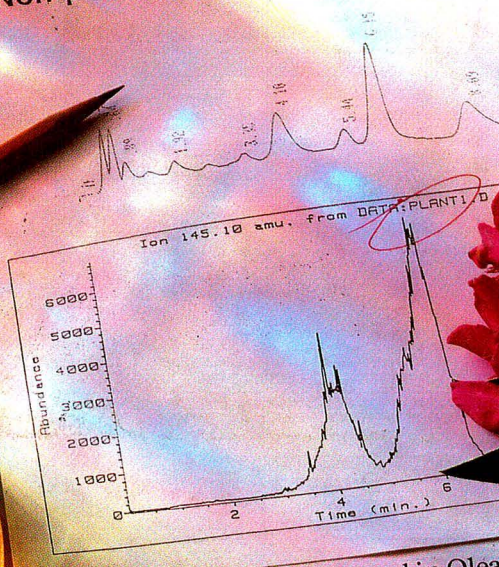


# Analytical CHEMISTRY

UV 220 nm and SIM at 145 amu  
chromatograms of partially purified  
oleander cardiac glycosides  
(Non-polar fraction)



...mination of Sugar Con  
...nents

Injected 250 ng of e

Ion 163.00 amu

k - Strophanth

Ion 151.00

20.

## Ex-Mortician Charged in Oleander Poisoning

BY JOHN JOHNSON  
Times Staff Writer

In what is believed to be the first murder prosecution in American history for oleander poisoning, authorities filed charges Friday against a former Pasadena funeral home worker accused of poisoning a

human remains, the theft of body parts and the removal of gold teeth from cadavers at the funeral home. It was these activities that Glas alleges Scione was trying to keep secret by poisoning Waters.

Scione's parents, Laureano Lamb Scione and Jeffrey Scione are awaiting trial on charges of mingling remains and other on charges connected with activities at the funeral home. The allegations amounted to "a worst scandal I've ever seen, or that I could ever imagine," California Cemetery and Burial Officer John W. Gill said.

Bruce Lamb, an uncle of David Scione, is now running the family mortuary. He believes in his nephew's innocence.

According to Glas, the case began in the 1970s when Laureano Lamb Scione took over the operation of the 67-year-old Lamb Funeral Home.

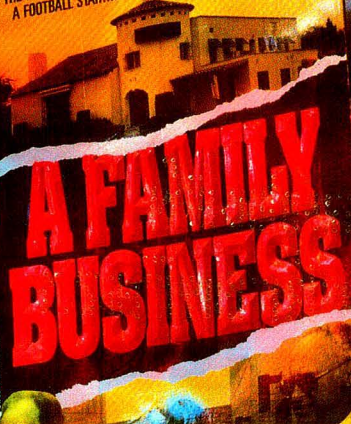
In 1982, according to Glas, David Scione took control of the family operation. In Altadena, a part of the Pasadena Creations Inc., taking in bodies for cremation on behalf of other mortuaries throughout Southern California for as little as \$25 each.

"They tried to corner the market," said Joe Rafterian, the funeral director of the Cremation Society of California.

At the same time, Waters began operating the Alpha Society cremation service in Burbank, Glas said. In January, 1985, Glas said, Waters told a friend, Richard Gray, that the Lamb Funeral Home was doing

Please see CHARGE, B8

THE SHOCKING TRUTH BEHIND A FUNERAL HOME FORTUNE...  
A FOOTBALL STAR...AND PERHAPS THE PERFECT MURDER



## A QUEST FOR OLEANDRIN

857 A

at 10 Cee

By BOB BAKER  
Times Labor Writer

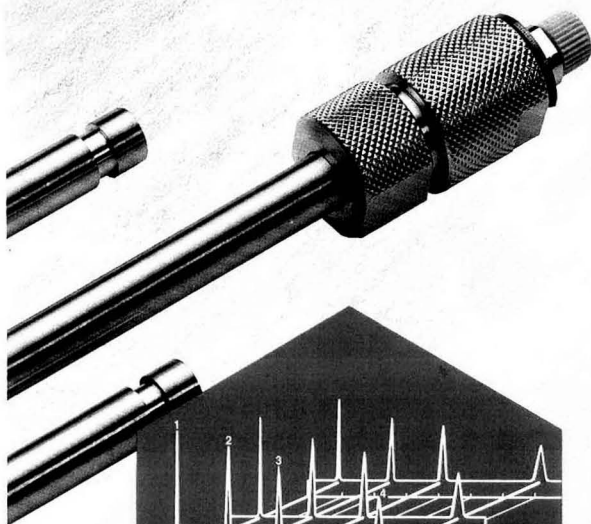
In an election Church strong organized cemetery over





# Guaranteed Reproducibility Reversed Phase HPLC *from* EM SEPARATIONS

Consistent, accurate results - sample after sample,  
column after column, year after year  
...and then scale up to prep. We guarantee it.



Guaranteed Reproducibility  
from Analytical to  
Prep Scale

## LiChrospher® RP-18, RP-8, and RP-select B Guaranteed Reproducibility Reversed Phases

E. Merck LiChrospher Guaranteed Reproducibility Reversed Phase HPLC Packings are produced to exacting specifications from the base silica gel through the bonded phases with special testing procedures to assure precise selectivities.

## Available in Economical LiChroCART® Cartridge Columns

LiChrospher Reversed Phases are available packed in LiChroCART Cartridge Columns. This newest innovation in HPLC column design from E. Merck provides the highest degree of flexibility and cost saving advantages. Column cartridges are available in three packs at considerable savings.

## Introducing Aluspher™ RP-select B For Basic Pharmaceutical Compounds

Aluspher RP-select B is the newest Reversed Phase from E. Merck, which provides a unique selectivity for basic pharmaceutical compounds. As an added advantage Aluspher RP-select B can be used with high pH mobile phases with no detrimental effects on column life.

Order E. Merck Chromatography  
Products directly from EM Separations



## EM SEPARATIONS

A Division of EM Industries, Inc.

480 Democrat Road • Gibbstown, New Jersey 08027  
(609) 224-0742 • (800) 922-1084 • FAX: (609) 423-4389

CIRCLE 30 ON READER SERVICE CARD

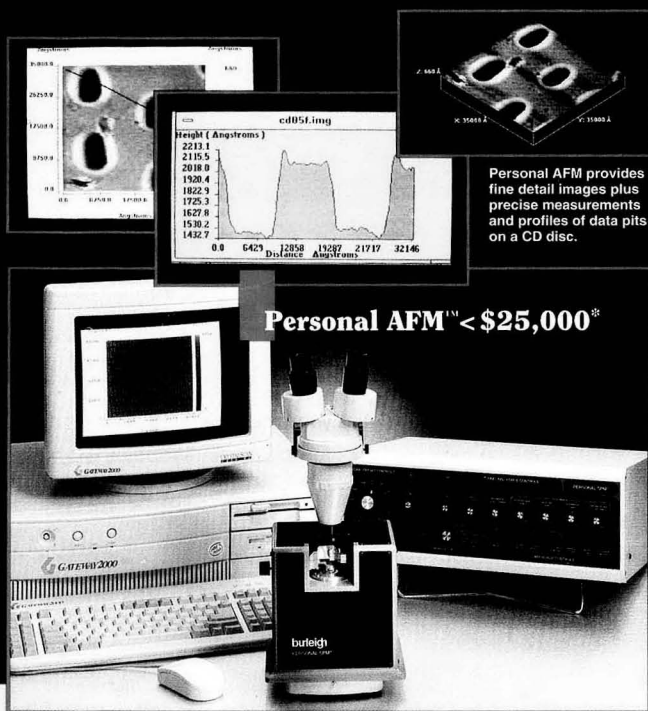
RP-select B • RP-18 • RP-8 • RP-18e • RP-8e



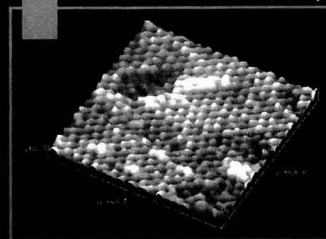
# SPM Technology

## So Affordable It's Personal

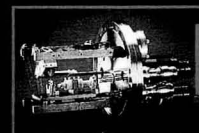
**Introducing Personal SPM™ – A New Generation of Affordable AFM and STM Systems Providing Research Grade Performance at Breakthrough Pricing**



**Personal STM™ < \$25,000\***



Personal STM surface image of Au (111) on mica substrate reveals gold adatom chains and vacant site.



**Personal UHV/STM™ < \$50,000\***

The Burleigh Personal SPM family of AFM, STM, and UHV/STM Systems puts powerful SPM imaging and 3D measurement capability in your lab at a price more affordable than ever before. Fully expandable, Personal SPM Systems are very easy to operate providing fast imaging and measurement of virtually any surface detail... even down to atomic scale.

\*U.S. List Price

### **FAX for Brochure and Demonstration Video**

- To receive your copy of the new Personal SPM brochure and a demonstration video faster call us at 1-716-924-9355 or fill out below and FAX to us at 1-716-924-9072.

Name/Title \_\_\_\_\_  
 Company \_\_\_\_\_  
 Address \_\_\_\_\_  
 City/ State/Zip \_\_\_\_\_  
 Phone \_\_\_\_\_

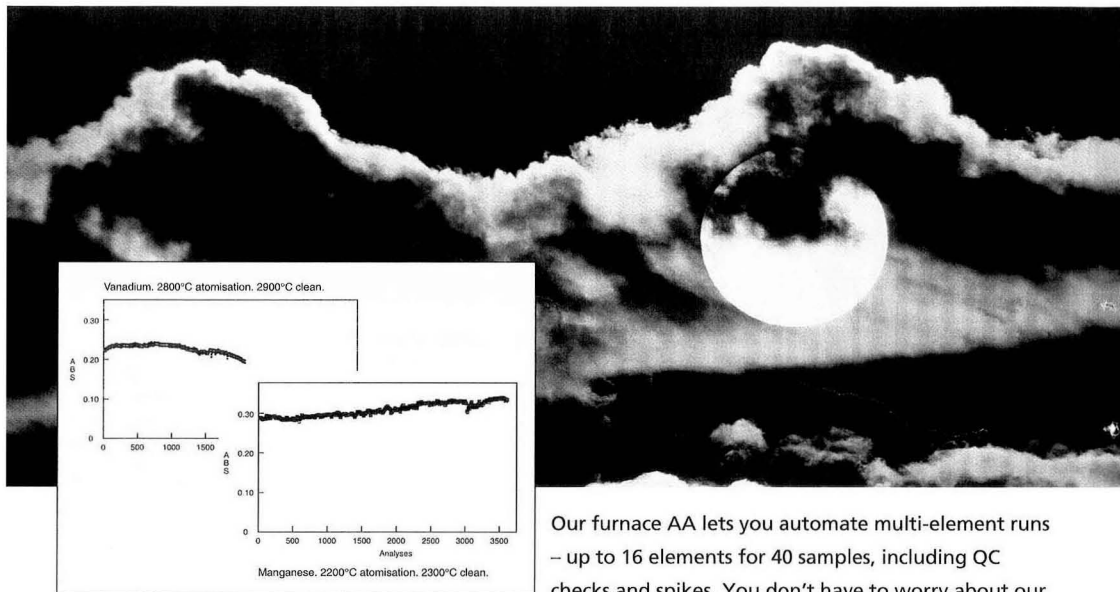
# burleigh

**Burleigh Instruments Inc.**  
 Burleigh Park, Fishers, NY 14453  
 716/924-9355 • FAX: 716/924-9072

In the U.K.: Burleigh Instruments LTD (0582) 766888 • FAX: (0582) 767888 In Europe: Burleigh Instruments GmbH (06157) 3047 • FAX: (06157) 7530 In Japan: Techscience Ltd. 0489 (64) 3111 • FAX: 0489 (65) 1500



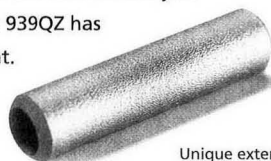
**Concerned about productivity?**  
**Our Furnace AA works non-stop**  
**throughout the night.**  
**Guaranteed!**



Our furnace AA lets you automate multi-element runs – up to 16 elements for 40 samples, including QC checks and spikes. You don't have to worry about our

ELC cuvette burning out in the middle of the run. We'll guarantee that! And we won't make you choose between Zeeman and Deuterium background correction either. Our 939QZ has both, with unique combined capability for the fastest methods development.

- **Up to 2000 firings per cuvette - guaranteed**
- **Automated 16-element analysis**
- **Automated method development**
- **Zeeman, Deuterium and Combined mode background correction**



Unique extended  
lifetime cuvette (ELC)

With an ATI-Unicam AA, you can reduce your cost of operation by up to 50%. You'll get better sample throughput too. To find out more, call us at (608) 831-5515, or fax (608) 831-2093.

In Canada, call (416) 507-9399, fax (416) 507-2436.

**ATI** UNICAM  
ANALYTICAL TECHNOLOGY INC.

ORION  
MATTSON  
UNICAM  
RUSSELL  
CAHN

CIRCLE 60 ON READER SERVICE CARD



OCTOBER 1, 1993  
VOLUME 65  
NUMBER 19



ANCHAM  
65(19) 815A-866A/2553-2712 (1993)  
ISSN 0003-2700

Registered in U.S. Patent and Trademark Office;  
©Copyright 1993 by the American Chemical Society

EDITOR: ROYCE W. MURRAY, University of North Carolina

ASSOCIATE EDITORS: Catherine C. Fenselau, University of Maryland Baltimore County, William S. Hancock, Genentech, James W. Jorgenson, University of North Carolina, Robert A. Ostryoung, North Carolina State University, Edward S. Yeung, Iowa State University/Ames Laboratory

Editorial Headquarters, research section  
Department of Chemistry  
Venable and Kenan Laboratories  
University of North Carolina  
Chapel Hill, NC 27599-3290  
Phone: 919-962-2541  
Fax: 919-962-2542  
E-mail: Murray @ uncvx1.oit.unc.edu

Editorial Headquarters, A-page section  
1155 Sixteenth St., N.W.  
Washington, DC 20036  
Phone: 202-872-4570  
Fax: 202-872-4574  
E-mail: rmh96 @ acs.org

Managing Editor: Mary Warner

Senior Editor: Louise Voreess

Associate Editor: Grace K. Lee

Assistant Editor: Felicia Wach

Editorial Assistant: Deborah Noble

Contributing Editor: Marcia Vogel

Head, Graphics and Production: Leroy L. Corcoran

Art Director: Alan Kahan

Designers: Sarah Chung, Peggy Corrigan

Production Editor: Elizabeth Wood

Electronic Composition: Wanda R. Gordon

Circulation: David Schulbaum

#### LabGuide

Managing Editor of Directories and Databases:  
Kathleen Strum

Associate Editor: Joanne Mullican

Assistant Editor: Susan Barclay

#### Journals Dept., Columbus, Ohio

Editorial Office Manager: Mary E. Scanlan

Journals Editing Managers: Kathleen E. Duffy,  
Anne C. O'Melia, Joseph E. Yurvat

Associate Editor: Lorraine Gibb

Assistant Editor: Brenda S. Wooten

Advisory Board: Michelle V. Buchanan, Bruce Chase, M. Bonner Denton, Joseph G. Gordon, David M. Haaland, Joel M. Harris, Timothy D. Harris, Franz Hillenkamp, Kiyokatsu Jinno, Dennis C. Johnson, Richard A. Keller, Philip D. LaFleur, Gary E. Maciel, Geraldine Richmond, Ralph Riggan, Michael Thompson  
Ex Officio: Joseph L. Glajch

Instrumentation Advisory Panel: Anna Bräjer-Toth, Raymond E. Clement, Therese M. Cotton, Norman J. Dovichi, Jack D. Henion, Mary Ellen P. McNally, John W. Olesik, Dallas L. Rabenstein, J. Michael Ramsey

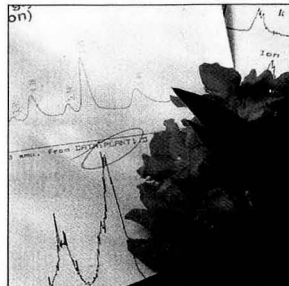
#### Publications Division

Director: Robert H. Marks

Head, Special Publications: Anthony Durniak

Head, Journals: Charles R. Bertsch

# Analytical<sup>®</sup> CHEMISTRY



## REPORT

835 A

**Nonlinear multivariate calibration methods.** The data explosion created by the increased resolving power of analytical instruments has placed more emphasis on data analysis. Sonja Sekulic, Bruce Kowalski, and co-workers at the University of Washington present an overview of multivariate calibration methods and apply them to six data sets from different spheres of analytical chemistry

## ANALYTICAL APPROACH

857 A

**On the cover. A quest for oleandrin.** In 1985 a young funeral parlor owner died from what was then reported as cardiac arrest; the case was reopened in 1991 when an informant suggested that death had been caused by intentional poisoning. Jack Henion and co-workers at Cornell University describe the LC/MS protocol developed to determine whether oleandrin was present in the decomposed tissue samples

Cover photo by Lee Anderson. Reproduction of *A Family Business* cover courtesy of St. Martin's Press, Inc. Newspaper article by John Johnson, staff writer, © 1990 *Los Angeles Times*, reprinted by permission.

## UPCOMING RESEARCH

827 A

## EDITORIAL

831 A

**The ubiquitous laser: or, let all spectroscopists enjoy the radiance.** Lasers have played a pervasive role in the development of, and remain a frontier of, analytical chemistry. Lasers are clearly a bright spot in our discipline's future, both basic and applied, and it will be fascinating to watch analytical laser spectroscopy grow

## NEWS

833 A

**1994 ACS awards** will go to Edward S. Yeung, Barbara J. Garrison, Adam Heller, Paul Kebarle, William H. Pirkle, Philip C. Wankat, and George M. Whitesides. • **ASA and Perkin Elmer awards** for outstanding technical papers. • **Golay award** presented to Konrad Grob

## FOCUS

846 A

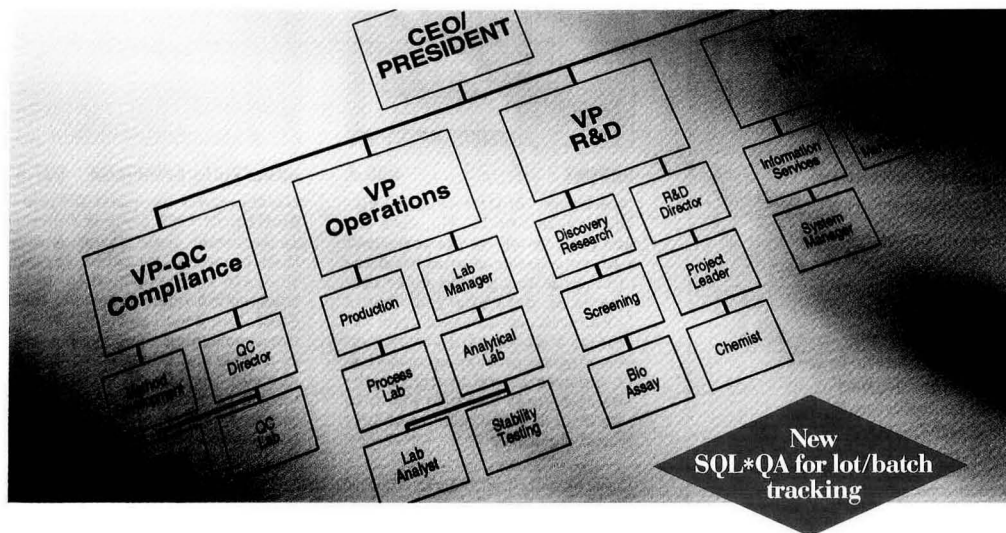
**Capillary chromatography** has been traditionally associated with terms such as high resolution, speed, and low detection limits. Wolfgang Bertsch of the University of Alabama reports on the 15th International Symposium on Capillary Chromatography, held in Riva del Garda, Italy, in May

## NEW PRODUCTS AND MANUFACTURERS' LITERATURE

852 A



# SQL\*LIMS Gets The Job Done For Everybody. Especially You.



An MIS system manager. Lab analyst.  
An R&D director. A project leader.  
QC/Compliance officer. SQL\*LIMS gets  
the job done. For everybody.

SQL\*LIMS is the only LIMS  
designed to maximize the power  
of ORACLE's® Relational Data-  
base and 4GL software tools. It  
makes the right connections with  
MDL's ISIS and MACCS, SAS  
statistical software, and BBN's  
RS-1. That means free flow of data  
between networks, databases, computers,  
and workstations today. And a secure



bridge to whatever information tech-  
nology develops tomorrow.

And SQL\*LIMS is the only LIMS with  
SQL\*STABILITY, SQL\*BARCODE,  
SQL\*QC, and SQL\*SCHEDULE.  
That's why SQL\*LIMS has more  
ORACLE-based installations  
than any other LIMS.  
Because it gets the job  
done. For everybody.



For more information, con-  
tact PE Nelson or your local Perkin-Elmer  
office. For product literature in the U.S.,  
call 1-800-762-4000.

## PE NELSON

PE Nelson, 10040 Bubb Road, Cupertino, CA 95014 USA. PE Nelson Europe, Hanzeweg 16, Gouda 2800 AL, Netherlands.  
PE Nelson is a division of The Perkin-Elmer Corporation. PE Nelson, SQL-LIMS, SQL-STABILITY, SQL-BARCODE, SQL-QC, and SQL-SCHEDULE are trademarks of The Perkin-Elmer Corporation.  
ORACLE is a registered trademark of the ORACLE Corporation. ISIS and MACCS are trademarks of Molecular Design Ltd. SAS is a registered trademark of SAS Institute, Inc. RS-1 is a registered trademark of BBN Software Products.  
All analytical instruments and systems manufactured by Perkin-Elmer are certified under the quality requirements of ISO 9001.

Come see us at FACSS Booth Nos. 601, 603, 605, 607 and 609.  
Circle 70 for Literature only Circle 71 for Literature and Sales Call.

ANALYTICAL CHEMISTRY (ISSN 0003-2700) is published semimonthly by the American Chemical Society, 1155 Sixteenth St., N.W., Washington, DC 20036. Second-class postage paid at Washington, DC, and additional mailing offices. Postmaster: Send address changes to ANALYTICAL CHEMISTRY, Member & Subscriber Services, P.O. Box 3337, Columbus, OH 43210. Canadian GST Reg. No. R127571347.

**Copyright Permission:** An individual may make a single reprographic copy of an article in this publication for personal use. Reprographic copying beyond that permitted by Section 107 or 108 of the U.S. Copyright Law is allowed, provided that the appropriate per-copy fee is paid through the Copyright Clearance Center, Inc., 27 Congress St., Salem, MA 01970. For reprint permission, write Copyright Administrator, Publications Division, ACS, 1155 Sixteenth St., N.W., Washington, DC 20036.

**Registered names and trademarks, etc.,** used in this publication, even without specific indication thereof, are not to be considered unprotected by law.

#### Subscription and Business Information

**1993 subscription rates** include air delivery outside the U.S., Canada, and Mexico. Canadian subscriptions are subject to 7% GST.

	Members	Nonmembers (personal)	Nonmembers (institutional)
U.S.	\$ 36	\$ 78	\$ 415
Canada and Mexico	72	114	451
Europe	117	230	496
Other countries	141	254	520

**Nonmember rates in Japan:** Rates above do not apply to nonmember subscribers in Japan, who must enter subscription orders with Maruzen Company Ltd., 3-10, Nihonbashi 2-chome, Chuo-ku, Tokyo 103, Japan. Tel: (03) 272-7211.

**For multi-year and other rates,** call toll free 800-227-5558 in the U.S. and Canada; in the Washington, DC, metropolitan area and outside the U.S., call 202-872-4363; fax 202-872-4615.

**Single issues,** current year, \$18.00 except review issue, \$50.00, and LabGuide, \$50.00; **back issues and volumes and microform editions** available by single volume or back issue collection. For information or to order, call the number listed for subscription orders by phone; or write the Microform & Back Issues Office at the Washington address.

**Subscription orders by phone** may be charged to VISA, MasterCard, or American Express. Call toll free 800-333-9511 in the continental U.S.; in the Washington, DC, metropolitan area and outside the continental U.S., call 202-872-8065. Mail orders for new and renewal subscriptions should be sent with payment to American Chemical Society, Department L-0011, Columbus, OH 43268-0011.

**Changes of address** must include both old and new addresses with ZIP code and a recent mailing label. Send all address changes to the ACS Columbus address. Please allow 6 weeks for change to become effective. **Claims for missing numbers** will not be allowed if loss was due to failure of notice of change of address to be received in the time specified; if claim is dated (a) North America—more than 90 days beyond issue date, (b) all other foreign—more than 180 days beyond issue date. Hard copy claims are handled at the ACS Columbus address.

**ACS membership information:** Lorraine Bowlin (202-872-4567)

## Articles

- Piezoelectric pH Sensors: AT-Cut Quartz Resonators with Amphoteric Polymer Films **2553**  
*Juan Wang, Michael D. Ward\*, Richard C. Ebersole\*, and Robert P. Foss*

- Analytical Applications of Catalytic Properties of Modified Cyclodextrins **2563**  
*Ellen Tuanying Chen and Harry L. Pardue\**

- Piezoelectric Detection of Water with A Separated Electrode **2568**  
*Wenhong Zhu, Wanzhi Wei, Zhihong Mo, Lihua Nie, and Shouzhao Yao\**

- Schiff Base Complexes of Cobalt(II) as Neutral Carriers for Highly Selective Iodide Electrodes **2572**  
*Ruo Yaun, Ya-Qin Chai, Dong Liu, De Gao, Jun-Zhong Li, and Ru-Qin Yu\**

- High-Frequency Generation of Electrochemiluminescence at Microelectrodes **2576**  
*Maryanne M. Collinson and R. Mark Wightman\**

- Behavior and Calibration of the Copper(II) Ion-Selective Electrode in High Chloride Media and Marine Waters **2583**  
*Stuart L. Belli\* and Alberto Zirino*

- High-Performance Flow Flame Atomic Absorption Spectrometry for Automated On-Line Separation and Determination of Cr(III)/Cr(VI) and Preconcentration of Cr(VI) **2590**  
*Jozsef Posta, Harald Berndt\*, Shen-Kay Luo, and Gerhard Schaldach*

- Helium Microwave Induced Plasma Atomic Emission Detection for Liquid Chromatography Utilizing a Moving Band Interface **2596**  
*Peter B. Mason, Liming Zhang, Jon W. Carnahan\*, and Randall E. Winans\**

- Solid-Matrix and Solution Luminescence Photophysical Parameters and Analytical Aspects of the Tetrols of Benzo[a]pyrene-DNA Adducts **2601**  
*Johannes Corley and Robert J. Hurtubise\**

- Liquid Mixtures for Matrix-Assisted Laser Desorption **2608**  
*D. Shannon Cornett, Michael A. Duncan, and I. Jonathan Amster\**

- Detection of Electrospray Ionization Using a Quadrupole Ion Trap Storage/Reflection Time-of-Flight Mass Spectrometer **2614**  
*Steven M. Michael, Benjamin M. Chien, and David M. Lubman\**

- Ultrahigh Resolution Matrix-Assisted Laser Desorption/Ionization of Small Proteins by Fourier Transform Mass Spectrometry **2621**  
*John A. Castoro and Charles L. Wilkins\**

- On-Line Fermentation Process Monitoring of Carbohydrates and Ethanol Using Tangential Flow Filtration and Column Liquid Chromatography **2628**  
*Torbjörn A. Buttler\*, Kristina A. J. Johansson, Lo G. O. Gordon, and György A. Marko-Varga*

\*Corresponding author

continued on p. 823 A



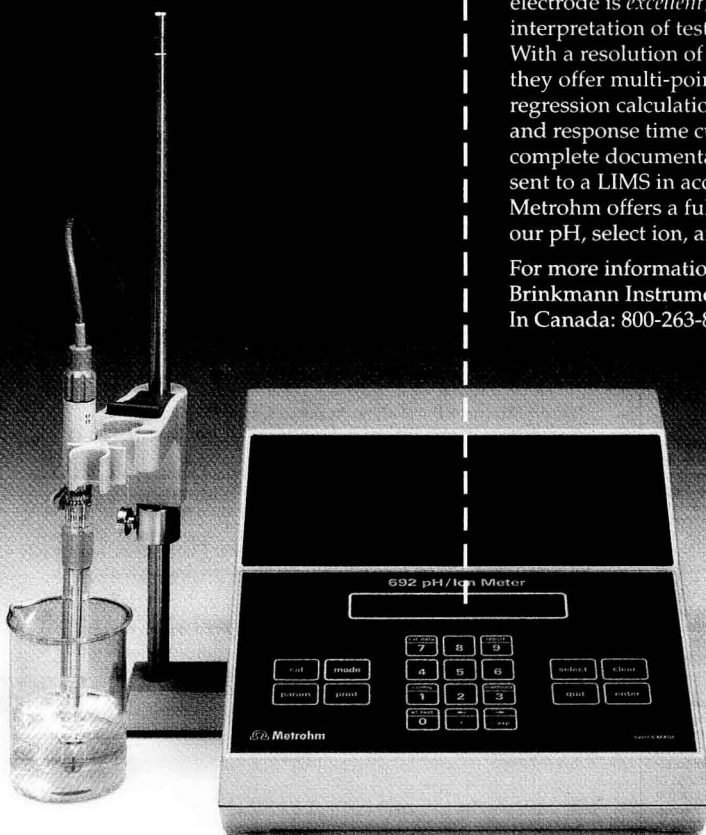
# EXCELLENT ELECTRODE

**Metrohm solves  
the #1 problem  
with pH meters.**

**Introducing  
the only pH meters  
with built-in  
electrode testing.**

The best pH meter is only as good as its electrode. Now, Metrohm's new pH meters feature built-in testing to tell you if the electrode is *excellent*, *good*, or *bad*. No interpretation of test results, no guesswork. With a resolution of 0.001 pH and 0.1 mV, they offer multi-point calibration with regression calculation. Slope, y-intercept and response time curves are printed for complete documentation and results can be sent to a LIMS in accordance with GLP. Metrohm offers a full line of electrodes for our pH, select ion, and hand-held meters.

For more information, call  
Brinkmann Instruments at 800-645-3050.  
In Canada: 800-263-8715.



 **Metrohm**

**BRINKMANN** Quality products for research and control.

Outside U.S. and Canada: Metrohm Ltd., Switzerland. Phone 071/53 85 85 or Telefax 071/53 89 01

CIRCLE 10 ON READER SERVICE CARD

AD 136-ME

**Editorial Information**

**Instructions for authors** of AC RESEARCH are published in the January 1 issue, p. 91. Guidelines for the INSTRUMENTATION, REPORT, ANALYTICAL APPROACH, and A/C INTERFACE features are published in the January 1 issue, p. 90. Please consult these instructions and guidelines prior to submitting a manuscript for consideration for publication.

**Manuscripts for publication** in AC RESEARCH (4 copies of text and illustrative material) should be submitted to the Editor at the University of North Carolina address. Please include a signed copyright status form; a copy of this document appears on p. 95 of the January 1 issue. Manuscripts for publication in the A-page section should be submitted to the Washington editorial staff.

**For individual reprints** of AC RESEARCH or A-page articles, please contact the authors directly. Bulk reprints of individual articles are available from ACS. For information, write or call the Distribution office at the ACS Washington address (202-872-4539; fax 202-872-4615).

**ACS Division of Analytical Chemistry**

Chair, Janet Osteryoung (919-515-2355)  
Secretary, Sarah Rutan (804-367-1298)

**ACS Information**

Library Services	202-872-4515
Education Division	202-872-4388
Meetings Dept.	202-872-4397
Member Services	202-872-4414
Employment Services	202-872-6120
Public Outreach	202-872-4091

**Supplementary material** is noted in the table of contents with a ■. It is available as photocopy (\$10.00 for up to 3 pages and \$1.50 per page for additional pages, plus \$2.00 for foreign postage) or as 24X microfiche (\$10.00, plus \$1.00 for foreign postage). Canadian residents should add 7% GST. See supplementary material notice at end of journal article for number of pages. Orders must state whether for photocopy or for microfiche and give complete title of article, names of authors, journal, issue date, and page numbers. Prepayment is required and prices are subject to change. Order from Microforms & Back Issues Office at the ACS Washington address.

The paper used in this publication meets the minimum requirements of American National Standard for Information Sciences—Permanence of Paper for Printed Library Materials, ANSI Z39.48-1984.

**Journals Department**

American Chemical Society  
2540 Olenetangy River Road  
P.O. Box 3330  
Columbus, OH 43210  
614-447-3600, Ext. 3171  
TELEX 6842086; Fax 614-447-3745

**Member & Subscriber Services**

American Chemical Society  
P.O. Box 3337  
Columbus, OH 43210  
614-447-3776  
800-333-9511

Advertising Office: Centcom Ltd., 1599 Post Road East, P.O. Box 231, Westport, CT 06881

The American Chemical Society and its editors assume no responsibility for the statements and opinions advanced by contributors. Views expressed in the editorials are those of the editors and do not necessarily represent the official position of the American Chemical Society.

Glass Chips for High-Speed Capillary Electrophoresis Separations with Submicrometer Plate Heights **2637**

*Carlo S. Effenhauser\*, Andreas Manz, and H. Michael Widmer*

New Parameters for the Characterization of Relationship between Gas Chromatographic Retention and Temperature **2643**

*M. de Frutos, J. Sanz\*, I. Martinez-Castro, and M. I. Jiménez*

Separation and Identification of Higher Molecular Weight Fullerenes by High-Performance Liquid Chromatography with Monomeric and Polymeric Octadecylsilica Bonded Phases **2650**

*Kiyokatsu Jinno\*, Takashi Uemura, Hatazuichi Ohta, Hideo Nagashima, and Kenji Itoh*

Mathematical Treatment of Electrophoretically Mediated Microanalysis **2655**

*Bryan J. Harmon, Dale H. Patterson, and Fred E. Regnier\**

Axial Thermal Gradient Microbore Liquid Chromatography by Flow Programming **2663**

*Leslie K. Moore and Robert E. Synovec\**

Affinity of Antifluorescein Antibodies Encapsulated within a Transparent Sol-Gel Glass **2671**

*Run Wang, Upvan Narang, Paras N. Prasad\*, and Frank V. Bright\**

Engineering Protein Orientation at Surfaces To Control Macromolecular Recognition Events **2676**

*Mark A. McLean, Patrick S. Stayton, and Stephen G. Sligar\**

Purification and Analysis of Drug Residues in Urine Samples by On-Line Immunoaffinity Chromatography/High-Performance Liquid Chromatography/Continuous-Flow Fast Atom Bombardment Mass Spectrometry **2679**

*Enrico Davoli, Roberto Fanelli, and Renzo Bagnati\**

**Correspondence**

Molecular Basis of Peak Width in Capillary Gas Chromatography under High Column Pressure Drop **2686**

*Leonid M. Blumberg\* and Terry A. Berger*

Ascorbic Acid Interferences in Hydrogen Peroxide Detecting Biosensors Based on Electrochemically Immobilized Enzymes **2690**

*Francesco Palmisano and Pier G. Zambonin\**

**Technical Notes**

On-Line Peptide Mapping by Capillary Zone Electrophoresis **2693**

*Lawrence N. Amankawa and Werner G. Kuhr\**

In Situ Elimination of Metal Inhibitory Effects Using Ligand-Containing Carbon Paste Enzyme Electrodes **2698**

*Joseph Wang\* and Qiang Chen*

Radiochemical Determination of Low-Level Lead-210 in Environmental Water Samples **2701**

*Dominic To*

continued on p. 825 A



**On why we do what we do.** My family used to take long car trips. We traveled Route 66 and learned about small town America before it was bypassed by the interstates. I still love cars and travel. Later, a summer job in Idaho convinced me that a chemist with a Ph.D. has more opportunities. So I veered at the next fork in the road, went back to school, and proceeded toward today's destination.

**On electrochemistry as an analytical technique.**  
My next stop was a NASA fellow-



electrochemical immunoassay. I have also been very involved in nuclear medicine and radiopharmaceutical development with Ed Deutsch using electrochemistry and chromatography. More recently, we've been working with polymer-modified electrodes in the development of sensors and in EXAFS spectroelectrochemistry (extended x-ray absorption fine structure), in a collaboration with Dick Elder.

**On stating a point of view.**  
Electrochemistry is becoming more important because of the development of materials

## Touring the two-lane blacktop and research as a two-way street.

ship at the University of North Carolina where I had the good fortune to study under Royce Murray, who taught electrochemistry, which I found to be an intellectually satisfying combination of math, physical phenomena and fairly complex processes.



William Heineman

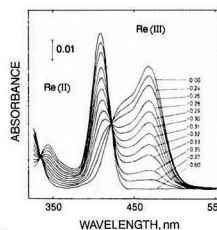
Now I had my vehicle! But the road called again and, after obtaining my Ph.D., I went into industry where I worked on ion selective electrodes and coulometry. Then, in completely unrelated developments I got married and left industry for postdoc work with Ted Kuwana at Case Western Reserve in spectroelectrochemistry. After a year, Kuwana moved to OSU and I kept going south on I-71 to the University of Cincinnati which has been home for more than 20 years.

**On where electrochemistry fits in.** Though I've maintained an interest in spectroelectrochemistry, for more than a decade Brian Halsall and I have collaborated on studies of

and fabrication techniques that allow mass production of disposable EC cells. We've worked on biosensors for detecting glucose in diabetics and solid state electrochemical cells that we hope to use to determine the oxygen status in premature infants. One of our electrochemical immunoassay techniques has reached a detection limit in the zeptomole range.

I see fundamental and applied research as a two-way street. Both are important and invigorating. The instrument companies—BAS among them—supply the tools that allow us to focus on results, not the complexity of the techniques.

Southern Ohio still has intriguing two-lane roads where it's fun to take a swing in my old Triumph. But modern, computerized instrumentation is what makes work in electrochemistry the stimulating and productive field it has become. *Serious science for serious scientists*



**BAS**  
Bioanalytical  
Systems, Inc.

BAS Japan • 36-4, 1-Chome • Oshiage, Sumida-Ku • Tokyo 131, Japan • PH (81) 3 3624 0367 • FAX (81) 3 3624 0940  
BAS Europe • Dellingstraat, 34-1, B-2800 Mechelen Belgium • PH (32) 15 43 22 31 • FAX (32) 15 43 23 85  
Bioanalytical Systems, Inc. • 2701 Kent Ave • West Lafayette, IN USA 47906 • PH (317) 463-4527 • FAX (317) 497-1102

CIRCLE 12 ON READER SERVICE CARD

**LabGuide**

The LabGuide is published as the August 15 issue of ANALYTICAL CHEMISTRY. Begun 38 years ago by the JOURNAL, the annual LabGuide edition is designed to be the ultimate buyers' resource for chemists. Its comprehensive coverage includes 2250 categories of laboratory products and services from more than 1700 companies.

The 1994 edition featured ~40,000 informative listings detailing manufacturers and distributors of each product and service. Each listing includes the company's phone number for fast action; a more complete listing of the company's address and branch offices is located in a separate section at the back of the book. Sections include Chromatography; Spectroscopy; Instruments and Accessories; Equipment and Supplies; Chemicals and Standards; and Research, Analytical, Consulting, Education, and Training Services.

Putting together such a comprehensive and useful guide would be impossible without the suggestions and guidance of our advisory board. Current members include Duane Bartak (University of North Iowa), Bob Hoesly (Mettler Toledo), Paul Preidecker (Gilson), K. C. Warawa (K. C. Associates), Anne Cerino (Anne Cerino Marketing Communications), H. M. Kingston (Duquesne University), Tim Heil (Radian), Susan Olesik (Ohio State University), Rodger Stringham (Merck), Bob Wright (Battelle Pacific Northwest Laboratories), and Sherman Hamel (Parr Instruments).

**Instrumentation in Analytical Chemistry  
1988-1991**

This recently published book continues a series begun as *Instrumentation in Analytical Chemistry* in 1973 by Alan J. Senzel, and continued by Stuart A. Borman in the 1980s as *Instrumentation in Analytical Chemistry: Volume 2* and *Instrumentation in Analytical Chemistry: 1982-86*. Like its predecessors, *Instrumentation in Analytical Chemistry 1988-1991* is designed to provide readers with updated overviews of analytical techniques and instrumentation drawn from articles originally published in ANALYTICAL CHEMISTRY's A pages.

The volume begins with an introduction by Royce Murray designed to help readers put into perspective the methodological and instrumental developments that have occurred during the period. The book is divided into six topical areas: Robotics, Computers, and Laboratory Data Management; Atomic and Molecular Spectroscopy; Electroanalytical Chemistry and Chemical Sensors; Separations; Mass Spectrometry; and Surface Analysis. Each section begins with a short introduction designed to provide a context for interpreting the articles that follow and to answer questions such as "What are recent changes in this field?" and "Why are these techniques important?". Copies of *Instrumentation in Analytical Chemistry 1988-1991* are available in clothbound (\$44.95), paperbound (\$28.95), and student (\$16.95) editions from the ACS Distribution Office, Dept. 390, 1155 16th St., N.W., Washington, DC 20036 (800-ACS-5558).


**Lithium Ion Selective Optical Sensor Based on a Novel Neutral Ionophore and a Lipophilic Anionic Dye**

*Kazuhiko Watanabe, Rieko Nakagawa, Hiroyuki Yamada, Hideaki Hisamoto, and Koji Suzuki\**

**2704****Correction****Analysis of Diffusional Broadening of Vesicular Packets of Catecholamines Released from Biological Cells during Exocytosis**

*Timothy J. Schroeder, Jeffrey A. Jankowski, Kirk T. Kawagoe, R. Mark Wightman\*, Christine Lefrou, and Christian Amatore*

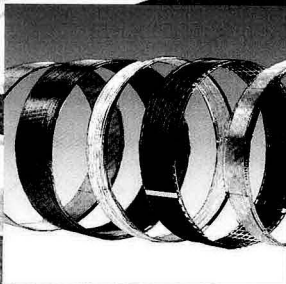
**2711****Author Index****2712**



There's an infinite variety of flowers, just like Chrompack's range of fused silica columns. But unlike the evolutionary change that flowers undergo, there's no such slippage with our columns. In fact, Chrompack columns perform to a repeatability that's literally unmatched anywhere inside or outside of nature.

And there's more:

- extremely inert
- no interference with sample
- accurate and reproducible quantitative analysis
- a complete range of columns plus tailor-made solutions.



Fused silica columns.  
The complete range plus  
tailor-made solutions.

*Just like our  
columns - an  
infinite variety*

 **CHROMPACK**

*From chromatographers  
for chromatographers*

For more info' phone The Netherlands +31 1180 71000, USA phone 800 526 3687

CIRCLE 22 ON READER SERVICE CARD



# UPCOMING RESEARCH

## Effect of Surface Roughness on the Response of Thickness-Shear Mode Resonators in Liquids

The effect of random surface roughness on the response of thickness-shear mode resonators in contact with liquids is examined.

**Stephen J. Martin\***, **Gregory C. Frye**, and **Antonio J. Ricco**, Microsensor Research and Development Department, Sandia National Laboratories, Albuquerque, NM 00087, and **Stephen D. Senturia**, Department of Electrical Engineering and Computer Science, Massachusetts Institute of Technology, Cambridge, MA 02139

## Laser-Light Scattering Instrument for the Measurement of Solute Vaporization Rates in Analytical Flames

An instrument is developed to measure the size of individual solute particles in an air-acetylene flame. The system is applied to the measurement of vaporization rates; instrumental design criteria are considered, and measurement performance is assessed.

**A. G. Childers** and **G. M. Hieftje\***, Department of Chemistry, Indiana University, Bloomington, IN 47405

## Measurement of Solute Vaporization Rates in an Analytical Flame by Laser-Light Scattering

The kinetics of alkali-chloride particle vaporization in a laminar air-acetylene flame are determined by laser-light scattering and compared with vaporization theory.

**A. G. Childers** and **G. M. Hieftje\***, Department of Chemistry, Indiana University, Bloomington, IN 47405

## Pulsed Amperometric Detection of Carbohydrates Separated by Capillary Electrophoresis

A 10- $\mu$ m Au electrode enables fmol detection of eight carbohydrates separated in NaOH electrolyte; the working range is  $10^{-6}$  to  $10^{-4}$  mol/L, and peak height reproducibility is 2%.

**Wenzhe Lu** and **Richard M. Cassidy\***, Chemistry Department, University of Saskatchewan, Saskatoon, Saskatchewan, Canada S7N 0W0

## Step-Scan FT-IR External Reflection Spectrometry of the Electrode/Electrolyte Interface by Potential Modulation

The absorption band of carbon monoxide adsorbed on a platinum electrode is measured by phase-modulated step-scanning FT-IR spectrometry. The wavenumber of the band is modulated through electrochemical Stark effect.

**Bioana O. Budevska** and **Peter R. Griffiths\***, Department of Chemistry, University of Idaho, Moscow, ID 83843

These articles are scheduled to appear in AC RESEARCH in the near future.

\*Corresponding author

## High Mass Resolution Glow Discharge Mass Spectrometry Using an External Ion Source FT-ICR Mass Spectrometer

Coupling a glow discharge source with an external ion source FT-ICR mass spectrometer produces results for NIST stainless steel standards in which peaks from nominally isobaric atomic isotopes are observed with high mass resolution ( $m/\Delta m_{1/2} \geq 290,000$ ). Detection limits in the high-ppb to low-ppm range are achieved for analysis of trace metals, and concentrations of the trace elements are determined with good accuracy (average error of 14%).

**Clifford H. Watson**, **John Wronka**, **Frank H. Laukien**, Bruker Instruments, Inc., Manning Park, Billerica, MA 01821, **Christopher M. Barshick**, Oak Ridge National Laboratory, Oak Ridge, TN 37831-6375, and **John R. Eyster\***, Department of Chemistry, University of Florida, Gainesville, FL 32611-2046

## Fragmentation Reactions of Multiply-Protonated Peptides and Implications for Sequencing by Tandem Mass Spectrometry with Low-Energy Collision-Induced Dissociation

Dissociation reactions of multiply-protonated peptides demonstrate that intramolecular coulombic repulsions alone do not guarantee structurally informative fragmentation. Complications include a new rearrangement in which C-terminal residues are transferred to a Lys sidechain near the N-terminus.

**Xue-Jun Tang**, **Pierre Thibault**, and **Robert K. Boyd\***, Institute for Marine Biosciences, National Research Council, 1411 Oxford Street, Halifax, Nova Scotia, Canada B3H 3Z1

## DNA Sequencing by Capillary Electrophoresis with Replaceable Linear Polyacrylamide and Laser-Induced Fluorescence Detection

Replaceable linear polyacrylamide is used to overcome gel instability for DNA sequencing by CE. The developed protocol provides reproducible sequencing (RSD = 2.4%) for 350 bases in close to 30 min, employing a simple single-laser, two-photomultiplier fluorescence detection system.

**Marie C. Ruiz-Martinez**, **Jan Berka**, **Alexei Belenkii**, **Frantisek Foret**, **Arthur W. Miller**, and **Barry L. Karger\***, Barnett Institute, Northeastern University, 360 Huntington Avenue, Boston, MA 02115

## Separation and Characterization of Components of Catalytic Cracker Feed Using Centrifugal Partition Chromatography

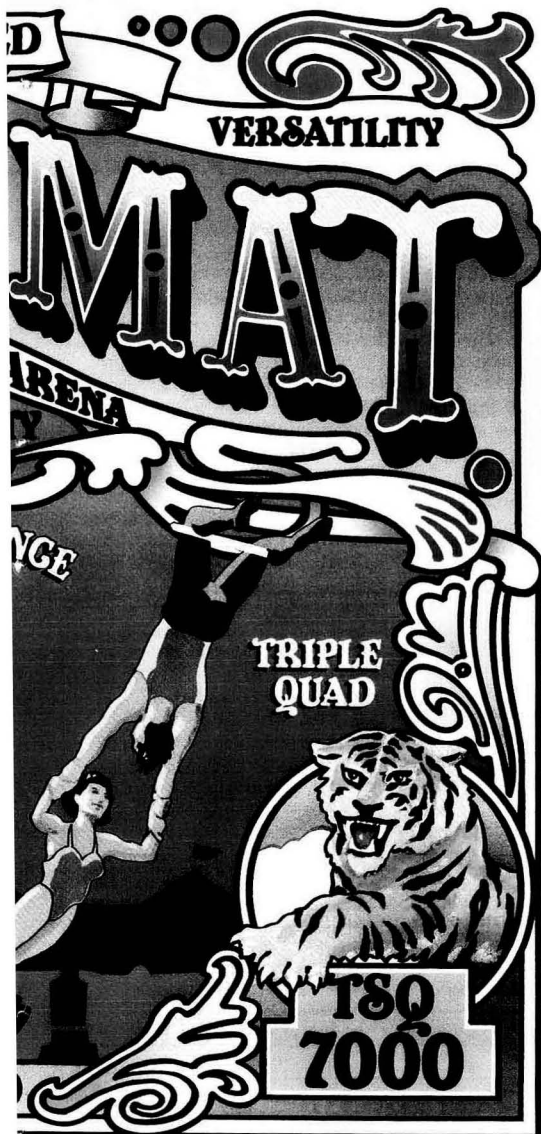
Petroleum catalytic cracking feedstock is separated into 21 fractions using centrifugal partition chromatography. Each fraction is analyzed spectroscopically and quantitated gravimetrically.

**Randy A. Menges**, **Larry A. Spino**, and **Daniel W. Armstrong\***, Department of Chemistry, University of Missouri-Rolla, Rolla, MO 65401



Circle the reader service number and we'll send you details of our new 7000 series and this colorful poster for your laboratory.

# PARDON OUR ENTHUSIASM.



It's not every day that something as exciting as Finnigan MAT's new generation of single and triple-stage quadrupole mass spectrometers comes to town. Our SSQ<sup>®</sup> and TSQ<sup>®</sup> 7000 family is the greatest show in LC/MS and GC/MS. We proudly present the spectacular power, sensitivity and value to outperform any competing system.

Choose MS or MS/MS, and combine it with our full range of inlet and ionization options, including: electrospray, APCI, PBI, EI/CI and many others.

These systems are, in a word, sensational. Their significantly longer quadrupole mass analyzers raise resolution to new heights, while the new detection system substantially improves sensitivity. Unlimited power and flexibility are yours with our advanced digital signal processing. And new Finnigan MAT software makes these research-grade instruments easier to use and more productive.

The 7000 systems are attractively priced and come with our world-renowned safety net of support and service. Only Finnigan MAT can bring you the experience and unwavering quality that comes from over 25 years of leadership in mass spectrometry.

Find out what the excitement is all about, and receive a free poster, by circling the reader service number below.



A subsidiary of Thermo Instrument Systems Inc.

California (408) 433-4800 • Georgia (404) 424-7880 • Ohio (513) 891-1255 • New Jersey (201) 740-9177 • Canada (416) 890-1034  
Germany (0421) 54 93 0 • UK (0442) 233555 • France (0169) 41 98 00 • Italy (02) 66011742 • Netherlands (08385) 27266 • Sweden (08) 6800101  
Japan (03) 3372-3001 • Australia (02) 646-2211

CIRCLE 34 ON READER SERVICE CARD



in conjunction with the

## Eastern Analytical Symposium

**November 1993**  **Somerset, New Jersey**

Receive Up-to-the-Minute Training in the Latest Technologies,  
Methods, and Research Approaches in

### **Activated Carbon Adsorption: Principles and Applications**

Monday-Tuesday, November 15-16, 1993

Acquire an in-depth knowledge of activated carbon and its applications.

### **Air Toxics Analysis by U.S. EPA Methods**

Thursday-Friday, November 18-19, 1993

Receive the latest word on advanced sampling and analysis techniques for air toxics measurement.

### **Analytical Methods for Proteins**

Thursday-Friday, November 18-19, 1993

Gain expertise in assessing the purity, integrity, and shelf life of recombinant proteins.

### **Chemical Engineering and Process Fundamentals for Chemists**

Monday-Wednesday, November 15-17, 1993

This course will help bridge the gap between research lab and the plant.

### **Effective Management of Chemical Analysis Laboratories**

Monday-Tuesday, November 15-16, 1993

Learn to do more with less.

### **Environmental Laboratory Data Quality Assurance QA/ QC**

Tuesday-Wednesday, November 16-17, 1993

Increase laboratory data quality and meet user needs—present and future laboratory goals.

### **Gas Chromatography**

Monday-Tuesday, November 15-16, 1993

Learn modern GC techniques in this intensive two-day course.

### **Gas Chromatography/Mass Spectrometry**

Thursday-Friday, November 18-19, 1993

Learn how GC/MS can solve your sample separation and identification problems.

### **Interpretation of IR Spectra**

Tuesday-Thursday, November 16-18, 1993

Improve your IR problem-solving skills.

### **Laboratory Information Management Systems**

Wednesday, November 17, 1993

Examine the impact a LIMS would have on your laboratory.

### **New Sample Preparation Methods for Chemical Analysis**

Thursday-Friday, November 18-19, 1993

Improve the productivity, reproducibility, and analyte recovery of your analytical laboratory, while decreasing sample preparation time and cost.

### **Quality Management/Quality Assurance in Industry and in the Laboratory**

Monday-Tuesday, November 15-16, 1993

Acquire the success skills necessary to keep your company competitive and profitable.

### **Technical Writing Workshop**

Thursday-Friday, November 18-19, 1993

Learn from a master teacher how to improve your professional writing skills.

### **Thermal Analysis in Polymer Characterization**

Monday-Tuesday, November 15-16, 1993

Learn to apply the methods of thermal analysis to a broad range of polymers.

### **Water and Waste by U.S. EPA Methods**

Thursday-Friday, November 18-19, 1993

Master the fundamentals of applied environmental measurements of pollutants in liquid and solid samples.

## Register Today!

For more information mail in the coupon below. FAX: (202) 872-6336. Or call the ACS Continuing Education Short Course Office at (800) 227-5558 (TOLL FREE) or (202) 872-4508.

Please send me information on the ACS Short Course Program to be held in conjunction with the Eastern Analytical Symposium, November 1993, in Somerset, NJ.

NAME

TITLE

ORGANIZATION

ADDRESS

CITY, STATE, ZIP

## EDITORIAL

# The Ubiquitous Laser Or, Let All Spectroscopists Enjoy the Radiance

At a round table gathering of ACS journal Editors some time ago, *Journal of Physical Chemistry* Editor and my colleague Mostafa El-Sayed remarked that the most significant instrumental developments in chemistry in recent decades have been the laser and the microprocessor. How true that is, for analytical as well as physical chemistry! Lasers have played a pervasive role in the development of, and remain a frontier of, analytical chemistry.

I suppose many analytical chemists, on hearing in the 1960s of the invention of the laser, imagined that the tungsten light bulbs in our absorption spectrophotometers would shortly be replaced by brighter, more sharply focused, and more highly monochromatic lasers. That thought was soon dispelled. Lasers, for all their virtues, are not even today gracefully configured as general-purpose scanning light sources. The intense irradiance, small beam divergence, and excellent stability and low noise properties of modern pulsed and CW lasers have, on the other hand, engendered numerous inventions and improvements in our analytical tools. Many applications are based simply on the intense but controllable irradiance of lasers. Enticing nonvolatile samples into the gas phase by deposition of an energy burst is an extremely profitable tactic, with a bonus that microscopic surface regions can be sampled. MS and atomic spectroscopy are notable beneficiaries of energy deposition in the forms of matrix-assisted laser desorption/ionization (MALDI) and the laser microprobe. Energy bursts have also been used to ablate barrier layers off carbon electrodes in studies of electrode kinetic phenomena.

The small beam divergence of lasers finds application for alignment and positioning control, as in FT-IR spectroscopy, scanning tunneling microscopy, and photo-thermal spectroscopy. This property, coupled with high irradiance, yields remote aerosol sampling techniques such as LIDAR and versions of microscopy, fluorescence, and Raman microspectrophotometry, in which quantitative photometric images are obtained. Near-field optical spectroscopy offers avenues to previously inaccessible images of liquid-solid interfaces at sub-Bragg-limit SEM-level resolution levels.

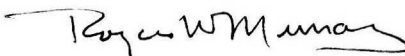
Large laser irradiance (and stable operation) also permits greatly enhanced sensitivity in older analytical tools, including

Raman spectroscopy and laser-induced fluorescence (LIF) of molecules in solutions and of atoms in the gas phase (LEAFS). At the Spectrochemical Analysis Award Symposium at the recent Chicago ACS meeting, there were fascinating lectures on the LIF detection of single molecules and of small herds of several hundred, and of the electrophoretically separated contents of single erythrocytes. LIF really shows its power as a detector in chemical separations, both when samples are tagged with appropriate fluorescent labels and increasingly based on native fluorescence only.

I am also impressed with the extent to which the laser spectroscopy community employs spaghetti soup acronyms and fanciful labels. An intelligent nonscientist hearing words such as thermal blooming, mirage effect, second harmonic, and mode locking, would logically think: flower gardening, a trek in the desert, good music, and highway trance. Although fanciful words don't aid chemists' ability to communicate with the public, they do give a little relief from our otherwise bland technical language.

Lasers are clearly a bright spot in our discipline's future, both basic and applied. Applications in provoking fluorescence and scattering will grow, especially in chemical sensor systems, but lower cost devices and diode wavelengths with more desirable wavelengths will be welcome. The spread of laser uses in microscopy seems far from over, especially in providing improved element or molecule-specific surface maps. Laser photo-initiated chemical reactions and holography should find places in analytical methods. There will be others. It will be fascinating to watch analytical laser spectroscopy grow; my bet is that uses will be found that have not yet been imagined.

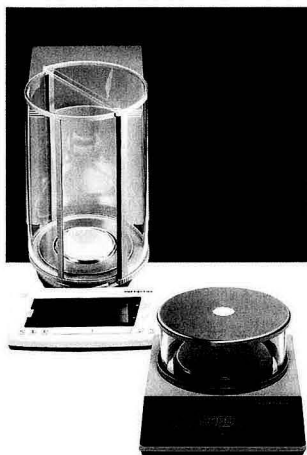
I would be remiss in not calling attention to how pervasive lasers have become in our society's technology. Welding, supermarket bar code readers, CD players, earthquake prediction, and eye surgery are samples that illustrate the breadth of their impact. The diversity of these applications offers a potent illustration of how hard it is to predict the specific benefits of basic research to society.



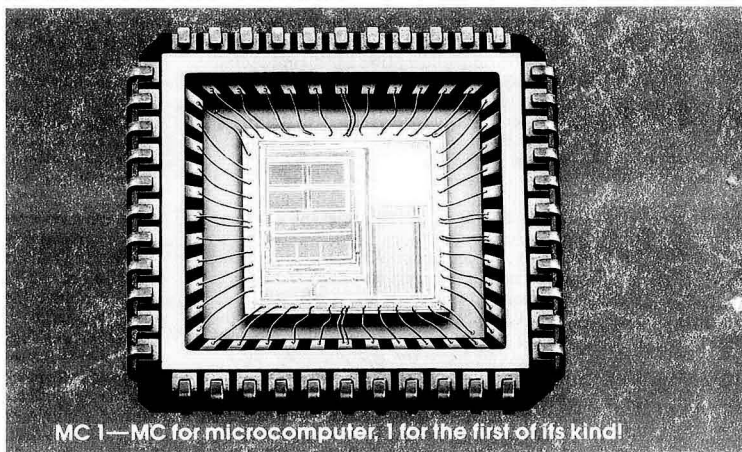
SARTORIUS KNOWS

# Technology

**Why a smarter balance  
is a smarter value.**



The MC 1 microchip is integrated into Sartorius top-loading, analytical and research balances.



MC 1—MC for microcomputer, 1 for the first of its kind!

With 40 MHz of power, Sartorius MC 1 balances are more powerful than most desktop computers. That power translates to speed, stability and programmability—unmatched by all microprocessor balances.

No other balance technology provides a rock-solid readout down to 0.01mg in as few as 2.5 seconds. Just as important, no other balance offers as many application programs: from simple percent calculations and over/under checkweighing routines to statistical weight analysis and formulation routines.

Sartorius has always stood for quality. Now, MC 1 stands for unique microcomputer capability. No matter how small or large the sample or how complex the weighing routine required, Sartorius knows how to put more computing power *into* its balances so you can get much more out of them.

**sartorius**

Sartorius Corporation  
131 Heartland Blvd.  
Edgewood, NY 11717  
Phone: 800-635-2906  
FAX: 516-254-4253

CIRCLE 82 ON READER SERVICE CARD



## 1994 ACS Awards

Seven scientists in the analytical chemistry community will receive 1994 American Chemical Society awards. The awards will be presented next March at the 207th ACS national meeting in San Diego.



**Edward S. Yeung**, professor of chemistry at Iowa State University of Science and Technology, senior scientist at Ames Laboratory, and spectroscopy editor for *ANALYTICAL CHEMISTRY*, will receive the ACS Award in Analytical Chemistry, sponsored by Fisher Scientific. The award is given in recognition of outstanding contributions to the science of pure or applied analytical chemistry.

Yeung received his A.B. degree from Cornell University in 1968 and his Ph.D. from the University of California–Berkeley in 1972. He then joined the faculty at Iowa State University of Science and Technology and was promoted to professor in 1981.

Yeung's research interests include sensitive detection in chromatography and electrophoresis, laser vaporization for the study of materials and large biomolecules, chemical analysis of single mammalian cells, and high-speed DNA sequencing. Yeung holds 10 patents and has published more than 200 papers.

His awards include the Division of Analytical Chemistry's Award in Chemical Instrumentation (1987); the Pittsburgh Analytical Chemistry Award, sponsored by the Society for Analytical Chemists of Pittsburgh (1993); and the Society of Applied Spectroscopy's Lester Strock Award (1990).



**Barbara J. Garrison**, professor of chemistry at The Pennsylvania State University, will receive the Francis P. Garvan–John M. Olin Medal. The award, sponsored by the Olin Corp., is given in recognition of distinguished service to chemistry by women chemists in the United States.

Garrison received her B.S. degree in physics from Arizona State University in 1971 and her Ph.D. in chemistry from the University of California–Berkeley in 1975. Garrison was a postdoctoral assistant at Purdue University, taught at the University of California–Berkeley and Purdue University, and then joined the faculty of The Pennsylvania State University in 1979. She was promoted to professor in 1986.

Garrison's research interests include interaction of gases with solid surfaces, keV ion bombardment of solids, etching of semiconductors, molecular beam epitaxial growth of semiconductors, and ionization phenomena near metal surfaces. She has published over 120 papers.

Her awards include the Alfred P. Sloan Fellowship (1980–84) and The Pennsylvania State Faculty Scholar Award for Outstanding Achievement in the Physical Sciences and Engineering (1990). Garrison is active in The Pennsylvania State University's affairs at the college, department, and university levels.



**Adam Heller**, professor of chemical engineering at the University of Texas–Austin, will receive the ACS Award in the Chemistry of Materials. The award, sponsored by DuPont, recognizes creative work in the chemistry of materials.

Heller received his M.Sc. degree in chemistry and physics in 1957 and his Ph.D. in chemistry in 1961,

both from the Hebrew University–Jerusalem. Heller was a postdoctoral associate at the University of California–Berkeley and was on the staffs of both Bell and GTE Laboratories. He returned to AT&T Bell Laboratories in 1975 and joined the faculty at the University of Texas–Austin in 1988.

Heller's research interests include hydrogen-evolving solar cells, electrical microengineering of enzymes, oil spill cleanup technology using buoyant coated cenospheres, and transparent metals. Heller has more than 30 patents and has published more than 130 papers and books.

His awards include the Battery Research Award (1978) and the David C. Grahame Physical Electrochemistry Award (1987), both from the Electrochemical Society. In 1987 he was elected to the National Academy of Engineering.



**Paul Kebarle**, professor of chemistry at the University of Alberta, will receive the Frank H. Field and Joe L. Franklin Award for Outstanding Achievement in Mass Spectrometry, sponsored by Extrel Corp. The award recognizes outstanding achievement in the development or application of MS.

Kebarle received his Diploma from the Swiss Federal Institute of Technology in 1952 and his Ph.D. in physical chemistry from the University of British Columbia in 1955. He then held a postdoctoral fellowship at the National Research Council of Canada until 1958, when he joined the faculty at the University of Alberta. He was promoted to professor in 1967.

Kebarle's research interests include gas-phase reaction kinetics, ion–molecule interactions at high pressure, ionic solvation and reactivity in the gas phase, and ion–molecule equilibria.

His awards include the Chemical Institute of Canada Medal (1986) and the University of Alberta's Kaplan Award for Excellence in Research (1989). He is an



elected member of the New York Academy of Sciences and an elected Fellow in the Chemical Institute of Canada and the Royal Society of Canada. Kebarle has published more than 200 papers.



**William H. Pirkle**, professor of chemistry at the University of Illinois, Urbana-Champaign, will receive the ACS Award in Chromatography, sponsored by Supelco, Inc. The award honors outstanding achievements in the field of chromatography.

Pirkle received his B.S. degree from the University of California-Berkeley in 1959 and his Ph.D. from the University of Rochester in 1963. He spent a year as a postdoctoral research associate at Harvard, then joined the faculty of the University of Illinois in 1964. He was promoted to professor in 1980.

Pirkle's research interests include the development of chiral stationary phases, NMR spectroscopy of chiral materials, and the elucidation of chromatographic fundamentals. He has published more than 180 papers.

Pirkle's awards include the Chromatography Society's A.J.P. Martin Medal (1990) and the Chicago Chromatography Discussion Group's Merit Award (1991). In addition, he received a National Science Foundation Fellowship (1963) and an Alfred P. Sloan Fellowship (1970-73).



**Phillip C. Wankat**, professor of chemical engineering at Purdue University, will receive the ACS Award in Separations Science and Technology, sponsored by Rohm and Haas. The award recognizes outstanding accomplishments in fundamental or applied research directed toward separations science and technology.

Wankat received his B.S. degree from Purdue University in 1966 and his Ph.D. from Princeton University in 1970, as well as an M.S. degree in education, counseling, and personnel services from Purdue University in 1982. He joined the faculty at Purdue University in 1970 and was promoted to professor in 1978.

His research interests include separation techniques, cascade theory, parametric pumping and cycling zone adsorption, chromatography, and biochemical separations. Wankat has published more than 120 papers.

Wankat's awards include the American Society for Engineering Education's George Westinghouse Award (1984), the Western Electric Award (1984), the Chester F. Carlson Award (1990), and Purdue University's Marion B. Scott Award (1982).



**George M. Whitesides**, professor of chemistry at Harvard University, will receive the James Flack Norris Award in Physical Organic Chemistry, sponsored by the ACS North-eastern Section. The award recognizes outstanding contributions to physical organic chemistry.

Whitesides received his A.B. degree from Harvard University in 1960 and his Ph.D. from the California Institute of Technology in 1964. He joined the faculty at the Massa-

chusetts Institute of Technology in 1963 and the faculty at Harvard in 1982 as a professor.

His research interests include the use of enzymes in organic synthesis, applied biochemistry, structure-property relationships in organic materials science, heterogeneous catalysis, and NMR spectroscopy. Whitesides has published more than 370 papers.

Whitesides' awards include the Alfred P. Sloan Fellowship (1968), the ACS Award in Pure Chemistry (1975), and the ACS Arthur C. Cope Scholar Award (1989).

## ASA, Perkin Elmer, and Golay Awards

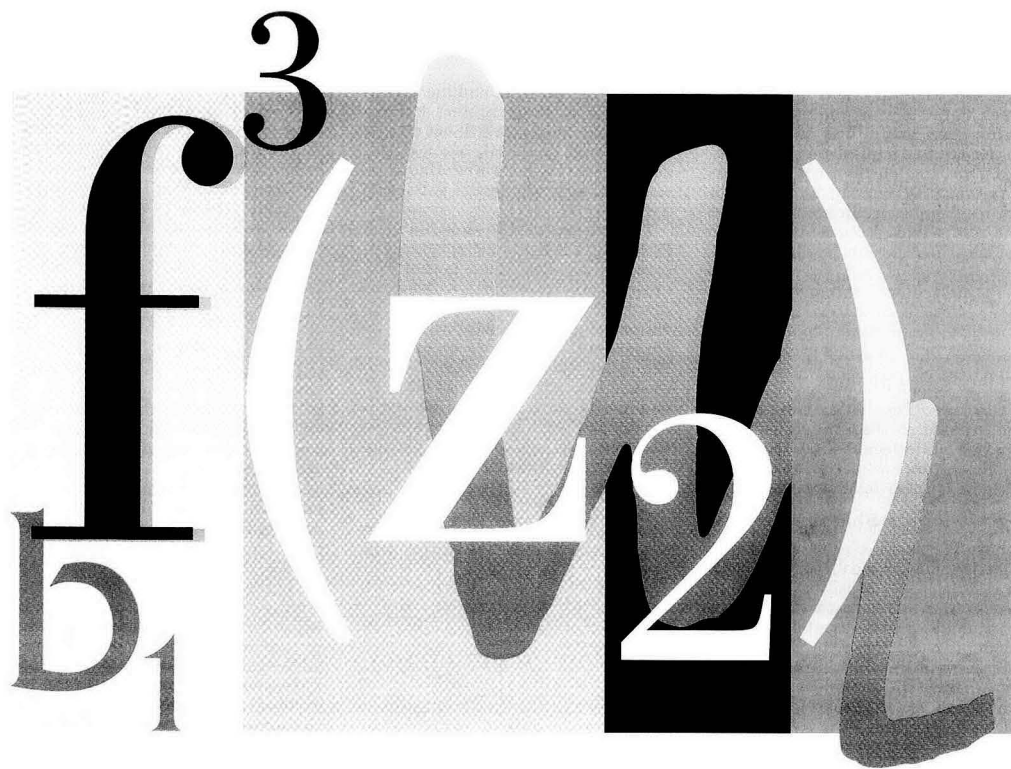
**Charles K. Bayne** of the Computing Applications Division and **Cheng Yu Ma** of the Analytical Chemistry Division, Oak Ridge National Laboratory, received the 1993 Statistics in Chemistry Award, sponsored by the American Statistical Association (ASA). Bayne and Ma were presented with citations and a check for \$2000 at the Joint Statistical Meeting in San Francisco in August. They won the award for their paper, "Differentiation of Aroclors Using Linear Discrimination for Environmental Samples Analyzed by Electron Capture Negative Ion Chemical Ionization Mass Spectrometry" (*Anal. Chem.* **1993**, *65*, 772-77). The award recognizes outstanding collaborative efforts between statisticians and chemists for a paper published in a refereed chemometrics, chemistry, or statistics journal.

**John Frenz**, **Cynthia P. Quan**, **William S. Hancock**, and **James Bourell** of Genentech won first prize in the Perkin Elmer International Liquid Chromatography Technical Paper Award contest. Their paper, "Characterization of a Tryptic Digest by High-Performance Displacement Chromatography and Mass Spectrometry" (*J. Chromatogr.* **1991**, *557*, 289-305), describes increasing the column capacity for the isolation of minor components in a tryptic digest. The award was presented in May at HPLC '93 in Hamburg, Germany. The prize entitles Genentech to \$20,000 worth of Perkin Elmer analytical equipment.

Papers are now being accepted for the 4th Perkin Elmer International Liquid Chromatography Technical Paper Award. Papers published within the past year are eligible. The technical content of the papers is unrestricted as long as LC is the analytical technique used and the LC system used (from any manufacturer) is listed. A second-place prize is also given; the winner receives \$5000 worth of items from the PE XPRESS catalog. For information, contact Laura Lauman, Perkin Elmer International Liquid Chromatography Award, The Perkin-Elmer Corp., 761 Main Ave., Norwalk, CT 06859-0250 (203-761-2932; fax 203-761-2887). Deadline is Dec. 31.

**Konrad Grob** of Kontonales Labor (Switzerland) was awarded the 1993 M.J.E. Golay Award in Capillary Chromatography at the International Symposium on Capillary Chromatography, held in Riva del Garda, Italy, in May. The award, also sponsored by Perkin Elmer, honors the late Marcel Golay, inventor of the capillary column. It is given for significant contributions to the evolution of capillary chromatography and consists of a medal, a scroll, and an endowment.

Nominations are being accepted for the 1994 Golay award. All nominations should be sent to Carel Cramers, Eindhoven University of Technology, Department of Chemistry, Lab Instrument Analysis, P.O. Box 513, 5600 MB Eindhoven, The Netherlands (31-40-473024; fax 31-40-453762). Deadline is Nov. 30.



# Nonlinear Multivariate Calibration Methods in Analytical Chemistry

Sonja Sekulic<sup>1</sup>, Mary Beth Seasholtz<sup>2</sup>, Ziyi Wang, and Bruce R. Kowalski\*

Laboratory for Chemometrics  
Department of Chemistry, BG-10  
University of Washington  
Seattle, WA 98195

Samuel E. Lee<sup>3</sup> and Bradley R. Holt

Department of Chemical Engineering,  
BF-10  
University of Washington  
Seattle, WA 98195

Over the years the role of the analytical chemist has evolved in step with technological advancements and the quest to explore and understand issues of increasing complexity. The

data explosion created by the increased resolving power of analytical instruments and the relative ease of access to computing facilities has placed more emphasis on data analysis. Even the relatively small area of calibration model construction has undergone a transition whereby the analytical chemist is presented with an ever-increasing palette of multivariate calibration methods.

## REPORT

During the past decade or so, methods such as principal components regression (PCR) and partial least squares regression (PLS) have gained acceptance in multivariate calibration, as evidenced by the increased number of applications (1-7) and reviews (8-11). With emphasis now shifting to the ability to model nonlinear information, several tech-

niques have been adapted or created to deal with such information, including locally weighted regression (LWR), projection pursuit regression (PPR), alternating conditional expectations (ACE), multivariate adaptive regression splines (MARS), and neural networks (NN). PCR and PLS can also be used to describe nonlinear systems by either incorporating a larger number of latent variables than would be required for a linear system (12) or using the nonlinear or quadratic versions of the algorithms (13, 14). Whatever the method origin, each of these techniques aims at describing the nonlinear relationship that exists between a given sample attribute (in analytical chemistry this is most often solute concentration) and its measured instrument responses.

In this REPORT we present an overview of these methods and apply them to six data sets, one simulated and five originating from different

Present addresses: <sup>1</sup> P.O. Box 534, Fairfield, NSW, Australia. <sup>2</sup> Dow Chemical Co., Bldg. 1712, Midland, MI 48679. <sup>3</sup> Ford Motor Co., 15031 S. Commerce Dr., Dearborn, MI 48120.

spheres of analytical chemistry. Each data set was analyzed, and a calibration model was constructed using the individual methods. Because more often than not a calibration model is constructed for use in future sample predictions, we used the relative prediction error as the comparison criterion. Scalars are denoted by lower-case letters, column vectors by bold lower-case letters, row vectors by column vectors transposed (using a superscript T), and matrices by bold upper-case letters.

### Method descriptions

**PCR and PLS.** These two popular calibration methods have been described and discussed at length in the literature (15–24). Both methods assume a linear inverse model

$$\mathbf{c} = \mathbf{R}\mathbf{b} + \mathbf{e} \quad (1)$$

where  $\mathbf{R}$  is the instrument response matrix (such as a collection of spectra) for a series of calibration samples,  $\mathbf{c}$  is a vector with the concentrations of all the samples (here a model is constructed for one sample attribute at a time),  $\mathbf{b}$  is a vector containing the model parameters, and  $\mathbf{e}$  is a vector of concentration residuals. PLS and PCR estimate the regression vector  $\hat{\mathbf{b}}$  by calculating an estimate of the pseudo-inverse (16),  $\mathbf{R}^+$

$$\hat{\mathbf{b}} = \mathbf{R}^+ \mathbf{c} \quad (2)$$

Estimating the pseudo-inverse in PCR and PLS is a three-step procedure. First, the response matrix is decomposed into three matrices

$$\mathbf{R} = \mathbf{U}\mathbf{S}\mathbf{V}^T \quad (3)$$

where the columns of  $\mathbf{U}$  and  $\mathbf{V}$  are orthonormal and  $\mathbf{S}$  is either diagonal (PCR) or bidiagonal (PLS) (16). A low-dimension approximation of the data is then made so that all the relevant information is retained while the noise is filtered out. Finally, the pseudo-inverse of this approximation is calculated:

$$\mathbf{R}^+ = \bar{\mathbf{V}} \bar{\mathbf{S}}^{-1} \bar{\mathbf{U}}^T \quad (4)$$

where the bars over the matrices indicate that this is the decomposition truncated to the optimal pseudo-rank (i.e., the number of latent variables or factors incorporated into the model such that the noise is minimized and predictive ability is optimized). The selection of pseudo-rank is important because the model should describe the significant sources of variance but not overfit the data (25, 26). The determination of the appropriate pseudo-rank is

not a trivial problem and has generated much research interest and discussion. Although we will not discuss this problem in detail, two methods demonstrated here are also presented later in the model validation section.

The greatest difference between PCR and PLS methods, as often discussed in the literature, is that PLS incorporates information from the concentration vector whereas principal component analysis (PCA, the intrinsic part of PCR) does not. Each PLS latent variable direction is modified so that the covariance between it and the concentration vector is maximized (27). More generally, in PLS the response matrix is decomposed into two matrices

$$\mathbf{R} = \mathbf{T}\mathbf{P}^T \quad (5)$$

where only  $\mathbf{T}$ , the scores matrix, is orthogonal and  $\mathbf{P}$  is the loadings matrix.

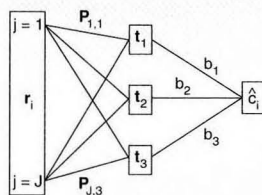


**Figure 1.** Flow diagram showing the transfer of information during the prediction phase of PCR and PLS.

Key:  $r_i$  represents the measurement vector of a future sample  $i$ ,  $\mathbf{P}$  is the loadings matrix calculated during calibration,  $t_1$ – $t_3$  are the scores calculated for sample  $i$  (assuming that three latent variables are required in the model),  $c_i$  indicates the predicted concentration value for the unknown sample, and  $b_1$ – $b_3$  are the regression parameters calculated during the calibration phase.

Figure 1 shows a flow diagram of the PCR and PLS methods using the decomposition in Equation 5. In this figure,  $t_1$ ,  $t_2$ , and  $t_3$  are the first three score vectors calculated from linear combinations of the original  $J$  sample measurements, represented by  $\mathbf{P}$  (the loadings matrix). Once the pseudo-inverse of  $\mathbf{R}$  is calculated during calibration, and thereby the regression vector estimated (represented by  $b_1$  to  $b_3$ ), it is easy to see how the concentration of an unknown sample can be obtained.

**Nonlinear PCR and PLS.** There are several different options, which generally involve the decompositions described by Equations 3 and 5, for

the implementation of nonlinear PCR and PLS algorithms. The instrument response matrix is decomposed into what is now commonly referred to as the score vectors ( $\mathbf{US}$  in Equation 3 and  $\mathbf{T}$  in Equation 5) and the loading vectors ( $\mathbf{V}$  in Equation 3 and  $\mathbf{P}$  in Equation 5). Once the decomposition is complete, the scores matrix is augmented and the inverse calibration model is modified to

$$\mathbf{c} = [t_1 \ t_2 \ t_1^2 \ t_2^2] \mathbf{b} + \mathbf{e} \quad (6)$$

The concentration vector  $\mathbf{c}$  is related to the augmented scores matrix denoted [...] via the regression vector  $\mathbf{b}$ . In Equation 6 the augmented scores matrix contains the first two score vectors and their quadratic transforms. This is the approach adopted here, although other algorithms are available for the PLS method that also enable incorporation of interaction terms (such as  $t_1 \cdot t_2$ ) (13).

Figure 2 shows the flow diagram for the quadratic PLS algorithm in which two latent variables are incorporated into the model. It is also possible to incorporate any appropriate functional transformation to the individual score vectors to construct the appropriate model. In some of the more recently published methods attempts have been made to avoid the necessity of specifying an exact functional form of the transformations by applying either smoothing functions (28) or splines (29) to the individual score vectors.

**LWR.** Calibration with LWR was introduced into analytical chemistry in 1990 by Naes, Isaksson, and Kowalski (12), after appearing in the statistics literature (30). Further results were reported in 1992 by Naes and Isaksson (31). LWR is based on the premise that a smooth nonlinear function can be locally approximated

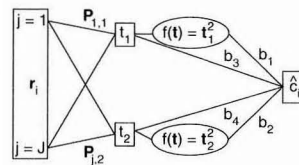


**Figure 2.** Flow diagram of the nonlinear PCR and PLS algorithms used for the prediction phase.

Note that here  $f(t)$  is the quadratic transform on the score vectors calculated during the calibration phase, as are the matrix  $\mathbf{P}$  and the regression parameters  $b_1$ – $b_4$ .  $J$  refers to the total number of measurements made on each sample.

with a simple model (linear or quadratic).

The model used in LWR is also the inverse least-squares model described by Equation 1. For each future sample  $\mathbf{r}_{un}$  to be predicted, a weighted regression is performed with only the  $q$  closest calibration samples. The weights are a function of the Euclidean distance between the  $q$  calibration samples and the unknown sample so that

$$w_i(\mathbf{r}_{un}) = \mathbf{W} [\rho(\mathbf{r}_{un}, \mathbf{r}_i) / d(\mathbf{r}_{un})] \quad (7)$$

where  $w_i(\mathbf{r}_{un})$  is the weight associated with the  $i$ th sample in the weighted regression for the prediction of  $\mathbf{r}_{un}$ ,  $\rho(\mathbf{r}_{un}, \mathbf{r}_i)$  is the Euclidean distance between the unknown sample and the  $i$ th calibration sample, and  $d(\mathbf{r}_{un})$  is the largest  $\rho(\mathbf{r}_{un}, \mathbf{r}_i)$  over the  $q$  points involved in the regression.

$$\mathbf{W}(u) = \begin{cases} (1 - u^3)^3 & 0 \leq u \leq 1 \\ 0 & \text{otherwise} \end{cases} \quad (8)$$

The weight function decreases as the distance from  $\mathbf{r}_{un}$  to the respective  $\mathbf{r}_i$  increases. Mathematically, Equation 1 is multiplied by the diagonal weight matrix  $\mathbf{W}$ , containing  $q$  non-zero diagonal elements corresponding to  $q$  closest calibration samples chosen. The regression vector  $\hat{\mathbf{b}}$  is found with a least-squares estimate according to

$$\hat{\mathbf{b}} = (\mathbf{WR})^+ \mathbf{Wc} \quad (9)$$

where  $(\mathbf{WR})^+$  is the pseudo-inverse of  $\mathbf{WR}$ .

In the work of Cleveland and Devlin (30), the distance  $\rho$  was the ordinary Euclidean distance in the original variables, but in our study it is a Mahalanobis distance in the principal component space (12). The optimal value of  $q$  and the number of principal components can be determined by one of the validation criteria described in the model validation section.

It has been shown (32) that in many cases a smaller number of principal components is needed for LWR compared with PCR or PLS simply because the most relevant information is present in the first few latent variables, but in a nonlinear fashion. LWR is a generalization of the PCR method (or PLS if PLS latent variables are used), but it does require that a local linear model be constructed for each unknown sample. Because the model is local, only a few latent variables and samples are required to construct it, making the prediction relatively fast. Note the similarity of Figure 3, the LWR flow diagram, to the flow diagram

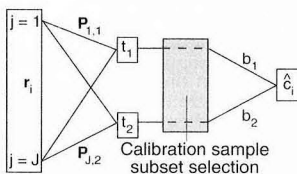


Figure 3. Flow diagram of the LWR method.

The shaded region indicates the local nature of the method in which a subset of calibration samples is selected to construct a local linear model in the PCA space (on scores space rather than on the raw variable space). Note that a model is constructed for each future sample  $\mathbf{r}_i$  and that the model parameters  $b_1$  and  $b_2$  are determined by the samples selected for local model construction.

for PCR and PLS shown in Figure 1. In LWR the loadings,  $\mathbf{P}$ , are calculated for all the available calibration samples. In order to obtain the concentration estimate,  $\hat{c}_i$ , the future sample response  $\mathbf{r}_i$  is introduced and the scores ( $t_1$  and  $t_2$ ) are calculated. A subset of samples is selected for the construction of the local model where  $b_1$  and  $b_2$  are the local model parameters.

**PPR.** The name of this method refers to the pursuit of an optimal projection axis for least-squares regression. The optimal projection axis is calculated using an optimization procedure that produces a vector,  $\alpha$ , containing the coefficients for an optimal linear combination of the original variables in the instrument response matrix,  $\mathbf{R}$ . The optimization is accomplished by minimizing the least-squares residual over the values of  $\alpha$  after a smoothing function approximation,  $S_{\alpha_m}$ , is applied to the projected data. The PPR model (33, 34) can be written as

$$\mathbf{c} = \phi(\mathbf{R}) = \sum_{m=1}^M \mathbf{b}_m \mathbf{S}_{\alpha_m}(\mathbf{R}\alpha_m) \quad (10)$$

where  $\mathbf{c}$  is the vector containing the sample concentrations,  $\mathbf{R}$  is the instrument response matrix,  $\alpha_m$  contains the optimal linear combination information,  $m$  is the index to the maximum number of such projections  $M$  (which is required to explain the observed variance), and  $\mathbf{b}_m$  is the regression parameter for optimal projection  $m$ . Once the instrument responses have been projected onto an axis defined by  $\alpha_m$ , a smoothing function estimate,  $S_{\alpha_m}$ , is used to obtain the least-squares estimate of the functionality observed on the

two-dimensional scatter plot ( $\mathbf{c}$  against  $\mathbf{R}\alpha_m$ ). This process is repeated with the residual values until sufficient variance is explained (Figure 4).

The use of the smoothing function estimate makes this method particularly suited to identifying nonlinear functions. The validation criterion is employed to select the model parameters such as the number of terms,  $M$ , required.

**ACE.** The underlying assumption of this method is that if the vector  $\mathbf{c}$  and columns in  $\mathbf{R}$  are not linearly related, then by applying suitable transforms on  $\mathbf{c}$  and the columns in  $\mathbf{R}$  the transformed  $\mathbf{c}$  and transformed columns in  $\mathbf{R}$  will be linearly related. The model can be expressed as

$$\mathbf{S}_c(\mathbf{c}) = \sum_{j=1}^J \mathbf{S}_j(\mathbf{R}_j) + \mathbf{e} \quad (11)$$

where  $\mathbf{S}_c(\mathbf{c})$  is the optimal transform on the vector  $\mathbf{c}$  and  $\mathbf{S}_j(\mathbf{R}_j)$  refers to the optimal transformation on column  $j$  in the response matrix (35, 36). In practice, the optimal transforms are approximated using a smoothing function. If there are  $J$  columns in  $\mathbf{R}$ , then  $J$  transforms are calculated. The transforms are calcu-

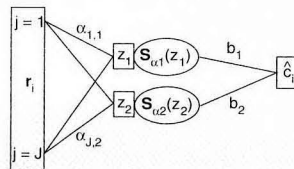


Figure 4. Flow diagram of the PPR method module for prediction.

Here,  $z_m$  is equal to  $\mathbf{r}_i \alpha_m$  and refers to the projection of the sample response along the optimal projection axis  $m$ .  $\mathbf{S}_{\alpha_m}$  refers to the smoothing function approximation of the scatter plot created by the projection of the calibration samples along the optimal axis  $m$ . The regression parameters  $b_1$  and  $b_2$  are estimated during the calibration phase.

lated by minimizing  $e^2$ , the least-squares model residual, in an iterative fashion

$$e^2(\mathbf{S}_c, \mathbf{S}_1, \mathbf{S}_2, \dots, \mathbf{S}_J) = E[\mathbf{S}_c(\mathbf{c}) - \sum_{j=1}^J \mathbf{S}_j(\mathbf{R}_j)]^2 \quad (12)$$

This minimization is undertaken by alternatively keeping either  $J-1$  of



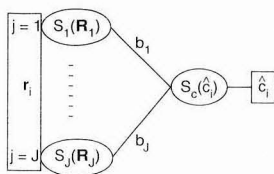


**Figure 5.** Flow diagram of the ACE method as defined by Equation 11.

$S_1$  to  $S_J$  refers to the smoothing function approximation of the optimal transformation on column or measurement 1 to  $J$  in matrix  $\mathbf{R}$  calculated for the calibration set of samples.  $S_c$  refers to the smoothing function approximation of the optimal transformation on the concentration vector of the calibration set of samples. During the prediction phase, the estimate of the smoothed concentration  $S_c(\hat{c})$  is obtained by a series of interpolations through the  $S_1$  to  $S_J$  smoothed functions. An additional interpolation is then required to obtain the prediction sample concentration estimate.

the transforms  $S_i(\mathbf{R}_i)$  or  $S_c(\mathbf{c})$  constant and estimating the conditional expectation of the remaining function. In each iteration the data are projected onto a two-dimensional surface (creating a scatter plot of the sample responses) after which a supersmoother is used to obtain the least-squares estimate of the observed functionality. (The supersmoother is a smoothing function with variable span capability particularly aimed at nonlinear function estimation.) The iterations cease when  $e^2$  no longer decreases.

The ACE algorithm does not provide the functional transformations for the final model. By plotting the original values of the  $j$ th column in  $\mathbf{R}$  against the optimal transformed values,  $S_j(\mathbf{R}_j)$ , the user may be able to deduce the required analytical transformation. ACE has been used more often for identifying appropriate data transformations than it has been for full multivariate regression. It does not perform variable selection and is therefore very sensitive to nonrelevant information. As shown in the flow diagram for this method (Figure 5), an additional step is required to obtain the actual sample concentration estimate from the smoothed concentration transform.

The two validation criteria found in the model validation section were used to select the best models constructed with this method. For data sets requiring initial dimensionality reduction, the best model was determined by calculating the criteria for models constructed with different numbers of score vectors.

**MARS.** The most complex method presented here, MARS is based on the idea that only a few variables contribute significantly in any one subregion of the multidimensional response space (37–39). By correctly identifying the subregions and the associated significant variables, it is possible to obtain linear or cubic spline estimates of the observed functionality for individual subregions. The entire model can be simply stated as

$$\mathbf{c} = \mathbf{f}(\mathbf{R}) + \mathbf{e} \quad (13)$$

where  $\mathbf{c}$  contains the sample concentration information,  $\mathbf{R}$  is the instrument response matrix,  $\mathbf{f}$  refers to the nonlinear functionality of the data, and  $\mathbf{e}$  refers to the concentration residuals.

The term *adaptive* in MARS refers to the ability of the algorithm to adapt to the specific features of a given data set in locating the appropriate subregions. In simplified terms, the subregions are identified by locating suitable splitting points, or knot locations, by minimizing a lack-of-fit criterion (least-squares residual with an incorporated complexity penalty). This is a highly iterative procedure whereby the sample responses are projected onto an axis defined by each of the independent variables in  $\mathbf{R}$ . Each projection is tested for possible knot locations with the aid of the lack-of-fit criterion, and the combination of variable and knot location that explains the greatest amount of variance is incor-

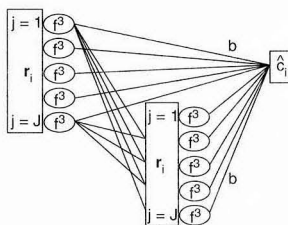


**Figure 6.** Flow diagram of a MARS model constructed with an allowed interaction level equal to 2 (i.e., interaction allowed between two variables).

The  $f^3$  indicates that a cubic spline approximation is carried out on the raw measurement variables. Note that cubic spline transformations performed on the same variable are not connected. The unknown sample concentration is obtained by passing the sample response vector through the variable transforms calculated during the calibration procedure.

porated into the model. The procedure is then continued on the residual values until sufficient variance has been described. This description refers only to univariate projections.

With MARS it is possible to subdivide the response space into multidimensional subregions mathematically by incorporating response variable interaction terms. Figure 6 shows the flow diagram of a model constructed using cubic spline approximations of the measurement variables ( $f^3$ ) and an allowable interaction level equal to 2. The interaction level determines the number of hidden  $\mathbf{R}_i$  layers, which is similar to NN architecture determination. However, unlike NN, no information is passed between two nodes at the same level (e.g.,  $j = 1$ ).

To construct the best model with MARS, the optimal number of terms (or subregions) must be selected.

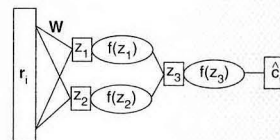


**Figure 7.** Flow diagram of typical NN architecture (MLF network).

The  $\mathbf{W}$  matrix containing the weights of the individual variable contributions to the  $z$  nodes is analogous to the loading matrix  $\mathbf{P}$  used in PCR and PLS.

This is accomplished by using a method validation criterion, two of which are described later. Dimensionality reduction was performed for several data sets used in this study. For those situations, to identify the best model constructed with MARS, it was also necessary to select the optimum number of score vectors used during model construction.

**NN.** A multilayer feedforward (MLF) (40) network with the sigmoid activation function is an appropriate network structure only when the data set is nonlinear. The flow diagram for an MLF network is shown in Figure 7. When the functional relationship between the input data (analogous to the instrument response information) and the output data (analogous to the concentration vector) is linear, MLF networks require a long training time because a nonlinear model structure is being used to model linear data.

In this study, the direct linear feedthrough (DLF) network structure shown in Figure 8 has been used. The weighted input patterns are directly added to the output layer of the standard nonlinear network, and an output datum from a DLF network is calculated according to the following equation

$$\text{output}_k = \frac{1}{1 + e^{-(\sum w_{ik}o_i + \theta_{ik})}} + (\sum w_{ik}o_i + \theta_{ik}) \quad (14)$$

where  $w_{ik}$  and  $\theta_{ik}$  represent the weight and bias terms between the  $i$ th and  $k$ th layers, respectively, and  $o_i$  represents the output value of a node in the  $i$ th layer. The DLF network structure is most useful when the functionality between the input and output data patterns is unknown. During the training of a linear input-output relationship, the contribution from the nonlinear part of the network will gradually diminish until it is invisible to the network. When this input-output pattern has purely nonlinear functionality, the linear and nonlinear components of the DLF network will both contribute to provide the best model for the data (41).

The process of training an artificial NN can be viewed as a nonlinear optimization for which the goal is to minimize the sum of the squared differences between predictions of the network and the desired outputs over all the training patterns. The optimization technique used in this study was a sequential quadratic programming (SQP) routine (42, 43). This method approximates the objective function (training criterion) locally by a quadratic function so that quadratic programming can be used recursively.

From an optimization viewpoint, the traditional back propagation or steepest descent method can be interpreted as searching for a solution in the direction orthogonal to the linear approximation of the objective function. Thus the search direction is simply the derivative of the objective function with respect to the weights in the NN. SQP, on the other hand, makes a quadratic approximation of the objective function that takes into account the curvature of the objective function and identifies a better search direction.

In most training algorithms for MLF networks, the objective is to make the output data from the NN

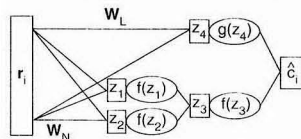


**Figure 8.** Flow diagram of the DLF network.

Note that two sets of weights are used here:  $W_N$  refers to the weights calculated for the nonlinear portion of NN and  $W_L$  refers to the weights calculated for the DLF part of the NN. Two different function transformations are used.

as close as possible to the desired values. One approach is to set the objective function to the sum of the squares of the differences between the desired and NN output for all outputs and all training patterns, and to find the proper weights that will minimize this objective function. However, finding the minimum of the objective function computed using the training data does not guarantee that the final model will have good prediction ability. In fact, when the objective function reaches the minimum, the model tends to fit the training data set exactly. To avoid overfitting, the procedures described in the model validation section have been adopted.

When the number of training samples is large, the prediction error is optimized on the number of hidden nodes, training iterations, and initial points. However, when the number of training samples is small, the selection criterion must also be optimized on the number of principal component scores. The learning speed of the DLF neural network can be improved by using the PCR regression vector,  $\mathbf{b}$ , to initialize the linear weights of the DLF network and by using principal component scores as input to the DLF network (dimensionality reduction) (44).

#### Model validation

The purpose of calibration in analytical chemistry is, more often than not, the prediction of calibrated properties in unknown samples. If only the calibration data are available, an approximation to the prediction error is calculated using a method called cross validation (45, 46). In this method, part of the data is left out, a model is constructed using the remaining data, and a prediction is made on the left-out data samples. This process is repeated until all of the data samples have been left out once. The most com-

monly applied method in calibration is called leave-one-out cross validation, in which each sample is left out, one at a time. The corresponding statistic, root mean squared error of cross validation (RMSECV) is

$$\text{RMSECV} = \sqrt{\frac{1}{I} \sum_{i=1}^I (c_i - \hat{c}_i)^2} \quad (15)$$

where  $I$  is the number of calibration samples and  $\hat{c}_i$  is the predicted concentration when a model is constructed without sample  $i$ . The simplest model selection scheme for PCR and PLS is to choose the pseudo-rank corresponding to the first minimum in a plot of pseudo-rank versus RMSECV (47). A similar approach is adopted for the nonlinear methods whereby the optimal model parameters are selected on the basis of a minimum calculated RMSECV value with respect to the available model parameters.

Alternatively, when both a calibration set and an additional prediction set are available, it is possible to use the root mean squared error of prediction (RMSEP) to select the appropriate model according to

$$\text{RMSEP} = \sqrt{\frac{1}{I} \sum_{i=1}^I (c_i - \hat{c}_i)^2} \quad (16)$$

where  $c_i$  is the  $i$ th prediction set concentration,  $\hat{c}_i$  is the estimate of that concentration value obtained with the model constructed using the available calibration set of samples, and  $I$  indicates the number of samples in the prediction data set. The major assumption with this type of approach to model selection is that the prediction data set must be representative of the expected future samples.

In this study the RMSECV statistic was employed for best model selection with data sets where only the calibration set of samples was available. For cases in which both calibration and prediction sets were available, the RMSEP statistic was used for model selection. All values have been converted to indicate the percent relative prediction (or cross validation) error according to

$$\% \text{ Rel. RMSEP} = \frac{\text{RMSEP} * 100}{\bar{c}} \quad (17)$$

where  $\bar{c}$  is the mean concentration value in the prediction set of sam-

Table I. Available software packages

Package	Methods	Supplier
Pirouette	PCA, PCR, PLS	Infometrix, Inc. 2200 Sixth Ave., Suite 833 Seattle, WA 98121
Unscrambler II	PCA, PCR, PLS, NN	Camo AS Olav Tryggv. gt 24 N-7011 Trondheim Norway
S-PLUS	PCA, PCR, PPR, ACE	Statistical Sciences, Inc. 1700 Westlake Ave. North, Suite 500 Seattle, WA 98109
MARS	MARS	Data Patterns 528 S. 45th St. Philadelphia, PA 19104
NeuralWorks Professional II-Plus	NN	NeuralWare, Inc. Building IV, Suite 227 Penn Center West Pittsburgh, PA 15276

ples. A similar expression is used for the percent relative RMSECV error where  $\bar{c}$  indicates the mean concentration value of the calibration set of samples.

#### Dimensionality reduction

For several data sets it was necessary to carry out a dimensionality reduction step before model construction with the various nonlinear methods. The dimensionality reduction step requires that the original instrument response matrix be decomposed into scores and loadings using either PCA or PLS. The nonlinear models are then constructed in a space spanned by a limited number of score vectors (12, 27, 44). In principle, the technique has the effect of increasing the numerical stability of the model construction process and reducing the amount of collinearity between variables (especially for spectroscopic methods of detection) along with the usual noise filtering.

The dimensionality reduction process can be reduced to four steps. First, the instrument response matrix ( $\mathbf{R}$ ) is decomposed into score and

loading vectors using either PCA or PLS. The model is then redefined to describe the relationship between the concentration vector ( $\mathbf{c}$ ) and the score vectors from the first step. The nonlinear models are then constructed to describe the relationship in the second step, and the best model is selected using the calculated statistics described in the model validation section.

#### Software and data sets

The routines for PCR, PLS, and LWR were written in house using Matlab, which was also used for generating the simulated emission data set. The PPR, ACE, and MARS programs (in Fortran) were obtained from Jerome H. Friedman (Department of Statistics, Stanford University, Stanford, CA). The NN calculations were performed using routines written in house (in Fortran), and the NPSOL package developed at the Department of Operations Research, Stanford University, was used for optimization. Table I contains a list of commercially available software; it is meant as a starting point for those

interested in obtaining further information but is not intended to be a comprehensive list of packages containing multivariate regression modules.

The attributes of the data sets analyzed in this study are summarized in Table II. The question of outlier detection was addressed for each data set. In cases where outliers were detected, the data set descriptions below do not include such samples.

#### Results

The criteria calculated and used to provide an estimate of the model predictive ability are listed in Table III for all the data sets and methods used in this study. All the values are percent relative prediction errors and are calculated using the approach described by Equation 16.

**Simulated emission data.** This data set was constructed to simulate the IR emission of a thin layer of material on a hot metal surface (48). Emissivity for the  $i$ th sample at the  $j$ th wavelength, given as a function of the absorbance  $A_{ij}$ , is

$$\epsilon_{ij} = \frac{[1 - p_1][1 - p_2 e^{-2A_{ij}/\log(e)}]}{1 - p_1 p_2 e^{-2A_{ij}/\log(e)}} \quad (18)$$

where  $p_1 = 0.05$ ,  $p_2 = 0.95$ , and the absorbance is linearly related to the concentration. The calibration data consists of 30 samples containing one chemical component, with evenly spaced concentrations ranging from 0 to 2.9. The emissivity was simulated for 40 channels, or wavelengths. Random numbers with zero mean and variance equal to 1% of the maximum emissivity were added to the  $\epsilon_{ij}$  values to simulate measurement error. A prediction set of 10,000 samples was similarly created and randomly covered the calibration space.

From Table III it can be seen that models constructed with PCR and PLS using two factors have the same predictive ability, and that the models constructed with the quadratic PCR and PLS algorithms have the same predictive ability compared with PCR and PLS. Both quadratic models require that the first two score vectors be transformed and incorporated into the model. The models are then constructed to describe the relationship between the concentration vector ( $\mathbf{c}$ ) and the augmented scores matrix (see Equation 6). Using a quadratic transformation on the score vectors does not improve the predictive ability of the con-

Table II. Characteristics of data sets

Data set	Calibration samples	Prediction samples	Independent variables	Model selection statistic
Emission	30	10,000	40	RMSEP
Taguchi	50	50	8	RMSEP
FIA	46	—	100	RMSECV
3M	163	—	32	RMSECV
Cargill-1	208	195	350	RMSEP
Cargill-2	60	—	700	RMSECV

**Table III. Percent relative prediction errors for data sets and methods**

Data set	C	PCR	PLS	PCR <sup>2</sup>	PLS <sup>2</sup>	LWR	PPR	ACE	MARS	NN
Emission (RMSEP)		2.07 (2)	2.07 (2)	2.07 (2, 4)	2.07 (2, 4)	0.90 (1, span = 0.1)	0.76 (1, M = 1)	0.76 (1)	0.83 (1, nk = 20)	0.76 (h = 1, DLF = 6)
Taguchi (RMSEP)	c1	22.57 (7)	21.61 (5)	18.34 (8, 15)	18.21 (7, 13)	11.06 (5, span = 0.4)	16.18 (0, M = 1)	13.80 (0)	10.25 (0, nk = 20)	5.82 (0, h = 2)
	c2	22.11 (8)	22.62 (3)	21.57 (5, 6)	21.46 (5, 6)	10.68 (5, span = 0.5)	16.87 (0, M = 1)	12.54 (0)	11.23 (0, nk = 20)	6.81 (0, h = 2)
FIA (RMSECV)	c1	3.69 (4)	3.65 (4)	3.72 (6, 10)	3.72 (4, 8)	3.26 (6, span = 0.9)	2.15 (9, M = 2)	3.79 (7)	4.10 (2, nk = 20)	3.28 (h = 1, DLF = 8)
3M (RMSECV)	c1	4.92 (10)	4.92 (7)	4.92 (8, 8)	4.92 (7, 7)	2.93 (4, span = 0.1)	2.74 (4, M = 1)	2.90 (7)	3.39 (7, nk = 20)	2.65 (0, h = 6)
Cargill-1 (RMSEP)	c1	2.18 (14)	2.12 (11)	2.28 (10, 10)	2.18 (8, 6)	2.17 (14, span = 1.0)	2.06 (6, M = 1)	2.23 (6)	2.19 (6, nk = 20)	2.07 (22, h = 5)
Cargill-2 (RMSECV)	c1	5.32 (4)	5.67 (2)	3.80 (9, 15)	2.85 (5, 9)	4.53 (5, span = 0.7)	2.72 (6, M = 1)	4.01 (4)	2.56 (6, nk = 20)	2.07 (25, h = 4)
	c2	1.34 (17)	1.28 (11)	0.71 (10, 16)	0.76 (11, 17)	0.67 (10, span = 0.6)	0.59 (9, M = 2)	0.75 (12)	0.76 (10, nk = 20)	0.56 (13, h = 4)

Values in parentheses describe model parameters of the best model constructed with each method.

PCR: No. of factors incorporated into the model.

PCR<sup>2</sup>: No. of transformed score vectors used to augment the score matrix; no. of principal components incorporated into the model.

PLS: No. of latent variables incorporated into the model.

PLS<sup>2</sup>: No. of transformed score vectors used to augment the score matrix; no. of latent variables incorporated into the model.

LWR: No. of factors; span equals fraction of total samples used.

PPR: No. of latent variables; M equals no. of terms/projection axes.

ACE: No. of latent variables.

MARS: No. of latent variables; nk is the maximum no. of subregions used.

NN: No. of factors as input; h is the no. of hidden nodes in NN architecture, DLF = length of PCR regression vector used to initialize the linear portion of the network.

Zero latent variables incorporated into the model denote that a model was constructed on the raw data and that no dimensionality reduction was carried out.

structed models because the relationship was generated by an exponential expression.

PPR, ACE, and MARS are actually PLS-PPR, PLS-ACE, and PLS-MARS, and the number of principal components listed in Table III refers to the number of score vectors supplied to the nonlinear algorithms. The best LWR model was constructed using the first principal component and a sample span equivalent to a 0.1 fraction of samples (or, alternatively, using 10% of the samples). For NN, the best model was obtained with 1 hidden node (h = 1). Here, the linear part of the DLF network was initialized with a 6-factor regression vector calculated using PCR.

Substantial improvements are obtained with the nonlinear methods (excluding the quadratic PCR and PLS algorithms) compared with PCR and PLS. No significant differences in the calculated predictive ability are observed among these nonlinear methods. Because the data set was simulated with an exponential term

in the relationship between concentration and responses, it is not surprising that all the nonlinear methods were capable of producing models with better predictive ability than that of PCR and PLS. Also, it shows the ability of the algorithms to construct good predictive models without having to assume any particular functionality. In this case, the quadratic transformation was not beneficial. In cases where there is uncertainty regarding the appropriate transformation, exploratory data analysis can be used to identify the appropriate transformation.

**Taguchi gas sensor data.** This data set was supplied by Pat Carey from the Department of Electrical Engineering, University of Washington (49), and consisted of 50 calibration samples and 50 prediction samples. An array of eight Taguchi gas sensors was used to measure responses to varying gaseous mixtures of toluene and benzene. Concentration information was provided for both constituents.

Table III lists the calculated rela-

tive prediction errors for toluene (c1) and benzene (c2) models. The PCR and PLS models constructed for toluene concentration prediction contained similar prediction errors. However, the fact that fewer PLS components were used to construct the PLS model is an indication that the PLS decomposition more efficiently spanned the concentration-dependent variance in the first few latent variables. The quadratic PCR and PLS models did not provide a significant improvement in predictive ability. Similar results were observed with the benzene concentration models.

Because the detection array consists of only eight sensors, it was not necessary to perform dimensionality reduction before constructing a model with PPR, ACE, MARS, and NN. Therefore, the values listed in Table III represent the relative prediction errors of the models constructed on the raw response data. However, dimensionality reduction was carried out for LWR in the form of PCA decomposition.



The LWR, PPR, ACE, and MARS models for both toluene and benzene had lower prediction errors compared with the PCR and PLS models. The NN approach constructs the model with the best predictive ability for both the toluene (c1) and benzene (c2) concentrations. The constructed NN models were substantially better than any other nonlinear models, and the best NN models for both toluene and benzene were constructed with a two-hidden-node DLF network architecture.

**FIA data.** This data set was provided by the FIA group at the Center for Process Analytical Chemistry at the University of Washington and consisted of 46 samples with varying concentrations of iron and nickel (50). Double-injection flow injection analysis with UV detection at 390 nm was used to calibrate for the iron concentration in the presence of the interfering nickel ions. All 46 samples were corrected with the aid of a reference sample, after which only mean-centering was employed as a preprocessing technique. The range of iron concentrations was 0–6 mM, with the mean concentration at 2.9 mM.

The prediction error of the model constructed with PPR provided the only result that is noticeably better than the remaining models (see Table III). Note that dimensionality reduction was carried out before the construction of LWR, PPR, ACE, and MARS models. Both PCR and PLS required four factors to construct a model, whereas the remaining methods used anywhere from two (MARS) to nine (PPR) factors. The NN model was constructed on the raw data using one hidden node, and the DLF weights were initialized with an eight-factor regression vector.

The fact that nine PLS score vectors were used to construct the PPR model indicates that some useful information contained in factors five through nine is not incorporated into the PCR and PLS models. For the remaining nonlinear models (excluding NN), various score vectors are used to construct models. The extent of nonlinearity in these score vectors is thus very small. Investigation of the score vectors and various constructed models confirms that the extent of curvature or nonlinearity in the data is very small and that good linear approximations may be obtainable.

**3M data.** These data, provided by the 3M company in St. Paul, MN, consisted of 163 samples. Each sample contains a quality control variable determined by 32 measurements. The

data set was taken from an optical-based measurement system so that the measurements are from either the raw sensor data or features derived from the raw sensor data.

The constructed PCR and PLS models have the same relative predictive ability as shown in Table III. Once again the PLS model uses fewer factors than the PCR model, indicating that PLS decomposition is a suitable method for dimensionality reduction before PPR, ACE, and MARS. The models constructed with the quadratic PCR and PLS algorithms did not provide improvements in predictive ability, and the remaining nonlinear methods provided substantial improvement in the calculated predictive ability compared with that of the PCR and PLS mod-

smooth, a fact confirmed by the knowledge that the response matrix is made up of discontinuous measurements (i.e., not spectroscopic). Methods relying on a specific transformation (quadratic PCR and PLS) were less suitable in this situation.

**Cargill-1 data.** These data were received from the Cargill Research Center in Minneapolis, MN. Near-IR reflectance spectra (1100–2498 nm, 4-nm spacing) were collected for each sample (soybeans harvested in 1990), and the second derivative was taken from the log (1/R) intensities. Calibration models were constructed for the prediction of the oil content (ranging from 17.1 to 23.1). There were originally 413 samples; 10 were removed as a result of outlier detection, 208 were used for calibration, and 195 were used for prediction.

All the models constructed for this data set have the same relative predictive ability. Looking at the number of latent variables used for the various methods (Table III), it may be observed that PPR, ACE, and MARS have constructed models with six latent variables. Dimensionality reduction was performed for this data set, which means that these nonlinear models were constructed on six PLS score vectors. This difference in the number of score vectors used for the nonlinear methods (6) and the number of components used for PCR (14) and PLS (11) tends to indicate that some nonlinearity exists in the first 6 latent variables. The same predictive ability can be achieved with PCR and PLS by incorporating a larger number of factors into the model.

Investigation of model concentration residuals showed that although the best predictive ability is obtained with 11 PLS factors, little improvement is obtained after incorporating 6 PLS factors into the model. This result may indicate that the data set is actually linear. An additional piece of evidence supporting the linear status of this data set is observed with the LWR model. Here, the best model is constructed using all the available calibration samples and the same number of factors used in the PCR model. Any nonlinearity would have required that a smaller number of samples be used to construct the regional or piecewise linear function approximations. The use of graphical diagnostics helped to determine that the models constructed with PPR, ACE, and MARS contained only a small degree of nonlinearity. Good linear approximations of the true underlying function-

**Several  
methods can do an  
equally good job  
at constructing  
models with  
good predictive  
ability**

els. The model constructed with MARS was noticeably better than the PCR and PLS models, but it was also substantially worse than the remaining nonlinear models. The NN model for this data set was constructed on the raw data using six hidden nodes.

Note that LWR constructs a model on the first four principal components and PPR constructs a nonlinear model on the first four PLS components. Thus these two methods are more efficient at modeling the relevant information present in the first few latent variables. Also, the fact that only 10% of the calibration samples were used to construct the local models for LWR indicates that the nonlinear functionality is not

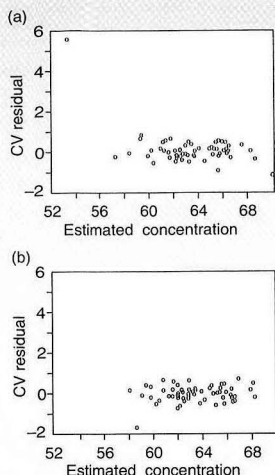


**Figure 9.** Cross validation concentration residual plots for the Cargill-2 data set (protein content). (a) PLS and (b) PPR. Note the presence of the point in the upper left-hand region of the PLS plot and the absence of the same point in the PPR plot.

ality were possible, as is evident by the good predictive ability obtained with the PCR and PLS models.

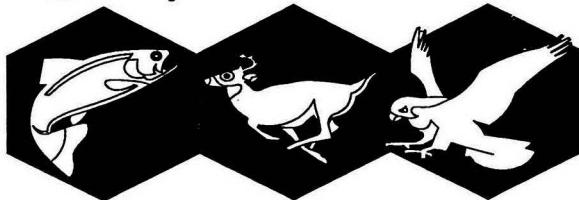
**Cargill-2 data.** This data set was received from Cargill Milling Division in Memphis, TN, and consisted of 60 calibration samples of corn gluten meal from a wet milling process. Continuous spectra were collected from a scanning monochromometer using 2-nm steps from 1100 to 2498 nm. Moisture and protein concentration values were supplied. The mean concentration values for moisture and protein were 10.5 and 63.3 percent w/w, respectively.

Table III shows that some improvement in the prediction ability is obtained by constructing nonlinear models for both moisture (c1) and protein (c2). Once again PLS was used for dimensionality reduction for PPR, ACE, and MARS, whereas PCA was used for LWR and NN. Note that the PLS models required fewer latent variables to obtain the same prediction error.

Further investigation resulted in the plot of the cross validation residuals for the PCR, PLS, and PPR models constructed for both c1 and c2. Note that for the PLS cross validation residuals one point has a very high value (Figure 9a) but that no

## Environmental Standards

### Quality is our #1 standard



#### Quantitative Standards Available from CIL:

- Chlorinated & Brominated Dioxins
- Chlorinated & Brominated Furans
- Polychlorinated Biphenyls (PCBs)
- Polynuclear Aromatic Hydrocarbons
- Performance Evaluation Standards
- Pollutants and Pesticides

# CIL

Call for product information  
and a free catalog.

**CAMBRIDGE ISOTOPE LABORATORIES**  
20 Commerce Way, Woburn, Massachusetts 01801  
800-322-1174 or 617-938-0067 (USA) 617-932-9721 (Fax) 800-643-7239 (Canada)

CIRCLE 18 ON READER SERVICE CARD

## NEWS FROM THE FRONTIERS OF RESEARCH

### Organometallics

The Monthly Journal of Vital  
Research Results  
Edited by Dr. Dietmar Seyferth  
Massachusetts Institute of Technology

ACS PUBLICATIONS

No other source brings you the latest breakthroughs in organometallic chemistry to light faster or more reliably than *Organometallics*. From the most current applications and findings on synthesis, structure, bonding, chemical reactivity and reaction mechanisms, this leading journal delivers it all!

See for yourself how you can shed new light on a field where change is a daily occurrence. Subscribe to *Organometallics* today!

#### Organometallics Subscription Rates

	U.S.	Canada & Mexico	Europe*	All Other Countries*
<b>ACS Members</b>				
1 year	\$ 79	\$104	\$141	\$160
2 years	\$142	\$192	\$266	\$304
<b>Nonmembers</b>	\$850	\$875	\$912	\$931

\* Air Delivery Included

#### Discover It Now

Call 1-800-333-9511

(U.S. only)

Outside the U.S. Call

614-447-3776

FAX 614-447-3671

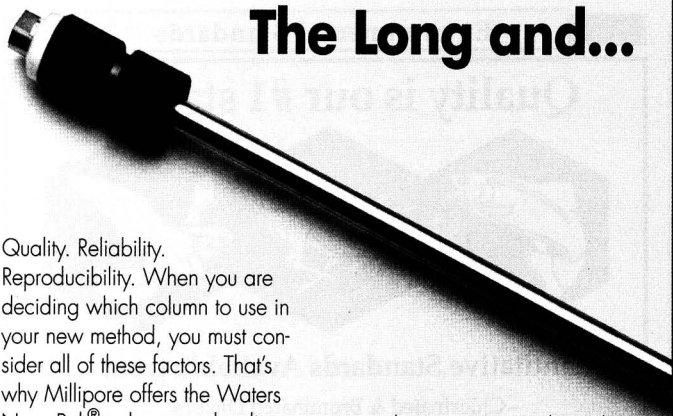
Or write to: American

Chemical Society (ACS)

Member and Subscriber Service

P.O. Box 3

Columbus, OH 43210-0003



# The Long and...

Quality. Reliability. Reproducibility. When you are deciding which column to use in your new method, you must consider all of these factors. That's why Millipore offers the Waters Nova-Pak® column product line. But what good is a column that offers all these features if it isn't the size column you want? Millipore knows that a variety of column choices is just as important as the quality of the column you buy. That's why we are

expanding our Nova-Pak product line from 3.9 diameter columns to include NEW Steel Cartridge columns in 4.6 x 150 mm and 4.6 x 250 mm dimensions. These steel cartridge columns are available in C<sub>18</sub> and C<sub>8</sub>, and with reusable, finger-tight endfittings.

CIRCLE 95 ON READER SERVICE CARD

such value is present for the PPR residuals (Figure 9b), an indication that the sample was not well described by the PCR and PLS models constructed without that sample. This is a high leverage point for PCR and PLS that influences the models so that the fit error for that sample is minimized.

The sample in question was not an obvious outlier in the score 1 versus score 2 space. It was, however, distinguishable in the third score vector. The cause of this deviation was a slight shift in the respective sample spectrum. It appears as though PPR and the remaining nonlinear methods are more robust to small perturbations in the instrument responses. This example represents the difficulties involved in defining what exactly an outlier is with respect to a nonlinear calibration model.

## Conclusions

We have seen that several methods can do an equally good job at constructing models with good predictive ability and that all the nonlinear methods construct models with better predictive ability than that of PCR and PLS when the data set contains nonlinearities. When the data set was predominantly linear (FIA

and Cargill-1 data sets), all the nonlinear methods were able to construct models with equivalent predictive ability compared with the models constructed using PCR and PLS.

Another interesting issue brought up during this study is the question of outlier definition and detection in nonlinear systems. As shown in the last data set, an outlier detected in a linear system may not necessarily be an outlier in a nonlinear system. The use of graphical diagnostics should be encouraged to aid outlier detection and model interpretation as well as to increase the level of confidence in the constructed multivariate calibration model. A good model is not just the result of a good model construction method, but rather it is the culmination of efforts incorporating sampling and experimental design, prior knowledge and experience, available data preprocessing techniques, data analysis methods, and statistical methods with which to evaluate the performance of the constructed model.

S.S. acknowledges the financial support of the ICI Chemometrics Fellowship. M.B.S. acknowledges the financial assistance of The Calgon Corporation for a Merck Fellowship. This work was also supported by the Center for Process Analytical Chemistry (CPAC), a National Sci-

## REPORT

ence Foundation Industry/University Cooperative Research Center at the University of Washington. All the authors would like to thank the following people and organizations for supplying the data sets and enabling us to carry out this study: the FIA group at CPAC, Tony Ervin at 3M, Mike Blackburn and Robert Kean from Cargill Inc., and Pat Carey at the Department of Electrical Engineering at the University of Washington.

## References

- (1) Miller, C.; Eichinger, B. E. *Appl. Spectrosc.* **1990**, *44*, 496.
- (2) Carey, W. P.; Wangen, L. E.; Dyke, J. T. *Anal. Chem.* **1989**, *61*, 1667.
- (3) Pell, R. J.; Erickson, B. C.; Hannah, R. W.; Callis, J. B.; Kowalski, B. R. *Anal. Chem.* **1988**, *60*, 2824.
- (4) Haaland, D.; Thomas, E. *Anal. Chem.* **1988**, *60*, 1202, 1208.
- (5) Miller, C. *Appl. Spectrosc.* **1989**, *43*, 1435.
- (6) Lindberg, W.; Clark, G. D.; Hanna, C. P.; Whitman, D. A.; Christian, G. D.; Ruzicka, J. *Anal. Chem.* **1990**, *62*, 849.
- (7) Seasholtz, M. B.; Archibald, D.; Lorber, A.; Kowalski, B. R. *Appl. Spectrosc.* **1989**, *43*, 1067.
- (8) Brown, S. D.; Bear, R. S.; Blank, T. B. *Anal. Chem.* **1992**, *64*, 22 R.
- (9) Beebe, K. R.; Kowalski, B. R. *Anal. Chem.* **1987**, *59*, 1007 A.
- (10) Gemperline, F. J.; Miller, K. H.; West, T. L.; Weinstein, J. E.; Hamilton, J. C.; Bray, J. T. *Anal. Chem.* **1992**, *64*, 523 A.
- (11) Erickson, C. L.; Lysaght, M. J.; Callis, J. B. *Anal. Chem.* **1992**, *64*, 1155 A.
- (12) Naes, T.; Isaksson, T.; Kowalski, B. R. *Anal. Chem.* **1990**, *62*, 664.
- (13) Vogt, N. B. *Chemom. Int. Lab. Sys.* **1989**, *7*, 119.
- (14) Wold, S.; Kettaneh-Wold, N.; Skagerberg, B. *Chemom. Int. Lab. Sys.* **1989**, *7*, 53.
- (15) Manne, R. *Chemom. Int. Lab. Sys.* **1987**, *2*, 187.
- (16) Lorber, A.; Wangen, L.; Kowalski, B. R. *J. Chemom.* **1987**, *1*, 19.
- (17) Martens, H.; Karstang, T.; Naes, T. *J. Chemom.* **1987**, *1*, 201.
- (18) Haaland, D.; Thomas, E. *Anal. Chem.* **1988**, *60*, 1193.
- (19) Höskuldsson, A. *J. Chemom.* **1988**, *2*, 211.
- (20) Thomas, E.; Haaland, D. *Anal. Chem.* **1990**, *62*, 1091.
- (21) Kowalski, B. R.; Seasholtz, M. B. *J. Chemom.* **1991**, *5*, 129.
- (22) Geladi, P.; Kowalski, B. R. *Anal. Chim. Acta* **1986**, *185*, 1.
- (23) Wold, S.; Esbensen, K.; Geladi, P. *Chemom. Int. Lab. Sys.* **1987**, *2*, 37.
- (24) Vogt, N. B. *Chemom. Int. Lab. Sys.* **1987**, *1*, 213.
- (25) Martens, H.; Naes, T. *Multivariate Calibration*; John Wiley and Sons: New York, 1989.
- (26) Martens, H.; Naes, T. *TRAC* **1984**, *3*, 204.
- (27) Simpson, D. G.; Guo, S.; Sacks, J.; Bietz, J. A.; Huebner, F.; Nelsen, T. *Chemom. Int. Lab. Sys.* **1991**, *10*, 155.
- (28) Frank, I. *Chemom. Int. Lab. Sys.* **1990**, *8*, 109.
- (29) Wold, S. *Chemom. Int. Lab. Sys.* **1992**, *14*, 71.
- (30) Cleveland, W.; Devlin, S. J. *Am. Stat. Assoc.* **1988**, *83*, 596.
- (31) Naes, T.; Isaksson, T. *Appl. Spectrosc.* **1992**, *46*, 34.
- (32) Naes, T. *Near InfraRed Spectroscopy*; Ellis Harwood: London, England, 1992.

- (33) Friedman, J. H.; Stuetzle, W. *J. Am. Stat. Assoc.* **1981**, 7, 817.  
 (34) Beebe, K. R.; Kowalski, B. R. *Anal. Chem.* **1988**, 60, 2273.  
 (35) Breiman, L.; Friedman, J. H. *J. Am. Stat. Assoc.* **1985**, 80, 580.  
 (36) De Veaux, R. D.; Steele, J. M. *Technometrics* **1989**, 31, 91.  
 (37) Friedman, J. H. Stanford University Technical Report No. 101, Stanford University, Stanford, CA, August 1988.  
 (38) Friedman, J. H. *Ann. Stat.* **1991**, 19, 1.  
 (39) Sekulic, S.; Kowalski, B. R. *J. Chemom.* **1992**, 6, 199.  
 (40) McClelland, J. L.; Rumelhart, D. E.; Hinton, G. E. In *Parallel Distributed Processing: Explorations in the Microstructure of Cognition, Vol. 1: Foundation*; Rumelhart, D. E.; McClelland, J. L., Eds.; MIT Press: Cambridge, MA, 1986.  
 (41) Lee, S. E.; Holt, B. R. *Proceedings of International Joint Conference of Neural Networks*; Baltimore, 1992; IV-549.  
 (42) Fletcher, R. *Practical Methods of Optimization, Vol. 2: Constrained Optimization*; John Wiley and Sons: New York and Toronto, 1981.  
 (43) Gill, P. E.; Murray, W.; Wright, M. H. *Practical Optimization*; Academic Press: London and New York, 1981.  
 (44) Gemperline, P. J.; Long, J. R.; Gregoriou, V. G. *Anal. Chem.* **1991**, 63, 2313.  
 (45) Stone, M. J. *Roy. Stat. Soc. B* **1974**, 36, 111.  
 (46) Wold, S. *Technometrics* **1978**, 20, 397.  
 (47) Osten, D. J. *Chemom.* **1989**, 2, 39.  
 (48) Pell, R. J. Ph.D. Dissertation, University of Washington, Seattle, 1990.  
 (49) Carey, W. P.; Yee, S. S. *Sens. Actuators* **1992**, 9, 113.  
 (50) Whitman, D. A.; Seasholtz, M. B.; Christian, G. D.; Ruzicka, J.; Kowalski, B. R. *Anal. Chem.* **1991**, 63, 775.



Ziyi Wang (left) is a Ph.D. candidate at the University of Washington. He holds a B.E. degree in computer science and engineering and M.S. degrees in computer science and analytical chemistry from the University of Science and Technology in China. His research focuses on nonlinear multivariate analysis, instrument standardization, and chemical neural networks.



Bruce R. Kowalski (right) is an Endowed Professor of Analytical Chemistry and chair of the faculty Board of Directors of the Center for Process Analytical Chemistry at the University of Washington. He received his B.S. degree from Millikin University (IL) in 1965 and his Ph.D. from the University of Washington in 1969. Kowalski's research interests include the use of chemometrics to enhance industrial process control and optimization.



Samuel E. Lee (left) is employed at Ford Motor Co. in Dearborn, MI, where he is pursuing his interest in process monitoring, identification, and control in combination with neural networks. He received his B.S. degree in 1983 from the University of California, Berkeley, his M.S. degree in 1985 from Northwestern University, and his Ph.D. in chemical engineering in 1993 from the University of Washington.




Bradley R. Holt (right) is an associate professor of chemical engineering at the University of Washington. He received his B.S. degree in 1979 from the University of Minnesota and his Ph.D. in chemical engineering in 1984 from the University of Wisconsin. Before joining the faculty of the University of Washington, he held positions with General Motors, Atlantic Richfield, and Shell Oil.



Sonja Sekulic (left) received her B.Sc. degree in chemistry and computer science and her Ph.D. in analytical chemistry from the University of New South Wales. She then began working for ICI Pharmaceuticals, which granted her a fellowship to do postdoctoral research under the direction of Bruce Kowalski at CPAC. Her research interests include linear and nonlinear multivariate calibration techniques.



Mary Beth Seasholtz (right) received her B.S. degree in chemistry from Lebanon Valley College (PA) and her M.S. degree in applied math and Ph.D. in chemistry from the University of Washington. She is currently employed at the Dow Chemical Co. in Midland, MI, where she uses chemometrics to improve process analytical measurement systems.



## ...short of it.

And now Nova-Pak® cartridge columns come in NEW, short lengths—5, 10 and 15 cm, and in the chemistries you need—C<sub>18</sub>, C<sub>8</sub>, Phenyl, CN and Silica. We have long columns, short columns, five chemistries and sixteen dimensions, making Nova-Pak the most complete line of columns available. Choosing Waters™ Nova-Pak steel cartridges or columns for your method guarantees top quality and offers unlimited choices. And that's the long and short of it!

If you act today, you will receive a free set of endfittings with the purchase of any three Nova-Pak cartridge columns.

Call **1-800-252-4752, Press 1** and ask for promotion XC6 to receive your free offer.

**MILLIPORE**  
Waters Chromatography

CIRCLE 95 ON READER SERVICE CARD

# Mozart and Microcolumns

## The 15th International Symposium on Capillary Chromatography



---

**Wolfgang Bertsch**

Department of Chemistry  
University of Alabama  
Lloyd Hall, Box 870336  
Tuscaloosa, AL 35487-0336

---

Capillary chromatography has traditionally been associated with terms such as high resolution, speed, and low detection limits. For some time now, chromatographers have relied on capillary and microcolumn methods to solve a variety of separation problems, so it's not surprising that after 18 years the International Symposium on Capillary Chromatography, held each spring in Riva del Garda, Italy, is always well attended.

The symposium has a long and distinguished history. In 1975 Rudolf

E. Kaiser of the Institute for Chromatography in Bad Dürkheim, Germany, organized the first meeting in the picturesque village of Hindelang, located in the Bavarian Alps of southern Germany. Some 143 chromatographers, more than had been expected, attended the conference and enjoyed three exciting days of

### **FOCUS**

presentations and live experiments conducted on stage by speakers such as Kurt Grob. Gas cylinders were laid flat under tables at the front of the lecture hall and, on more than one occasion, the room went dark because the wiring of the hotel was not equipped to handle the electrical

peak loads of the instruments used in the demonstrations.

Success has its price. The first four symposia, conducted biennially, grew larger and larger. The hotel and conference facilities in Hindelang were no longer adequate for the large number of visitors, and Kaiser, who had almost single-handedly organized all aspects of the conference, withdrew after the fourth symposium in 1981. Pat Sandra of the State University of Ghent in Belgium filled the void. He moved the symposium from Hindelang to the equally picturesque Riva del Garda, where it thrived—the 1983 conference boasted 93 presentations.

Participants in the early meetings were die-hard capillary (open-tubular) column gas chromatographers. The newer generation includes a siz-



able contingent of scientists who specialize in supercritical fluid extraction (SFE) technology, electro-driven separations and instrument interfacing, and other applied fields. But they all have one thing in common: the exploitation of miniaturized systems to solve difficult analytical problems.

This year's symposium, which was held May 24–27, hosted 749 participants and guests—about the same number present at the previous meeting. Chromatographers from 38 countries attended. The Italian colleagues were the largest group, followed by German, British, and Swiss scientists. In addition, a respectable force of 60 chromatographers from the United States participated. (In the early years of the symposium, very few American scientists took the trip to Europe.)

The organizers attempted to retain some of the concepts that made the original symposia so successful. Three or four short plenary lectures were presented each day in the morning and early afternoon. An exhibition, poster sessions, workshop seminars, short courses, and users meetings were held throughout the rest of the day, and panel discussions took place in the evenings.

The organizers have preserved another special feature of the Hinde-lang symposia. In addition to chromatography, participants at Riva del Garda are exposed to a healthy dose of classical music. This year, the 30-member Milano Classica Ensemble played a Mozart program that included the well-known Concert in A Major for clarinet and orchestra. The sponsored social program offered everything from catered receptions in front of the harbor to nights at the disco.

The conference opened with the presentation of the M.J.E. Golay Award to Konrad Grob of Kantonales Labor in Zürich, Switzerland. Grob was honored for his contributions in the general area of GC and related techniques. In his lecture, "What Hinders the Further Development of Capillary GC?", Grob contended that the current environment of GC has begun to stagnate with regard to innovation, and he pointed out that in spite of the relatively high profile the technique has achieved over the years, much remains to be done. He noted the rise of "expert bottle crimpers" and "cookbook recipes" in the field and lamented that incentives for experimentation are often taken away by laboratory managers interested only in efficiency.

A general session on capillary methods followed Grob's lecture. M. Novotny of Indiana University in Bloomington discussed high-performance capillary electrophoresis (HPCE) of biopolymers under pulsed fields. In contrast to conventional chromatography, which suffers size limitations for large ions and molecules, CE with free buffers or entangled polymer solutions imposes virtually no limitations with respect to the size of the ion, he said.

In a discussion of new developments in miniaturized systems, A. Manz of Ciba-Geigy in Basel, Switzerland, reported on advances in silicon chip technology that allow greater precision in the manufacture

selective phases, was followed by a lively discussion.

R. S. Ramsey of Oak Ridge National Laboratory in Oak Ridge, TN, said that the ion trap mass spectrometer generally offers greater sensitivity and broader capabilities than other mass analyzers in obtaining structural information. Ramsey presented applications of ion trap MS for conventional chromatography and for CE, including an example of broadband collisionally activated dissociation that was used to elucidate the structure of neurotensin from a sample of only 0.9 pg.

F. Dondi of the University of Ferrara in Ferrara, Italy, introduced the audience to Fourier analysis for de-



of well-defined microchannels and cells. Manz described the performance of a chip-based absorbance detector with an optical pathlength of 1 mm and a volume of only 1 nL and demonstrated that in some applications of CE, more than 100,000 theoretical plates could be produced in < 20 s.

J. L. Brazier of the Université Claude Bernard in Lyon, France, showed that GC coupled with atomic emission detection can be a highly specific method for detecting biomolecules and metabolites labeled with stable isotopes. He said that detection limits achieved with GC and atomic emission detection are often considerably better than those obtained by other methods, including MS.

The afternoon session also covered a wide range of topics. G. Schomburg of the Max-Planck Institut für Kohlenforschung in Mülheim-Ruhr, Germany, discussed the use of cyclodextrins and derivatives as chiral selectors in chromatography and CE. The presentation, which contained a wealth of information on enantio-

termining chromatographic performance and peak overlapping in multicomponent mixtures. The lecture started with a demonstration of the severe overlap that often occurs in practice, even with so-called high-resolution columns. Dondi then presented a general expression of the power spectrum of a chromatogram.

#### Capillary column GC

The morning session on the second day focused on capillary column GC. Before the start of the scientific program, H. McNair of Virginia Polytechnic Institute and State University in Blacksburg, VA, and K. Cramers of Eindhoven Institute of Technology in Eindhoven, The Netherlands, were honored with the Tswett Medal for their contributions to chromatography. The presentation was made by K. I. Sakodinskii of the Association of Chromatographers M. S. Tswett in Moscow, Russia.

P. Ciccioli of CNR in Monterotondo, Italy, presented a broad-based lecture on the analysis of volatile organic compounds (VOCs) in the atmosphere. He reviewed technical

approaches to VOC analysis and discussed optimization strategies for sampling and sample preparation. Although on-line sampling is preferable, he said, it cannot always be used, especially in cases where samples must be taken from remote locations. In addition, passivated canisters must be used for highly volatile components in spite of problems with container reactivity and background contributions. Ciccioli also discussed water problems. Present in huge excess, water often overshadows trace components of interest. With cryogenic sample introduction, ice can form at the column inlet, effectively shutting down sample transfer.

These problems were also addressed by A. Tipler of Perkin Elmer in Beaconsfield, U.K., who presented an on-line system for VOC analysis and discussed the role of drying agents. Most drying agents are either reactive or adsorptive, and Tipler compared the performance of membrane-based systems to dryer/adsorbent approaches. The latter seem to be superior, and  $\text{CaCO}_3$  appears to be the most suitable drying agent for VOC analysis, he concluded.

The last two presentations of the session dealt with polychlorinated biphenyl (PCB) determinations and narrow-bore, thick-film columns. B. Larsen of CEC Joint Research Center in Ispra, Italy, discussed routine isomer-specific determination of PCBs using multicolumn techniques. Presenting retention and resolution data for about a dozen stationary phases, Larsen pointed out that no single phase is capable of resolving all 209 possible isomers or even all 150 of the isomers that might be present in the environment. Depending on the specific situation, serial, parallel, and multidimensional systems all have analytical advantages and disadvantages.

Pat Sandra demonstrated the usefulness of 50- $\mu\text{m}$ -i.d. thick-film columns for fast analysis. He showed that either GC or SFC can readily be performed with these columns but that LC is more limited. Although LC separations in these columns suffer from low efficiency, proteins can still be separated by this method because the inertness of well-deactivated fused silica favors the separation.

#### Hyphenated techniques

On the afternoon of the second day, U.A.T. Brinkman of the Free University in Amsterdam, The Netherlands, introduced a fully automated water

analyzer based on on-line solid-phase extraction (SPE) and capillary column GC for the determination of pesticides. Organics dissolved in water are preconcentrated on a polymeric LC-type stationary phase. After cleanup and drying, the analyte is desorbed with ethyl acetate and transferred to a GC column via a retention gap under conditions of concurrent solvent evaporation. By using MS as a detector, Brinkman said, detection limits as low as 5 pg can be obtained.

J.G.J. Mol of Eindhoven University of Technology provided a different approach to the general problem of determining trace organics in water. He suggested a valve-based

## Pressure-counterbalanced CE increases the time analytes spend in the applied electric field

sample introduction system to eliminate water prior to introduction into a capillary column via a programmed-temperature vaporizer injector.

Another presentation, by P. Uden of the University of Massachusetts at Amherst, concerned the determination of metals by GC with atomic emission detection. Emission spectrometry has matured to the point where it can be considered routine, he said.

#### Micro LC

On the third morning of the conference, R. T. Kennedy of the University of Florida in Gainesville presented a system for rapid high-resolution separation of peptides by packed capillary column LC. The best results were obtained for pellicular particles packed into 50- $\mu\text{m}$  col-

umns, and 7000 theoretical plates were achieved in 10 s on these slurry-packed columns.

M. Ursem of LC Packings in San Francisco, CA, discussed the benefits of capillary column LC in protein or peptide sequencing and showed how information can be gained from picomole quantities of the peptide. Ursem introduced an on-line blotting procedure based on the deposition of the eluate onto a membrane. Capillary LC followed by 2D polyacrylamide gel electrophoresis was also used for mapping proteins.

K. E. Karlson of Astra Hässle in Mölndahl, Sweden, showed how HPLC microcolumns can be used in conjunction with MS methods. He compared conventional electrospray MS in sector instruments with a system in which deuterated water is used as the mobile phase. Hydrogen atoms bound to heteroatoms are readily exchanged for deuterium under such conditions, and reference compounds are not necessary.

A. C. van Asten of the University of Amsterdam, The Netherlands, introduced the audience to the use of thermal field-flow fractionation (ThFFF) for the separation and characterization of polymers. Polymer species are separated according to both size and chemical characteristics. Large temperature gradients favor separation, and ThFFF becomes more efficient with increasing molecular weight of the polymer. It is advantageous to make the channel as narrow as possible, van Asten said, but there are practical limitations.

#### Electromigration

In the Thursday morning session, J. W. Jorgenson of the University of North Carolina at Chapel Hill described pressure-counterbalanced CE, in which pressure is used to counterbalance the electroosmotic flow, thereby increasing the time analytes spend in the applied electric field. In this new approach, resolution can be improved by moving the analytes back and forth over the detection window. Jorgenson used the separation of tagged leucine and isoleucine to demonstrate the concept. The system generated around 4 million plates for 15 passes, although some loss of peak area resulted.

S. Terabe of the Himeji Institute of Technology in Hyogo, Japan, talked about the effect of surfactant structures on conductivity in micellar electrokinetic chromatography. Sodium salts of fatty acids were used to investigate the relationship between the structures of surfactants, the dis-

tribution coefficients between the micellar and aqueous phases, and the thermodynamic properties of micellar solubilization. Terabe showed that a change of entropy in the system had a significant effect on selectivity for many substances.

M.W.F. Nielen of Akzo in Arnhem, The Netherlands, demonstrated the enantioseparation of basic drugs by cyclodextrin-modified CE. Ten compounds with rather different molecular structures were separated by adding a suitable cyclodextrin chiral selector to the buffer. For several commercially available cyclodextrins tested, Nielen said, resolution depended not only on the particular cyclodextrin and its concentration, but also on the strength of the applied field. Impurities down to 0.5% of the isomer are detectable by this method, and sample throughput can be increased by injecting samples while the previous analysis is still in progress.

The advantages of diode array detection in CE were discussed by D. N. Heiger of Hewlett Packard in Waldbronn, Germany. Various strategies can be used to overcome some of the sensitivity limitations imposed by minimum volume and pathlength requirements in detector cells. In addition to the optimization of chemical parameters leading to background noise reduction, cell geometries other than the conventional cylindrical arrangements can be used. Heiger compared the performance of a "bubble cell" design with those of conventional cells. The bubble cell design improved the detection limit by three- to fivefold, with no appreciable loss in efficiency or resolution.

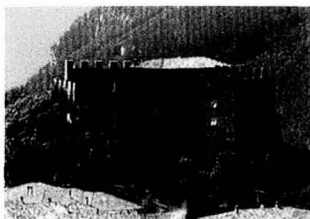
#### Dovetailing with SFE

The last session of the symposium also constituted the first session of the 2nd European Symposium on Analytical Supercritical Fluid Chromatography and Extraction. That meeting, held on Thursday afternoon and Friday, was organized by K. Markides, K. Bartle, H. Engelhardt, and P. Sandra. The timing was influenced by considerations of convenience and cost; many attendees of the chromatography symposium decided to stay for one extra day in Riva del Garda.

Some 220 chromatographers registered for the SFC/SFE meeting. The first speaker of the joint session was M. Lee of Brigham Young University in Provo, UT. Lee's presentation, "Supercritical Fluid Chromatography with Packed Columns," came as something of a surprise, considering

his pioneering work in capillary column SFC. Lee said that many limitations of conventional short packed columns can be overcome with new packing techniques and the use of  $\text{CO}_2$  as the carrier fluid. More than 240,000 theoretical plates were generated on a 10-m packed SFC column, and the chromatograms shown resembled those typically seen for capillary column GC.

P. Peterson of Uppsala University in Sweden presented information on retention time and peak width models for chiral separations in open-tubular SFC. Peterson demonstrated a factor analysis approach to optimizing the influence of temperature and density on retention time and peak width and showed that a small number of experiments is adequate to model the performance of different stationary phases under varying conditions. The system was demonstrated with the enantioseparation of an anticonvulsant drug.



F. David of the Research Institute for Chromatography in Kortrijk, Belgium, presented a paper on optimizing selectivity in SFE with capillary GC and HPLC for the determination of pollutants in different matrices. Careful optimization of the conditions used in SFE largely eliminates unnecessary background contributions from the matrix, leading to improved chromatographic separation. David showed that polycyclic aromatic hydrocarbons (PAHs) and PCBs can be extracted effectively from fat-containing matrices by using  $\text{CO}_2$  at medium density, but that selectivity is lost as the extraction fluid becomes more dense. However, selectivity can be introduced into a system even if fats are co-extracted with a high-density fluid if a solid-phase trap with silica gel is used to remove fats from the PAH samples after the initial extraction.

In the last presentation, T. Chester of Procter & Gamble in Cincinnati, OH, discussed retention and selectivity in high-temperature, high-pressure, open-tubular column SFC with  $\text{CO}_2$  as the mobile phase. Using

a variety of test mixtures, he investigated the three most effective phases and recorded selectivities for difficult solute pairs of interest. Large shifts in selectivity were observed for the biphenyl and cyanopropyl stationary phases. Chester said that adjusting the temperature is an effective way to exploit relatively small differences in molecular structures on such selective phases, but that unfortunately, the pressures needed often exceed the capabilities of currently available instrumentation. He expressed the hope that instrument manufacturers would recognize the benefits of expanding the range and introduce hardware capable of providing higher pressures.

L. Ettre of Perkin Elmer in Norwalk, CT, gave the closing address. He noted that the attendance at lectures was good up to the last day—no mean feat considering the multitude of parallel activities taking place at the symposium. He also praised symposium organizers for making available a large number of scholarships to students from both Europe and overseas.

The conference proceedings were published in two hefty volumes containing 1744 pages. Copies of these proceedings and some from previous capillary column meetings may be obtained from IOPMS (see below).

The 16th Capillary Chromatography Symposium will be held in September 1994 to avoid overlap with HPLC '94, which is scheduled for May 1994 in Minneapolis, MN. Information can be obtained from IOPMS, Kennedy Park 20, B-8500 Kortrijk, Belgium, phone (32) 56-204960; fax (32) 56-204859.



*Wolfgang Bertsch received his B.S. degree in chemical engineering from the Technicum für Chemie und Physik in Isny, Germany, and his Ph.D. in chemistry from the University of Houston under the direction of Al Zlatkis. His research interests lie primarily in the analysis of volatiles by GC/MS. Since 1974 he has been a member of the chemistry faculty at the University of Alabama in Tuscaloosa. He is an editor of the Journal of High Resolution Chromatography.*

# NEW PRODUCTS



**Field emission scanning electron microscope Model 1910FE** contains a three-element Schottky field emission gun and operates in the range of 0–30 kV with resolution of 1.5 nm at 30 kV. The microscope and controlling software perform automatic image focusing, digital image processing, and image archiving. The microscope contains a 5-axis, 4-in.-motion universal specimen stage, accommodates samples up to 6 in. in diameter, and uses a three-stage pump to maintain vacuum in the range of  $10^{-12}$  Pa. Amray **402**

## Instrumentation

**Spectroscopy.** SpectraPro-150 compact imaging spectrograph and monochromator features an astigmatism-corrected optical system and imaging capabilities for multichannel CCD-based spectroscopy and has a footprint of 7 × 7 in. The spectrograph, which has a 155-mm focal length and a 25-mm-wide focal plane, offers 5 nm/mm dispersion. The unit contains a built-in stepping motor wavelength drive for use as a monochromator with 0.4-nm resolution and can be integrated into an automated spectral data acquisition system. Acton Research **401**

**Particle size analysis.** Fractional sample cell for the LA-900 Particle Size Analyzer is designed for measuring very small amounts of sample

or for minimizing dispersed-phased volumes. The 10-mL cell can be interchanged with either a flow-through cell or a dry feed cell and can be used for measurements in the size range of 0.04–1000  $\mu\text{m}$ . Horiba **403**

**MALDI-TOFMS.** LaserTec Bench-Top II mass spectrometer for MALDI-TOF is compact (20 × 24 × 36 in.) and contains a vertical 0.7-m linear flight tube and a nitrogen laser. It includes a video monitor for viewing samples and a joystick for fast adjustment of sample position on a 100-sample, 50 × 50 mm plate. Intelligent automation optimizes laser intensity and sample position for unattended operation. A 1.2-m linear flight tube and a high-performance 2.4-m reflector analyzer are optional. Vestec **404**

**UV-vis spectroscopy.** UV-vis detector Model 119 operates in single- or dual-wavelength and scan modes. The detector can scan from 190 to 700 nm without manual interruption and uses digital signal processing to filter out noise and stabilize baselines. Features include automatic parameter changes during a run, on-screen help, autorepeat, and autozero. Gilson Medical Electronics **405**

**Electrochemistry.** Electrochemical impedance analyzer Model 6310 combines potentiostatic circuitry with phase-sensitive detection. Impedance software allows performance of single-sine measurements from 100 kHz down to 50  $\mu\text{Hz}$  as well as pseudo-random noise or multisine measurements from 50  $\mu\text{Hz}$  to 10 Hz. Additional electrochemical software provides real-time plotting with high-resolution graphics. EG&G Princeton Applied Research **406**

**DNA analysis.** QPCR System 5000 for quantitative polymerase chain reaction analyses uses electrically initiated chemiluminescence rather than radiolabeling for quantitation of PCR products or of the original copies of target DNA down to the attomole level. The computer-controlled system can process 50 samples per hour. Perkin Elmer **407**

**IR.** Multicomponent IR process analyzer Model 2550 with single-beam optics is designed for continuous process or environmental monitoring of up to four gases in a sample stream. Intrinsic error and linear error are within 1% full-scale deflection, and repeatability is within 0.5%. The microprocessor-controlled analyzer can be placed up to 1650 ft. away from the control panel for hazardous applications. Options include electrically heated or steam-heated sample cells as well as pressure sensors for barometric and sample pressure compensation. Servomex **408**

For more information, please circle the appropriate numbers on one of our Reader Service Cards.





**Laser reflectance measurement system Model LRMS-600** measures total integrated reflectance from surfaces in the spectral region of 250–2500 nm in setups with a user's laser source. The system contains a 150-mm-diameter integrating sphere with a diffuse reflectance surface coating, transfer optics, a detector assembly, and a controller for manual or computer control. Labsphere 409

**Data acquisition.** Single-channel chromatography data acquisition and integration system Model 717

for GC or HPLC contains an A/D converter board that runs at a 100-Hz sampling rate and fits into a half-length PC bus slot. Also included are chromatography software as well as detector and flag cables. The system expands, scales, or displays data in two different time axes simultaneously during collection, then optimizes integration parameters, draws baselines, and labels peaks after the run. Manual baseline changes can be reintegrated, and options are included for HPLC pump control, vial barcode identification, and linking to networks. Axiom Chromatography 410

## Software

**FT.** Fourier Toolkit software contains the calculation capabilities of Fourier Analyzer, Transfer Function Analyzer, and Harmonic Analyzer software packages. It performs time domain and frequency domain transforms, including fast and discrete FT and their inverses, and calculates power spectral density. Data filters include exponential and moving average filters for time domain trans-

forms and low, high, or bandpass filters for frequency domain transforms. The software includes Hanning, Hamming, Blackman, and Bartlett windowing functions. It calculates autocorrelation and covariance, cross-correlation and cross-covariance, and convolution for complex data sets. Dynacomp 411

**Spectrometry.** Xspec modular spectrometry data processing and analysis software for UNIX computers includes programs for  $n$ -dimensional NMR, FT-MS and TOFMS, IR, and EPR, as well as a program for automated peak assignment and spectral interpretation. The modules all feature a mouse-manipulated graphics user interface, multiple spectral display capability, and WYSIWYG plotting and annotation for HPGL and PostScript output devices. The software runs on Sun SPARC, Silicon Graphics, IBM, and Macintosh platforms. Bruker 412

**Property prediction.** InStep v1.0 category and property prediction software package uses macro tools and statistical models produced by Pirouette software to generate an ex-

# The BURLEIGH INSTRUCTIONAL STM™ Transforms Atomic Theory Into Atomic Reality



**Complete System <\$15,000\***  
Includes control electronics, STM scanning head, sample set, sampling kit, instruction manual, and student workbook.

**High Performance, Student Proof Experiential Learning System Allows First Time Users to View Atoms and Measure Them... Quickly and Easily**

- Comprehensive Scanning Tunneling Microscope System designed specifically for classroom use.
- Easy to operate even for first time users — supplied with step-by-step Quick Start instructions.
- Laboratory workbook provides predefined experiments along with theory and history of microscopy — prequalified sample set enclosed.
- Windows-based True Image™ software for your 386/486 computer provides sub-angstrom image resolution and precise three dimensional measurements.
- Proven system with over 150 in use by colleges, universities, and high schools worldwide.

For more information and a demonstration video call 716/924-9355, FAX: 716/924-9072 or write:

**burleigh**

Reliable Precision  
Burleigh Instruments Inc.  
Burleigh Park, Fishers, NY 14453  
716/924-9355 • FAX: 716/924-9072

\*U.S. Prices

In the U.K.: Burleigh Instruments LTD (0582) 766888 • FAX: (0582) 767888 In Europe: Burleigh Instruments GmbH (06157) 3047 • FAX: (06157) 7530 In Japan: Techscience Ltd. 0489 (64) 3111 • FAX: 0489 (65) 1500

CIRCLE 15 ON READER SERVICE CARD

ANALYTICAL CHEMISTRY, VOL. 65, NO. 19, OCTOBER 1, 1993 • 853 A



## NEW PRODUCTS

pert system based on classification, regression, or combined models for a particular application. The software can be coupled to analytical instrument systems to function as a turn-key custom analyzer that produces control charts and tables for QC. The package runs under Windows 3.0 on a 386 or higher level PC with 4 MB RAM and 5 MB free hard disk space. InfoMetrix **413**

**HPLC.** "Separation Modes in HPLC" software tutorial package presents stationary phases, separation mechanisms, and practical applications for HPLC, RPLC, SEC, IEC, and chiral separations. The topics are illustrated with animated graphics in an interactive mouse-controlled user interface. The software requires a 286 or higher level PC with 1 MB RAM, 2 MB free space on a hard disk, and Windows 3.0. Phenomenex **414**

### Manufacturers' Literature

**HPCPC.** Literature describes a method for determining the hydrophobicity of drugs by measuring

their partition coefficients in an octanol/water system using high-performance centrifugal partition chromatography. The literature features the Series 1000X benchtop HPCPC column module. Sanki **415**

**GC.** Brochure describes the use of retention indexes as a specification for capillary GC column performance. Equations, definitions, and sample chromatograms are included. 4 pp. J&W Scientific **416**

**OES.** Data sheet describes the Spectrovac 2000 arc/spark optical emission spectrometer, a vacuum spectrometer system with 60-channel capacity. Specifications and operational requirements are listed, as are software features and the advantages of using a DC arc source. Baird Analytical **417**

**GC/MS.** Technical note describes advantages of a chemical ionization source in the MD 800 GC/MS system. The system contains CI and EI sources, and a turbo pump-based vacuum system switches between them for a downtime of 15–20 min. 2 pp. Fisons **418**

**Biopolymer analysis.** Brochure describes four systems for separating, determining, and sequencing proteins, peptides, and nucleotides. Included are the Quanta 4000E CE system with membrane fraction collection for real-time membrane blotting; the AccQ-Tag amino acid analysis system, a dedicated HPLC system with prepackaged eluent and fluorescence-labeling derivatizing reagents; the Bioscovery System for peptide mapping, protein microisolation, and DNA or RNA analysis; and LC/MS systems. 4 pp. Millipore/Waters Chromatography **419**

**GC.** Brochure describes the use of a purge-and-trap system for headspace and thermal desorption GC determinations of VOCs in foods and beverages. Also mentioned are an autosampler and an off-line purge unit for large samples ranging from 350 to 1000 mL. Sample chromatograms and run conditions are included. 8 pp. Chrompack **420**

**TOFMS.** "Proceedings of the International Conference on Instrumentation for Time-of-Flight Mass Spec-

Sample preparation for XRF-AA-ICP-CHEM.

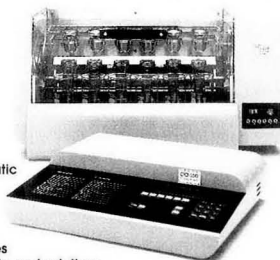
**To Bis! or not to Bis!**  
That is the question!

**claisse**  
FLUXER BIS!

The most sophisticated automatic microprocessor controlled fusion apparatus that...

- processes almost all kinds of samples
- prepares glass disks and solutions
- makes six samples at one time
- can be modified to make 100 solutions per hour
- uses propane or butane, no oxygen.

Most competitive pricing. With sale, free training trip to Quebec City.



Call or write to the most experienced people on fusion for information.



corporation  
scientifique  
claisse inc.

2522, chemin Sainte-Foy  
Sainte-Foy (Québec)  
Canada G1V 1T5  
Tel: (418) 656-6453  
Fax: (418) 656-1169  
Telex: 051-31731

**The First and Finest in Fusion**

CIRCLE 20 ON READER SERVICE CARD

## Great Research Is Surfacing...

...every month in **LANGMUIR**,  
the Journal of Surfaces and Colloids

If you are involved with any aspect of surface and colloid chemistry, *Langmuir* is required reading. Published by the American Chemical Society, this monthly journal presents cutting-edge primary research as well as applied and theoretical perspectives on all aspects of this dynamic, multidisciplinary field. Get the most comprehensive coverage of the latest and most important developments in one convenient source.

**Benefit from original, peer-reviewed research on:**

Liquid State Surface Chemistry...  
Surface Chemical Physics...Disperse  
Systems...Electrochemistry...Surface Structure...and more!

**Stay on top of the latest developments...Subscribe today!**

**By phone:** Toll-free: 1-800-333-9511 (within U.S.), (614) 447-3776 (outside U.S.); **By fax:** (614) 447-3671; **By mail:** American Chemical Society, Member and Subscriber Services, P.O. Box 3337, Columbus, OH 43210

	U.S.	Canada and Mexico	Europe Air Service Included	All Other Countries Air Service Included
<b>ACS Members</b>				
One Year	\$ 68	\$ 89	\$116	\$129
Two Years	\$122	\$164	\$218	\$244
<b>Nonmembers</b>	\$715	\$736	\$763	\$776

trometry" contains 17 technical papers and a report of the meeting, which was held Nov. 11-12, 1992. Topics include instrument design, continuous ion sources, detectors and signal processing, and hyphenated techniques. The book also provides a list of participants and an author index. 244 pp. LeCroy 421

## Catalogs

**Environmental QC.** Catalog of certified EPA and A2LA environmental standards lists constituents and ampule volumes for EPA standards for Method series 500, 600, and 8000, as well as for A2LA certified GC/MS high-concentration reference materials; semivolatiles internal, surrogate, and matrix spike standards; and certified pesticide, TCLP, and PCB solution standards. EPA standards in neat form are also listed. The catalog includes an illustrated description of the certification process as well as a question-and-answer section. 18 pp. Ultra Scientific 422

**Microfiltration.** Product selection guide describes microfiltration membranes and devices. Micrographs, specification and conversion tables, and typical applications are provided. Membrane types include polycarbonate and polyester screen, silver, silica-free PVC, nylon, and mixed cellulose ester. Ceramic and glass fiber filters, water purification systems, and centrifugal separators are presented. 76 pp. Poretics 423

**Labware.** Catalog of platinum laboratory supplies includes illustrations and specifications for evaporating dishes, crucibles, beakers, combustion boats, implements such as tongs and spatulas, gauze cylinder electrodes and wire-form anodes, and miniaturized versions of most of these supplies for microanalyses. Conversion charts and a section describing the use and care of platinum labware are also included. 24 pp. Engelhard 424

**Chromatography.** Catalog No. 300 describes columns, instrumentation, and accessories for capillary chromatography, GC, HPLC, and TLC. Included are specification tables, photos and diagrams, applications, and sample chromatograms. The catalog contains listings for sample preparation products, autosampler vials, and analytical standards and includes product indexes. 800 pp. Alltech 425

# THERMAL ANALYSIS IN POLYMER CHARACTERIZATION

EDITH A. TURI, COURSE DIRECTOR

Monday-Tuesday, November 15-16, 1993

Somerset, New Jersey

in conjunction with the Eastern Analytical Symposium

## Ten Key Ways You'll Benefit from Attending This Course:

- 1 Learn the basic principles of thermal techniques
- 2 Understand the characteristics of commercial instruments; learn their applicability to your needs
- 3 Learn the systematic application of thermal analysis to a broad range of polymers
- 4 Learn ways to enhance polymer performance
- 5 Learn how to optimize experimental conditions and interpret thermal data obtained by different techniques
- 6 Optimize processes and quality control methods
- 7 Learn how to increase your direct input in achieving marketing objectives
- 8 Eliminate expensive trial-and-error experiments by cost-efficient, speedy, small-scale thermal analysis
- 9 Enhance your capability to conduct experiments targeted to improving quality and increasing productivity
- 10 Discuss with leading experts your specific questions such as problem solving, troubleshooting, and operation safety

For more information on this dynamic, new course, mail in the coupon below.

FAX: (202) 872-6336. Or call the American Chemical Society Continuing Education Short Course Department at (800) 227-5558 (TOLL FREE) or (202) 872-4508.

**YES!** Please send me more information on the new ACS Short Course, *Thermal Analysis in Polymer Characterization*, to be held November 15-16, 1993, in conjunction with the Eastern Analytical Symposium.

NAME \_\_\_\_\_

TITLE \_\_\_\_\_

ORGANIZATION \_\_\_\_\_

ADDRESS \_\_\_\_\_

CITY, STATE, ZIP \_\_\_\_\_

MAIL TO: American Chemical Society, Dept. of Continuing Education, Meeting Code TAPC9311, 1155 Sixteenth Street, N.W., Washington, DC 20036

# Mastering today's analytical tools isn't as elementary as it used to be.

Without proper training, adding powerful tools like the electron-impact mass spectrometer to your analytical arsenal can just add to the mystery. That's why ACS developed *Introduction to Mass Spectrometry* — a video series that takes an uncomplicated look at complex technology.

From using the instruments to analyzing mass spectra, easy-to-follow tapes present a visual explanation of the entire process. Your students or lab technicians won't be confounded by concepts presented in jargon-filled manuals — because computer-animated graphics show exactly what to expect at each stage! And after completing the course, they'll be fully versed in basic instrumental techniques,

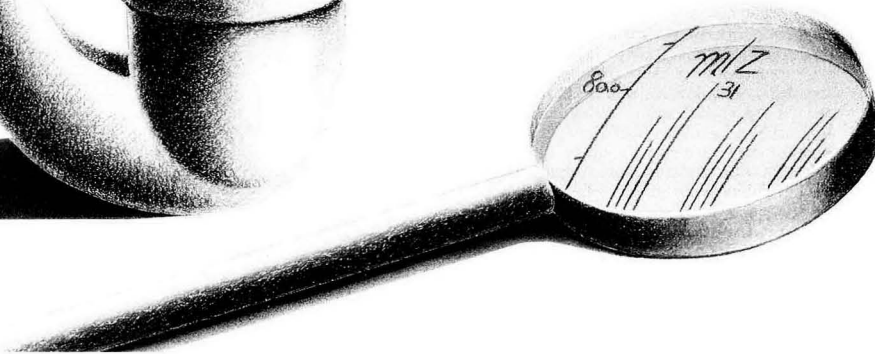
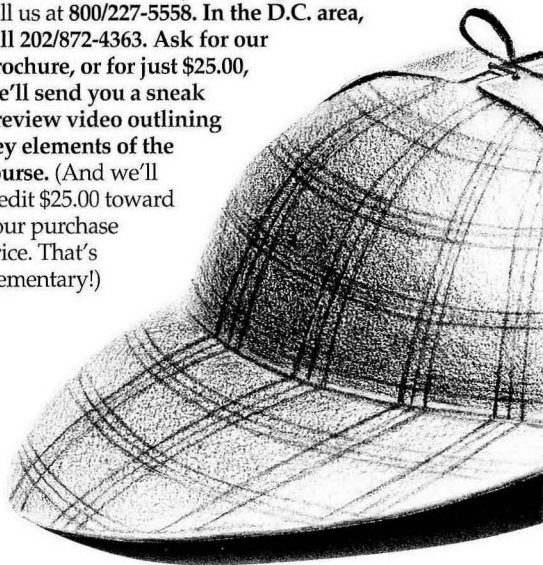
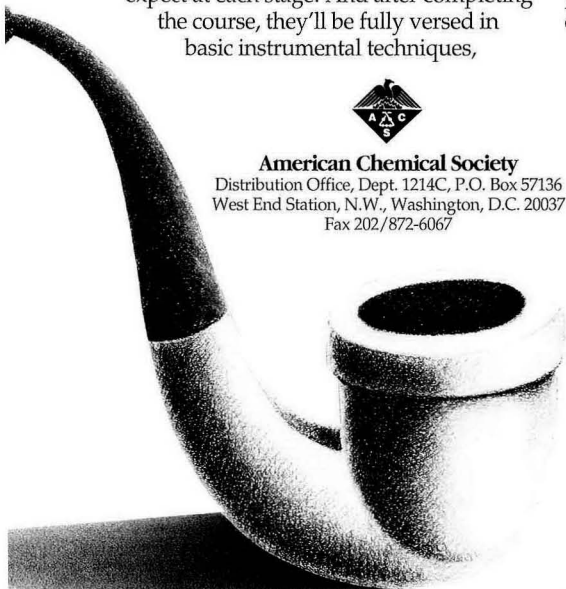
strategies for interpretation, and procedures for sample handling. It's enlightening for working chemists and students alike.

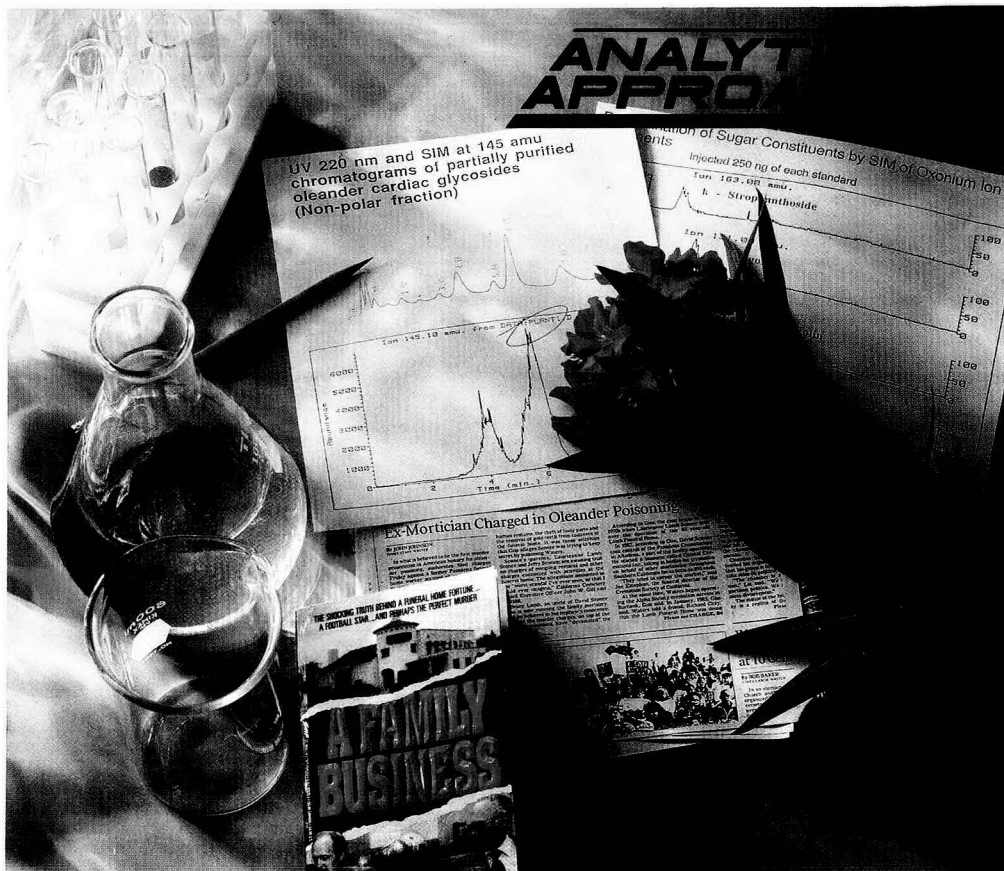
For more information about *Introduction to Mass Spectrometry*, call us at 800/227-5558. In the D.C. area, call 202/872-4363. Ask for our brochure, or for just \$25.00, we'll send you a sneak preview video outlining key elements of the course. (And we'll credit \$25.00 toward your purchase price. That's elementary!)



**American Chemical Society**

Distribution Office, Dept. 1214C, P.O. Box 57136  
West End Station, N.W., Washington, D.C. 20037  
Fax 202/872-6067





# A QUEST FOR OLEANDRIN IN DECAYED HUMAN TISSUE

**Geoffrey Rule, Lee G. McLaughlin, and Jack Henion**  
Diagnostic Laboratory  
College of Veterinary Medicine  
Cornell University  
Ithaca, NY 14851-0786

In early February 1991 we were asked to perform LC/MS analyses of badly decayed human autopsy tissues from a suspected homicide victim. The death had occurred almost six years earlier and was believed to have been caused by cardiac arrest. The victim, a young funeral parlor owner, was overweight and had led a stressful life. Although the case was closed in 1985 following a medical examiner's report of death from nat-

ural causes, a report by an informant five years later suggested that death had been caused by intentional poisoning at the hand of a competitor—a nearby funeral parlor and crematorium owner. The case was reopened in early 1991 and had all the elements of a television or paperback book mystery (1).

The trial was scheduled to be held in Ventura County, CA, and was a frequent, much-discussed topic in Los Angeles area newspapers (2). When the case was reopened, the defendant could have received the death penalty; however, our LC/MS data did not substantiate the presence of the suspect toxin in the deceased's body tissues or preservation fluids. Thus the case never went to

trial. In this ANALYTICAL APPROACH we describe the protocol and experimental difficulties we encountered in using LC/MS analysis of badly decomposed human tissue samples to determine the presence or absence of a toxic cardiac glycoside.

The body had been entombed for five years in a glass, above-ground casket for easy viewing by family and friends. The case was being reopened because the informant, a former employee of the rival funeral parlor owner, stated that death was caused by intentional poisoning with an oleander plant (*Nerium oleander*) extract. Oleandrin, one of several toxic components of the oleander plant, is present in its leaves and bark. The plant commonly grows in

warm, subtropical climates (3). Previous reports of death by ingestion of oleander leaf extracts have been reported (4, 5). Similarly, there have been undocumented reports of poisonings that occurred after ingestion of meat roasted on oleander stems (3).

Body tissues remaining in the casket from the original autopsy were recovered in early 1991 to determine whether oleandrin or a related compound, oleandrogenin, could be identified. Routine preliminary nonquantitative thin layer chromatography (TLC) and radioimmunoassay (RIA) screening from two different toxicology laboratories indicated the possible presence of oleandrin. These data, which suggested that the defendant may have murdered his competitor, were later entered into court as evidence. Because the defendant could have received the death penalty if convicted, attorneys for both sides requested additional definitive evidence based on the use of more specific analytical tools.

A well-known toxicology consultant was hired by the defense to review the available incriminating scientific evidence and to make recommendations regarding whether more definitive methods might prove the innocence of the defendant. The consultant concluded that the recent TLC and RIA results supported the possible presence of oleandrin in the autopsy body tissues. However, these results were not supported by conclusive proof generally provided by GC/MS, the technique routinely used in important forensic cases.

At the same time, attorneys for the prosecution decided that although their case was going well at that point, their request for more definitive evidence also required them to obtain more accurate data to further strengthen their case. Because the suspect cardiac glycosides are not easily characterized by GC/MS (6), it was recommended that LC/MS techniques might be more appropriate for the unequivocal identification of the suspected oleandrin poison. Both the defense's consultant and the prosecution's attorneys independently provided the name of one of us (JH) as a source of additional scientific expertise that could be used for the case.

Before accepting this potentially entangling forensic matter we chose to determine whether our ion spray LC/MS technology (7) was suitable for tackling the problem. First, we asked the attorneys and their con-

sultants to specify exactly which analytes should be targeted in the decayed autopsy tissues; it was impractical to look for all possible "toxins." The defense's consultant recommended—and we agreed—that the search could be confined to oleandrin and its aglycone, oleandrogenin (Figure 1). The latter is a logical breakdown product of oleandrin (although there are several other possible candidates that we could have targeted). To lessen the anticipated difficulty of isolating, detecting, and identifying very low levels of the compounds and their chemical or enzymatic breakdown products, we limited our search to the two target analytes.

We purchased authentic standards of oleandrin and oleandrogenin (Sigma Chemical Co., St. Louis, MO) and prepared dilute synthetic mixtures for LC with UV detection and LC/MS analysis. At the same time, we spiked fresh bovine liver samples with the two compounds to develop the extraction procedure. We anticipated that LC/MS coupled with tandem MS (LC/MS/MS) in the selected reaction monitoring (SRM) mode (8) would be required for selective detection of the target analytes. Preliminary experiments were carried out to see whether this technique would

have the requisite sensitivity and selectivity to accomplish the goal of determining the presence of oleandrin and oleandrogenin in badly decayed human tissue.

A full-scan collision-induced dissociation (CID) mass spectrum was obtained for each compound by infusion of each analyte dissolved in CH<sub>3</sub>OH/H<sub>2</sub>O (50/50, v/v) containing 5 mM NH<sub>4</sub>OAc under ion spray conditions. The latter compound was added as a "desorption reagent" for electrospray ionization MS so that ammonium ion adducts could be attached to the polar, neutral functional groups present on the oleandrin and oleandrogenin molecules. These molecules could then be converted to protonated molecules in the free-jet expansion region of the atmospheric pressure ionization (API) mass spectrometer (7) by CID without premass selection to cause loss of neutral NH<sub>3</sub>. The resulting protonated molecules are excellent precursor ions for CID because they yield abundant primary fragment ions of the analyte. A full-scan CID mass spectrum for each compound, as well as the processes taking place during ion spray MS/MS, are shown in Figure 2.

In these experiments the protonated molecules observed at *m/z* 577

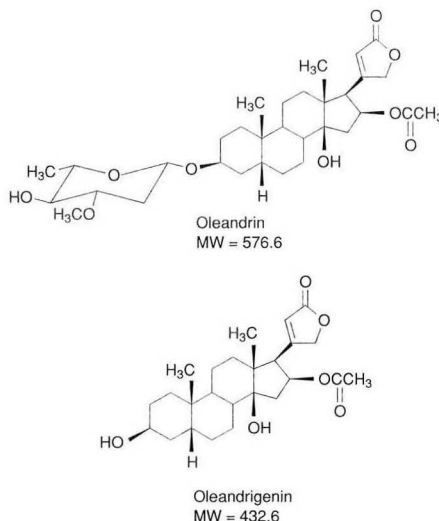


Figure 1. Chemical structures of oleandrin and oleandrogenin.



for oleandrin and at  $m/z$  433.1 for oleandrigenin are preselected and are focused by the first quadrupole (Q1) into the collision cell (Q2). This region is pressurized to  $2 \times 10^{-14}$  atoms/cm<sup>2</sup> with argon collision gas where CID and the resulting fragmentation occurs. The family of product ions (e.g.,  $m_1^+$ ,  $m_2^+$ ,  $m_3^+$ ) resulting from the CID of the protonated molecule precursor ions is mass-analyzed by the third quadrupole (Q3) to give the mass spectra shown in Figure 2. These full-scan mass spectral "fingerprints," which are unique for each compound, provide a means for unequivocal identification. In addition, when this information is obtained from on-line HPLC (LC/MS/MS), we have the additional retention time information afforded by LC. Thus LC/MS/MS provides the combination of retention time and mass spectral fragmentation information commonly provided by GC/MS.

LC/MS/MS is useful for the analysis of very polar, thermally labile compounds that cannot be determined by GC/MS. The CID mass spectra obtained in this work, however, are not those obtained from the more common electron ionization MS. Nevertheless, the mass spectra in Figure 2 are reproducible and structurally informative. On the basis of our preliminary results with spiked bovine liver and ion spray MS experiments, we accepted the analytical challenge presented to us. Because the defense and the prosecution were retaining us for the forensic analysis of the samples, both agreed to accept our findings—whatever the outcome.

#### Analysis of decayed tissue

Portions of the deceased's tissues were sent to Cornell under "chain of custody" (a documented, thorough forensic security measure) by both the defense and the prosecution. The defense also sent a forensic toxicology consultant to our laboratory to deliver the tissue samples and brief us on the available evidence and history of the case. We were supposed to analyze these two sample sets separately and provide the corresponding results only to the respective sides.

The difficulty of our task soon became apparent. The human autopsy tissues were nearly six years old and were extensively decomposed. A literature search provided little help in finding an analytical protocol for handling such decomposed material. Given our previous experience with

tissue analyses for trace residues of growth-promoting agents (9), we returned to the three-phase liquid-liquid extraction procedure that we had reported for the determination of dexamethasone in bovine liver and muscle (10). By using a unique solvent mixture consisting of acetonitrile, water, hexane, and dichloromethane, three distinct solvent phases are formed that selectively isolate substances of differing polarities.

Typically, the analytes of interest partition into the middle acetonitrile layer while the fats and other nonpolar material partition into the upper hexane layer. The heavier dichloromethane layer remains at the bottom and usually contains material of intermediate polarity. The middle acetonitrile layer is removed, concentrated, and subjected to either further purification by solid-phase extraction (SPE) or column-switching

(LC/LC) techniques (11). LC/LC offers automation, quantitative sample transfer during the column-switching steps, and considerable separating power because of its high separation efficiency. Considerable selectivity is also available with LC/LC because different stationary phases may be used in each of the sequenced HPLC columns. Finally, this approach can be used for direct coupling with MS/MS.

To evaluate the degree of "analytical horsepower" required for this project, we obtained a control sample of decayed human autopsy tissue. One-gram portions of the control tissue were fortified with 30 ppb of oleandrin and oleandrigenin, and the homogenized sample was subjected to the three-phase liquid-liquid extraction procedure reported previously (9, 10). However, when we performed the SPE procedure that we had developed for fresh bovine liver,

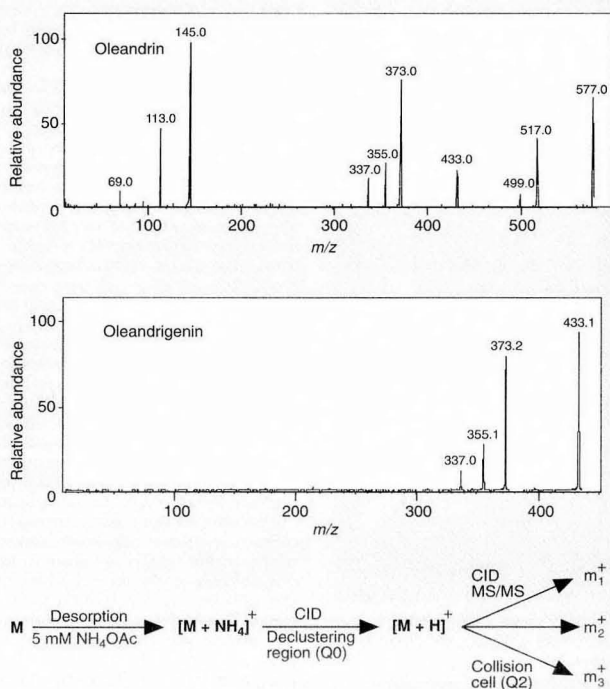


**Figure 2.** Full-scan CID mass spectra for oleandrin and oleandrigenin.

The protonated molecule precursor ions at  $m/z$  577.0 and 433.1 were subjected to collisions with argon in the central collision cell of the triple quadrupole mass spectrometer.

we immediately began to have difficulty purifying the rotten control and suspect tissue samples.

These difficulties were likely caused by the presence of adipocere, a product of microbial tissue decomposition (12). Also known as white grave wax, adipocere is a complex mixture of fatty acids that proved to be extremely difficult to separate from the target analytes under the time constraints imposed on us. We opted to omit the SPE step and injected the crude extracts directly onto the LC column after filtration. A concentrated extract of a control decayed tissue that had been fortified with 30 ppb of oleandrin and analyzed by LC under conditions developed for the chromatographic separation of oleandrin and oleandri-

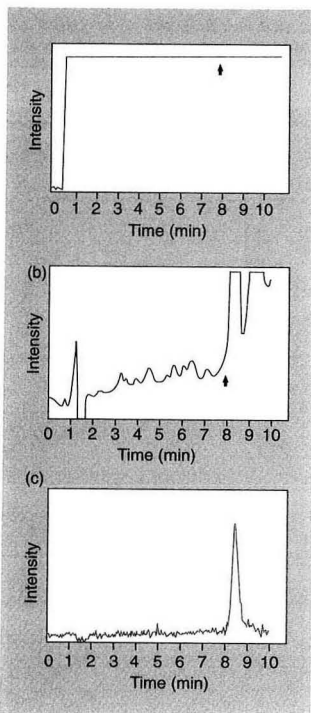


**Figure 3.** Analysis of an extract obtained from a 30-ppb fortified tissue homogenate.

The tissue homogenate was subjected to three-phase liquid-liquid extraction, filtered, and injected onto an LC column. The three panels shown were obtained from the same extract analyzed by (a) LC with UV detection, (b) LC/LC with UV detection, and (c) LC/LC/MS/MS under SRM conditions.

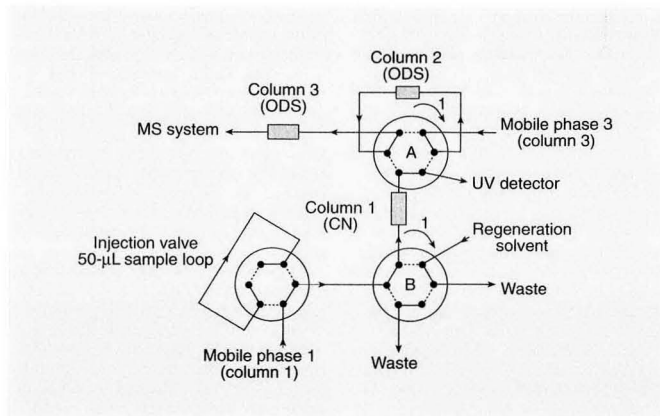


**Figure 4.** Coupled-column system schematic composed of two HPLC pumps, three columns, and two automatic switching valves (A and B).

genin is shown in Figure 3a. The arrow indicates the expected retention time for oleandrin. These results clearly show major chemical interference from tissue matrix components in the region of interest.

Coupled-column HPLC was integrated into the sample cleanup procedure to improve the selectivity of the LC procedure. The coupled-column system (Figure 4) consists of three HPLC columns, two switching valves, and two pumping systems. Typically, 15  $\mu$ L of the sample extract (100 mg of tissue equivalent) was injected onto column 1 (4.6 mm i.d.  $\times$  100 mm cyanopropyl) to provide initial separation of oleandrin. When the retention time window for oleandrin was reached, the effluent from column 1 was switched to column 2 (4 mm i.d.  $\times$  10 mm Spherisorb ODS 2) where the "heart cut" oleandrin and any co-eluting matrix components are trapped on the intermediate "peak compression" column.

This step in the column-switching procedure allows selective trapping of the target analytes onto the second column while the remainder of the effluent from column 1 goes to waste. The next timed event switches the second pumping system to deliver a different HPLC eluent whose composition is optimized to back-flush column 2 and provide an analytical separation on column 3 (2 mm i.d.  $\times$  100 mm ODS 2). It is helpful to think of column 2 as a trapping column and as the "injector" for column

3. Essentially, column 2 performs both of these tasks in sequence. A variable-wavelength UV detector (220 nm) was placed at the exit of column 3 to provide a UV chromatogram for these LC/LC experiments.

The unsuccessful sample analysis (Figure 3a) was repeated using the column-switching sequence described above. The LC/LC chromatogram obtained from the analysis of the 30-ppb fortified human tissue extract is shown in Figure 3b. This chromatogram at least has a recognizable baseline with defined chromatographic peaks, but the 7.9-min retention time location for oleandrin is still masked by high levels of other sample matrix components. Although coupled-column sample cleanup of the three-phase liquid-liquid extraction significantly improved the condition observed in Figure 3a, it was clear that still more selectivity would be required.

#### The ultimate analytical weapon

We might have accomplished our goal by exploring alternative approaches such as improved sample purification after the initial extraction, column-switching protocols using different HPLC column stationary phases, or perhaps derivatization followed by more specific detection schemes. However, an answer was required within one week of our acceptance of the request for analysis. Therefore, we used the coupled-column technology used to obtain the chromatogram in Figure 3b, but we replaced the UV detector with our

tandem triple quadrupole API mass spectrometer.

By using the ion spray LC/MS interface the collisionally induced protonated molecule for oleandrin at  $m/z$  577 was focused by the first quadrupole into the collision cell of the mass spectrometer where it was subjected to CID with argon gas. The product ions at  $m/z$  517, 373, and 145 (Figure 2, top) were selected and repetitively monitored by the third quadrupole using SRM to provide an additional dimension of selectivity. We hoped to detect oleandrin and oleandrinigenin in the extracts of fortified tissues and, if present, in the suspect human autopsy tissues.

The total selected ion current profile for the four different ions from oleandrin fortified at 30 ppb in a homogenized control tissue sample is shown in Figure 3c. Using the same sample treatment procedure as described above, we performed the LC/LC/MS/MS analysis in which an ion current chromatographic profile shows only oleandrin in spite of the high levels of interfering matrix components. The retention time for oleandrin in Figure 3c is slightly longer than that in Figure 3b because of changes in HPLC column performance resulting from repetitive analysis of these chemically complex samples. However, the relative ion abundance ratios and appropriate chromatographic behavior are obtained for oleandrin, and thus its presence in the fortified sample is documented. LC/LC/MS/MS determination of oleandrinigenin in a fortified tissue extract revealed similar results. Analysis of control or blank tissue extracts showed no evidence of the analytes at their corresponding retention times.

Once we demonstrated that oleandrin and oleandrinigenin could be confirmed by LC/LC/MS/MS under SRM conditions at levels fortified to 30 ppb in a control human liver tissue homogenate, we analyzed several target tissues from the deceased. In addition to tissues from the heart, liver, and kidney, we analyzed a formalin-fixing solution in which some of the tissues had been stored. The analysis of these samples revealed no scientific evidence for the presence of either target analyte.

There are several possible explanations for these negative results. First, the deceased may not have been poisoned by oleandrin. Second, chemical and microbial degradation could have easily broken down oleandrin and oleandrinigenin to other

products that we would not have detected from our targeted approach. Third, our cutoff was 30 ppb, but the target analytes could have been present at lower levels given that the samples had been stored at ambient temperatures for a long time. The combination of these potentially very low levels and the high chemical complexity of the decayed tissues could have precluded their detection under our experimental conditions.

#### Analysis of crude oleander extract

Accompanying the human tissue samples was a sample of oleander leaf extract. The attorneys had also requested analysis of this sample and a comparison of the results with those from the human tissue analyses. The supposed logic of this approach was that other known cardiac glycosides in the oleander plant might also be detected in the tissue samples if in fact the death had been caused by oleander ingestion. A review of the literature showed that more than a dozen toxic cardiac glycosides have been identified in the oleander plant (13).

The LC/LC and LC/LC/MS/MS data for the analysis of a crude solvent extract of oleander leaves performed under experimental conditions comparable with those for the tissue samples analysis are shown in Figure 5. The LC/LC chromatogram with UV detection (Figure 5a) shows a rather complex mixture with significant interference in the expected retention region for oleandrin. When this experiment is repeated with LC/LC/MS/MS, while monitoring the  $m/z$  517, 373, and 145 product ions

from  $m/z$  577  $[(M+H)^+]$ , the individual selected ion current profiles shown in Figure 5b readily confirm the presence of oleandrin in the leaf extract at the expected retention time of 7.3 min.

Two other compounds with the same mass as oleandrin but different retention times were also found in the plant extract. In all likelihood, these compounds are cryptograndoside A and nerigoside; both are isomeric with oleandrin and were previously identified in the oleander plant (14). When the tissue extracts from the deceased were inspected, there was no evidence of the presence of these additional oleander components—perhaps because of the same reasons discussed above.

#### Summary

This forensic case taught us several lessons. First, there is a need for improved sample cleanup and treatment of severely decayed tissue samples when trace determinations of target analytes are needed. With the exception of a few reports (15, 16), the literature is lacking in information with regard to the most modern sample preparation techniques. Second, the coupling of LC/LC with tandem MS provides an effective means of "on-line" sample cleanup for complex sample matrices. The improvements in selectivity shown in Figure 3 reveal the analytical power available when these techniques are combined. Third, once we decided to use LC/LC/MS/MS, we were able to analyze more than 50 samples in a semi-automated fashion over approximately three days. The reliability and ruggedness of the combined

**Table I. Column-switching timetable for the determination of oleandrin in tissue homogenate extract**

Time (min)	Switching valve A	Switching valve B	Event
0	Position 2	Position 2	Inject sample
2.8 <sup>a</sup>	Position 1		Begin collection of oleandrin on column 2
4.4	Position 2		End collection; begin separation on column 3; start integrator and MS acquisition
4.6		Position 1	Begin regeneration of column 1
9.6		Position 2	End regeneration and begin equilibration of column 1
17.6	Position 2	Position 2	End equilibration; inject next sample

<sup>a</sup> The collection window for oleandrinigenin was 2.7–4.4 min.

# ACS Congressional Fellowship

Available Fall 1994

The Fellowship places an ACS member in a staff position in Congress to

- Gain firsthand knowledge of the operation of the legislative branch of the federal government,
- Make scientific and technical expertise available to the government, and
- Forge links between the scientific and government communities.

Applications due January 1, 1994.

For more information contact:  
Mr. William Gray  
Department of Government  
Relations and Science Policy  
American Chemical Society  
1155 Sixteenth Street, N.W.  
Washington, DC 20036,  
(202) 872-4467.

Applications consist of a letter of intent, a resumé, and two letters of reference. Arrangements should be made to send the letters of reference directly to ACS. Candidates should contact ACS prior to submitting an application to determine the type of information needed in the letter of intent.



## ANALYTICAL APPROACH

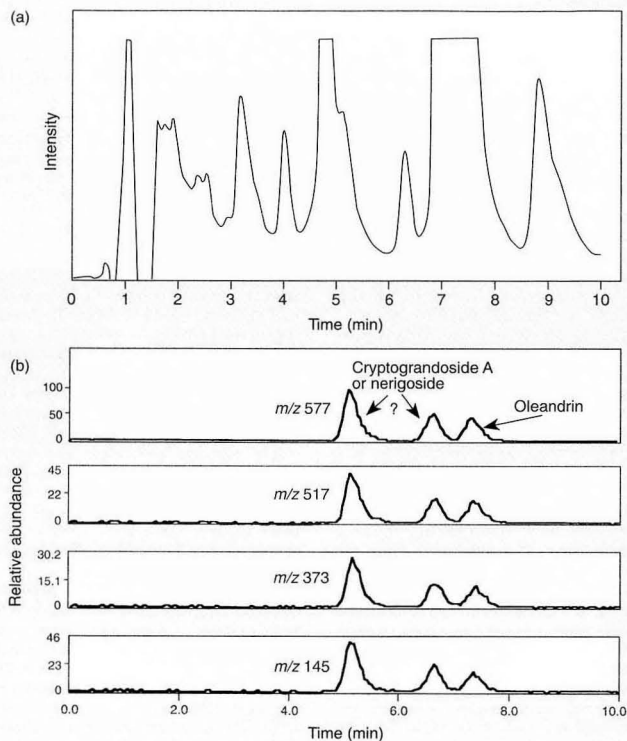


**Figure 5.** Analysis of liquid-liquid extract from an oleander leaf by (a) LC/LC with UV detection and (b) LC/LC/MS/MS under SRM conditions.

techniques and equipment suggest this approach may have merit for common applications in which large numbers of biological samples (e.g., plasma and urine) must be analyzed.

As a postscript, when this project was completed we proposed that the use of antibodies for isolating oleandrin and its relatives might be a more selective means for trace enrichment of the target analytes (17). For example, a high-pressure immunoaffinity column could have been coupled on line as column 1 in Figure 4. After pumping a relatively high volume of aqueous tissue extract through an immunoaffinity column during trapping and trace enrichment conditions, the column could be rinsed with phosphate-buffered saline. Then the pH could be lowered to unfold the antibody protein and allow release of the trapped analyte from this column with subsequent

trapping on column 2 in Figure 4. Back-flushing column 2 with an appropriate eluent could then elute the trapped analytes and any additional matrix components resulting from nonspecific binding onto column 3, which would provide an analytical separation followed by MS/MS detection.

We have demonstrated the feasibility of an immunoaffinity chromatography (IAC) and LC/MS approach with several simple drug and environmental applications. For example, a polyclonal antibody specific for propranolol was used to trace-enrich this drug from human urine. When we use IAC/LC/MS on a modified single quadrupole mass spectrometer operated in the SIM mode, we determined propranolol at a concentration of 2.5 ng/mL directly from urine (18).

Other applications in our laboratory include the IAC/LC/MS deter-

mination of lysergic acid diethylamide (LSD) in urine as well as carbofuran in environmental water and food matrix samples (19). This approach appears to have significant advantages for particularly complex matrices and may be a modern alternative to current liquid-liquid or SPE sample preparation techniques. It also could be an alternative to the analysis of decayed tissue samples in future legal cases such as the one described here.

We thank the prosecuting attorney, Kevin De-  
noce, and the defense attorney, Roger Diamond,  
for bringing this problem to our attention, and  
James Conboy for operation of the API LC/MS/MS  
system used to obtain the mass spectral data  
described in this work. We also thank Bryan Finkle  
for recommending our laboratory and for briefing us  
on matters pertaining to the case. Finally, we thank  
the Strong Memorial Hospital in Rochester, NY, for  
providing control decayed human tissue samples.

#### References

- (1) Engle, K. *A Family Business*; St. Martin's Press: New York, 1992.
- (2) *LA Times*, Spring 1991 (several articles).
- (3) Ellenhorn, M. J.; Barceloux, D. G. *Medical Toxicology—Diagnosis and Treatment of Human Poisoning*; Elsevier: New York, 1988; p. 1252.
- (4) Osterloh, J.; Herold, S.; Pond, S.

- JAMA* **1982**, 247(11), 1596–97.
- (5) Blum, L. M.; Reiders, F. J. *Anal. Toxicol.* **1987**, 11, 219–21.
- (6) Szabuniewicz, M.; McCrady, J. D.; Camp, B. J. *Arch. Int. Pharmacodyn.* **1971**, 189, 12–21.
- (7) Huang, E. C.; Wachs, T.; Conboy, J. J.; Henion, J. D. *Anal. Chem.* **1990**, 62, 713 A–728 A.
- (8) Busch, K. L.; Glish, G. L.; McLuckey, S. A. *Mass Spectrometry/Mass Spectrometry: Techniques and Applications of Tandem Mass Spectrometry*; VCH Publishers: New York, 1988.
- (9) Chichila, T. M.; Edlund, P. O.; Wilson, R.; Epstein, R. L.; Henion, J. D. *J. Chromatogr.* **1989**, 488, 389–406.
- (10) McLaughlin, L. G.; Henion, J. D. *J. Chromatogr.* **1990**, 529, 1–19.
- (11) Edlund, P. O.; Bowers, L.; Henion, J. D. *J. Chromatogr.* **1989**, 487, 341–56.
- (12) Mellen, P. F.; Lowry, M. A.; Micozzi, M. S. *J. Forensic Sci.* **1993**, 38(1), 91–93.
- (13) Wagner, H.; Blatt, S.; Zgainski, E. M. *Plant Drug Analysis*; Springer Verlag: New York, 1983.
- (14) Jager, H.; Schindler, O.; Reichstein, T. *Helv. Chim. Acta* **1959**, 42, 977–1013.
- (15) Curry, A. S. *Poison Detection in Human Organs*, 3rd ed.; Charles C. Thomas Publishers: Springfield, IL, 1976.
- (16) Curry, A. S. In *Toxicology, Mechanisms, and Analytical Methods*; Steward, C. P.; Stolman, A., Eds.; Academic Press: New York, 1960; Vol. 1.
- (17) Henion, J. D.; Rule, G. S.; Cornell University, unpublished results.
- (18) Rule, G. S.; Henion, J. D. *J. Chromatogr.* **1992**, 582, 103–12.
- (19) Rule, G. S.; Mordehai, A. V.; Henion, J. D., submitted for publication in *Anal. Chem.*



Geoffrey Rule (left) completed his M.S. degree in analytical toxicology at Cornell in June 1993. His thesis, based on work completed in Henion's laboratory, focused on the use of immunoaffinity chromatography combined with on-line coupled-column HPLC and LC/MS. He received his B.S. degree in chemistry from Syracuse University.

Lee G. McLaughlin received her Ph.D. in May 1993 from Cornell, where she gained experience in Henion's laboratory with coupled-column HPLC analysis of tissue extracts and ion spray LC/MS. She received her B.S. degree from Bowdoin College and is currently employed by Bristol-Myers Squibb in New Brunswick, NJ.

Jack Henion is professor of toxicology in the Diagnostic Laboratory of the New York State College of Veterinary Medicine at Cornell University. He received his B.A. degree from Alfred University and his Ph.D. in analytical organic chemistry from the State University of New York at Albany. His research integrates sample preparation and analysis with modern mass spectrometric techniques to solve real-world problems.

# SciWords

**A technical dictionary  
that saves hours of  
spell-checking!**

Save time by eliminating "word not found" messages—and be confident your scientific documents are correct with SciWords, an automatic spell-checker developed specifically for scientific writing.

**Over 75,000 organic  
and inorganic names**

Regular spell-checkers alone can't handle your complex scientific documents. The new SciWords spell checker contains over 75,000 technical words used in chemistry, physics, and biology with special emphasis on pharmaceuticals, agrochemicals, pesticides, and biochemical materials. You'll be able to check thousands of chemical trade names and trivial names, element symbols, many individuals' surnames, common acronyms, and more—from Aacaptan to Zyzyum!

**Integrates easily . . .  
works automatically!**

Sciwords works with your standard WordPerfect, MicroSoft Word or FrameMaker dictionary. It integrates easily and is activated automatically every time you request a spell check. With SciWords, you ensure spelling accuracy on all your documents—from technical reports to grant proposals, letters, and theses—in a fraction of the time!

Available in DOS, Macintosh, and Windows for WordPerfect, MSWord, and FrameMaker.

#### Hardware requirements:

**IBM:** MS-DOS 2.1 or higher OR running Windows 3.0 or higher; WordPerfect 5.0/5.1 (DOS or Windows version).

**Macintosh:** Macintosh WordPerfect 2.0/2.1.

List price: \$50

Member price: \$50

Academic price: \$50

**30-day**

\*\*\*  
**money back**

\*\*\*  
**guarantee**

 **ACS Software**

#### Order from

American Chemical Society, Distribution Dept., Office 66, 1155 Sixteenth Street, N.W., Washington, DC 20036  
Or call TOLL FREE 1-800-227-5558.  
In Washington, D.C. 202-872-4363.  
Or FAX your order to 202-872-6067.



# CLASSIFIED—HELP WANTED

## DIRECTOR, CORE ANALYTICAL LABORATORY

THE CENTER FOR CLINICAL PHARMACOLOGY at the University of Pittsburgh Medical Center is seeking an outstanding analytical chemist to administer a core assay facility that serves as a centralized analytical resource for experimental protocols being conducted by investigators for the General Clinical Research Center and also within the University of Pittsburgh Medical Center. The successful candidate must have postdoctoral experience with a demonstrated ability to develop, validate and apply RIAs, EIAs, HPLC assays and GC-MS assays. Preference will be given to candidates who have experience with pharmacokinetic modeling and/or who have medicinal chemistry training and an independent scientific research program. It is anticipated that the appointment will be made at the Assistant or Associate Professor level. Interested candidates should submit a curriculum vitae and a letter of introduction to Dr. Edwin K. Jackson, Ph.D., Associate Director, Center for Clinical Pharmacology, 623 Scaife Hall, University of Pittsburgh Medical Center, Pittsburgh, PA 15261, Tel: (412) 648-1808, Fax: (412) 648-7107. An Equal Opportunity/Affirmative Action employer.

## FREE DATA, FAST

To quickly amass data on all of the products you need, consult the Lab Data Service Section on our *Analytical Chemistry* reader reply card insert.

## HELP WANTED ADS

ROP display at ROP rates. Rate based on number of insertions within contract year. Cannot be combined for frequency.

Unit	1-TI	6-TI
1" (25 mm)	\$210	\$190
	12-TI	24-TI
	\$180	\$170

CALL OR WRITE JANE GATENBY

### ANALYTICAL CHEMISTRY

1599 Post Road East  
P.O. Box 231  
Westport, CT 06881  
203-256-8211  
FAX: 203-256-8175

## LABORATORY SERVICE CENTER

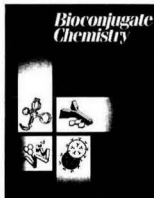
(Equipment, Materials, Services, Instruments for Leasing), Maximum space — 4 inches per advertisement. Column width, 2-3/16"; two column width, 4-9/16". Artwork accepted. No combination of directory rates with ROP advertising. Rates based on number of inches used within 12 months from first date of first insertion.

Per inch: 1" — \$185; 12" — \$180; 24" — \$175; 36" — \$170; 48" — \$165.

CALL OR WRITE JANE GATENBY

### ANALYTICAL CHEMISTRY

1599 Post Road East  
P.O. Box 231  
Westport, CT 06881  
203-256-8211  
FAX: 203-256-8175



Unifying the Field of Conjugation Chemistry...

# Bioconjugate Chemistry

Editor: Claude F. Meares, University of California, Davis

## Centralized Access is Here!

Featuring highly technical, primary literature in biomedically related R&D, *Bioconjugate Chemistry* centralizes information previously published in some 200 different scholarly journals. It brings together—in one source—research forming the core of breakthroughs in biotechnology from universities, research institutes, biomedical firms, drug companies, and chemical laboratories. Specifically, *Bioconjugate Chemistry* addresses the joining of two different molecular functions by chemical or biological means. No other journal has this unique, topical focus: Conjugation of...

antibodies (and their fragments) nucleic acids and their analogues ( $\alpha$ -anomers, phosphonates, ...) liposomal components other biologically active molecules (receptor-binding proteins, hormones, peptides, ...)

with each other or with any molecular groups that add useful properties...

drugs, radionuclides, toxins, fluorophores, photoprobes, inhibitors, enzymes, haptens, ligands, etc.

In bimonthly issues you'll explore the chemical aspects of conjugate preparation and characterization, including:

- *In vivo* applications of conjugate methodology;
- Molecular biological aspects of antibodies, genetically engineered fragments, and other immunochemicals;
- The relationships between conjugation chemistry and the biological properties of conjugates.

ACS **PUBLICATIONS**  
Essential Resources for the Chemical Sciences

### 1993 Subscription Rates

	ACS Members*		Nonmembers
	One Year	Two Years	One Year
U.S.	\$ 29	\$ 52	\$273
Canada & Mexico	\$ 36	\$ 66	\$280
Europe**	\$ 41	\$ 76	\$285
All Other Countries**	\$ 44	\$ 82	\$288

\*Subscriptions at member rates are for personal use only. \*\*Air service included.

### Order Today!

American Chemical Society  
Member and Subscriber Services  
P.O. Box 3337

Columbus, OH 43210

Toll free: 1-800-333-9511 Local: (614) 447-3776

FAX: (614) 447-3671

For nonmember subscriptions in Japan contact Maruzen Co., LTD.

# INDEX TO ADVERTISERS IN THIS ISSUE

CIRCLE  
INQUIRY NO.                      ADVERTISERS                      PAGE NO.

60. .... \*ATI ..... 818A  
Fourier Court Advertising

12. .... Bioanalytical Systems, Inc. .... 824A  
Kissinger Advertising Associates

10. .... Brinkmann Instruments, Inc. .... 822A  
Lavey/Wolff/Swift Inc.

14, 15 .... Burleigh Instruments, Inc. .... 817A, 853A  
Scientific Marketing Services, Inc.

18. .... \*Cambridge Isotope Laboratories ..... 843A

22. .... \*Chrompack ..... 826A

20. .... Corporation Scientifique Claise, Inc. .... 854A

30. .... EM Separations ..... IFC  
Scientific Marketing Services, Inc.

34. .... Finnigan MAT ..... 828A-829A  
Pinné/Herbers, Inc.

52. .... Leco Corporation ..... OBC  
Lecom

70, 71 .... \*PE Nelson ..... 820A  
Keller & Company

82. .... Sartorius Corporation ..... 832A  
Dunlap, Schulze & Associates

95. .... Waters Chromatography/Div. of Millipore 844A-845A  
Blitz Media

Advertising Management for the American Chemical Society Publications

## CENTCOM, LTD.

*President*

**James A. Byrne**

*Executive Vice President*

**Benjamin W. Jones**

**Joseph P. Stenza, Production Director**

**Laurence J. Doyle, Director of Marketing**

1599 Post Road East  
P.O. Box 231  
Westport, Connecticut 06881-0231  
(Area Code 203) 256-8211  
Fax No. 203-256-8175

## DIRECTOR, ADVERTISING SALES, LABORATORY PRODUCTS

**Bruce E. Poorman**

## ADVERTISING PRODUCTION MANAGER

**Jane F. Gatenby**

## SALES REPRESENTATIVES

Philadelphia, PA. . . . CENTCOM, LTD. GSB Building, Suite 405, 1 Belmont Ave., Bala Cynwyd, PA. 19004. Telephone: 215-667-9666, FAX: 215-667-9353

New York/New Jersey . . . Dean A. Baldwin, John F. Raftery, CENTCOM, LTD., Schoolhouse Plaza, 720 King Georges Post Road, Fords, NJ 08863. Telephone: 908-738-8200, FAX: 908-738-6128

Westport, CT/Boston, MA. . . Dean A. Baldwin, Michael J. Pak, CENTCOM, LTD., 1599 Post Road East, P.O. Box 231, Westport, CT 06881-0231. Telephone: 203-256-8211, FAX: 203-256-8175

Cleveland, OH. . . . Bruce E. Poorman, Dean A. Baldwin, CENTCOM, LTD., 19035 Old Detroit Road, Suite 203, Rocky River, OH 44116. Telephone: 216-331-5151, FAX: 216-331-3432

Chicago, IL. . . . Michael J. Pak, CENTCOM, LTD., 540 Frontage Rd., Northfield, IL. 60093. Telephone: 708-441-6383, FAX: 708-441-6382

Houston, TX/Atlanta, GA. . . . Edward M. Black, CENTCOM, LTD., P.O. Box 820966, Houston, TX 77082-0966. Telephone: 713-493-1560, FAX: 713-493-6673

San Francisco, CA. . . . Paul M. Butts, CENTCOM, LTD., Suite 808, 2672 Bayshore Parkway, Mountain View, CA 94043. Telephone: 415-969-4604, FAX: 415-969-2104

United Kingdom, Scandinavia and Europe (Except: Germany, Switzerland, Austria, Italy, Spain) . . . Malcolm Thiele, Technomedia Ltd., Wood Cottage, Shurlock Row, Reading RG10 0QE, Berkshire, England. Telephone: 0734-343302, FAX: 0734-343948

Germany, Switzerland, Austria . . . IMP InterMediaPartners, GmbH, Deutscher Ring 40, 42327 Wuppertal, Germany. Telephone: (0202) 711091, FAX: (0202) 712431

Italy, Spain . . . Tess Serranti, Serranti Communications, 43 Van Sant Road, New Hope, PA 18938. Telephone: 215-598-0668, FAX: 215-598-0670

Tokyo, Japan . . . Sumio Oka, International Media Representatives Ltd., 1-11-5-502, Tamazutsumi, Setagaya-ku, Tokyo 158 Japan. Telephone: 502-0656, Telex #22633, FAX: 5706-7349

Asia (Except Japan) . . . Bruce E. Poorman, CENTCOM, LTD., 19035 Old Detroit Road, Suite 203, Rocky River, OH 44116. Telephone: 216-331-5151, FAX: 216-331-3432

South America . . . Bruce E. Poorman, CENTCOM, LTD., 19035 Old Detroit Road, Suite 203, Rocky River, OH 44116. Telephone: 216-331-5151, FAX: 216-331-3432

*Classified section, see page 864A.*

*\*See ad in 1994 LabGuide Edition.*



**CHEMICAL REVIEWS single thematic issue.**

# PHOTOCHEMISTRY

**GET YOUR OWN COPY NOW ONLY \$20** (ACS Member Rate, nonmembers \$30.)

## ARTICLES BY:

- Schuster, Lem, and Kaprinids; Arai and Tokumaru; Kohler; Givens and Kueper; Maciejewski and Steer; Muller and Mattay; Das; Becker; and Wan and Shukla illustrate how photochemistry has benefited from the development of new concepts, techniques synthetic, strategies and from the involvement of spectroscopists.
- vanWilligen, Levstein, and Ebersole; Gehlen and De Schryver; Wilson and Schnapp; Leigh; and Johnston summarize the impact of instrumentation, newer techniques, and methods of data handling on photochemical investigations.
- Kamat; Thomas; Yoon; Fox and Dulay focus on the study of reactions under microheterogeneous conditions.
- De Keukeleire and He; Duxbury; Monroe and Weed; and Law present the applications of photochemistry.
- And reviews by Bhattacharyya and Chowchury; Khudyakov, Serebrennikov, and Turro illustrate the effect of magnetic field on photoprocesses.

**Four more PHOTOCHEMISTRY related articles to appear in the March 1993 CHEMICAL REVIEWS issue are authored by:**

Cornelisse; Lissi, Encinas, Lemp, and Ruibio; Winnik; Legrini, Oliveros, and Braun.

**598 PAGES**

**24 ESSENTIAL REVIEWS.**

**41 ESTEEMED, INTERNATIONAL CONTRIBUTORS.**

**1 EXCEPTIONAL RESOURCE.**

## Guest Editors

V. Ramamurthy & N.J. Turro

**Order Now!  
Mail the Card Below Today  
Or Call:**

TOLL FREE: 1-800-227-5558,

IN DC: 202-872-4363, FAX: 202-872-6067

## 1993 CHEMICAL REVIEWS Subscription

**\$33 for ACS members** (Includes 4 single-topic thematic issues)

TOLL FREE: 1-800-333-9511, FAX: 614-447-3671

## CHEMICAL REVIEWS

*For top-ranking, international, primary chemistry literature*

- Comprehensive, topical articles by distinguished specialists
- Editorial policy of rigorous, outside peer review
- Definitive summaries of progress in all fields of chemistry
- Expert, monograph-coverage of emerging disciplines
- Current impact factor: 9.6

## Editor

Josef Michl, *University of Colorado, Boulder*

## Associate Editors

John A. Gladysz, *University of Utah*

Steven M. George, *University of Colorado, Boulder*

*Published eight times a year by the American Chemical Society*

## ORDER CARD

**Get your limited-edition, Photochemistry Thematic Issue today**

*A Special Opportunity from CHEMICAL REVIEWS*

PLEASE USE THIS FORM to order your copy of *Photochemistry* (Vol. 93, No. 1) OR your 1993 subscription to *CHEMICAL REVIEWS* at the appropriate rate(s) below. As a SUBSCRIBER you will receive eight peer-reviewed issues in all, including these single-topic thematic issues: *Photochemistry* (Jan/Feb), *New Perspectives in Coordinated Chemistry* (May), *Marine Chemistry* (July/Aug), and *Molecular Mechanics* (Nov). Your subscription is guaranteed by the ACS, if you are dissatisfied, you may cancel service at any time for a prompt refund on all unmailed issues.

### PHOTOCHEMISTRY THEMATIC ISSUE

☐ ACS-Member Rate ~~\$44~~ \$20

☐ Nonmember/Library Rate ~~\$44~~ \$30

### CHEMICAL REVIEWS 1993 SUBSCRIPTION

☐ ACS Member Rate \$33

☐ Nonmember/Library Rate \$346

☐ Send my copy of *Photochemistry* at the discounted rate of: \$ \_\_\_\_\_ **OR**

☐ Start my *CHEMICAL REVIEWS* 1993 subscription at the regular rate of: \$ \_\_\_\_\_

PLEASE NOTE: Member rates are for personal use only. Prices listed U.S. only. For rates abroad please contact the ACS.

### IMPORTANT BILLING INFORMATION

☐ My check payable to ACS is enclosed. Please address envelope to:

American Chemical Society, Room 609, 1155 16th Street, N.W., Washington, DC 20036

☐ Please debit my VISA/Mastercard ☐ Please bill me as indicated.

Acct. # \_\_\_\_\_ Expires \_\_\_\_\_

Name on Card \_\_\_\_\_

Address \_\_\_\_\_ City \_\_\_\_\_

State \_\_\_\_\_ Zip \_\_\_\_\_ Country \_\_\_\_\_

Signature \_\_\_\_\_

# AC RESEARCH

## Piezoelectric pH Sensors: AT-Cut Quartz Resonators with Amphoteric Polymer Films

Juan Wang and Michael D. Ward\*

Department of Chemical Engineering and Materials Science, University of Minnesota, Amundson Hall, 421 Washington Avenue SE, Minneapolis, Minnesota 55455

Richard C. Ebersole\* and Robert P. Foss

Central Research and Development Department, E. I. duPont de Nemours & Co., Experimental Station, P.O. Box 80173, Wilmington, Delaware 19880-0173

Piezoelectric AT-cut quartz resonators immersed in aqueous media, coated with cross-linked films of the random copolymer  $-\{[\text{CH}_2\text{CH}(\text{CO}_2\text{H})]_a-[\text{CH}_2\text{C}(\text{CH}_3)(\text{CO}_2\text{CH}_3)]_b-[\text{CH}_2\text{C}(\text{CH}_3)(\text{CO}_2\text{CH}_2\text{CH}_2\text{NMe}_2)]_c\}_n$  (1), exhibit large frequency changes when the pH is changed in the vicinity of the isoelectric point of the polymer film. The frequency changes are attributed to changes in the viscoelastic properties of the films that occur during phase transitions between the isoelectric form and the cationic polymer ( $1\text{-NMe}_2\text{H}^+$ ) present at low pH or the anionic polymer ( $1\text{-CO}_2^-$ ) present at high pH. These phase transitions are accompanied by dramatic changes in acoustic energy attenuation, film thickness changes, and film surface energy, as indicated by acoustic impedance analysis, phase measurement interferometric microscopy, and contact angle measurements. The results are consistent with pH-dependent segregation of the isoelectric and ionic phases within the bulk and between the bulk and the surface. The unique pH-sensing capabilities of the coated resonators, combined with their robustness, ease of fabrication, and low cost, provide a convenient approach for the measurement of "threshold" pH changes. Real-time measurements of enzymatic activity and microbe metabolism are demonstrated as examples of potential applications of these sensors.

### INTRODUCTION

The ability of piezoelectric acoustic wave devices to respond to small changes in mass at their surfaces while immersed in liquids has led to numerous fundamental investigations of

interfacial phenomena with these devices.<sup>1</sup> The technological significance of these devices is also becoming increasingly appreciated in that sensors can be readily designed by appropriate modification of the transducer surfaces with a chemically active film. For example, different acoustic wave sensors (shear,<sup>2</sup> surface acoustic,<sup>3</sup> flexure,<sup>4</sup> and shear-horizontal acoustic plate mode<sup>5</sup> devices) have been reported for the detection of biologically significant analytes,<sup>6</sup> metal ions,<sup>5</sup> and nerve toxin analogs.<sup>7</sup> These devices generally rely on interfacial chemical events that result in mass changes, which alter the frequency of the acoustic wave that propagates through the transducer and the chemically active film.

The most extensively studied transducer in this regard has been the shear mode AT-cut quartz resonator, commonly referred to as the quartz crystal microbalance (QCM), which comprises an AT-cut crystal sandwiched between two metal excitation electrodes that generate a standing shear wave

(1) (a) Ward, M. D.; Buttry, D. A. *Science* 1990, 249, 1000-1007. (b) Frye, G. C.; Martin, S. J. *Appl. Spectrosc. Rev.* 1991, 26, 73.

(2) (a) King, W. H., Jr. *Anal. Chem.* 1964, 36, 1735. (b) Ho, M. H. In *Applications of Piezoelectric Quartz Crystal Microbalances*; Lu, C., Czanderna, W., Eds.; Elsevier: New York, 1984; pp 351-388. (c) Guibault, G. G.; Jordan, J. M. *CRC Crit. Rev. Anal. Chem.* 1988, 19, 1. (d) Guibault, G. G. *Ion-Sel. Electrode Rev.* 1980, 2, 3. (e) McCallum, J. J. *Analyst* 1989, 114, 1173. (f) Okahata, Y.; Ebato, H.; Ye, X. *J. Chem. Soc., Chem. Commun.* 1988, 1037. (g) Lai, C. S.; et al. *J. Chem. Soc., Perkin Trans. 2* 1988, 319. (h) Ngh-Ngwaibini, J.; Foley, P. H.; Kuan, S. S.; Guibault, G. G. *J. Am. Chem. Soc.* 1986, 108, 1986.

(3) (a) Wohltjen, H. *Sens. Actuators* 1984, 5, 307. (b) Wohltjen, H.; Ballantine, D. S.; Jarvis, N. L. *ACS Symp. Ser.* 1989, No. 403, 157. (c) Wohltjen, H.; Dessy, R. *Anal. Chem.* 1979, 51, 1458. (d) Roederer, J. E.; Baastians, G. J. *Anal. Chem.* 1983, 55, 2333.

(4) Wenzel, S. W.; White, R. M. *IEEE Trans. Electron Devices* 1988, 35, 735.

(5) Ricco, A. J.; Martin, S. J.; Niemczyk, T. M.; Frye, G. C. *ACS Symp. Ser.* 1989, No. 403, 191.

(6) (a) Muramatsu, H.; Dieks, J. M.; Tamiya, E.; Karube, E. T. *Anal. Chem.* 1987, 59, 2760. (b) Muramatsu, H.; Kajiwara, K.; Tamiya, E.; Karube, I. *Anal. Chim. Acta* 1986, 188, 257261. (c) Muramatsu, H.; Watanabe, Y.; Hikuma, M.; Ataka, T.; Kubo, I.; Tamiya, F.; Karube, I. *Anal. Lett.* 1989, 22, 2155. (d) Ebersole, R. C.; Ward, M. D. *J. Am. Chem. Soc.* 1988, 110, 8623. (e) Ebersole, R. C.; Miller, J. A.; Moran, J. R.; Ward, M. D. *J. Am. Chem. Soc.* 1990, 112, 3239.

(7) Kepley, L. J.; Crooks, R. M.; Ricco, A. J. *Anal. Chem.* 1992, 64, 3191.

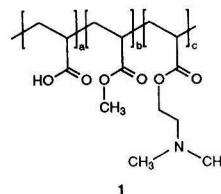
\* Authors to whom correspondence should be addressed.

across the thickness of the quartz crystal. The shear acoustic wave experiences an antinode at the surface of the quartz crystal and therefore can propagate into a film immobilized on the surface of the crystal. The thickness (or mass per unit area) of the film and the nature of the shear wave propagation in the film determine the frequency response. The mass change is generally determined from the frequency response according to the Sauerbrey relationship<sup>8</sup> (eq 1), where  $\Delta f$  is

$$\Delta f = -2f_0^2 \Delta m / A(\rho_q \mu_q)^{1/2} \quad (1)$$

the measured frequency shift,  $f_0$  the initial (resonant) frequency of the quartz crystal,  $\Delta m$  the mass change,  $A$  the piezoelectrically active area defined by the two excitation electrodes,  $\rho_q$  the density of quartz (2.648 g/cm<sup>3</sup>), and  $\mu_q$  the shear modulus (2.947 × 10<sup>11</sup> dyn cm<sup>-2</sup> for AT-cut quartz).

Sensor design based solely on mass changes, however, can be somewhat limiting if the analytes have low molecular mass. For example, the mass increase associated with binding of a protein to an active surface of a shear mode AT-cut quartz crystal may not be sufficient to achieve a frequency response of practical significance.<sup>6d</sup> While other piezoelectric transducers may provide somewhat greater sensitivity to mass changes, detection of analytes with low molecular mass remains difficult, particularly at low coverages. Other considerations include the rigidity of the bound analyte; for example, cell layers that bind to the surface of a QCM give frequency shifts that are much smaller than predicted by eq 1, suggesting that these films behave more like fluids than rigid masses when attached to the resonator surface.<sup>9</sup> Under these conditions, the acoustic wave propagation and the resonant frequency of piezoelectric resonators can be sensitive to the viscosity and density of materials in contact with the resonator.<sup>10</sup> In the case of thin films immobilized on the quartz resonator, it is becoming increasingly apparent that the viscoelastic properties of the films can play a large role in the frequency response of piezoelectric transducers.<sup>11,12</sup> The suggestion that thin films whose viscoelastic properties change dramatically upon interaction with an analyte could serve as a basis for the design of piezoelectric sensors prompted us to examine this approach for the detection of low molecular weight analytes. We have been particularly interested in developing piezoelectric sensors for pH measurements that are economical, robust to hostile environments, and amenable to miniaturization and small sample volumes. The need for a pH measurement system with these qualities is embodied in recent reports describing a light-addressable pH sensor which can be utilized for small-volume microbiological and cytotoxicity applications<sup>13,14</sup> and optical fibers modified with pH indicator dyes.<sup>15</sup> We describe herein a unique, highly sensitive, piezoelectric pH sensor based on composite resonators fabricated from AT-cut quartz resonators coated with cross-linked films of the amphoteric polymer 1. The phase behavior and viscoelasticity of these composite resonators are strongly dependent upon pH, and this behavior is



manifested as dramatic changes in the resonant frequency and electrical characteristics of the composite resonator during phase transitions between ionic and isoelectric forms of 1. The sensors are capable of detecting "threshold" pH changes in which significantly large frequency changes are observed over very small pH changes. These studies also provide insight into the unique fundamental properties of this polymer and illustrate the sensitivity of the QCM to factors other than mass changes. We also provide some illustrative examples of applications of these sensors which demonstrate their utility, namely, measurement of the rates of an enzymatic reaction and microbial metabolism. While our studies have employed a QCM as the piezoelectric element, the concepts can be transferred readily to other piezoelectric transducers capable of operating in liquids.

## EXPERIMENTAL SECTION

**Apparatus.** The pH sensor comprises a 1-in. diameter 5-MHz AT-cut quartz crystal coated with a cross-linked polymer film of 1 and an oscillator circuit designed to drive the crystal at its resonant frequency as described recently.<sup>16</sup> Gold electrodes (2000 Å thick) on titanium underlayers (500 Å) were deposited on both sides of the crystal by electron beam evaporation. The quartz crystal is inserted into the feedback loop of a broad-band rf amplifier via the two gold electrodes, and an alternating potential field across the crystal induces oscillation in the shear mode (displacement parallel to the electrodes) at the series resonant frequency. The quartz crystal was mounted between two 9-mm O-rings confined by standard 18/9 glass O-ring fittings, such that the upper glass joint comprised the sample chamber. The gold electrode facing the solution is at hard ground. The output of the oscillator circuit is connected to a Hewlett-Packard 5384A frequency counter, which is interfaced to a Macintosh personal computer for data collection. The sensitivity of a 5-MHz QCM as given by eq 1 is 0.057 Hz cm<sup>2</sup> ng<sup>-1</sup>. An asymmetric electrode format was employed in which the side having the larger gold pad is coated with the polymer film and faces the solution ( $A = 0.35$  cm<sup>2</sup> polymer side,  $A_{\text{plano}} = 0.18$  cm<sup>2</sup> on opposite side).

Impedance analysis was performed with a Hewlett-Packard 4194A impedance/gain-phase analyzer capable of performing measurements over a frequency range of 100 Hz–40 MHz in the impedance mode. Data collection was accomplished via an HPIB interface with a Macintosh personal computer. Programs were configured to measure impedance ( $Z$ ), susceptance ( $B$ ), conductance ( $G$ ), and phase angle ( $\theta$ ) over the entire frequency range at an appropriate resolution or to measure key parameters related to the properties of the composite resonator (that is, the quartz crystal and polymer film). These parameters included the maximum conductance ( $G_{\text{max}}$ ) and the frequency of that value ( $f_{G_{\text{max}}}$ ), minimum and maximum impedance ( $Z_{\text{min}}$ ,  $Z_{\text{max}}$ ) and the frequencies of those values ( $f_{Z_{\text{min}}}$ ,  $f_{Z_{\text{max}}}$ ), the frequencies of the half-power points ( $f_1$ ,  $f_2$ ), minimum and maximum susceptance ( $B_{\text{min}}$ ,  $B_{\text{max}}$ ) and the frequencies of those values ( $f_{B_{\text{min}}}$ ,  $f_{B_{\text{max}}}$ ). Equivalent circuit values based on the Butterworth–van Dyke model<sup>17</sup> were determined using the internal simulation program

(8) Sauerbrey, G. Z. *Phys.* 1959, 155, 206.

(9) Gryte, D.; Ward, M. D.; Hu, W.-S. *Biotechnol. Prog.* 1993, 9, 105.

(10) (a) Kanazawa, K. K.; Gordon, J. G., II. *Anal. Chem.* 1985, 57, 1771–1772. (b) Kanazawa, K. K.; Gordon, J. G. *Anal. Chim. Acta* 1985, 175, 99. (c) Martin, S. J.; Granstaff, V. E.; Frye, G. C. *Anal. Chem.* 1991, 63, 2272.

(11) (a) Martin, S. J.; Frye, G. C. *Appl. Phys. Lett.* 1990, 57, 1867. (b) Reed, C. E.; Kanazawa, K. K.; Kaufman, J. H. *J. Appl. Phys.* 1990, 68, 1993. (c) Martin, S. J.; Frye, G. C. *IEEE Ultrason. Symp.* 1991, 393.

(12) Lasky, S. J.; Buttry, D. A. *ACS Symp. Ser.* 1989, No. 403, 237. (13) Parce, J. W.; Owicki, J. C.; Kercso, K. M.; Sigal, G. B.; Wada, H. G.; Muir, V. C.; Bousse, L. J.; Ross, K. L.; Sikic, B. J.; McConnell, H. M. *Science*, 1989, 246, 243–247.

(14) McConnell, H. M.; Owicki, J. C.; Parce, J. W.; Miller, D. L.; Baxter, G. T.; Wada, H. G.; Pitchford, S. *Science* 1992, 257, 1906–1912.

(15) Tan, W.; Shi, Z.-Y.; Kopelman, R. *Anal. Chem.* 1992, 64, 2985.

(16) Ward, M. D. *J. Phys. Chem.* 1988, 92, 2049.

(17) (a) Bottom, V. E. *Introduction to Quartz Crystal Unit Design*; Van Nostrand Reinhold: New York, 1982. (b) Mason, W. P. *Piezoelectric Crystals and Their Application to Ultrasonics*; Van Nostrand: New York, 1960. (c) Bahadur, H.; Parashad, R. In *Physical Acoustics*; Mason, W. P., Thurston, R. N., Eds.; Academic Press: New York, 1982; pp 37–171.



of the HP4194A. Quality factors were calculated using the relationship  $Q = f_{\text{meas}}/(f_2 - f_1)$ .

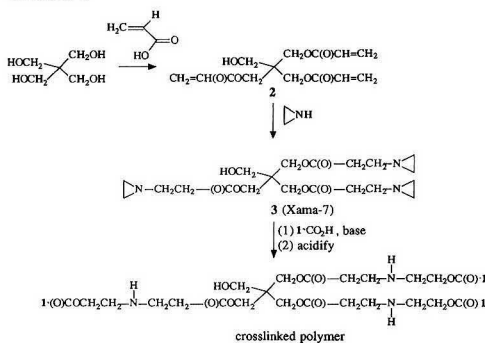
Measurements of pH were made simultaneously with frequency measurements or network analysis with a Beckman Model #32 pH meter. The analog output of the pH meter was connected to an IO/Tech analog-digital converter which was interfaced to the HPIB bus, enabling automatic measurement of pH.

Film thicknesses in aqueous solutions were measured directly with a phase measurement interferometric microscope (Zygo, Inc.). Cross-linked films of 1 were coated on evaporated gold films on quartz substrates according to the procedure described below and were immersed under a thin film (ca. 1 mm) of water contained over the sample with a glass cover slip. The pH of the solution was changed by replacing the water between the sample and the cover slip with water adjusted to the desired pH value. This replacement was performed with a syringe so that the sample compartment and optical path length was not disturbed. A reference height difference for calibration was provided by the edge of the gold films, whose thickness was established from the frequency shift of the quartz crystal microbalance during electron beam evaporation. Sessile contact angle measurements were performed with a Rame-Hart contact angle goniometer using a 10- $\mu$ L water droplet.

**Polymer Preparation and Film Immobilization.** The polymer 1 (with  $a = b = c = 1$ ) was synthesized according to a previously reported procedure.<sup>18</sup> Under a nitrogen atmosphere, an emulsifier solution consisting of 1000 mL of distilled water, 10 g of Triton QS-30 surfactant (Rohm & Haas), and 10 g of (*N,N*-dimethylamino)ethanol was heated to 60 °C. Then a mixture containing 0.58 mol of methyl acrylate, 0.58 mol of methyl methacrylate, and 0.58 mol of (dimethylamino)ethyl methacrylate was added at 4 mL/min. When the solution became saturated (saturation is evident when the solution begins to exhibit translucency), addition of an initiator solution containing 5 g of ammonium persulfate in 250 mL of distilled water was started at 0.75 mL/min while the monomer addition was continued simultaneously. Addition of the initiator results in immediate polymerization, as evidenced by a temperature increase. After all the monomer was added, the mixture was stirred for an additional 15 min and then poured into 2-L polyethylene beaker. Acetone was added until the product coagulated. The product was then collected by filtration and washed with water to remove remaining emulsifier and other impurities. The polymer was transferred to a flask equipped with a high-shear blade stirrer, ethanol added, and the mixture heated to 80 °C. After the polymer had dissolved, a solution of 32.65 g of KOH in 100 mL of distilled water was added via an addition funnel to selectively convert the methyl acrylate to the potassium salt of acrylic acid. The addition rate should be controlled so that polymer does not precipitate during this step. After the addition was complete, the mixture was stirred for an additional 30 min at 80 °C. The product either can be retained in the ethanol solution in this basic form or can be neutralized by addition of an amount of acid equivalent to the amount of base added during the hydrolysis step. The product was isolated by isoelectric precipitation by transferring the ethanol solution of the polymer to a large excess of distilled water and then adding acid to precipitate the isoelectric polymer. The polymer was isolated by centrifugation, washed with water, and then redissolved in water at a pH either above or below its isoelectric point. It is important to store the polymer as a solution because redissolution of the dried polymer is difficult.

Films of 1 were cross-linked with a multifunctional aziridine (Xama-7; Virginia Chemical Co.) according to the procedure depicted in Scheme I. Xama-7 is the pentaerythritol-tris( $\beta$ -aziridinyl)propionate 3 which is prepared by the reaction of ethyleneimine with 2, the ester of pentaerythritol and acrylic acid. Cross-linked films of 1 were prepared by spin coating a basic solution ( $\text{NH}_4\text{OH}$ ) containing 5.44% 1 and a required amount of 3, followed by heating for 5 min at 100 °C. It was found that generally a 50:1 molar ratio of 1:3 gave the best results. The heating step eliminates  $\text{NH}_3$ , thereby acidifying the coating and enabling cross-linking the polymer via a proton-assisted ring-opening reaction between the aziridine groups and a small number of the  $\text{CO}_2\text{H}$  groups of 1. The film thickness was controlled by

Scheme I



spin-coating rotational speeds, which ranged from 1000 to 4000 rpm. Film thicknesses were determined independently with a Sloan Dektak IIA stylus profilometer.

**Enzyme Activity Measurements.** The response to pH changes induced by urease-catalyzed hydrolysis of urea was measured in 2 mL of a buffer solution in which the resonator coated with cross-linked 1 was immersed. The buffer solution was prepared from 1.48 mL of 1.0 mM NaOH, 8 mL of 0.2 mM EDTA, and 100 mL of deionized water adjusted to a pH of 5.5. Determinations of the response dependence upon urease concentration were performed by adding known amounts of a urease solution (1 mg of urease in 100 mL of deionized water) to the buffer solution containing 0.25 M urea while the resonator was immersed in the solution. Conversely, the response dependence upon urea was determined by adding known amounts of a urea solution to the buffer solution containing 0.1  $\mu\text{g/mL}$  urease.

**Microbe Metabolism.** The aqueous growth medium (pH = 7.4) for microbe metabolism measurements contained 1.0% (w/v) protease peptone No. 3 (Difco), 0.1% beef extract (Bacto), 0.002% Bromo Cresol Purple, 0.5% NaCl, and 0.1%  $1\text{-CO}_2^-$ . The base medium was supplemented with carbohydrates (1% w/v) where required and filtered through a 0.2- $\mu\text{m}$  Corning sterilization filter. Response of the piezoelectric sensor to bacterial metabolism was investigated using reference strains obtained from the American Type Culture Collection (ATCC). *Escherichia coli* (ATCC 25922) was first grown overnight in a 3% trypticase soy broth (TSB) medium at 37 °C to a cell density of  $\sim 10^8$  cells/mL. Just before use, the cells were diluted to minimal media composed of 1 part in 20 in Difco Bacto Purple broth (BPB) containing no carbohydrates. The cell density was determined microscopically in a hemocytometer using a light microscope. Portions of the diluted culture are then used as a starting inoculum for the piezoelectric sensor experiments. Cell numbers determined on aliquots removed from the QCM growth chamber were obtained by first arresting the cell growth of the aliquot by addition of a 0.1% sodium azide solution. The samples were vortexed and counted visually in a Petroff Hauser counting chamber. In some cases the cell concentrations were counted automatically using an Olympus Q2 image analyzer equipped with a Compaq 386/25 computer.

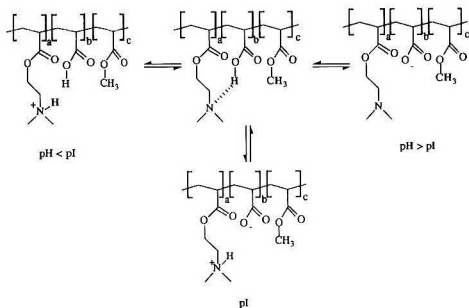
## RESULTS AND DISCUSSION

We recently reported an approach to pH sensing employing AT-cut quartz resonators and an acrylate-based polymer derivatized with  $\text{NMe}_2$  and  $\text{CO}_2\text{H}$  functionalities (1) whose solubility was dependent upon the pH of the medium (Scheme II).<sup>19</sup> As the pH of the medium approached the isoelectric point of the polymer, deposition of the isoelectric insoluble polymer onto the surface of the resonator resulted in a corresponding shift in the resonant frequency of the resonator.

(19) Ebersole, R. C.; Foss, R. P.; Ward, M. D. *Bio/Technology* 1991, 9, 450-454.

(18) Foss, R. P. U. S. Patent 4,749,762, 1988.

## Scheme II



This approach was employed successfully for the measurement of microbe metabolism.

The polymer 1 can be prepared readily from acrylate monomers so that the (dimethylamino)ethyl methacrylate, methyl methacrylate, and acrylic acid groups are present in controlled amounts (see Experimental Section). The experiments described herein were all performed with the polymer formulation  $a = b = c = 1$ . Light scattering studies suggested that  $pI \approx 6.1$  for this composition; at this value the optical density of aqueous solutions of this polymer was maximum due to scattering by the insoluble polymer. At pH values below or above the  $pI$ , however, the polymer was very soluble owing to its high degree of ionicity under these conditions. For  $pH > pI$  values, the polymer can be considered as consisting of neutral  $NMe_2$  and anionic  $CO_2^-$  groups, whereas for  $pH < pI$  the polymer can be considered as consisting of neutral  $CO_2H$  and cationic  $NMe_2H^+$  groups. Accordingly, the ionic forms of the polymer are herein referred to as 1- $CO_2^-$  ( $pH > pI$ ) and 1- $NMe_2H^+$  ( $pH < pI$ ). Light scattering and buffering capacity studies of non-cross-linked 1 indicated that the width of the isoelectric region was approximately 1 pH unit. In this region the polymer's buffering capacity is reduced, presumably owing to its decreased solubility and lower activity of the acid and base centers resulting from hydrogen bonding or electrostatic bonding of zwitterionic pairs. The buffering capacity studies actually suggested that  $pI \approx 5.5$ ; this value may be more accurate because the light scattering studies are susceptible to errors associated with the size of the polymer particles and their agglomeration. The  $pI$  and the width of the isoelectric region can be adjusted synthetically by altering the molecular weight and/or the ratio of the monomers. For example, the width of the isoelectric region would be decreased by increasing polymer uniformity (i.e., minimizing the variability of  $a$ ,  $b$ , and  $c$  among different chains).

The utility of the aforementioned sensing approach that relies on polymer precipitation is limited because it requires the presence of the pH-sensitive polymer in the medium. We therefore pursued a strategy employing polymer films immobilized on the AT-cut quartz resonator; wherein mass and viscoelastic properties were sensitive to pH changes. We surmised that the mass and viscoelastic properties of polymer films of 1 would depend upon pH for several reasons. At pH values below and above the isoelectric point the polymer film is positively and negatively charged, respectively. Under these conditions it was expected that the film would swell with solvent and electrolyte to minimize the repulsion between the charged centers. At the isoelectric point, however, the polymer can be considered as either neutral or zwitterionic. Hydrogen bonding between functional groups, the absence of charge repulsion, and hydrophobic effects were expected to reduce the swelling of the polymer. Such dimensional

changes would presumably be accompanied by large changes in viscoelasticity and surface energy (i.e., hydrophobicity)<sup>20</sup> of the polymer that could be manifested in large QCM frequency shifts. Changes in mass due to exchange of electrolyte ions and solvent between the film and solution are also to be expected. Indeed, impedance analysis indicated that precipitated films of un-cross-linked 1 on an AT-cut quartz resonator exhibited large bandwidths in the conductance spectrum and a corresponding decrease in the quality factor, suggesting energy dissipation associated with viscoelastic behavior.

**Preparation of Cross-Linked Polymer Films.** Composite resonators comprising the AT-cut quartz crystals with immobilized films of 1 were prepared by a procedure in which an esterified pentaerythritol reagent containing reactive aziridine groups served to cross-link 1 by an acid-assisted ring-opening reaction between the aziridine groups and a small number of  $CO_2H$  functionalities of 1. Films were prepared by spin coating a mixture of 1 and the cross-linking agent 3 onto a 1-in. AT-cut quartz crystal from a solution basified with  $NH_4OH$ , the basic medium suppressing the cross-linking step. Cross-linking in the film was then induced by gentle heating at 100 °C for ~10 min, which eliminated  $NH_3$  and decreased the basicity of the film. We have found that, for our purposes, films with a 50:1 ratio of 1:3 gave optimum combination of negligible solubility and large frequency responses to pH changes. Smaller amounts of cross-linking agent resulted in films that were either soluble or very tacky, with significant instability in the composite resonator. Conversely, large amounts of cross-linking agent resulted in films that are highly cross-linked and rigid and are not responsive to pH changes.

**Frequency Response to pH.** Composite resonators with the coated side of the crystal immersed in aqueous solution exhibited stable oscillation provided the film thickness did not exceed 1  $\mu m$ . Films with thicknesses exceeding this value resulted in severe acoustic losses, as indicated by the low quality factors of the resonator. These losses likely result from viscous damping associated with coupling between polymer chains and between polymer chains and solvent. Stable oscillation in air was achieved when these films were dry, corroborating the participation of solvent in the energy loss mechanism.

The series resonant frequency ( $f_s$ ), measured with the composite resonator in the feedback loop of a broad-band rf amplifier, and the frequency of maximum conductance ( $f_{G_{max}}$ ) measured by impedance analysis, were found to depend significantly upon the pH of the solution in contact with the resonator (we will assume throughout that the difference between  $f_s$  and  $f_{G_{max}}$  is negligible<sup>21</sup>). When the pH of an aqueous solution, previously acidified with  $H_3PO_4$ , was gradually increased from  $pH = 3$  the onset of an abrupt frequency decrease at  $pH \approx 4.6$  was observed (Figure 1). The magnitude of the frequency shift increased with polymer film thickness, giving exceptionally large shifts approaching -6000

(20) (a) Thompson, M.; Arthur, C. L.; Dhaliwal, G. K. *Anal. Chem.* 1986, 58, 1206-1209. (b) Rajakovic, L. V.; Covic-Viasak, B. A.; Ghaemmaghami, V.; Kallury, K. M. R.; Kipling, A. L.; Thompson, M. *Anal. Chem.* 1991, 63, 615-621. (c) Duncan-Hewitt, W. C.; Thompson, M. *Anal. Chem.* 1992, 64, 94.

(21) The values of  $f_s$  and  $f_{G_{max}}$  are rigorously different for the quartz resonator owing to the dielectric contribution of the quartz crystal, which effectively adds a capacitance in parallel to the series "motional branch" of the oscillator, in accord with the Butterworth-van Dyke electrical equivalent representation. In the feedback mode,  $f_s$  is actually measured since this mode requires oscillation at  $\theta = 0^\circ$ , where the reactance of the series branch is zero and the actual conductance is less than  $G_{max}$ . Impedance analysis, however, gives  $G_{max}$  and  $f_{G_{max}}$  explicitly, the latter occurring at a slightly lower frequency than  $f_s$ . In practice, the difference between the two is negligible, and factors that result in a shift in  $f_s$  will give a corresponding shift in  $f_{G_{max}}$ .

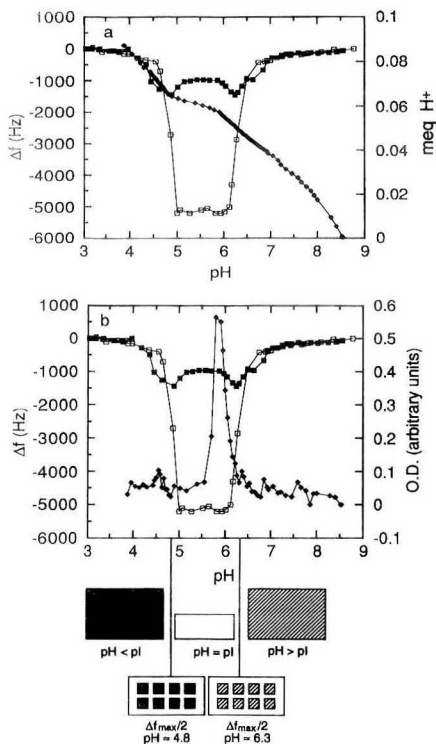
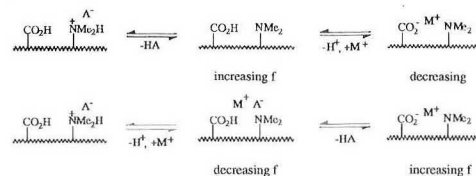


**Figure 1.** (a) Comparison of  $f_{\text{max}}$  at different pH values for a 5-MHz AT-cut quartz resonator coated with cross-linked polymer films of 1 with the buffering capacity ( $\diamond$ ) of a solution of non-cross-linked 1. (b) Comparison of  $f_{\text{max}}$  at different pH values for a 5-MHz AT-cut quartz resonator coated with a cross-linked polymer film of 1 with the optical density ( $\diamond$ ) of a solution of non-cross-linked 1. The pH was adjusted by addition of NaOH to an aqueous solution previously acidified with  $H_3PO_4$ ; thickness, 0.4 ( $\blacksquare$ ) and 0.8  $\mu\text{m}$  ( $\square$ ). Below: Schematic representation of the dimensional changes in the film and segregated domain structure when both ionic and isoelectric phases are present. No spatial ordering of the domains is implied by this representation. Key for the lower portion of the figure that identifies these phases: 1-NMe<sub>2</sub>H<sup>+</sup> ( $\blacksquare$ ); 1(isoelectric) ( $\square$ ); 1-CO<sub>2</sub><sup>-</sup> ( $\boxtimes$ ).

Hz for an 0.8- $\mu\text{m}$ -thick polymer film. The frequency exhibited a slight maximum at pH = 5.5, followed by an abrupt increase when the pH  $\approx$  6.1. The width and pH range of this isoelectric region was similar to that indicated by the buffering capacity studies of soluble 1. These data strongly suggested that the observed frequency changes were related to the changes accompanying the transitions between the ionic and isoelectric forms of 1. The small maximum in the center of the isoelectric region at pH = 5.5 was more apparent for the thinner films, which also exhibited a broader isoelectric region based on the frequency changes.

Under ideal rigid-layer conditions the frequency changes of the composite resonator would correspond only to mass changes in the polymer film that result from exchange of electrolyte required to maintain electroneutrality in the film. Electrolyte ion pairs and solvent exchange, which would contribute to the degree of swelling of the polymer, are also likely. For example, the egress of  $H_2PO_4^-$  or  $HPO_4^{2-}$  counterions from the film (depending on the actual pH;  $pK_a = 2.12$ ;  $pK_a^2 = 7.21$ ) can provide electroneutrality during the transition from 1-NMe<sub>2</sub>H<sup>+</sup> to isoelectric 1 upon increasing

### Scheme III



the pH, resulting in a mass decrease and a corresponding frequency increase (Scheme III). When pH > pI, electroneutrality could be provided by insertion of Na<sup>+</sup>, which would result in a frequency decrease. This mechanism, however, is contrary to observation. It is also feasible that upon entering the isoelectric region from the low-pH side electroneutrality is preserved by loss of H<sup>+</sup> with concomitant insertion of Na<sup>+</sup> and retention of phosphate ions, which would give a net decrease in frequency. Leaving the isoelectric region on the high-pH side the frequency increase may then correspond to loss of anions from the film with retention of the Na<sup>+</sup> ions. While this latter scheme corresponds qualitatively to the observed behavior, the frequency of the composite resonator on opposite sides of the isoelectric region, however, were identical. In addition, the frequency changes for the 0.4- and 0.8- $\mu\text{m}$ -thick films correspond to mass changes of approximately 20 and 90  $\mu\text{g}/\text{cm}^2$ , respectively. These mass changes are not proportional to film thickness and are comparable to the total areal mass ( $\Delta m/A$ ) of these films after spin coating (estimated as 40 and 80  $\mu\text{g}/\text{cm}^2$  based on a film density of 1 g/cm<sup>3</sup>). These observations strongly suggest that the frequency changes are due to factors other than mass changes.

Phase measurement interferometric microscopy (PMIM)<sup>22</sup> provides further evidence that factors other than mass changes contribute to the observed frequency decreases. PMIM relies on the measurement of a change in the phase angle of a He-Ne laser reflected from the surface of the polymer film immersed under a thin film (in this case 1 mm) of the aqueous solution. The change in phase angle with respect to a reference beam is used to calculate the actual height changes, provided the refractive indices of the solution and the film are known and constant. PMIM clearly revealed a rather dramatic decrease in the thickness of the cross-linked polymer film of 1 upon formation of the isoelectric phase. Typically, the film thickness at the center of the isoelectric region at pH = 5.5 was half that of the thickness at the pH extremes. Topographical maps of the film obtained with PMIM over large areas (200  $\mu\text{m} \times 200 \mu\text{m}$ ) indicated that the thickness change was uniform across the entire film. The thickness change is fairly abrupt and mirrors the observed frequency dependence upon pH. The significant film compaction argues against an increase in film mass as the source of the frequency decrease during the transition to the isoelectric phase, strongly suggesting an important role for changes in the viscoelastic properties of the film.

In order to determine whether stress effects were responsible for the observed frequency response, we employed the double-resonator technique, in which AT-cut and BT-cut quartz crystals are used as piezoelectric substrates simultaneously or under identical conditions.<sup>23</sup> The stress coefficients for these crystals are nearly equal in magnitude but are opposite in sign ( $K^{\text{AT}} = 2.75 \times 10^{-12} \text{ cm}^2 \text{ dyn}^{-1}$ ;  $K^{\text{BT}} = -2.65$

(22) Biegen, J. F.; Smythe, R. A. *Proc. Soc. Photo-Opt. Instrum. Eng.* **1988**, 897, 207. (b) Smith, C. P.; Fritz, D. C.; Tirrell, M.; White, H. S. *Thin Solid Films* **1991**, 198, 369.

(23) (a) EerNisse, E. P. *J. Appl. Phys.* **1973**, 44, 4482-4485. (b) EerNisse, E. P. *J. Appl. Phys.* **1972**, 43, 1330-1337. (c) Cheek, G. T.; O'Grady, W. E. *J. Electroanal. Chem.* **1990**, 277, 341.

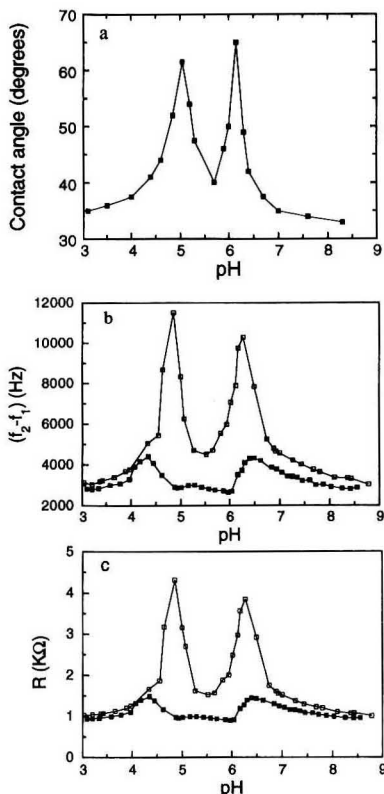


**Figure 2.** (a) The contact angle,  $\theta$ , of the polymer films measured with water drops of different pH values. (b) The bandwidth  $f_2 - f_1$  at different pH values for a 5-MHz AT-cut quartz resonator coated with a cross-linked polymer film of 1: thickness, 0.4  $\mu\text{m}$  (■) and 0.8  $\mu\text{m}$  (□). (c) The equivalent resistance,  $R$ , for a 5-MHz AT-cut quartz resonator coated with a cross-linked polymer film of 1: thickness 0.4  $\mu\text{m}$  (■) and 0.8  $\mu\text{m}$  (□).

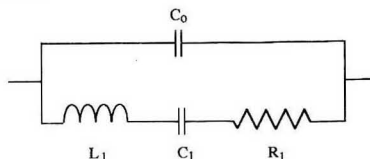
$\times 10^{-12} \text{ cm}^2 \text{ dyn}^{-1}$ ), enabling isolation of the stress contributions from other contributions such as mass changes. The stress can be directly measured using eq 2, where  $t_q^{\text{AT}}$  and  $t_q^{\text{BT}}$  are the thicknesses of the AT-cut and BT-cut quartz crystals, respectively. However, these experiments indicated identical frequency response for AT- and BT-cut crystals in the entire pH range, indicating that  $\Delta S = 0$ .

$$\Delta S = (K^{\text{AT}} - K^{\text{BT}})^{-1} [t_q^{\text{AT}} \Delta f^{\text{AT}} / f_s^{\text{AT}} - t_q^{\text{BT}} \Delta f^{\text{BT}} / f_s^{\text{BT}}] \quad (2)$$

Sessile contact angle measurement using water drops of different pH demonstrated that the polymer is very hydrophilic at the pH extrema where the polymer is ionic (Figure 2a). As the pH of the drop was increased from pH = 3, the contact angle sequentially increased from  $\theta = 35^\circ$  to a maximum of  $62^\circ$  at pH  $\approx 5$ , decreased to  $40^\circ$  at the isoelectric point, increased again to  $65^\circ$  at pH  $\approx 6.5$ , and then decreased to  $35^\circ$  at pH  $> 8$ .

**Impedance Analysis.** The shear vibration of the quartz crystal results in mechanical interactions between the crystal and the polymer film on its surface. The mechanical properties of the film therefore influence the mechanical properties of the resonator, which because of piezoelectric coupling results in corresponding changes in the electrical

**Scheme IV**



properties of the QCM. These changes can be examined readily by impedance analysis methods in which current across the quartz crystal is measured at constant voltage over a specified range of frequencies. The electrical characteristics of an unperturbed QCM are generally analyzed in terms of the Butterworth-Van Dyke equivalent circuit (Scheme IV), which comprises a LCR series branch corresponding to the mechanical motion of the crystal and a parallel capacitance associated with the static dielectric properties of the quartz crystal. The electrical properties of this circuit result in a maximum current at the resonant frequency where the capacitive and inductive reactances ( $X_C$  and  $X_L$ , respectively) cancel and the circuit becomes purely resistive in the series branch. When operating the crystal is operating in a feedback loop of an rf amplifier, the series resonant frequency is measured directly because the feedback loop operates at the highest value of the conductance at zero phase angle, which occurs when  $X_L = X_C$ . Impedance analysis, however, provides other parameters that can be used to evaluate the changes in mechanical properties occurring in the polymer film. The Butterworth-Van Dyke equivalent circuit values obtained with impedance analysis represent the mechanical properties of the composite resonator, in that  $L$  corresponds to the inertial mass,  $C$  the energy stored during oscillation, and  $R$  the energy dissipation during oscillation.<sup>24</sup> The latter term is especially significant as it reflects the energy attenuation of the acoustic wave by the film.

In principle, the Butterworth-Van Dyke equivalent circuit is applicable only when the QCM does not experience losses due to viscous coupling resulting from contact with a fluid. It has been noted, however, that near the resonant frequency, the electrical characteristics can be used to evaluate this perturbed QCM with reasonable accuracy, thus enabling measurement of the energy loss and mass loading associated with viscous coupling.<sup>10c</sup> Several reports have used this model to interpret QCM data.<sup>25</sup> Particularly useful is the electrical conductance ( $G$ ) spectrum, which reaches a maximum at  $f_{G_{\text{max}}}$ , where the real part of the electrical admittance reaches a maximum value.

The bandwidth,  $f_2 - f_1$ , where  $f_1$  and  $f_2$  are the frequencies at  $G_{\text{max}}/2$  ( $\sim 3 \text{ dB}$  below  $G_{\text{max}}$ ), is proportional to the damping of the acoustic wave energy in the composite resonator. Impedance analysis of a 5-MHz uncoated AT-cut quartz crystal revealed that  $f_2 - f_1$  typically has values of  $\sim 100 \text{ Hz}$  in air and  $\sim 3000 \text{ Hz}$  in water. Significant increases in  $f_2 - f_1$  are observed when the crystal is coated with the cross-linked films of 1, typically with values of  $3000 \text{ Hz}$  in air and values in water that depended on the solution pH (vide infra). The values of  $f_2 - f_1$  increase with polymer film thickness. This indicates appreciable attenuation of the acoustic energy due to the damping of the shear wave by viscous coupling to the polymer. Notably, the bandwidth decreases with in-

(24) (a) Buttry, D. A.; Ward, M. D. *Chem. Rev.* 1992, 92, 1355. (b) Buttry, D. A. In *Electroanalytical Chemistry*; Bard, A. J., Ed.; Marcel Dekker: New York, 1990; Vol. 17. (25) Muramatsu, H.; Tamiya, E.; Karube, I. *Anal. Chem.* 1988, 60, 2142. (b) Beck, R.; Pittnerman, U.; Weil, K. G. *Ber. Bunsen-Ges. Phys. Chem.* 1988, 92, 1363. (c) Kipling, A. L.; Thompson, M. *Anal. Chem.* 1990, 62, 1514-1519. (d) Tien, Z.; Liehwa, N.; Zhou, Y. *J. Electroanal. Chem. Interfacial Electrochem.* 1990, 293, 1.

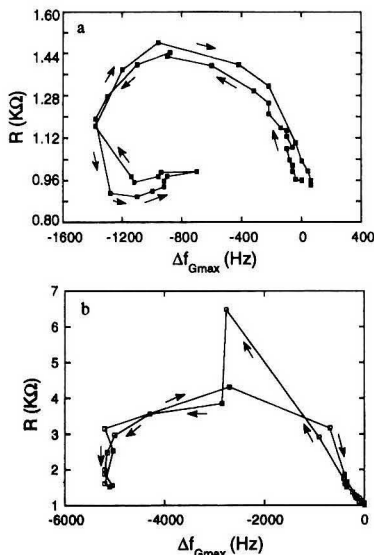


Figure 3. Equivalent resistance,  $R$ , vs  $\Delta f_{G_{\max}}$  for 5-MHz AT-cut quartz resonators coated with cross-linked polymer films of 1: (a) thickness 0.4  $\mu\text{m}$ , (b) thickness 0.8  $\mu\text{m}$ .

creasing amount of cross-linking agent during film preparation, suggesting that increased rigidity provided by greater number of cross-links reduces the viscous damping, in accord with expectations.

Impedance analysis reveals that  $f_2 - f_1$  exhibits a "double-peak" dependence upon pH, with two maxima at pH values of 5.0 and 6.4 (Figure 2b). These maxima occur at pH values corresponding to  $\Delta f_{G_{\max}}/2$  (Figure 1). The value of  $f_2 - f_1$  in the center of the isoelectric region at pH = 5.5 approached the values observed at the pH extrema. The equivalent resistance,  $R$ , which is related to the bandwidth because both are a measure of the acoustic energy loss in the coated resonator, exhibits the same dependency (Figure 2c). Remarkably, this double-peak behavior mimics the contact angle dependence upon pH, indicating that the energy dissipation and contact angles are manifestations of the same phase transition behavior.

The correspondence between  $R$  and  $\Delta f_{G_{\max}}$  is depicted in Figure 3 for polymer films of two different thicknesses. As the pH is increased from an initial value of pH = 3,  $\Delta f_{G_{\max}}$  decreases with a concomitant increase in  $R$ , with  $R$  reaching a maximum near  $\Delta f_{G_{\max}}/2$ . Further pH increases into the isoelectric region result in a decrease in  $R$  while  $\Delta f_{G_{\max}}$  still decreases. The slight increase in  $\Delta f_{G_{\max}}$  in the center of the isoelectric region is evident here for the thin film by the short-lived shift to less negative  $\Delta f_{G_{\max}}$  values. The data then essentially retrace themselves with  $R$  now increasing with more positive values of  $\Delta f_{G_{\max}}$  to  $\Delta f_{G_{\max}}/2$ , followed by a decrease in  $R$  until pH = 9, where the value of ( $\Delta f_{G_{\max}}$ ,  $R$ ) is identical to the value obtained at pH = 3. We note that these data are functionally equivalent to traces of  $\Delta\alpha/k$  vs  $\Delta\nu/\nu_0$  reported recently to describe the glassy transitions in polymer films immobilized on surface acoustic wave devices, where  $\Delta\alpha/k$  is the attenuation per wavenumber and  $\Delta\nu/\nu_0$  is the fractional velocity change.<sup>14</sup>

The frequency changes, network analysis data, and physical characterization clearly indicate that the chemical, physical, and rheological properties of 1 depend upon pH in a rather

complicated manner. Based on our previous experiments with soluble 1, it is reasonable to suggest that for pH  $\ll$  pI and pH  $\gg$  pI the polymer is highly ionized. Under these conditions the tendency of the film to minimize Coulombic repulsion by solvent incorporation can result in swelling that leads to the observed dimensional changes. Alternatively, the expulsion of water and accompanying deswelling upon transformation to the isoelectric form of the polymer may be driven by entropic effects associated with the release of bound water molecules from the increasingly hydrophobic polymer, as has been postulated for temperature- and pH-sensitive hydrogels.<sup>26</sup>

The contact angle behavior corroborates complicated phase transitions in the polymer film. The low contact angles observed at the pH extremes were expected, based on the ionicity of the polymer in these regions, similar to contact angle behavior at low pH reported for polyethylene modified with surface carboxylic acid functionality.<sup>27</sup> The increase in contact angle to the maximum values at  $\Delta f_{G_{\max}}/2$  is consistent with decreasing ionicity or the emergence of hydrophobic methyl methacrylate regions on the surface. Upon approaching the center of the isoelectric region from these maxima resregation of the hydrophobic and hydrophilic regions of the polymer is suggested by the decrease in contact angle, with the hydrophobic withdrawing to the interior of the polymer film. The similar pH dependence of the energy dissipation strongly suggests that these two phenomena are related to the same phase transitions involving the formation of ionic and isoelectric phases throughout the pH range. At the pH extremes and at the isoelectric point, a single phase exists and energy dissipation will depend upon viscous losses associated with interfacial friction between polymer chains, and between polymer chains and solvent. In contrast, at pH values approaching the isoelectric region, the polymer will consist of isoelectric and ionic phases whose relative amounts will depend upon pH. If  $\Delta f_{G_{\max}}$  is assumed to be proportional to the fraction of the ionic and isoelectric phases, the observation of maximum energy attenuation when  $\Delta f = \Delta f_{G_{\max}}/2$  suggests that the maximum energy attenuation occurs when these phases are present in equal amounts. It is reasonable to suggest that this energy dissipation is a consequence of scattering of the acoustic wave off phase domains formed from segregation of ionic and isoelectric regions (or the interfacial regions between the phase domains), as scattering would be most significant when the isoelectric and ionic phases are present in equal amounts. The viscous loss is apparently much more significant between the isoelectric and ionic phases than between polymer chains and solvent in the single-phase regions. Further examination of the data suggests that the energy attenuation is greater for the isoelectric phase than for the ionic phase. We emphasize that the postulate of phase domains is speculative, as we have no independent corroboration of their existence. Measurements of thin cross-linked films of 1 with PMIM did not indicate any evidence of phase segregation, which would have been observable because of the difference in experimentally measured refractive indices of the ionic ( $n_D = 1.37$ ) and isoelectric forms ( $n_D = 1.42$ ). However, the limited lateral

(26) (a) Franks, F. In *Chemistry and Technology of Water Soluble Polymers*; Finch, C. A., Ed.; Plenum Press: New York, 1983; Chapter 9. (b) Hoffman, A. S. *J. Controlled Release* 1987, 6, 297. (c) Afrassiabi, A.; Hoffman, A. S.; Cadwell, L. A. *J. Membr. Sci.* 1987, 33, 191. (d) Schneider, M. Reversibly Precipitable Immobilized Enzyme Complex and a Method for its Use. U.S. Patent 4,088,538, 1978. (e) Tanaka, T.; Hirokawa, Y. Reversibly Discontinuous Volume Changes of Ionized Isopropylacrylamide Cells. U.S. Patent 4,732,930, 1988. (f) Tanaka, T. *Phys. Rev. Lett.* 1978, 40, 820. (g) Tanaka, T.; et al. *Phys. Rev. Lett.* 1977, 38, 771. (h) Tanaka, T.; et al. *Phys. Rev. Lett.* 1980, 45, 1636. (i) Ilavsky, M. *Macromolecules* 1982, 15, 782. (j) Hrouz, J.; Ilavsky, M.; Ulbrich, K.; Kopecek, J. *Eur. Polym. J.* 1981, 17, 361.

(27) Bain, Colin D.; Whitesides, G. M. *Langmuir* 1989, 5, 1370.



resolution of PMIM would prevent detection of domains smaller than  $\sim 2 \mu\text{m}$ .

The pH-induced dimensional changes occurring in the polymer suggest changes in the viscoelasticity and density of the polymer film; these changes are expected to result in frequency shifts because of changes in the propagation characteristics of the shear acoustic wave in the polymer film. The double-resonator experiments indicated that there are negligible contributions from stress changes in the polymer film during the phase transitions; that is, contributions from changes in the film modulus are negligible. This behavior is not entirely unexpected because the elasticity of the film is associated with the restoring force of the chains after application of a shear stress. This property is affected primarily by the polymer network structure (i.e., cross-linking density and polymer chain configuration), which does not necessarily change during phase transitions.<sup>28</sup> Indeed, it has been shown that the shear modulus of gels does not change substantially during a phase transition, when normalized for the polymer network concentration.<sup>29</sup> The frequency changes clearly are not consistent with mass changes alone, as it is unlikely that film mass would double during deswelling or that the mass of the film would be identical at both pH extremes.

If changes in the polymer film modulus are ignored, the changes in the properties of the composite resonator may best be understood by considering contributions from changes in the viscosity of the polymer film. This can be accomplished by treating the film as a viscous Newtonian fluid, in which the shear wave amplitude decreases with distance from the resonator surface as an exponentially damped cosine function given by eq 3, where  $V_x(z,t)$  is the instantaneous velocity of

$$V_x(z,t) = Ae^{-kz} \cos(kz - \omega t) \quad (3)$$

$$\Delta f = -f_0^{3/2}(\rho_L \eta_L / \pi \rho_q \mu_q)^{1/2} \quad (4)$$

$$\delta = (\eta_L / \pi f_s \rho_L)^{1/2} \quad (5)$$

the shear wave parallel to the surface of the quartz resonator at a distance  $z$  from the resonator surface at time  $t$ ,  $A$  is the maximum amplitude of the shear wave, and  $\omega$  the resonant frequency.<sup>10ab</sup> The solution of this equation indicates that increases in the viscosity and density give corresponding decreases in the resonant frequency according to eq 4, where  $\eta_L$  and  $\rho_L$  are the absolute viscosity and density of the liquid, respectively. This dependence stems from the increase in the decay length of the shear wave ( $\delta$ ) with increasing  $\eta_L$  and decreasing  $\rho_L$  (eq 5), the decay length representing the distance from the resonator surface over which the acoustic wave amplitude decreases to  $1/e$  of its original value. Compaction of the film during transformation to the isoelectric phase results in a higher viscosity film confined closer to the resonator surface where the amplitude of the shear wave is greater, the higher viscosity increasing the amplitude and decay length of the shear wave (Figure 4). Under these conditions, the shear wave will also extend further into the solution above the polymer film as well. The enhanced coupling of the acoustic wave with the film during compaction thereby increases the effective mass detected by the propagating shear wave. The decay length of the shear wave in water for a 5-MHz QCM is  $\sim 0.25 \mu\text{m}$ . The  $R$  values for the polymer film at  $\text{pH} > \text{pI}$  and  $\text{pH} < \text{pI}$  are not much greater than those for a bare resonator (ca. 700  $\Omega$ ), suggesting similar damping characteristics and decay lengths for these two cases.

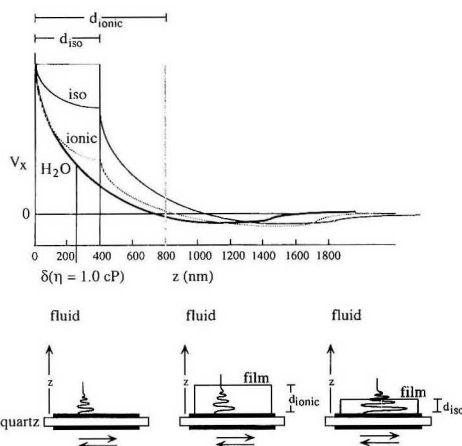


**Figure 4.** Schematic representation of the velocity profile of a shear wave, and the effect on shear wave propagation of compaction and increasing viscosity of the polymer film resulting from the phase transition between the ionic and isoelectric forms. The thick line represents the decay of the acoustic wave in water at room temperature, where the decay length for a 5-MHz shear wave is  $\delta = 250 \text{ nm}$ . The dashed lines represent the thickness of the ionic phase ( $d_{\text{ionic}} = 0.8 \mu\text{m}$ ) and shear wave propagation in this phase. The thin solid lines represent the thickness of the higher viscosity, compacted isoelectric phase ( $d_{\text{iso}} = 0.4 \mu\text{m}$ ). Compaction of the film during transformation to the isoelectric phase results in a higher viscosity film confined closer to the resonator surface where the amplitude of the shear wave is greater, the higher viscosity increasing the amplitude and decay length of the shear wave. Under these conditions, the shear wave will also extend further into the solution above the polymer film. The enhanced coupling of the acoustic wave with the film during compaction thereby increases the effective mass detected by the propagating shear wave.

Therefore, the thicknesses of the films ( $0.4\text{--}0.8 \mu\text{m}$ ) and the dimensional changes (ca.  $0.2\text{--}0.4 \mu\text{m}$ ) are of the same magnitude as the shear wave decay length. It is not surprising that substantial frequency decreases would be observed upon compaction under these conditions. We therefore attribute the frequency decrease in the isoelectric region to viscosity effects and corresponding changes in the shear wave propagation during the dimensional changes of polymer film.

Interfacial viscosities and the corresponding surface energies at the polymer film–water interface may also play a role in the observed behavior, particularly if the films are rigid enough so that the shear wave has significant amplitude at this interface. An increase in the surface energy of the polymer film interface is equivalent to an increase in the interfacial viscosity, which would favor the “no-slip” condition that is generally assumed for shear mode AT-cut resonators in liquid media. When slip occurs, the mass of the liquid layer above the interface will effectively “decouple” from the shear motion, resulting in an apparent mass decrease and a corresponding frequency increase. The data, however, cannot be interpreted on the basis of changes in the slip condition because  $\Delta f$  does not correspond to the contact angle behavior. Indeed, the resonator frequency is highest at the pH extremes where the contact angle is largest and the no-slip condition is expected to be most applicable. We conclude that, while interfacial viscosity effects may be present, their contribution is not sufficient to dominate the frequency of the composite resonator.

**Piezoelectric Measurement of Enzymatic Reactions Rates.** In order to demonstrate the possible utility of cross-linked films of 1 in sensing applications, we have examined

(28) Ullman, R. In *Elastomers and Rubber Elasticity*; Mark, J. E., Lal, J., Eds.; ACS Symposium Series 193; American Chemical Society: Washington, DC, 1982; p 257.

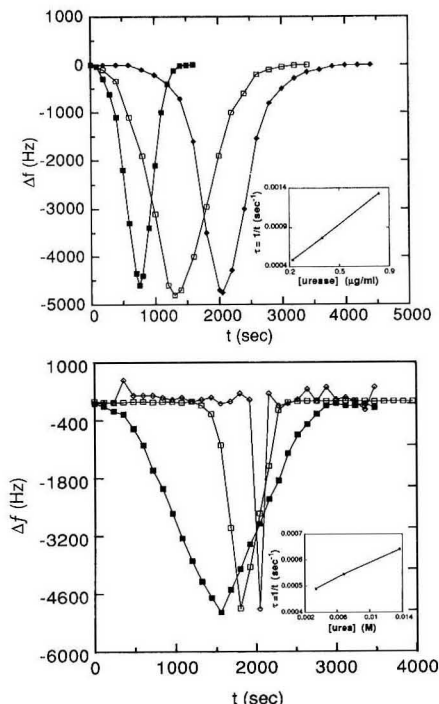


**Figure 5.** (upper) Frequency response of a 5-MHz AT-cut quartz resonator coated with a cross-linked polymer film of **1** to the urease-catalyzed hydrolysis of urea at three different urease concentrations: 0.83 (■), 0.43 (□), and 0.22 μg/mL (◆). Conditions: phosphate buffer solution containing 0.015 M NaOH, 0.016 M EDTA, and 0.25 M urea adjusted to a pH of 5.5 with  $\text{H}_3\text{PO}_4$ . Inset: Dependence of  $\tau$ , the time of minimum frequency on urease concentration. (lower) Frequency response of a 5-MHz AT-cut quartz resonator coated with a cross-linked polymer film of **1** to the urease-catalyzed hydrolysis of urea at three different urea concentrations:  $3.4 \times 10^{-3}$  M (◆),  $6.8 \times 10^{-3}$  M (□),  $13.6 \times 10^{-3}$  M (■). Conditions: phosphate buffer solution containing 0.015 M NaOH, 0.016 M EDTA, and 0.1 μg/mL urease adjusted to a pH of 5.5 with  $\text{H}_3\text{PO}_4$ . Inset: Dependence of  $\tau$ , the time of minimum frequency on urea concentration.

the frequency response of the composite resonator to the urease-catalyzed hydrolysis of urea. This reaction results in the formation of  $\text{NH}_3$  with a corresponding increase in the pH of the medium. Accordingly, when urea is added to a phosphate buffer solution (initial pH = 4.0) containing urease a monotonic frequency decrease is observed after a short time, followed by a monotonic increase until the original frequency is attained (Figure 5). The rates of frequency change in both branches are essentially identical. The time at which the frequency reaches the minimum shifts to longer values with decreasing urease concentration. These data are consistent with the pH-dependent frequency of the composite resonator: urease-catalyzed hydrolysis increases the pH of the medium, resulting in conversion of the 1-NMe $_2$ H $^+$  polymer film to its isoelectric form where the frequency decreases. Further urease-catalyzed increases in pH result in conversion from the isoelectric form to the 1-CO $_2^-$  film with a concomitant increase in frequency. The relative rates for different urease concentrations can be discerned from the inverse of the time of the frequency minimum,  $\tau$ . The experiments were performed at large urea concentrations to ensure a saturated concentration of the enzyme-substrate complex and an

enzymatically catalyzed reaction occurring at the maximum velocity,  $V_{\text{max}}$ . Under these conditions  $\tau \propto V_{\text{max}}$ , as indicated by the linear dependence of  $\tau$  on [urease]. Similarly, experiments in which [urea] is varied at constant urease concentration (but not at saturation of the enzyme-substrate complex) indicate that  $\tau$  increases with urea concentration.

**Piezoelectric Measurement of Microbe Metabolic and Growth Rates.** The growth of microorganisms and cells alters the composition of their growth medium as nutrients are consumed and converted into metabolic end products. During this process, the pH of a medium is altered by conversion of carbohydrates into smaller molecules, such as lactic acid, succinic acid, and acetic acid, or through the conversion of amino acids to ammonia and bicarbonate. The production of metabolic acids has long been recognized as a useful and broadly applicable indicator of cell metabolism and growth. For example, acid production has been used to monitor changes in cellular metabolism due to environmental influences, toxins, and chemicals.<sup>13,14</sup> We previously reported that the metabolic and growth rates of *Escherichia coli* could be determined by measuring the frequency changes due to pH-induced deposition of soluble **1** resulting from *E. coli* metabolism of carbohydrates.<sup>19</sup> Our results and previous work<sup>30</sup> indicate that *E. coli* readily metabolizes carbohydrate with a concomitant decrease in the pH of its medium; at 37 °C the population doubling rate is  $\sim 1800$  s.

The pH-dependent frequency of AT-cut quartz resonators coated with cross-linked polymer films of **1** provides a unique and convenient approach for evaluating metabolism and growth rates. Cell metabolism rates were measured with the coated side of the composite resonator submerged in a growth medium (pH = 7.5; 37 °C) containing a carbohydrate nutrient. The medium was then inoculated with *E. coli* and covered with type A immersion oil to exclude air. Under these conditions the bacteria metabolize carbohydrates to organic acids and carbon dioxide, thus lowering the pH of the medium. After an induction time required for the medium to reach the pH of the upper end of the isoelectric region of the polymer film, the decreasing pH results in a gradual decrease in frequency due to formation of the isoelectric phase (Figure 6). This is followed by a gradual increase in the frequency to the initial frequency as the pH of the medium decreases through the isoelectric region. The time of the frequency minimum is inversely proportional to the metabolic and growth rate. The inverse of this time,  $\tau$ , therefore corresponds to the rate. The value of  $\tau$  varies for different carbohydrate nutrients. Smaller values of  $\tau$  are accompanied by a broader minimum and a slower approach to the minimum frequency, behavior which is internally consistent with slower metabolic rates. The observed nutrient profiles were consistent with the known metabolic requirements of this strain with lactose > mannitol > arabinose. Experiments performed in carbohydrate-deficient media did not afford a significant response.

## CONCLUSIONS

The resonant frequency of composite resonators fabricated from AT-cut quartz crystals and cross-linked films of the amphoteric polymer **1** is very sensitive to the pH of the medium in which the resonator is immersed. While the frequency changes are not linear across the entire pH range,

(29) Ilavsky, M.; Hrouz, J. *Polym. Bull. (Berlin)* **1983**, *9*, 159.

(30) (a) Ingraham, J. L. In *Escherichia Coli and Salmonella Typhimurium Cellular and Molecular Biology*; Neidhardt, F. C., Ingraham, J. L., Brooks, K., Magasanik, M., Schaechter, M., Umberger, H. E., Eds.; American Society for Microbiology: Washington, DC, 1987. (b) Gottschalk, G. *Bacterial Metabolism*; Verlag-Springer: New York, 1987.

(31) Riccio, A. J.; Martin, S. J.; Niemczyk, T. M.; Frye, G. C. *ACS Symp. Ser.* **1989**, No. 403, 191.

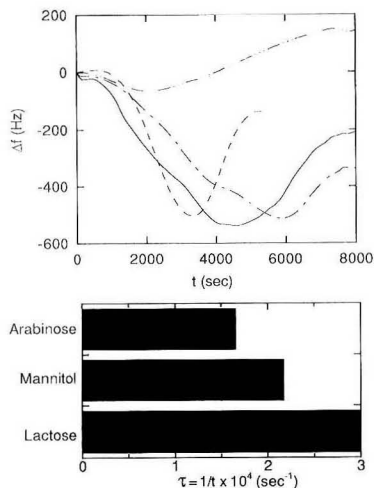


**Figure 6.** (upper) Frequency response of a 5-MHz AT-cut quartz resonator coated with a cross-linked polymer film of 1 to *E. coli* in different carbohydrates: lactose (—), mannitol (—), arabinose (---), no carbohydrate (----); polymer film thickness 0.8  $\mu\text{m}$ ; cell concentration  $10^7$  cells/mL; 1% carbohydrate nutrient in Bacto beef broth with beef extract. (lower) Relative frequency responses of the sensor in different carbohydrate nutrients based on  $\tau$ , the inverse of the time for the response curve to reach the minimum value of  $f_0$ .

they are very large within two very narrow ranges, exceeding 5000 Hz for a change of 0.1 pH unit. Assuming a reasonable signal-to-noise requirement of 2.5 and a minimum detectable frequency change of 1 Hz, this sensor is capable of detecting

pH changes of 0.001 unit in this region. This property suggests that pH sensors based on this design are particularly well suited for detecting "threshold" pH changes that may be especially useful in process control such as fermentation, enzyme-based sensors, or microbiological applications. These films are very robust, exhibiting reproducible pH response to at least 25 cycles through the isoelectric region. The ability to shift the isoelectric region, and accordingly the threshold pH, by chemically altering the acid/base ratio in the polymer enables the sensor to be tailored for a particular application and pH range. Moreover, these studies illustrate that the resonant frequency of composite resonators comprising AT-cut quartz crystals and swellable polymer films can be very sensitive to effects other than mass changes. In these cases caution must be exercised when the QCM response is interpreted so that viscoelastic effects are taken into account.

The unique properties of these polymer films suggest that modification of the polymer with specific receptors such as antibodies can provide composite resonators capable of specific binding to antigens. Phase transitions and corresponding changes in the viscoelastic properties of the polymer upon binding can afford frequency responses that are substantially greater than those expected from mass changes alone. In addition, the behavior described here for AT-cut quartz resonators is transferable to other piezoelectric transducers, such as shear horizontal plate mode<sup>31</sup> and flexure mode devices.<sup>32</sup> These strategies are likely to lead to piezoelectric sensors that are economical, robust, and widely applicable toward various applications.

#### ACKNOWLEDGMENT

The authors are grateful for the generous donation of equipment and research support from E. I. duPont de Nemours & Co.

(32) (a) Wenzel, S. W.; White, R. M. *IEEE Trans. Electron Devices* 1988, 35, 735. (b) Wenzel, S. W.; White, R. M. *Appl. Phys. Lett.* 1989, 54, 1976.

RECEIVED for review March 9, 1993. Accepted June 11, 1993.

# Analytical Applications of Catalytic Properties of Modified Cyclodextrins

Ellen Tuanying Chen and Harry L. Pardue\*

Department of Chemistry, 1393 BRWN Building, Purdue University, West Lafayette, Indiana 47907-1393

This paper describes the evaluation of the catalytic properties of modified cyclodextrins for analytical applications. The  $\beta$ -dimethylcyclodextrin was modified by adding one and two imidazolyl groups at carbon three positions. The modifications produced enhancements of catalytic activity for the hydrolysis of *p*-nitrophenyl acetate at neutral pH by factors of 1000 or more relative to the unmodified cyclodextrins. The catalytic properties of the monosubstituted cyclodextrin were evaluated for the quantification of *p*-nitrophenyl acetate in the concentration range of 10–90  $\mu\text{mol/L}$ . Results obtained by equilibrium, initial-rate, and error-compensating predictive kinetic methods were compared. The equilibrium and predictive kinetic options yielded virtually identical results, with linear changes with concentration throughout the range studied and severalfold larger than the initial-rate option and dependencies on temperature, pH, and catalyst concentration that are 5–10-fold smaller than the initial-rate option.

Cyclodextrins are macrocyclic compounds consisting of 6–12 D-glucose units joined at the  $\alpha$ -1,4 positions. The most common forms consist of 6, 7, and 8 glucose units and are identified as the  $\alpha$ -,  $\beta$ -, and  $\gamma$ -cyclodextrins, respectively.<sup>1</sup> The cyclodextrins mimic enzymes in the sense that they catalyze certain types of chemical reactions such as hydrolyses of esters and phosphates; moreover, the catalytic activities can be enhanced by modifying the cyclodextrins to contain functional groups involved in the catalytic action of enzymes.<sup>1–8</sup>

Although there have been extensive studies of the catalytic behavior of both unmodified and modified cyclodextrins (CD and M-CD),<sup>3–8</sup> there have been few if any studies of possible analytical applications of the catalytic properties of these compounds. This paper describes a study of the use of the catalytic behavior of cyclodextrins for the kinetic determination of selected organic compounds.

We chose *p*-nitrophenyl acetate (*p*-NPA) as a model substrate because the hydrolysis product, *p*-nitrophenolate ion (*p*-NP<sup>−</sup>) is easily monitored by its absorbance near 400 nm. Because preliminary studies indicated that  $\beta$ -cyclodex-

trin was the more active of the three most common CDs, most of the study was done with unmodified and modified forms of this compound. Two modified forms of  $\beta$ -CD were prepared and studied. The two modifications involved addition of one and two imidazole groups to  $\beta$ -dimethylcyclodextrin ( $\beta$ -DMCD). The two modified CDs are identified throughout as the mono- and bis-modified  $\beta$ -dimethylcyclodextrins (mM- $\beta$ -DMCD and bM- $\beta$ -DMCD). Some results are reported for unmodified  $\alpha$ -cyclodextrin ( $\alpha$ -CD) for comparison purposes. Results are reported and compared for data-processing methods without and with error-compensating capabilities.<sup>9</sup> The latter method is shown to reduce effects of experimental variables such as temperature and the concentration of catalyst.

## EXPERIMENTAL SECTION

**Instrumentation.** Data for absorbance vs time were obtained with a diode-array-based spectrophotometer (Model 8450A, Hewlett Packard Co., Palo Alto, CA). Data were transferred to and processed by a supermicrocomputer (Model 5500 workstation, Masscomp, Westford, MA) as described earlier.<sup>10</sup>

**Reagents.** All reagents except the substrate were prepared in doubly distilled (Megapure distillation apparatus, Corning Inc., Corning, NY) deionized water.

**Substrate.** The *p*-nitrophenyl acetate (Aldrich Chemical Co., St. Louis, MO) was purified by recrystallization from hexane and tested for purity by using gas chromatography. Serial dilutions of *p*-NPA were prepared in freshly distilled acetonitrile (Fisher Scientific, Chicago, IL) and stored at 4 °C until used.

**Modified Cyclodextrins.** The mono- and bis-modified dimethyl cyclodextrins were synthesized by using a slightly modified procedure described earlier.<sup>8</sup> Briefly, 0.80 g of 80% sodium hydride (Aldrich) was washed three times with degassed *n*-hexane to obtain 0.6 g (0.026 mol) of purified sodium hydride. The purified sodium hydride was added to 5 g of  $\beta$ -DMCD (Aldrich) in 0.040 L of dry tetrahydrofuran under nitrogen at 0 °C. The solution was heated and maintained at 35–38 °C for 10 h. After the solution was again cooled to 0 °C, 1.0 g of 2-(4-imidazolyl)-ethyl bromide (synthesized as described previously<sup>11</sup>) in 10 mL of degassed tetrahydrofuran was added and the solution was maintained at 25 °C for 10 h to obtain the monosubstituted cyclodextrin (mM- $\beta$ -DMCD) or 20 h to obtain the bis-substituted product (bM- $\beta$ -DMCD). Products were isolated by column chromatography on silica gel (C-60, 200–240 mesh) by elution with a ternary mixture of *n*-butanol, dimethyl formamide, and water in volume ratios of 2:1:1, respectively. The product of the 10-h reaction is a yellowish solid; the product of the 20-h reaction is a green solid.

The products were characterized by using elemental (C, H, N) determinations, fast-atom-bombardment mass spectrometry (FAB-MS), two-dimensional nuclear magnetic resonance spectrometry (in D<sub>2</sub>O), and ultraviolet absorption. The yellow precipitate from the 10-h reaction was expected to be *c*-3-[2-(4-imidazolyl)ethyl]dimethyl- $\beta$ -cyclodextrin; the green precipitate from the 20-h reaction was expected to be *c*-3,3'-[bis(2-

(1) Bender, M. L.; Komiyami, M. *Cyclodextrin Chemistry*; Springer-Verlag: Berlin, 1978.

(2) Breslow, R.; Bovy, P.; Hersh, C. L. *J. Am. Chem. Soc.* 1980, 102, 2115–2117.

(3) Tabushi, I. *Acc. Chem. Res.* 1982, 15, 1566–1572.

(4) Szejtli, J. *Cyclodextrin Technology*; Kluwer Academic Publishers: Boston, 1988.

(5) Stoddart, F. *Cyclodextrins*; Royal Society of Chemistry: London, 1989.

(6) Ikeda, H.; Kojin, R.; Yoon, C.-I.; Ikeda, T.; Toda, F. *J. Inclusion Phenom.* 1989, 7, 117–124.

(7) Breslow, R. *Acc. Chem. Res.* 1991, 24, 317–324.

(8) Schneider, H.-J.; Dürr, H. *Frontiers in Supramolecular Organic Chemistry and Photochemistry*; VCH: New York, 1991.

(9) Pardue, H. L. *Anal. Chim. Acta* 1989, 216, 69–107.

(10) Skoug, J. W.; Weiser, W. E.; Cyliax, L.; Pardue, H. L. *Trends Anal. Chem.* 1986, 5, 32–34.

(11) Stenislö, K.-E.; Wahlberg, K.; Wahren, R. *Acta Chim. Scand.* 1973, 27, 2179–2183.

(4-imidazolyl)ethyl]]dimethyl- $\beta$ -cyclodextrin. The elemental results (percent found) for the yellow precipitate were C (48.65), H (7.34), and N (1.97), corresponding to  $C_{61}H_{104}O_{36}N_2 \cdot 4H_2O$ , MW = 1425 + 4 $H_2O$ . Results for the green precipitate were C (42.8), H (7.27), and N (3.57), corresponding to  $C_{66}H_{110}O_{36}N_4 \cdot 18H_2O$ , MW = 1519.6 + 18 $H_2O$ . Molecular weights determined by FAB-MS were 1425.0 and 1519.6 for the yellow and green solids, respectively. Two NMR peaks for each compound, corresponding to chemical shifts of  $\delta$  = 7.7 and 8.25, are consistent with peaks found for the starting imidazole compound. Areas of these peaks for the yellow compound correspond to one hydrogen per peak while areas for the green compound corresponded to two hydrogens per peak.

The two-dimensional NMR results indicated that the imidazole groups are attached through the ethyl group to carbon 3 on one of the glucose units in the cyclodextrin.

Both compounds gave an ultraviolet absorption maximum at 250 nm when dissolved in water. With the exception of the carbon content for the green solid, all these results are consistent with mono- and bis-substituted  $\beta$ -dimethylcyclodextrin and the products are identified below as mM- $\beta$ -DMCD and bM- $\beta$ -DMCD, respectively.

**Procedures.** Catalyst (in buffer) and substrate (in acetonitrile) solutions were prepared fresh each day and equilibrated to the desired temperature by immersion in a temperature-controlled water bath. For each run, 1.00 mL of catalyst solution and 5.0  $\mu$ L of substrate solution were added to the temperature-controlled cuvette in the spectrophotometer and the resulting solution was stirred briefly with a small stirring rod. Data acquisition was initiated 6 s after addition of sample, and absorbance values at 400 nm were recorded at 2-s intervals. Equilibrium results were computed as the average of 10 data points collected between 786 and 806 s ( $\sim 23 t_{1/2}$ ). Predicted equilibrium absorbance changes were computed by fitting first-order<sup>12</sup> and Michaelis-Menten<sup>13</sup> models to time-dependent data during the first 75–80% of each reaction. Initial rates were computed by applying a moving-window derivative method<sup>14</sup> to time-dependent data during the first 10% of the reaction.

## RESULTS AND DISCUSSION

Imprecision is reported at the level of one standard deviation ( $\pm 1$  SD) throughout.

**Kinetic Behavior.** To facilitate comparisons with earlier reports,<sup>3–8</sup> some studies were done initially at pH 7.2 and 8.2 in phosphate buffer (0.067 M) at 30 °C. Plots of reciprocal velocity vs reciprocal concentration (Lineweaver–Burke plots) were linear. Michaelis constants,  $K_m$ , and maximum velocities,  $V_{max}$ , were evaluated in the usual way from the slopes and intercepts, respectively, of these plots. Catalytic rate constants,  $k_c$ , were computed, as the maximum velocity divided by the catalyst concentration  $k_c = V_{max}/C_{cat}$ .

Values of selected constants obtained for the mono- and bis-substituted  $\beta$ -dimethylcyclodextrin are included in Table I along with the rate constants for the uncatalyzed reaction and results obtained in an earlier study.<sup>6</sup> There is reasonable agreement among constants determined in this study and those reported earlier. The largest discrepancy (32%) is between Michaelis constants determined at pH 8.2 and 25 °C in the two studies. Even here, similar orders of magnitude were obtained.

**Response Curves.** Because reactions were quite slow for pH values described in the previous section, the remainder of these studies were done at pH 10.6 where reactions were faster. Figure 1A compares responses for the hydrolysis of *p*-nitrophenyl acetate under conditions that are the same except for the catalysts used. Plots a and b represent responses for the bis- and monosubstituted  $\beta$ -DMCD whereas

**Table I. Kinetic Parameters for the Hydrolysis of *p*-Nitrophenyl Acetate with and without Different Catalysts**

catalyst	pH <sup>a</sup>	temp (°C)	$k_c$ (10 <sup>-2</sup> s <sup>-1</sup> )	$k_{un}$ (10 <sup>-3</sup> s <sup>-1</sup> )	$K_m$ (10 <sup>-3</sup> M)	( $k_c/k_{un}$ )
bM- $\beta$ -DMCD	7.2	30	6.06 $\pm$ 0.4 <sup>b</sup>	1.26	1.45 $\pm$ 0.2 <sup>b</sup>	4810
mM- $\beta$ -DMCD	7.2	30	1.57	1.26	7.24	1246
mM- $\beta$ -DMCD	7.2	25	1.45 $\pm$ 0.01 <sup>b</sup>	1.31	2.82 $\pm$ 0.04	1106
mM- $\beta$ -DMCD <sup>c</sup>	7.2	25	1.44	1.31	2.60	1100
mm- $\beta$ -DMCD	8.2	25	3.12 $\pm$ 0.4 <sup>b</sup>	2.85	1.97 $\pm$ 0.6 <sup>b</sup>	1095
mM- $\beta$ -DMDD <sup>c</sup>	8.2	25	2.67	2.9	2.90	921

<sup>a</sup> Phosphate buffer (0.067 M). <sup>b</sup> Average of three runs. <sup>c</sup> Reference 6.

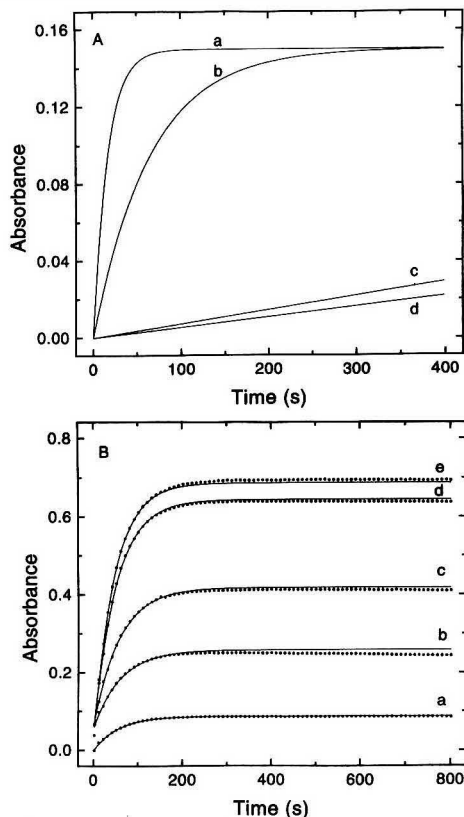


**Figure 1.** Response curves for hydrolysis of *p*-nitrophenyl acetate. (A) Catalysts: (a) bM- $\beta$ -DMCD, (b) mM- $\beta$ -DMCD, (c) and (d) none. (B) Effects of substrate concentration: (a) 9.95, (b) 27.2, (c) 45.3, (d) 64.7, and (e) 84.6  $\mu$ mol/L. Catalyst, mM- $\beta$ -DMCD;  $C_{cat}$  = 4.2 mmol/L; temp, 25.0 °C; pH 10.6 (carbonate buffer); ionic strength, 63.2 mmol/L. Experimental data (---); first-order fit (—).

curve c is for the hydrolysis without a catalyst and curve d is for hydrolysis in the presence of unmodified  $\beta$ -DMCD. Clearly both the mono- and bis-substituted cyclodextrins yield enhanced reaction rates. Either catalyst could have been used in this study. However, because larger amounts of monosubstituted product (mM  $\beta$ -DMCD) were synthesized, it was used in the remainder of this study.

(12) Mielsing, G. E.; Pardue, H. L.; Thompson, J. E.; Smith, R. A. *Clin. Chem.* 1979, 25, 1581–1590.

(13) Hamilton, S. D.; Pardue, H. L. *Clin. Chem.* 1982, 28, 2359–2365.

(14) Savitzky, A.; Golay, J. E. *Anal. Chem.* 1978, 50, 1611–1618.



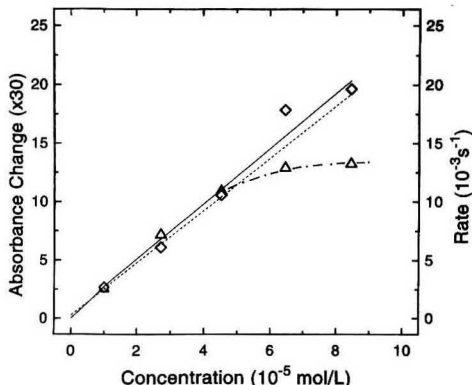


Figure 2. Calibration plots for predictive and initial-rate methods. Conditions as in Figure 1B. Linear least-squares fits through first three points: predictive method ( $\diamond$ , —); rate method ( $\Delta$ , ---).

Figure 1B represents time-dependent response curves for the catalyzed hydrolysis of different concentrations of *p*-nitrophenyl acetate in the presence of equal concentrations of mM- $\beta$ -DMCD. Individual points represent experimental data, and the solid lines represent fits of a first-order model to the data. The first-order model fits the data quite well and was used for all subsequent studies.

**Calibration Results.** Calibration results for the initial-rate and predictive methods are given in Figure 2. The ordinate values for the predictive method are multiplied by a constant factor (30) to adjust the numerical values of the two data sets to be about the same for the three lowest concentrations where both plots are linear. The linear plots in the figure represent linear-least squares fits through the first three points in each case. The least-squares statistics for these fits are included as the first two rows in Table II.

The relative standard deviations for the slopes are about the same, 7.2% for the rate method and 6.7% for the predictive method. In each case, the standard error of the estimate is 5.9% of the midpoint value and the correlation coefficients are essentially the same. The primary difference between the two data sets is the curvature of the rate data toward the concentration axis at higher concentrations. The larger intercept for the rate method probably results from the fact that the plot is already beginning to curve toward the concentration axis at the highest concentration value included in the least-squares fit. Although there is some scatter at higher concentrations for the predictive method, both points at higher concentrations are much closer to the least-squares line than for the rate data. Clearly, the predictive method is linear to much higher concentrations than the rate method.

Other data in Table II represent least-squares statistics for equilibrium results and predictive results with different fitting ranges. There are only small differences between results by the equilibrium and predictive methods for fitting ranges of two half-lives or more. It is noted that the relative standard deviations of the slopes for the predictive method (~2.6%) are better than those for the equilibrium (9.6%) and initial-rate (7.2%) methods. The same is true for the standard errors of the estimate relative to midpoint values (2.6% for the predictive method relative to 11% and 5.9% for the equilibrium and rate methods, respectively).

**Variable Dependencies.** One goal of this study was to evaluate the effects of changes in selected experimental variables on results obtained by the different data-processing options. Variable studied were temperature, pH, and catalyst

concentration. Relative error coefficients (rec) were used to quantify and summarize effects of these variables on the initial-rate, equilibrium, and predictive data-processing methods.

**Relative Error Coefficients.** The relative error coefficient for any variable,  $V$ , is equal to the change in concentration,  $\Delta C$ , produced by a change,  $\Delta V$ , in the variable of interest divided by the concentration [ $\text{rec} (\%) = 100(\Delta C/\Delta V)/C$ ]. There are different ways to quantify relative error coefficients.<sup>15,16</sup> In this study, we obtained signals for a single analyte concentration at each of several values of each variable. The error coefficients were evaluated in linear regions of calibration plots for each data-processing option.

Assuming a linear calibration plot with intercept,  $a$ , two measured signals,  $S_i$  and  $S_r$ , at a single analyte concentration, and two values,  $V_i$  and  $V_r$ , of the variable of interest, one can compute a ratio

$$R_i = (S_i - a_r)/(S_r - a_r) \quad (1)$$

in which the subscripts,  $i$  and  $r$ , refer to test and reference values, respectively, of the variable. For several such ratios obtained in this way, it is easily shown<sup>15</sup> that the slope of a plot of the ratios,  $R_i$ , as ordinate vs different values,  $V_i$ , of the variable is equal to the relative error coefficient at the value of the variable at which the slope is measured.

In this study, all the intercepts in eq 1 were very small and relative error coefficients were determined from plots of ratios computed with intercepts assumed to be zero, i.e.,  $R_i = S_i/S_r$ . Results for temperature, pH, and catalyst concentration are given below.

**Temperature.** Effects of temperature change are illustrated in Figure 3 for the three data-processing options. The ordinate is the ratio of signals at 29, 33, and 35 °C to that at 31 °C. Whereas plots for the equilibrium and predictive methods are virtually flat, the plot for the initial-rate method has a significant positive slope indicating a positive error coefficient. Numerical values of the error coefficients computed from the slopes of these plots are summarized in the first data column of Table III for the equilibrium, predictive, and initial-rate methods. The equilibrium and predictive methods have essentially the same temperature coefficients, and both options are ~15–20-fold less dependent on temperature than the initial-rate option used in the concentration range for which initial-rate varies linearly with concentration. For higher substrate concentrations for which the rate changes less rapidly with change in concentration, the temperature coefficient for the rate option would be significantly larger than that computed above whereas the error coefficients for the equilibrium and predictive methods would be essentially the same. Correlation coefficients,  $r$ , for least-squares fits of signal ratios vs variable values are also included in parentheses in the table. Results for the equilibrium and predictive methods are much less correlated with temperature than are results by the rate option.

The temperature coefficients for the equilibrium and predictive options are somewhat larger than we had expected relative to the value for the rate option. In an attempt to identify the source of this larger temperature dependency for these two options, we evaluated the effect of temperature on the absorbance after the reaction had been permitted to react to equilibrium. At 31 °C, the molar absorptivity of the reaction product (at 400 nm) was determined to be  $11.7 \times 10^3$  L/mol-cm and varied linearly with temperature between 25 and 35 °C with a slope of 160 L/mol-cm-°C. This slope corresponds to a relative temperature coefficient of 1.4%/

(15) Lim, K. B.; Pardue, H. L. *Anal. Chem.*, in press.

(16) Li, J.; Pardue, H. L. *Anal. Chem.*, in press.

**Table II. Least-Squares Results for Different Data-Processing Options<sup>a</sup>**

method	slope (SD) ( $10^{-3}$ L/ $\mu$ mol) <sup>b</sup> ( $10^{-4}$ L/ $\mu$ mol-s) <sup>c</sup>	intercept (SD) (absorbance) <sup>b</sup> ( $10^{-4}$ s <sup>-1</sup> ) <sup>c</sup>	SE (absorbance) <sup>b</sup> ( $10^{-4}$ s <sup>-1</sup> ) <sup>c</sup>	correl coeff
rate <sup>d</sup>	2.36(0.17)	3.8(5.3)	4.2	0.997
predictive ( $4t_{1/2}$ ) <sup>d</sup>	7.45(0.5)	0.01(0.015)	0.012	0.998
equilibrium <sup>e</sup>	7.79(0.75)	0.0092(0.04)	0.044	0.997
predictive <sup>e</sup> (range, $t_{1/2}$ ) <sup>f</sup>				
8	7.69(0.2)	0.0022(0.01)	0.011	0.9993
6	7.74(0.2)	0.0041(0.01)	0.012	0.9992
4	7.65(0.2)	0.0051(0.01)	0.010	0.9995
3	7.66(0.2)	0.0053(0.01)	0.012	0.9992
2	7.75(0.2)	0.010(0.02)	0.017	0.9984

<sup>a</sup> Conditions as in Figure 1B. <sup>b</sup> Equilibrium, predictive methods. <sup>c</sup> Rate method. <sup>d</sup> Lowest three concentrations. <sup>e</sup> All concentrations. <sup>f</sup> Fitting range.

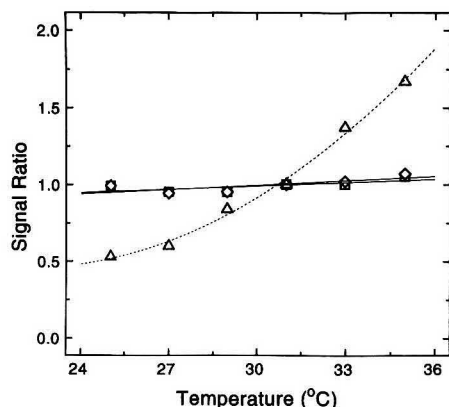


**Figure 3.** Effects of temperature on results obtained by different data-processing options. Conditions as in Figure 1B except  $C_{P-NPA} = 50$   $\mu$ mol/L and  $C_{cat} = 60$   $\mu$ mol/L. Equilibrium ( $\square$ ); predictive ( $\diamond$ ); initial rate ( $\Delta$ ). Reference signals at  $T = 31.0$  °C: ( $\square$ ),  $0.599 \times 10^{-3}$ ; ( $\diamond$ ),  $0.611 \times 10^{-3}$ ; ( $\Delta$ ),  $4.43 \times 10^{-3}$  s<sup>-1</sup>.

**Table III. Relative Error Coefficients for Three Variables and Three Data-Processing Options**

option	temp (%/°C)	pH (%/pH unit)	catalyst (%/mmol-L)
rate	14.3 (0.99) <sup>b</sup>	316 (0.997) <sup>c</sup>	84 (0.98)
equilibrium	0.7 (0.73)	-3.8 (-0.68)	1.4 (0.22)
predictive	1.0 (0.78)	3.0 (0.50)	1.6 (0.15)

<sup>a</sup> Correlation coefficients for least-squares fits of signal ratio vs variable of interest over full range in Figures 3-5 except as noted below. <sup>b</sup> 29-35 °C. <sup>c</sup> pH 10.6-12.0.

°C. Thus, most of the temperature coefficients for the equilibrium and predictive options probably result from the temperature coefficient of the absorptivity of the reaction product rather than the kinetic behavior of the reaction.

**pH.** Figure 4 includes data for the effects of pH on results obtained by the three data-processing options. For pH values between 9 and 10, all three options have relatively small dependencies on pH. However, above pH 10, the dependency of the initial-rate method on pH increases sharply. The error coefficients in this pH range for the three data-processing options are summarized in the second data column in Table III. The rate method is roughly 100-fold more dependent on pH above pH 10.6 than are the other two options. For higher analyte concentrations (see Figure 2) the difference would be larger.

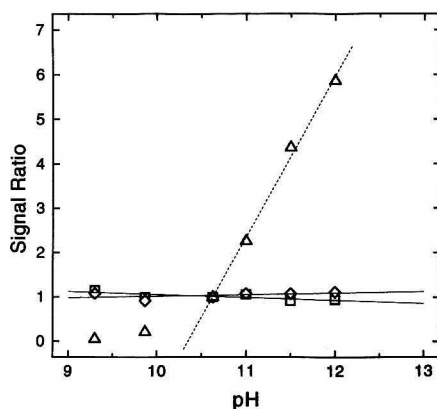


**Figure 4.** Effects of pH on results obtained by different data-processing options. Conditions as in Figure 1B except  $C_{P-NPA} = 50$   $\mu$ mol/L and  $C_{cat} = 27$   $\mu$ mol/L. Symbols as in Figure 3. Reference signals at pH 10.6: ( $\square$ )  $0.52 \times 10^{-3}$ ; ( $\diamond$ )  $0.59 \times 10^{-3}$ ; ( $\Delta$ )  $3.04 \times 10^{-3}$  s<sup>-1</sup>.

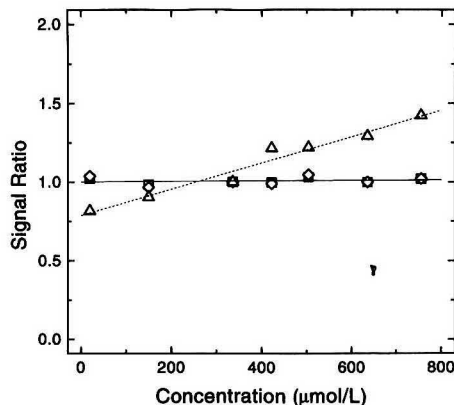


**Figure 5.** Effects of catalyst concentration on results obtained with different data-processing options. Conditions as in Figure 1B except  $C_{P-NPA} = 50$   $\mu$ mol/L. Symbols as in Figure 3. Reference signals at  $C_{cat}$  values: ( $\square$ )  $0.450 \times 10^{-3}$  s<sup>-1</sup> at 336  $\mu$ mol/L; ( $\diamond$ )  $0.464 \times 10^{-3}$  s<sup>-1</sup> at 756  $\mu$ mol/L; ( $\Delta$ )  $1.63 \times 10^{-3}$  s<sup>-1</sup> at 336  $\mu$ mol/L.

**Catalyst Concentration.** Figure 5 shows plots of signal ratios,  $S_y/S_x$ , vs catalyst concentration. Plots for the equilibrium and predictive options are virtually flat whereas that for the initial-rate option has a positive slope. The error

coefficients obtained from the slopes of these plots are summarized in the third data column in Table III. The equilibrium and predictive options are  $\sim 50$ -fold less dependent on catalyst concentration than the initial-rate option. As with temperature and pH, correlation coefficients for  $R$  vs  $V$  show much less correlation between equilibrium and predictive results and catalysts concentration than for the rate option.

**Time Dependence.** The effect of storage time on the modified cyclodextrin was evaluated by preparing a stock solution of catalyst ( $1.86 \mu\text{mol/L}$ ) in carbonate buffer (pH 10.6) and storing a portion at room temperature ( $\sim 25^\circ\text{C}$ ) and at  $4^\circ\text{C}$ . Measurements were made at six different times during a 16-day period by using  $50 \mu\text{mol/L}$  substrate. The apparent first-order rate constant, initial rate, measured equilibrium absorbance, and predicted equilibrium absorbance were determined for each data set and regressed (linear least-squares) against time. For catalyst stored at  $25^\circ\text{C}$  and at  $4^\circ\text{C}$ , the slopes for rate constants vs time were  $-1.9 \times 10^{-5}$  and  $-3 \times 10^{-6} \text{ s}^{-1} \text{ day}^{-1}$  with initial values of  $4.7 \times 10^{-3}$  and  $4.9 \times 10^{-3} \text{ s}^{-1}$ , respectively. These slopes correspond to changes of about  $-0.4$  and  $-0.6\%$ /day. Slopes for initial rates and measured and predicted equilibrium absorbances vs time all corresponded to changes of about  $(2 \pm 1)\%$ /day for samples stored at both  $25$  and  $4^\circ\text{C}$ . We had expected that any change in catalytic activity would have larger effects on rate constants and initial rates than on measured or predicted absorbances. We are unable to explain why this is not the case. In any event, time-dependent changes were relatively small.

**Reproducibility.** We evaluated the within-run reproducibility for each of the three data-processing options by making 10 runs on a fixed concentration ( $50 \mu\text{mol/L}$ ) of substrate at a fixed set of conditions ( $25^\circ\text{C}$ , pH 10.6, ionic strength of 0.0632, and catalyst concentration of  $26.7 \mu\text{mol/L}$ ). Average values of rates and absorbance changes for the initial-rate equilibrium, and predictive options were  $6.68 \text{ s}^{-1}$ , 0.740, and 0.86, respectively, and the relative standard deviations were 5.12, 3.10, and 1.74%, respectively.

## CONCLUSIONS

Addition of one or two imidazolyl groups to  $\beta$ -cyclodextrins enhances the catalytic activity several thousandfold relative to unmodified cyclodextrins. The modified compounds can be used to quantify esters such as *p*-nitrophenyl acetate in the submillimolar range. The combination of the catalytic properties of the modified cyclodextrins with error-compensating data-processing methods can extend linear ranges and reduce variable dependencies by 10-fold or more relative to initial-rate options.

## ACKNOWLEDGMENT

This work was supported in part by Grant GM13326-24 from the National Institutes of Health.

RECEIVED for review December 28, 1992. Accepted July 2, 1993.\*

\* Abstract published in *Advance ACS Abstracts*, August 15, 1993.

# Piezoelectric Detection of Water with a Separated Electrode

Wenhong Zhu, Wanzhi Wei, Zhihong Mo, Lihua Nie, and Shouzhao Yao\*

New Material Research Institute, Hunan University, Changsha, 410082, Peoples Republic of China

**A new detector of water based on the piezoelectric crystal with separated electrode (PCSE) is proposed. The frequency response of the PCSE to the dielectric constant of nonelectrolyte solution is derived. The detector was applied to determine the microcontent of water in organic solvents. The detection limits are 0.022, 0.013, and 0.010 g/L in acetone, tetrahydrofuran, and dioxane, respectively. For the water content in ethanol, linear and nonlinear regression methods are employed, and the average relative errors of prediction are 1.67% and 2.77%, respectively.**

## INTRODUCTION

There have been hundreds of publications dealing with the determination of water.<sup>1,2</sup> Among the procedures based on chemical reactions, Karl Fischer titration may be the most conventional method in terms of accuracy and sensitivity,<sup>3-5</sup> but it is somewhat difficult to perform due to reagent dehydration and toxicity. Modern physical methods prove to be useful in this field,<sup>6-12</sup> but some of them are inconvenient owing to sophisticated instrumentation. In addition, piezoelectric quartz crystal (PQC) and surface acoustic wave (SAW) sensors were employed in detecting water by merit of their high mass sensitivity,<sup>13,14</sup> but they were restricted within water detection in the gas phase.

In the past 10 years, PQCs have acquired increasing applications in the liquid phase, based on its mass and nonmass effect.<sup>15-17</sup> Recently, a new type of piezoelectric crystal with separated electrode (PCSE) was proposed,<sup>18,19</sup> in which one or two metal excitation electrodes were separated from the surface of the crystal, and the space between the electrode and the crystal was filled with liquid. We herein report the application of the PCSE in the determination of

micromatter content in organic solvents based on its high sensitivity to the dielectric property of liquids.

## THEORY

The construction of the PCSE detection cell reported in this paper is shown in Figure 1. Physically, the PCSE can be represented by the equivalent circuit shown in Figure 2. In this equivalent circuit,  $R_1$ ,  $L_1$ ,  $C_1$ , and  $C_o$  stand for the motional resistance, motional inductance, motional capacitance, and static capacitance of the quartz crystal, respectively.  $R_s$  and  $C_s$  are the solution resistance and the solution capacitance. In nonelectrolyte solution,  $R_s$  is very large and it is reasonable to neglect the contribution of  $R_s$  to the total impedance of the PCSE. Thus the total impedance can be expressed as follows:

$$Z = \frac{R_1}{M^2 + N^2} + j \left( \frac{M}{(M^2 + N^2)\omega C_o} - \frac{1}{\omega C_o} - \frac{1}{\omega C_s} \right) \quad (1)$$

where  $M = 1 + C_o/C_1 - \omega^2 L_1 C_o$ ,  $N = R_1 \omega C_o$ , and  $\omega = 2\pi f$ ,  $f$  being the frequency of the PCSE.

When a PCSE is connected in the input and output terminals of an oscillator as the positive feedback network, the ratio of the imaginary part of the impedance to the real part of the impedance should be equal to  $-Y$ ,  $Y = \tan \theta$ ,  $\theta$  being the phase shift in the oscillator. Based on eq 1, we get the following equation:

$$BM^2 - M - YN + BN^2 = 0 \quad (2)$$

where  $B = 1 + C_o/C_s$ .

As the frequency of the PCSE is determined by eq 2, it is difficult to obtain an accurate expression of the oscillating frequency. But we can assume that the frequency is determined only by  $M$  with  $N$  regarded as a constant. The reason is that  $M$  is much more sensitive to small changes in frequency than  $N$ . According to eq 2, there are two roots for  $M$ . Nevertheless, only the following value of  $M$  can be used as the series frequency measured in our experiments. The value of  $M$  is given by

$$M = \frac{1 + (1 + 4BN(Y - BN))^{1/2}}{2B} \quad (3)$$

According to the equation  $M = 1 + C_o/C_1 - \omega^2 L_1 C_o$ , the frequency of the PCSE is expressed as follows:

$$f = f_s \left[ 1 + \frac{C_1}{2C_o} \left( 1 - \frac{1 + (1 + 4BN(Y - BN))^{1/2}}{2B} \right) \right] \quad (4)$$

where  $f_s = 1/(L_1 C_1)^{1/2}$ .  $f_s$  is the resonant frequency of the quartz crystal, which is relevant to the density and viscosity of the solution.<sup>20</sup> The value of  $N$  is calculated by using  $f_s$ .

Under our experimental conditions,  $-0.1 < YBN - B^2 N^2 < 0.1$ ; thus eq 3 can be simplified as follows:

$$f = f_s \left[ 1 + \frac{C_1}{2(C_o + C_s)} + \frac{C_1(C_o + C_s)}{2C_o C_s} N^2 - \frac{C_1 Y N}{2C_o} \right] \quad (5)$$

Equation 5 indicates that the oscillating frequency of the PCSE is sensitive to changes in  $C_s$ . With the increase of  $C_s$ ,

(20) Kanazawa, K. K.; Gordon, J. G. *Anal. Chim. Acta* 1985, 177, 99.

\* Author to whom correspondence should be addressed.

(1) Mitchell, J., Jr.; Smith, D. M. *Aquametry*; Wiley: New York, 1977-1984; Parts I-III.

(2) Carr-Brion, K. *Moisture Sensors in Process Control*; Elsevier: New York, 1986.

(3) Dahms, H. U.S. Patent 4,786,602, November 22, 1988.

(4) Liang, C.; Vácha, P.; Vander Linden, W. E. *Talanta* 1988, 35, 59.

(5) Liang, Y. Y. *Anal. Chem.* 1990, 62, 2504.

(6) Ludvik, J.; Hilgard, S.; Volke, J. *Analyst* 1988, 113, 1729.

(7) Matsubara, K.; Kawata, S.; Minami, S. *Appl. Spectrosc.* 1988, 42, 1375.

(8) Ho, F. F. L.; Kohler, R. R. *Anal. Chem.* 1974, 46, 1302.

(9) Gast, T.; Talebi, R. *Thermochim. Acta* 1987, 119, 32.

(10) Karim, M. R. O. *Analyst* 1987, 112, 1369.

(11) Atanasoski, R. T.; Lew, H. H.; McIntosh, R. C.; Tobias, C. W. *Electrochim. Acta* 1987, 32, 877.

(12) Boltinghouse, F.; Abel, K. *Anal. Chem.* 1989, 61, 1863.

(13) McCallum, J. J. *Analyst* 1989, 114, 1173.

(14) Ballantine, D. S., Jr.; Wohltjen, H. *Anal. Chem.* 1989, 61, 704a.

(15) Yao, S. Z.; Nie, L. H. *Anal. Proc. (London)* 1987, 24, 336.

(16) Duttry, D. A. In *Electroanalytical Chemistry*; Bard, A. J., Ed.; Marcel Dekker: New York, 1991; Vol. 17, pp 1-85.

(17) Thompson, M.; Kipling, A. L.; Duncan-Hewitt, W. C.; Rajaković, L. V.; Cavić-Vlasak, B. A. *Analyst* 1991, 116, 881.

(18) Mo, Z. H.; Nie, L. H.; Yao, S. Z. *J. Electroanal. Chem.* 1991, 316, 79.

(19) Nomura, T.; Yanagihara, T.; Mitsui, T. *Anal. Chim. Acta* 1991, 248, 329.

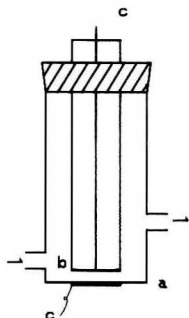


**Figure 1.** PCSE detection cell: (a) piezoelectric quartz crystal with one electrode dissolved; (b) aluminum disk fixed on the end of a glass tube; (c) leading wires. The volume of the cell is  $\sim 0.5$  mL.

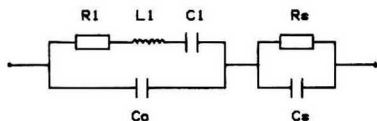


**Figure 2.** Equivalent circuit of PCSE.

$f$  decreases. It is well-known that the solution capacitance is proportional to the dielectric constant of the solution. Therefore, the PCSE is a useful dielectric constant sensor. The PCSE is applied to detect the microcontent of water in organic solvents as an example of the applications.

Since the dielectric constant of water is remarkably greater than most other materials, one of the reliable methods for detecting water is based on the direct determination of dielectric constants, which is usually measured by the capacitance method and the impedance method.<sup>21,22</sup> The capacitance method was applied to detect the moisture content in crude oil, agricultural, and manufactured products by extraction with a solvent.<sup>23</sup> However, the sensitivity of this method was relatively low. In the linear range,  $C_{\max} = 1.0\%$  and the sensitivity was 1% per meter reading.

Under ideal conditions, the dielectric constant of a binary mixture can be calculated from the linear relation<sup>21</sup>

$$\epsilon = \epsilon_1 p_1 + \epsilon_2 p_2 \quad (6)$$

where  $p_1 + p_2 = 1$ ,  $p_1$  and  $p_2$  being the relative volume fractions of each component. Oehme found,<sup>24</sup> however, that most systems did not behave ideally. Hence, a calibration curve is required for the analysis of each system. If the water content ( $x$ ) is small in a binary mixture of water and organic solvent, the approximate dielectric constant of the mixture can be calculated by eq 6. Then we obtain

$$\epsilon = \epsilon_o + (\epsilon_w - \epsilon_o)x \quad (7)$$

where  $\epsilon_o$  and  $\epsilon_w$  are the dielectric constants of the organic solvent and water. For the PCSE detection cell, the  $C_s$  value is calculated by the following equation:

$$C_s = k\epsilon + C' \quad (8)$$

where  $\epsilon$  is the dielectric constant of the solution,  $k = A/d$  is the cell constant of the detection cell,  $A$  the area of the electrode,  $d$  the distance between the separated electrode

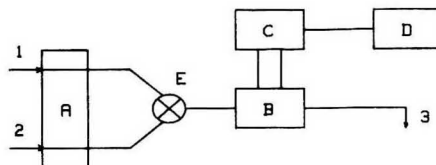


**Figure 3.** Schematic diagram of PCSE flow-through in-situ detection system: (A) electronic peristaltic pump; (B) PCSE detection cell; (C) oscillator; (D) frequency counter; (E) three-way valve; (1) reference solution, (2) sample solution, (3) waste solution.

and the crystal, and  $C'$  is the parasitic capacitance between the leading wires. The typical value of  $C'$  is  $\sim 1.8$  pF under our experimental conditions.

Frequency shifts rather than frequencies are generally used in piezoelectric sensors. The frequency shift ( $\Delta f$ ) used in this paper is  $\Delta f = f_o - f$ ,  $f_o$  and  $f$  being the frequencies of the PCSE in reference and sample solutions. With the organic solvent as the reference solution, the frequency shift of the PCSE in a sample solution can be obtained by combining eqs 5, 7, and 8. Neglecting the changes of the value of  $N$ , the frequency shift is approximately expressed as

$$\Delta f = \frac{f_o C_1 k (\epsilon_w - \epsilon_o) x}{2(C_o + C_s)^2} + \frac{f_o C_1 k (\epsilon_w - \epsilon_o) N^2 x}{2C_o^2} - \frac{\Delta Y f_o C_1 N}{2C_o} - \Delta f_s \quad (9)$$

where  $\Delta f_s$  is the resonant frequency shift of the crystal,  $\Delta Y$  is the change caused by the phase shift of the oscillator, and the values of  $\Delta f_s$  and  $\Delta Y$  are negative in the binary system used in this paper.

Equation 9 indicates that the frequency shift of the PCSE has a linear relationship with the water content. The sensitivity of the method, as indicated by the slope of the calibration curve, is relevant to differences in dielectric constant between the organic solvent and the water. The greater the difference, the greater the slope. In dioxane-water mixture, the approximate slope of the calibration curve may be estimated by virtue of the normal values of the parameters of the crystal. With  $f_o = 9 \times 10^6$  Hz,  $C_o = 8 \times 10^{-12}$  F,  $C_1 = 4 \times 10^{-14}$  F,  $C' = 1.8 \times 10^{-12}$  F,  $k = 6 \times 10^{-2}$  m,  $R_1 = 3 \times 10^2 \Omega$ , and  $x = 0.1\%$ , the frequency shift arising from the first and second terms is  $\sim 80$  Hz. If  $\Delta Y$  and  $\Delta f_s$  are taken into account, the frequency shift is a little larger. Obviously, the sensitivity is satisfactory.

## EXPERIMENTAL SECTION

**Apparatus and Reagents.** The PCSE detector used in this work was illustrated in Figure 1. A separated electrode, an aluminum disk, and a piezoelectric crystal were fixed separately by epoxy resin to the ends of two glass tubes. The distance between the separated electrode and the crystal was ca. 0.5 mm, and the volume of the detection cell was ca. 0.5 mL. The crystal oscillator and the frequency counter were described in the previous paper.<sup>25</sup> A flow-through detection system for in-situ monitoring of water content in organic solvents was illustrated in Figure 3. Solutions were introduced into the detection cell with an electronic peristaltic pump. The solution temperature was controlled at  $25 \pm 0.1$  °C by a water bath in all experiments, and the room temperature was air-conditioned at  $25 \pm 0.5$  °C.

Analytical-grade chemicals and deionized-distilled water were used. All the organic solvents were used without being dehydrated. It should be mentioned here that dioxane, flammable and harmful to health, must be handled with care in the determination of the water content. Undoubtedly, an in-situ method is preferable in this respect.

**Procedure and Calibration.** The reference solution was first passed through the detection cell with a three-way valve, and the

(21) Thomas, B. W. In *Treatise on Analytical Chemistry*, Part I; Kolthoff, I. M., Elving, P. J., Eds.; Wiley: New York, 1963, Vol. 4, p 2641.

(22) Mitchell, J., Jr. In *Treatise on Analytical Chemistry*, Part II; Kolthoff, I. M., Elving, P. J., Eds.; Wiley: New York, 1961, Vol. 1, p 158.

(23) Katz, S.; Bach, W. W.; Reiche, W. A. *Anal. Chem.* 1969, 41, 1270.

(24) Oehme, F. *Angew. Chem.* 1956, 68, 467.

(25) Yao, S. Z.; Mo, Z. H. *Anal. Chim. Acta* 1987, 193, 97.



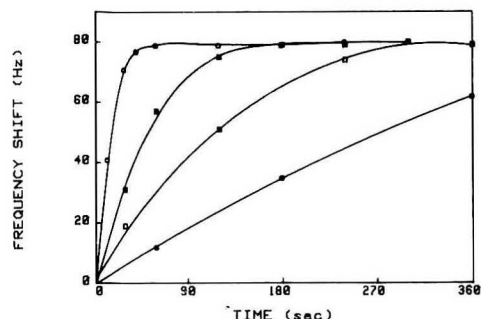


Figure 4. Relationship between frequency shift and time for ethanol containing 2.0 g/L water with detection cell at different flow rates: (●) 3, (□) 10, (■) 20, and (○) 30 mL/min.

Table I. Linear Regression Result for Water in Acetone, Tetrahydrofuran, and Dioxane<sup>a</sup>

solv	$\epsilon_r^{27}$	slope (Hz/L/g)	SD (g/L)	$r$
dioxane	2.2	100	0.003 33	0.998
THF	7.4	78	0.004 40	0.998
acetone	20.7	46	0.005 95	0.999

<sup>a</sup>  $\epsilon_r$  is the relative dielectric constant; SD is standard deviation;  $r$  is correlation coefficient.

stable oscillating frequency was recorded as the reference frequency ( $f_0$ ). The sample solution was then passed through the detection cell, and the stable frequency was recorded again as the sample frequency ( $f$ ). In this way the frequency shift,  $\Delta f = f_0 - f$ , was obtained.

The standard solutions were prepared by precisely adding different amounts of water to each organic solvent. Frequency shifts for each standard solution were measured by using the corresponding solvent as the reference solution. Obviously, to obtain an absolute water content, the reference solution should be anhydrous. If the reference solution contains a small quantity of water ( $x_0$ , for example), the actual water content in the sample solution should be  $x + x_0$ , provided the water content is in the linear range. The water contents in reference solvents were determined by Karl Fischer titration.

## RESULTS AND DISCUSSION

**Response Rate.** The ethanol solution containing 2.0 g/L water was passed through the detection cell at different flow rates. The changes in frequency vs time were shown in Figure 4. It can be seen that the frequency becomes stable within 1 min when the flow rate is greater than 30 mL/min. Although the response rate of the piezoelectric crystal is fast, the replacing rate of solution is relatively slow. Therefore, the replacing rate is the dominant factor for the stable time. It is obvious that the replacing rate is dependent on the construction or volume of the detection cell and the flow rate of solutions, and an effective way to accelerate the response rate of this new detector can be obtained by decreasing the volume of the detection cell and increasing the flow rate of solutions. With regard to the piezoelectric detector described above, a flow rate of 30 mL/min is used in our analysis. The volume of the sample was 25 mL.

**Sensitivity, Accuracy, and Precision.** The correlations of the frequency shift and the water content in dioxane, tetrahydrofuran, and acetone are summarized in Table I. The frequency shift is in a good linear relation with the water content in the range of 0.03–10, 0.04–15, and 0.07–20 g/L in dioxane, tetrahydrofuran (THF), and acetone, respectively. The corresponding detection limits are 0.010, 0.013, and 0.022

Table II. Effect of Foreign Organic Solvents on Data of Water in Dioxane<sup>a</sup>

	$\epsilon_r^{27}$	$\Delta f$ (Hz) A/B	RD (%) A/B
dioxane	2.2	60/60	
methanol	32.6	59/51	1.7/15
ethanol	24.3	59/55	1.7/8
<i>n</i> -propanol	20.1	60/58	−/3
cyclohexanol	15.0	60/59	−/2
ethyl ether	4.34	60/60	
furan	2.95	60/60	
acetic acid	6.15	61/63	1.7/5

<sup>a</sup>  $\Delta f$  is the frequency shift of the sensor in dioxane containing 0.6 g/L water and 1% (A) or 10% (B) foreign solvent. RD is relative deviation.

Table III. Regression Analysis of Data for Eight Unknowns

sample no.	concn (% v/v)		rel error (%)	
	actual	predicted (1) <sup>a</sup> (2)	(1)	(2)
1	0.100	0.103 0.104	3.00	3.50
2	0.300	0.305 0.303	1.67	1.00
3	0.600	0.595 0.591	0.83	1.50
4	1.00	1.04 1.03	4.00	3.00
5	1.40	1.40 1.39	0.00	0.71
6	1.77	1.79 1.78	1.13	0.56
7	2.15	2.10 2.09	2.33	2.79
8	2.53	2.52 2.51	0.43	0.79
av			1.67	1.73

<sup>a</sup> (1) linear regression; (2) nonlinear regression.

g/L, which are much lower than that of the classical capacitance method ( $\sim 4$  g/L).<sup>26</sup> In addition, it can be seen that the less the dielectric constant of the solvent, the higher the sensitivity of the PCSE detector to the water content, which is consistent with the prediction of eq 9.

**Effect of Foreign Substances.** In the case of dioxane containing a foreign substance as the reference solution, the frequency shifts due to the water content are listed in Table II. It can be seen that only the frequency shifts in the solutions containing a high concentration (10%) of methanol or ethanol are decreased. The reason is that the dielectric constant of the solution becomes larger in such a case, and increase in dielectric constant reduces the sensitivity. This indicates that the effect of the foreign substance is relevant to the difference of dielectric constants between the foreign substance and the main solvent (dioxane). Similar experiments have been carried out in ethanol, and the results indicate that the foreign substances, including methanol, acetic acid, and ethyl ether, do not affect the determination.

**Effect of Temperature.** As the temperature of a solution rises, the dielectric constant of the solution usually decreases, thus increasing the frequency of the PCSE. Besides, the parameters of the crystal are also functions of the temperature. The effect of temperature on measurement was tested. The frequency temperature coefficients (Hz/°C) of the PCSE are 4.8 in dioxane, 7.9 in tetrahydrofuran, 9.6 in acetone, and 9.3 in ethanol at temperatures ranging from 20 to 30 °C. Therefore, keeping the measurement temperature constant is important for precise quantitation.

**Application.** The PCSE was applied to determine the water content in ethanol samples with linear and nonlinear regression calibration techniques. Seven calibration samples

(26) Wolfe, W. C. *Anal. Chem.* 1963, 35, 1884.

(27) Weast, R. C.; Astle, M. J.; Beyer, W. H. *CRC Handbook of Chemistry and Physics*, 65th ed.; CRC Press Inc.: Boca Raton, FL, 1984.

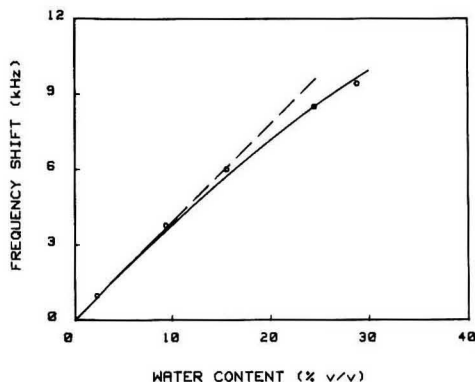


**Figure 5.** Correlation of frequency shift and water content ranging from 0 to 30% for ethanol: points, experimental data; line, regression results.

of ethanol with water content ranging from 0 to 3% were prepared, the frequency shifts were measured, and a linear model was fitted to the experimental data. The regression equation is given by

$$\Delta f = -0.8 + 3.732 \times 10^4 x \quad (10)$$

where  $x$  is the water content (v/v) and  $\Delta f$  is the frequency shift in hertz. Then eight separately prepared samples as the unknowns were measured under the same experimental conditions. The model was used to predict their water content. Table III lists the actual and predicted water content for the eight samples, and the average relative error is 1.67%.

As can be seen in eq 9,  $\Delta f$  is proportional to  $x$  under the condition of  $x \ll 1$ . In a sample solution with high water content, the relation between  $\Delta f$  and  $x$  is no longer linear as  $C_s$  increases. The high content of water also brings about changes in parameters of the crystal and circuit, which is related to  $x$ . Figure 5 illustrates the correlation of the frequency shift and the water content ranging from 0 to 30% for six calibration samples; the deviation from the straight

**Table IV.** Nonlinear Regression Analysis of Data for Five Unknowns

sample no.	concn (% v/v)		rel error (%)
	actual	predicted	
1	1.96	1.99	1.53
2	9.09	9.50	4.51
3	15.25	15.97	4.72
4	24.24	24.02	0.91
5	28.57	27.94	2.20
av			2.77

line can be seen in the water content ranging from near 10 to 30%. In order to establish a suitable method to determine the water content in wider ranges, a nonlinear regression model was utilized to fit the experimental data. The equation we got is

$$\Delta f = -1.4 + 3.774 \times 10^4 x - 90x^2 - 3.1x^3 \quad (11)$$

The water contents of five unknown samples predicted by eq 11 are listed in Table IV. The average relative error is 2.77%. The results show that the nonlinear regression model is suitable for water analysis in wider concentration ranges.

To test the suitability of the nonlinear regression model, the experimental data for the lower water contents were analyzed by eq 11 and the results are also listed in Table III. The average relative error for the eight unknown samples is 1.73%.

To test the efficiency of the procedure, a dioxane sample was analyzed by means of the PCSE method and Karl Fischer titration. The water content (g/L) of three samples is  $0.221 \pm 0.0043$  for the former and  $0.223 \pm 0.0067$  for the later method.

#### ACKNOWLEDGMENT

The authors thank Dr. Shen Dazhong in this laboratory for his helpful discussions. This work was supported by the Natural Science Foundation and the Education Commission Foundation of China.

RECEIVED for review April 3, 1992. Accepted June 16, 1993.

# Schiff Base Complexes of Cobalt(II) as Neutral Carriers for Highly Selective Iodide Electrodes

Ruo Yuan, Ya-Qin Chai, Dong Liu, De Gao, Jun-Zhong Li, and Ru-Qin Yu\*

Department of Chemistry and Chemical Engineering, Hunan University, Changsha, 410082, China

A new solvent polymeric membrane electrode based on Schiff base complexes of Co(II) is described which demonstrates excellent selectivity toward the iodide ion. The resulting electrode exhibits fairly low detection limits and good selectivity properties. The selectivity sequence observed is iodide > thiocyanate ~ nitrite > perchlorate ~ bromide > nitrate > chloride > sulfate. The excellent selectivity for iodide is related to the unique interaction between the central Co(II) ion and iodide. The response mechanism of the electrode was also studied with the ac impedance and spectroscopic techniques.

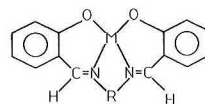


Figure 1. Structures of Schiff base complexes of metal(II) used to prepare membrane electrodes [Co(II)(salen), M = Co(II), R = C<sub>6</sub>H<sub>4</sub>; Co(II)(salophen), M = Co(II), R = C<sub>6</sub>H<sub>4</sub>; Ni(II)(salen), M = Ni(II), R = C<sub>6</sub>H<sub>4</sub>].

Co(II) are incorporated into plasticized PVC membranes with 2-nitrophenyl dodecyl ester (o-NPDE) as the plasticizer to prepare electrodes with substantially improved selectivity toward the iodide ion.

## EXPERIMENTAL SECTION

**Reagents.** Bis(salicylaldehyde)ethylenediiminecobalt(II) [Co(II)(salen)], bis(salicylaldehyde)phenyldiiminecobalt(II) [Co(II)(salophen)], and bis(salicylaldehyde)ethylenediiminenickel(II) [Ni(II)(salen)] were prepared as described by refs 15-17 (see Figure 1). Bis(salicylaldehyde)ethylenediimineiodocobalt(III) [Co(III)(salen)] was synthesized as described by refs 18-20. The products were identified by elemental analysis. The 2-nitrophenyl dodecyl ether (o-NPDE) was synthesized as described by Horning.<sup>21</sup> The synthesis of hexadecyltriethylammonium iodide (HTOAI) was described in ref 22. Poly(vinyl chloride) (PVC) powder of chromatographic grade was a product of Shanghai Chemical Co. Redistilled deionized water and analytical-grade reagents were used throughout.

**Apparatus.** Potentiometric and pH measurements were made with a Model 901 microprocessor analyzer (Orion, Cambridge, MA). The cells used for millivolt measurements were of the following type: Hg; Hg<sub>2</sub>Cl<sub>2</sub>, KCl (satd)|NaNO<sub>3</sub> (3 mol/L)|sample solution|membrane|NaNO<sub>3</sub> (3 mol/L), pH 5.6 buffer|AgCl, Ag. The pH 5.6 buffer solution used was 1.0 mol/L in citrate and 1.0 mol/L in KCl. The external reference electrode was a double-junction saturated calomel electrode. Before use, the electrodes were conditioned in the 0.1 mol/L KI aqueous solution for 1 day.

The membrane composition was optimized by using an orthogonal experimental design with the electrode linear response range for iodide ion as the object function for optimization. The optimum composition found was 2.5% (w/w) in ionophore, 31% (w/w) in PVC, and 66.5% (w/w) in o-NPDE. The PVC membrane electrodes were fabricated from various carriers and assembled according to Thomas and co-workers.<sup>23,24</sup>

## INTRODUCTION

Anion-sensitive membrane electrodes based on ion exchangers such as lipophilic quaternary ammonium or phosphonium salts display classical Hofmeister behavior in which the membrane selectivity is controlled by the free energy of hydration of ions involved.<sup>1,2</sup> Recently, electrodes using plasticized poly(vinyl chloride) (PVC) membranes incorporating derivatives of vitamin B<sub>12</sub>, Co(III), Sn(IV), Mo(IV), and Mn(III) porphyrin complexes, and electropolymerized Co(II) porphyrin derivative films demonstrated potentiometric anion-selectivity sequences which deviated from the Hofmeister pattern.<sup>3-12</sup> These deviations result from the direct interaction between the central metal and the analyte ion and steric effect associated with the structure of the porphyrin ring.

The complexes bis(salicylaldehyde)ethylenediiminecobalt(II) and similar Schiff base complexes of Co(II) can reversibly coordinate oxygen and have been extensively studied as "model compounds" to simulate natural oxygen carriers which contain a transition metal [e.g., iron (myoglobin), copper (hemocyanin)].<sup>13,14</sup> In this paper, Schiff base complexes of

\* To whom correspondence should be addressed.

(1) Sollner, K.; Shean, G. M. *J. Am. Chem. Soc.* 1964, 86, 1901-1902.  
(2) Wuthier, U.; Pham, H. V.; Zund, R.; Welti, D.; Funck, R. J. J. Bezegh, A.; Ammann, D.; Pretsch, E.; Simon, W. *Anal. Chem.* 1984, 56, 535-538.

(3) Schulthess, P.; Ammann, D.; Krautler, B.; Caderas, C.; Stepanek, R.; Simon, W. *Anal. Chem.* 1985, 57, 1397-1401.

(4) Stepanek, R.; Krautler, B.; Schulthess, P.; Lindemann, B.; Ammann, D.; Simon, W. *Anal. Chim. Acta* 1986, 182, 83-90.

(5) Ammann, D.; Huser, M.; Krautler, B.; Rusterholz, B.; Schulthess, P.; Lindemann, B.; Halder, E.; Simon, W. *Helv. Chim. Acta* 1986, 69, 849-854.

(6) Chaniotakis, N. A.; Chasser, A. M.; Meyerhoff, M. E.; Groves, J. T. *Anal. Chem.* 1988, 60, 185-188.

(7) Hodinar, A.; Jyo, A. *Chem. Lett.* 1988, 993-996.

(8) Hodinar, A.; Jyo, A. *Anal. Chem.* 1989, 61, 1169-1171.

(9) Chang, Q.; Meyerhoff, M. E. *Anal. Chim. Acta* 1986, 186, 81-90.

(10) Chaniotakis, N. A.; Park, S. B.; Meyerhoff, M. E. *Anal. Chem.* 1989, 61, 566-570.

(11) Abe, H.; Kokufuta, E. *Bull. Chem. Soc. Jpn.* 1990, 63, 1360-1364.  
(12) Daunert, S.; Wallace, S.; Florido, A.; Bachas, G. *Anal. Chem.* 1991, 63, 1676-1679.

(13) Ochiai, E. I. *J. Chem. Educ.* 1973, 50, 610-611.

(14) Appleton, T. G. *J. Chem. Educ.* 1977, 54, 443-444.

(15) Bailes, R. H.; Calvin, M. J. *Am. Chem. Soc.* 1947, 69, 1886-1893.

(16) Deiasi, R.; Holt, S. L.; Post, B. *Inorg. Chem.* 1971, 10, 1498-1500.

(17) Chen, B. T. *Experimental Manual of Inorganic Chemistry*; Beijing Normal University Press: Beijing, 1984; pp 210-217.

(18) Floriani, C.; Puppis, M.; Calderazzo, F. *J. Organomet. Chem.* 1968, 12, 209-223.

(19) Marzilli, L. G.; Marzilli, P. A.; Halpern, J. J. *Am. Chem. Soc.* 1971, 93, 1374-1378.

(20) Burness, J. H.; Dillard, J. G.; Taylor, T. *Syn. React. Inorg. Metal-Organ. Chem.* 1976, 6, 165-177.

(21) Horning, E. C. *Organic Syntheses*; John Wiley: New York, 1955; Collect. Vol. III, pp 140-141.

(22) Yu, R. Q.; Huang, S. S. *Talanta* 1983, 30, 427.

(23) Moody, G. J.; Oke, R. B.; Thomas, J. D. R. *Analyst* 1970, 95, 910-918.

(24) Gragg, A.; Moody, G. J.; Thomas, J. D. R. *J. Chem. Educ.* 1974, 51, 541-544.

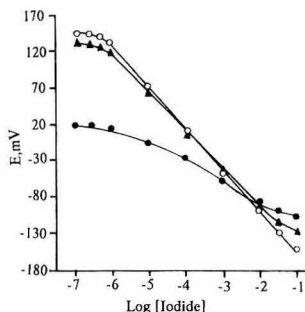


**Figure 2.** Potentiometric response curves of Schiff base complexes of metal(II), Co(II)(salophen) (○), Co(II)(salen) (▲), and Ni(II)(salen) (●), in 0.01 mol/L  $\text{H}_3\text{PO}_4$ -NaOH solution, pH 2.5.

**Determination of emf Response and Selectivity of the Electrodes.** Anion selectivity coefficients,  $\log K_{\text{I}^-}^{\text{pot}}$ , were determined by separate solution method. The solutions were buffered with 0.01 mol/L  $\text{H}_3\text{PO}_4$  and adjusted to pH 2.5 with a concentrated NaOH solution. The single-ion activities were calculated by using the extended Debye-Hückel equation.

**Determination of emf Response of the Electrodes in an Oxygen-Free Environment.** The fabricated PVC membrane containing various ionophores was dried in vacuo. Before use, the electrodes were conditioned in 0.1 mol/L KI aqueous solutions which were deoxygenated by bubbling nitrogen through the solutions for 24 h. The various KI solutions were prepared with deoxygenated buffered solutions and then  $\text{N}_2$  was allowed to flow over the freshly prepared KI solution during the determination of emf response of the electrodes.

**ac Impedance Experiments.** The ac impedance of the electrode membrane, plasticized with *o*-NPDE and containing 5.46 mmol of Co(II)(salen), was recorded with the PAR M 368-2 system (EG&G Princeton Applied Research, Princeton, NJ) in 0.01 mol/L  $\text{H}_3\text{PO}_4$ -buffered solutions adjusted to pH 2.5 with NaOH. The frequency range used was  $10^0$ – $10^2$  Hz (at 14 °C).

**UV-Visible Absorption Spectra.** Spectra of the chloroform phase, obtained by shaking a solution of Schiff base complexes of metal(II) in  $\text{CHCl}_3$  with aqueous 0.1 mol/L KI for 30 min, were recorded on a PE Lambda 17 spectrophotometer (Bodenseewerk Perkin-Elmer & Co. GmbH, D-7770 Ueberlingen, Germany).

## RESULTS AND DISCUSSION

**emf Response Characteristics and Selectivity of Electrodes Doped with Schiff Base Complexes of Metal(II).** Potentiometric response characteristics of the electrodes containing different carriers are shown in Figure 2. The electrode incorporating Co(II)(salophen) showed a near-Nernstian potentiometric response for  $1 \times 10^{-4}$ – $1 \times 10^{-6}$  mol/L  $\text{I}^-$  with a detection limit of  $7 \times 10^{-7}$  mol/L and a slope of  $56.2 \pm 0.2$  mV/pI $^-$  (20 °C) in 0.01 mol/L  $\text{H}_3\text{PO}_4$  buffer solutions adjusted to pH 2.5 with NaOH. The time required for the electrode to reach 90% response was less than 1 min. The dc resistance of the electrode membrane was  $124.7 \pm 0.3$  k $\Omega$  (average of six determinations,  $n = 6$ ). The standard deviation of the electrode potential readings over a period of 12 h in 0.01 mol/L phosphate-buffered solution (pH 2.5) containing 0.001 mol/L KI was 0.3 mV ( $n = 72$ ), and the potential readings for the electrode dipped alternately into stirred solutions of 0.01 and 0.001 mol/L KI showed a standard deviation of 0.8 mV over 2 h ( $n = 6$ ). An electrode conditioned by continuous contact with 0.01 mol/L KI aqueous solution (pH 5.6) for 2 months did not show detectable loss of performance characteristics. The electrode doped with Co(II)(salen) showed a linear response for  $6 \times 10^{-2}$ – $2 \times 10^{-6}$  mol/L with a slope of  $55.8 \pm 0.3$  mV/pI $^-$  ( $n = 5$ , 20 °C) in phosphate-buffered solutions of pH 2.5. The other potentiometric response

**Table I.** Selectivity Coefficients,  $\log K_{\text{X}^-}^{\text{pot}}$  for the Solvent Polymeric Membrane Containing Different Carriers<sup>a,b</sup>

anion	Co(salophen)	Co(salen)	HTOAI
$\text{I}^-$	0	0	0
$\text{Cl}^-$	-4.3	-4.1	-3.1
$\text{Br}^-$	-2.5	-2.6	-2.0
$\text{ClO}_4^-$	-2.4	-2.4	1.9
$\text{SCN}^-$	-2.2	-2.1	0.5
$\text{NO}_3^-$	-4.2	-4.2	-1.4
$\text{NO}_2^-$	-2.2	-2.1	-2.8
$\text{SO}_4^{2-}$	-4.5	-4.4	-4.2

<sup>a</sup> Selectivity coefficient obtained with the separate solution method, in a 0.01 mol/L phosphate-buffered solution (pH 2.5). <sup>b</sup> Membrane compositions: 2.5% (w/w) in carrier; 31% (w/w) in PVC; 66.5% (w/w) in *o*-NPDE.

characteristics of the electrode containing Co(II)(salen) are very similar to those of the electrode incorporating Co(II)(salophen). The potentiometric response characteristics of the electrode doped with Ni(salen) are rather poor (see Figure 2).

The potentiometric selectivity coefficients for membranes containing different carriers are shown in Table I. The electrode containing Co(II)(salophen), for instance, showed a selectivity sequence of anions in the following order: iodide > thiocyanate ~ nitrite > perchlorate > bromide > nitrate > chloride > sulfate.

**Mechanism of Iodide Response and Selectivity.** The electrodes doped with a Co(III) porphyrin derivative exhibit fairly high selectivity toward the thiocyanate ion.<sup>5,7</sup> The potentiometric selectivity coefficient  $K_{\text{I}^-}^{\text{pot}}$  were 1.3<sup>5</sup> and 5.6.<sup>7</sup> This was partially explained in terms of the stability constant of the Co(III) complex of porphyrin derivatives with anions which decreases according to the following order: thiocyanate > iodide > bromide > chloride.<sup>26</sup> The sensors based on poly[cobalt(II)tetrakis(2-aminophenyl)porphyrin] or poly[Co(*o*-NH<sub>2</sub>)TPP] films demonstrated excellent selectivity toward the thiocyanate ion.<sup>12</sup> The value of the  $K_{\text{I}^-}^{\text{pot}}$  of electropolymerized [Co(*o*-NH<sub>2</sub>)TPP] films was  $2.0 \times 10^3$ .<sup>12</sup> The high selectivity toward thiocyanate seemed to be related to the ion-recognition properties of the poly[Co(*o*-NH<sub>2</sub>)TPP] films.<sup>12</sup> It was noticeable that the value of the  $K_{\text{I}^-}^{\text{pot}}$  of the membrane doped with Schiff base complexes of Co(II) was  $6.3 \times 10^{-3}$ . The high potentiometric selectivity for iodide must be related to the unique interaction between cobalt(II) complexes and iodide in acid solution. Indeed, oxygen could oxidize iodide ion to iodine in low-pH aqueous solutions<sup>26</sup> and the reaction of cobalt(II) Schiff base complex with iodine was accompanied by electron transfer between the central cobalt and iodine in iodide complexes which could be described as  $\text{Co}^{3+} \cdots \text{I}^-$ .<sup>20,27</sup> The following reactions took place:

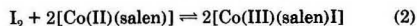
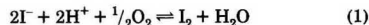
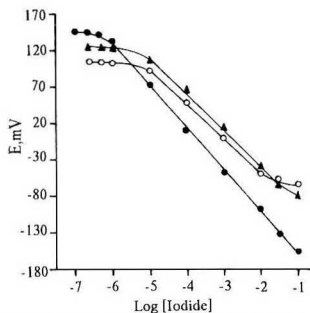


Figure 3 illustrates the influence of pH on potentiometric response of an electrode containing Co(II)(salophen) toward the iodide ion. The linear response range and the slope deteriorated with increasing solution pH. Figure 4 shows that the potentiometric response characteristics of the electrodes doped with Co(II)(salen) and Co(II)(salophen)

(25) Ashley, K. R.; Berggren, M.; Cheng, M. *J. Am. Chem. Soc.* 1975, 97, 1422–1426.

(26) Heslop, R. B.; Jones, K. *Inorganic Chemistry*; Elsevier: New York, 1976.

(27) Burness, J. H.; Dillard, J. G.; Taylor, L. T. *J. Am. Chem. Soc.* 1975, 97, 6080–6088.



**Figure 3.** Potentiometric response curves of membrane electrode doped with Co(salophen) in 0.01 mol/L  $\text{H}_3\text{PO}_4$  buffer adjusted with NaOH to pH (●) 2.5, (▲) 4.5, and (○) 6.5.

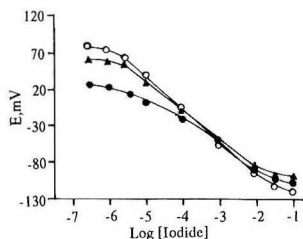


**Figure 4.** Potentiometric response curves of Schiff base complexes of metal(II), Co(II)(salophen) (○), Co(II)(salen) (▲), and Ni(II)(salen) (●), in deoxygenated 0.01 mol/L  $\text{H}_3\text{PO}_4$ -NaOH solution, pH 2.5.

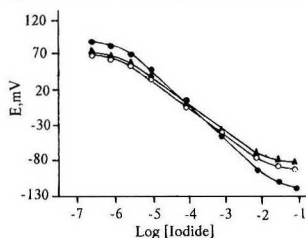


**Figure 5.** Potentiometric response curves of membrane electrode doped with Co(salophen) in deoxygenated 0.01 mol/L  $\text{H}_3\text{PO}_4$  buffer adjusted with NaOH to pH (●) 2.5, (▲) 4.5, and (○) 6.5.

deteriorated in an  $\text{O}_2$ -free environment under the same experimental conditions as in the Figure 2, whereas the presence of oxygen did not have a remarkable effect on the performance of Ni(II)(salen). The slopes of the electrodes containing Co(II)(salen) and Co(II)(salophen) in the absence of oxygen were 41–46 mV/pI, whereas the slope of the electrode incorporating Ni(II)(salen) in an  $\text{O}_2$ -free environment was nearly the same as that of the electrode exposed to air (compare Figures 2 and 4). The effect of oxygen on the performance of the electrode containing Co(II)(salophen) was more significant in solutions of pH 2.5, whereas in solutions of pH 4.5 and 6.5 this effect was not so remarkable (compare Figures 3 and 5). On the one hand, hydroxide-coordinated central metal might interfere with the response toward iodide. A similar effect of pH on potentiometric response was observed previously with Mn(III) and Sn(IV) porphyrin derivatives.<sup>6,10</sup> On the other hand, the reaction of iodide with oxygen from air and formation of iodine would be hindered by the increase of solution pH. The formation of iodine should be prohibited also by adding agents such as ascorbic acid. Figure 6 shows the potentiometric response of the membrane doped with

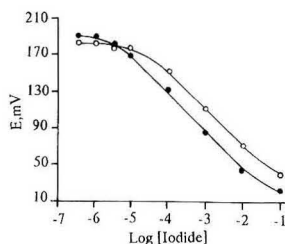


**Figure 6.** Effect of ascorbic acid on the iodide response of Co(II)-(salophen)-based membrane electrode in 0.01 mol/L  $\text{H}_3\text{PO}_4$ -NaOH solution, pH 2.5. [(●) 0.01 mol/L ascorbic acid; (○) 0.0005 mol/L ascorbic acid].

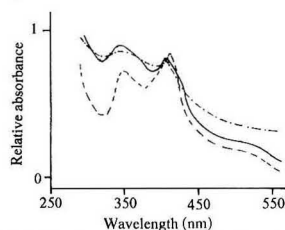


**Figure 7.** UV-visible absorption spectra of chloroform solutions of Co(II)(salen) (---), Co(III)(salen)I (-.-.-), and Co(II)(salen) treated with 0.1 mol/L KI (—).

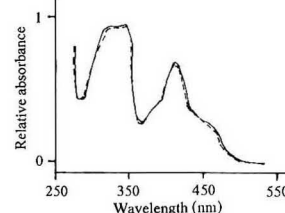


**Figure 8.** UV-visible absorption spectra of chloroform solutions of Ni(II)(salen) (---) and Ni(II)(salen) treated with 0.1 mol/L KI (—).

Co(II)(salophen) toward iodide ion in pH 2.5 phosphate buffer solutions containing ascorbic acid. The addition of ascorbic acid deteriorated the potentiometric response of the membrane for iodide. The iodine in solution was reduced by ascorbic acid, and the interaction between the carrier and iodine was weakened.

It is possible to study the interaction between central metal of carriers and iodide with UV-visible spectroscopy. Figure 7 shows the absorption spectra of Schiff base complexes of Co(II) and Co(III) in  $\text{CHCl}_3$ . The spectrum of the chloroform solution of Co(II)(salen) treated with 0.1 mol/L KI aqueous solution was similar to that of [Co(III)(salen)I] and rather different from that of the Co(II)(salen). When 1.5 mmol/L Co(II)(salen) in  $\text{CHCl}_3$  with 0.1 mol/L KI aqueous solution was shaken for 2 h, [Co(III)(salen)I], a brownish-black powder, slightly soluble in  $\text{CHCl}_3$ , was collected and identified by elemental analysis. The UV-visible spectrum of Co(III)(salen)I showed relatively little change in the low-energy portion of the spectrum compared with that of Co(II)(salen). It was probable that the Co(III)(salen)I complex possessed weaker d-d transitions ( $I^- \rightarrow \text{Co(III)}$ ). The spectrum of Ni(II)(salen), on the other hand, was identical with that of the product of Ni(II)(salen) in  $\text{CHCl}_3$  treated with 0.1 mol/L KI aqueous solution (see Figure 8). This observation seems to support the hypothesis that the potentiometric selectivity of



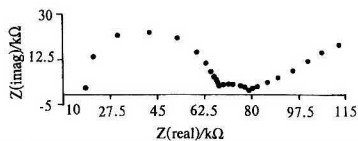


**Figure 9.** Impedance plots of a 5.46 mmol Co(II)(salen) membrane with *o*-NPDE as plasticizer immersed in 0.01 mol/L  $\text{H}_3\text{PO}_4$ -NaOH buffered solution containing 0.0001 mol/L KI, pH 2.5, for 4 h (frequency,  $1 \times 10^5$ – $1 \times 10^{-2}$  Hz at 14 °C).

the membrane was correlated with the unique coordination of iodide to the Co(II)(salen).

The ac impedance of a membrane containing 5.46 mmol of Co(II)(salen) conditioned in pH 2.5 phosphate buffer for 4 h displayed a well-resolved bulk and surface impedance plot (see Figure 9). The bulk resistance decreased with increasing KI concentration: 98.0 kΩ cm in  $10^{-5}$  mol/L KI, 63.5 kΩ cm in  $10^{-4}$  mol/L and 47.6 kΩ cm in  $10^{-3}$  mol/L KI. This indicated

that Co(II)(salen) could take up iodide across the membrane and the transfer process is diffusion controlled.

**Preliminary Application.** Iodide in drug preparations were determined with the membrane electrode containing Co(II)(salophen). A sample of 25–30 mg of *Oleum iodisum* was burned in an oxygen bomb with 15 mL of 6%  $\text{H}_2\text{O}_2$  and 4.0 mL of 0.5 mol/L KOH as the absorbate. The absorbate heated, acidified with  $\text{H}_2\text{SO}_4$ , and diluted with water was analyzed by potentiometric titration method with 0.005 mol/L  $\text{Ag}_2\text{SO}_4$  as the titrant and the Co(II)(salophen) electrode as the indicating electrode. The result obtained was  $37.46 \pm 0.3$  (w/w) in iodide ( $n = 5$ ), which was in fair agreement with the result given by precipitation method<sup>28</sup> [ $37.72 \pm 0.2$  (w/w) in iodide,  $n = 5$ ].

#### ACKNOWLEDGMENT

This work was supported by the National Natural Science Foundation of China and partially by Laboratory of Electroanalytical Chemistry, Changchun Institute of Applied Chemistry, Chinese Academy of Sciences.

(28) *Chinese Pharmacopoeia*; Pharmacopoeia Committee of the Ministry of Health of China, Eds.; Chinese Health Press: Beijing, 1990; Vol. 2.

RECEIVED for review January 13, 1993. Accepted June 17, 1993.

# High-Frequency Generation of Electrochemiluminescence at Microelectrodes

Maryanne M. Collinson and R. Mark Wightman\*

Department of Chemistry, University of North Carolina at Chapel Hill, Chapel Hill, North Carolina 27599-3290

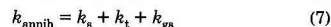
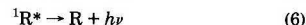
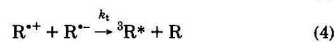
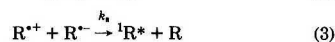
High-frequency generation of electrochemiluminescence (ECL) from ion-annihilation reactions has been investigated at microelectrodes. Well-defined, stable, reproducible luminescence curves were obtained when a multicycle square wave was applied to a microelectrode in the presence of either 9,10-diphenylanthracene, 9,10-dimethylantracene, or 9-phenylanthracene. ECL efficiencies of ca. 5%, 2%, and 2% were obtained for these compounds, respectively, using ruthenium(II) tris(bipyridine) as a standard. Due to the reduced effects of double-layer capacitance and ohmic drop, the microelectrode can be pulsed at a more rapid rate than electrodes of conventional size. The electrochemical-time constant, which was directly evaluated from the luminescence data, determined the upper frequency limit. For a 5  $\mu\text{m}$  radius electrode in acetonitrile containing 0.1 M electrolyte, this corresponded to 20–30 kHz. The rapidity of the experiment improved the stability of the luminescence and enabled ECL to be investigated from dilute solutions as well as from solutions containing 10% added water. Through variation in both the time scale of the experiment and the precursor concentration, a lower limit on the ion-annihilation rate constant for DPA of  $2 \times 10^9 \text{ M}^{-1} \text{ s}^{-1}$  was determined. This is close to the diffusion-controlled value of  $10^{10} \text{ M}^{-1} \text{ s}^{-1}$  theoretically expected.

## INTRODUCTION

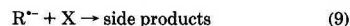
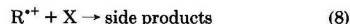
During the past decade, high-speed voltammetry involving microelectrodes has become increasingly important for the acquisition of thermodynamic and kinetic information from rapid electrochemical reactions.<sup>1–11</sup> In particular, it has been possible to measure redox potentials of conventionally unstable compounds with half-lives below 10  $\mu\text{s}$ , heterogeneous rate constants greater than 2 cm/s, and homogeneous

bimolecular rate constants near the diffusion-controlled limit.<sup>2–8</sup> Due to the reduced effects of double-layer capacitance and ohmic drop, scan rates greater than 200 kV/s have been employed without significant distortion of the voltammetric data.<sup>6</sup> The upper limit is dictated by both the time constant of the electrochemical cell (the product of the uncompensated solution resistance and the double-layer capacitance) and the instrumental time constant.<sup>1,11</sup> More recently, high-speed voltammetry has been successfully used to investigate the kinetics and mechanisms of the electrochemical polymerization of polymer films.<sup>12–14</sup> Likewise, high-frequency techniques, specifically pulsed voltammetry, should also play a significant role in the investigation of electrogenerated chemiluminescence (ECL). In particular, the reduced time scale should enable the reaction kinetics, which are near the diffusion-controlled limit, to be assessed, and side reactions, which interfere with the efficient generation of light, to be outrun.

ECL is the production of light from electrochemically generated species. This technique has been thoroughly investigated since the early 1960s and has been extensively reviewed.<sup>15–18</sup> A simplified reaction sequence for ECL is shown below for convenience where  $\text{R}^{++}$  and  $\text{R}^{\cdot-}$  can be formed from the same or different precursor



The radical ions are very susceptible to side reactions with impurities, designated as X below, which decrease the ECL efficiency.



When  $\text{R} = 9,10\text{-diphenylanthracene (DPA)}$ , the principal compound used in this work, the energy supplied by the radical-ion annihilation reaction, 3.2 eV, is sufficient to promote DPA to its first excited singlet state, 3.0 eV. Emission is believed to occur almost entirely from the singlet state

\* To whom correspondence should be addressed.

- (1) Wightman, R. M.; Wipf, D. O. *Acc. Chem. Res.* 1990, 23, 64–70.
- (2) Howell, J. O.; Wightman, R. M. *Anal. Chem.* 1984, 56, 524–529.
- (3) Andrieux, C. P.; Garreau, D.; Hapiot, P.; Pinson, J.; Saveant, J.-M. *J. Electroanal. Chem.* 1988, 243, 321–325.
- (4) Howell, J. O.; Wightman, R. M. *J. Phys. Chem.* 1984, 88, 3915–3918.
- (5) Howell, J. P.; Gonçalves, J. M.; Amatore, C.; Klsinc, L.; Wightman, R. M.; Kochi, J. K. *J. Am. Chem. Soc.* 1984, 106, 3968–3976.
- (6) Amatore, A. A.; Jutand, A.; Pfluger, F. J. *Electroanal. Chem.* 1987, 218, 361–365.
- (7) Wipf, D. O.; Wightman, R. M. *J. Phys. Chem.* 1989, 93, 4286–4291.
- (8) Wipf, D. O.; Wightman, R. M. *Anal. Chem.* 1988, 60, 2460–2464.
- (9) Andrieux, C. P.; Hapiot, P.; Saveant, J.-M. *J. Phys. Chem.* 1988, 92, 5992–5995.
- (10) Bowyer, W. J.; Engelman, E. E.; Evans, D. H. *J. Electroanal. Chem.* 1989, 262, 67–82.
- (11) Wightman, R. M.; Wipf, D. O. *Electroanalytical Chemistry*; Bard, A. J., Ed.; Marcel Dekker: New York, 1988; Vol. 15, pp 267–353.

- (12) Andrieux, C. P.; Audibert, P.; Hapiot, P.; Nechtschein, M.; Odin, C. *J. Electroanal. Chem.* 1991, 305, 153–162.
- (13) Andrieux, C. P.; Audibert, P.; Hapiot, P.; Saveant, J.-M. *J. Phys. Chem.* 1991, 95, 10158–10164.
- (14) Yang, H.; Bard, A. J. *J. Electroanal. Chem.* 1991, 306, 87–109.
- (15) Hercules, D. M. *Acc. Chem. Res.* 1969, 2, 301–307.
- (16) Faulkner, L. R.; Bard, A. J. *Electroanalytical Chemistry*, Bard, A. J., Ed.; Marcel Dekker: New York, 1977; Vol. 10, pp 1–95.
- (17) Park, S.-M.; Tryk, D. A. *Rev. Chem. Intermed.* 1981, 41, 43–79.
- (18) Velasco, J. G. *Electroanalysis* 1991, 3, 261–271.

(reaction 6), although the lowest lying triplet state is also energetically accessible, 1.8 eV, and hence populated.<sup>16</sup> Since the reactions leading to the singlet, triplet, and ground states are electron-transfer reactions, their respective rate constants can be estimated by Marcus theory. In this regard, measurement of  $k_{\text{annih}}$  can provide experimental information on such exoergic electron-transfer reactions.

To date, high-frequency generation of ECL has only been employed in a limited number of studies. Van Duyne and co-workers,<sup>19,20</sup> for example, employed a triple-potential step at short step times to measure the rate constant for the annihilation reaction between the radical ions of 9,10-diphenylanthracene,  $k_{\text{annih}}$ . This experiment involves stepping the electrode potential sequentially for a certain time,  $t_f$  and  $t_r$ , to form the radical ions and then back to the rest potential to regenerate the initial starting conditions.<sup>16,21</sup> From the shape of the luminescence curves, Van Duyne and Fischer<sup>19</sup> were able to put an upper limit on  $k_{\text{annih}}$  as  $10^{10} \text{ M}^{-1} \text{ s}^{-1}$ . Bard and co-workers, however, provided a lower limit on  $k_{\text{annih}}$  of  $10^7 \text{ M}^{-1} \text{ s}^{-1}$  using the rotating ring-disk experiment (RRDE) coupled with digital simulation.<sup>22</sup> The difficulty associated with rotating the RRDE at faster rotation rates precluded an actual determination of  $k_{\text{annih}}$ .

In this work, we were able to obtain a more reliable estimate for the annihilation-rate constants using high-frequency multicycle generation of ECL at microelectrodes. Multicycle ECL involves the alternate generation of the cation and anion radicals by continuously pulsing the electrode sequentially between the oxidative and reduction potentials.<sup>16,23,24</sup> The cation and anion radicals react in the diffusion layer at a point where the inward and outward fluxes meet and subsequently produce light. In contrast to Van Duyne's work,<sup>19,20</sup> both the step time and concentration were varied in order to estimate a value for  $k_{\text{annih}}$ . At the high-pulse frequencies employed, ECL stability was not a significant problem since side reactions with impurities, which interfere with the efficient generation of light, were outrun. Furthermore, from the data obtained at higher concentrations where kinetic limitations were negligible, we were able to evaluate the magnitude of the electrochemical-time constant under different solvent and electrolyte conditions. This enabled an upper limit to be placed on the maximum square-wave frequency which can be applied before significant signal distortion occurs. In this paper, 9,10-diphenylanthracene (DPA) was chosen as a typical model compound to evaluate this technique because its ECL properties are well documented,<sup>16,17</sup> it is stable,<sup>25,26</sup> and it has a high fluorescence efficiency.<sup>27</sup> However, high-frequency generation of ECL at microelectrodes is amenable to other less commonly studied compounds particularly those which are not as stable as DPA such as 9,10-dimethylanthracene (DMA) and 9-phenylanthracene (PA).<sup>25,26</sup> By use of  $\text{Ru}(\text{bpy})_3^{2+}$  as a standard, the ECL efficiencies for DPA, DMA, and PA were determined.

## EXPERIMENTAL SECTION

**Electrode Preparation.** Platinum or gold microdisks were prepared by sealing microscopic wires (Goodfellow) with nominal

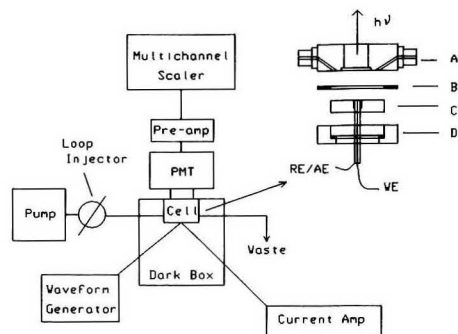


**Figure 1.** Simplified block diagram of ECL flow cell and equipment: (A) stainless-steel cell body housing an optical window; (B) polyethylene spacer; (C) epoxy-encased microelectrode; (D) stainless-steel electrode retainer.

radii of 5–30  $\mu\text{m}$  in 4 mm o.d. soft tubing.<sup>11</sup> A Pt-band electrode ( $w = 2 \mu\text{m}$ ,  $l = 2.5 \text{ mm}$ ) was constructed by sealing a piece of platinum foil between two microscope slides with epoxy as previously described.<sup>11</sup> A silver foil or tube (ca. 0.3 mm thick) placed around the microelectrode served as the counter electrode. This assembly was secured in a Teflon mold which was then filled with epoxy (EPON 828 with 14% metapenylenediamine, Miller Stephenson) and cured for at least 4 h at 150 °C. The epoxy-encased microelectrodes were polished with fine sandpaper (600–1000 grade) until the working and reference electrodes were completely exposed. They were then polished with 6- and 1- $\mu\text{m}$  diamond paste on Nylon cloths (all, Buehler). Prior to each experiment, the epoxy-encased microelectrode was polished with the 1- $\mu\text{m}$  diamond paste and thoroughly rinsed with acetonitrile.

**Apparatus.** A simplified view of the ECL flow cell, the flow-injection analysis (FIA) system and single-photon counting equipment used in this work are shown in Figure 1. The ECL flow cell consists of a stainless-steel body housing an epoxy-sealed glass window, a 150  $\mu\text{m}$  thick polyethylene spacer, and a stainless steel electrode retainer plate. The epoxy-encased microelectrode fits snugly in the electrode retainer plate which secures to the cell body with stainless steel screws. The volume of the cell defined by the rectangular groove cut into the polyethylene spacer is ca. 12  $\mu\text{L}$ . Solvent was continuously pumped through the cell via glass-lined, stainless-steel tubing ( $1/16$  in. o.d., Alltech) with an ISCO microflow pump at a flow rate of 300  $\mu\text{L}/\text{min}$ . A SSI valve equipped with a pneumatic actuator was used to inject ca. 100  $\mu\text{L}$  of the deoxygenated sample in the flow stream. The ECL flow cell was placed in a light-tight box ca. 4 cm from the photocathode of a Hamamatsu 4632 photomultiplier tube (PMT). This tube was chosen because of its low dark counts, i.e., 50–100 counts per second (CPS), which eliminated the need for an external PMT cooling device. A high-voltage power supply (Bertan Series 230) applied  $\sim 800 \text{ V}$  to the PMT. The PMT signal was amplified by a fast preamplifier (EGG Ortec VT120A, 150 MHz bandpass, 200 gain) and the output was directed to the discriminator of a multichannel scaler (EGG Ortec T-914). The discrimination level was set at  $\sim 600 \text{ mV}$ . A Wavetek Model 143 function generator applied a symmetrical square wave to the silver counter electrode and triggered the multichannel scaler. The microelectrode was either connected directly to ground or to a current amplifier. The waveforms were monitored with a Nicolet 320 digital oscilloscope. Any emission from the counter electrode, although highly unlikely at these high frequencies, was prevented by masking the counter electrode with black electrical tape placed on the outside of the glass optical window.

**Procedures.** In order to ensure the electrode potentials are chosen so that the cation and anion radicals are produced at a diffusion-controlled rate at all frequencies, the following procedure was used. Following frequency selection of the square wave, the cathodic and anodic potentials were adjusted so that they roughly correspond to those of the redox potentials for the

(19) Van Duyne, R. P.; Fischer, S. F. *Chem. Phys.* 1974, 5, 183–197.  
(20) Drake, K. F. Ph.D. Thesis, Northwestern University, Evanston, IL, 1979.

(21) Feldberg, S. W. *J. Am. Chem. Soc.* 1966, 88, 390–393.

(22) Maloy, J. T.; Prater, K. B.; Bard, A. J. *J. Am. Chem. Soc.* 1971, 93, 5959–5968.

(23) Laser, D.; Bard, A. J. *J. Electrochem. Soc.* 1975, 122, 632–640.

(24) Crusier, S. A.; Bard, A. J. *J. Am. Chem. Soc.* 1969, 91, 267–275.

(25) Marcoux, L. S.; Fritsch, J. M.; Adams, R. N. *J. Am. Chem. Soc.* 1967, 89, 5766–5769.

(26) Adams, R. N. *Electrochemistry at Solid Electrodes*; Marcel Dekker: New York, 1969; Chapter 10.

(27) Berlman, I. B. *Handbook of Fluorescence Spectra of Aromatic Molecules*, 2nd ed.; Academic Press: New York, 1974.

generation of the cation and anion radicals. The compound under study was injected into the flow stream and the size and shapes of the two luminescence peaks obtained for each cycle were observed. The applied potentials were then adjusted with each new injection of DPA until luminescence peaks of equal or nearly equal size and of the highest possible intensity were obtained. This procedure was repeated for each frequency.

The ECL efficiency for DPA, defined as the number of photons generated per reaction event,<sup>16</sup> was determined by directly comparing the integrated-light intensity emitted during the forward step to that emitted from a standard compound under identical conditions, i.e., electrode, electrolyte, frequency.<sup>28</sup> The standard chosen was Ru(bpy)<sub>3</sub>PF<sub>6</sub> for which an efficiency of 0.05 has previously been obtained.<sup>29</sup> The slightly different diffusion coefficients and PMT spectral response at the wavelengths of emission for these two compounds were taken into account. The diffusion coefficients of  $9.0 \times 10^{-6}$  and  $1.3 \times 10^{-6}$  cm<sup>2</sup>/s were used for Ru(bpy)<sub>3</sub>PF<sub>6</sub> and DPA in ACN, respectively.<sup>30</sup>

**Reagents.** Acetonitrile (ACN, UV, Burdick & Jackson), toluene (TOL, Burdick & Jackson), and dimethylformamide (DMF, Burdick & Jackson) were used as received. 9,10-Diphenylanthracene (DPA, Aldrich) was recrystallized twice from absolute ethanol. Tris(2,2'-bipyridyl)ruthenium(II) hexafluorophosphate, Ru(bpy)<sub>3</sub>PF<sub>6</sub>, was prepared by metathesis of tris-(2,2'-bipyridyl)ruthenium chloride hexahydrate (Aldrich) and ammonium hexafluorophosphate in water. The filtered product was recrystallized twice in an ethanol/acetonitrile mixture. Tetrabutylammonium hexafluorophosphate (TBAH, Aldrich) was recrystallized twice from 95% ethanol. 9,10-Dimethylanthracene (DMA, Aldrich) and 9-phenylanthracene (PA, Aldrich) were used as received. All chemicals were dried under reduced pressure at 60 °C and stored in a desiccator. Solutions were prepared fresh each day and were deoxygenated with solvent-saturated nitrogen.

## RESULTS

**High-Frequency ECL of DPA.** Figure 2 shows two cycles of the potential waveform applied to a gold disk ( $r = 5 \mu\text{m}$ ) and the resulting luminescence from a 0.6 mM solution of DPA. As expected from theory, two pulses of light are observed from each cycle.<sup>16,23,24</sup> When the potential is stepped positive, the cation radical reacts with the anion radical formed on the previous step in a reaction zone lying near the electrode surface. The light increases sharply as the diffusion layers meet and then decays as the reactants are depleted.<sup>16,23,24</sup> If the cation and anion radical are both stable during the time scale of the experiment, equal-size light pulses should be obtained on the forward and reverse steps.<sup>24</sup> Increasing the frequency of the applied square wave usually results in more equivalent luminescent curves. In Figure 2 at 1 kHz, a slightly smaller pulse of light is observed when the electrode is stepped from a negative to a positive potential indicating that the DPA anion is less stable than the cation on this time scale. At 20 kHz, both the cation and anion radicals are stable as evident from the equivalent light pulses.

The system yields reproducible results with multiple injections at both low and high frequencies, Figure 3. Since DPA is only in contact with the electrode for ca. 60 s, impurities do not have a chance to build up in solution or on the electrode

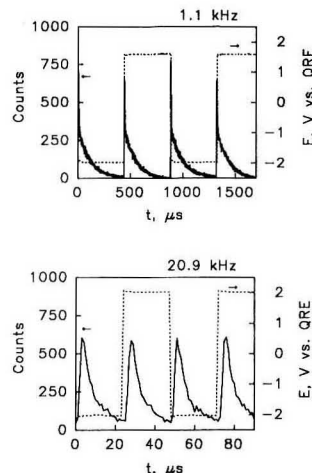


**Figure 2.** Potential waveform with the corresponding ECL curves from 0.6 mM DPA at a gold disk ( $r = 5 \mu\text{m}$ ) in acetonitrile containing 0.2 M TBAH at two different frequencies. The ordinate represents the number of counts collected during 1- $\mu\text{s}$  time bins. The luminescence curves were summed 100 times.

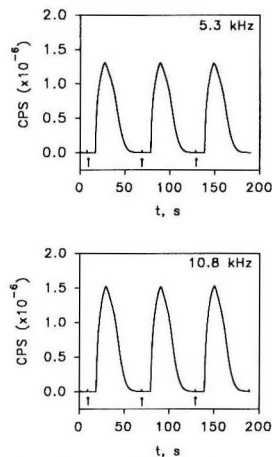


**Figure 3.** ECL from three repetitive injections of 0.5 mM DPA in acetonitrile containing 0.05 M TBAH at two different applied frequencies at a gold disk ( $r = 5 \mu\text{m}$ ). Arrows indicate the point of sample injection. Flow rate = 300  $\mu\text{L}/\text{min}$ .

and degrade the ECL response. As evident in Figure 3, when the electrode is pulsed at 10 kHz, a larger amount of light is observed. The relationship between applied frequency and light intensity can more easily be observed in Figure 4. At this electrode, ca. a 3-fold increase in the amount of light is observed when the electrode is pulsed at 20 kHz compared to 1 kHz. Even though the amount of light produced per cycle is smaller at the higher frequencies (see Figure 2), the amount of light produced per unit time is considerably larger. Although not shown in this figure, the light intensity drops off when the applied frequency is increased to 30 kHz. This can be directly attributed to the electrochemical-time constant of the cell.

(28) The usual method for determining an ECL efficiency involves taking a ratio of the integrated-light intensity to the faradaic charge (16–18). In the case of pulsed amperometry at these frequencies involving a microelectrode, it is not possible to accurately separate the faradaic charge from the non-faradaic charge. However, the faradaic charge passed is related to the diffusion coefficient and concentration by the integrated-Cottrell equation. Providing all other values in this equation remain constant and the diffusion coefficient and concentration for these two species are taken into account, an ECL efficiency can be estimated by directly comparing integrated-light intensities.

(29) Tokel-Takvoryan, N. E.; Hemingway, R. E.; Bard, A. J. *J. Am. Chem. Soc.* 1973, 95, 6582–6589.

(30) Bartlett, J. E. Ph.D. Thesis, Indiana University, Bloomington, IN, 1990.

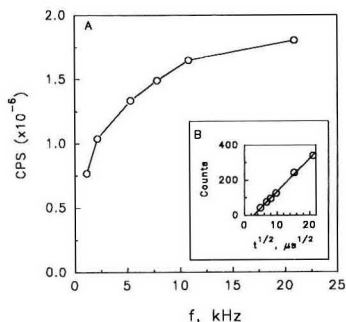


**Figure 4.** Frequency dependence of light intensity during ECL (A) and chronoluminescence plot (B) from 0.6 mM DPA in acetonitrile containing 0.05 M TBAH at a gold disk ( $r = 5 \mu\text{m}$ ). The solid line in panel B represents the linear regression fit to the experimental data.  $x$ -intercept corresponds to  $7.5 \mu\text{s}$ .

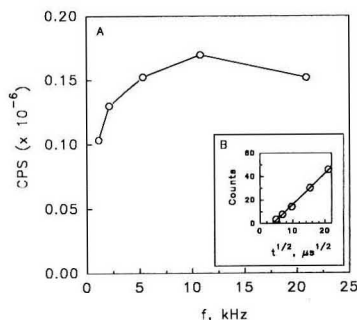


**Figure 5.** Frequency dependence of light intensity (A) and chronoluminescence plot (B) from 0.46 mM DPA in DMF containing 0.1 M TBAH at a Pt disk ( $r = 5 \mu\text{m}$ ). The solid line in panel B represents the linear regression fit to the experimental data.  $x$ -intercept corresponds to  $15.8 \mu\text{s}$ .

If the integrated-light intensity per step is plotted versus the square root of the step time, a linear curve is obtained, Figure 4b. This is the behavior expected for a diffusion-controlled reaction. The nonzero  $x$ -intercept reflects the time it takes to charge the interface to a potential sufficient to generate the radical ions. For DPA in ACN containing 0.1 M TBAH at  $r = 5 \mu\text{m}$  electrodes, the  $x$ -intercept is typically  $2.5 \mu\text{s}^{1/2}$ , which corresponds to a time delay of ca.  $6 \mu\text{s}$ . The voltammetric time constant estimated from cyclic voltammetry agrees with this value. Increasing the resistance of the solution or increasing the electrode size increases this intercept. For example, in Figure 5B the chronoluminescence behavior of DPA in DMF, a more resistive solvent, gives an intercept which corresponds to ca.  $16 \mu\text{s}$ . This increase agrees with the ca. 2-fold increase in the specific resistances of electrolyte ions in DMF compared to ACN.<sup>31</sup> Since the electrode takes longer to charge to the applied potential, both the upper-frequency limit and the total number of counts decrease. In addition, the smaller diffusion coefficient of DPA in DMF results in a lowered light output. For this electrode, an ca. 4-fold decrease in the amount of light is observed when DMF is used as a solvent compared to ACN.

When small amounts of water are added to the DPA solutions, two light pulses can still be observed, although they

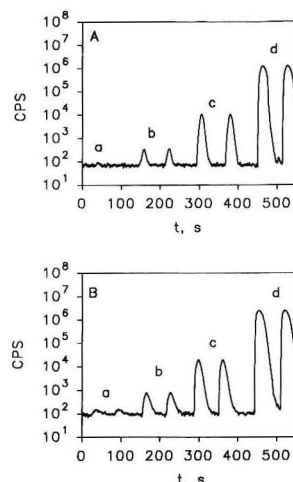


**Figure 6.** Repetitive injections of different concentrations of DPA in 50:50 acetonitrile/toluene containing 0.1 M TBAH at an applied frequency of 0.6 kHz (A) and 10.9 kHz (B) at a Pt band ( $w = 2 \mu\text{m}$ ,  $l = 2.5 \text{ mm}$ ). The data were smoothed by performing a nine-point running average. DPA concentrations: (a) 0.07, (b) 6.8, (c) 68, (d)  $170 \mu\text{M}$ . Flow rate =  $300 \mu\text{L}/\text{min}$ .

are no longer of equal intensity. Under these conditions, the radical anion is less stable than the radical cation as evident from the smaller light pulse observed when the electrode potential is stepped negative to positive (data not shown). When the amount of added water is increased to 5–10%, either one light pulse per cycle or asymmetric light pulses are observed. In addition, when the electrode is pulsed at 0.5–1 kHz, a significant diminution in the light intensity is observed, e.g., only 30% of the original signal remains. At 10–20 kHz, however, ca. 70% of the original light level remains. This result indicates that the reaction of the radical ions with water can be competed with at high frequencies.

High-frequency generation of ECL should be ideal for measuring dilute solutions of DPA since this technique is less sensitive to the concentration of impurities and a greater amount of light is produced at higher applied frequencies. Figure 6 shows ECL from dilute solutions of DPA at both high and low frequencies. A microband electrode was used instead of a disk because the electrode area, and hence the luminescence, is greater. However, since the band was only  $2 \mu\text{m}$  wide, it can still be pulsed at a rapid rate.<sup>11</sup> When the applied frequency was 0.6 kHz, Figure 6A, the most dilute DPA solution cannot be distinguished from background. However, at 10.9 kHz (Figure 6B) ECL can be observed from this solution (ca.  $70 \text{ nM}$ ). The lowest detectable concentration depends on a number of factors including the applied frequency, the electrode size, the amount of impurities (water, oxygen) in solution, and the collection efficiency of the PMT detector system. The ECL intensity, however, is nonlinear with respect to concentration. This can be attributed primarily to the reaction kinetics which further reduce the light intensity at low concentrations (*vide infra*).

**Kinetics of ECL.** Feldberg<sup>21</sup> and later Van Duyne et al.<sup>19,20</sup> digitally simulated the ECL temporal characteristics for reactions 1–7 generated by square-wave pulses. At relatively high frequencies or with low concentrations, a distinct change in the size and shape of the luminescence curves becomes apparent. The peak height decreases, the width at half-height increases, and the peak maximum shifts toward longer

(31) Sawyer, D. T.; Roberts, J. L. *Experimental Electrochemistry for Chemists*; John Wiley and Sons: New York, 1974.



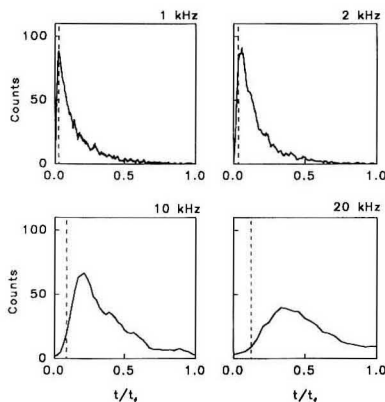


**Figure 7.** ECL curves from 0.2 mM DPA in 50:50 acetonitrile/toluene containing 0.1 M TBAH as a function of applied frequency at a Pt disk ( $r = 5 \mu\text{m}$ ). The dashed lines represent the theoretical position of the luminescence peak maximum in the absence of kinetics.<sup>32</sup> The luminescence obtained when the electrode potential is stepped positive is shown. The ordinate represents the number of counts collected during 1- $\mu\text{s}$  time bins. The luminescence curves were summed 100 times.

times.<sup>19-21</sup> This behavior becomes apparent when the kinetic parameter,  $k_{\text{anion}}t_fC$ , is less than 100. If  $k_{\text{anion}}$  is between  $10^7$  and  $10^{10} \text{ M}^{-1} \text{ s}^{-1}$  as proposed by Bard et al.<sup>22</sup> and Van Duyne et al.,<sup>19</sup> the product of the forward step time ( $t_f$ ) and the precursor concentration ( $C$ ) should be between  $10^{-5}$  and  $10^{-8} \text{ M s}$  in order to begin to access this kinetically limited region. Experimental luminescence curves are shown in Figure 7 when the concentration is kept fixed at 0.2 mM and the frequency changed from 1 to 20 kHz. The behavior observed here is similar to that predicted for a transfer between kinetic and diffusion control as described by Feldberg<sup>21</sup> and Van Duyne et al.<sup>19,20</sup> As can be seen in this figure, the luminescence curves broaden, drop in intensity, and shift toward longer times relative to the diffusion-controlled position<sup>32</sup> as theoretically expected when  $t_fC$  drops from 88 to  $4.5 \times 10^{-9} \text{ M s}$ . Likewise, similar results are obtained when the applied frequency is kept constant and the concentration varied from 120 to  $2 \mu\text{M}$  ( $t_fC$  varies from 6 to  $0.1 \times 10^{-9} \text{ M s}$ ) (data not shown).

An estimate of  $k_{\text{anion}}$  can be obtained by plotting the logarithm of the normalized rate of light emission versus the logarithm of  $t_fC$ , Figure 8. The rate of light emission ( $I$ ) was evaluated at 30% of the potential-step time from the background-subtracted luminescence curves.<sup>33</sup> The data in Figure 8 represent the results from two experiments in which a microband electrode was pulsed between 1 and 5 kHz and the concentration varied from 1.7 to 200  $\mu\text{M}$ . The solid line is from the Feldberg model assuming  $k_{\text{anion}}$  is  $2 \times 10^9 \text{ M}^{-1} \text{ s}^{-1}$ .

(32) The position at which the peak maximum occurs, however, depends not only on the value of  $k_{\text{anion}}t_fC$  but also on the time it takes to charge the interface as well as the position of the reaction plane relative to the electrode surface. In the absence of kinetic limitations, the position of the peak maximum should actually decrease as the frequency is increased because the position of the reaction plane lies closer to the electrode surface by the square root of the forward step time. If this variable is taken into account by taking a ratio of the square root of the forward step time at a given frequency relative to 1 kHz, the peak maximum in the decay curves increases as expected when the value of  $t_fC$  decreases.

(33) The rate of light emission was evaluated at 30% of the potential step time in an attempt to minimize the contributing effects of the residual radical ions generated from prior steps to the observed ECL. ECL from residual ions would effect the latter half of the luminescence curve more than the former half. At times smaller than 30% of the potential step, however, the finite amount of time required to charge the interface significantly interferes with this measurement.

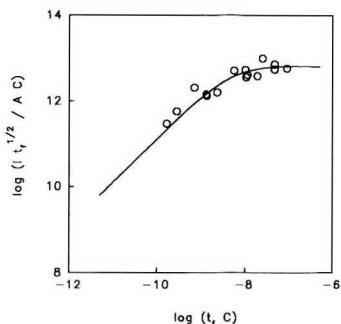


**Figure 8.** Modified Feldberg plot. The rate of light emission ( $I$ ) was evaluated at 30% of the potential step time from the background-subtracted luminescence curves obtained from DPA in 50:50 acetonitrile/toluene containing 0.1 M TBAH at a Pt band electrode ( $w = 2 \mu\text{m}$ ,  $l = 2.5 \text{ mm}$ ). The data points represent results from two different experiments when the DPA concentration and the applied frequency were varied from 1.7 to 200  $\mu\text{M}$  and 1 to 5 kHz, respectively.

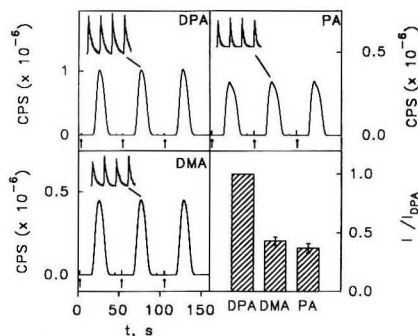


**Figure 9.** Repetitive injections of 0.4 mM solutions of (A) DPA, (B) 9-phenylanthracene (PA), and (C) 9,10-dimethylanthracene (DMA) in 50:50 acetonitrile/toluene containing 0.1 M TBAH at a gold disk ( $r = 5 \mu\text{m}$ ), applied frequency 5 kHz. The ECL curves for two cycles are shown above the second injection (see Figure 2 for details). Arrows indicate the point of sample injection. Panel D represents the average ECL intensity of PA and DMA relative to DPA from three separate experiments.

**Other Compounds.** Since ECL is incorporated in an FIA system, it was relatively straightforward to examine other compounds to determine their relative luminescence efficiency. In Figure 9, the ECL of 9,10-dimethylanthracene (DMA) and 9-phenylanthracene (PA) are compared to DPA. As evident from the nearly equivalent light pulses obtained on the cathodic and anodic steps, the radical ions are stable on this time scale. The three successive injections produced the same light intensity indicating the ECL response is reproducible with multiple injections. In Figure 9D, the intensities of these compounds relative to DPA are shown. DPA has a considerably greater intensity than DMA or PA, in part, because the fluorescence efficiency of DPA is 1 compared to 0.49 for DMA, for example.<sup>27</sup>

## DISCUSSION

The experiments described here clearly demonstrate that high-frequency potential pulses can be used to pursue both fundamental and practical applications of ECL. The ECL observed at both high and low frequencies is considerably

more stable than that observed in previous work,<sup>24,34-37</sup> which makes it more amenable for extracting mechanistic information. Even the low frequencies used in this work are still 10–1000 times faster than the upper frequencies normally used in multicycle ECL.<sup>24,36-40</sup> Based on the use of Ru(bpy)<sub>3</sub><sup>2+</sup> as a standard, an ECL efficiency of  $5 \pm 1\%$  was determined for DPA. This ECL efficiency is in good agreement with values previously reported.<sup>30,38,41,42</sup> In general, greater stability was observed when higher frequencies (5–30 kHz) were employed (Figure 2). This is in agreement with previous work which shows that either sweeping or pulsing the applied potential at an increased rate results in more equivalent light pulses.<sup>24,43</sup> As the time scale of the experiment is reduced, the reactions of the cation and anion radicals with impurities such as water or oxygen become less significant. When the electrode is pulsed at a frequency greater than 5–10 kHz, 70% of the original light intensity can still be observed in DPA solutions containing 10% added water. This result could provide a means for using high-frequency ECL involving radical ions in more practical applications.

In addition to providing greater stability, high-frequency ECL usually produces a greater light output because a greater amount of ECL reagents are generated per unit time. However, as shown in Figures 4 and 5, there is an upper limit on how fast a given electrode/solvent system can be pulsed before the light intensity drops off. Bard and co-workers<sup>37-40</sup> typically saw 5–40-fold increases in ECL intensities over the frequency range of 0.2–100 Hz (estimated from logarithmic frequency dependence plots). In all cases, the ECL intensity significantly dropped off as the frequency was increased past 50–100 Hz. In this work, we see a 2–3-fold increase in the ECL intensity over the frequency range of 1–21 kHz with an upper-frequency limit typically of 21 kHz. Figures 4 and 5 clearly demonstrate that this rolloff is due to the finite amount of time it takes to charge the interface. The magnitude of this time constant, which can be determined directly from the luminescence data, is critical in determining the upper frequency or scan rate limit that can be used before distortion in the voltammetric or ECL signal occurs.

In order to achieve the highest possible light output from a given analyte, it is imperative that solvent conditions be chosen so that the electrochemical-time constant is minimized as much as possible. If a significant amount of time is spent charging the electrode to the applied potential, the radical ions generated on the previous step have a greater probability for diffusing away, being consumed by the electrode, or reacting with impurities present in solution. DMF and propylene carbonate (data not shown), which are more resistive than ACN, are not ideal solvents to use in this regard. Decreasing the electrode area will also decrease the electrochemical-time constant, but at the expense of the light level. In this respect, a compromise needs to be made in the choice of electrode size and the value of the time constant that can

be tolerated. Since the microelectrode can be pulsed 200–400 times faster than a conventional sized electrode, ca. 30 times more light is emitted per unit area. This increase in ECL intensity along with the greater stability of the cation and anion radicals at high frequencies compensates for the decreased light intensity resulting from the smaller electrode area. Indeed, the characteristic blue light emitted from 0.5 mM DPA solutions at  $r = 33 \mu\text{m}$  microdisks can be observed in a dimly lit room.

Since ECL is coupled to a FIA system, it was relatively straightforward to examine, or rather to "screen", other compounds to determine their ECL characteristics. High-frequency ECL should be advantageous for examining luminescence from conventionally unstable compounds because chemical reactions which consume the electrogenerated unstable compounds are less significant. DMA and PA were chosen because, unlike DPA, the cation radicals are not stable on the conventional time scale.<sup>25,26</sup> In particular, the 9,10-positions of the radicals are more reactive than those for DPA. Considering their apparent instabilities and the lower fluorescence efficiency ( $\phi_f = 0.49$  for DMA<sup>27</sup>), it is not surprising that ECL generated from these two compounds has received little attention.<sup>44-46</sup> However as evident in Figure 9, stable, reproducible ECL can be obtained from both these compounds when the time scale of the experiment is sufficiently reduced. From the relative intensities of PA and DMA to DPA, an estimated ECL efficiency of ca. 2% was determined for DMA and PA using DPA as a standard ( $\phi_{\text{ECL}} = 5\%$ ).<sup>47</sup> Since the ECL efficiency is defined as the product of the fluorescence efficiency ( $\phi_f$ ) times the fraction of molecules producing the excited state ( $\phi_{\text{ex}}$ )

$$\phi_{\text{ECL}} = \phi_f \phi_{\text{ex}} \quad (10)$$

then the efficiency for producing the emitting species ( $\phi_{\text{ex}}$ ) appears to be similar for the two compounds.

High-frequency ECL can be used to measure the ion-annihilation reaction kinetics. Van Duyn and Fisher,<sup>19</sup> in particular, attempted to measure  $k_{\text{annih}}$  but were only able to set an upper limit on  $k_{\text{annih}}$  to be  $10^{10} \text{ M}^{-1} \text{ s}^{-1}$ . In later work, an attempt was made to fit the experimental luminescence curves to simulated curves but had limited success due to the difficulty in separating instrumental effects from the results.<sup>20</sup> Bard et al.<sup>22</sup> and later Itoh et al.<sup>48</sup> were able to set a lower limit on  $k_{\text{annih}}$  of ca.  $10^7$  and  $2.5 \times 10^6 \text{ M}^{-1} \text{ s}^{-1}$ , respectively. Bard and co-workers were limited by the rotation rate of the RRDE while Itoh and co-workers were limited by the time constant of the instrument used in their work. In this work, microelectrodes<sup>11</sup> enabled more reliable estimates of  $k_{\text{annih}}$  to be made by reducing the time scale of the experiment sufficiently to access the reaction kinetics without significantly distorting the results.

In order to determine  $k_{\text{annih}}$  for DPA, we have fit the luminescence data obtained from dilute solutions to Feldberg's theoretical model<sup>21</sup> recognizing there are some discrepancies between the model, which is for a triple-potential step, and the multicycle-potential step experiments employed in this work. In the triple-potential step experiment, the initial boundary conditions are such that the concentrations of the radical ions are zero at  $t = 0$ . In the multicycle experiment employed in this work, the potential is continuously stepped.

(34) Kim, J.; Faulkner, L. R. *J. Electroanal. Chem.* 1988, 242, 107–121.

(35) Bezman, R.; Faulkner, L. R. *J. Am. Chem. Soc.* 1972, 94, 6317–6323.

(36) Chang, M.-M.; Saji, T.; Bard, A. J. *J. Am. Chem. Soc.* 1977, 99, 5399–5403.

(37) Keszthelyi, C. P.; Tachikawa, H.; Bard, A. J. *J. Am. Chem. Soc.* 1972, 94, 1522–1527.

(38) Keszthelyi, C. P.; Tokel-Takvoryan, N. E.; Bard, A. J. *Anal. Chem.* 1976, 47, 249–256.

(39) Tokel, N. E.; Keszthelyi, C. P.; Bard, A. J. *J. Am. Chem. Soc.* 1972, 94, 4872–4877.

(40) Wallace, W. L.; Bard, A. J. *J. Phys. Chem.* 1979, 83, 1350–1357.

(41) Itoh, K.; Honda, K.; Sukigara, M. *Electrochim. Acta* 1979, 24, 1195–1198.

(42) Maness, K. M.; Bartelt, J. E.; Wightman, R. M. Submitted for publication in *J. Phys. Chem.*

(43) Hercules, D. M.; Lansbury, R. C.; Roe, D. K. *J. Am. Chem. Soc.* 1966, 88, 4578–4583.

(44) Parker, C. A.; Short, G. D. *Trans. Faraday Soc.* 1967, 63, 2618–2622.

(45) Werner, T. C.; Chang, J.; Hercules, D. M. *J. Am. Chem. Soc.* 1970, 92, 763–768.

(46) Fleet, B.; Keliher, P. N.; Kirkbright, G. F.; Pickford, C. J. *Analyst* 1969, 94, 847–854.

(47) The diffusion coefficients of DPA, PA, and DMA were not taken into account in this calculation which could lead to some uncertainty in these numbers.

(48) Itoh, K.; Sukigara, M.; Honda, K. *Chem. Lett.* 1977, 1269–1272.

Therefore, the initial conditions are such that the concentration of the radical ions are not zero at the beginning of each cycle. As the reaction becomes increasingly kinetically limited, there will be residual radical ions in the diffusion layer generated from prior steps which will contribute to the observed ECL. This is reflected in Figure 7 as the nonzero luminescence baseline which becomes apparent as the applied frequency is increased. To partially correct for this disparity, the time-dependent luminescence was background subtracted and the rate was evaluated at 30% of the potential-step time.<sup>33</sup> The background in each case was determined by averaging the number of counts before and after the decay curve. According to Feldberg's theory, a plot of the logarithm of the normalized rate of light emission versus the logarithm of  $(t_r C)$  should yield a slope of 1 when the reaction is kinetically limited and a slope of zero when the reaction proceeds under diffusion control.<sup>21</sup> The data shown in Figure 8 follow the shape predicted by this model. The rate determined by this procedure is an order of magnitude smaller than the diffusion-controlled value theoretically expected,<sup>19,24,49,50</sup> ca.  $10^{10} \text{ M}^{-1} \text{ s}^{-1}$ . Due to the contributing effects of the electrochemical-time constant on the light intensity, it is likely that our present estimate of  $k_{\text{annih}}$  is at least an order of magnitude low. Indeed, a comparison of the background light levels from the experimental curves (Figure 7, 20 kHz) to curves simulated for similar conditions<sup>20</sup> indicates that  $k_{\text{annih}}$  could be as high as  $3 \times 10^{10} \text{ M}^{-1} \text{ s}^{-1}$ . A more precise experimental value of  $k_{\text{annih}}$  will require development of a more suitable model as well as a correction for the electrochemical-time constant. Nevertheless, these experiments demonstrate the unique ability to electrochemically measure a bimolecular rate constant near the diffusion-controlled limit.<sup>5,61</sup>

(49) Rehm, D.; Weller, A. *Isr. J. Chem.* 1970, 8, 259-271.

(50) Schomburg, H.; Staerk, H.; Weller, A. *Chem. Phys. Lett.* 1973, 22, 1-4.

(61) Andrieux, C. P.; Moiroux, A. A. J.; Saveant, J.-M. *J. Electroanal. Chem.* 1991, 307, 17-28.

## CONCLUSIONS

High-frequency ECL can be used to explore both fundamental and practical applications of ion-annihilation reactions. The reduced time scale enables reaction kinetics to be accessed and affords a means for investigating ECL without rigorously purifying solvents or working on a vacuum line or in a drybox. The ability to access the reaction kinetics provides a means for obtaining fundamental experimental information concerning electron-transfer reactions. The upper frequency limit is caused by the electrochemical-time constant. This can be determined directly from the luminescence data, and should be incorporated in simulations of luminescence curves. This could provide a way for determining  $k_{\text{annih}}$  under a variety of different solvent and electrolyte conditions. High-frequency generation of ECL is not limited to investigations involving DPA but can be routinely used to examine ECL from other compounds, particularly those which are not as stable. A wide variety of practical analytical applications should now be possible since efficient ECL can be observed from conventionally unstable compounds in conventionally unstable environments. Future work will explore these applications.

## ACKNOWLEDGMENT

We thank Steve Woodward for helpful discussions concerning the instrumentation and K. M. Maness for preparation of  $\text{Ru}(\text{bpy})_3^{2+}$ . We gratefully acknowledge support of this work from the National Science Foundation (CHE).

RECEIVED for review April 29, 1993. Accepted June 30, 1993.\*

\* Abstract published in *Advance ACS Abstracts*, August 15, 1993.

# Behavior and Calibration of the Copper(II) Ion-Selective Electrode in High Chloride Media and Marine Waters

Stuart L. Belli\* and Alberto Zirino

Code 521, RDT & E Division, Naval Command, Control and Ocean Surveillance Center, San Diego, California 92152

The response of the solid-state Cu(II) ion-selective electrode in high chloride media was investigated and found to be Nernstian under normal laboratory and field measurement conditions. The previously reported "non-Nernstian" behavior has been identified as a combination of electrode fouling, due to specific storage and measurement conditions, and the action of stoichiometric levels of a Lewis base on the standard addition method of electrode calibration. Electrode calibration by external Cu(II) activity buffers in artificial seawater is described. The copper activity of the buffers is calculated from an ion-interaction model, and the electrode response in these buffers is shown to be consistent with that in chloride solutions over 10 orders of magnitude copper concentration and from pH 8 to 2.

## INTRODUCTION

Copper is an important metal pollutant due to its widespread use and subsequent distribution into the environment, coupled with its toxicity at excess levels. The toxicity is generally attributed to the aquo-complexed "free" cupric ion ( $\text{Cu}^{2+}$ ) rather than the inorganic or organic complexes,<sup>1</sup> and therefore, the measurement of free Cu(II) is extremely important both in assessing copper toxicity and for environmental monitoring. Of the many analytical methods available for determining copper in aquatic environments, only potentiometry with copper ion-selective electrodes (ISEs) can directly measure the free copper ion in situ without perturbing the natural speciation. Cu ISEs have found widespread use in both toxicological studies and the environmental monitoring of freshwater but have not found general use in marine environments due to reported interference by high levels ( $>0.1$  M) of chloride in the sample matrix.

The nature of this interference has been characterized principally as an increase in electrode response from an expected 29.6 mV/decade (at 25 °C) per decade increase in Cu concentration to a nominal 59.2 mV/decade in high chloride solutions such as seawater.<sup>2,3</sup> Oglesby<sup>4</sup> indicated that the interference was not due to ionic strength effects, and Westall<sup>5</sup> suggested that the interference was caused by the reduction of Cu(II) to Cu(I) at the electrode surface with consequent adsorption of the Cl<sup>-</sup> stabilized  $\text{CuCl}_2^-$  ion at the

electrode surface. The exact reduction mechanism was not described although they indicated that both high Cu ( $>4.5 \times 10^{-5}$  M) and high chloride (0.5 M) were necessary to produce the 59 mV/decade slope condition. In order to study the reduced state, their experiments were conducted in unstirred, oxygen-free solutions. These conditions are rarely, if ever, met in natural seawater.

In spite of the alleged interference, the electrode has been used by A.Z. as an indicator of changes in the Cu content of seawater,<sup>5-8</sup> but the interpretation of the electrode potential in terms of Cu activity was precluded by an inability to produce a fully Nernstian behavior (Zirino et al.<sup>6</sup> obtained a response of 34 mV/decade) and by a lack of a clear understanding of the redox chemistry at the electrode surface. Indeed, the presence of Cl<sup>-</sup> by itself does not lead to the reduced form of the Cu ion but only stabilizes it, and Hoyer<sup>9</sup> was able to show that a Cu ISE responded normally in 0.5 M Cl<sup>-</sup> solutions.

The present work reexamines the behavior of the Cu ISE in Cl<sup>-</sup> solutions, in artificial seawater, and in natural seawater and proposes that the Cu ISE may be used as a divalent electrode if (1) the extreme conditions which lead to non-Nernstian response are avoided and (2) electrode potentials are interpreted in terms of the concentration of the free Cu ion (pCu) rather than in terms of the total added Cu concentration. In order to calibrate the electrode in terms of activity we developed two new pCu buffers prepared in artificial seawater. The Cu activity of the buffers was calculated using an ion-interaction model.<sup>10,11</sup>

## METHODS

The Orion 94-29 copper ion-selective electrode was used in conjunction with an Orion double-junction Ag/AgCl reference electrode containing 10%  $\text{KNO}_3$  as the outer filling solution. Two electrodes of undetermined age (at least 10 years old) were used for the majority of the work and were cleaned by polishing with fine grit alumina when needed as determined by deteriorating response slopes. At one point, a new electrode was put into service and found to give good response without pretreatment, as recommended by the manufacturer's literature. The cell emf was measured to 0.1 mV with a Radiometer pH/ion meter and recorded on a strip chart recorder. Solution pH was simultaneously recorded during each experiment with a combination pH electrode calibrated against standard pH buffers. The presence of the pH electrode in the same cell was determined to have negligible effect on the response of the copper electrode.

Solutions were made from analytical-grade reagents as purchased without further purification. The set of limited component test solutions is listed in Table I. Nitrate is a noncomplexing anion and was used to adjust ionic strength. Sodium bicarbonate established the solution pH and provided some pH

\* Permanent address: Department of Chemistry, Vassar College, Poughkeepsie, NY, 12601.

(1) Anderson, D. M.; Morel, F. M. M. *Limnol. Oceanogr.* 1978, 23, 283-295.

(2) Jasinski, R.; Trachtenberg, I.; Andrychuk, D. *Anal. Chem.* 1974, 46, 364-369.

(3) Westall, J. C.; Morel, F. M. M.; Hume, D. N. *Anal. Chem.* 1979, 51, 1792-1798.

(4) Oglesby, G. B.; Duer, W. C.; Millero, F. J. *Anal. Chem.* 1977, 49, 877-879.

(5) Zirino, A.; Seligman, P. F. *Mar. Chem.* 1981, 10, 249-255.

(6) Zirino, A.; Clavell, C., Jr.; Seligman, P. F. *Nav. Res. Rev.* 1978, 31, 26-38.

(7) Zirino, A.; Hightower, J. D. *Ocean Sci. Eng.* 1984, 9, 239-252.

(8) Zirino, A.; M. C.; Dotson, P.; Seligman, P. F.; Bower, D. *Abstracts of Papers*, 189th National Meeting of the American Chemical Society, Miami Beach, FL, American Chemical Society: Washington, DC, 1985.

(9) Hoyer, B. *Talanta* 1991, 38, 115-118.

(10) Westall, J. C. MICROQL: a chemical equilibrium program in basic. Dept. Chem. Tech. Rep.; Oregon State University, 1986.

(11) Zirino, A.; Yamamoto, S. *Limnol. Oceanogr.* 1972, 17, 661-671.

**Table I. Component Test Solutions**

soln	KNO <sub>3</sub> (M)	NaCl (M)	NaHCO <sub>3</sub> (M)	ionic strength
1	0.5	0	0.01	0.53
2	0.4	0.1	0.01	0.53
3	0.3	0.2	0.01	0.53
4	0.2	0.3	0.01	0.53
5	0.1	0.4	0.01	0.53
6	0	0.5	0.01	0.53
7	0	1	0.01	1.03

buffering. The concentration of NaCl in the test solutions was varied from 0 to 1.0 M. Artificial seawater (ASW) was formulated as per Kester et al.<sup>12</sup> with deletion of the strontium component. In all cases, the test solutions were allowed to equilibrate with atmospheric CO<sub>2</sub> before use, at which time the pH was found to be in the range of 7.9–8.2, and experiments were run in open beakers. The solutions were stirred at a constant speed using an overhead (nonmagnetic) stirrer. All calibrations were carried out at room temperature, 24 ± 1 °C. The electrode slopes were calculated by a linear least-squares regression and reported to 0.1 mV/decade. The slopes were reproducible to within ±2 mV/decade over several months.

Electrode response was determined after addition of aliquots of the standard copper solution, which brought the total Cu concentration through the range of 1 ppb to the onset of Cu precipitation. Precipitation was initially noted as a slow emf drift, generally occurring near a concentration of 100 ppm copper. In most cases the solutions were then acidified to a pH of ~2. This stabilized the emf and dissolved the precipitate. Copper additions were then resumed. The cell emf was recorded upon stabilization after each addition, generally within 6 min. Changes in ionic strength occurring over the course of the titration were considered negligible.

The chemical speciation in each test solution was calculated from a specific ion-interaction model<sup>13–15</sup> using the BASIC program MICROQL<sup>10</sup> and the appropriate ligand binding constants. It is important to make an accurate estimate of the individual carbonate species in the solutions because of the high affinity of CO<sub>3</sub><sup>2-</sup> for copper; however, this estimate can be difficult due to the sensitivity of carbonate species to pH and the tendency to equilibrate with atmospheric CO<sub>2</sub>. The amount exchanged with the atmosphere can be calculated from the equilibrium pH. Since the exchange process is slow, this calculation was done for each solution after sufficient time for equilibration had been allowed and then total carbonate was assumed constant during the time frame of the titration. The concentration of free copper species [Cu(II)] was calculated at each point in the titration from the total copper and the pH.

Copper ion activity buffers for electrode calibration were prepared by adding copper in the form of CuSO<sub>4</sub> and a copper-complexing agent, ethylenediamine or glycine, in known proportions to artificial seawater. The amounts of copper and ligand were chosen to fall near the center of the buffering region as shown by the calculated Cu titration curve for that ligand (Figure 1). Both buffers were 1 mM in organic ligand and 0.2 mM in total copper. Ethylenediamine and glycine were chosen as they bracket a wide range of copper activity including the expected levels in natural marine waters. The free [Cu(II)] for the standards was calculated using the ion-interaction model. Because the copper ion activity of these Cu buffers is pH dependent (Figure 2), and the buffer solutions are subject to small pH variations, a pH measurement of the buffer is required before the pCu level of the buffer can be assigned.

## RESULTS AND DISCUSSION

**Electrode Behavior.** Our analysis of the electrode behavior will examine the performance at two levels: the

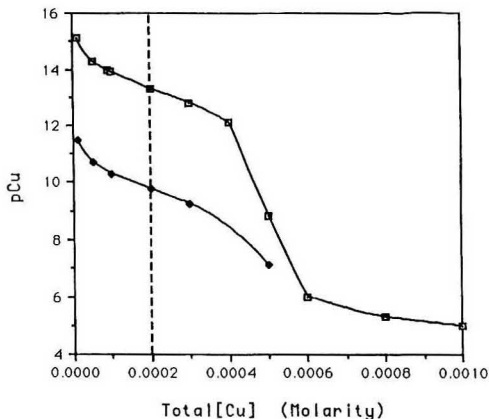


**Figure 1.** Ethylenediamine (□) and glycine (◆), 0.001 M, in artificial seawater. Calculated titration curve at pH 8.20. Line shows total copper concentration used in standard buffers.

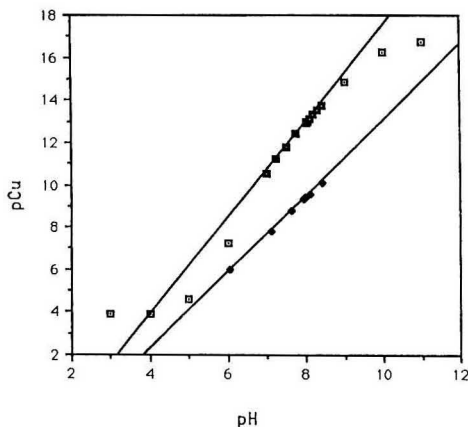


**Figure 2.** Copper activity buffers, 0.001 M ethylenediamine (□) and glycine (◆) containing 0.0002 M total copper. Calculated pCu at various pH. The linear approximations are used to assign buffer pCu as a function of measured pH.

actual raw data of the electrode emf as recorded on a stripchart during a "calibration" experiment and the response plot of the data as it is displayed in a calibration curve. The strip chart shows the electrode response to changes in the sample matrix and gives information on the dynamics of the electrode. The calibration curve represents the equilibrium response behavior, which can be interpreted in terms of the Nernstian equation and the equilibrium speciation of the sample matrix.

**I. Nitrate Medium.** We first studied the Cu ISE where one expects good behavior, in a non-chloride medium, a solution of 0.5 M KNO<sub>3</sub> buffered to pH ~8 with 0.01 M NaHCO<sub>3</sub>. In this solution dissolved copper is expected to distribute among the solution species Cu<sup>2+</sup>, CuCO<sub>3</sub>, CuHCO<sub>3</sub><sup>+</sup>, Cu(CO<sub>3</sub>)<sub>2</sub><sup>2-</sup>, Cu(OH)<sup>+</sup>, Cu(OH)<sub>2</sub>, Cu(OH)<sub>3</sub><sup>-</sup>, and Cu(OH)<sub>4</sub><sup>2-</sup> according to the respective equilibrium formation constants.

Figure 3a presents a reproduction of the strip chart record, showing the Cu electrode emf and pH trace during a typical Cu titration. For each low (ppb) addition of Cu, the record shows the ISE's emf to increase (become more positive),

(12) Kester, D. R.; Duedall, I. W.; Connors, D. N.; Pytkowicz, R. M. 1967, 12, 176–178.

(13) Turner, D. R.; Whitfield, M. *Geochim. Cosmochim. Acta* 1987, 51, 3231–3239.

(14) Turner, D. R.; Dickson, A. G.; Whitfield, M. *Geochim. Cosmochim. Acta* 1981, 45, 855–881.

(15) Dickson, A. G.; Whitfield, M. *Mar. Chem.* 1981, 10, 315–333.



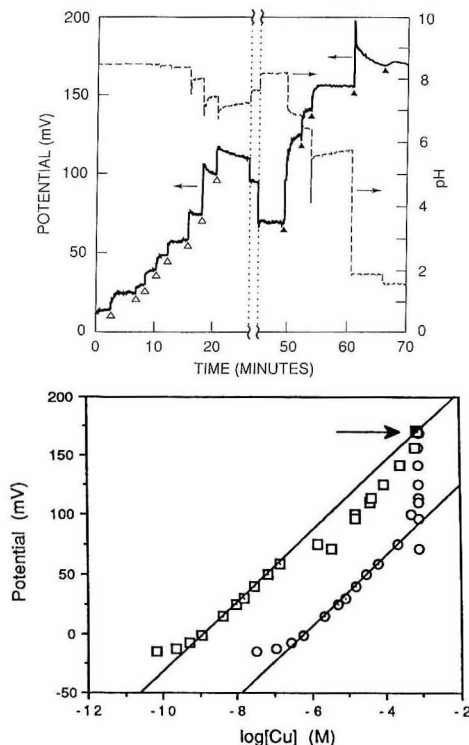


**Figure 3.** Copper electrode response in 0.5 M  $\text{KNO}_3$ –0.01 M  $\text{NaHCO}_3$ . (a, top) Strip chart recording of known addition experiment with simultaneous measurement of pH. Standard copper additions ( $\Delta$ ) and  $\text{HNO}_3$  ( $\blacktriangle$ ) marked on plot. Recording was stopped twice as marked to allow equilibration. (b, bottom) Data graphed as copper concentration vs. potential. Total copper (O) with regression applied to linear portion, slope 29.6 mV/decade. Free copper ( $\square$ ) was calculated with MICROQL using the total copper and pH at each point. Regression applied to the linear portion plus the fully acidified point, indicated by arrow, slope 29.5 mV/decade.

reaching a constant value (equilibrium); solution pH changes very little. On the other hand, at higher copper concentrations, we observed that the emf appears to drift after each Cu addition. This has been attributed to electrode instability. However, the copper additions change the solution pH due to the acidity of the standards and subsequent pH drift is seen on reequilibration with the atmosphere. In this system,  $\text{CO}_3^{2-}$  and  $\text{OH}^-$  are the main copper ligands and slight pH shifts dramatically alter the free  $\text{Cu(II)}$  concentration. In addition, a copper precipitate is observed in this region. The electrode "drift" is actually a true measure of copper activity as the sample reequilibrates with the atmosphere. Finally, as the pH is lowered to  $\sim 2$  by addition of  $\text{HNO}_3$  at constant total copper the emf increases, due to both the dissolution of the precipitate and the removal of  $\text{OH}^-$ ,  $\text{CO}_3^{2-}$ , and  $\text{HCO}_3^-$  as copper ligands.

The electrode response, plotted in Figure 3b, shows a linear region with Nernstian, divalent slope of 29.5 mV/decade. At the high copper range, corresponding to electrode drift and precipitation, the electrode still follows the free  $\text{Cu(II)}$ , although the points fall below the line due to the precipitation of  $\text{Cu(OH)}_2$  and to the exchange of  $\text{CO}_2$  with the atmosphere not accounted for in the model. The last point, taken at pH

1.82, where no carbonate or hydroxide complexation will occur and the precipitate has dissolved, lies on the Nernstian line. This supports our calculation of free  $\text{Cu(II)}$  using the speciation model.

At low copper levels, the curvature is attributed to both low levels of copper in our reagents and the presence of low levels of a Lewis base. While both cause initial curvature in a standard addition calibration, they must be handled very differently and will have a profound effect on the interpretation of the electrode behavior. The initial concentration of copper impurity is calculated from the known electrode response slope and the electrode potentials as measured in a standard addition experiment.<sup>16</sup> Once determined, this initial copper can be added to all the subsequent known additions to give a "corrected" total copper value, which should then extend the linear region to the lowest measurements. However, we often find that when this correction is made, the electrodeslope increases and becomes "super-Nernstian"; for the experiment shown in Figure 3b, the electrode response increases to 32.4 mV/decade when corrected in this manner.

The second reason for the initial curvature and one that may explain the observation made above as well as provide insight into trace metal speciation in seawater is that the initial Cu additions are not resulting in as much free  $\text{Cu(II)}$  as the latter additions. This behavior would occur in the presence of a low, but unaccounted for, concentration of a Lewis base. The initial additions of copper in the ppb range are substantially lost to the base and show low response. Once the binding sites are filled, the subsequent additions partition differently, giving a higher, in this case, linear electrode response. We have seen evidence of this in a wall effect; the curvature exhibited by inorganic solutions is reduced, or even eliminated, when the sample beaker is switched from glass to Teflon. Also, this effect is well-known for natural waters where the change in electrode response is used to measure the "complexation capacity", e.g., the excess Lewis bases available for complexation, primarily humic substances.<sup>17</sup>

**II. High Chloride Medium.** Figure 4 shows that the electrode behaves much the same in high chloride medium (0.5 M  $\text{NaCl}$ ) as in 0.5 M  $\text{KNO}_3$ . In the calibration curve, Figure 4b, we see the initial curvature at low copper additions, then the linear portion with a slope of 26 mV/decade, and a break at  $\text{pCu} = 7.0$  corresponding to the onset of precipitation at pH 8. On acidification to pH 2.2, the copper is no longer bound by carbonates and hydroxides and the free copper becomes equivalent to the total copper. Further additions of copper at pH 2.2 result in electrode response identical and, in fact, collinear with that at pH 8.

There are differences, however, which are apparent on consideration of the strip chart recording of the raw electrode emf. We see the expected response to copper addition at low levels, but an interesting effect is observed. The electrode's response becomes faster and the high-frequency noise level increases as the copper concentration increases. The high-frequency noise is often attributed to instrument noise due to the high impedance of the electrode but in this case, because of its clear correlation to copper concentration, may be attributable to other sources, such as a reaction occurring at the electrode surface. At  $\sim 10^{-4}$  M copper, an appreciable electrode drift is noted. This was not accompanied by a significant pH drift as we saw with the  $\text{KNO}_3$  calibration but the solution did become cloudy, indicating a solubility problem. The cloudiness cleared when acid was added and the emf rose as expected due to the freeing of  $\text{Cu(II)}$ . The acidification was carried out by several additions of  $\text{HNO}_3$  at

(16) Smith, M. J.; Manahan, S. E. *Anal. Chem.* 1973, 45, 836–839.

(17) Buffle, J.; Greter, F.-L.; Haerdi, W. *Anal. Chem.* 1977, 49, 216–222.

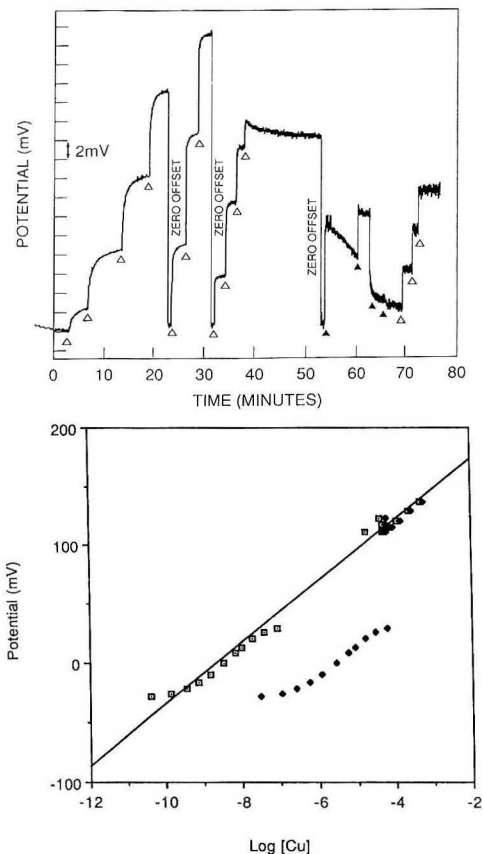


**Figure 4.** Copper response in 0.5 M NaCl-0.01 M NaHCO<sub>3</sub>. (a, top) Strip chart recording of Cu electrode emf showing response to Cu additions (Δ) and HNO<sub>3</sub> additions (▲). (b) Electrode calibration curve in terms of total copper (◆) and free copper (□), regression slope 26.0 mV/decade.

constant total copper as shown on the graph. It was observed that the measured potential reached a maximum value at pH ~6 and then dropped on further acidification. This effect was not further studied but indicates copper complexation at low pH. After stabilization at low pH (=2.25), additional copper was added. The electrode response was very fast and accompanied by high-frequency noise, but retained the 26 mV/decade slope as previously noted.

One additional point not shown but consistently observed is the electrode potential and also the noise level become very dependent on the stirring rate in the high chloride media. When the stirring is stopped, either by turning off the motor or removing the drive belt, the high-frequency noise is greatly diminished. This indicates the noise may be a result of the turbulent nature of Cu(II) delivery to the electrode by stirring as opposed to the smoother, diffusional transport in the still solution. These observations may be explained by the work of Westall et al.,<sup>3</sup> where the anomalous +1 response slopes were observed under conditions of high chloride, high copper, and low oxygen. The condition of no stirring may allow the products of an electrode surface reaction to build up fouling the electrode surface. We have consistently left the electrode

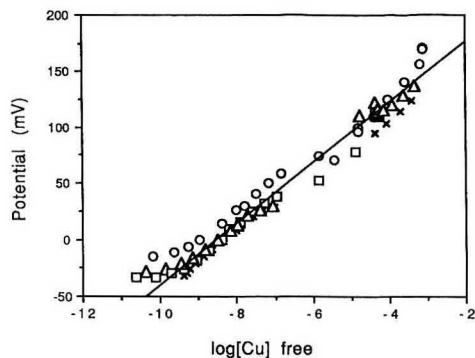


**Figure 5.** Copper electrode response in high chloride buffers: 0.1 M NaCl (□), 0.5 M NaCl (Δ), 1.0 M NaCl (X), and 0.5 M KNO<sub>3</sub> (O). Free [Cu<sup>2+</sup>] calculated from total [Cu] and pH at each point, regression slope 27.0 mV/decade.

soaking in the high chloride solution overnight with no adverse effects, but if high copper is also present, the electrode shifts to +1 response which is then observed in either chloride or nitrate solutions. This apparent electrode shift is accompanied by discoloration of the electrode surface, which must be removed to restore normal response.

Several experiments were run at varying ratios of chloride to nitrate, maintaining constant ionic strength and even at substantially higher ionic strength; see Table I. The various plots of electrode EMF vs log (free) copper were found to define essentially the same line, Figure 5. An important point to note here is the coincidence of the calibration for the chloride solutions with the non-chloride solutions when the electrode potential is plotted against the free copper. This indicates that there is no chloride interference under the conditions used here.

**III. Artificial Seawater.** The next step in our investigation was to test the electrode in a solution containing all the major inorganic components of natural seawater. Again the critical step was to model the chemical speciation with MICROQL in order to assign the electrode response to free Cu(II) concentration.

In artificial seawater at pH 8, the electrode response is clearly super-Nernstian, approaching, but never fully reaching 59 mV/decade, indicative of the univalent behavior. This is seen for both total and free copper, Figure 6. This super-Nernstian response has been attributed to a mechanistic change in the electrode toward a univalent response mode through the stabilization of the Cu<sup>+</sup> by the high chloride in the medium. But we have seen normal divalent response in high chloride medium. In fact, the electrode exhibits divalent response in artificial seawater when the pH is initially set to 2; see Figure 6. In one experiment, shown in Figure 7, the pH was adjusted from 8 to 2 midway through a calibration and the response shows a clear, immediate shift from 36.9 mV/decade at pH 8 to 27.8 mV/decade at pH 2. This in itself does not rule out the possibility of altered electrode sensitivity in seawater at pH 8, but does suggest solution speciation as the source of this "response shift". We believe the difference between the pH 8 and 2 response is due to the simplified speciation at pH 2, specifically by the removal of Lewis bases through protonation at low pH.

The super-Nernstian response obtained when calibration is carried out by the known addition method in artificial seawater at pH 8 can be explained using the Nernst equation and assuming the presence of low levels of Lewis base. The standard addition method requires that the added analyte

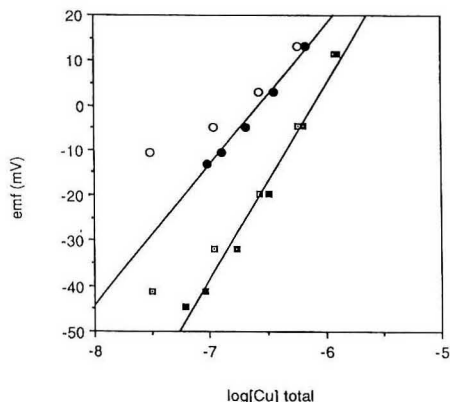


**Figure 6.** Copper determination by standard addition method in artificial seawater spiked with 6 ppb copper. Determination made at pH 8 (□) and pH 2 (○). The solid symbols represent data corrected for background by the method of Smith and Manahan<sup>18</sup>: pH 8 (■), regression slope 43.2 mV/decade indicating 3.8 ppb initial copper; pH 2 (●), regression slope 31.1 mV/decade, indicating 5.9 ppb initial copper.

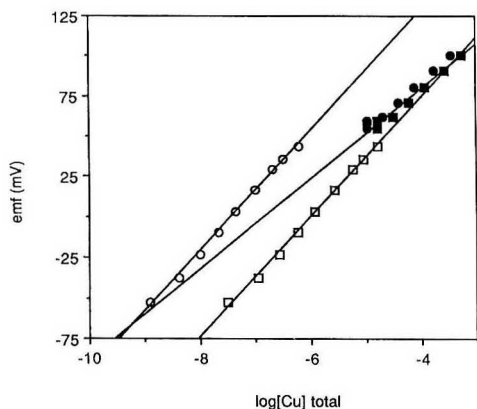


**Figure 7.** Electrode response in artificial seawater. pH 8: total (□) and free (○) copper with regression slopes of 37 mV/decade. pH 2: total (■) and free (●) copper with regression slope of 28 mV/decade.

partition in the sample matrix to the same extent as the sample analyte independent of the analyte concentration. Only when this occurs will the electrode yield correct response slopes according to the Nernst equation:

$$E = E' + \frac{0.0592}{n} \log [\text{Cu}^{2+}] \quad (1)$$

The copper partitioning can be represented with a partitioning factor,  $\alpha$ :

$$[\text{Cu}^{2+}] = [\text{Cu}_T] \alpha \quad (2)$$

which on substitution into the Nernst equation shows the electrode response is dependant on the total copper and on the matrix partitioning.

$$E = E' + \frac{0.0592}{n} \log ([\text{Cu}_T] \alpha) \quad (3)$$

$$E = E' + \frac{0.0592}{n} \log [\text{Cu}_T] + \frac{0.0592}{n} \log \alpha \quad (4)$$

When  $\alpha$  is constant throughout a calibration, the partitioning

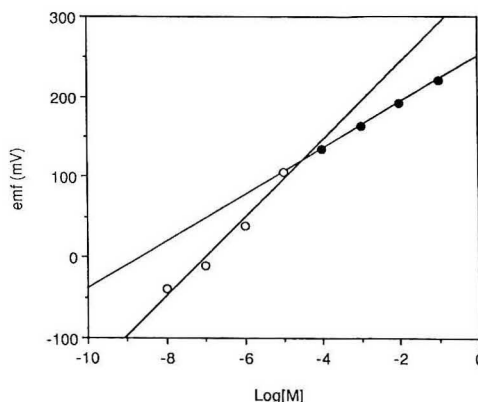


**Figure 8.** Calculated standard addition curve with consideration of partitioning effect ( $E = K + 29 \log [\text{M}\alpha]$  (3)). Varying partitioning (○),  $\alpha = 0.01$  to  $\alpha = 1$ , slope 48.4 mV/decade; constant partitioning (●), slope 29.0 mV/decade.

term can be included with the constant offset term:

$$E'' = E' + \frac{0.0592}{n} \log \alpha \quad (5)$$

and normal Nernstian slope is observed:

$$E = E'' + \frac{0.0592}{n} \log [\text{Cu}_T] \quad (6)$$

However, when  $\alpha$  changes during the calibration, this simplification can no longer be made. A shift in  $\alpha$  will occur if a strong Lewis base is present at low concentration, that is, at stoichiometric levels, and is titrated during the calibration. The result of this can be seen in Figure 8 where eq 3 was used to calculate electrode response in a "thought experiment" where  $\alpha$  shifts from 0.01 to 1 during the course of a known addition calibration.

What implication does this have on the validity of the electrode response? It certainly forces one to question the method of standard additions as applied to ASW at pH 8. One of the basic assumptions of the standard additions method is that the matrix will bind the same constant fraction of the copper independent of the copper concentration. This condition is apparently not being met in ASW at pH 8 (at present we can only speculate that this uptake of  $\text{Cu}^{2+}$  is due to the presence of colloidal substances such as hydrated iron oxides and carbonates). This does not mean the electrode response is in error, only that our forcing it to fit the assumptions inherent in the standard addition method is. Therefore, calibration in ASW and in natural seawater under natural conditions (pH 8) must be by external standards such as copper activity buffers. Of course, it may be possible to use the information from a standard addition, such as the initial curvature and slope, to gain insight about the matrix.<sup>18</sup>

When the  $\text{KNO}_3$  or  $\text{NaCl}$  solutions were acidified during calibration (see Figures 3 and 4), a large emf shift was observed, but the slope of the response remained constant. This abrupt shift of emf was explained as a real increase in free  $\text{Cu}(\text{II})$  through the loss of carbonate (present in much higher concentrations than in the artificial seawater) and hydroxide copper complexes and could be accounted for with the solution model. For the ASW, the smooth transition with no large potential change on acidification at  $\text{pCu}$  near  $10^{-6}$  M indicates

(18) Buffle, J. *Complexation Reactions in Aquatic Systems: An Analytical Approach*; Ellis-Horwood: Chichester, England, 1988.

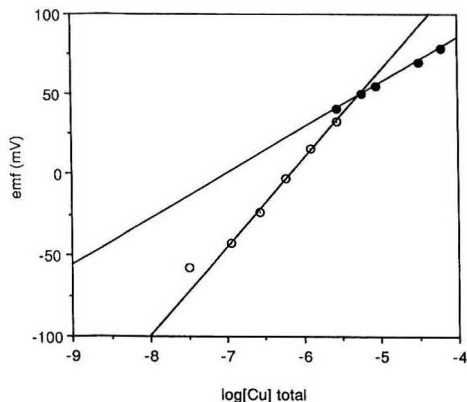


**Figure 9.** San Diego Bay sample, standard addition at pH 8 (O), response slope 55 mV/decade. Standard addition continued after acidification to pH 2 (●), response slope 28 mV/decade.

that, first, copper is not bound to pH-dependent complexes (the speciation model tells us the carbonates and hydroxides are bound up by the calcium and magnesium) and, second, the fundamental electrode reaction is not changing, as no major shift in  $E_o'$  is observed. We attribute the high calibration slope at pH 8 (at  $pCu < 10^{-6}$  M) to complex chemical speciation in the seawater matrix which we have not been able to correct with the model due to neglected species.

The electrode is capable of determining correct total copper concentration by the standard addition method as shown in Figure 6. The sample was spiked with 6 ppb copper and the determination made at both pH 8 and 2. The copper concentration was calculated from the equation<sup>16</sup>

$$C_o = C_s V_s / (V_o 10^{-(E_1 - E_2)/S} - V_o)$$

Where  $C_o$  and  $C_s$  are the copper concentrations in the original sample and the added standard, respectively, and  $V_o$  and  $V_s$  are the volumes.  $E_1$  and  $E_2$  are the cell potentials before and after the spike.  $S$  is the experimental response slope in the solution. The value returned for the pH 2 determination was in agreement with our known spiked level and also with an independent determination by anodic stripping voltammetry. The low value for the pH 8 determination is indicative of the presence of a Lewis base. This supports our claim of a low concentration Lewis base, even in the artificial seawater, that is effectively removed on acidification of the solution.

**IV. San Diego Bay Water.** The result of a copper titration of San Diego Bay water is shown in Figure 9. The electrode behavior is identical to that in ASW with an apparent high, super-Nernstian slope at pH 8 and normal divalent slope at pH 2. It is interesting that the pH 8 slope in bay water (54 mV/decade) is considerably greater than the equivalent slope in ASW (40 mV/decade). We believe that this difference is caused by the (presumed) higher concentration of Lewis bases in natural seawater.

**Copper Activity Calibration Buffers.** The pH and copper electrode emf was measured in each buffer and the free copper concentration was calculated using MICROQL. A plot of the  $\log [Cu^{2+}]$  vs emf gives a slope of 28 mV/decade as expected for the electrode. In another experiment, we saw strong electrode response to the addition of nitric acid to the buffer. When the pH effect on copper speciation was calculated with MICROQL, the electrode was found to be responding to free copper at 28 mV/decade over 6 orders of

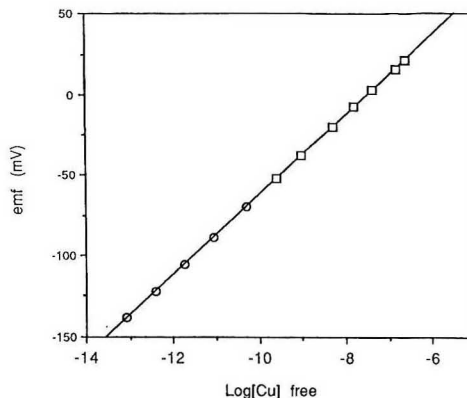


**Figure 10.** Copper activity buffers in artificial seawater. Ethylenediamine (O) and glycine (◇), both at 0.001 M ligand and 0.0002 M total copper. Electrode potential measured at various pHs; free copper calculated at each pH using MICROQL. Regression slope 25.4 mV/decade.

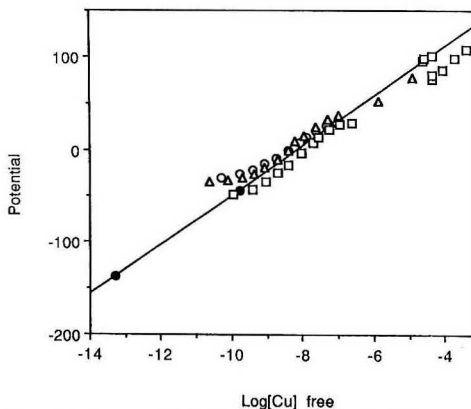


**Figure 11.** Copper activity buffers in artificial seawater (●) compared to the standard addition calibration in 0.1 (Δ), 0.5 (O), and 1.0 (□) M NaCl. Regression slope 26.5 mV/decade.

magnitude, Figure 10. In addition, these two points fall on the same line described by the free copper calibration curve from the NaCl matrix solutions at pH 8 and pH 2; see Figure 11. With no independent method available for determining free copper we are faced with assigning values to these standards strictly from the parameters included in our seawater model. Nevertheless, our results are internally consistent and agree with the results reported by Hoyer<sup>9</sup> in 0.5 M NaCl in which he showed linear response with 30 mV/decade upon copper titration of the ethylenediamine and glycine.

## CONCLUSION

Comparison of the  $KNO_3$  with the NaCl calibrations clearly show no chloride interference from the matrix. The electrode emf may seem to vary with  $[Cl^-]$  but this can be attributed to effects on the Cu speciation; when expressed in terms of  $[Cu^{2+}]$ , the electrode response is independent of  $[Cl^-]$ . In artificial seawater the electrode gives apparent super-Nernstian Cu response, but again this can be attributed to copper

speciation. The very complex nature of the matrix produces many copper binding species at submicromolar concentrations. These Lewis bases are actually titrated by the added copper in the traditional known-addition calibration method, yielding the apparently anomalous response curves.

Earlier researchers have observed complex, non-Nernstian electrode response to copper in high chloride medium such as seawater. We found this anomalous response only under specific conditions of operation and storage which can be avoided in routine analytical applications. We found +1 response slopes only when the electrode had been stored in high chloride, high copper, low oxygen solutions. This +1 response was then observed in both high and low chloride buffers and seemed to be due to some changes at the electrode surface, not to the sample matrix itself. This behavior can be understood in terms of the reactions proposed by Westall et al.,<sup>3</sup> which would be favored by the above conditions. However, whereas he concluded that this made the electrode unsuitable for seawater measurements, we believe that avoiding the particular conditions that lead to a +1 mode will maintain the electrode in its normal Nernstian response. We have seen evidence of electrode surface reactions in the increase in high-frequency noise and decreasing response times in chloride media but have found this does not interfere with measurement of free Cu(II).

Normal potential measurements in natural marine waters, even for extended times, do not appear to expose the electrode to conditions which foul the surface. Storage of the electrode in stagnant natural seawater is to be avoided because (1) the electrode dissolves in Cl<sup>-</sup> solution giving high values of Cu<sup>2+</sup> and (2) oxygen is consumed by microbiological activity. These

conditions lead to the +1 state and render the electrode unuseable. On the other hand, storage of the electrode in fresh, flowing seawater "cleans" by removing Cu ion from the electrode surface by ablation and does not appear to produce undesirable results.<sup>8</sup>

The unquantified weak bases do not preclude the measurement of Cu activity by the ISE in the conventional sense. We believe that the emf produced by the electrode in natural seawater is an accurate reflection of the free Cu(II) concentration but that the electrode must be calibrated by the external copper activity buffers. In fact the electrode appears to be giving useful information on the copper complexing capacity of the natural water when the standard addition technique is used to titrate the Lewis bases.

Electrode potentials can be calibrated in terms of free Cu(II) using the seawater ethylenediamine and glycine buffers we describe. Our assignment of free Cu(II) activity in the buffer solutions based on the speciation model is supported by experiments in simplified systems as discussed in the results section. We have seen self-consistency in the model through variation of total copper concentration and through variation of pH. Finally, the buffer potentials fall on the same calibration curve as the much simplified nitrate and chloride solutions, including the acidified condition in which all the copper is expected to be "free". This establishes a connection between free Cu(II) and the more easily determinable "total" copper.

RECEIVED for review February 10, 1993. Accepted June 16, 1993.



# High-Performance Flow Flame Atomic Absorption Spectrometry for Automated On-Line Separation and Determination of Cr(III)/Cr(VI) and Preconcentration of Cr(VI)

Jozsef Posta,<sup>†</sup> Harald Berndt,\* Shen-Kay Luo, and Gerhard Schaldach

Institut für Spektrochemie und angewandte Spektroskopie, Bunsen-Kirchhoff-Strasse 11, D-44139 Dortmund, Germany

High-performance flow atomic spectrometry permits the fully automated separation of Cr(III)/Cr(VI) species and subsequent flame AAS determination within only 1 min. An HPLC integrator at the output of the flame AA spectrometer renders possible the simultaneous signal processing of both oxidation states. Samples of drinking water, waste water, and extracts of soils were investigated. The relevant detection limits are 0.03 Cr(III) or 0.02  $\mu\text{g/mL}$  Cr(VI) ( $3\sigma$  values,  $N = 25$ ). The relative standard deviation amounts to  $\sim 1\%$  ( $N = 10$ ,  $1 \mu\text{g/mL}$ ). With the same type of chromium speciation column (modified C18 type), Cr(VI) can be preconcentrated from drinking water and then determined online by flame AAS within 3.5 min. A detection limit of  $0.5 \mu\text{g/L}$  ( $3\sigma$  value) can be attained when a sample volume of 5 mL is used; the standard deviation is 3.1 ( $10 \mu\text{g/L}$  Cr(VI)) or  $1.5\%$  ( $100 \mu\text{g/L}$  Cr(VI)).

## INTRODUCTION

In high-performance flow atomic spectrometry (HPF-AS) the aerosol generation is caused by hydraulic high-pressure nebulization (HHPN). This very efficient nebulization mode, which is widely used in technical fields (e.g., diesel oil injection, combustion jets of aeroplane turbines, and spray drying) has now, by the availability of the HPF/HHPN system (Knauer/Varian), also gained entry in the field of sample introduction in atomic spectrometry. The pressure is generated by an HPLC pump. As is common practice in HPLC, the sample is brought into a high-pressure carrier stream by means of a sample introduction valve. The liquid is then injected into the nebulization chamber by a pressure of  $\sim 17 \text{ MPa}$  (170 bar) (high-pressure injection) and consequently nebulized (flow rate  $2.5 \text{ mL/min}$ ). The opening of the special nebulization nozzle measures only  $20 \mu\text{m}$ . Dependent on the type of flame AA spectrometer, the aerosol yield amounts to more than 50%.<sup>1</sup> Using this nebulization mode, a high-performance flow system becomes a functional component of an atomic spectrometer.<sup>1,2</sup> High-pressure flow systems can be equipped with columns of large bed length and fine-grained packing material. An additional HPLC column placed between the sample introduction valve and the HHPN nozzle facilitates an interface-free coupling of the HPLC separation technique and atomic spectrometry. Due to the great number of theoretical plates of HPLC columns, a separation of oxidation

states and bonding forms becomes possible.<sup>3,4</sup> As regards the on-line separation of Fe(II)/Fe(III) and the subsequent determination by flame AAS, the resulting detection power improved by  $\sim 1$  order of magnitude compared to that obtained by coupling with pneumatic nebulization.<sup>3</sup> By equipping the system with two valves and a small ion-exchange or C18 RP column, on-line trace element preconcentrations/matrix separations can be performed.<sup>5,6</sup> An inert HPLC autosampler serves for automation of sample introduction.

The toxic behavior of chromium and its compounds in different oxidation states is already described in numerous scientific papers of medicine, biology, and environmental and analytical chemistry. Surveys containing general information on the element and its behavior can be found in refs 7 and 8. In 1992, Sperling et al. gave a description of Cr(VI) and total chromium determination by electrothermal AAS after preconcentration. The paper contains detailed statements about chromium distribution as well as about former and recent analytical determination methods.<sup>9</sup> In this paper, for the first time is described the rapid and automated separation and determination of Cr(III) and Cr(VI) by HPF flame AAS using an HPLC integrator for signal processing. At the separation of Cr(III)/Cr(VI), flame AAS measurements yield two peak signals (two transient signals). Standard software of the flame AA spectrometer permits the measurement of only one transient signal at a time. This was the reason that hitherto the detection of both species after separation could only be handled in a rather complicated way. However, connection of an HPLC or GC integrator to the analog output of the atomic spectrometer offers a simple solution to this problem. Another excellent method for processing several transient signals in atomic spectrometry (speciation analysis) is offered by the availability of HPF-AS software (Knauer), which is quite similar in its structure to HPLC software. Additional investigations centered on the preconcentration of Cr(VI) traces. Samples of drinking water, waste water, and extracts of contaminated soil served as matrices.

## EXPERIMENTAL DETAILS AND RESULTS

**General Procedures.** (1) *Apparatus.* (a) *Automated Separation of Cr(III)/Cr(VI).* The following equipment was used: Varian flame AA spectrometer SpectraAA 400 (double-beam spectrometer with external PC), additional 1-V analog output (modified by Varian, Darmstadt, Germany). Varian/

<sup>†</sup> On leave at Varian GmbH, Alsfelder Str. 6, D-64289 Darmstadt, Germany.

(1) Berndt, H.; Müller, A. *Fresenius J. Anal. Chem.* 1993, 345, 18-24.

(2) Berndt, H. *Fresenius Z. Anal. Chem.* 1988, 331, 321-323.

(3) Weber, G.; Berndt, H. *Chromatographia* 1990, 29, 254-258.

(4) Weber, G.; Berndt, H. *Int. J. Environ. Anal. Chem.*, in press.

(5) Ivanova, E.; Schaldach, G.; Berndt, H. *Fresenius J. Anal. Chem.* 1992, 342, 47-50.

(6) Berndt, H.; Müller, A.; Schaldach, G. *Fresenius J. Anal. Chem.* 1993, 346, 711-716.

(7) Berman, E. *Toxic Metals and Their Analysis*; Heyden: London; 1980; Chapter 10.

(8) Bowen, H. J. M. *Environmental Chemistry of the Elements*; Academic Press: London, 1979.

(9) Sperling, M.; Yin, X.; Welz, B. *Analyst* 1992, 117, 629-635.

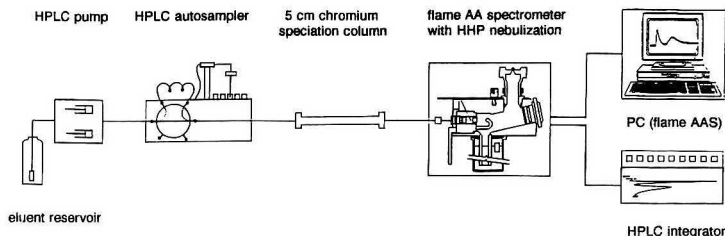


Figure 1. HPF flame AAS arrangement for on-line separation and determination of Cr(III) and Cr(VI).

Knaauer HPF/HHPN system, basic system with original Varian HHP nebulization chamber plug, HPF/HHPN autosampler (inert HPLC autosampler), 100- $\mu$ L sample loop (PEEK), chromium speciation column (5 cm, 4.6-mm inner diameter, modified C18 type, Knaauer), Knaauer Wissenschaftliche Geräte, D-14163 Berlin, Germany. Hewlett-Packard HPLC/GC integrator HP 3396 A.

(b) *Preconcentration of Cr(VI)*. There was an additional sample introduction valve (PEEK) with a 5-mL sample loop.

(2) *Reagents*. The following reagents were used: tetrabutylammonium acetate (TBAA, Fluka 86849), acetic acid, phosphoric acid, methanol, and ammonium acetate (reagents of AR grade). Cr(III) stock solutions were prepared from Titrisol ampules. Cr(VI) stock solutions were made from  $K_2Cr_2O_7$  (Merck, Darmstadt, Germany).

(3) *HPF/HHPN Arrangement for Separation of Cr(III)/Cr(VI)*. Figure 1 shows the apparatus arrangement for the automated separation and determination of both oxidation states of chromium via flame AAS, functioning as an element-specific detector. In contrast to the commonly used coupling of HPLC with flame AAS, the exit of the HPLC column is not connected to a pneumatic nebulizer, but via a high-pressure capillary with an HHPN nozzle. Thus, the high-pressure flow system ends with the high-pressure nebulization (interface-free coupling). In order to protect the Pt/Ir nozzle with an inner diameter of only 20  $\mu$ m against blockage by particles, a 3- $\mu$ m titanium sieve filter is positioned in front of the nozzle. At a flow rate of 2.5 mL/min, a pressure of  $\sim$ 17 MPa (170 bar) is required for the nebulization. The HPLC pump produces a maximum pressure of 40 MPa (400 bar); thereby, a pressure of more than 20 MPa was available for chromatographic separation. Using the Cr speciation column (5-cm bed length, 5- $\mu$ m packing material), the total pressure at a flow rate of 2.5 mL/min was  $\sim$ 25 MPa. The sample (100- $\mu$ L sample loop) is introduced (time-controlled) into the carrier stream by a programmable HPLC autosampler, which also gives a read signal to the AA spectrometer. The delay time and the measuring time are determined (signal representation via PC of the AAS instrument) via the spectrometer software; it is also possible to attain an automated calibration using the standard addition method. The corrected AAS signal is additionally transferred to an HPLC/GC integrator via the analog output of the spectrometer. For flame AAS measurement, standard conditions for the determination of chromium were chosen (wavelength 357.8 nm, slit width 0.7 nm, slightly reduced air/acetylene flame, measuring height 8 mm above the burner slit).

**Separation and Determination of Cr(III)/Cr(VI).** (1) *Investigations for Optimization of Separation*. The separation of Cr(III) and Cr(VI) by ion pair chromatography was initially followed as described in the literature. But unlike Syty et al.,<sup>10</sup> who used tetrabutylammonium phosphate, acetate was chosen in this case. Phosphoric acid served for

adjustment of the pH value (3.0–3.2). The concentration of phosphoric acid in the solution was  $3.7 \times 10^{-3}$  mol/L. For separation, a flow rate of 2 mL/min is cited in the literature.<sup>10</sup> For hydraulic high-pressure nebulization, a flow rate of 2.5 mL/min has proved optimal with respect to flame AAS working conditions (20- $\mu$ m HHPN nozzle). Therefore, all subsequent investigations were carried out at this flow rate. In agreement with ref 10, the approximate time used for separation was 3 min. In order to optimize the separation step, the concentration of tetrabutylammonium acetate and phosphoric acid was varied. However, only insignificant improvements resulted. Methanol is generally used for elution of complexed trace elements from C18 RP columns. In subsequent determinations of the trace elements by flame AAS, an additional advantage is given by methanol, which causes considerable improvement in sensitivity. Therefore, during further experiments, methanol was added to the carrier (eluent). At fixed concentrations of tetrabutylammonium acetate ( $1 \times 10^{-4}$  M), ammonium acetate ( $1 \times 10^{-4}$  M), and phosphoric acid ( $4 \times 10^{-3}$  M), the stepwise variation of the methanol concentration of 2.5 vol % differed between 0 and 40%. When low methanol concentrations (<10%) were used, a sharp Cr(III) peak was initially observable, whereas the Cr(VI) signal appeared relatively late and very flat (Figure 2, 5% methanol). At an increasing methanol concentration the Cr(VI) signal improved significantly; it became higher and narrower; in addition, the time intervals of both maxima decreased (Figure 2, 15% methanol). Although a further increase in the methanol concentration to 40% led to an increase in the peak height of the Cr(VI) signal, the two oxidation states are no longer completely separated (Figure 2, 40% methanol). During subsequent experiments, again variations of the other chromatographic parameters were tested under conditions of prescribed methanol concentrations of 10, 15, and 20% for each run. It was observed that the TBAA concentration exerted a strong effect on the separation. At low concentrations, the two oxidation states overlapped (Figure 3, top); at high concentrations, the Cr(VI) signal grew very broad (Figure 3, bottom). An optimal separation resulted from tests made with 20% methanol and  $1.5 \times 10^{-4}$  TBAA (Figure 3, center). Under these operational conditions, 90 s is sufficient for the separation including flame AAS measurement.

(2) *Results of Flame AAS Measurement (Sequential Determination)*. With the evaluation of the signals by means of the original AAS software, the advantage of the simultaneous processing of the two oxidation states gets lost. By limiting the measuring time to 30 s, only Cr(III) is detected. In a second separation and measurement procedure, a delay time of 30 s is chosen and the signal area is measured in the time interval between 30 and 75 s (Cr(VI)). Table I contains the relative standard deviations ( $N = 10$ ) resulting from separation and determination procedures at identical concentrations of Cr(III) and Cr(VI) in each case; during each single measurement, only one of the two species was deter-

(10) Syty, A.; Christensen, R. G.; Rains, T. C. *J. Anal. Atom. Spectrom.* 1988, 3, 193–197.

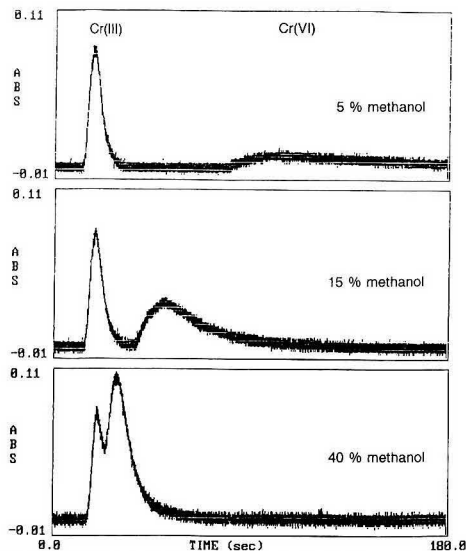


**Figure 2.** Influence of methanol concentration in the carrier on the separation process involving  $2 \mu\text{g/mL}$  Cr(III)/Cr(VI) (screen print, AA spectrometer).

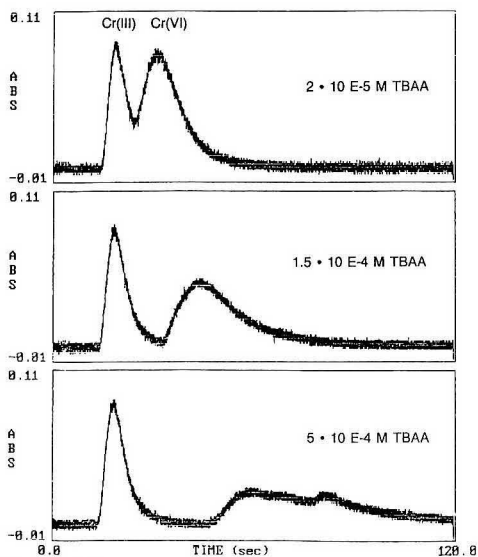


**Figure 3.** Influence of tetrabutylammonium acetate concentration in the carrier on the separation process involving  $2 \mu\text{g/mL}$  Cr(III)/Cr(VI) (screen print, AA spectrometer).

mined. It was found that the reproducibility of the Cr(III) determination was better than that of the Cr(VI) determination. In order to learn more about the mutual influence of the two oxidation states, mixtures of  $1 \mu\text{g/mL}$  Cr(III) or Cr(VI) were doped with increasing concentrations of the other oxidation state ( $0$ – $20 \mu\text{g/mL}$ ). At concentration ratios of Cr(III)/Cr(VI) or Cr(VI)/Cr(III) above  $1:10$ , a partial overlapping of the signals could be observed. By increasing the TBAA concentration in the carrier from  $1.5 \times 10^{-4}$  to  $3 \times 10^{-4}$

**Table I.** Relative Standard Deviations for Cr(III) and Cr(VI) Determination by Original Flame AAS Software Operation

concn of Cr(III) and Cr(VI) ( $\mu\text{g/mL}$ )	rel SD (%) ( $N = 10$ )	
	Cr(III)	Cr(VI)
0.1	4.8	9.0
0.25	4.8	2.4
0.5	3.6	1.5
1.0	1.1	1.2
2.0	0.5	1.9

**Table II.** Mutual Influence by Cr(III)/Cr(VI) on Cr(III) and Cr(VI) Separation and Determination

concn ( $\mu\text{g/mL}$ )		Cr(III)	concn ( $\mu\text{g/mL}$ )		Cr(VI)
Cr(III)	Cr(VI)	measd ( $\mu\text{g/mL}$ )	Cr(VI)	Cr(III)	measd ( $\mu\text{g/mL}$ )
1	0	1.01	1	0	0.99
1	1	0.96	1	1	0.96
1	2	0.98	1	2	0.96
1	5	0.98	1	5	0.99
1	10	0.96	1	10	0.99
1	20	1.01	1	20	1.01

mol/L, the two oxidation states could be completely separated (Table II). The detection limit was established using 25 separation procedures (undoped water); it amounted to  $0.05 \mu\text{g/mL}$  in respect to both Cr(III) and Cr(VI). These measurements were performed with a column which had been in analytical use for as long as 4 months (several thousand separations). With a new column, the detection limit for Cr(III) improved to  $0.03 \mu\text{g/mL}$  ( $3\sigma$  value).

(3) *Results of Flame AAS Measurement (Simultaneous Data Acquisition).* The simultaneous evaluation of the separated peak signals is only possible if HPLC software or an HPLC/GC integrator is used in the operation. Via an additional 1-V analog output fitted into the system by Varian, the corrected AAS signal was transmitted to the HPLC/GC integrator. Figure 4 shows the signal printout of  $2 \mu\text{g/mL}$  Cr(III) and Cr(VI); the evaluation was based on the signal areas established by the integrator. The relative standard deviation ( $N = 10$ ) amounted to  $1.9$  (Cr(III)) or  $3.7\%$  (Cr(VI)).

(4) *Drinking Water.* The mode of separation established in the above manner was also applied to the analysis of spiked drinking water (taken from the Dortmund region). As noted under the Investigations for Optimization of Separation for pure trace solutions, the two oxidation states of these real samples could only be separated incompletely (slight overlapping of peaks). This phenomenon is also mentioned in ref 10. By doubling the concentration of TBAA ( $3 \times 10^{-4}$  M), a complete separation was possible. All measurements were carried out with the HPLC integrator. The relative standard deviations ( $N = 10$ ) in respect to doped samples of drinking water ( $0.1$ – $2.0 \mu\text{g/mL}$  Cr(III) or Cr(VI)) lie between  $3$  and  $10\%$ .

(5) *Soil Samples.* Separation was also carried out on aqueous extracts of contaminated soil samples. Figure 5 shows an example of a soil sample that contained chromium only as Cr(VI). The aqueous extract was doped with  $1$  or  $2 \mu\text{g/mL}$  Cr(III) and Cr(VI). At the point where the Cr(III) signal of the soil sample should have appeared, only the base line was displayed, whereas the doped samples showed both oxidation states. The Cr(VI) concentration found was  $2.51 \mu\text{g/mL}$ , so there was ground for the suspicion that the soil sample was contaminated (sample taken from an industrial area).

(6) *Improved Conditions for Separation.* After the measurements with flame AAS were finalized, experiments were made to apply the mode of on-line separation to the determination by ICP/OES. The high aerosol yield required a desolvation of the aerosol. But inside the desolvation unit,

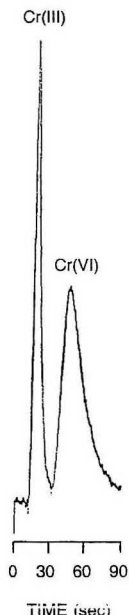


**Figure 4.** Signals attained from 2  $\mu\text{g/mL}$  Cr(III)/Cr(VI), during measurements with an HPLC integrator (simultaneous evaluation of the signal areas).

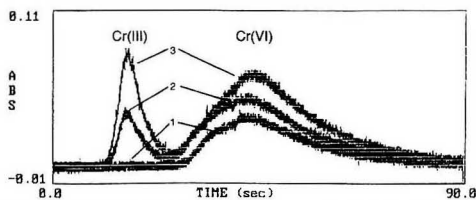


**Figure 5.** Determination of chromium in a contaminated soil sample by standard addition: (1) extract from original soil sample; (2) addition of 1  $\mu\text{g/mL}$  Cr(III)/Cr(VI); (3) addition of 2  $\mu\text{g/mL}$  Cr(III)/Cr(VI).

a strong dispersion of the sample occurred, so that the present separation conditions no longer sufficed. Therefore, it became necessary to optimize again, specially for ICP/OES. The most significant improvement was achieved by the direct and relatively large addition of tetrabutylammonium acetate to the sample. This probably caused the formation of the complex compound required for the ion pair chromatography before the HPLC column was reached, whereby a better separation was attained.<sup>11</sup> The experiences with ICP/OES were later used in the on-line separation of Cr(III)/Cr(VI) with subsequent determination by flame AAS.

**New Conditions for Separation (Drinking Water).** Carrier:  $3 \times 10^{-4}$  M tetrabutylammonium acetate,  $1 \times 10^{-4}$  M ammonium acetate,  $4 \times 10^{-2}$  M acetic acid, 40% (v/v) methanol (pH 3.0–3.2). Sample:  $5 \times 10^{-3}$  M tetrabutylammonium acetate,  $\sim 4 \times 10^{-2}$  M acetic acid. Using acetic acid, a pH value is adjusted between 3.0 and 3.2. Depending of the type of water sample, the required volume of the acetic acid varies. The total time for the on-line separation and determination could be reduced to less than 60 s. The obtained Cr(VI)

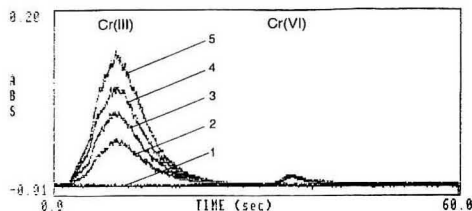


**Figure 6.** Separation/measurement of Cr(III)/Cr(VI) in a waste water sample: (1) blank; (2) sample; (3–5) addition of 1, 2, and 3  $\mu\text{g/mL}$  Cr(III), respectively.

signal was observed to be higher and narrower and the separation of the two signals was significantly better. Cr(VI) added to drinking water caused a display of a signal identical in shape and height to that obtained from deionized water. The signal obtained from Cr(III) in samples of drinking water appeared some time later and was smaller than that of deionized water. This resulted in different slopes of the calibration curve. Therefore, Cr(III) had to be determined in this case by the standard addition method. The relative standard deviation was established with respect to Cr(III)/Cr(VI) concentrations of 0.1, 0.25, 0.5, 1, and 2  $\mu\text{g/mL}$ ; it was found to lie in each case between 1 and 2%. Resulting limits of detection ( $3\sigma$  values,  $N = 25$ ) were 0.03 (Cr(III)) or 0.02  $\mu\text{g/mL}$  (Cr(VI)).

**(7) Waste Water.** For these measurements, the Improved Conditions for Separation were followed. The samples used were waste waters from industrial plants and drained into the public sewage. These samples were assumed to contain too high concentrations of chromium; they were stabilized with nitric acid. Figure 6 illustrates the separation (AAS measurement) of a waste water sample (diluted at a ratio 1:5 with deionized water); it also shows the different signal heights resulting from the same sample after addition of 1, 2, or 3  $\mu\text{g/mL}$  Cr(III). Within 60 s, a complete separation and measurement of both oxidation states are achievable. The chemical behavior of the added Cr(III) is identical to the behavior of the chromium contained in the original sample. The Cr(VI) signal remains uninfluenced by the change in the Cr(III) concentration (identical shape and same retention time). An operational time of 30 s was chosen for the determination of the Cr(III) concentration by standard addition; the Cr(VI) determination was carried out with a delay time of 30 s and a measuring time of 30 s. In this case 0.5, 1.0, and 1.5  $\mu\text{g/mL}$  Cr(VI) were added. The quantitative determination was done via standard additions automatically by synchronizing the autosampler and AA spectrometer. An operation time of  $\sim 5$  min was required for the determination of one oxidation state (blank, sample, three additions). Only by a change in delay time it is possible to determine the other oxidation state from the same sample.

In order to check the accuracy of measurement, two waste water samples were digested with nitric acid and  $\text{H}_2\text{O}_2$  and the total chromium concentration was determined with the nitrous oxide flame. The total chromium concentration of sample 1 (after digestion) was 8.5  $\mu\text{g/mL}$ ; sample 2 contained 2.3  $\mu\text{g/mL}$  chromium. These values were compared with those resulting from a chromatographic separation procedure. In respect to Cr(III), 6.6 (sample 1) and 2.2  $\mu\text{g/mL}$  (sample 2) were measured; in respect to Cr(VI), the values measured were 2.0 (sample 1) and  $<0.3$   $\mu\text{g/mL}$  (sample 2, value at detection limit). The resulting values in respect to the total chromium concentration are 8.6 (sample 1) and 2.2  $\mu\text{g/mL}$  (sample 2). Both determination methods thus lead to the same result for the total chromium concentration. (Note: In the course of routine investigations of waste waters, these

(11) Luo, S. K.; Posta, J.; Berndt, H., unpublished results.

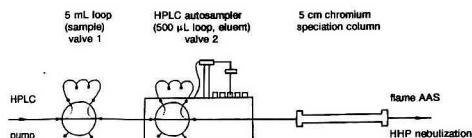


**Figure 7.** Extended HPF flame AAS arrangement for preconcentration of Cr(VI) in the lower microgram per liter range (additional valve with 5-mL sample loop).

measurements were carried out by the "Amt für Umweltschutz und Lebensmitteluntersuchung der Stadt Bonn" and results presented to the authors for publication.)

**Preconcentration of Cr(VI).** (1) *Investigations for Optimization of Preconcentration.* (a) *Arrangement of Apparatus.* The volume capacity of the built-in injection syringe in the autosampler is 2.5 mL. When the sample loops in flow systems are filled, ~2–3-fold the amount of sample volume is required because of the dispersion inside the sample loop, which means a maximum injection of only a 1-mL sample. In principle, one can inject a volume of 1 mL repetitively and, thereby, attain a preconcentration from a larger volume. However, in this investigation, preference was given to the operation with a second HPLC valve (manually operated) equipped with a 5-mL sample loop. The autosampler served in eluting the Cr(VI) traces collected on the column (valve with 500-µL loop). Figure 7 shows the apparatus arrangement for preconcentration of Cr(VI). The apparatus arrangement for separation (Figure 1) was thus merely extended by one valve with a 5-mL sample loop. The Cr(VI) traces contained in the sample are retained by the chromium speciation column. Since, during the elution, only a single peak signal is obtained, the evaluation can be made via standard AAS software.

(b) *Optimization.* In order to attain a sufficiently high detection power, a sample volume of 5 mL was chosen. The flow rate was 2.5 mL/min (optimum nebulization with a 20-µm HHPN nozzle). In all investigations,  $1 \times 10^{-4}$  M ammonium acetate was used as carrier. The pH value of the carrier (pH 3.0–3.2) was adjusted with acetic acid. Investigations included the effect of the TBAA concentration in the sample, the time spent for the process of preconcentration, and the concentration of methanol in the eluent. The used concentration of TBAA ranged from 0.01 to 100 mmol/L. The preconcentration began at a TBAA concentration of 0.1 mmol/L, the sensitivity increased to 5 mmol/L. At higher concentrations (to 100 mmol/L TBAA) a plateau is observed. Within a preconcentration time of only 2.5 min, 95% of the maximum signal area was attained. An optimum signal was obtained within 2.5–3 min. Longer preconcentration times (5 min) resulted in a signal broadening at identical signal area. Preconcentration times exceeding 5 min cause a decrease of signal area, because Cr(VI) is gradually washed out of the column by the carrier. Investigations of the elution efficiency were made using methanol/water mixtures ranging from 0 to 100% (v/v) and carrying out each test by the stepwise increase of 10% methanol. It was found that an acceptable elution can only be attained if 30% of methanol in the mixture is exceeded. At increasing methanol concentration, the elution time reduces (30% methanol, 43.5 s; 50% methanol, 32 s; 60% methanol, 29 s; 80–100% methanol, 26 s). The difference in the respective signal shapes resulting from methanol concentrations between 30 and 80% is insignificant; the maximum lies at 60% methanol. At excess of 80% methanol, the signals become lower and far broader. The following measurements were made with a mixture of 60%/40% (v/v) methanol/water.

(c) *Semiautomated Preconcentration of Cr(VI).* At the start of a timing cycle, the autosampler fills the 500-µL loop

(Figure 7, valve 2) with the eluent. At the same time, the sample volume (5 mL) is manually introduced into the carrier stream (valve 1) and the Cr(VI) traces are collected on the column. The actual time is shown on the autosampler display. After 148 s, the sample introduction valve is manually switched to the load position. When the display indicates 150 s, the autosampler injects the eluent (valve 2) and transmits a read signal to the AA spectrometer. After elution (40 s), the autosampler switches valve 2 back into its initial position and a rinse time of 20 s follows. While elution and AAS measurement are in progress, the 5-mL sample loop (valve 1) is refilled with the next sample. After 210 s, the autosampler starts a new cycle.

(2) *Preconcentration of Cr(VI) from Drinking Water (Results).* Samples of drinking water taken from the Dortmund region were used for analysis ( $5 \times 10^{-3}$  mol/L TBAA, pH 3–3.2 adjusted with acetic acid). None of these samples was found to contain inherent Cr(VI), when this method was used. Therefore, all investigations had to be carried out with doped samples. The investigated concentrations ranged from 10 to 100 µg/L Cr(VI). In comparison to the preconcentration from deionized water, the signal area attained was somewhat smaller (95–97%). The effect of the drinking water is therefore concluded to be relatively small. Acidified samples do not require the addition of acetic acid. A stabilization of the water sample by nitric acid is common practice. In that case, ammonia is taken for the adjustment of the pH value. When strongly acidified samples with nitric acid are used, the resulting neutralization causes a larger concentration of ammonium nitrate. A considerable effect is exerted on the preconcentration when ammonium nitrate concentration exceeds ~2 mmol/L. For that reason, any samples used for preconcentration of Cr(VI) should be stabilized with only very small volumes of nitric acid. Another problem is that a larger acid concentration leads to a lower recovery by the undesirable reduction of Cr(VI); the lifetime is considerably shortened under strongly acidic operation conditions.<sup>12</sup> The relative standard deviation was established by using differently spiked samples. It amounted to 3.1% at 10 µg/L, to 1.9% at 50 µg/L and to 1.5% at 100 µg/L Cr(VI) ( $N = 10$ ). The detection limit ( $3\sigma$  value) was established from measurements of 25 undoped samples; it lies at 0.5 µg/L Cr(VI).

## CONCLUSION

The aim of this work was the automated on-line separation and determination of Cr(III)/Cr(VI) traces by high-performance flow atomic spectrometry. The separation of the two oxidation states by HPLC and subsequent flame AAS determination was described earlier (coupling of HPLC and AAS<sup>10</sup>). Fully automated HPLC separation techniques are nowadays available. Using hydraulic high-pressure nebulization for sample introduction in flame AAS, an HPLC pump (pressure generator) becomes a functional unit of the atomic spectrometer. Equipped with standard HPLC accessories (e.g., autosampler) this procedure can be fully automated. Compared to pneumatic nebulization, a 4-times higher sensitivity in the determination of chromium is achieved (measurement of signal area 100-µL samples). An additional HPLC separation column permits an efficient and interface-free coupling of HPLC separation techniques and flame AAS determination of the separated traces. With commonly used AA spectrometers, the signals attained from Cr(III) and Cr(VI) cannot be measured simultaneously, since the AAS software can process only a single transient signal. Nevertheless, simultaneous signal processing is possible by the employment

(12) Pavel, J.; Kliment, J.; Stoerk, S.; Suter, O. *Fresenius Z. Anal. Chem.* 1985, 321, 587–591.



of an HPLC integrator or HPLC software. In this investigation, the AA spectrometer was additionally equipped with an analog output which was connected to an HPLC integrator. By modification of the separation conditions as known from the literature,<sup>10</sup> and especially by the addition of tetrabutylammonium acetate to the sample as well as methanol in the eluent (carrier), both oxidation states could be on-line-separated and measured fully automated within only 60 s. With regard to chromium concentrations in the range of 1  $\mu\text{g/mL}$ , the relative standard deviation is  $\sim 1\%$ . Such good reproducibility is probably due to the fully automated mode of operation (autosampler, time control). The detection limit lies at 0.03  $\mu\text{g/mL}$  with respect to Cr(III) and at 0.02  $\mu\text{g/mL}$  with respect to Cr(VI) ( $3\sigma$  values,  $N = 25$ ). Serving as matrices were samples of drinking water and samples of waste water, whereat the separation in even strongly acidic waste water samples was found to be possible ( $\text{pH} < 1$ ); in this case, however, the calibration has to be done by standard addition. The separation and determination was also possible using aqueous extracts of contaminated soil samples. The same type of chromium speciation column (modified C18 type) is also suitable for preconcentration of Cr(VI) traces. If the HPLC arrangement is extended by an additional, not automatic valve, Cr(VI) can be determined within the lower microgram per liter range (detection limit 0.5  $\mu\text{g/L}$ ,  $3\sigma$  value). The relative standard deviation is 3.1 (10  $\mu\text{g/L}$  Cr(VI)) or 1.5% (100  $\mu\text{g/L}$  Cr(VI)); the time duration for preconcentration and determination was only 3.5 min. Drinking water samples were used for the preconcentration procedure. An operation time of 26 min for the preconcentration (25-cm HPLC column, flame AAS, coupling via pneumatic nebulizer) has been quoted elsewhere.<sup>13</sup>

During the initial investigations, different techniques of sample pretreatment were chosen for the separation of Cr(III)/Cr(VI) and the preconcentration of Cr(VI). If tetrabutylammonium acetate is added to the sample and water is used as carrier, Cr(VI) is retained by the HPLC column, while Cr(III) passes the column (conditions for a preconcentration). Subsequently, Cr(VI) is eluted with "methanol" (60% methanol/40% water). During the separation of Cr(III)/Cr(VI) usually only the carrier contains TBAA; both species pass the column under different speeds. For real samples, e.g.,

strongly acidic samples, a separation is often no longer possible under the conditions as mentioned above, because the interaction of Cr(VI) and the C18 RP material in acidic solution is too weak. In a case where TBAA is added to the sample, Cr(VI) is totally collected on the column. However, since the aim was not a preconcentration of Cr(VI), but a chromatographic separation, methanol was added to the carrier in order to reduce the bonding strength. Using methanol in different concentrations, the retention times of Cr(III) and Cr(VI) can be varied over a wide range. With TBAA in the sample and 40% methanol in the carrier, a reduction to only 1 min of total time required for separation and flame AAS determination could be achieved, even in cases where difficult real samples, e.g., polluted waste water samples, were involved. The entire procedure was performed fully automated in this case.

### FUTURE AIMS

An HPLC integrator was still used in this investigation for the evaluation of the chromatographic signals. However, with an instrument-specific combination of hard- and software (HPF-AS software, representing in principle an HPLC control and evaluation software), not only simple separations such as those of Cr(III) and Cr(VI) may be carried out by high-performance flow atomic spectrometry but almost all other operational modes of HPLC can be coupled interface-free with atomic spectrometric determination methods. The elution, for example, could thus proceed via software control and under the application of a low-pressure gradient technique.

### ACKNOWLEDGMENT

This work was carried out with the financial support of the Bundesministerium für Forschung und Technologie as well as the Ministerium für Wissenschaft und Forschung des Landes Nordrhein-Westfalen. Additional support was given by the Deutscher Akademischer Austauschdienst (DAAD) as well as by Varian GmbH, Germany. The authors further extend their thanks to Frau A. Lorenz and Herrn Tilp, Bonn, for their excellent cooperation regarding the work with waste water samples.

(13) Syty, A.; Christensen, R. G.; Rains, T. C. *At. Spectrosc.* 1986, 7, 89-92.

# Helium Microwave Induced Plasma Atomic Emission Detection for Liquid Chromatography Utilizing a Moving Band Interface<sup>†</sup>

Peter B. Mason, Liming Zhang, and Jon W. Carnahan\*

Department of Chemistry, Northern Illinois University, DeKalb, Illinois 60115

Randall E. Winans\*

Chemistry Division, Argonne National Laboratory, Argonne, Illinois 60439

A moving band interface is used to separate HPLC solvent from analyte before introduction into a microwave-induced plasma atomic emission detector. Spectral scans indicate that all detectable solvent is removed prior to analyte introduction. Analyte memory effects are not detectable. Chlorine element selective detection limits are 140, 410, 220, and 770 pg/s for 9-chlorofluorene, *p*-chlorobiphenyl, 4-chlorobenzophenone, and  $\alpha,\alpha'$ -dichloro-*o*-xylene, respectively. If the vaporization region is heated significantly, chlorine selective response is dependent upon the boiling point of the compound due to analyte volatilization before it reaches the detector.

## INTRODUCTION

The need for a sensitive and selective detector for liquid chromatography (LC) is intrinsic to the method itself. Many commonly utilized LC detectors exploit eluent bulk physical or chemical properties, such as refractive index or UV-visible absorption. These types of detectors lack the combination of high sensitivity and selectivity. Due to the finite resolving capabilities of today's chromatographic columns, the problem of analyte coelution must be addressed. On a fundamental basis, the technique of atomic emission spectrometry used for LC detection has the potential to provide both enhanced sensitivity and selectivity. With the low detection limits afforded by typical atomic emission techniques and the inherent selectivity of elemental line emission, it would seem that an atomic emission detector would be ideally suited for use in chromatography.

One chromatographic technique which has successfully employed helium microwave-induced plasma (MIP) atomic emission detection is gas chromatography (GC).<sup>1-7</sup> Several operational aspects of GC make it a suitable partner for MIP coupling. In particular, helium gas may be used as both the GC mobile phase and the plasma support gas, flow rates of the mobile phase and the plasma gas are similar, and analyte is present in the vapor phase; thus lower power plasmas (~100

W) are capable of efficient atomization and excitation. Unfortunately, GC represents a unique case. The presence of the mobile phases of other chromatographic techniques may alter selected plasma characteristics, making mating to the MIP more problematic.

Most areas of LC plasma research focus on direct sample introduction. Several interfacing methods have been investigated, including the introduction of effluent vapor,<sup>8</sup> nebulization,<sup>9,10</sup> and thermospray.<sup>11</sup> While some success has been achieved, a fundamental limitation of this approach is that the bulk of the introduced material is the chromatographic mobile phase. Due to molecular emission (C<sub>2</sub>, CH, CO, CN, N<sub>2</sub>, etc.) caused by organic solvents, the mobile phase often contributes to increased noise due to increased spectral background. Additionally, lower power plasmas are generally incapable of desolvation, atomization, and excitation. The presence of even small amounts of mobile phase may cause analyte signal reduction or even extinguish the plasma.

It has been suggested by Jansen, Huff, and DeJong<sup>12</sup> that a means of achieving the desired sensitivity and low detection limits with liquid chromatography-plasma atomic emission interfaces requires the separation of the bulk solvent (i.e., mobile phase) from the analyte prior to introduction into the plasma. The use of a solvent evaporation-analyte transport-type interface between HPLC and MIP represents a potential means of solving this problem.

Zhang and co-workers<sup>13</sup> exploited the large differences in volatility between mobile phases and inorganic LC eluates. They examined the use of a moving wheel interface to couple HPLC with the He-MIP. The column effluent was nebulized and deposited on a rotating stainless steel wheel. As the wheel rotated, the effluent passed under a flow of hot nitrogen which served to vaporize and carry away the mobile phase. The dry analyte on the wheel then rotated into the plasma where it was vaporized, atomized, and excited. While temperature control was sufficient to separate solvent from inorganic solutes, the high heat capacity of the thick steel wheel coupled with direct plasma contact reduced the feasibility of the use of this system with organic analytes. Finer temperature control and more rapid temperature changes are required. Additionally, detection limits were limited by flicker noise induced by plasma-rotating wheel contact.

An ideal transport-type interface should possess the following characteristics: the sample-loading capacity should

<sup>†</sup> Presented in part at the 19th Annual Meeting of the Federation of Analytical Chemistry and Spectroscopy Societies, Cleveland, OH, 1990; Paper 44.

(1) Estes, S. A.; Uden, P. C.; Barnes, R. M. *Anal. Chem.* 1981, 53, 1829.

(2) Van Dalen, J. P. J.; de Lezenne Coulander, P. A.; de Galen, L. *Anal. Chim. Acta* 1977, 94, 1.

(3) Bradley, C.; Carnahan, J. W. *Anal. Chem.* 1988, 60, 858.

(4) Slatkavitz, K. J.; Uden, P. C.; Barnes, R. M. *J. Chromatogr.* 1986, 355, 117.

(5) Wu, M.; Lee, M.; Farnsworth, P. B. *J. Anal. At. Spectrom.* 1992, 7, 197.

(6) Webster, G. H.; Doggett, W. O.; Boss, C. B. *Anal. Chim. Acta* 1992, 257, 309.

(7) Quimby, B. D.; Sullivan, J. J. *Anal. Chem.* 1990, 62, 1027.

(8) Billiet, H. A. H.; Van Dalen, J. P. J.; Schoenmakers, P. J.; De Galen, L. *Anal. Chem.* 1983, 55, 847.

(9) Michlewicz, K. G.; Carnahan, J. W. *Anal. Chem.* 1986, 58, 3122.

(10) La Freniere, K. E.; Fassel, V. A.; Eckels, D. E. *Anal. Chem.* 1987, 59, 879.

(11) Roychowdhury, S. B.; Koropchak, J. A. *Anal. Chem.* 1990, 62, 484.

(12) Jansen, G. W.; Huff, F. A.; De Jong, H. J. *Spectrochim. Acta, Part B* 1985, 40, 307.

(13) Zhang, L.; Carnahan, J. W.; Winans, R. E.; Neill, P. H. *Anal. Chem.* 1989, 61, 895.

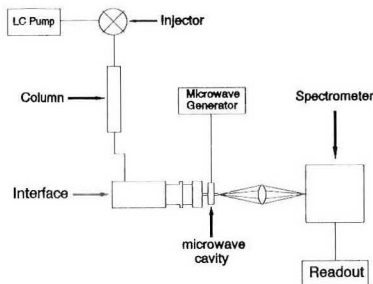


**Figure 1.** Overview diagram of the LC-MIP system with the moving band interface. Details appear in the text.

be high, the solvent removal process should be efficient, the analyte transport efficiency to the detector should approach 100%, sample memory effects should be nonexistent, and it should be possible to quickly alter the temperature of the sample transport surface to provide low-temperature sample deposition and high-temperature sample vaporization.

Designed for HPLC mass spectrometry, the moving band interface manufactured by Finnigan MAT (San Jose, CA)<sup>14</sup> possesses many of these characteristics. Applications of this interface to mass spectrometry were reported by several researchers.<sup>15-17</sup> This moving band interface maintains high sampling efficiency while removing enough solvent so that the remaining dry analyte can be introduced into the detector. The interface provides rapid temperature changes on the moving band so as to minimize sample loss due to decomposition and volatilization prior to entering the vaporization chamber. Presented in this paper are initial promising results based on HPLC-MIP coupling with the moving band interface.

## EXPERIMENTAL SECTION

A block diagram of the HPLC-MIP system is presented in Figure 1. The individual components of this system are described below.

**High-Performance Liquid Chromatography System.** The LC pump was a miniPump from Laboratory Data Control capable of flow rates from 0.48 to 4.8 mL/min. A Rheodyne (Cotati, CA) Model 7125 injector was utilized with a 20- $\mu$ L injection loop. Sample injection was performed manually. Separation was accomplished using a 25  $\times$  0.46 cm Chromanetics Spherisorb 5- $\mu$ m particle diameter ODS C-18 column. The 20% deionized water in methanol mobile phase was degassed ultrasonically for 10 min.

**Microwave-Induced Plasma System.** The plasma torches used throughout this research were capillary quartz tubes, nominally 2 mm i.d.  $\times$  7 mm o.d. The torch was inserted into a TM<sub>010</sub> resonant cavity (91.5-mm inner diameter, 12.2-mm depth) of the same basic design as that described by Beenakker.<sup>17</sup> Microwave power was provided by a 125-W, 2450-MHz Microtherm Model CMD<sub>4</sub> generator from Raytheon Manufacturing Co. (Waltham, MA) with a Times Fiber Corp. No. 07145RG-214/U (Wallingford, CT) coaxial cable. Impedance matching was performed using a Model 1878B 3-stub tuner from Maury Microwave (Cucamonga, CA). The plasma was maintained at 60 W with a helium flow of 20 mL/min.

**Spectrometer System.** Plasma emission was focused onto the entrance slit of the polychromator of a microwave plasma

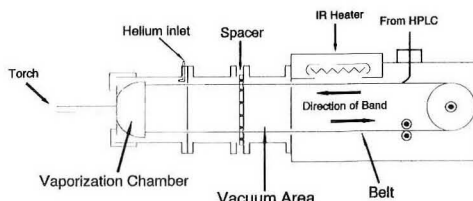


**Figure 2.** Moving band interface with the entire housing chamber. For initial spectral scans, the front portion of the housing surrounding the vaporization chamber was removed and helium was introduced directly into a port on the vaporization chamber.

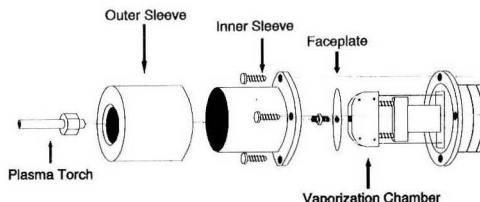


**Figure 3.** Exploded view of the front portion of the housing system to envelope the vaporization chamber. Details are discussed in the text.

detector (MPD) 850 organic analyzer from Applied Chromatography Systems Ltd. (Bedfordshire, England). This 0.75-m focal-length spectrometer employs the Rowland circle design with a 960 groove/mm grating and multiple exit slits to achieve simultaneous detection. For this study, the 479.54-nm chlorine ion line was monitored using an RCA 1P28 PMT (Lancaster, PA). The PMT was biased at  $\sim$ 900 V. The PMT output was converted to a voltage and amplified. The amplified signal was monitored using a Houston Instruments (Austin, TX) single-channel strip-chart recorder Model B5117-2. Initial spectral scans were obtained with a 0.5-m focal-length Model 82-000 Jarrell-Ash (Waltham, MA) Ebert spectrometer.

**Reagents.** Reagents employed in this research were analytical grade and used as received. The following chemicals were used: 4-chlorobenzophenone from Matheson Co., Inc. (Joliet, IL); *p*-chlorobiphenyl from Aldrich Chemicals (Milwaukee, WI);  $\alpha,\alpha'$ -dichloro-*o*-xylene from Eastman Organic Chemicals (Rochester, NY); 9-chlorofluorene from Aldrich Chemicals (Milwaukee, WI) and methanol. It was found using HPLC with UV-visible detection that at least one impurity was present in 9-chlorofluorene. A second sample of 9-chlorofluorene from Aldrich was obtained and yielded the same impurity. Pure helium (99.995%) was purchased from Great Lakes Airgas, Inc. (West Chicago, IL).

## RESULTS AND DISCUSSION

**Design and Operating Principles of the Moving Band Interface.** The modified moving band interface is diagrammed in Figures 2 and 3. Operation of the interface occurs in five steps. In the first step, the HPLC eluent is directed onto the moving band as shown in Figure 2. The band is a polyimide film 3.2 mm wide and 0.05 mm thick moving at a speed of 2.5 cm/s. The column eluent was directed onto the band through a 1/16-in.-o.d., 0.01-in.-i.d. flexible PEEK tube (Upchurch Scientific, Inc., Oak Harbor, WA) held 1 mm above the band with a 6-mm-o.d., 2-mm-i.d. glass sleeve which was bent 30° and mounted on the interface body with a Swagelok fitting. It may be calculated that a flow rate of 1 mL/min deposits a 0.2-mm-thick eluent layer on the band. The second step involves initial solvent evaporation as the band passes beneath an infrared heater. Third, the effluent passes into a vacuum region served by a roughing pump. In this region residual solvent vapors are removed. The dry analyte is then

(14) Finnigan MAT HPLC-MS Interface Operator's Manual, Manual No. 92000-9091, Revision B, February 1982.

(15) McFadden, W. H.; Schwartz, H. L.; Evans, S. J. *Chromatogr.* 1976, 122, 389.

(16) McFadden, W. H.; Bradford, D. C.; Games, D. E.; Gover, J. L. *Am. Lab.* 1977, 10, 55.

(17) Hayes, M. J.; Lankmeyer, E. P.; Vouros, P.; Karger, B. L.; McGuire, J. M. *Anal. Chem.* 1983, 55, 1745.

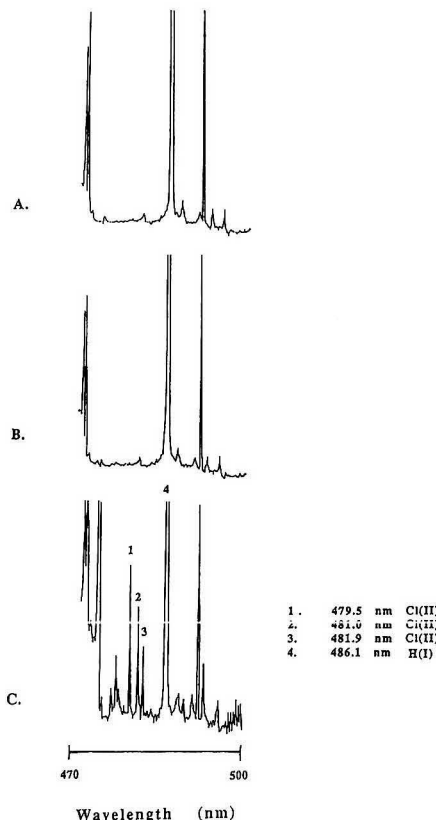


**Figure 4.** Spectral scans of the helium plasma in the 470–500-nm spectral region: (A) plasma of pure helium, helium introduced through the interface; (B) plasma with 0.5 mL/min methanol introduced onto the moving band; (C) plasma with 0.5 mL/min methanol containing 1 mg/mL 4-chlorobenzophenone deposited onto the moving band.

transported to the fourth functional region of the interface, the vaporization chamber. Here, flash vaporization of the analyte is achieved through radiant heating. Heating is accomplished by a nichrome heater within a quartz sleeve inside the chamber. Following sample volatilization, the band with remaining analyte residue exits the vaporization chamber and passes under a nichrome wire cleanup heater. This heater serves to remove any remaining sample and prepare the band for the solvent deposition step. The band then cools and is ready to repeat another cycle.

For initial vaporization and spectral characterizations, the Beenakker TM<sub>010</sub> cavity was affixed directly in front of the vaporization chamber. The quartz plasma torch was connected to the vaporization chamber with a Swagelok fitting. The configuration used for these experiments is similar to that of Figure 2 except that the forwardmost portion of the outer housing was not present and a 1/8-in. copper tube was soldered onto the vaporization chamber to deliver helium plasma gas through the chamber and into the torch. The plasma gas is introduced into the chamber and transports vaporized analyte into the plasma. The efficiency of solvent removal and analyte vaporization was examined by obtaining spectra in the region from 470 to 500 nm. These spectra are shown in Figure 4. The spectra with pure helium and with

the continuous introduction of 0.5 mL/min methanol are essentially identical. With the introduction of 0.5 mL/min methanol containing 1 ppt 4-chlorobenzophenone (bp 332 °C at 771 Torr), three intense chlorine ion emission lines were observed. Immediately upon the cessation of 4-chlorobenzophenone introduction and substitution of pure methanol, the spectra returned to that seen in Figure 4B. These results indicated that solvent analyte separation and high boiling point analyte desorption could be achieved with success.

Flow injection was used to simulate transient chromatographic signals.<sup>18</sup> When 4-chlorobenzophenone was monitored at the 479.5-nm chlorine emission line, it was found that solvent flows exceeding 0.5 mL/min suppressed the emission intensity. This behavior is probably due to incomplete removal of the greater solvent volume.

While this configuration was useful for initial studies, it is not ideal in terms of maximizing analyte transport to the plasma. Of particular note are the rectangular slots where the moving band enters and exits the vaporization chamber. The entrance and exit slots have dimensions of approximately 5 mm × 0.5 mm, or a combined area of 5 mm<sup>2</sup>. It is reasonable to assume a significant loss of helium, and consequently, a loss of analyte occurs through these slots. The inner diameter of the quartz plasma torch is 2 mm, which represents an area of 3.1 mm<sup>2</sup>. On the basis of areas alone, one would expect only 38% of the analyte to exit through the plasma torch. Plasma back pressure may decrease this fraction significantly.

To prevent this decrease in sample transport to the plasma, a modification to provide a helium overpressure outside of the vaporization slots was devised. Figures 2 and 3 detail this approach. A system employing inner and outer cylindrical sleeves and a 0.5 mm thick by 54 mm diameter metal face plate was machined. The inner sleeve was fitted over the vaporization chamber and secured with bolts. The outer sleeve slid over the inner sleeve and a gas-tight seal was formed by a nitrile O-ring located on the interior surface of the outer sleeve. The chamber was completely sealed by the metal face plate butting against a second nitrile O-ring located on the inner face of the outer sleeve. On Figure 2, note the placement of the thin metal spacer located between the housing and the adjacent chamber. This spacer had 12 holes (3-mm diameter) to allow access to the atmosphere. Without the spacer, the vacuum was sufficient to draw atmosphere through the outlet of the torch and prevent plasma ignition. By isolating the vacuum region from the helium overpressure region with the spacer, a net positive flow of helium through the torch was maintained. With the vaporization chamber completely enclosed, helium gas was introduced. This introduced gas had two outlets: into the vaporization chamber through the aforementioned vaporization chamber slots or out the back of the enclosed region through the moving band slots. This former flow serves as the analyte transport and plasma support gas. In this manner, the loss of analyte through the vaporization chamber slots was eliminated. To achieve a net flow of 20 mL/min through the plasma torch, approximately 1.5 L/min helium was provided to the enclosed overpressure region. The bulk of introduced gas was lost through the metal spacer to the surrounding environment.

Because the flash vaporization and cleanup heaters are completely enclosed in the metal sleeves, there was a 1-h period of time before the temperature of the vaporization chamber and the cleanup heater reached steady-state values. The interface was operated without introduction of mobile phase until the temperatures stabilized. The IR heater was set at 90% of maximum, yielding an approximate temperature of 100 °C. Vaporization and cleanup heater temperatures

(18) Zhang, L. Ph.D. Dissertation, Northern Illinois University, 1990.

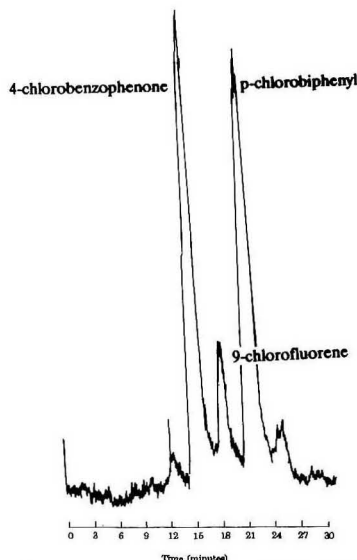


Figure 5. Chromatogram of 4-chlorobenzophenone, 9-chlorofluorene, and *p*-chlorobiphenyl. The vaporization and cleanup heaters are set at 226 and 214 °C, respectively.

were in the range of 200–250 °C. These temperatures are detailed with individual chromatograms. It should be noted that, even at the high temperatures maintained in the vaporization and cleanup regions, the polyimide band showed few signs of deterioration when operated continuously for periods of 6–7 h and intermittently over a period of 3 months.

Figure 5 is a chromatogram of a 20- $\mu$ L injected mixture of 8.9  $\mu$ g of chlorine as 4-chlorobenzophenone, 0.53  $\mu$ g of chlorine as 9-chlorofluorene, and 8.9  $\mu$ g chlorine as *p*-chlorobiphenyl in methanol. A mobile-phase flow rate of 0.43 mL/min was employed, with the vaporization heater set at 226 °C and the cleanup heater at 214 °C. Using UV-visible detection, the first and last peaks of this chromatogram were determined to be impurities in the 9-chlorofluorene. For this set of compounds, the peak areas per unit mass were similar. This observation is not surprising as the MIP is expected to produce peak areas proportional to chlorine mass. Further, because the boiling point range of these compounds is reasonably small (291–332 °C), their vaporization behaviors on the moving band interface are expected to be similar. (It should be noted that the boiling point of 9-chlorofluorene has not been determined. However, the boiling point of fluorene is 295 °C and the chlorinated species is expected to be slightly higher.)

A second set of mixtures was examined. This chromatogram was obtained using a vaporization temperature of 240 °C and cleanup heater temperature of 215 °C. The chromatogram in Figure 6 was obtained by injecting a 20- $\mu$ L sample containing chlorine masses of 3.3  $\mu$ g as  $\alpha,\alpha'$ -dichloro-*o*-xylene, 2.7  $\mu$ g as 4-chlorobenzophenone, and 4.2  $\mu$ g as *p*-chlorobiphenyl.

**Dynamic Ranges and Detection Limits.** Calibration plots were obtained for the compounds separated in Figure 5 and are shown in Figure 7. As stated previously, the responses for these compounds are similar. Response tends to be linear up to approximately 5  $\mu$ g. Masses above this level produce a "roll-over" in the calibration plot. The cause of this nonlinearity may be due to plasma "over-loading", vaporization effects, or a combination of the two.

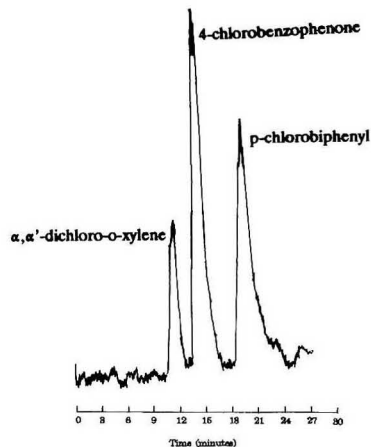


Figure 6. Chromatogram of  $\alpha,\alpha'$ -dichloro-*o*-xylene, 4-chlorobenzophenone, and *p*-chlorobiphenyl. The vaporization and cleanup heaters are set at 240 and 216 °C, respectively.

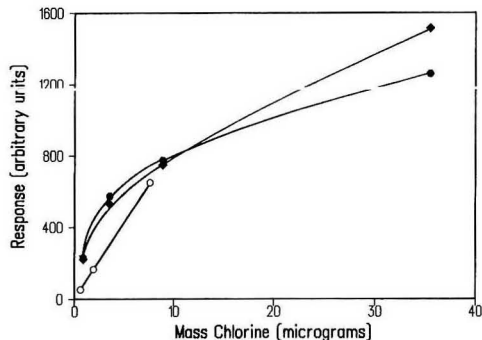


Figure 7. Calibration plots of compounds shown in the Figure 5 chromatogram: (●) 4-chlorobenzophenone; (◆) *p*-chlorobiphenyl; (○) 9-chlorofluorene.

Figure 8 is a plot of peak area versus chlorine mass for the mixture of 4-chlorobenzophenone, *p*-chlorobiphenyl, and  $\alpha,\alpha'$ -dichloro-*o*-xylene. This plot indicates a different detector response for each of the three compounds. Relative responses were 1.00 for 4-chlorobenzophenone, 0.55 for *p*-chlorobiphenyl, and 0.34 for  $\alpha,\alpha'$ -dichloro-*o*-xylene.

Examinations of the differences in response behaviors are important in optimizing the system for analytical use. The calibration plot shown in Figure 7 (4-chlorobenzophenone, 9-chlorofluorene, *p*-chlorobiphenyl) was taken with a vaporization temperature of 220 °C. Fairly uniform response was seen for all compounds. Calibration data for Figure 8 were taken with a vaporization heater temperature of 240 °C. In this case, response varied from compound to compound. It is likely that the temperature of the moving band within the housing plays a major role in determining response behavior. The metal sleeves which house the vaporization and cleanup heaters are significantly heated by the vaporization and cleanup heaters. One problem which this heating poses is the possible vaporization of analyte prior to entrance into the vaporization chamber. The boiling points and response factors for 4-chlorobenzophenone, *p*-chlorobiphenyl, and  $\alpha,\alpha'$ -dichloro-*o*-xylene are listed in Table I. As can be seen from



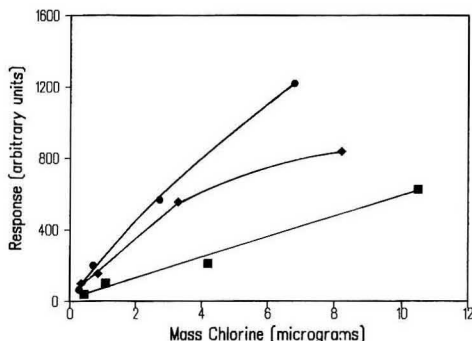


Figure 8. Calibration plots of compounds shown in the Figure 6 chromatogram: (●) 4-chlorobenzophenone; (◆) *p*-chlorobiphenyl; (■)  $\alpha,\alpha'$ -dichloro-*o*-xylene.

Table I. Boiling Points and Response Factors for Compounds Separated in Figure 6 and for Which Calibrations Are Shown in Figure 8

compound	bp (°C)	rel response
4-chlorobenzophenone	332	1.00
<i>p</i> -chlorobiphenyl	291	0.55
$\alpha,\alpha'$ -dichloro- <i>o</i> -xylene	239	0.34

this table, response factors increased as the analyte boiling point increased. It is likely that at the higher vaporization chamber temperature that the heating of the metal sleeve increases and this heat may be transferred to the moving band. Lower boiling point compounds may be partially vaporized before they reach the vaporization chamber and be carried out the back slots by helium in the overpressure region.

Reproducibility studies were performed with each of the compounds injected and the conditions of Figures 7 and 8. The average relative standard deviations were 5.0% and the range for the compound set was 1.0–12%.

Table II illustrates chlorine detection limits using a signal to baseline noise ratio of 3 for the compounds utilized in this study. The range of detection limits was 140 pg of Cl/s for 9-chlorofluorene to 770 pg of Cl/s for  $\alpha,\alpha'$ -dichloro-*o*-xylene. These detection limits approach those of the GC-MIP systems. Estes et al.<sup>1</sup> listed a chlorine detection limit for 1,1,2,2-tetrachloroethane of 43 pg/s. In this work, the listed detection limits average 380 pg/s. Thus, the average detection limit is only a factor of 9 higher than that obtained with GC-MIP and only a factor of 3 higher in the best case. Clearly, the detection limits for the LC-MIP system are approaching those of the GC-MIP.

Table II. Detection Limits for Compounds Separated and Detected with the Moving Band HPLC-MIP Interface<sup>a</sup>

compound	rel detectn limit (ng of Cl/s)	abs detectn limit (ng of Cl)
4-chlorobenzophenone	0.22	31
9-chlorofluorene	0.14	16
<i>p</i> -chlorobiphenyl	0.41	60
$\alpha,\alpha'$ -dichloro- <i>o</i> -xylene	0.77	97

<sup>a</sup> For all compounds except 9-chlorofluorene, detection limits were taken with the conditions of Figure 5. For 9-chlorofluorene, conditions are those of Figure 6.

## CONCLUSION

The moving band interface has been demonstrated to be an efficient tool for separation of liquid chromatography mobile phase from the analyte. Using this scheme, detection limits approach those of GC/MIP systems. It appears that improvements can be made to enhance system performance even more.

Accompanying the modified vaporization region was a significant amount of heating of the sleeves which surrounded the band. This heating may have caused significant loss of analyte due to vaporization in this region. Cooling of the sleeve by affixing a water coil to it may prevent this problem.

Additionally, the capillary quartz plasma torches typically used in a low power plasma system are degraded by the high temperature plasma. Eventual large increases in plasma noise and instability necessitates changing these torches. Initial design and construction of a water-jacketed torch, with the water jacket placed immediately after the cavity has improved the lifetime of the torch approximately 2–3 times. Implementation of this torch for LC/MIP will be examined.

Finally, future work should focus on the application of this system to other chromatographic separations. The He-MIP is capable of detecting a number of non-metals, including O, N, C, H, S, P, Cl, and Br. In particular, the advantage of selectivity offered by atomic emission detection should be exploited by examining separations which involve the co-elution of analytes by simultaneous monitoring of several emission lines. This system shows promise and should be examined for the separation, identification and quantitation of pesticides and pharmaceuticals.

## ACKNOWLEDGMENT

This work was performed in part under the auspices of the Office of Basic Energy Sciences, Division of Chemical Sciences, U.S. Department of Energy, under Contract W-31-109-ENG-38.

RECEIVED for review April 12, 1993. Accepted June 23, 1993.\*

\* Abstract published in *Advance ACS Abstracts*, August 15, 1993.

# Solid-Matrix and Solution Luminescence Photophysical Parameters and Analytical Aspects of the Tetrols of Benzo[a]pyrene-DNA Adducts

Johannes Corley and Robert J. Hurtubise\*

Department of Chemistry, University of Wyoming, Laramie, Wyoming 82071

Tetrols are the products obtained from the hydrolysis of benzo[a]pyrene-DNA adducts. The fluorescence and phosphorescence lifetimes and quantum yields were obtained for the tetrols both at room temperature and at low temperature with 10%  $\alpha$ -CD/NaCl and in solutions. Relatively large changes in the solution fluorescence lifetimes of the tetrols were observed from room temperature to 77 K. However, very small changes were observed for the fluorescence and phosphorescence lifetimes of the tetrols on 10%  $\alpha$ -CD/NaCl from room temperature to 93 K. Several photophysical rate constants and quantum yields for various photophysical processes were calculated. Comparisons were made between the room-temperature and low-temperature photophysical parameters. Also, several approaches for characterizing and identifying the tetrols by their solid-matrix luminescence properties and solution fluorescence properties were considered.

## INTRODUCTION

Polycyclic aromatic hydrocarbons (PAH) constitute an important class of mutagenic and carcinogenic environmental pollutants. One source of PAH is from the combustion of fossil fuels. The PAH are relatively inert and practically insoluble in aqueous solutions.<sup>1</sup> In living cells, however, these molecules are metabolized into a variety of oxygenated products which are more soluble in aqueous systems.<sup>1</sup> Benzo[a]pyrene (B[a]P) is one of the most widely studied PAH. The biologically active metabolites of B[a]P have been identified as B[a]P-7,8-diol-9,10-epoxide (BPDE) derivatives.<sup>1</sup> The conversion of B[a]P into DNA-reactive metabolites, the binding of these metabolites to DNA, and the hydrolysis of the BPDE-DNA adducts to the tetrols have been studied.<sup>1,2</sup> However, very little work has been done to identify and characterize the four stereoisomeric tetrols, which are products from B[a]P-DNA adducts.

Two general approaches are used to study the extent of chemical damage to DNA by B[a]P, namely, the direct detection and characterization of B[a]P-DNA adducts bonded to DNA, and the detection, characterization, and quantitation of tetrols obtained from the B[a]P-DNA adducts and other oxygenated products from the B[a]P-DNA adducts. Methods to study the adducts bonded to the DNA have been developed.<sup>1-14</sup> In particular, fluorescence line-narrowing

spectrometry has been used extensively to characterize intact DNA-PAH adducts.<sup>9-14</sup> Jankowiak and Small<sup>12</sup> have recently reviewed the use of fluorescence line-narrowing spectrometry in DNA and protein damage from chemical carcinogens. As an example of the detection of tetrols, Manchester et al.<sup>4</sup> developed a method for human placenta samples. They started with the separation of partially digested DNA samples, and the final step involved the detection of tetrols by synchronous fluorescence spectrometry, after hydrolysis from the B[a]P-DNA adducts. The amount of tetrols detected from human placental DNA samples was used as a measure of the amount of the B[a]P-DNA adducts present in the placenta samples. Rahn et al.<sup>6</sup> combined fluorescence spectrometry and high-performance liquid chromatography (HPLC) for the quantitation of tetrols after they were removed from DNA by acid hydrolysis. Shugart et al.<sup>8</sup> also employed fluorescence spectrometry and HPLC to quantify tetrols. They were interested in the analysis of adduct formation in the bluegill sunfish between B[a]P and DNA of the liver and hemoglobin of the erythrocyte. In another example, Wang and O'Laughlin<sup>15</sup> used HPLC and laser-induced fluorescence to determine tetrols. The data obtained were related to the DNA adduct level in liver samples from fish. The previous two examples show the importance of detecting tetrols in nonhuman samples.

In the area of solid-matrix luminescence analysis, Vo-Dinh and Uziel<sup>16</sup> reported a limit of detection of 15 fmol for the tetrols from B[a]P-DNA using laser-induced room-temperature phosphorescence (RTP) detection with filter paper as a solid matrix. Also, Johnson and Vo-Dinh<sup>17</sup> used fumed silica substrates for enhanced fluorescence spot-test analysis

(1) Geacintov, N. E. In *Polycyclic Aromatic Hydrocarbon Carcinogenesis: Structure-Activity Relationships*; Yang, S. K., Silverman, B. D., Eds.; CRC Press, Inc.: Boca Raton, FL, 1988; Vol. II, pp 181-206.

(2) *Polycyclic Hydrocarbons and Carcinogenesis*; Ronald G. Harvey, Ed.; ACS Symposium Series 283; American Chemical Society: Washington DC, 1985.

(3) Perera, F. P.; Poirier, M. C.; Yuspa, S. H.; Nakayama, J.; Jaretski, A.; Curnen, M. M.; Knowles, D. M.; Weinstein, I. B. *Carcinogenesis* 1982, 3, 1405-1410.

(4) Manchester, D. K.; Wilson, V. L.; Hsu, I.-C.; Choi, J. S.; Parker, N. B.; Mann, D. L.; Weston, A.; Harris, C. C. *Carcinogenesis* 1990, 11, 553-559.

(5) Rahn, R. O.; Chang, S. S.; Holland, J. M.; Shugart, L. R.; *Biochem. Biophys. Res. Commun.* 1982, 109, 262-268.

(6) Shugart, L.; McCarthy, J.; Jimenez, B.; Daniels, J. *Aquat. Toxicol.* 1987, 9, 319-325.

(7) Geacintov, N. E.; Zinger, D.; Ibanez, V.; Santella, R.; Grunberger, D.; Harvey, R. G. *Carcinogenesis* 1987, 8, 925-935.

(8) Jankowiak, R.; Cooper, R. S.; Zamzow, D.; Small, G. J.; Doskocil, G.; Jeffrey, A. M. *Chem. Res. Toxicol.* 1988, 1, 60-68.

(9) Jankowiak, R.; Lu, P.; Small, G. J.; Nishimoto, M.; Varanasi, U.; Kim, S. K.; Geacintov, N. E. *J. Pharm. Biomed. Anal.* 1990, 8, 113-121.

(10) Jankowiak, R.; Lu, P.-q.; Small, G. J. *Chem. Res. Toxicol.* 1990, 3, 39-46.

(11) Lu, P.; Jeong, H.; Jankowiak, R.; Small, G. J. *Chem. Res. Toxicol.* 1991, 4, 58-69.

(12) Jankowiak, R.; Small, G. J. *Chem. Res. Toxicol.* 1991, 4, 256-269.

(13) Devanesan, P. D.; Ramakrishna, N. V. S.; Todorovic, R.; Rojan, E. G.; Cavallieri, E. L.; Jeong, H.; Jankowiak, R.; Small, G. J. *Chem. Res. Toxicol.* 1992, 5, 302-309.

(14) Marsch, G. A.; Jankowiak, R.; Farhat, J. H.; Small, G. J. *Anal. Chem.* 1992, 64, 3038-3044.

(15) Wang, R.; O'Laughlin, J. W. *Environ. Sci. Technol.* 1992, 26, 2294-2297.

(16) Vo-Dinh, T.; Uziel, M. *Anal. Chem.* 1987, 59, 1093-1095.

(17) Johnson, R. W.; Vo-Dinh, T. *Anal. Chem.* 1989, 61, 2766-2769.

of B[a]P-DNA products. In general, solid matrices have been used very successfully to obtain room-temperature luminescence data in organic trace analysis.<sup>18-20</sup> This is mainly because good selectivity and low limits of detection have been achieved with this approach. Also, both fluorescence and phosphorescence information can be obtained at room temperature. A wide variety of solid materials have been used in solid-matrix luminescence, such as filter paper, silica gel chromatoplates with a polyacrylate binder, sodium acetate, polymers, and cyclodextrins. Bello and Hurtubise<sup>21</sup> demonstrated the use of  $\alpha$ -CD/NaCl matrices to study both the fluorescence and phosphorescence properties of a large number of organic compounds at room temperature. Richmond and Hurtubise<sup>22</sup> showed that  $\beta$ -CD/NaCl matrices are also very useful for room-temperature fluorescence and phosphorescence studies. In addition, they developed a room-temperature phosphorescence, time-resolved method for the determination of a mixture of two of the tetrols.<sup>23</sup> Recently, we investigated  $\alpha$ -,  $\beta$ -, and  $\gamma$ -CD/NaCl mixtures for the solid-matrix luminescence of the tetrols.<sup>24</sup> From this study, it was found that the 10%  $\alpha$ -CD/NaCl matrix was most effective in obtaining solid-matrix luminescence signals from the tetrols.

The work reported here was undertaken for several reasons. There has been no comparison of solid-matrix luminescence photophysical parameters for the tetrols. In addition, there has been no comparison of the solution luminescence photophysical parameters for the tetrols. In this work, both solid-matrix and solution luminescence parameters were obtained for the tetrols, but emphasis was placed on solid-matrix luminescence. Tetrols are important in cancer research because from the data obtained from the analysis of a mixture of tetrols it is possible to establish the stereochemical origin of the benzo[a]pyrene diol epoxides in DNA.<sup>6,25</sup> Also, Geacintov et al.<sup>6</sup> have emphasized that tetrols appear readily as products from B[a]P-DNA adducts in solutions, and the tetrols have very similar fluorescence properties to the B[a]P-DNA adducts. Thus, the tetrols have a great potential to interfere when one is characterizing intact B[a]P-DNA adducts. Finally, with appropriate analytical methodology the distribution and the amounts of the tetrols can be used as a means for human molecular dosimetry. For example, Weston and Bowman<sup>26</sup> characterized B[a]P-DNA adducts in human lung tissue with fluorescence spectrometry by measuring the fluorescence of tetrols.

## EXPERIMENTAL SECTION

**Reagents.** The  $\alpha$ -CD was supplied by American Maize Products Co., Hammond, IN. The methanol used was Baker analyzed HPLC grade. The water was HPLC grade purchased from Burdick and Jackson. The ethanol was redistilled before use. The cyclodextrin and sodium chloride (ACS Reagent grade, J. T. Baker) were washed with distilled ethanol before use. The tetrol isomers were purchased from Midwest Research Institute, Kansas City, MO. The names and abbreviations (in parentheses) for the tetrols are B[a]P-*r*-7,*t*-8,9,*c*-10-tetrahydrotetrol (I-1), B[a]P-*r*-7,*t*-8,9,10-tetrahydrotetrol (I-2), B[a]P-*r*-7,*t*-8,*c*-9,*t*-10-tetrahydrotetrol (II-1), and B[a]P-*r*-7,*t*-8,*c*-9,10-tetrahydrotetrol (II-2).

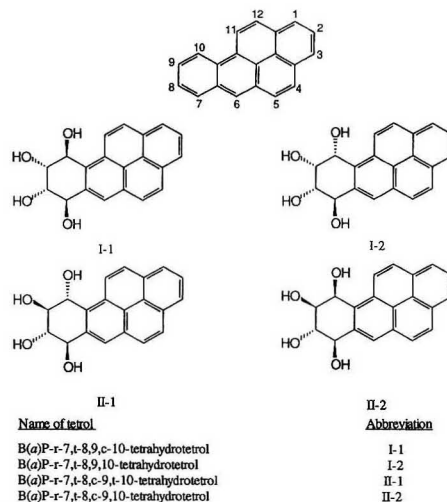


Figure 1. Structures and names of tetrols.

(II-2). The structures are shown in Figure 1. The sample preparation technique for obtaining solid-matrix luminescence data from 10%  $\alpha$ -CD/NaCl matrix was discussed earlier.<sup>24</sup>

**Instrumentation. Fluorescence and Phosphorescence Lifetimes.** The phosphorescence lifetimes were obtained with a Spex Fluorolog 2 spectrofluorometer using a 150-W pulsed xenon lamp and an RS 928 photomultiplier tube. The fluorescence lifetimes were acquired with a Photon Technology International LS-100 spectrofluorometer, using a pulsed nitrogen lamp as the source. For low-temperature measurements, the solid matrices were cooled to 93 K by passing  $N_2$  gas through a copper coil immersed in liquid  $N_2$  and then passing the cold  $N_2$  gas into a dewar assembly which contained the sample holder.<sup>27</sup> For low-temperature solution studies, the sample solution was placed in a Supracil quartz tube (2.8-mm i.d.) which was closed at one end. The tube was immersed in a dewar containing liquid  $N_2$ , and the solution in the tube formed a clear glass.

**Degassing Technique for Solutions.** The solutions were degassed to remove dissolved oxygen, by passing high-purity  $N_2$  gas (United States Welding, Denver, CO) through the solution for 1.5 h. For ethanol solutions, the degassing procedure was carried out in a plastic chamber under a nitrogen atmosphere. The ethanol solution was then placed in a quartz cuvette and the quartz cuvette was stoppered inside the chamber. This extra precaution was necessary in the case of the ethanol solutions because much lower lifetimes were obtained when the solutions were degassed under regular atmospheric conditions. This problem did not occur in the case of MeOH/ $H_2O$  solutions. The same degassing techniques were also used in obtaining the quantum yields of the tetrols.

**Quantum Yields.** The instrument that was used to determine the quantum yield values for both solid matrix and solutions was a Farrand MK-2 spectrofluorometer. The absorbance values for solutions of the tetrols were obtained on a Perkin-Elmer  $\lambda$ -9 UV-VIS-NIR spectrophotometer. The instrumental setup and the procedure used for measuring the quantum yield values were similar to the ones described by Ramasamy et al.<sup>27,28</sup> The procedures, however, were modified to a certain extent. Since the phosphorescence emission was scanned from 550 to 700 nm, with the excitation monochromator at 349 nm, the second-order scatter band near 694 nm was a serious problem. Thus, a cutoff filter (Oriel, No. 58891) was used in the path of the emitted

(18) Hurtubise, R. J. *Anal. Chem.* **1989**, *61*, 889A-895A.

(19) Hurtubise, R. J. *Phosphorimetry: Theory, Instrumentation, and Applications*; VCH: New York, 1990.

(20) Vo-Dinh, T. *Room-Temperature Phosphorimetry for Chemical Analysis*; Wiley: New York, 1984.

(21) Bello, J.; Hurtubise, R. J. *Appl. Spectrosc.* **1986**, *40*, 790-794.

(22) Richmond, M. D.; Hurtubise, R. J. *Anal. Chem.* **1989**, *61*, 2643-2647.

(23) Richmond, M. D.; Hurtubise, R. J. *Anal. Chim. Acta* **1991**, *255*, 335-341.

(24) Corley, J. S.; Hurtubise, R. J. *Anal. Lett.* **1992**, *25*, 1559-1572.

(25) Yang, S. K.; McCourt, D. W.; Gelboin, H. V.; Miller, J. R.; Roller, P. J. *Am. Chem. Soc.* **1977**, *99*, 5124-5134.

(26) Weston, A.; Bowman, E. D. *Carcinogenesis* **1991**, *12*, 1445-1449.

(27) Ramasamy, S. M.; Hurtubise, R. J. *Anal. Chem.* **1987**, *59*, 432-436.

(28) Ramasamy, S. M.; Senthilnathan, V. P.; Hurtubise, R. J. *Anal. Chem.* **1986**, *58*, 612-616.

**Table I. Fluorescence and Phosphorescence Lifetimes of the Tetrols on 10%  $\alpha$ -Cyclodextrin/ $\text{NaCl}^{\text{a,c}}$** 

	I-1	I-2	II-1	II-2
$\tau_{\text{RTF}}$	166 $\pm$ 2 ns	136 $\pm$ 2 ns	148 $\pm$ 2 ns	149 $\pm$ 1 ns
$\tau_{\text{LTF}}$	185 $\pm$ 2 ns	152 $\pm$ 4 ns	174 $\pm$ 2 ns	178 $\pm$ 1 ns
$\tau_{\text{RTF}}$	187 $\pm$ 3 ms	179 $\pm$ 0 ms	190 $\pm$ 9 ms	194 $\pm$ 1 ms
$\tau_{\text{LTF}}$	242 $\pm$ 3 ms	225 $\pm$ 1 ms	246 $\pm$ 1 ms	274 $\pm$ 0 ms

<sup>a</sup>  $\tau_{\text{RTF}}$ , room-temperature fluorescence (296 K) lifetimes of the tetrols on 10%  $\alpha$ -CD/ $\text{NaCl}$ ;  $\tau_{\text{LTF}}$ , low-temperature (93 K) fluorescence lifetimes of the tetrols on 10%  $\alpha$ -CD/ $\text{NaCl}$ ;  $\tau_{\text{RTF}}$ , room-temperature (296 K) phosphorescence lifetimes of the tetrols on 10%  $\alpha$ -CD/ $\text{NaCl}$ ;  $\tau_{\text{LTF}}$ , low-temperature (93 K) phosphorescence lifetimes of the tetrols on 10%  $\alpha$ -CD/ $\text{NaCl}$ . <sup>b</sup> The precision of the lifetimes are reported in terms of the standard deviation. <sup>c</sup> The average values of  $\tau_{\text{RTF}}$  were from tetrol samples at 50, 60, and 120 ng/mg, and the average values of  $\tau_{\text{LTF}}$  were from tetrol samples at 120 ng/mg. The average values of  $\tau_{\text{RTF}}$  were from tetrol samples at 2 ng/mg, and the average values of  $\tau_{\text{LTF}}$  were from tetrol samples at 10 ng/mg.

**Table II. Fluorescence and Phosphorescence Lifetimes of the Tetrols in Solutions of Ethanol and Methanol/Water<sup>a,d</sup>**

	I-1	I-2	II-1	II-2
$\tau_{\text{RTF}}$ , EtOH	196 ns	187 ns	183 ns	218 ns
$\tau_{\text{LTF}}$ , EtOH	390 $\pm$ 1 ns	305 $\pm$ 4 ns	378 $\pm$ 5 ns	380 $\pm$ 1 ns
$\tau_{\text{RTF}}$ , M/W	226 $\pm$ 2 ns	176 $\pm$ 4 ns	206 $\pm$ 2 ns	210 $\pm$ 4 ns
$\tau_{\text{LTF}}$ , EtOH	389 $\pm$ 0 ms	243 $\pm$ 6 ms	313 $\pm$ 4 ms	359 $\pm$ 2 ms

<sup>a</sup>  $\tau_{\text{RTF}}$ , EtOH, room-temperature fluorescence (296 K) lifetimes of the tetrols in ethanol;  $\tau_{\text{LTF}}$ , EtOH, low-temperature fluorescence (77 K) lifetimes of the tetrols in ethanol;  $\tau_{\text{RTF}}$ , M/W, room-temperature fluorescence (296 K) lifetimes of the tetrols in 1:1 MeOH/ $\text{H}_2\text{O}$ ;  $\tau_{\text{LTF}}$ , EtOH, low-temperature phosphorescence (77 K) lifetimes of the tetrols in ethanol. <sup>b</sup> The precision of the lifetimes is reported in terms of the standard deviation. <sup>c</sup> The average values of  $\tau_{\text{RTF}}$  for tetrols were obtained from EtOH and M/W solutions at 1  $\mu\text{g/mL}$ . Ethanol solutions at 5  $\mu\text{g/mL}$  were used to obtain the average values for  $\tau_{\text{LTF}}$  and  $\tau_{\text{LTP}}$ . <sup>d</sup> Average value of two different samples.

radiation. The correction factor for the optical filter was determined on a Perkin-Elmer  $\lambda$ -9 UV-VIS-NIR spectrophotometer by measuring the percent transmittance with and without the filter in the sample path of the spectrophotometer. The ratio of the percent transmittance areas (550–700 nm) with and without the filter in the path was used in correcting the area under the phosphorescence emission curve. Also, the technique used in positioning the sample was modified. In the work of Ramasamy et al.,<sup>27,28</sup> the angle of the sample was adjusted to give a reflectance band intensity of 60 (range setting 0.1) with the excitation and emission monochromators at 500 nm. In our work, due to the low phosphorescence intensity, the angle was adjusted to give a reflectance band intensity of 80 (range 0.1). This permitted a greater phosphorescence intensity to impinge on the detector.

## RESULTS AND DISCUSSION

**Fluorescence and Phosphorescence Lifetimes with 10%  $\alpha$ -CD/ $\text{NaCl}$ .** The fluorescence and phosphorescence lifetimes were determined for the four tetrols on 10%  $\alpha$ -CD/ $\text{NaCl}$  matrix (Table I), in ethanol, and in 1:1 MeOH/ $\text{H}_2\text{O}$  (Table II). For the solid matrices, the room-temperature measurements were carried out at 296 K, whereas the low-temperature experiments were carried out at 93 K for solid matrices and 77 K for solutions. Two-component analysis of the solid-matrix fluorescence lifetime data indicated that there were two components contributing to the fluorescence lifetimes of the tetrols at room temperature and at low temperature. The fluorescence lifetime data for the major component are shown in Table I. These lifetimes were used in calculating some of the photophysical parameters. On the average, the major component contributed 92% to the fluorescence intensity of the fluorescence lifetime curves. The

contribution of the second lifetime component was considered as minor and was not used in calculating the photophysical parameters. The source of the minor component is presently under investigation. As indicated in Table I, the fluorescence lifetimes for the tetrols on 10%  $\alpha$ -CD/ $\text{NaCl}$  increased by 11.4%, 11.8%, 17.6%, and 19.5%, respectively, from room temperature to low temperature. This indicated that the tetrol isomers in the singlet state were held more rigidly at 93 K than at room temperature. Also, comparison of the fluorescence lifetimes for I-1 and I-2 at 296 K shows that they are quite different. The same is true for these isomers at 93 K. The differences in the lifetimes suggest that the isomers are interacting in dissimilar ways with the solid matrix. Figure 1 shows that the only difference between these two isomers is in the positions of the hydroxyl groups in the 9 and 10 positions. For II-1 and II-2 at 296 K, the fluorescence lifetimes are the same. The same is true for these isomers at 93 K. These results indicate that II-1 and II-2 interact in a similar fashion with the solid matrix at the respective temperatures. Geacintov et al.<sup>7</sup> have reported solution fluorescence lifetimes of 200 (oxygen-free solution) and 130 ns (air-saturated solution) for tetrols derived from B[a]P-DNA adducts. It should be mentioned that each tetrol sample consisted of a racemic mixture, and the structures shown in Figure 1 represent one structure each for an enantiomeric pair.

The data analysis for the phosphorescence lifetimes indicated that only one component was contributing to the phosphorescence decay curve. The  $\ln(\text{phosphorescence intensity})$  versus time plots gave linear correlation coefficients of 0.995 or greater. Table I shows that the phosphorescence lifetimes increased from room temperature to low temperature for the four tetrols. The increase was 29.4%, 25.7%, 29.5%, and 41.2%, respectively, for I-1, I-2, II-1, and II-2. The room-temperature phosphorescence lifetimes of I-1 and I-2 are only marginally different, and the room-temperature phosphorescence lifetimes of II-1 and II-2 are very close to one another (Table I). Table I shows that at 93 K the low-temperature phosphorescence lifetimes of I-1 and I-2 give a greater difference in their lifetimes compared to the room-temperature values, and the same is true for II-1 and II-2 at 93 K. However, I-1 and II-1 have essentially the same phosphorescence lifetimes, and I-1 and II-2 have very different lifetimes at 93 K.

Because the four tetrols can be readily separated by HPLC,<sup>6,25</sup> solid-matrix fluorescence lifetimes and solid-matrix phosphorescence lifetimes could be used in conjunction with HPLC to identify and characterize the tetrols after isolation by HPLC. For example, I-1 and I-2 could be readily distinguished by their solid-matrix RTF lifetimes (Table I). Because the solid-matrix RTF lifetimes of II-1 and II-2 are the same, they could not be identified from HPLC fractions. However, Table I shows that the solid-matrix low-temperature phosphorescence lifetimes are very different. Thus, these lifetimes could be used in the identification of II-1 and II-2 from HPLC fractions. After the separation of the tetrols by HPLC, and collection and concentration of the HPLC fractions, all the tetrols could be identified by using a combination of RTF lifetimes and LTP lifetimes from the isomers adsorbed on solid matrices. A particular advantage of using solid-matrix luminescence lifetimes is that extensive degassing is not needed. It is only necessary to pass dry nitrogen through the cell compartment while the lifetimes are being measured. Recently, we have reported a RTF limit of detection of 62 fmol/mg for I-1 and a RTP limit of detection of 94 fmol/mg for I-1 on 10%  $\alpha$ -cyclodextrin/ $\text{NaCl}$ .<sup>24</sup> Very recently, we have found that much lower limits of detection can be obtained by using a heavy atom. These results will be reported later.

**Fluorescence and Phosphorescence Lifetimes in Solutions.** Table II shows the solution fluorescence and phosphorescence lifetimes of the four tetrals. There was an increase of 99.0%, 63.1%, 106%, and 74.3%, respectively, for I-1, I-2, II-1, and II-2, in the fluorescence lifetimes at 77 K in ethanol compared to the corresponding tetrals at 296 K. This large increase is most likely due to the inhibition of fluorescence quenching at low temperature. Even though the ethanol solutions were degassed for 1.5 h, most likely all of the oxygen was not removed completely from the ethanol, and thus the room-temperature fluorescence lifetimes are somewhat low. Also, the long lifetimes of the tetrals would favor quenching of these fluorescent species at room temperature in solution. Table II shows that with MeOH/H<sub>2</sub>O (1:1) the fluorescence lifetimes are greater at room temperature for I-1 and II-1 compared to the same compounds in ethanol at room temperature. For I-2 and II-2, the fluorescence lifetimes are smaller with methanol/water (1:1) compared to the same compounds in ethanol (Table II). In contrasting the fluorescence lifetimes in Tables I and II, it is seen that the room-temperature fluorescence lifetimes in ethanol are roughly the same as the corresponding tetrals at low temperature on 10%  $\alpha$ -CD/NaCl. The fact that the fluorescence lifetimes changed to a much larger extent from room temperature to low temperature with ethanol solutions indicated that quenching did not occur to a great extent with solid matrices. Table II shows that the low-temperature phosphorescence lifetimes in ethanol are very different from one another. Thus, the phosphorescence lifetimes could be used to characterize the individual samples of the pure tetrals isolated by HPLC. However, as will be discussed below, the low-temperature phosphorescence quantum yields in ethanol were very low, which would affect the sensitivity of the detection of phosphorescence at low temperature in ethanol.

Table II shows that fluorescence lifetimes at room temperature and low temperature could be used to identify I-1 and I-2 isolated from HPLC fractions. Also, II-1 and II-2 could be distinguished by fluorescence lifetimes at room temperature with ethanol, but I-2 and II-1 most likely could not be distinguished using ethanol as a solvent at room temperature. However, Table II shows that I-2 and II-1 could be differentiated by their low-temperature fluorescence lifetimes in ethanol or at room temperature with methanol/water as a solvent. The lifetime data in Tables I and II show that there are several ways of characterizing the tetrals; however, low-temperature solution phosphorescence would not be useful because of the very low phosphorescence intensities of the tetrals in solution. Also, we found that special precautions had to be taken to obtain reproducible room-temperature fluorescence lifetimes in ethanol solutions (See Experimental Section). In general, with solid matrices, the lumiphor fluorescence and phosphorescence lifetimes are not very sensitive to oxygen quenching compared to the lumiphor dissolved solutions. If dry nitrogen gas is passed through the cell compartment during the measurement step, then solid-matrix fluorescence and phosphorescence lifetimes are easily obtained. Also, the phosphorescence lifetimes can be obtained at room temperature with solid matrices, whereas with tetrals phosphorescence lifetimes cannot be obtained in solution at room temperature.

**Luminescence Quantum Yields of the Tetrals on 10%  $\alpha$ -CD/NaCl.** As examples of solid-matrix luminescence quantum yields, both the fluorescence and phosphorescence quantum yields of I-1 and I-2 were obtained (Table III). The quantum yields were acquired both at 296 ( $\phi_{\text{RTF}}$  and  $\phi_{\text{RTP}}$ ) and at 93 K ( $\phi_{\text{LTF}}$  and  $\phi_{\text{LTP}}$ ). Several interesting results can be seen from Table III. There are very large differences between the fluorescence and phosphorescence quantum yields for both

**Table III. Fluorescence and Phosphorescence Quantum Yields of the Tetrals on 10%  $\alpha$ -Cyclodextrin/NaCl<sup>a,b</sup>**

	I-1	I-2
$\phi_{\text{RTF}}$	$0.59 \pm 0.03$	$0.44 \pm 0.05$
$\phi_{\text{RTP}}$	$1.77 \times 10^{-3} \pm 0.5 \times 10^{-3}$	$2.45 \times 10^{-3} \pm 0.2 \times 10^{-3}$
$\phi_{\text{LTF}}$	$0.71 \pm 0.04$	$0.52 \pm 0.03$
$\phi_{\text{LTP}}$	$1.72 \times 10^{-3} \pm 0.09 \times 10^{-3}$	$2.25 \times 10^{-3} \pm 0.3 \times 10^{-3}$

<sup>a</sup>  $\phi_{\text{RTF}}$ , room-temperature (296 K) fluorescence quantum yield;  $\phi_{\text{RTP}}$ , room-temperature (296 K) phosphorescence quantum yield;  $\phi_{\text{LTF}}$ , low-temperature (93 K) fluorescence quantum yield;  $\phi_{\text{LTP}}$ , low-temperature (93 K) phosphorescence quantum yield. <sup>b</sup> The precision of the quantum yield values are reported in terms of the standard deviation. The concentration of the tetrals sample was 10 ng/mg.

I-1 and I-2. The fluorescence quantum yields are very high at room temperature, and there is a 20.3% and 18.2% increase in the fluorescence quantum yields for I-1 and I-2, respectively, at 93 K. As Table III shows, the phosphorescence quantum yields were very low, and they did not change much with temperature for either of the tetrals. In earlier work, Bello and Hurtubise<sup>29</sup> observed no change in the fluorescence quantum yields for phenanthrene and benzo[*f*]quinoline adsorbed on 80%  $\alpha$ -CD/NaCl from 296 and 93 K. Ramasamy and Hurtubise<sup>30</sup> reported only a slight increase in the fluorescence quantum yields of B[*f*]Q on filter paper from 296 to 93 K. Also, there was no increase in the fluorescence quantum yield for benzo[*f*]quinoline adsorbed on 30%  $\beta$ -CD/NaCl when the temperature was lowered from 296 to 93 K.<sup>31</sup> This is in contrast to the fluorescence quantum yield values obtained at 296 and 93 K for the two tetrals adsorbed on 10%  $\alpha$ -CD/NaCl. This indicates that the tetrals are not held as rigidly in the singlet state with 10%  $\alpha$ -CD/NaCl compared to the phenanthrene and benzo[*f*]quinoline adsorbed on the CD/NaCl matrices because of the greater increase in  $\phi_{\text{f}}$  for the tetrals. For the phosphorescence quantum yields in previous work with CD/NaCl matrices, the quantum yields increased about 2-fold for both phenanthrene and benzo[*f*]quinoline on 80%  $\alpha$ -CD/NaCl,<sup>29</sup> but there was no increase in the phosphorescence quantum yield for benzo[*f*]quinoline adsorbed on 30%  $\beta$ -CD/NaCl.<sup>31</sup>

**Luminescence Quantum Yields of Tetrals in Solutions.** Previously, Rahn et al.<sup>6</sup> reported the relative quantum yields of tetrals mixtures in 50% methanol by assigning a value of 1.0 for the relative fluorescence quantum yield at 77 K. However, in this work, we obtained the actual fluorescence and phosphorescence quantum yields for the tetrals isomers. Table IV gives the fluorescence and phosphorescence quantum yields of the tetrals in two different solvents. As Table IV shows, the fluorescence quantum yields of I-1 and I-2 in ethanol are considerably lower than the quantum yields of these tetrals in MeOH/H<sub>2</sub>O. This is probably due to the greater polarity of the MeOH/H<sub>2</sub>O solvent system resulting in greater hydrogen bonding between the tetrals and solvent molecules. As the data in Table IV indicate, the quantum yields of the tetrals in MeOH/H<sub>2</sub>O at room temperature are much higher than the quantum yields of the tetrals in ethanol at 77 K. This is an important analytical consideration because MeOH/H<sub>2</sub>O (1:1) can be used at room temperature for I-1 and I-2 to achieve high fluorescence sensitivity.

Table IV shows that the low-temperature phosphorescence quantum yield for the tetrals are very low, and thus low-temperature phosphorescence in ethanol may not be very useful analytically. However, the solution molar absorptivity

(29) Bello, J. M.; Hurtubise, R. J. *Anal. Chem.* 1988, 60, 1291-1296.

(30) Ramasamy, S. M.; Hurtubise, R. J. *Appl. Spectrosc.* 1989, 43, 616-621.

(31) Richmond, M. D.; Hurtubise, R. J. *Anal. Chem.* 1991, 63, 169-173.



**Table IV. Fluorescence and Phosphorescence Quantum Yields of the Tetrols in Solution<sup>a,b</sup>**

	I-1	I-2	II-1	II-2
$\phi_{\text{RTF}}$ , M/W	0.77 $\pm$ 0.03	0.66 $\pm$ 0.01		
$\phi_{\text{RTF}}$ , EtOH	0.20 $\pm$ 0.01	0.26 $\pm$ 0.04	0.17 $\pm$ 0.04	0.25 $\pm$ 0.01
$\phi_{\text{LTF}}$ , EtOH	0.42 $\pm$ 0.04	0.37 $\pm$ 0.02	0.28 $\pm$ 0.02	0.41 $\pm$ 0.03
$\phi_{\text{LTF}}$ , EtOH	1.59 $\times 10^{-4}$	2.71 $\times 10^{-4}$	3.66 $\times 10^{-4}$	4.41 $\times 10^{-4}$
	$\pm 0.5 \times 10^{-4}$	$\pm 0.6 \times 10^{-4}$	$\pm 1.5 \times 10^{-4}$	$\pm 0.74 \times 10^{-4}$
$\phi_t$ (77 K)	0.58	0.63	0.73	0.59

<sup>a</sup>  $\phi_{\text{RTF}}$ , M/W, room-temperature (296 K) fluorescence quantum yields of the tetrols in MeOH/H<sub>2</sub>O (1:1);  $\phi_{\text{RTF}}$ , EtOH, room-temperature (296 K) fluorescence quantum yields of the tetrols in ethanol;  $\phi_{\text{LTF}}$ , EtOH, low-temperature (77 K) fluorescence quantum yields of the tetrols in ethanol;  $\phi_{\text{LTF}}$ , EtOH, low-temperature (77 K) phosphorescence quantum yields of the tetrols in ethanol;  $\phi_t$  (77 K), quantum yield for the formation of the triplet state from the singlet state of the tetrols in ethanol at 77 K. <sup>b</sup> The precision of the quantum yield values are reported in terms of the standard deviation. The average values of  $\phi_{\text{RTF}}$  for the tetrols were obtained from EtOH and M/W solutions at 1  $\mu\text{g/mL}$ . Ethanol solutions at 5  $\mu\text{g/mL}$  were used to obtain the average values for  $\phi_{\text{LTF}}$  and  $\phi_{\text{LTF}}$ .

values are high for the tetrols, and thus, reasonable sensitivity may be obtained from low-temperature solution phosphorimetry. Another aspect of the quantum yield data in Tables III and IV is that they indicate that the stereoisomeric tetrols have photophysical features that are different from one another. Figure 1 shows that the tetrols only differ in the positions of their hydroxyl groups, and therefore, the positions of the hydroxyl groups determine the differences in the photophysical properties of the tetrols.

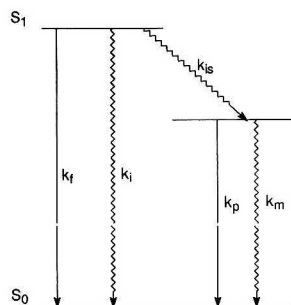
**Limits of Detection.** As discussed earlier, we reported the room-temperature solid-matrix fluorescence and phosphorescence limits of detection for I-1 to be 62 and 94 fmol/mg, respectively, on 10%  $\alpha$ -CD/NaCl.<sup>24</sup> The low limits of detection were obtained for phosphorescence in spite of the large differences between the fluorescence and phosphorescence quantum yield values (Table III). This was due primarily to two factors. The excitation and emission wavelengths for fluorescence are 346 and 398 nm, which are fairly close to each other, whereas they are quite well separated for phosphorescence (346 and 604 nm). Source radiation scattered from the solid matrix would be more of a problem with fluorescence measurements than with phosphorescence measurements. Also, the solution molar absorptivities are large for tetrols and most likely the absorption coefficients are high for the tetrols on 10%  $\alpha$ -CD/NaCl. A high absorption coefficient would favor low limits of detection. However, additional experimental data would have to be obtained to prove this.

**Photophysical Rate Constants of the Tetrols on 10%  $\alpha$ -CD/NaCl.** Table V shows the photophysical rate constants for I-1 and I-2 on 10%  $\alpha$ -CD/NaCl at both 296 and 93 K, and Figure 2 gives a summary of the rate processes. The rate constants were calculated using the equations derived by Parker<sup>32</sup> and Turro<sup>33</sup> and applied to solid-matrix luminescence.<sup>19,28-31</sup> Table V shows that the values of the fluorescence rate constant,  $k_f$ , and the phosphorescence rate constant,  $k_p$ , did not change very much with temperature for either I-1 or I-2, which would be expected. The internal conversion rate constants,  $k_i$ , were equal to zero because  $\phi_p/\tau_p$  was constant with temperature. Details of this calculation were discussed earlier.<sup>34,35</sup> The values of the intersystem crossing rate constant ( $S_1 - T_1$ ),  $k_{is}$ , decreased slightly with temperature for a given tetrol. Also, the respective values of

**Table V. Photophysical Rate Constants for the Tetrols on 10%  $\alpha$ -Cyclodextrin/NaCl<sup>a,c</sup>**

	tetrol I-1		tetrol I-2	
	296 K	93 K	296 K	93 K
$k_f$	3.54 $\times 10^6$ $\pm 0.18 \times 10^6$	3.85 $\times 10^6$ $\pm 0.22 \times 10^6$	3.23 $\times 10^6$ $\pm 0.37 \times 10^6$	3.41 $\times 10^6$ $\pm 0.22 \times 10^6$
$k_p$	0.023 $\pm 0.007$	0.021 $\pm 0.003$	0.024 $\pm 0.003$	0.021 $\pm 0.003$
$k_i$	0.00	0.00	0.00	0.00
$k_{is}$	2.46 $\times 10^6$ $\pm 0.18 \times 10^6$	1.57 $\times 10^6$ $\pm 0.22 \times 10^6$	4.11 $\times 10^6$ $\pm 0.37 \times 10^6$	3.15 $\times 10^6$ $\pm 0.21 \times 10^6$
$k_m$	5.30 $\pm 1.93$	2.95 $\pm 0.54$	5.46 $\pm 0.82$	4.43 $\pm 0.78$

<sup>a</sup>  $k_f$ , fluorescence rate constant;  $k_p$ , phosphorescence rate constant;  $k_i$ , internal conversion rate constant;  $k_{is}$ , intersystem-crossing rate constant ( $S_1 - T_1$ );  $k_m$ , intersystem-crossing rate constant ( $T_1 - S_0$ ). <sup>b</sup> All rate constants are reported in units of reciprocal seconds. <sup>c</sup> The standard deviations associated with the rate constants were calculated with propagation of error equations.

**Figure 2.** Summary of rate constants for excited-state processes.  $k_f$ , rate constant for fluorescence;  $k_i$ , rate constant for internal conversion;  $k_{fs}$ , rate constant for intersystem crossing from S<sub>1</sub> to T<sub>1</sub>;  $k_p$ , rate constant for phosphorescence;  $k_m$ , rate constant for intersystem crossing from T<sub>1</sub> to S<sub>0</sub>.

$k_f$  are very similar for the two tetrols at room temperature and at 93 K. The same is true for the  $k_p$  values at room temperature and at 93 K for I-1 and I-2. However, comparison of the values of  $k_{is}$  for I-1 and I-2 shows they are quite different (Table V). For example, the ratio of the  $k_{is}$  values for I-2 to I-1 at room temperature is 1.7 and at 93 K the ratio is 2.0. The differences in the  $k_{is}$  values are due to the minor structural differences in the two isomers. The dissimilarity in the  $k_{is}$  values can be used in the characterization of the two tetrols. This aspect will be discussed later. Table V shows that the values of the intersystem crossing rate constant ( $T_1 - S_0$ ),  $k_m$ , are larger than the values of  $k_p$  by greater than 2 orders of magnitude at 296 and at 93 K. This explains the very low solid-matrix phosphorescence quantum yields that were observed in Table III and shows that the nonradiative pathway is preferred over the radiative pathway in the triplet state. By adding a heavy atom to the 10%  $\alpha$ -CD/NaCl, it should be possible to increase the value of  $k_p$  and thus the phosphorescence quantum yields of the tetrols. This has been shown to be true for tetrols by Vo-Dinh and Uziel<sup>16</sup> with filter paper, Richmond and Hurtubise<sup>23</sup> with  $\beta$ -CD/NaCl solid matrices, and Wei and Hurtubise<sup>36</sup> with different types of filter paper. Additional aspects of the heavy atom effect are presently being studied in our work, and very encouraging results have been obtained.

(32) Parker, C. A. *Photoluminescence of Solutions*; Elsevier Publishing Co.: New York, 1968.

(33) Turro, N. J. *Modern Molecular Photochemistry*; The Benjamin Cummings Publishing Co.: Menlo Park, CA, 1978.

(34) Ramasamy, S. M.; Hurtubise, R. J. *Anal. Chem.* 1987, 59, 432-436.

(35) Ramasamy, S. M.; Hurtubise, R. J. *Anal. Chem.* 1987, 59, 2144-2148.

(36) Wei, T.; Hurtubise, R. J. *Anal. Lett.* 1993, 26, 557-572.

**Table VI. Photophysical Rate Constants of the Tetrols in Ethanol<sup>a,b</sup>**

	I-1	I-2	II-1	II-2
$k_f$	$1.02 \times 10^6$	$1.33 \times 10^6$	$0.93 \times 10^6$	$1.15 \times 10^6$
$k_t$ (77 K)	$1.08 \times 10^6$	$1.21 \times 10^6$	$0.73 \times 10^6$	$1.08 \times 10^6$
	$\pm 0.10 \times 10^6$	$\pm 0.07 \times 10^6$	$\pm 0.05 \times 10^6$	$\pm 0.08 \times 10^6$
$k_{ia}$ (77 K)	$1.49 \times 10^6$	$2.07 \times 10^6$	$1.93 \times 10^6$	$1.55 \times 10^6$
	$\pm 0.10 \times 10^6$	$\pm 0.07 \times 10^6$	$\pm 0.02 \times 10^6$	$\pm 0.08 \times 10^6$
$k_p$ (77 K)	$0.71 \times 10^{-3}$	$1.77 \times 10^{-3}$	$1.59 \times 10^{-3}$	$2.08 \times 10^{-3}$
	$\pm 0.23 \times 10^{-3}$	$\pm 0.09 \times 10^{-3}$	$\pm 1.00 \times 10^{-3}$	$\pm 0.35 \times 10^{-3}$
$k_m$ (77 K)	$2.57 \pm 0.95$	$4.11 \pm 0.93$	$3.18 \pm 1.51$	$2.78 \pm 0.10$

<sup>a</sup> All rate constants are reported in units of reciprocal seconds.<sup>b</sup> The standard deviations associated with the rate constants were calculated with propagation of error equations. <sup>c</sup> Fluorescence lifetimes were obtained as an average of two runs.

**Photophysical Rate Constants of the Tetrols in Solution.** Table VI shows the fluorescence rate constants for the tetrols in ethanol at room temperature and at 77 K. The fluorescence rate constants are approximately the same for the tetrols at both room temperature and at 77 K. This is not surprising considering the similarities in the structure of the four tetrols, and the fact that fluorescence rate constants are normally independent of temperature.<sup>32</sup> Because phosphorescence was not observed in solution at room temperature for the tetrols, it was not possible to calculate other photophysical rate constants at room temperature. Table VI shows that the  $k_{ia}$  values for the tetrols at 77 K are somewhat different for the four tetrols. The ratios of the  $k_{ia}$  values at 77 K for I-1, I-2, II-1, and II-2 are 1.00, 1.30, 1.30 and 1.04, respectively. These ratios are less than the  $k_{ia}$  ratios obtained for I-2 to I-1 at 296 and 93 K with 10%  $\alpha$ -CD/NaCl (Table V). As with the  $k_p$  values for I-1 and I-2 on 10%  $\alpha$ -CD/NaCl, the  $k_p$  values for the tetrols in ethanol at 77 K are very small for the four tetrols. They are approximately 3 orders of magnitude smaller than the  $k_m$  values. This shows that the nonradiative decay pathway from the triplet state dominates over the radiative pathway in ethanol at 77 K.

**Additional Comparison of Rate Constants with 10%  $\alpha$ -CD/NaCl and Solutions.** By further comparison of the rate constants for the tetrols in solution and on 10%  $\alpha$ -CD/NaCl in Tables V and VI, other differences are noticeable for the data from solid matrices compared to the data obtained from solutions.

1. The  $k_t$  values with 10%  $\alpha$ -CD/NaCl are approximately 3 times larger than the  $k_t$  values in ethanol. This is also indicated by the fluorescence quantum yield data in Tables III and IV. Comparison of the fluorescence quantum yields in Table IV obtained with ethanol to the fluorescence quantum yields in Table III shows that the quantum yields are considerably higher with 10%  $\alpha$ -CD/NaCl.

2. The  $k_{ia}$  values at low temperature for I-1 are quite similar both on 10%  $\alpha$ -CD/NaCl and in ethanol; however, they are somewhat different for I-2. Also, the  $k_{ia}$  (low-temperature) values are approximately the same for I-1 and I-2 in ethanol.

3. The respective  $k_m$  values at room temperature and low temperatures are roughly the same for I-1 and I-2 on 10%  $\alpha$ -CD/NaCl. The ratio of the  $k_m$  values at 296 K for I-1 with 10%  $\alpha$ -CD/NaCl to the  $k_m$  value with ethanol at 77 K is 2.1, whereas the equivalent ratio for I-2 is 1.0. The  $k_m$  ratio for I-1 indicates that the nonradiative deactivation from the triplet state is somewhat more effective for I-1 on 10%  $\alpha$ -CD/NaCl.

**Quantum Yield Ratios.** The ratios of low-temperature fluorescence to room-temperature fluorescence quantum yields and the ratios of low-temperature phosphorescence to room-temperature phosphorescence quantum yields of I-1 and I-2 are shown in Table VII. As can be seen from the

**Table VII. Ratios of Quantum Yields of the Tetrols on 10%  $\alpha$ -CD/NaCl<sup>a</sup>**

ratio	tetrol I-1	tetrol I-2
$\phi_{LTP}/\phi_{RTP}$	1.20	1.18
$\phi_{LTP}/\phi_{RTP}$	0.83	0.91
$\phi_{RTP}/\phi_{RTP}$	333	180
$\phi_{LTP}/\phi_{LTP}$	482	231

<sup>a</sup>  $\phi_{RTP}$ , room-temperature fluorescence quantum yield;  $\phi_{RTP}$ , room-temperature phosphorescence quantum yield;  $\phi_{LTP}$ , low-temperature fluorescence quantum yield;  $\phi_{LTP}$ , low-temperature phosphorescence quantum yield.

table, the ratios of fluorescence quantum yields at the two different temperatures are close to 1.2, and the ratios of phosphorescence quantum yields at 296 and 93 K are near 0.9. These results show that there is little change in the fluorescence or phosphorescence quantum yields as the temperature is lowered. The ratios of the room-temperature fluorescence to room-temperature phosphorescence quantum yields for I-1 and I-2 both increase upon going to 93 K as shown in Table VII. The changes in the fluorescence to phosphorescence quantum yield ratios as the temperature is lowered for compounds adsorbed on solid matrices has been discussed by Hurtubise and Ramasamy.<sup>37</sup> In general, they found that the quantum yield ratio for an organic compound adsorbed on a solid matrix was equal to a constant ( $k_f/k_p$ ) times either the reciprocal of the product of  $k_{ia}$  and phosphorescence lifetime or a constant [ $k_f/(k_p k_{ia})$ ] times the reciprocal of phosphorescence lifetime as the temperature was lowered (see eq 1). The constant was determined by

$$\phi_f/\phi_p = k_f/(k_{ia}k_p\tau_p) \quad (1)$$

which set of photophysical rate constants were independent of temperature. In Table V, the  $k_{ia}$  values for both I-1 and I-2 decrease slightly with temperature, but  $k_t$  and  $k_p$  were essentially constant with temperature. From the data in Table I, it is seen that the phosphorescence lifetimes of I-1 and I-2 on 10%  $\alpha$ -CD/NaCl changed with temperature. Thus, as the temperature was lowered, the fluorescence to phosphorescence quantum yield ratios for I-1 and I-2 are approximately equal to a constant, which is  $k_f/k_p$  times the reciprocal of  $k_{ia}$  times phosphorescence lifetime (see eq 1).

Table V shows that the  $k_{ia}$  values at room temperature (296 K) for I-1 and I-2 are quite different. Also, as mentioned, the RTP lifetimes are somewhat different. The same is true for the corresponding values of  $k_{ia}$  and  $\tau_p$  at 93 K (Tables I and V). Because of the difference in  $k_{ia}$  values between the two stereoisomers on 10%  $\alpha$ -CD/NaCl, eq 1 shows that with such a difference between the  $k_{ia}$  values the quantum yield ratios would thus be different for I-1 and I-2. The dissimilarity between the phosphorescence lifetimes for I-1 and I-2 is not large enough to cause a major change in quantum yield ratios between the two tetrols, although the phosphorescence lifetimes for I-1 and I-2 do contribute somewhat to the different luminescence quantum yield ratios for I-1 and I-2.

Because of the results obtained for  $k_{ia}$ , it is possible to characterize I-1 and I-2 by their  $k_{ia}$  values obtained from 10%  $\alpha$ -CD/NaCl. As indicated above, Table V shows the  $k_{ia}$  values are very different for I-1 and I-2 at both 296 and 93 K. However, as shown in Table VI, the  $k_{ia}$  values for I-1 and I-2 in ethanol at 77 K do not differ as much as the  $k_{ia}$  values for I-1 and I-2 on 10%  $\alpha$ -CD/NaCl. Thus, the calculated  $k_{ia}$  values from the solid-matrix approach would be more useful in distinguishing the two isomers. In addition, the room-

(37) Hurtubise, R. J.; Ramasamy, S. M. *Appl. Spectrosc.* 1993, 47, 283-286.

**Table VIII. Ratios of the Luminescence Areas of the Tetrols on 10%  $\alpha$ -CD/NaCl<sup>a,b</sup>**

tetrol	I-1	I-2	II-1	II-2
$F_{RTF}/P_{RTP}$	171 $\pm$ 21	97 $\pm$ 12	74 $\pm$ 9	115 $\pm$ 14
$F_{LTF}/P_{LTP}$	235 $\pm$ 14	140 $\pm$ 17	194 $\pm$ 19	276 $\pm$ 22

<sup>a</sup>  $F_{RTF}$ , room-temperature fluorescence area;  $P_{RTP}$ , room-temperature phosphorescence area;  $F_{LTF}$ , low-temperature fluorescence area;  $P_{LTP}$ , low-temperature phosphorescence area. <sup>b</sup> The standard deviations associated with the area ratios were calculated with propagation of error equations.

temperature solid-matrix data are easier to obtain rather than luminescence data with liquid nitrogen conditions.

The ratio of fluorescence quantum yield to phosphorescence quantum yield for I-1 is about twice the ratio for I-2 both at room temperature and at 93 K (Table VII). These results are important because the ratios of fluorescence to phosphorescence quantum yields at either room temperature or low temperature can be used to characterize I-1 and I-2. The differences in the ratios are a result of the structural differences between I-1 and I-2 (Figure 1).

Another very important consideration is that because the absorption areas used in calculating the fluorescence and phosphorescence quantum yields are identical for a given tetrol, the area terms cancel when the quantum yield ratios are calculated. Thus, it would only be necessary to obtain the ratios of the corrected fluorescence area to the corrected phosphorescence area to distinguish the tetrols. This was done for the four tetrols with the results presented in Table VIII. As shown in Table VIII, the area ratios are quite different among the four tetrols. They could then be identified by their luminescence area ratios after an HPLC separation step. Also, the room-temperature ratios would be easier to obtain than the low-temperature ratios.

In summary, the solid-matrix and solution photophysical data are presented for the first time for the tetrols. These data are important in understanding the differences in the photophysics among the tetrols both in solution and on solid matrices for analytical methods development. For example, the data reported can be used in the characterization of the tetrols in conjunction with HPLC or other separation methodology. Once the tetrols are separated, solution fluorescence data, such as lifetimes, can be acquired to identify the tetrols. Even more specific information can be obtained for the separated tetrols by using other solid-matrix luminescence data. Both solid-matrix fluorescence and phosphorescence lifetimes can be obtained for the tetrols. Also, as shown for I-1 and I-2, the ratios of fluorescence quantum yield to phosphorescence quantum yield can be used to identify these tetrols. In addition, it is possible to employ  $k_{12}$  to differentiate I-1 and I-2. Finally, the ratios of the solid-matrix-corrected fluorescence area to the solid-matrix-corrected phosphorescence area could be used to characterize all four tetrols.

#### ACKNOWLEDGMENT

Financial support for this project was provided by the U.S. Department of Energy, Division of Basic Energy Sciences, Grant DE-FG-02-86 ER13547. Partial support was provided by the U.S. Environmental Protection Agency under Grant R817678. The cyclodextrins were provided by American Maize Products Co., Hammond, IN.

Received for review April 22, 1993. Accepted June 23, 1993.\*

\* Abstract published in *Advance ACS Abstracts*, August 15, 1993.

# Liquid Mixtures for Matrix-Assisted Laser Desorption

D. Shannon Cornett, Michael A. Duncan, and I. Jonathan Amster\*

Department of Chemistry, University of Georgia, Athens, Georgia 30602

Binary matrix solutions are described which can be used for matrix-assisted laser desorption of peptides and proteins at 532 or 337 nm. The matrix solutions are composed of a strongly absorbing organic compound, such as rhodamine 6G or 1,4-diphenyl-1,3-butadiene, dissolved into a polar liquid, such as 3-nitrobenzyl alcohol or glycerol. Variations in absorber concentration are shown to affect the mass resolution, with higher resolution mass spectra being obtained at lower absorber concentrations. At the lowest absorber concentrations, mass resolution approaches that obtained with this instrument using the standard solid matrix, sinapinic acid. Peak broadening at high absorber concentration is shown to result from the formation of adducts of the absorber molecule and not the solvent molecule.

## INTRODUCTION

The technique of matrix-assisted laser desorption/ionization (MALDI), first described by Hillenkamp and Karas in 1988,<sup>1</sup> has greatly expanded the field of biological mass spectrometry. Using MALDI, many classes of biomolecules have been successfully mass analyzed at an accuracy matched only by the complementary technique of electrospray ionization.<sup>2-9</sup> Much of the success in the rapid development of MALDI can be attributed to the identification of a number of effective matrices.<sup>10-16</sup> The general utility of any matrix compound is determined by its efficiency in ionizing the biomolecule of interest and by a lack of sensitivity to the

numerous impurities commonly present in biological solutions. Matrices such as sinapinic acid and 2,5-dihydroxybenzoic acid have been shown to be effective for many biomolecules, even in the presence of relatively high concentrations of inorganic salts and buffer.<sup>13</sup> However, such properties are not universal for all known matrix compounds. We have been investigating matrices formed by combining two or more compounds which have properties that can be adjusted for specific experimental conditions. In this paper, we demonstrate that binary mixtures can be selected to operate at specific laser wavelengths and that component ratios can be adjusted to change the features of the mass spectra generated from the mixture.

The properties required of a matrix for MALDI experiments are that it absorbs strongly at the wavelength of the irradiating laser, that it can co-crystallize (solid matrix) or dissolve (liquid matrix) the sample, that it promotes the chemistry that leads to the ionization of the sample, and that it insulates the sample from thermal degradation during laser desorption. Multiple component matrices offer the capability to independently optimize the different properties required of the matrix by varying the identity and/or concentration of the components. On the other hand, matrices that consist of either a pure liquid or solid have fixed physical and chemical properties. Tanaka and co-workers, who independently reported MALDI-type experiments at the same time that Hillenkamp and Karas first announced their results, described a binary matrix which was composed of an ultrafine cobalt powder dispersed in glycerol.<sup>17</sup> This heterogeneous mixture allowed the energy of the laser to be coupled into the liquid at a wavelength (337 nm) at which the solvent was transparent. Williams and co-workers have observed a 10-fold increase in the intensity of DNA fragment ions desorbed from a frozen aqueous matrix when the desorption laser was tuned to resonant absorption lines of sodium and copper atoms, present in the desorbed plume and as a substrate, respectively.<sup>3</sup> More recent work from the Hillenkamp group has shown that, for 2,5-dihydroxybenzoic acid, the MALDI performance in the high mass region (>50 kDa) was improved when the matrix was combined with a structurally similar compound, presumably by lowering the energy required to disrupt the crystal lattice.<sup>18</sup> Similar to the Tanaka experiments, we have demonstrated that 532-nm radiation can be efficiently coupled into the liquid matrix, 3-nitrobenzyl alcohol, by preparing admixtures with the strongly absorbing laser dye, rhodamine 6G.<sup>19</sup>

Liquid matrices present some advantages over solid matrices for MALDI. One of the most important criteria for MALDI is the intimate mixing of the analyte and the matrix. For solid matrices, impurities can cause a considerable degree of heterogeneity in the resulting sample crystals, inhibiting

\* Author to whom correspondence should be addressed.

- (1) Karas, M.; Hillenkamp, F. *Anal. Chem.* 1988, 60, 2299-2301.
- (2) Spengler, B.; Pan, Y.; Cotter, R. J.; Kan, L.-S. *Rapid Commun. Mass Spectrom.* 1990, 4, 99-102.
- (3) Nelson, R. W.; Thomas, R. M.; Williams, P. *Rapid Commun. Mass Spectrom.* 1990, 4, 348-351.
- (4) Bornsen, K. O.; Schar, M.; Gassmann, E.; Steiner, V. *Biol. Mass Spectrom.* 1991, 20, 471-478.
- (5) Parr, G. R.; Fitzgerald, M. C.; Smith, L. M. *Rapid Commun. Mass Spectrom.* 1992, 6, 369-372.
- (6) Huth-Fehre, T.; Gosine, J. N.; Wu, K. J.; Becker, C. H. *Rapid Commun. Mass Spectrom.* 1992, 6, 209-213.
- (7) Nordhoff, E.; Ingendoh, A.; Cramer, R.; Overberg, A.; Stahl, B.; Karas, M.; Hillenkamp, F.; Crain, P. F. *Rapid Commun. Mass Spectrom.* 1992, 6, 771-776.
- (8) Tang, K.; Allman, S. L.; Chen, C. H. *Rapid Commun. Mass Spectrom.* 1992, 6, 365-368.
- (9) Lewis, S.; Korsmeyer, K. K.; Correia, M. A. *Rapid Commun. Mass Spectrom.* 1993, 7, 16-19.
- (10) Beavis, R. C.; Chait, B. T. *Rapid Commun. Mass Spectrom.* 1989, 3, 432-435.
- (11) Beavis, R. C.; Chait, B. T. *Rapid Commun. Mass Spectrom.* 1989, 3, 233-237.
- (12) Beavis, R. C.; Chait, B. T. *Rapid Commun. Mass Spectrom.* 1989, 3, 436-439.
- (13) Strupat, K.; Karas, M.; Hillenkamp, F. *Int. J. Mass Spectrom. Ion Proc.* 1991, 111, 89-102.
- (14) Zhao, S.; Somayajula, K. V.; Sharkey, A. G.; Hercules, D. M.; Hillenkamp, F.; Karas, M.; Ingendoh, A. *Anal. Chem.* 1991, 63, 450-453.
- (15) Chan, T.-W. D.; Colburn, A. W.; Derrick, P. J. *Org. Mass Spectrom.* 1992, 27, 53-56.
- (16) Beavis, R. C.; Chaudhary, T.; Chait, B. T. *Org. Mass Spectrom.* 1992, 27, 156-158.

- (17) Tanaka, K.; Waki, H.; Ido, Y.; Akita, S.; Yoshida, Y.; Yoshida, T. *Rapid Commun. Mass Spectrom.* 1988, 2, 151-153.
- (18) Karas, M.; Nordhoff, E.; Stahl, B.; Strupat, K.; Hillenkamp, F. Matrix mixtures for a Superior Performance of Matrix Assisted Laser Desorption Ionization Mass Spectrometry: *Proceedings of the 40th ASMS Conference on Mass Spectrometry and Allied Topics*; Washington, DC, May 31-June 5, 1992; pp 368-369.
- (19) Cornett, D. S.; Duncan, M. A.; Amster, I. J. *Org. Mass Spectrom.* 1992, 27, 831-832.

and possibly preventing the formation of ions.<sup>13,20</sup> Also, it is not uncommon for the distribution of crystals to vary widely over the entire sample probe, which can cause considerable fluctuation in mass spectra obtained from different regions of the sample. The inherent homogeneity provided by liquid matrices eliminates the problems associated with inhomogeneous crystallization. In addition, solutions provide an evenly distributed coverage of the sample over the probe surface which improves shot-to-shot reproducibility and, because of the combined effects of sample diffusion and liquid flow, many more laser shots per spot can be obtained than from solid samples.<sup>15,19</sup> Liquid matrices also show great promise for providing a direct interface with liquid separation techniques using either flow-injection or continuous-flow MALDI.<sup>21</sup>

We present here results obtained with a series of binary mixtures which utilize 3-nitrobenzyl alcohol or glycerol as the primary component. These compounds are liquids under typical MALDI conditions and have been reported to be effective matrices for both UV and IR MALDI.<sup>15,22,23</sup> However, in our experiments, the laser wavelengths used are not absorbed by these liquids but rather are absorbed by the second component of the mixture. In contrast to the metal powder used by Tanaka and co-workers, our absorbers are organic molecules which are soluble in the respective liquids, providing much greater control over the absorbance of the solution. This allows us to evaluate the energetics of the desorption process to determine possible effects on the quality of the resulting mass spectra. In a previous study, we demonstrated that two compounds, rhodamine 6G and 3-nitrobenzyl alcohol, could be combined to create a matrix which was effective for 532-nm MALDI.<sup>19</sup> Although we have produced ions in excess of 250 kDa using this mixture, the mass resolution reported in this earlier paper was significantly less than can be obtained by using solid matrices. In this paper, we present evidence that mass resolution can be improved by adjusting the concentration of the absorbing compound in the mixture.

## EXPERIMENTAL SECTION

All experiments were performed in a linear time-of-flight mass spectrometer constructed at the University of Georgia specifically for MALDI experiments. Details of the instrument have been published elsewhere.<sup>24</sup> Briefly, samples are deposited onto a 4.8-mm diameter stainless steel probe which is positioned flush with the surface of the acceleration plate. Laser desorption is accomplished by focusing either 532-nm (frequency doubled Nd-YAG, Quanta Ray) or 337-nm (N<sub>2</sub> laser, Laser Photonics) light onto the liquid droplet. The fluence of each laser was on the order of 10–100 mJ cm<sup>-2</sup> (calculated using a spot size measured from a solid sample), measured by placing a quartz disc in front of the window of the vacuum system to direct 8% of the laser beam onto a joulemeter (Laser Precision, Inc.). Desorbed ions are accelerated to 25 keV and passed through a 1.5-m flight tube before being detected by an electron multiplier tube (Hamamatsu R-595). Ion signals are digitized and summed by a CAMAC-based 100-MHz transient digitizer (DSP Technology) before being transferred to an IBM-compatible computer. With the liquid samples inserted, the typical background pressure of the instrument is 10<sup>-6</sup> Torr.

Matrix solutions are prepared by combining strongly absorbing compounds with a liquid, 3-nitrobenzyl alcohol (NBA) or glycerol, to concentrations of 10<sup>-1</sup>–10<sup>-3</sup> M. Absorbers we have evaluated include rhodamine 6G, coumarin 175, and 1,4-diphenyl-1,3-butadiene. Rhodamine/nitrobenzyl alcohol solutions are prepared by dissolving the absorber directly into the liquid. For the other combinations, the absorber is first dissolved into an appropriate solvent, 50% v/v toluene:ethanol for the butadiene compound and methanol for the rhodamine and coumarin dyes. An aliquot of this solution is injected into a 1.0–1.5-μL droplet of the liquid, previously deposited on the probe, to yield the desired concentration. Volatile solvents are allowed to evaporate before addition of the protein. Proteins are used as obtained (Sigma Co.) and dissolved to a concentration of 10<sup>-4</sup> M in a 0.05% solution of TFA in methanol. A total of 1–10 μL of protein solution is injected into the droplet of matrix solution to yield a total protein loading of approximately 1 nmol. After the methanol was allowed to evaporate at room temperature, samples are inserted into the mass spectrometer for analysis.

## RESULTS AND DISCUSSION

**Matrix Solutions.** Compared to NBA, glycerol is a more favorable solvent for biological molecules because of its greater polarity. In combination with a dissolved, light-absorbing compound, glycerol also works well as a matrix solution for MALDI experiments. (Matrices involving only NBA or glycerol are referred to as *liquid matrices*; admixtures involving an absorbing compound dissolved in NBA or glycerol are referred to as *matrix solutions*.) Figure 1 shows mass spectra of horse heart cytochrome c (12361 Da), horse skeletal apomyoglobin (16951 Da),<sup>25</sup> and bovine serum albumin (66431 Da)<sup>26</sup> that were obtained from a 0.1 M matrix solution of rhodamine 6G in glycerol. The laser wavelength used for desorption was 532 nm at a fluence of approximately 15 mJ cm<sup>-2</sup>. The general features of the spectra are similar to those reported for 0.1 M rhodamine in NBA matrix solution. In both cases, we observe the protein molecular ion as well as a broad distribution of protein cluster ions. Also, the mass resolution exhibited in Figure 1 is substantially less than that which can be obtained with solid matrices. However, these features can be changed by adjusting the absorber concentration, as we show below.

Glycerol is typically used as a liquid matrix only in conjunction with IR lasers, because of strong O-H absorption in this region of the optical spectrum.<sup>22,23</sup> Absence of a significant absorption band in the visible region has, thus far, prohibited its use as a liquid matrix for visible wavelength lasers. The mass spectra shown in Figure 1 demonstrate that by addition of a component with a strong absorption band in the visible spectrum, such as is provided by the rhodamine admixture, 532-nm radiation can be effectively coupled into a glycerol-based matrix. The ability to adjust the light-absorbing properties of a solution allows the use of glycerol as an alternative to NBA. The three mass spectra of Figure 1 (12–190 kDa) clearly demonstrate that this matrix solution is effective over a wide mass range.

The wide range of spectral properties exhibited by various organic compounds allows the wavelength dependence of the absorbance of a solution to be adjusted. We find that a solution of 0.1 M 1,4-diphenyl-1,3-butadiene in NBA can be used for 337-nm MALDI. The mass spectra of bovine insulin and cytochrome c shown in Figure 2 were obtained from solutions that have protein concentrations identical to those used for the rhodamine mixtures. Mass spectra obtained from the butadiene matrix solution exhibit features that are similar to those from the previous matrix solutions, namely,

(20) Beavis, R. C. Understanding Matrix-Protein Interactions in Matrix assisted Laser Desorption: *Proceedings of the 40th ASMS Conference on Mass Spectrometry and Allied Topics*; Washington, DC, May 31–June 5, 1992; pp 5–6.

(21) Li, L.; Wang, A. P. L.; Coulson, L. D. *Anal. Chem.* **1993**, *65*, 493–495.

(22) Overberg, A.; Karas, M.; Bahr, U.; Kaufmann, R.; Hillenkamp, F. *Rapid Commun. Mass Spectrom.* **1990**, *4*, 293–296.

(23) Overberg, A.; Karas, M.; Hillenkamp, F. *Rapid Commun. Mass Spectrom.* **1991**, *5*, 128–131.

(24) Cornett, D. S.; Amster, I. J.; Duncan, M. A. *J. Phys. Chem.* **1993**, *97*, 5036–5039.

(25) Zaia, J.; Annan, R. S.; Biemann, K. *Rapid Commun. Mass Spectrom.* **1992**, *6*, 32–36.

(26) Feng, R.; Konishi, Y.; Bell, A. W. *J. Am. Soc. Mass Spectrom.* **1991**, *2*, 387–401.



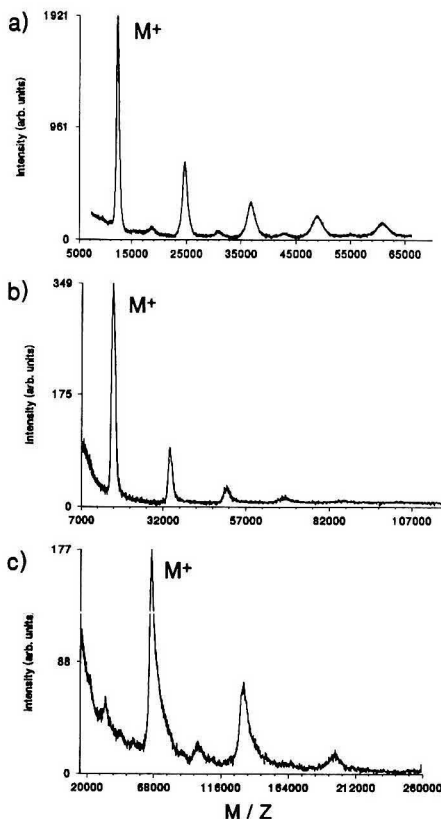


**Figure 1.** Positive ion mass spectra obtained by 532-nm MALDI from a 0.1 M matrix solution of rhodamine 6G in glycerol. (a) 1 nmol of horse heart cytochrome *c*; 500 laser shots; 20 kV acceleration. (b) 1 nmol of horse skeletal myoglobin; 250 laser shots; 25 kV acceleration. (c) 1 nmol of bovine serum albumin; 250 laser shots; 25-kV acceleration.

low mass resolution and a high degree of cluster formation. As with the glycerol solvent at 532 nm, NBA exhibits no significant absorption of the 337-nm light used in these experiments, thus it is classified as an ineffective liquid matrix at this wavelength.<sup>27</sup> Addition of the butadiene absorber ( $\epsilon_{337} \approx 67\,000\text{ M}^{-1}\text{ cm}^{-1}$ ) to NBA provides the pathway by which laser energy can be coupled into the liquid.

We have been able to verify that ion formation results from the cumulative properties of the mixture and not from matrix properties exhibited by a single component of the matrix solution. We have examined the two absorbing compounds individually as matrices at their respective wavelengths to determine if either compound is directly involved in producing the ions we observe. For these experiments, insulin was used as the test protein. Samples were prepared in an identical fashion to the solution experiments, with the exception that no liquid was present. Solutions of absorber and protein were combined to yield the same molar ratios used in the 0.1 M matrix solutions, 1:150 insulin:absorber. Also, the same quantity of insulin present in the matrix solutions, 1 nmol,

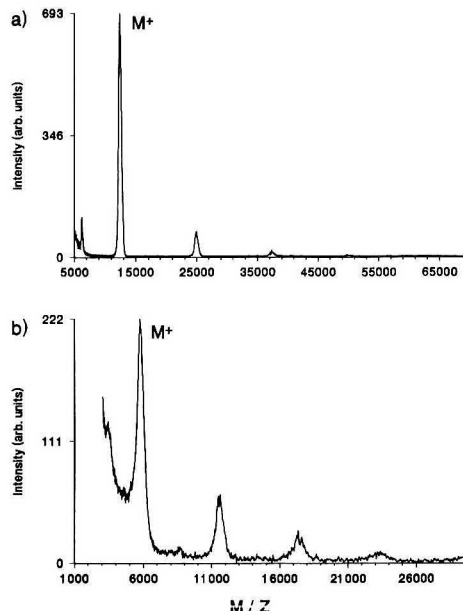


**Figure 2.** Positive ion mass spectra obtained by 337-nm MALDI from a 0.1 M matrix solution of 1,4-diphenyl-1,3-butadiene in NBA. (a) 1 nmol of horse heart cytochrome *c*; 500 laser shots; 20-kV acceleration. (b) 1 nmol of bovine insulin; 250 laser shots; 20 kV acceleration.

was deposited on the probe. At a laser fluence comparable to that used for matrix solutions, no positive ion formation is observed from either butadiene or rhodamine compounds. The solvents themselves are not effective matrices at the wavelengths employed in these experiments, as they do not absorb the laser radiation. Together, these data indicate that ions are formed from matrix solutions as a result of the combined properties of the absorber and liquid. Although rhodamine is not effective as a matrix for forming positive ions of peptides, there has been a report of its use for forming negative ions. Chen and co-workers have observed that 532-nm irradiation of a 10 000:1 molar ratio of rhodamine 6G: protein mixture produces negative ions of many of the proteins we have examined.<sup>28</sup>

Although the absorbing compound is not directly responsible for ion formation, the activity of the absorbing compound may not be limited only to the absorption of the laser energy. Some compounds which strongly absorb the laser energy do not produce effective matrix solutions. Using a matrix solution composed of the laser dye coumarin 175 and glycerol, no insulin or cytochrome *c* ions are observed for 337-nm MALDI. This result is surprising since the absorbance of the coumarin dye ( $\epsilon_{337} \approx 175\,000\text{ M}^{-1}\text{ cm}^{-1}$ ) is much greater than that of the butadiene absorber. Since coumarin 175 exists in solution as an anion, its basicity may be greater than that of the protein. In this case, proton transfer to the dye anions may be favored, resulting in the formation of negative protein ions. Unfortunately, the power supplies used for ion acceleration are monopolar and prevent the investigation of negative ions. Another possibility which must be considered is that the maximum output energy of our  $\text{N}_2$  laser, 200  $\mu\text{J}$ /pulse, may be insufficient to initiate desorption from glycerol,

(27) Overberg, A.; Hassenburger, A.; Hillenkamp, F. In *Mass Spectrometry in the Biological Sciences: A Tutorial*; Gross, M. L., Ed.; Kluwer Academic Publishers: Boston, 1992; pp 181–197.

(28) Tang, K.; Allman, S. L.; Jones, R. B.; Chen, C. H. *Org. Mass Spectrom.* 1992, 27, 1389–1392.

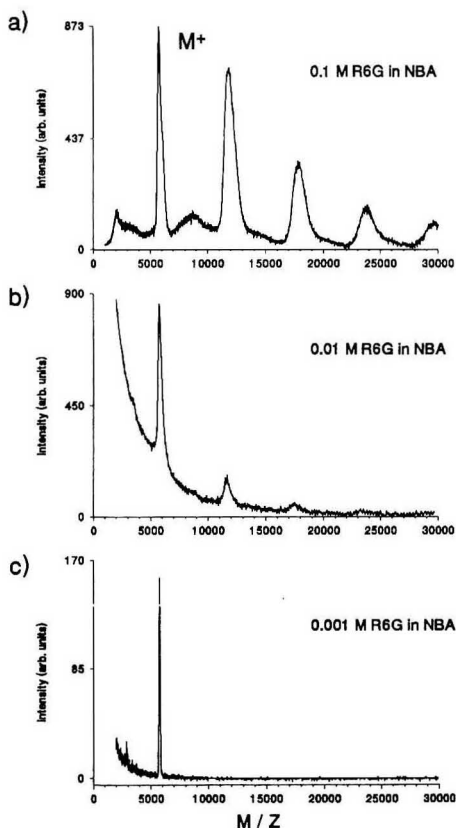


**Figure 3.** Positive ion mass spectra of bovine insulin obtained by 532-nm MALDI at three concentrations of rhodamine/NBA matrix solution: (a) 0.1 M, (b) 0.01 M, (c) 0.001 M. Experimental conditions for all spectra: 1 nmol of protein; 250 laser shots; 20-kV acceleration.

which is less volatile than the NBA solvent used with the butadiene absorber at 337 nm. We have been unable to verify this possibility with a matrix solution of coumarin 175 in NBA because of the low solubility of the dye in this solvent. Therefore, it remains unclear if the chemical nature of this particular absorber actively inhibits ion formation.

**Improved Mass Resolution.** In addition to changing the compounds used as an absorber and as the liquid solvent, these matrix solutions provide an additional experimental variable which may be manipulated to alter physical properties of the matrix, i.e., the concentration of the absorber. Using the rhodamine/NBA matrix solution, we have conducted experiments in which the absorber concentration was varied in order to gain a better understanding of the role of this species in the ion formation process. To ensure that any observed differences in the mass spectra were due solely to absorber concentration, three samples were prepared using a fixed amount of liquid and protein. Quantities of the rhodamine absorber were added to yield concentrations of  $10^{-1}$ ,  $10^{-2}$ , and  $10^{-3}$  M. Mass spectra were acquired at laser fluences just above threshold for observing protein ions. The results, shown in Figure 3, illustrate an inverse relationship between solution absorbance and mass resolution. We observe that decreasing the concentrations of absorber from  $10^{-1}$  to

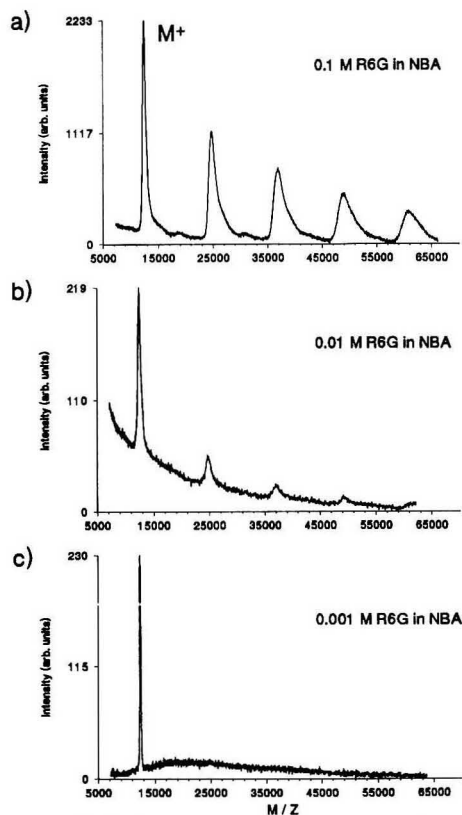


**Figure 4.** Positive ion mass spectra of horse heart cytochrome c obtained by 532-nm MALDI at three concentrations of rhodamine/NBA matrix solution: (a) 0.1 M, (b) 0.01 M, (c) 0.001 M. Experimental conditions for all spectra: 1 nmol of protein; 250 laser shots; 25-kV acceleration.

$10^{-3}$  M results in an improvement in mass resolution from an  $m/\Delta m$  of 12 in Figure 3a to an  $m/\Delta m$  of 52 in Figure 3b. This effect suggests a relation between the amount of energy deposited into the matrix solution and mass resolution. Such a relationship has been shown to exist for solid matrices.<sup>11,20</sup> Formation of adducts between the protein and the absorber must also be considered as a possible cause of poor mass resolution.

Formation of cation or matrix adducts is frequently cited as a major cause of peak broadening in MALDI mass spectra.<sup>10,11,13</sup> With multiple species present, as in a matrix solution, the possibility of forming many different adduct ions increases. In this event, we would expect that by decreasing the amount of absorber species, as in the above experiments, the population of adduct ions having specific masses would decrease, resulting in a narrower distribution of masses. This conclusion is supported by the mass spectra of cytochrome c shown in Figure 4. These spectra were obtained using matrix solutions identical to those used to

(29) Verentchikov, A.; Ens, W.; Martens, J.; Standing, K. G. Experimental Study of Ion Ejection Processes in Matrix Assisted Laser Desorption: *Proceedings of the 40th ASMS Conference on Mass Spectrometry and Allied Topics*; Washington, DC, May 31–June 5, 1992; pp 360–361.

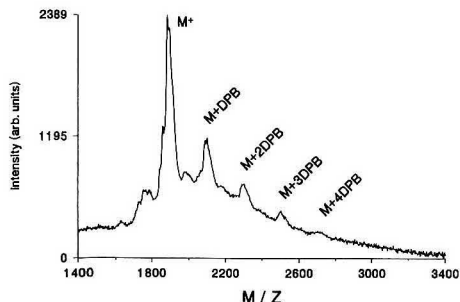


**Figure 5.** Positive ion mass spectrum of gramicidin D obtained by 337-nm MALDI from 0.1 M solution of 1,4-diphenyl-1,3-butadiene in NBA. Conditions: 500 pmol of peptide; 250 laser shots; 20-kV acceleration.

obtain the mass spectra of Figure 3. For cytochrome *c*, we see that decreasing the concentration of the absorbing compound results in an improvement in mass resolution of similar magnitude to that observed for insulin. As a benefit of the narrower peak width, the mass accuracy for the cytochrome *c* molecular ion improves from 0.2% to 0.5%. The significant higher mass tailing exhibited by the cluster ion peaks in Figure 4a suggests the attachment of several of the absorber molecules. Another feature common to the mass spectra in Figures 3 and 4 is that a decrease in the rhodamine concentration produces not only an increase in mass resolution but also a decrease in the abundance of cluster ions relative to the molecular ion intensity. One explanation of this trend is that the cluster ions are comprised of protein molecules connected by rhodamine molecules, and so their abundance increases as the concentration of rhodamine increases.

To determine whether the absorber does in fact form an adduct with the analyte, MALDI mass spectra have been obtained for the peptide gramicidin D in both butadiene and rhodamine matrix solutions. Gramicidin D is a mixture of five components of similar mass, with the most abundant peptide having a mass of 1881 Da. Because of its relatively low molecular weight, the mass resolution of our instrument is sufficient to distinguish any solvent or absorber adduct ions which may be formed. This peptide can be used as a model for larger protein molecules to determine the extent of adduct ion formation. Figure 5 is a mass spectrum of gramicidin D obtained from a 0.1 M butadiene/NBA matrix solution using 337 nm. Clearly observed are ions corresponding to as many as four of the butadiene molecules attached to the peptide ion,  $[M + (206)_N]^+$ . Unfortunately, we have been unable to observe ion formation at lower concentrations of this absorber, possibly because of the limited laser power available at 337 nm. It is therefore unknown whether the population of adduct ions decreases at lower concentrations of butadiene. Figure 6 shows results obtained from 0.1 and 0.001 M rhodamine/NBA matrix solutions. From this data, it is apparent that lower concentrations of absorber do result in a decreased intensity of adduct ions. The mass spectrum in Figure 6a, obtained from a solution with a higher concentration of the absorber, contains an ion peak centered at 2324 Da, which corresponds to the attachment of one rhodamine molecule. In the mass spectrum obtained with a lower absorber concentration, shown in Figure 6b, no adduct ion is present. The absorber concentrations are representative of the minimum and maximum concentrations used to obtain

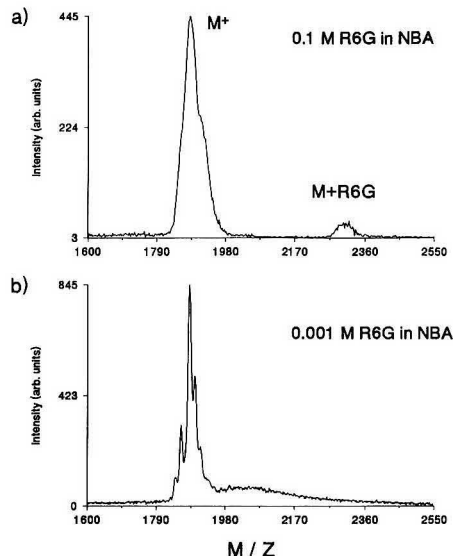


**Figure 6.** Positive ion mass spectra of gramicidin D obtained by 532-nm MALDI from (a) 0.1 M rhodamine 6G in NBA and (b) 0.001 M rhodamine 6G in NBA. Conditions: 500 pmol of peptide; 250 laser shots; 25-kV acceleration.

the mass spectra in Figures 3 and 4. Although only a small number of absorber adducts are observed for gramicidin D, it is not unlikely that larger protein molecules would contain many more sites to which absorber molecules could attach. As a side note, it is interesting that no solvent adduct ions ( $M + 153$ )<sup>+</sup> are observed in either of the mass spectra shown in Figures 5 and 6. A small, very broad peak centered at an  $m/z$  of  $M + 104$  does appear in Figure 5. A speculative assignment for this ion is that it is an adduct of the protein with styrene, a possible photodecomposition product of the absorber, 1,4-diphenylbutadiene.

The formation of adduct ions explains in part the poor resolution observed for higher mass ions, but further examination of Figure 6 shows that other factors may also contribute to broad peaks. In the mass spectrum obtained with the higher concentration of the rhodamine absorber, Figure 6a, the five components of gramicidin D appear as a single, unresolved peak. For the mass spectrum obtained with a lower concentration of absorber, Figure 6b, all five components are sufficiently resolved. Certainly, this effect cannot be attributed to the formation of adduct ions. We believe that this contribution to peak broadening is due to energetic factors. Varying the absorber concentration changes the amount of energy that is absorbed by the solution. This, in turn, may have an effect on the kinetic energy distribution of the desorbed ions or on the length of time over which desorption/ionization occurs.

The laser fluence necessary to observe ion formation increases with decreasing solution absorbance. However, the required fluence increases by only 1 order of magnitude in response to a decrease in absorber concentration of 2 orders of magnitude. This nonlinear behavior indicates that the

(30) Salehpour, M.; Perera, I.; Kjellberg, J.; Hedin, A.; Islamian, M. A.; Hakansson, P.; Sundqvist, B. U. R. *Rapid Commun. Mass Spectrom.* 1989, 3, 259-263.

(31) Ens, W. E.; Mao, Y.; Mayer, F.; Standing, K. G. *Rapid Commun. Mass Spectrom.* 1991, 5, 117-123.

total energy deposited into the weakly absorbing solution is still less than for the higher absorber concentration. For solid matrices, the observation of a fluence threshold for producing ions indicates that a critical energy flux into the matrix is necessary to initiate the desorption process.<sup>1,11,30-32</sup> One model proposed for ion ejection from solid matrices is that laser irradiance initiates a rapid phase change in the matrix from a solid to gas, producing a rapidly expanding jet.<sup>33,34</sup> The vapor pressure of NBA, however, is significantly higher than that of common solid matrices, and therefore, there is no distinct and rapid phase change. In using the ultrafine cobalt powder as an absorber in glycerol, Tanaka and co-workers have described its role in the desorption process as that of a "volatility enhancer", i.e., absorbed laser energy is converted to heat causing ion desorption through a rapid evaporation of glycerol matrix. This explanation likely applies to our observations from organic solutions and is consistent with prior observations of photothermal-induced vaporization of laser irradiated solutions.<sup>35-37</sup> It has been suggested that protein ion production from desorbed solid matrices occurs above a critical matrix sublimation rate.<sup>38</sup> Similarly, we might expect to observe a critical evaporation rate for liquids, which is the minimum rate for which protein ions are emitted from the surface in detectable quantities. Lower laser fluence is known to result in improved resolution from solid matrices, probably because of a decrease in the length of time in which ions are produced. This reasoning may also apply to the matrix solution data presented in Figure 6. The higher absorber concentration would be expected to result in a greater temperature increase than for the weakly absorbing solution. The evaporation rate for the 0.1 M solution would be much greater, producing a greater ion yield, consistent with the observed decrease in protein ion intensity at lower concentrations of rhodamine. Depending on the thermal conductivity of the liquid matrix, the time required for the solution to cool below the critical evaporation rate would be much longer, perhaps even longer than the laser pulse. This would increase the time over which protein ions are formed, resulting in lower mass resolution. However, confirmation of this model will require a mass analyzer that is not time dependent.

(32) Spengler, B.; Kirsch, D.; Kaufmann, R. *Rapid Commun. Mass Spectrom.* **1991**, *5*, 198-202.

(33) Beavis, R. C.; Chait, B. T. In *Methods and Mechanisms for Producing Ions from Large Molecules*; Standing, K. G., Ens, W., Eds.; Plenum Press: New York, 1991; pp 227-234.

(34) Beavis, R. C.; Chait, B. T. *Chem. Phys. Lett.* **1991**, *181*, 479-484.

(35) Sigrist, M. W.; Kneubuhl, F. K. *J. Acoust. Soc. Am.* **1978**, *64*, 1652-1663.

(36) Emmony, D. C. *Appl. Phys.* **1985**, *25*, 133-139.

(37) Braslavsky, S. E.; Heibel, G. E. *Chem. Rev.* **1992**, *92*, 1381-1410.

(38) Vertes, A. In *Methods and Mechanisms for Producing Ions from Large Molecules*; Standing, K. G., Ens, W., Eds.; Plenum Press: New York, 1991; pp 275-286.

(39) Beavis, R. C.; Chait, B. T. In *Methods and Mechanisms for Producing Ions from Large Molecules*; Standing, K. G., Ens, W., Eds.; Plenum Press: New York, 1991; pp 227-234.

(40) Spengler, B.; Kirsch, D.; Kaufmann, R. *J. Phys. Chem.* **1992**, *96*, 9678-9684.

(41) Orlando, R. *Anal. Chem.* **1992**, *64*, 332-334.

It is important to note that the sensitivity of the experiments presented here is rather low in comparison to MALDI experiments using solid matrices. This limitation appears to be due to instrumental factors and not to the liquid-based matrices, as a number of investigators have reported picomole sensitivity with NBA and glycerol as liquid matrices.<sup>16,21,23</sup> The mass spectrometer presented here is designed for a number of different types of experiments and as such is not optimized for sensitivity and mass resolution with MALDI experiments. For example, the sample probe tip diameter of 4.8 mm requires more sample for optimum coverage than the 1-2-mm probe tips previously described.<sup>11,16</sup> Sensitivity is also reduced because the ion signal is sampled directly from the unamplified output of an electron multiplier tube rather than using the dual microchannel plate (MCP) or hybrid MCP-electron multiplier used by others.<sup>39</sup> The acceleration region has a length of 3.3 cm to facilitate the introduction of the desorption laser. This feature allows ions that have a high radial velocity to expand perpendicular to the flight axis prior to attaining full acceleration, with the result that only a fraction of the desorbed ions are focused onto the detector. A long flight distance of 1.5 m in combination with the higher pressure from the liquid matrix is expected to enhance collisionally induced decomposition and scattering relative to solid matrix experiments, which would lead to peak broadening and signal loss.<sup>40</sup>

## CONCLUSIONS

Using two-component mixtures, it is possible to create matrices which are effective at a number of laser wavelengths and to optimize the performance for MALDI experiments. These results suggest that it should be possible to combine more than two components to create matrices which are optimized for many of the problems relating to impurities, as well as for novel compounds encountered in working with biological systems. For example, an additional component may be used to reduce the adverse effects that high concentrations of salts can exert on matrix performance. It may be possible to eliminate off-line purification steps by simply adding a component which eliminates cation interferences, such as 18-crown-6-ether, which has been successfully demonstrated to reduce this interference in NBA solutions in fast-atom bombardment mass spectrometry.<sup>41</sup> Further, the ability to choose solvent systems and to adjust mass resolution should prove useful for the development of continuous-flow MALDI.<sup>21</sup>

## ACKNOWLEDGMENT

The authors gratefully acknowledge financial support from the University of Georgia Research Foundation as well as the National Science Foundation through Grants CHE-9008246 (M.A.D.) and CHE-9024922 (J.J.A.).

RECEIVED for review April 30, 1993. Accepted July 6, 1993.\*

\* Abstract published in *Advance ACS Abstracts*, September 1, 1993.

# Detection of Electrospray Ionization Using a Quadrupole Ion Trap Storage/Reflectron Time-of-Flight Mass Spectrometer

Steven M. Michael, Benjamin M. Chien, and David M. Lubman\*

Department of Chemistry, The University of Michigan, Ann Arbor, Michigan 48109

A quadrupole ion trap storage/reflectron time-of-flight mass spectrometer has been developed as a detector for electrospray ionization of peptides. It is shown that the ion trap provides a means of storing externally generated electrospray ions prior to mass analysis via pulsed dc extraction into a reTOFMS. The IT/reTOF storage capabilities allow for nearly 100% duty cycle in converting a continuous electrospray ion beam into a pulsed source for TOF. In addition, the storage capabilities of the device provide enhanced sensitivity and resolution, where a typical resolution of  $\sim 3500$  at  $m/z = 1000$  is obtained. A sensitivity level in the low femtomole region is demonstrated for several peptides. It is further shown that this high duty cycle can be achieved using a low pulse-out rate and that the rapid acquisition of ESI/MS can be obtained with excellent  $S/N$  in even less than 1 s.

## INTRODUCTION

Electrospray ionization (ESI) has become a powerful means of ionizing high molecular weight and fragile nonvolatile molecules for analysis by mass spectrometry.<sup>1-7</sup> The electrospray source, in particular, has properties which make it very attractive for biomolecule analysis. The atmospheric pressure ion evaporation process which produces ions in electrospray results in multiply charged ions. The detection of ions in mass spectrometry is based upon the  $m/z$  ratio so if the extent of multiple charging is sufficient, high molecular weight ions can be detected in a mass spectrometer with a very limited mass range. Thus electrospray has become widely used as an ionization source for biomolecular analysis, using relatively inexpensive quadrupole mass spectrometers and more recently quadrupole ion traps<sup>8</sup> and Fourier transform ion cyclotron resonance mass spectrometers.<sup>9-11</sup>

A second key advantage of ESI is that it involves the production of ions from species dissolved in solution. Thus, ESI has become a widely used method for on-line interfacing of microbore liquid chromatography and capillary electrophoresis to mass spectrometry.<sup>4,8,7</sup> Several important issues in these experiments are high sensitivity, resolution, mass accuracy, and scan speed. The first three of these properties are important in analysis of large biomolecules, while the scan speed becomes particularly important in applications where rapidly eluting species are detected, such as in LC and CE separations.

An alternative means of detecting ions produced by ESI with certain distinct advantages is the time-of-flight mass spectrometer.<sup>12</sup> In particular, the TOF can provide speed in the acquisition of an entire mass spectrum over an extended mass range. This attribute is important for detection of rapidly eluting species in liquid chromatography or for any application involved in monitoring transient species in fast reactions. In addition, TOFMS is capable of detecting and analyzing high mass ions, which can potentially allow one to observe a broad range of charged states in electrospray MS. Further, the use of reflectron devices can provide relatively high resolution<sup>13-17</sup> and high mass accuracy for biomolecule analysis, as well as the capabilities for metastable energy analysis.<sup>17</sup> TOF devices can provide high sensitivity for biomolecule analysis based upon their high transmission and microchannel plate detectors. Finally, TOF mass spectrometers are simple devices with no slits, moving parts, or scanning fields.

There have been several recent attempts to interface ESI to TOFMS.<sup>18-20</sup> As noted in previous work,<sup>18</sup> the main problem involved in interfacing ESI to TOFMS is that ESI produces a continuous ion beam while TOF requires a pulsed operation. Thus a method is required to pulse a continuous ion beam resulting in discrete ion packets with a sufficiently narrow time profile to provide high resolution in a TOF. In particular, the work of Boyle<sup>18</sup> and Dodonov<sup>19</sup> has successfully interfaced an ESI source to TOF with a method involving orthogonal pulsed extraction of ions produced by ESI from the TOF acceleration region. In this work, resolution of around 1000 was typically achieved for a number of peptides with excellent sensitivity often reaching down into the femtomole regime. This sensitivity could be achieved through

(1) Fenn, J. B.; Mann, M.; Meng, C. K.; Wong, S. F.; Whitehouse, C. M. *Science* 1989, 246, 64.

(2) Fenn, J. B.; Mann, M.; Meng, C. K.; Wong, S. F.; Whitehouse, C. M. *Mass Spectrom. Rev.* 1990, 9, 37.

(3) Covey, T. R.; Bonner, R. F.; Shushan, B. I.; Henion, J. D. *Rapid Commun. Mass Spectrom.* 1988, 2, 249.

(4) Huang, E. C.; Wachs, T.; Conboy, J. J.; Henion, J. D. *Anal. Chem.* 1990, 62, 713A.

(5) Smith, R. D.; Olivares, J. A.; Nguyen, N. T.; Udseth, H. R. *Anal. Chem.* 1988, 60, 436.

(6) Loo, J. A.; Udseth, H. R.; Smith, R. D. *Anal. Biochem.* 1989, 179, 404.

(7) Chowdhury, S. K.; Katta, V.; Chait, B. T. *Rapid Commun. Mass Spectrom.* 1990, 4, 81.

(8) McLuckey, S. A.; VanBerkel, G. J.; Glish, G. L.; Huang, E. C.; Henion, J. D. *Anal. Chem.* 1991, 63, 375.

(9) Hofstadler, S. A.; Laude, D. A. *J. Am. Soc. Mass Spectrom.* 1992, 3, 613.

(10) Loo, J. A.; Quinn, J. P.; Ryu, S. I.; Henry, K. D.; Senko, M. W.; McLafferty, F. W. *Proc. Natl. Acad. Sci. U.S.A.* 1992, 89, 286.

(11) Loo, R. R. O.; Loo, J. A.; Udseth, H. R.; Fulton, J. L.; Smith, R. D. *Rapid Commun. Mass Spectrom.* 1992, 6, 159.

(12) Wiley, W. C.; McLaren, I. H. *Rev. Sci. Instrum.* 1955, 26, 1150.

(13) Mamyrin, B. A.; Karataev, V. I.; Shmikh, D. V.; Zagulin, V. A. *Sov. Phys. JETP* 1973, 37, 45.

(14) Boesl, U.; Neusser, H. J.; Weinkauff, R.; Schlag, E. W. *J. Phys. Chem.* 1982, 86, 4851.

(15) Bergmann, T.; Martin, T. P.; Schaber, H. *Rev. Sci. Instrum.* 1989, 60, 347.

(16) Cotter, R. J. *Anal. Chem.* 1992, 64, 1027A.

(17) LaFortune, F.; Ens, W.; Hruska, F. E.; Sadana, K. L.; Standing, K. G.; Westmore, J. B. *Int. J. Mass Spectrom. Ion Processes* 1987, 78, 179.

(18) Boyle, J. G.; Whitehouse, C. M. *Anal. Chem.* 1992, 64, 2084.

(19) Dodonov, A. F.; Chernushevich, I. V.; Laiko, V. V. Poster presented at the 12th International Mass Spectrometry Conference, Amsterdam, Holland, August 28-30, 1991.

(20) Boyle, J. G.; Whitehouse, C. M.; Fenn, J. B. *Rapid Commun. Mass Spectrom.* 1991, 5, 400.



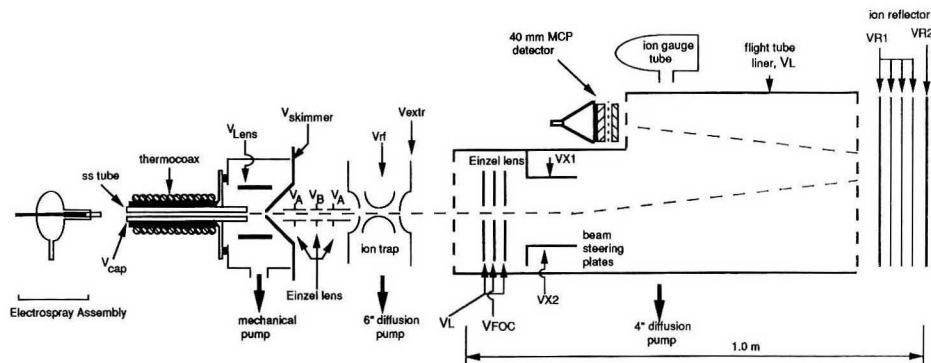


**Figure 1.** External ion injection/ion trap reflectron time-of-flight instrument with electrospray source:  $V_A$ ,  $V_B$ , pretrap Einzel lens voltages;  $V_{rf}$ , radio frequency potential;  $V_{extr}$ , dc extraction voltage;  $V_L = V_{X1}$ , flight tube liner voltage;  $V_{loc}$ , focusing voltage;  $V_{X2}$ , beam steering voltage;  $V_{R1}$ , ion repeller voltage;  $V_{R2}$ , ion reflector voltage.

the high duty cycle in the experiment which is believed to be  $\sim 2\%$ . However, this orthogonal extraction method may suffer several potential disadvantages that should be noted. In order to achieve this high duty cycle a very high pulsed extraction repetition rate must be used, i.e.  $\sim 2000/s$ . As noted previously<sup>18</sup> this high repetition rate in combination with the potentially large record lengths involved and speed with which the acquired spectra must be stored require specially designed circuitry and software. In addition the transverse velocity associated with an orthogonally expanding beam will limit the mass range observed at the detector and also the resolution of the ion peaks over a wide mass range.

In this work we explore the use of a quadrupole ion trap storage/reTOF device<sup>21</sup> as a means of interfacing a continuous ion beam produced by electrospray ionization to a TOF device. The idea here is that a quadrupole ion trap is used to store ions injected from ESI for an extended period of time ranging from tens of microseconds to several seconds. The endcaps of the trap then act as the acceleration region of the reTOF and the stored ions are ejected via a dc pulse applied to the exit endcap into the reTOF for analysis. Since the extraction time is short compared to the storage time, the trap converts a continuous ion beam into a pulsed beam with essentially 100% duty cycle. It is demonstrated herein that the IT/reTOF is an effective means of interfacing electrospray to a TOF, achieving a high duty cycle using a relatively low pulse-out extraction rate. This low pulse-out rate in turn can simplify the required electronics and data processing relative to other methods which require high pulse-out rates to achieve a reasonable duty cycle. Further it is shown that the enhancement of the signal due to the storage properties of the trap can provide rapid acquisition of ESI/MS with excellent  $S/N$  in even less than 1 s. In addition it is shown that the storage properties of the trap can enhance the resolution of the electrospray reTOF mass spectra, where a resolution of up to 3500 is observed at  $m/z \sim 1000$ . As shown in previous work,<sup>25</sup> the resolution in the trap is improved markedly with the use of a buffer gas. The broadening effect of the energy distribution of the ions on the resolution in the reTOF is decreased by relaxation of the translationally hot ions by the buffer gas, likewise the spatial effect is minimized since the ions are rapidly relaxed to a small volume in the center of the trap from which they are ejected. Also, the use of the trap as a front end storage device can potentially provide enhanced sensitivity through storage and integration of the

ion signal prior to TOF mass analysis. Indeed typical sensitivities for ESI of peptides are demonstrated in the low femtomole regime.

## EXPERIMENTAL SECTION

The experimental setup is shown in Figures 1 and 2. It consists of a differentially pumped reflectron time-of-flight mass spectrometer (Model D950) interfaced to a quadrupole ion trap storage device (Model C-1251 manufactured by R. M. Jordan Co., Grass Valley, CA)<sup>21</sup> and an electrospray sample ionization source. A syringe pump was used to deliver the sample, dissolved in a solvent, through a fused silica capillary tube into an electrospray assembly where the sample was ionized. The droplets produced were sampled through a heated ss inlet capillary which desolvates the droplets.<sup>22</sup> The remaining ions are injected into a differentially pumped region ( $\sim 1.5$  Torr) where the on-axis component of the ion beam passes through a 325- $\mu$ m skimmer into the mass spectrometer region and was collimated by a set of Einzel lenses into the quadrupole ion trap device. The ions were stored or accumulated until an extraction pulse is applied to the exit endcap of the ion trap. This extraction pulse ejects the ions from the trap and triggers the start for the TOF mass analysis. Upon leaving the trap, the ion packet enters a field-free drift region  $\sim 1$  m long at the end of which its velocity is slowed and reversed by the ion reflector. The newly focused ion packet then retraverses the drift region and is detected by a dual 40-mm microchannelplate detector with a gain of  $\sim 10^6$ - $10^7$ .

**A. Sample Ionization and Injection.** An ISCO Model  $\mu$ LC-500 micropump LC syringe pump was used to deliver the sample through a 100- $\mu$ m fused silica capillary directly to the electrospray assembly. The flow rates were typically 0.5–10.0  $\mu$ L/min and the solvent used was MeOH/H<sub>2</sub>O/HOAc (80:20:5 (v/v)) degassed in an ultrasonic bath. All peptide samples were obtained from the Sigma Chemical Co. St. Louis, MO, and used without further purification. This fused silica capillary was inserted through a stainless steel zero-dead-volume-tee into a 27-gauge flat tipped stainless steel needle. A nebulizing gas flow could be applied through this tee, and the tee/needle assembly was maintained at 3.5–4.5 kV relative to the stainless steel inlet capillary tube to produce the electrospray.

The sprayer assembly is axially directed onto a  $1/16$  in. 200 mm long 0.5 mm i.d. heated stainless steel capillary inlet tube. The typical needle to tube distance is 10 mm. A tightly fitting  $1/8$  in. copper tube was placed over this stainless steel tube and was tightly wound with  $1/16$  in. thermocoax cable heater. The temperature of the inlet was measured using a thermocouple and maintained at a constant temperature with a temperature controller. The temperature used in these experiments was generally 85–160 °C to assist in desolvating and declustering the

(21) Michael, S. M.; Chien, M.; Lubman, D. M. *Rev. Sci. Instrum.* 1992, 63 (10), 4277.

(22) Iribarne, J. V.; Thomson, B. A. *J. Chem. Phys.* 64, 2287.

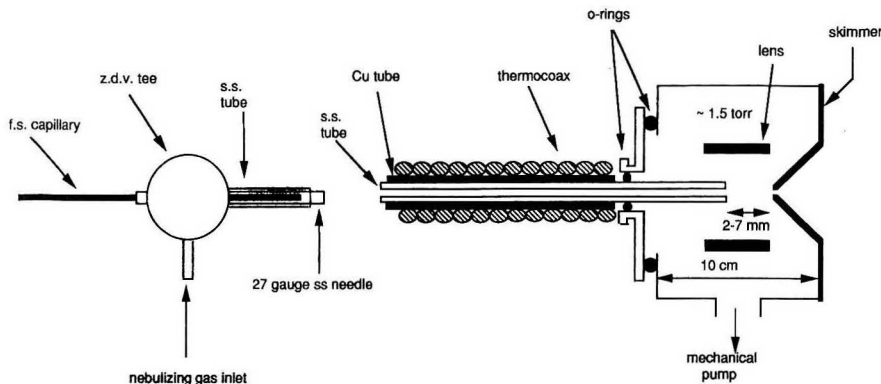


Figure 2. Detail of the electrospray ionization source.

sampled electrosprayed droplets. The actual sample temperature is expected to be somewhat lower due to ambient gas flow through the tube. This inlet tube is directly inserted through a Cajon Ultratorr fitting into the first vacuum chamber which was pumped to a pressure of approximately 1.5 Torr by a 650 L/min mechanical pump. The exit end of the inlet tube is axially directed onto the 325- $\mu$ m orifice skimmer. The inlet tube and skimmer were maintained at potentials of 350–50 V and 120–0 V, respectively. The distance between the tube and skimmer was adjustable and was usually maintained between 2 and 7 mm and was optimized as required. There was a cylindrical condenser lens around the space between the exit of the tube and the skimmer which focused the ion beam into the skimmer's orifice. This lens had an applied potential of 70–200 V.

The analyte solution was electrosprayed at atmospheric pressure producing highly charged droplets. These charged droplets are pushed toward the inlet tube via the electric field present. Some of these droplets enter the tube and pass through it with the help of the applied potential and the ambient pressure gradient. The ions exiting the tube are drawn into the skimmer via the potential difference between the inlet tube and the skimmer. In this space between the tube's exit and the skimmer, the ions undergo collisions. By alteration of the potential difference, the distance between the tube and skimmer, and the pressure of this region, the ions can be collisionally activated to either produce or minimize fragmentation.<sup>7</sup>

**C. Trapping.** The ions passing through the first vacuum region were sampled through the skimmer and entered the mass spectrometer region. The ions underwent a supersonic jet expansion and were then collimated by a set of Einzel lenses into the quadrupole ion trap device.

The quadrupole ion trap consists of two endcap electrodes with hyperbolic surfaces and a ring electrode situated between these endcaps. The quadrupole ion trap was completely enclosed with ceramic spacers placed between the ring and endcaps except for an inlet and exit aperture 3.1 mm in diameter on the endcaps. A  $1/16$  in. stainless-steel tubing with 0.02 in. i.d. was tightly fitted into a hole on the ring electrode in order to introduce helium or other gases into the trap to increase the local pressure as desired. A Vernier needle valve was used to finely control the amount of gas admitted into the trap. Typical pressure in the quadrupole ion trap ranged from  $5 \times 10^{-4}$  to  $10^{-3}$  Torr. During operation, both endcaps are held at 0 V while an rf signal of constant frequency (1.1 MHz) and variable amplitude (0–2200 V<sub>pp</sub>) is applied to the ring electrode. This applied rf field serves to trap ions present within the volume of the trap. Varying the rf amplitude varies the  $m/z$  range of ions that are stable within the trap. Ions with appropriate  $m/z$  for a particular rf amplitude have a stable trajectory within the trap and, therefore, are trapped.<sup>23</sup> The mass range of the ions that are trapped was

approximated by computer simulation.<sup>24</sup> After a selected  $m/z$  range has been trapped, a dc pulse was applied to the exit endcap to simultaneously extract all ions from the trap for TOF analysis as detailed below.

The trapping, extraction, and detection processes were as follows: A Global Specialties Co. 4001 pulse generator (PG) was used to trigger a California Avionics Laboratories, Inc., Model 112 AR digital delay generator (DDG). A modified EAI rf power supply with variable amplitude 0–2200 V<sub>pp</sub>, 1.1 MHz output was used to trap ions with  $m/z$  greater than 200. The DDG output pulse triggered the extraction pulser and this pulser passed its pulse to trigger the Lecroy Model 9400A digital oscilloscope (DOSC). The signal from the detector was amplified by a Stanford Research Systems Model SR445 DC 300 MHz amplifier.

DDG output pulse can be delayed from a few microseconds to as long as 10 s after triggering. Therefore, the delay of the DDG determined the duration of ion trapping, i.e., how long the ions could be stored or accumulated in the trap. After its set delay, the DDG outputs a pulse (20 ns rise time, +10 V amplitude, 10  $\mu$ s fwhm) which triggers the extraction pulser. The extraction pulser serves the dual purpose of both providing a start time reference for the TOF mass analysis and providing an extraction pulse to the exit endcap of the ion trap, thereby ejecting the ions from the trap. Upon the arrival of the rising edge of the DDG pulse, the extraction pulser passes this trigger pulse, the DDG output pulse, to the DOSC's external trigger. This provides the start time reference for the TOF mass analysis. After the arrival of the rising edge of the DDG output pulse (1.5  $\mu$ s), the extraction pulser sends the extraction pulse to the exit endcap of the ion trap. This extraction pulse was a dc square wave –330 V in amplitude and 2  $\mu$ s in width with 10-ns rise and fall times. The repetition rate of the entire experimental cycle varies from 0.1 to 10 kHz limited by the ions with the longest flight time.

**D. TOF Operation.** Upon exiting the ion trap, the ions pass through a set of accelerating plates and Einzel lens which serve to focus the ion packet and accelerate it into the field-free flight tube region through a potential difference of ~1500 V. A pair of beam deflecting plates are then used to steer the ions toward the ion repeller/reflector assembly, where the ion packet is more tightly focused, reversed in direction, and reaccelerated through the flight tube (with angular displacement from its initial axis of trajectory) onto the 40-mm dual microchannel plate detector. The field free region is held at a potential of ~1500 V using a liner inside the flight tube. The quadrupole ion trap is held at 0 V dc potential except for the dc extraction pulse applied to the exit endcap to eject ions from the trap into the acceleration region. The reflectron flight tube is pumped by a Varian VHS 4 diffusion pump while the main chamber is pumped by Varian VHS 6 diffusion pump. A restriction of 1 in. tubing is placed between the flight tube and the main chamber, which produced typical operating pressures of  $8 \times 10^{-6}$  and  $1 \times 10^{-6}$  Torr, respectively.

(23) March, R.; Hughes, R. *Quadrupole Storage Mass Spectrometry*; Wiley: New York, 1989.

(24) Ma, C.; Lee, H.; Lubman, D. M. *Appl. Spectrosc.* 1992, 46, 1769.

Electrospray ionization of Phenylalanine-alanine-valine, MW 371, 931 ms trapping time, Resolution ~ 3350

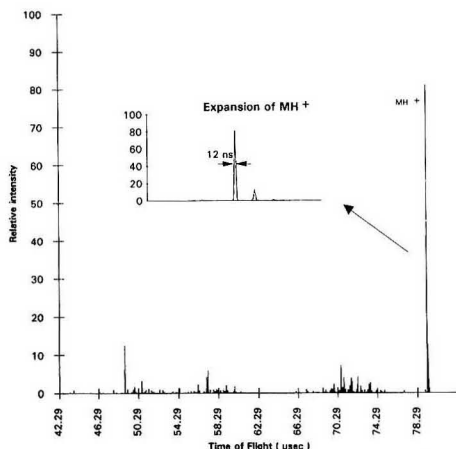


**Figure 3.** Electrospray ionization spectrum of phenylalanine-alanine-valine with  $V_{r.f.} = 685$  V<sub>pp</sub>,  $V_{cap} = +105$  V,  $V_{skimmer} = +30$  V,  $V_{lens} = +90$  V,  $V_{extr.} = -400$  V,  $V_A = -17$  V,  $V_0 = -65$  V,  $V_1 = V_{X1} = -1500$  V,  $V_{loc} = -1250$  V,  $V_{X2} = -1380$  V,  $V_{R1} = -197$  V,  $V_{R2} = +410$  V.

The TOF of the extracted ion packets was measured on the DOSC. Signal averaging was used to enhance the signal-to-noise ratio and reported spectra are averages of 100 single waveforms unless noted otherwise. In the experiment, DDG simultaneously triggered the DOSC and the extraction pulser. The ion signals from the detector were sent to the input of the DOSC, and the time difference between various ion peaks and the trigger ( $t = 0$ ) reference provides the time of flight of each ion.

The TOF spectra in the DOSC were transferred to a 386 IBM compatible PC using an RS 232 interface bus established between the DOSC and the computer. A user-written QUICKBASIC program was used to control the transfer processes. The size for each data point was 16 bit for our experiments. The raw data from DOSC were in ASCII form. It was converted into signed decimal form by a user-written program. The stored data in binary form was converted into ASCII form by a user-written program and loaded into a commercial spreadsheet software such as EXCEL for further data analysis.

Mass calibration was performed by measuring the time of flight ( $T$ ) of a few known masses (such as background water or methanol cluster ion signal) to find out the constant  $x$  and  $y$  in the empirical equation by linear regression analysis,  $m/z = xT^2 + y$ .

## RESULTS AND DISCUSSION

The results of interfacing the quadrupole ion trap/reTOF mass spectrometer with an electrospray ionization (ESI) source are demonstrated in Figures 3–10 for various peptide samples. Figure 3 shows the ESI mass spectrum of phenylalanine-alanine-valine using  $2.7 \times 10^{-6}$  M phenylalanine-alanine-valine dissolved in MeOH/H<sub>2</sub>O/HOAc (80:20:5 (v/v)) solvent. This solvent was used to obtain ESI spectra for all of the samples reported in this work. The production and transmission of ions to the trap were performed as described in the Experimental Section. The spectrum obtained was a 200 waveform average with a storage time of 931 ms per cycle. The amount of phenylalanine-alanine-valine sample consumed over the entire time period was ~84 pmol. Figure 3 also shows the expansion diagram of the protonated molecular ion peak with  $m/z$  of 372 and its <sup>13</sup>C isotope with  $m/z$  of 373. The fwhm of the MH<sup>+</sup> peak is 12 ns which corresponds to a mass resolution of ~3350. The rf voltage on the ring electrode

Electrospray ionization of Bradykinin, MW 1060, 931 ms trapping time, 400 waveforms average

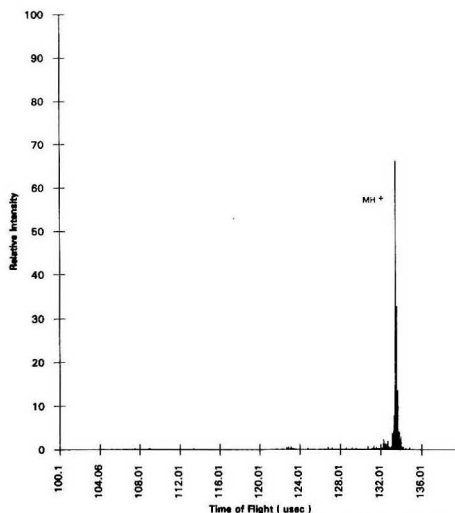


**Figure 4.** Electrospray ionization spectrum of bradykinin with  $V_{r.f.} = 1975$  V<sub>pp</sub>,  $V_{cap} = +50$  V,  $V_{skimmer} = +10$  V,  $V_{lens} = +190$  V,  $V_{extr.} = -330$  V. All other conditions were the same as those of Figure 3.

was optimized to provide the optimal trapping efficiency and was 685 V<sub>pp</sub> for this molecule.

Similar resolution has been achieved on higher  $m/z$  samples as shown in Figures 4 and 5. Figure 4 is the ESI mass spectrum of bradykinin protonated molecular ion injected into the IT/reTOF using  $2.3 \times 10^{-6}$  M bradykinin solution. The spectrum obtained was a 400 waveform average using a storage time of 931 ms per cycle. The bradykinin sample actually consumed in obtaining this spectrum is ~12 pmol. The rf voltage used to obtain this spectrum was 1975 V<sub>pp</sub>. Figure 5 is the expansion spectrum of Figure 4. The largest peak in this spectrum is the protonated molecular ion with a  $m/z$  of 1061. The fwhm of this peak is only 20 ns which corresponds to a mass resolution of ~3300. This spectrum clearly shows the completely resolved <sup>13</sup>C isotope peaks with  $m/z$  of 1062 and 1063. The ions with  $m/z$  of 1060 and 1059 were also observed. These two ions are the result of loss of one and two hydrogens, respectively. The appearance of these ions is most prominent when higher rf voltage was employed suggesting that the loss of H's most probably occurred from collisions inside the trap.

Figure 6 shows a mass spectrum of Leu-enkephalin-arginine with  $m/z$  of 711 using an analyte concentration of  $2.4 \times 10^{-6}$  M. The ions from ESI were stored for 931 ms using an rf voltage of 1500 V<sub>pp</sub> and the spectrum was averaged over 50 waveforms to provide improved S/N. In Figure 6A, both the singly and doubly protonated Leu-enkephalin-arginine molecular ions were observed with a focusing lens voltage of +180 V. In Figure 6B, when the focusing lens voltage was increased to +280 V, only the singly charged molecular ion was observed. It was found consistently that more multiply charged ions were observed when lower lens voltage was applied.

In Figures 7 and 8 are shown ESI/IT/reTOF mass spectra of gramicidin S obtained using different storage times. The spectra were obtained using  $10^{-6}$  M gramicidin S solution. In Figure 7, the spectrum was obtained using a 3.1-ms storage time and was averaged 50 times. This corresponds to a total

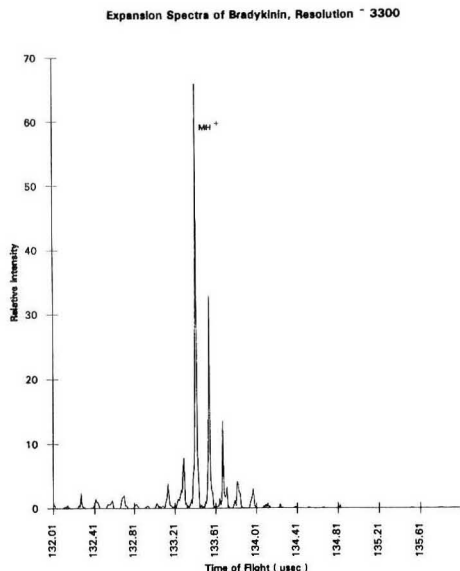
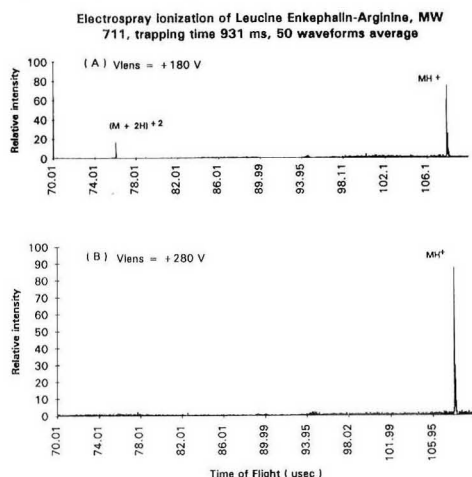
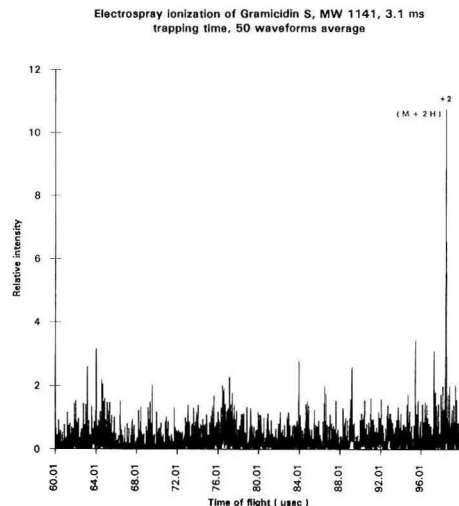


Figure 5. Expansion of Figure 4.



**Figure 6.** Electrospray ionization spectra of Leu-enkephalin-arginine with  $V_{rf} = 1500$  V<sub>pp</sub>,  $V_{cap} = +150$  V,  $V_{skimmer} = +30$  V, and  $V_{extr.} = -330$  V. All other conditions were the same as those of Figure 3 with the exception of  $V_{lens}$ .

analysis time of only 1.5 s. The gramicidin S sample actually consumed in obtaining this spectrum is 240 fmol. The major peak observed in this spectrum is the doubly charged molecular ion with a  $m/z$  of 571.5. The singly charged gramicidin S molecular ion with a  $m/z$  of 1142 is not shown in this spectrum. A rf voltage of 2200 V<sub>pp</sub> was used in this analysis. Under the same conditions, another spectrum was obtained using a 931-ms storage time and was averaged 50 times as shown in Figure 8. The amount of gramicidin S consumed in obtaining this spectrum was 7.2 pmol. Both the singly and doubly charged molecular ions were observed with the major peak being the singly charged gramicidin S



**Figure 7.** Electrospray ionization spectrum of gramicidin S with  $V_{rf} = 2200$  V<sub>pp</sub>,  $V_{cap} = +50$  V,  $V_{skimmer} = +10$  V,  $V_{lens} = +195$  V, and  $V_{extr.} = -330$  V. All other conditions were the same as those of Figure 3.

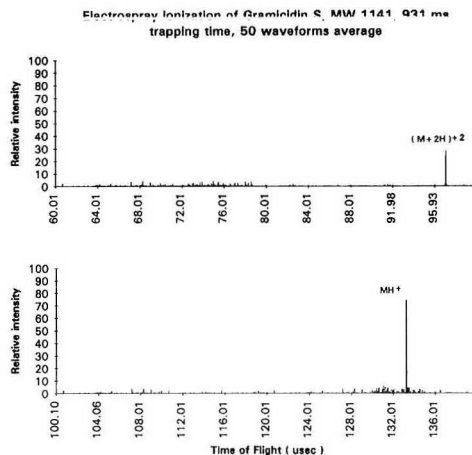


**Figure 8.** Electrospray ionization spectrum of gramicidin S. All conditions were the same as those of Figure 7.

molecular ion. The  $S/N$  is greatly improved in this spectrum because of the ability of the quadrupole ion trap to accumulate the ions through longer trapping time. This capability is especially prominent when interfaced to a ESI source as opposed to a plasma source where space charge effects may be present because of the high ion current (1–10 mA) produced in the ionization source.<sup>25</sup> Usually, the ion current measured in the quadrupole ion trap region is less than 1 pA in our current experimental setup. This low current results in the reduction of space charge effects inside the quadrupole ion trap. Thus, the resolution of all the spectra obtained by using the ESI source is generally improved over that obtained from

(25) Chien, B. M.; Michael, S. M.; Lubman, D. M. *Anal. Chem.* 1993, 65, 1916.

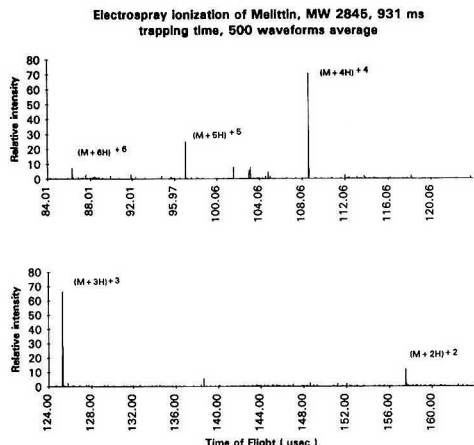


**Figure 9.** Electrospray ionization spectrum of melittin with  $V_{rf} = 2200$  V<sub>pp</sub>,  $V_{cap} = +100$  V,  $V_{skimmer} = +30$  V,  $V_{lens} = +160$  V, and  $V_{extr} = -330$  V. All other conditions were the same as those of Figure 3.

the API plasma source, where space charge may limit the spatial component of the resolution in the reTOF. The fwhm of gramicidin S doubly charged molecular ion peak in Figures 7 and 8 is  $\sim 35$  ns which corresponds to a mass resolution of  $\sim 1900$ .

The ability of this mass spectrometer to analyze higher molecular weight samples, such as melittin and horse heart cytochrome *c*, is demonstrated in Figures 9 and 10. The spectrum in Figure 9 was obtained by using  $3.5 \times 10^{-6}$  M melittin solution. In Figure 9 the spectrum was acquired with 931-ms trapping time and was averaged over 500 waveforms. The total sample consumed in this spectrum was  $\sim 27$  pmol. Since melittin has five amino acid basic sites plus one N-terminal base, a maximum of six charges on a molecule should be possible. Indeed, all of the different charge states were observed although the singly charged molecular ion is not shown in this figure. This is due to the fact that the maximum rf voltage output of our EAI rf power supply (2200 V<sub>pp</sub>) is not sufficiently high to trap  $m/z$  of 2845 with appreciable intensity. The fwhm of  $(M+2H)^{3+}$  peak is 65 ns, which corresponds to a mass resolution of  $\sim 1200$ . Figure 10 is the ESIIT/reTOF mass spectrum of cytochrome *c* ( $m/z$  12 327) where multiply charged ions from  $(M+20H)^{20+}$  to  $(M+11H)^{11+}$  are observed. This spectrum was acquired using  $4.8 \times 10^{-6}$  M cytochrome *c* solution with 931-ms trapping time and was averaged over 200 waveforms. The total sample consumed in this spectrum was  $\sim 17$  pmol. The fwhm of  $(M+16H)^{16+}$  peak is 45 ns, which corresponds to a mass resolution of  $\sim 1500$ . The highest rf voltage available to us was used to obtain these spectra.

An important potential advantage of the IT/reTOF is the duty cycle of the device. The actual pulse-out time of the device is  $\sim 2$   $\mu$ s. Thus if one uses a storage time of  $>10$  ms per cycle for sampling a continuous ion beam, the duty cycle approaches nearly 100%. Other methods have been used to sample continuous ion beams into TOF such as beam modulation<sup>20,26,27</sup> and pulsed extraction.<sup>18,19</sup> The pulsed extraction technique appears to be a particularly promising method for interfacing a continuous ion beam such as electrospray to a TOF device. In this method an ion beam

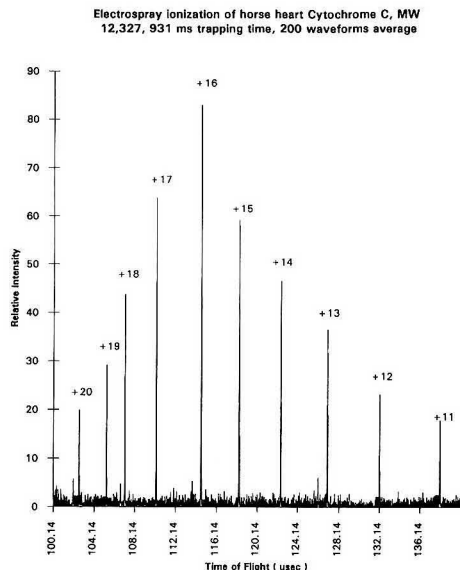


**Figure 10.** Electrospray ionization spectrum of horse heart cytochrome *c*. All conditions were the same as those of Figure 9.

is transmitted between the acceleration plates of the TOF and then rapidly pulsed out with an extraction pulse into the TOF drift tube which is transverse to the ion beam. The duty cycle is limited by the length of the extraction plates and velocity of the ion beam but has been estimated to be as high as 2% at a repetition rate of 5 kHz.<sup>18</sup> The duty cycle of these two techniques will decrease when detecting ions with larger  $m/z$  where a lower repetition rate must be used.

Another important advantage of the ion trap is that it can achieve an excellent duty cycle for continuous ion beams independent of repetition rate. As shown in this work, a trapping time of 931 ms can be used to enhance the signal and resolution of ions generated by an ESI source. Under these conditions, a pulse-out rate of only 1 Hz is required, which can easily be processed even with relatively modest electronics and software. When fast spectrum acquisition must be performed, such as applications in GC or LC when detecting rapidly eluting species or monitoring transient species, a 10-ms trapping time and a pulse-out rate of 100 Hz can be used to obtain the same 100% duty cycle. However, in the beam modulation and pulsed extraction methods a high extraction rate (2–10 kHz) is always required to achieve a reasonable duty cycle.

In our experiments the total ion current measurement at the entrance endcap in our interface design was  $\sim 1 \times 10^{-13}$  A. This is  $\sim 2$ –3 orders of magnitude lower than that reported in the literature, which used a three-stage pumping interface to achieve a total ion current of a few hundred picoamperes.<sup>18</sup> Nevertheless, the limit of detection measurement obtained in our experiment so far is quite comparable to those reported. In this work, a longer trapping time (931 ms) provided the best results for most of the samples studied. A trapping time shorter than 10 ms normally results in poor signal averaged spectra.

There are other potential advantages of the IT/reTOF over pulsed extraction methods without storage. Simulations performed on the SIMION program show that orthogonal extraction of ions becomes difficult above 50 eV of energy

(26) Bakker, J. M. B. *J. Phys. E: Sci. Instrum.* 1973, 6, 785.

(27) Ma, C.; Michael, S. M.; Chien, M.; Zhu, J.; Lubman, D. M. *Rev. Sci. Instrum.* 1992, 63, 139.



where the ions cannot be easily turned around and transmitted down the flight tube.<sup>28</sup> In comparison, the IT/reTOF is capable of slowing down and trapping ions of high energy with resulting high resolution due to the storage properties of the trap. Also, the orthogonal pulsed extraction method will be limited in the observed mass range due to the transverse velocity component of the ion beam. However, the mass storage range of the IT/reTOF is determined by the voltage and frequency applied to the trap and can be made extremely large in conjunction with the use of a buffer gas in the trap.<sup>24</sup> In the present work the actual trapping range is limited by the voltage range of the rf power supply available due to the actual voltage required to trap externally generated ions.<sup>29</sup> However, storage and trapping of ions over a relatively large mass range has been demonstrated in the trap.<sup>30,21</sup> The subsequent pulse-out of the stored ions from the trap into the reTOF occurs on-axis so that any further difference in the kinetic energy of ions of different masses in the extraction process is no longer important in determining the mass range of the device as compared to the orthogonal pulsed extraction method. In addition, a further possible advantage of the IT/reTOF in these experiments that has not been demonstrated herein is the possibility for MS/MS studies in the trap and for the studies of long-lived metastable decay in the IT/reTOF combination.

A measurement of the limit of detection attainable for liquid injection into the ESI source was examined using arginine,

leucylalanine, and gramicidin S dissolved separately in MeOH/H<sub>2</sub>O/HOAc (80:20:5 (v/v)) solvent. Initial solutions of  $7 \times 10^{-5}$  M were prepared and successive dilutions were made down to  $6.55 \times 10^{-8}$  M. These samples were run as detailed in the Experimental Section but with the conditions optimized for each analyte and concentration. A lower limit of detection of 35, 20, and 80 fmol, respectively, were determined using a  $S/N = 3$  as our limit of detection criterion. Later work on ESI incorporated a 40-mm triple microchannel plate detector in our IT/reTOF mass spectrometer where limits of detection of 4.5, 0.7, and 0.5 fmol were achieved for gramicidin S, arginine, and leucylalanine respectively. Future work will involve improving the ion transmission efficiency in the interface region, which should allow even lower detection limits.

In conclusion, the capabilities of a quadrupole ion trap storage/reflectron time-of-flight mass spectrometer combination have been demonstrated for detection of ions generated by liquid injection into an electrospray ionization source. The IT/reTOF can provide nearly 100% duty cycle in converting a continuous ion beam into a pulsed source for TOF. It is also shown that the storage capabilities of the device provide enhanced sensitivity and resolution as the storage time is increased. The detection limit of the device was also studied and found to be in the low femtomole regime.

#### ACKNOWLEDGMENT

We thank Bruce Thomson of Sciex for the loan of an electrospray source. This work received partial support from the National Science Foundation under Grant BIR-9223677.

RECEIVED for review April 15, 1993. Accepted June 29, 1993.\*

\* Abstract published in *Advance ACS Abstracts*, August 15, 1993.

(28) Fountain, S. T.; Lee, H.; Lubman, D. M. Unpublished results, 1992.

(29) Chambers, D. M.; Goeringer, D. E.; McLuckey, S. A.; Glish, G. L. *Anal. Chem.* 1993, 65, 14.

(30) Cooks, R. G.; Kaiser, R. E., Jr. *Acc. Chem. Res.* 1990, 23, 213.

(31) Cooks, R. G.; Williams, J.; Cox, K.; Kaiser, K.; Schwartz, J. *Rapid Commun. Mass Spectrom.* 1990, 4, 427.

# Ultrahigh Resolution Matrix-Assisted Laser Desorption/Ionization of Small Proteins by Fourier Transform Mass Spectrometry

John A. Castoro and Charles L. Wilkins\*

Department of Chemistry, University of California, Riverside, Riverside, California 92521

Recent research has demonstrated that matrix-assisted laser desorption/ionization (MALDI) is feasible for Fourier transform mass spectrometric analysis of biomolecules with masses in excess of 50 000 Da. Here, the effects of electrostatic deceleration times and laser energy upon mass resolution are reported. It is demonstrated that optimum deceleration times for singly-charged MALDI-generated protein ions ranging in mass from 2627 to 29 000 Da are a linear function of  $m^{1/2}$  when a 9.5-V decelerating potential is used. Furthermore, higher resolution is obtained with laser fluences close to the threshold for MALDI. Slow metastable decay of molecular ions in the absence of co-matrix is demonstrated for melittin and bovine insulin. It appears that the resolution enhancing effect of co-matrix may result from slowing molecular ion unimolecular decomposition rates sufficiently to allow infrared emission to compete with metastable decay, thus providing the requisite population of long-lived ions for high mass resolution. A spectrum of bovine insulin molecular ion with mass resolution of 30 000 is presented, together with several spectra of lower mass proteins with mass resolution in excess of 100 000. Detection of a doubly-charged carbonic anhydrase trimer ion with a mass of 87 000 Da is reported.

## INTRODUCTION

In recent years, there have been important advances in the mass spectrometric analysis of large thermally labile molecules. Widespread research employing electrospray ionization (ESI)<sup>1</sup> and matrix-assisted laser desorption/ionization (MALDI)<sup>2-4</sup> sources have extended the practical mass range above several hundred kilodaltons. As a result, there have been numerous applications of these promising new methods to mass spectral investigations of biomolecules and particularly to studies of proteins. Concurrently, there is great interest in improving the performance of the mass analyzers, including mass measurement accuracy, mass range, and resolution.

MALDI requires the use of matrices that absorb laser radiation at the wavelength used for desorption and has been used for analysis of proteins with masses >200 000 Da. A variety of wavelengths are suitable for desorption,<sup>5,6</sup> and

ultraviolet (UV),<sup>7-12</sup> visible (VIS),<sup>13-15</sup> and infrared (IR) radiation<sup>16,17</sup> have been employed for this purpose, with a variety of matrices. For example, 3-nitrobenzyl alcohol, nicotinic acid, 2,5-dihydroxybenzoic acid, and a number of cinnamic acid derivatives have been used for UV-MALDI. Solvent (water, benzene) matrices frozen by deposition on cryogenically cooled copper probes and a mixture of nitrobenzyl alcohol and rhodamine 6G have been used for VIS-MALDI, and nicotinic acid, glycerol, succinic acid, and urea have been successful for IR-MALDI.

The great majority of MALDI experiments thus far reported utilized the high mass detection capability of time-of-flight mass spectrometers (TOF-MS). Unfortunately, mass resolution obtainable for MALDI-TOF experiments rarely exceeds 1000.<sup>8</sup> On the other hand, Fourier-transform mass spectrometry (FTMS) is a demonstrated ultrahigh resolution technique<sup>18,19</sup> which has substantial potential as a tool for high resolution MALDI analysis of biomolecules. For this type of mass analyzer, theory suggests that an upper mass limit of at least  $m/z$  375 000 Da should be obtainable using a 2.54-cm cubic cell, 8-T spectrometer<sup>20</sup>. Accordingly, a number of researchers devoted considerable effort to coupling the extended mass range provided by MALDI with the high mass resolution capabilities of FTMS.<sup>21-23</sup> Initial MALDI-FTMS experiments for small peptides<sup>24,25</sup> and oligonucle-

(1) Whitehouse, C. M.; Dreyer, R. N.; Yamashita, M.; Fenn, J. *Anal. Chem.* 1985, 57, 675-679.

(2) Karas, M.; Bachmann, D.; Bahr, U.; Hillenkamp, F. *Int. J. Mass Spectrom. Ion Process.* 1987, 78, 53-68.

(3) Karas, M.; Hillenkamp, F. *Anal. Chem.* 1988, 60, 2299-2301.

(4) Tanaka, K.; Hiroaki, W.; Ido, Y.; Akita, S.; Yoshida, Y.; Yoshida, T. *Rapid Commun. Mass Spectrom.* 1988, 8, 151-153.

(5) Vertes, A.; Levine, R. D. *Chem. Phys. Lett.* 1990, 171, 284-290.

(6) Vertes, A.; Gijbels, R.; Levine, R. D. *Rapid Commun. Mass Spectrom.* 1990, 4, 228-233.

(7) Karas, M.; Bahr, U.; Hillenkamp, F. *Int. J. Mass Spectrom. Ion Process.* 1989, 92, 231-242.

(8) Spengler, B.; Cotter, R. J. *Anal. Chem.* 1990, 62, 793-796.

(9) Beavis, R. C.; Chait, B. T. *Anal. Chem.* 1990, 62, 1836-1840.

(10) Chan, T.-W. D.; Colburn, A. W.; Derrick, P. J. *Org. Mass Spectrom.* 1991, 27, 53-56.

(11) Zhao, S.; Somayajula, K. U.; Sharkey, A. G.; Hercules, D. M.; Hillenkamp, F.; Karas, M.; Ingendoh, A. *Anal. Chem.* 1991, 63, 450-453.

(12) Strupat, K.; Karas, M.; Hillenkamp, F. *Int. J. Mass Spectrom. Ion Process.* 1991, 111, 89-102.

(13) Nelson, R. W.; Rainbow, M. J.; Lohr, D. E.; Williams, P. *Science* 1989, 246, 1585-1587.

(14) Nelson, R. W.; Thomas, R. M.; Williams, P. *Rapid Commun. Mass Spectrom.* 1990, 4, 348-351.

(15) Cornett, D. S.; Duncan, M. A.; Amster, I. J. *Org. Mass Spectrom.* 1992, 27, 831-832.

(16) Overberg, A.; Karas, M.; Bahr, U.; Hillenkamp, F. *Rapid Commun. Mass Spectrom.* 1990, 4, 293-296.

(17) Overberg, A.; Karas, M.; Hillenkamp, F. *Rapid Commun. Mass Spectrom.* 1991, 5, 128-131.

(18) James, C. F.; Wilkins, C. L. *J. Am. Chem. Soc.* 1988, 110, 2687-2688.

(19) Beu, S. C.; Senko, M. W.; Quinn, J. P.; McLafferty, F. W. *J. Am. Soc. Mass Spectrom.* 1993, 4, 190-192.

(20) Russell, D. H. *Mass Spectrom. Rev.* 1986, 5, 167-189.

(21) Köster, C.; Kahr, M. S.; Castoro, J. A.; Wilkins, C. L. *Mass Spectrom. Rev.* 1992, 11, 495-512.

(22) Marshall, A. G.; Grosshans, P. B. *Anal. Chem.* 1991, 63, 215A-229A.

(23) Buchanan, M. V.; Hettich, R. L. *Anal. Chem.* 1993, 65, 245A-259A.

(24) Nuwaysir, L. M.; Wilkins, C. L. SPIE Proceeding No. 1437; SPIE: Bellingham, WA, 1991; pp 112-123.

(25) Hettich, R. L.; Buchanan, M. V. *J. Am. Soc. Mass Spectrom.* 1991, 2, 22-28.

otides<sup>26</sup> were relatively successful for detection of biomolecules with masses up to 3000 Da. However, until recently, efforts to extend the technique to analysis of such substances with higher masses were relatively unsuccessful. On the basis of TOF-MS experiments which demonstrated that ions generated by MALDI have significant translational energies that increase with increasing mass,<sup>27,28</sup> Beavis and Chait suggested that larger molecules might be difficult or impossible to trap in a FTMS, because of the low trapping potentials normally required for reliable spectral measurements. Use of collisional cooling of the MALDI-generated ions provided some mass range enhancement by removing excess energy, allowing the detection of bovine insulin ( $m/z = 5734$ ) and its dimer with  $m/z > 10\,000$ .<sup>29</sup> This is consistent with expectations, if the earlier TOF observations were relevant to FTMS conditions.

These observations prompted us<sup>30</sup> to investigate an experimental approach involving electrostatic deceleration of the ions generated by MALDI, minimizing the translational energy of the trapped ion population and permitting low voltage trapping in a FTMS cell. This technique employs a modification of the gated trapping method previously used for  $z$ -axis injection<sup>31</sup> of externally generated ions, but using a larger voltage applied to the rear trap plate (9.0 V, rather than 2.0 V), while maintaining the front trap plate at 0 V, resulting in a higher potential energy gradient. Low energy ions are ejected along the  $z$ -axis while ions with translational energies greater than 9.0 V pass through the cell or are neutralized by collision with the rear trapping plate. In this respect, the use of a decelerating potential is similar in effect to that of a kinetic energy band pass filter.<sup>32,33</sup> An additional advantage of this procedure, when the retarding potential is maintained for sufficient duration, is that higher velocity low mass ions can enter and exit the trap during the deceleration time, but lower velocity higher mass ions with the same kinetic energies are trapped. Therefore, ions are trapped as a function of both their  $z$ -axis translational energy and their  $z$ -axis velocity. Analytically, this has the advantage that there is discrimination against low mass contaminants and matrix-related ions, thus reducing chemical noise. Furthermore, because the dynamic range of the trap is limited,<sup>34</sup> trapping efficiency for the analyte ions is enhanced by trapping few unwanted matrix ions, thus avoiding interfering space-charge effects.

Use of the gated trapping decelerating potential approach allowed MALDI-FTMS measurements of poly(ethylene glycol) of 10 000, including oligomers with masses up to 14 000 Da, molecular ions of cytochrome *c* ( $m/z$  12 384), myoglobin ( $m/z$  17 000), trypsinogen ( $m/z$  24 000), and the dimer of myoglobin ( $m/z$  34 000).<sup>30</sup> However, although this technique was successful in coupling the extended mass range of MALDI with FTMS, the resolution obtained in the first experiments was disappointing (between 50 and 300). It was evident, particularly for the proteins, that metastable decomposition of molecular ions,  $[M + H]^+$ , formed in the gas phase during

the MALDI process,<sup>35</sup> limited molecular ion observation time, and as a consequence, precluded high mass resolution. Similar metastable decay behavior has been observed in MALDI-TOF-MS experiments.<sup>36</sup> To address this problem, the MALDI matrix was modified by the addition of a sugar co-matrix which minimized metastable decay and permitted mass resolution of 10 000–12 000 for bovine insulin ( $m/z$  5734), ubiquitin (from bovine red blood cells) ( $m/z$  8562), and cytochrome *c* (from horse heart) ( $m/z$  12 349).<sup>37</sup>

These experiments demonstrated the necessity of using low trapping potentials during the observation period to obtain high resolution MALDI-FTMS spectra. This is because high trapping potentials cause space-charge effects,<sup>38</sup> which perturb ion motion and reduce trapping efficiency, both of which degrade resolution. In an earlier effort to extend the range of trapping potentials available, we investigated the use of a "screened" electrostatic ion trap cell (first introduced by Wang and Marshall)<sup>39</sup> designed to minimize the trapping potential within the trap for analysis of high mass MALDI ions.<sup>40</sup> Resolution was indeed enhanced at high trapping voltages, but was not higher than mass resolution obtained with lower voltage trapping in the absence of screening potentials. Therefore, following a series of preliminary studies using the screened trap procedure, additional effort was directed toward more careful examination of MALDI-FTMS experimental parameters using a standard nonscreened dual cell cubic trap.

Here, the effects of electrostatic deceleration times and laser energy upon mass resolution are reported. It is demonstrated that optimum deceleration times for singly-charged MALDI-generated protein ions, ranging in mass from 2627 to 29 000 Da are a linear function of  $m^{1/2}$  when a 9.5-V decelerating potential is used. Furthermore, higher resolution is obtained with laser fluences close to the threshold for MALDI. Slow metastable decay of molecular ions in the absence of co-matrix is demonstrated for melittin and bovine insulin. It appears that the resolution-enhancing effect of co-matrix may result from further slowing of the molecular ion unimolecular decomposition rates, which is sufficient to allow IR emission to compete with metastable decay, thus providing the requisite population of long-lived ions necessary for high mass resolution. A spectrum of bovine insulin molecular ion with mass resolution of 30 000 is presented, together with several spectra of lower mass proteins with resolution in excess of 100 000. Detection of a doubly-charged carbonic anhydrase trimer with mass of 87 000 Da is reported.

## EXPERIMENTAL SECTION

**Instrumentation.** Experiments were performed using a Millipore-Extrel (Madison, WI) FTMS-2000 Fourier-transform mass spectrometer equipped with a 7-T superconducting magnet, differentially pumped  $1\frac{1}{8}$ -in. source and analyzer cubic cells separated by a 2-mm conductance limit, and an automatic solids probe. The FTMS is interfaced to a Lambda Physik (Göttingen Germany FL-2001) dye laser, pumped by a Lambda Physik EMG201-MSC excimer laser (operating at 308 nm, 180 mJ/28 ns pulse). All MALDI experiments employed the dye laser operating at 355 nm with a 0.6 g/L dioxane solution of 2,2'-dimethyl-*p*-quaterphenyl (BMQ, Lambda Physik), resulting in a maximum output energy of 5 mJ/pulse. The 355-nm laser light was grossly

(26) Hettich, R. L.; Buchanan, M. V. *J. Am. Soc. Mass Spectrom.* **1991**, *2*, 402–412.

(27) Beavis, R. C.; Chait, B. T. *Chem. Phys. Lett.* **1991**, *181*, 479–484.

(28) Pan, Y.; Cotter, R. J. *Org. Mass Spectrom.* **1992**, *27*, 3–8.

(29) Solouki, T.; Russell, D. H. *Proc. Natl. Acad. Sci. U.S.A.* **1992**, *89*, 5701–5704.

(30) Castoro, J. A.; Köster, C.; Wilkins, C. L. *Rapid Commun. Mass Spectrom.* **1992**, *6*, 239–241.

(31) Hofstadler, S. A.; Laude, D. A., Jr. *Int. J. Mass Spectrom. Ion Process.* **1990**, *101*, 65–78.

(32) Hofstadler, S. A.; Beu, S. C.; Laude, D. A., Jr. *Anal. Chem.* **1993**, *65*, 312–316.

(33) Lebrilla, C. B.; Anster, I. J.; McIver, R. T., Jr. *Int. J. Mass Spectrom. Ion Process.* **1989**, *87*, R7–R13.

(34) Limbach, P. A.; Grosshans, P. B.; Marshall, A. G. *Anal. Chem.* **1993**, *65*, 135–140.

(35) Wang, B. H.; Dreisewerd, K.; Bahr, U.; Karas, M.; Hillenkamp, F. *J. Am. Soc. Mass Spectrom.* **1993**, *4*, 394–398.

(36) Spengler, B.; Kirsch, D.; Kaufmann, R. *Rapid Commun. Mass Spectrom.* **1991**, *5*, 198–202.

(37) Köster, C.; Castoro, J. A.; Wilkins, C. L. *J. Am. Chem. Soc.* **1992**, *114*, 7572–7574.

(38) Jeffries, J. B.; Barlow, S. E.; Dunn, G. H. *Int. J. Mass Spectrom. Ion Process.* **1983**, *54*, 169–187.

(39) Wang, M.; Marshall, A. G. *Anal. Chem.* **1989**, *61*, 1288–1293.

(40) Castoro, J. A.; Köster, C.; Wilkins, C. L. *Anal. Chem.* **1992**, *65*, 784–788.

attenuated by an iris and finely attenuated by a fused silica variable attenuator, Model 935-5 (Newport Corp., Fountain Valley, CA). The resulting output energy was measured by a RLP-734 energy probe and a RJ-7610 energy radiometer (Laser Precision Corp., Utica, NY). The beam enters the mass spectrometer through a fused-silica window and is focused to a 500- $\mu\text{m}$ -diameter beam impinging upon a probe tip (incidence angle  $90^\circ$ ), which is positioned 1–2 mm from the source trap plate, by a 12.5-cm focal-length optical glass lens. This lens is mounted on a lens assembly attached to the analyzer flange, allowing the lens to be rotated out of the way when electron ionization or chemical ionization measurements are made. The laser output energy is fine-tuned by attenuation of the beam to obtain a power density of approximately  $10^6$ – $10^7$  W/cm $^2$ .

**Sample Preparation.** 2,5-Dihydroxybenzoic acid, DHB (Fluka Chemical Co., Buchs, Switzerland), was used as the matrix for all MALDI experiments. All biomolecules were purchased from Sigma Chemical Co. (St. Louis, MO). Samples were prepared by mixing a suitable quantity of 0.5 mmol/L analyte solution in 0.1% aqueous trifluoroacetic acid, TFA (Mallinckrodt Inc., St. Louis, MO) with a 50 mmol/L matrix solution (0.1% TFA in methanol). Where noted, the matrix was modified by the addition of a 50 mmol/L D-fructose (Aldrich Chemical Co., Milwaukee, WI) co-matrix methanol solution. The molar ratios are reported with each spectrum. The MALDI solutions were sprayed as aerosols onto a rotating stainless steel probe tip for homogenous deposition.

**Spectral Measurements.** MALDI spectra were obtained using both the source cell and the analyzer cell. A simple experimental sequence was used with the typical quench, ionization, ion excitation, and image current detection events. The uniqueness of the experiment involves the careful timing of a deceleration potential allowing the minimization of  $z$ -axis translational energy of the MALDI-generated ions for subsequent low potential field trapping. The duration of this switching from deceleration to trapping potential is controlled during the ionization event. For source cell detection, the probe and the front trap plate of the source cell are held at ground potential while the rear trap plate (conductance limit) is held at 9 V, during the ionization event. The deceleration time after firing the laser is varied between 10 and 600  $\mu\text{s}$  and is optimized for each sample. Following this event, the potentials of the front and rear trapping plates are adjusted to final trapping voltages, between 0.2 and 3 V. This takes approximately 30  $\mu\text{s}$ . For high resolution measurements, a 200–1000-ms delay was imposed (following the application of the trapping potential) so that laser-desorbed neutrals can be pumped away and to permit analyte ions to relax to the center of the cell and equilibrate within the trap. A similar experimental sequence is employed for analyzer cell detection. For this detection mode, the probe tip, source trap plate, and conductance limit are all held at ground potential while the analyzer rear trap plate is maintained at 9 V during the MALDI. The total experiment time is increased, to allow the time necessary for desorbed ions to traverse the source cell and enter the analyzer cell where they are electrostatically decelerated and trapped. Thus, for source cell detection, melittin ions are decelerated by holding the conductance limit at 9 V for 80  $\mu\text{s}$  after the desorption event while for analyzer cell detection, the analyzer rear trap plate is held at 9 V for 190  $\mu\text{s}$  after the desorption event. In general, the highest resolution is obtained by using analyzer heterodyne detection.

**Data Processing.** For a typical scan, 200-V peak-to-peak frequency sweep excitation was applied from 1 to 200 KHz with a 200 Hz/ $\mu\text{s}$  sweep rate and source cell direct mode detection. Low resolution data, including those for the deceleration timing study and the carbonic anhydrase spectrum, were obtained using a 3-V trapping potential and averaging 10–30 time-domain data set of 32 768 data points at a data acquisition rate of 1 MHz. For the laser desorption energy fluence studies of metastable decay of insulin and melittin a 2-V trapping potential was used, averaging the 16 time-domain data sets of 32 768 data points acquired with a 200-kHz bandwidth. Background pressure was maintained at  $3\text{--}4 \times 10^{-8}$  Torr. High resolution insulin data were obtained using similar conditions but with data acquired for 2.2 s while maintaining trapping voltages between 0.2 and 0.6 V. High resolution heterodyne detection was performed in the

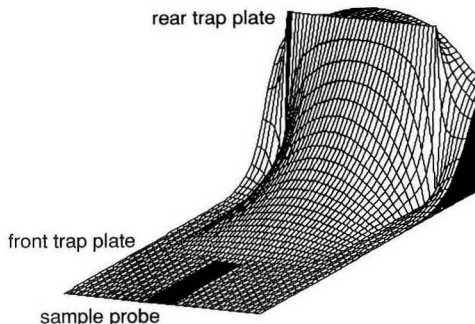


**Figure 1.** MacSimion plot of cubic FTMS cell electric field with a 9.0-V rear trap plate potential and a 0-V front trap plate potential.

analyzer cell. The spectrum of gramicidin S was measured using 0.2 V for trapping, a reference frequency (REF) of 93.7 KHz, and a bandwidth (BWI) of 6.25 KHz. Spectral data were acquired for a single 5.25-s transient. The high resolution spectrum of  $\alpha$ -melanocyte stimulating hormone was acquired using 0.4-V trapping, with REF = 72.3 KHz and BWI = 10 KHz. A single 65 536 data point transient 3.28 s in duration was obtained. For melittin, the trapping voltage was 3 V, REF = 41 KHz, and BWI = 20 KHz. The time-domain data were obtained by ensemble-averaging 13 1072 data points obtained over a 3.28-s transient for each of four laser shots. To obtain frequency domain mass spectra, each data set was augmented by an equal number of zeros and baseline-corrected prior to magnitude-mode Fourier transformation. No apodization was used. Sodium-cationized poly(ethylene glycol) 1000 was used as an external calibrant, with the same trapping voltage, trapping cell, and excitation conditions as the analyte. The Extrel-supplied isotopic distribution program (IDP) was used to calculate theoretical isotopic distributions. Resolution in all cases is estimated from the ratio of peak position to peak width at half-height.

## RESULTS AND DISCUSSION

A high voltage decelerating potential applied to the rear trap plate of the trapped ion cell permits trapping of ions with high  $z$ -axis translational energies. This is possible because of the high electric field gradient the desorbed ions encounter when they enter the cell. Figure 1 is a SIMION<sup>41</sup> plot of the cell and probe potentials under deceleration conditions. When the mass dependence of the optimum deceleration time (following desorption and prior to restoration of normal trapping potentials for mass spectral measurements) is examined, the results shown in Figures 2 and 3 are obtained. For this set of experiments, using a 9.5-V decelerating potential, the molecular ion abundances of a series of proteins ranging in mass from 2627 to 29 000 Da were determined as a function of deceleration time. The data in Figure 2 show that molecular ion abundances for each compound rise, pass through a maximum (at the optimum time), and fall as the deceleration time is increased. The duration of the optimal time increases as molecular mass increases. Furthermore, when that optimum time is plotted versus the square root of mass (Figure 3), a linear dependence is seen, indicating that ion flight time is an important parameter. At first, this might seem to contradict the reported observations of common velocities for MALDI-generated ions,<sup>28,29</sup> however, it does not because the trapping method used here discriminates against ions with energies greater than the decelerating potential and, as a consequence, results in sampling different portions of the velocity distributions

(41) McGilvery, D. C.; Morrison, R. J. S.; MacSimion, Version 2.0, Montech Pty. Ltd., Victoria, Australia.

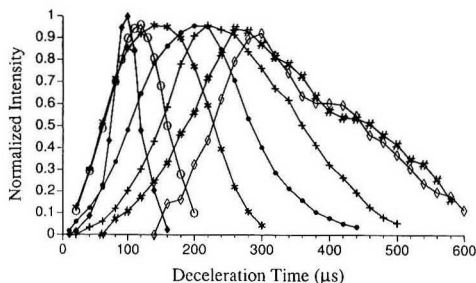


**Figure 2.** Normalized molecular ion abundance as a function of 9.5-V deceleration time for spectra obtained using 1:1000 molar ratio of analyte to 2,5-dihydroxybenzoic acid. A three-point smooth was applied to each plot. (◆) insulin a chain ( $m/z$  2627); (○) bovine insulin ( $m/z$  5734); (\*) ubiquitin ( $m/z$  = 8562); (●) cytochrome *c* ( $m/z$  12 385); (+) myoglobin ( $m/z$  17 000); (#) trypsin ( $m/z$  24 000); (◇) carbonic anhydrase ( $m/z$  29 000).

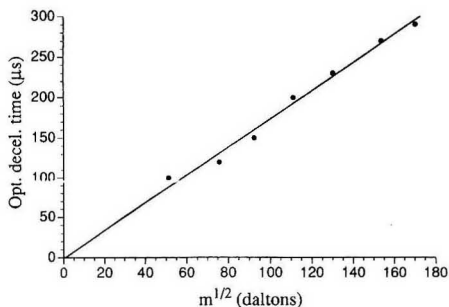


**Figure 3.** Optimum deceleration time ( $\mu$ s) for observation of the molecular ion of each compound in Figure 1 as a function of the square root of the ion mass (daltons).

for molecular ions of different mass. From an experimental standpoint, Figure 2 provides a useful guide for the selection of appropriate deceleration times (between ca. 100 and 300  $\mu$ s) for ions with masses from 2000 to 29 000 Da. For unknowns, it is evident that deceleration times should be varied in steps of at least 100  $\mu$ s, when one searches for molecular ion signals.

**Extended MALDI-FTMS Mass Range.** These low resolution experiments establish that the gated-trapping decelerating potential method we reported last year<sup>30</sup> does make possible significant extension of the practical mass range for laser desorption FTMS. Figure 4, which is a MALDI-FTMS positive ion spectrum obtained from a carbonic anhydrase sample using a DHB matrix, documents the highest mass ions yet observed by laser desorption in an FTMS. In this spectrum, in addition to the expected carbonic anhydrase molecular ion ( $m/z$  29 000) and a singly-charged dimer ion ( $m/z$  58 000), a doubly-charged trimer ion (87 000 Da,  $m/z$  43 500) is detected. The relative spectral abundances of these three ions is related to choice of deceleration time. Longer deceleration times favor trapping a greater abundance of the slower moving singly-charged dimer ions, while shorter deceleration times favor trapping more of the singly-charged molecular ion and the doubly-charged trimer, which are expected to have similar higher velocities under the experimental conditions.

**Factors Affecting Mass Resolution.** Although Figures 2 and 4 document extended mass range, the spectra from which the data in Figure 2 are derived show uniformly poor

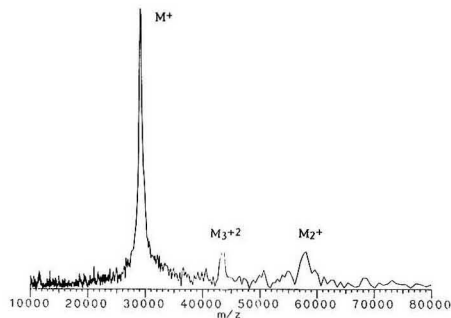


**Figure 4.** UV-MALDI-FT mass spectrum of carbonic anhydrase with a 1:5000 molar ratio of carbonic anhydrase to 2,5-dihydroxybenzoic acid matrix.

mass resolution (typically, between 50 and 300) which is worse than that routinely available with TOF-MALDI. This low resolution results from rapid damping of the transient ion signal during data acquisition, as resolution is strictly limited by observation time. There are several possible explanations for such signal damping: (a) signals could be damped by collisional relaxation; (b) ion signal could diminish as a result of trapping losses by a number of mechanisms; (c) ions could be lost due to unimolecular metastable decay with rates sufficiently rapid to preclude prolonged observation. Because cell pressures were maintained at  $10^{-8}$  Torr or less during mass spectral detection, collisional relaxation can be ruled out. Observation of metastable decay for MALDI of both insulin and melittin molecular ions is not unprecedented and has been observed in MALDI-TOF-MS.<sup>36</sup> Metastable fragmentation of bovine insulin ions produced by <sup>252</sup>Cf plasma desorption<sup>42</sup> and by fast atom bombardment<sup>43</sup> has also been reported. More recently, Ngoka and Lebrilla<sup>44</sup> reported the relatively slow metastable decay of protonated oligosaccharide molecular ions detected by FTMS, with half-lives on the order of several milliseconds. Metastable decay rates with half-lives on the order 10 ms or less, as reported here, are consistent with the RRKM theory<sup>45</sup> which suggests a general increase in fragmentation time as molecular size and the number of vibrational degrees of freedom of a molecule increases.

**Metastable Decay of Molecular Ions.** To test whether metastable decay is responsible for low mass resolution, a series of time-resolved measurements of bovine insulin and melittin were carried out. In these experiments, the delay between trapping desorbed ions and measuring their spectra was systematically varied. In this way, metastable decay of molecular ions could be observed by monitoring decreases in molecular ion abundances with concurrent increases in fragment ion abundances. In addition, the approximate half-life of this process can be estimated. Figure 5 shows low resolution time-resolved spectral data for melittin and bovine insulin. These data are consistent with the metastable decay mechanism, as there is a clear time-dependent increase of fragment ion abundances at the expense of molecular ion abundance. Figure 6 contains kinetic plots for MALDI of this sample, which contained both melittin and insulin in the presence of a 2000-fold molar excess of 2,5-dihydroxybenzoic

(42) Chait, B. T.; Field, F. H. *Int. J. Mass Spectrom. Ion Process.* 1985, 65, 169-180.

(43) Barber, M.; Bordoli, R. S.; Elliot, G. J.; Tyler, A. N.; Bill, J. C.; Green, B. N. *Biomed. Mass Spectrom.* 1984, 11, 182-186.

(44) Ngoka, L.; Lebrilla, C. B. *J. Am. Soc. Mass Spectrom.* 1993, 4, 210-215.

(45) Bunker, D. L.; Wang, F.-M. *J. Am. Chem. Soc.* 1977, 99, 7457-7459.



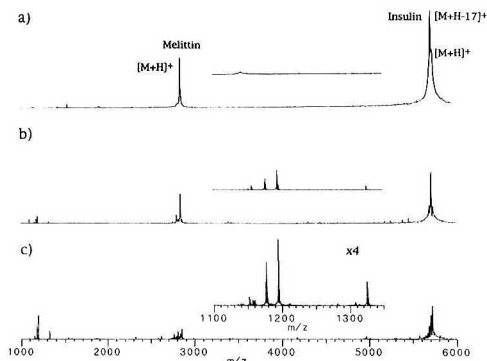


**Figure 5.** Time-resolved MALDI-FT mass spectra for melittin and insulin obtained using a 1:1:2000 molar ratio of melittin to insulin to 2,5-dihydroxybenzoic acid: (a) 0-ms delay after desorption and before observation; (b) 10-ms delay; (c) 100-ms delay. Expanded mass and ion abundance scale insets show growth of fragment ion abundances.

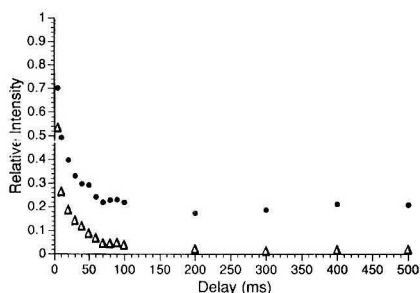


**Figure 6.** Kinetic plot of molecular ion abundance for melittin and bovine insulin as a function of delay time following MALDI.

acid. The data were obtained by stepwise variance of the delay between firing the laser and acquiring the spectra. Particularly significant for melittin is the observation that the relative molecular ion abundance appears to reach a steady state, which does not decline with delays longer than the minimum required to reach that relative abundance. Unimolecular rate constants were calculated from semilog plots of relative molecular ion abundances ( $[M + H]^+$  ions) versus delay after firing the laser. These rate constants are  $62 \text{ s}^{-1}$  for melittin and  $98 \text{ s}^{-1}$  for insulin (half-lives of 11 and 7 ms, respectively).

**Effects of Laser Power.** In order to obtain further evidence of the role of metastable decay when low resolution spectra of insulin are measured, the dependence of mass resolution upon laser power was investigated. Because metastable fragmentation occurs as a result of excess energy deposited into molecular ions during the desorption process, it is logical to predict that laser power levels and/or matrix ratios would affect the rates of such reactions. Table I summarizes these results. When spectra of an insulin/DHB (1:1000) sample are acquired after 100 ms of trapping following laser desorption, molecular ion lifetimes and mass resolution increase as laser power is decreased. Thus, no molecular ions are observed for laser pulse energies above 2.0 mJ, but high resolution spectra are obtained with energies just above threshold for MALDI (1.25 mJ in this case). Figure 7a is the high resolution MALDI-FTMS spectrum of bovine insulin using a 1.5 mJ laser pulse and trapping the molecular ion species for more than 2 s. In this spectrum, average resolution

**Table I.** Comparison of Relative Abundances of Bovine Insulin Molecular Ion and Most Abundant Fragment Ion for MALDI Using 2,5-Dihydroxybenzoic Acid Matrix and Mixed 2,5-Dihydroxybenzoic Acid, D-Fructose Matrix for Range of Laser Pulse Energies

matrix ratio <sup>a</sup>	energy (mJ)	$[M + H]^+$	$[M + H - 17]^+$	abundance ratio <sup>b</sup>
1:10000:0	2.3	0	0.62	0
	2.0	0	1.00	0
	1.5	0.32	0.63	0.51
	1.3	0.05	0.13	0.41
1:1000:1000	4.0	0.45	0.90	0.51
	3.0	0.98	1.00	0.98
	2.3	0.73	0.65	1.12
	1.5	0.04	0.06	0.71

<sup>a</sup> Molar ratio, insulin:2,5-dihydroxybenzoic acid D-fructose. <sup>b</sup> Ratio  $[M + H]^+$  to  $[M + H - 17]^+$ .

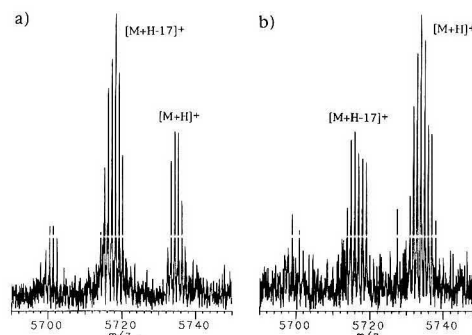
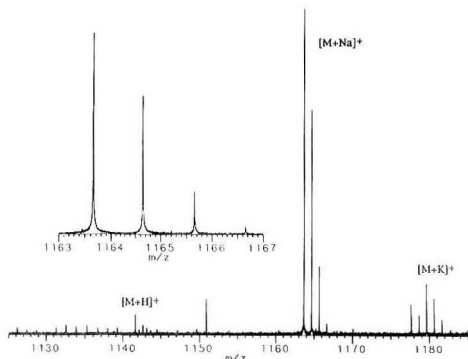


**Figure 7.** High resolution UV-MALDI-FT mass spectra of bovine insulin: (a) obtained using a 1:1000 insulin to 2,5-dihydroxybenzoic acid ratio and 1.5 mJ laser energy, (b) obtained using a 1:1000:1000 insulin to 2,5-dihydroxybenzoic acid to D-fructose ratio and 2.3 mJ laser energy.

of 27 300 is obtained for the isotopic multiplet of the protonated molecular ion, with mass measurement error of 0.01 % for the most abundant of those ions (those containing three  $^{13}\text{C}$  atoms).

**Use of Sugar Co-Matrix.** In view of these results, we conclude that short molecular ion lifetimes and consequent low mass resolution result primarily from metastable decay induced by deposition of excess energy during the MALDI process. Lowering the laser fluence is one means of obviating this effect. An alternative means is to alter the MALDI matrix by the addition of a volatile co-matrix which might pyrolyze during the desorption event and produce a momentary high pressure of small molecules that could cool the desorbing analyte species, rendering it less likely to decompose. Accordingly, following an earlier suggestion by Beavis and co-workers,<sup>46</sup> the effect of modifying the MALDI matrix by the addition of sugars was investigated. For their infrared desorption experiments, they suggested that the sugar in the sample pyrolyzed at a lower temperature than the analyte, thereby decreasing the temperature of desorption. In our laboratory, for UV-MALDI-FTMS, fructose was found to be an effective co-matrix, making possible high mass resolution. This was demonstrated by obtaining unit mass resolution mass spectra of insulin, ubiquitin, and cytochrome *c*.<sup>37</sup> We suggested that the function of the sugar co-matrix might be to collisionally cool the desorbing proteins. The results in

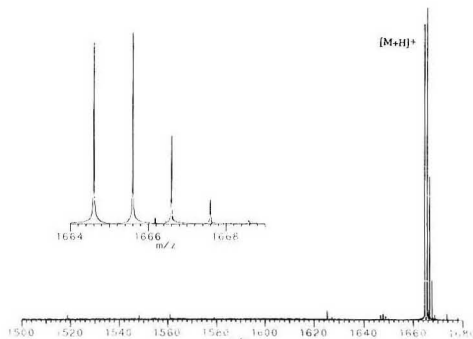
(46) Beavis, R. C.; Lindner, J.; Grottemeyer, J.; Schlag, E. W. *Chem. Phys. Lett.* 1988, 146, 310-313.



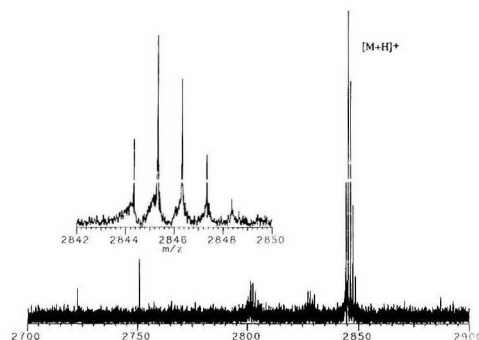
**Figure 8.** UV-MALDI-FT heterodyne analyzer cell mass spectrum of gramicidin S obtained using a 1000-fold molar excess of 2,5-dihydroxybenzoic acid matrix. Inset shows the sodium-attached gramicidin S molecular ion isotopic multiplet.

Table I for a sample comprised of a 1:1000:1000 molar ratio of insulin:DHB:D-fructose show the dramatic effect of this matrix modification. With this change in the matrix, molecular ions can be detected even following a 1-s delay after desorption. Furthermore, laser pulse powers as high as 4 mJ still result in the observation of molecular ions after a 1-s delay. However, the highest mass resolution is still obtained for laser pulse powers just above the desorption threshold for MALDI. Figure 7b is the high resolution MALDI-FTMS spectrum of bovine insulin in the presence of co-matrix using a 2.3 mJ laser pulse and trapping molecular ion species for more than 2 s. In this spectrum, average resolution of 24 100 is obtained for the isotopic multiplet of the protonated molecular ion, with mass measurement error of 0.005% for the most abundant of those ions (three  $^{13}\text{C}$ ).

**Ultrahigh Mass Resolution.** For smaller peptides, which seem to desorb with lower excess energy, it is possible to obtain exceptionally high mass resolution by careful attention to experimental details. For example, MALDI-FTMS of oxidized insulin b chain was obtained with molecular ion resolution of 24 000 and a potassium-attached lysine-loss fragment of the octapeptide Val-His-Leu-Thr-Pro-Val-Glu-Lys with an average resolution of the isotopic multiplet of 141 000.<sup>47</sup> Figures 8 and 9 show the molecular ion regions of MALDI-FTMS spectra of gramicidin S and  $\alpha$ -melanocyte stimulating hormone obtained using a 9-V deceleration potential and heterodyne analyzer cell detection. The spectrum in Figure 8 shows an inset of the sodium-adduct molecular ion region of the spectrum with a resolution of 153 000 and a 0.005% mass measurement error for the all  $^{12}\text{C}$  isotope-containing ion. The relative isotopic abundances of 100:69:21:4 agree qualitatively with the theoretical values of 100:73:28:7. The  $\alpha$ -MSH spectrum in Figure 9 contains an inset with an expanded scale plot of the molecular ion region showing average resolution of 131 000 for the three most abundant ions of the isotopic multiplet and a 0.013% mass error for the all  $^{12}\text{C}$  isotope-containing ion. The relative isotopically substituted molecular ion abundances of 95:100:46:13:2 are also in qualitative agreement with the theoretical values of 100:97:54:22:6. When fructose co-matrix is added, equally good or better results are obtained. The high resolution mass spectrum of melittin is shown in Figure 10, where an average resolution of 99 300 was obtained for the



**Figure 9.** UV-MALDI-FT heterodyne analyzer cell mass spectrum of  $\alpha$ -melanocyte stimulating hormone using a 1000-fold molar excess of 2,5-dihydroxybenzoic acid matrix. Inset shows the proton-attached  $\alpha$ -MSH molecular ion isotopic multiplet.



**Figure 10.** UV-MALDI-FT heterodyne analyzer cell mass spectrum of melittin using a 1:3000:3000 analyze:DHB:D-fructose molar ratio. Inset shows the proton-attached melittin molecular ion isotopic multiplet.

four most abundant ions in the isotopic multiplet with a mass measurement error of 0.05% for the most abundant ion species, containing a single  $^{13}\text{C}$  isotope. Here, too, the experimental values of 46:100:78:38:15 are in qualitative agreement with the theoretical relative abundances of 60:100:86:51:23. This spectrum was obtained from a sample with a 1:3000:3000 molar ratio of melittin:DHB:D-fructose using a higher than usual trapping voltage of 3 V. Finally, because MALDI-FTMS has recently been employed for off-line analysis of capillary electrophoresis effluents,<sup>48</sup> it was useful to determine whether high buffer salt concentrations would compromise the ability to obtain high resolution mass spectra. Figure 11 is the partial MALDI-FT mass spectrum obtained from a sample comprised of a 1:1000:1000:100 molar ratio of insulin:DHB:D-fructose:NaHCO<sub>3</sub>. Here, the addition of sodium bicarbonate to the matrix has resulted in formation of abundant molecular ion adducts containing one, two, or three sodium atoms, in addition to the protonated molecular ion. However, these reactions do not adversely affect the stability of the resulting species; mass resolution of 32 000 is obtained.

**Disposal of Excess Energy.** Considering these results, it seems likely that the factor which controls experimental mass resolution for proteins generated by MALDI and observed with the FTMS is the excess energy deposited in

(47) Castoro, J. A.; Wilkins, C. L. In *Lasers and Optics in Surface Analysis*; SPIE Proceeding No. 1857; SPIE: Bellingham WA, 1993; pp 51-59.

(48) Castoro, J. A.; Chiu, R. W.; Monnig, C. A.; Wilkins, C. L. *J. Am. Chem. Soc.* **1992**, *114*, 7572-7574.

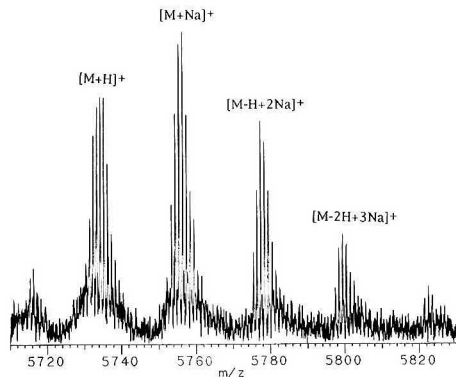


**Figure 11.** UV-MALDI-FT source cell direct mode MALDI-FT mass spectrum of bovine insulin, obtained using a 1:1000:1000:100; analyte: DHB:D-fructose:NaHCO<sub>3</sub> molar ratio.

the molecular ion during the desorption process. There is evidence from the data reported for both melittin and bovine insulin that excess energy can be controlled by the adjustment of laser fluence or modification of the matrix. For these and other proteins and peptides with masses less than 6000 Da, high resolution can be obtained with or without a co-matrix. In general, higher laser powers can be used and better sensitivity can be obtained for this category of compounds if fructose is added to DHB as a mixed matrix.

From the time-resolved metastable decay studies, which establish that molecular ion abundances approach a steady state at longer delay times, it seems that there may be

competition between two mechanisms for energy loss. Because the molecular ions are trapped under collision-free conditions, they may either undergo metastable decay, as demonstrated here or, alternatively, may dispose of excess energy by infrared emission, with rate constants ( $k_a$ ) of the same order of magnitude as those for metastable decay ( $k_m$ ).<sup>49,50</sup> Experimental changes, such as changing the laser power or modifying the matrix, can have differential effect on reaction rates and, therefore, the ratio  $k_a/k_m$ . Obviously, even if ions are generated with excess energy, high mass resolution should be possible if  $k_a/k_m$  can be made large enough.

## CONCLUSIONS

The present results demonstrate that, under certain experimental conditions, excess energy deposition during the MALDI process plays an important role in limiting attainable FTMS molecular ion mass resolution for small proteins. This is a consequence of metastable decay processes with half-lives of ca. 10 ms or less. However, with the proper choice of matrix and laser power, it is possible to obtain ultrahigh mass resolution for proteins with masses less than about 6000 Da and nearly unit mass resolution for proteins as large as cytochrome c. Thus, it seems likely that it will be possible to develop strategies for obtaining high mass resolution by MALDI-FTMS of even larger biomolecules by using techniques which can remove excess energy of laser-desorbed ions. One possible approach would be to use collisional methods, combined with quadrupolar excitation, as recently demonstrated by both Marshall and Amster and co-workers.<sup>51,52</sup>

## ACKNOWLEDGMENT

We thank I. Jon Amster for providing a preprint of ref 52 reporting his group's work on quadrupolar excitation. Support from NIH Grant GM-44606 and NSF Grant CHE-92-01277 is gratefully acknowledged.

RECEIVED for review May 18, 1993. Accepted July 13, 1993.\*

\* Abstract published in *Advance ACS Abstracts*, September 1, 1993.

(49) Van de Guchte, W. J.; Van der Hart, W. J.; de Koning, L. J.; Nibbering, N. M. M.; Dunbar, R. C. *Int. J. Mass Spectrom. Ion. Process.* **1993**, *123*, 11–17.

(50) Huang, F. S.; Dunbar, R. C. *Int. J. Mass Spectrom. Ion. Process.* **1991**, *109*, 151–170.

(51) Schweikhard, L.; Guan, S.; Marshall, A. G. *Int. J. Mass Spectrom. Ion. Process.* **1992**, *120*, 71–83.

(52) Speir, J. P.; Groman, G. S.; Pitsenberger, C. C.; Turner, C. A.; Wang, P. P.; Amster, I. J. *J. Anal. Chem.* **1993**, *65*, 1746–1752.

# On-Line Fermentation Process Monitoring of Carbohydrates and Ethanol Using Tangential Flow Filtration and Column Liquid Chromatography

Torbjörn A. Buttler,\* Kristina A. J. Johansson,<sup>†</sup> Lo G. O. Gorton, and György A. Marko-Varga

Department of Analytical Chemistry, University of Lund, P.O. Box 124, S-221 00 Lund, Sweden

This paper describes a fully automated on-line system for the unattended monitoring of bioprocesses. Removal of solids and macromolecules from fermentation broth is achieved with a tangential flow filtration unit (Waters Filter/Acquisition Module). The obtained filtrate is transported in a flow system to a cleanup step, based on solid-phase extraction, followed by introduction into a column liquid chromatographic system. Carbohydrates are then detected by refractive index and ethanol content using a laboratory-made selective amperometric alcohol biosensor. Data acquisition and processing, as well as switching of the system valves, are performed by a computer. The on-line system was used for continuous monitoring of five carbohydrates and ethanol during 24-h ethanol fermentations. Waste water from the Swedish pulp industry was used as the technical substrate. Typical RSD values of the entire setup were on the order of 5–6% over a 24-h period of operation.

## INTRODUCTION

Total utilization of biomass is very important from environmental, industrial, and agricultural points of view. As an energy source, it could be utilized to a much greater extent if proper technological solutions could be developed. New environmental regulations introduced worldwide have put greater pressure on industrial waste treatments. These facts have been realized by pulp industries in both Europe and North America; effort and research are being invested in a search for more efficient plants where environmental aspects are taken into consideration. Waste water from pulp industries has been utilized as a technical fermentation medium for ethanol production<sup>1</sup> in this context. This is an especially interesting alternative, due to the restricted oil reserve, because ethanol could be used as an alternative energy source, e.g., as fuel for cars.

Waste waters from paper pulp plants contain lignocellulose, a soluble fraction originating from the hydrolyzed wood. The lignocellulose consists of both high and low molecular weight components with a very complex composition. The hemi-cellulose part of this waste comprises high levels of carbohydrates, poly-, oligo-, and monosaccharides (both hexoses and pentoses) that can be used as the carbon source in bioprocess production of ethanol. This fraction is also known to contain high levels of breakdown products of lignin, such as phenolic derivatives and related aromatic compounds,

which may act as inhibitors in the bioprocess. The exact composition is not really known and may vary significantly depending on small changes in the industrial process.

A collaborative project at the Chemical Center, University of Lund, has been for several years occupied in finding new and more economical ways to use both technical substrates and solid wood as substrates for ethanol production. The main ideas are the following:

(1) Find technical solutions for chemical and enzymatic hydrolysis of solid wood from fast-growing energy woods like *Salix caprea* and/or use waste water from the pulp industry.<sup>2,3</sup> Enzymatic hydrolysis is preferable since it gives a less complex composition of the liquefied wood.<sup>3,4</sup> The key factors, i.e., origin, production, and reuse of the enzyme, have to be taken into consideration.

(2) Highly efficient microorganisms with the ability to withstand high inhibitory levels present in these substrates are needed.<sup>5</sup> Only *Saccharomyces* strains can withstand the toxic environment, but they are unable to ferment pentoses to ethanol.

(3) Mechanistic studies of pentose fermentations are therefore necessary for increased efficiency of the overall process. *Saccharomyces* yeasts can be made to ferment both hexoses and pentoses to ethanol by gene cloning.<sup>6</sup>

(4) On-line analysis systems are developed for monitoring the processes described above. Methods giving a high degree of selectivity are needed in the types of fermentations where complex substrates are used.

Today, there is a great need to follow bioprocesses on-line by analyzing the content of the substrate (most often various sugars), intermediates, and products. On-line analysis is done to recognize and optimize the process. Once the process is optimized, on-line process monitoring can be used for feedback control of, for example, carbon source supply, regulation of molecular oxygen, or pH control. All of these steps are performed to achieve maximum product yield. The monitoring system can also be used as an "alarm" control for infections by measuring compounds that might be used as markers in the process.<sup>7,8</sup>

Lately, there has been rapid development in on-line analysis of biotechnological processes with regard to sampling and its coupling to column liquid chromatography (CLC) and flow

<sup>†</sup> Current address: Department of Analytical Chemistry, Astra Draco AB, P.O. Box 34, S-221 00 Lund, Sweden.

(1) Lindén, T.; Hahn-Hägerdal, B. *Enzyme Microb. Technol.* 1989, 11, 583–89.

(2) Lindén, T.; Peetre, J.; Hahn-Hägerdal, B. *Appl. Environ. Microbiol.* 1992, 58, 1661–9.

(3) Eklund, R.; Galbe, M.; Zacchi, G. *J. Wood Chem. Technol.* 1988, 8, 379–92.

(4) Eklund, R.; Galbe, M.; Zacchi, G. *VIII Int. Symp. Alc. Fuels*, Tokyo, November 13–16, 1988; pp 101–5.

(5) Clark, T. A.; Mackie, K. L. *J. Chem. Technol. Biotechnol.* 1984, 34B, 101–10.

(6) Hallborn, J.; Walfridsson, M.; Ajraskinen, U.; Ojamo, H.; Hahn-Hägerdal, B.; Penttilä, M.; Keränen, S. *Biotechnology* 1991, 9, 1090–5.

(7) Sonesson, A.; Larsson, L.; Fox, A.; Westerdaal, G.; Odham, G. *J. Chromatogr.* 1988, 431, 1–15.

(8) Elmroth, L.; Valeur, A.; Odham, G.; Larsson, L. *Biotechnol. Bioeng.* 1992, 35, 787–92.

(9) Håkanson, H.; Nilsson, M.; Mattiasson, B. *Anal. Chim. Acta* 1991, 249, 61–5.

injection (FI).<sup>9,10</sup> Most often, on-line configurations are used, although automated off-line configurations have also appeared. The fermentation times vary depending on the type of process, but typically last 1–7 days using microorganisms and may last for several months using mammalian cells. This, of course, puts completely different requirements on the analytical setup. For shorter fermentations, the setup may be sufficient under aseptic conditions, for example, in ethanol fermentations using *Saccharomyces cerevisiae*, where keeping the pH below 6 will avoid contamination from bacterial growth. In longer fermentation runs, this approach is not possible; therefore, sampling sterility and the risk of infections become key factors to consider.

The sample drawn by the sampling unit is often analyzed by FI and/or CLC. The number of FI applications has grown rapidly over the last few years.<sup>11</sup> This is also reflected in the number of papers using this technique for bioprocess monitoring. One of the first reports on the use of FI for this purpose was published in 1984 by Kroner and Kula<sup>12</sup> and was later followed by several others.<sup>13–16</sup> Recently, FI was used for the determination of a variety of analytes.<sup>17–19</sup> Earlier papers included the determination of ethanol<sup>13</sup> and lactose, galactose, and lactate.<sup>20</sup>

The number of enzyme-based detection systems has increased rapidly with both FI and CLC techniques. However, since FI is not a separation method, only one component at a time is usually determined. When several substrates (for which the enzyme is active) are present in the sample, a signal reflecting the sum will result. Some research groups have specialized in multicomponent FI analysis using immobilized enzyme reactors (IMERs) in multiple flow lines<sup>21,22</sup> or a parallel setup.<sup>23,24</sup> However, when the separation of a number of solutes is required for complex samples, CLC is the most commonly used technique. A number of different substances have been monitored using enzyme-based detection, e.g., glucose and ethanol<sup>25,26</sup> and different carbohydrates.<sup>27</sup> Coupled methods have also appeared, e.g., multichannel FI in combination with on- and off-line CLC,<sup>28</sup> and also a FI system coupled to tandem MS.<sup>29</sup>

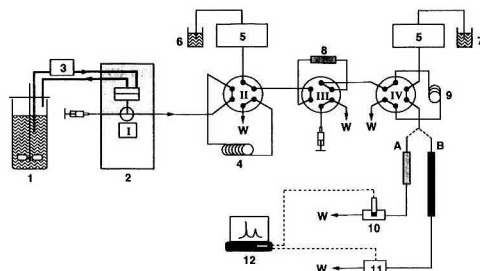


**Figure 1.** Schematic illustration of the experimental setup: (1) bioreactor, (2) sampling unit (Waters filter/acquisition module), (3) peristaltic pump, (4) sampling loop, (5) LC pump, (6) eluent for the flow system, (7) mobile phase for the chromatographic system, (8) cleanup column, (9) analytical loop, (10) alcohol biosensor, (11) refractive index detector, and (12) data collection and processing; (A and B) analytical columns for ethanol and carbohydrate analyses, respectively; (W) waste; (I–IV) switch valves.

Selectivity for on-line process monitoring in a CLC system can be introduced before or after the analytical separation. In the first case, this can be done in a sample cleanup step, e.g., by sterile membrane filtration and/or solid-phase extraction (SPE). In the second case, selective detection is often made in a chemical or biochemical derivatization step after the separation column.<sup>30</sup> In the field of catalytic reaction detection, most attention has been focused on immobilized enzymes over the years.<sup>31–33</sup>

In a previous paper,<sup>34</sup> we reported on the characterization and optimization of a tangential flow filtration unit and its use as a sampling device in small-scale fermentations. This paper deals with the integration of this unit, Waters filter/acquisition module (FAM), into a fully automated on-line monitoring system. A CLC setup is described, including precolumn sample cleanup and postcolumn enzyme-based detection of ethanol. Each part in the system was individually optimized and then pieced together. Five carbohydrates and ethanol were then monitored during 24-h ethanol fermentation processes.

## EXPERIMENTAL SECTION

**Apparatus.** The entire experimental setup is shown in Figure 1. It consists of the sampling unit (denoted 2 in Figure 1), Waters (Millipore, Milford, MA) filter/acquisition module (FAM), containing a tangential flow filtration module and an electrically driven six-port injection valve (Rheodyne Model 7045, Cotati, CA; II in Figure 1), on which a 100- $\mu$ L sampling loop (4 in Figure 1) was placed. Membranes from Millipore (MF and Durapor, pore sizes 0.22 and 0.45  $\mu$ m, respectively) were used. The eluent and the mobile phase were delivered by a Waters Model 590 programmable solvent delivery module and an LKB LC pump (Model 2150, Bromma, Sweden), respectively (both denoted 5 in Figure 1). The two six-port valves (Waters automated switching valve; III and IV in Figure 1) were pneumatically activated with air or nitrogen. The 20  $\times$  3.2 mm i.d. cleanup precolumn (8 in Figure 1) contained a mixture of anion- and cation-exchange resins [Dowex 1 (Fluka AG, Buchs SG, Switzerland) and Bio-Rad AG 50W-X8 (Bio-Rad Labs., Richmond, CA)]. Carbohy-

- (10) Scheper, T.; Brandes, W.; Grau, C.; Hundek, H. G.; Reinhardt, B.; R  ther, F.; Pl  tz, F.; Schelp, C.; Sch  gerl, K.; Schneider, K. H.; Giffhorn, F.; Rehr, B.; Sahm, H. *Anal. Chim. Acta* 1991, 249, 25–34.
- (11) Ruzicka, J.; Hansen, E. H. *Flow Injection Analysis*, 2nd ed.; Wiley: New York, 1988.
- (12) Kroner, K. H.; Kula, M. R. *Anal. Chim. Acta* 1984, 163, 3–15.
- (13) Garn, M.; Gisin, M.; Thommen, C.; Cevey, P. *Biotechnol. Bioeng.* 1989, 34, 423–8.
- (14) L  di, H.; Garn, M.; Bataillard, P.; Widmer, H. M. *J. Biotechnol.* 1990, 14, 71–9.
- (15) Nielsen, J.; Nikolajsen, K.; Villadsen, J. *Biotechnol. Bioeng.* 1989, 33, 1127–34.
- (16) Gram, J.; de Bang, M.; Villadsen, J. *Chem. Eng. Sci.* 1990, 45, 1031–42.
- (17) Chung, S.; Wen, X.; Vilholm, K.; de Bang, M.; Christian, G.; Ruzicka, J. *Anal. Chim. Acta* 1991, 249, 77–85.
- (18) Christensen, L. H.; Nielsen, J.; Villadsen, J. *Anal. Chim. Acta* 1991, 249, 123–36.
- (19) Forman, L. W.; Thomas, B. D.; Jacobson, F. S. *Anal. Chim. Acta* 1991, 249, 101–11.
- (20) Nielsen, J.; Nikolajsen, K.; Benthin, S.; Villadsen, J. *Anal. Chim. Acta* 1990, 237, 165–75.
- (21) Matsumoto, K.; Kamikado, H.; Matsubara, H.; Osajima, Y. *Anal. Chim. Acta* 1988, 60, 147–51.
- (22) Matsumoto, K.; Matsubara, H.; Hamada, M.; Uked, H.; Osajima, Y. *J. Biotechnol.* 1990, 14, 115–26.
- (23) Marko-Varga, G.; Dom  nguez, E.; Hahn-H  gerdal, B.; Gorton, L. *J. Pharm. Biomed. Anal.* 1990, 8, 817–23.
- (24) Marko-Varga, G.; Dom  nguez, E. *Trends Anal. Chem.* 1991, 10, 290–7.
- (25) Dincer, A. K.; Kalyanpur, M.; Skea, W.; Ryan, M.; Kierstead, T. In *Developments in Industrial Microbiology*; Society for Industrial Microbiology: Arlington, VA, 1984; Vol. 25 p 603.
- (26) Dinwoodie, R. C.; Mehner, D. W. *Biotechnol. Bioeng.* 1985, 27, 1060–2.
- (27) van de Merbel, N. C.; Kool, I. M.; Lingeman, H.; Brinkman, U. A. Th.; Kolhorn, A.; de Rijke, L. C. *Chromatographia* 1992, 33, 525–32.

- (28) Sch  gerl, K.; Brandes, L.; Dullau, Holzhauser-Rieger, T. K.; Hotop, S.; H  bner, U.; Wu, X.; Zhou, W. *Anal. Chim. Acta* 1991, 249, 87–100.
- (29) Hayward, M. J.; Kotiaho, T.; Lister, A. K.; Cooks, R. G.; Austin, G. D.; Narayan, R.; Tsao, G. T. *Anal. Chem.* 1990, 62, 1798–1804.
- (30) Gorton, L.; J  nsson-Pettersson, G.; Cs  regi, E.; Johansson, K.; Dom  nguez, E.; Marko-Varga, G. *Analyst* 1992, 117, 1235–41.
- (31) Schmid, R. D.; K  nnecke, W. *J. Biotechnol.* 1990, 14, 3–31.
- (32) Marko-Varga, G. *Electroanalysis* 1992, 4, 403–27.
- (33) Marko-Varga, G.; Gorton, L. *Anal. Chim. Acta* 1990, 234, 13–29.
- (34) Buttler, T.; Gorton, L.; Marko-Varga, G. *Anal. Chim. Acta* 1993, 279, 27–37.



drates were separated on a ligand-exchange column in  $\text{Pb}^{2+}$  form [Aminex HPX-87P, Bio-Rad Labs., dimensions  $300 \times 7.8$  mm i.d. (B in Figure 1)] at an elevated operating temperature of 85 °C (Waters column heater module, controlled by Waters temperature control module). Water was used as the mobile phase, pumped with a flow rate of 0.6 mL/min. The injection volume was 1  $\mu\text{L}$ , and the sugars were monitored with a refractive index (RI) detector (Model 2142, LKB; 11 in Figure 1). The alcohol sensor (10 in Figure 1) was used in a CLC system using a PLRP-S reversed-phase column (5  $\mu\text{m}$ , 100 Å,  $50 \times 4.6$  mm i.d., Church Stretton, Shropshire, UK; A in Figure 1) and an injection volume of 20  $\mu\text{L}$ . The mobile phase was a 0.025 M phosphate buffer at pH 7.5, pumped with a flow rate of 0.6 mL/min. Data acquisition and processing were performed by a chromatography workstation (Baseline 810, Millipore; 12 in Figure 1). The signal from the detector was also monitored on a chart recorder [Model 2210, LKB (not shown in Figure 1)].

In the breakthrough measurements, a flow system consisting of a peristaltic pump (Gilson Minipuls 2, Villiers-le-Bel, France; 3 in Figure 1), a six-port injection valve (Rheodyne), and a UV detector (Model 2151, LKB) were used. Results were observed on a chart recorder.

**Reagents.** The carbohydrates, L(+)-arabinose, D(+)-cellobiose, D(+)-galactose, D(+)-glucose, D(+)-mannose, and D(+)-xylose, were of reagent grade from Sigma (St. Louis, MA). Ethanol (spectrographic grade, 99.5%) was obtained from Kemetyl, Stockholm, Sweden. The fermentation substrate, spent sulfite liquor (SSL) was a gift from MoDo, Örnsköldsvik, Sweden.

All solutions were prepared by dissolving the substance in water obtained from a Millipore Milli-Q water purification system (Bedford, MA). This water was also used as the eluent in the flow system and the mobile phase in the CLC system for carbohydrate analysis.

**Preparation of the Alcohol Sensor.** An alcohol biosensor containing coimmobilized horseradish peroxidase and alcohol oxidase was used to monitor ethanol. The enzymes were coimmobilized in a carbon paste electrode as described previously.<sup>30</sup> Alcohol oxidase (AOD, EC 1.1.3.13, from *Candida boidinii*, Serva, Heidelberg, Germany, Catalog No. 12085, 30.3 units/mg) and horseradish peroxidase (HRP, EC 1.11.1.7, Sigma, Catalog No. P 8375, 270 units/mg) were used as received. The electrodes were prepared as follows: modification of the graphite powder (Catalog No. 50870, Fluka, Buchs, Switzerland) was made by heat treatment in air at 700 °C for 15 s in a muffle furnace. The graphite powder was then activated with carbodiimide (1-cyclohexyl-3-(2-morpholinoethyl)carbodiimide metho-*p*-toluenesulfonate, Sigma, Catalog No. C 6011) and followed by addition of the enzymes to be covalently bound to the graphite. Glutaraldehyde was also added to cross-link the enzymes and polyethyleneimine to act as a promoter in the sensor.<sup>30</sup> Phenylmethylsilicone oil (40  $\mu\text{L}$ /100 mg of graphite; Silicone DC 710, Alltech Associates, Arlington Heights, IL) was added to the vacuum-dried graphite with the immobilized enzymes and mixed thoroughly to form a uniform paste. The chemically modified carbon paste was filled into the tip of a syringe barrel (1.0-mL syringe, Brunswick 81/79J03) and rubbed on a smooth glass surface, resulting in a flat shining electrode surface with a surface area of  $\sim 0.024$  cm<sup>2</sup>. A silver thread was placed in the paste to provide electric contact. Next, the surface of the electrodes was covered with an electropolymerized membrane layer of *o*-phenylenediamine by inserting the electrode surface in a 0.1 M acetate buffer solution at pH 5.2 containing 5 mM of *o*-phenylenediamine and running five cyclic voltammograms between 0 and +650 mV vs standard calomel electrode, with a sweep rate of 50 mV/s. The electrode was thereafter rinsed with Milli-Q water and allowed to dry. Six layers of an anionic membrane (Eastman AQ-29D) were then applied by dipping the electrode in a solution containing 0.5% of the AQ ionic membrane. Between each layer, the electrode was dried for 20 min. The ready-made electrode was allowed to dry for 1 h and was then mounted in a three-electrode amperometric flow cell of wall-jet type<sup>36</sup> in the CLC system; see Figure 1.

(35) Appelqvist, R.; Marko-Varga, G.; Gorton, L.; Torstensson, A.; Johansson, G. *Anal. Chim. Acta* 1985, 169, 237-47.

**Fermentation Conditions.** A 450-mL portion of crude SSL was used as the fermentation substrate. First the pH was adjusted to 6.1 with concentrated NaOH and then the substrate was transferred to the bioreactor, a well-stirred 500-mL Erlenmeyer flask with a rubber stopper (1 in Figure 1). Next, 1.25 g of yeast extract (Difco, Detroit, MI) and 0.12 g of ammonium sulfate (PA, Merck, Darmstadt, Germany) were added. The bioreactor solution was circulated by a peristaltic pump (Gilson Minipuls 2) at a feed rate of 12 mL/min, and the membrane in the filtration unit with a Millipore Durapor with 0.22- $\mu\text{m}$  pores. At time zero, 40 g/L bakers' yeast (*Saccharomyces cerevisiae*; Jästbolaget, Stockholm, Sweden) was added, giving a total broth volume of ca. 500 mL. Aseptic conditions were established by washing all parts with pure ethanol followed by thorough rinsing with Milli-Q water.

## RESULTS AND DISCUSSION

The technical substrate used in the ethanol fermentation, spent sulfite liquor (SSL), is a waste product from the pulp industry containing high amounts of soluble sugars. It is a very complex fermentation substrate and very little is known about the composition and reaction products.<sup>32,38</sup> In earlier investigations<sup>36</sup> on ethanol fermentations based on SSL, it was found that a CLC separation is mandatory for both carbohydrate and ethanol analysis. The reason is obvious in carbohydrate analysis since refractive index is a nonselective detection system. The enzyme-based alcohol sensor is in that sense a much more selective detection unit. Nevertheless, alcohol oxidase, known as an enzyme with broad substrate specificity, catalyzes the oxidation of other alcohols besides ethanol such as methanol, propanol, 2-propanol, and butanol.<sup>37</sup> Some organic acids and aldehydes have also been found to be substrates for AOD, e.g., lactate, formaldehyde, and acetic acid.

An on-line sampling and analysis system consists of several parts that must be optimized separately. The system we have developed, shown in Figure 1, comprises the following parts: bioreactor, sampling unit, cleanup, separation, detection, and data acquisition and processing. Below, the sampling unit and cleanup, separation, and detection, are discussed.

The two main types of sampling units used for continuous monitoring of bioprocesses are correlated to their position relative to the fermenter. A filtrate is more easily obtained and less apparatus demanding with an in situ module (situated inside the fermenter). However, it is not possible to change the membrane of the sampling unit during one fermentation. It may also be difficult to calibrate and sometimes the response time is slow. The second type (placed outside) uses a pump for broth feeding, which in turns means that circulation of extensive volumes is necessary. After filtration, the retained substances are pumped back again. Although it is possible to change the membrane during fermentation, the risk of contamination, as well as the risk of affecting the microorganisms due to the circulation, is increased.

As mentioned earlier, in a recent paper we characterized the Waters FAM unit, which hitherto has only been used to sample from larger scale bioreactors, as a sampling unit in small-scale fermentations.<sup>34</sup> The membrane recovery (defined as the amount in the filtrate divided by the amount in the bioreactor, as analyzed by CLC) was found to be very high (>90%) for pure carbohydrate solutions. Discriminating effects toward amino acids and organic acids were found to result in recovery values of  $\sim 50\%$ , which means that some selectivity in the sampling step was introduced, besides the

(36) Marko-Varga, G.; Domínguez, E.; Hahn-Hägerdal, B.; Gorton, L.; Irth, H.; de Jong, G. J.; Frei, R. W.; Brinkman, U. A. Th. *J. Chromatogr.* 1990, 523, 173-88.

(37) Johansson, K.; Jönsson-Petersson, G.; Gorton, L.; Marko-Varga, G.; Csöregi, E. *J. Biotechnol.*, in press.

exclusion of solids and macromolecules. No significant operational differences regarding its sterility and stability could be seen when the sampling unit was incorporated into the on-line flow system. Results obtained in the previous characterization and optimization were directly transferable into the on-line system. This is because the sampling unit is operated separately as such, but is still a part of the total on-line setup.

Two modes of sampling were considered, continuous and discontinuous. The choice of operation mode is in most cases determined by the volume of the bioreactor, the composition of the fermentation broth, the flow rate of the filtrate, and the volume that is outside the fermenter at a given time. In a continuous mode, the filtrate may be returned to the fermenter or passed to waste. If the filtrate is returned to the fermenter after having passed the injection loop of the analytical system, the risk of contamination must be considered. In a recent study,<sup>27</sup> a sterile filter barrier was used to circumvent this risk, although it is generally meant that it is hazardous to the fermentation to return the filtrate. On the other hand, if the filtrate is not returned, the fermenter must be large enough so that the loss of filtrate does not affect the fermentation.<sup>28</sup> This means that when the restrictor of the FAM (which controls the flow rate of the filtrate) was adjusted to 0.1 mL/min, only half of the fermentation broth would remain after 24 h, with an initial volume of 300 mL. For continuous sampling, a fermentation volume of at least 10 L is required. The loss per day (24 h) will then be ca. 1.5%, which is acceptable. However, for very long fermentations (several weeks or months), this mode is obviously unsuitable. In order to run small-scale fermentations (~500 mL), the discontinuous mode of operation is the only choice if the filtrate is to be eluted to waste. Therefore, discontinuous sampling was optimized, resulting in the following procedure. The filtrate line is open for 60 s, closed, and not opened again until the next sampling occasion. This procedure has two effects. First, the loss of filtrate to waste is very limited even during long runs. Second, the pressure difference over the membrane is zero. When the filtrate line is open, a pressure difference is established, which will lead to an accumulation of retained molecules on the membrane surface, increasing the mass transport resistance. This effect is called concentration polarization and has great influence on the rate of filtration, which will initially decrease fast and then level out to a constant lower value.<sup>27,34</sup> By keeping the filtrate line closed most of the time, this effect is avoided or minimized, resulting in highest possible flow rate of the filtrate on every sampling occasion.

**Sample Pretreatment.** Today, automated sample handling is used extensively in the clinical, medical, pharmaceutical, and environmental areas and is also becoming more important in the biotechnological field. Sample handling techniques have moved from simple dilution/membrane filtration steps toward the introduction of more selective chromatographic techniques such as solid-phase extraction. The most commonly used SPE phases are silica-based, with a broad range of functional groups, polystyrene divinylbenzene supports and carbonaceous phases.<sup>36,38</sup> Nielsen et al. already showed in 1987 the utility of programmable on-line SPE systems coupled to CLC separations.<sup>39</sup> Disposable cartridges, slurry packed with 5- $\mu$ m analytical column materials, were used in a totally closed flow system, including cartridge exchange, transport, and sealing. This work was the basis for the fully automated SPE instrument that is now commercially

available under the name PROSPEKT. Similar cleanup methods by SPE have been used successfully both off- and on-line coupled to CLC separation.<sup>40-43</sup>

Earlier adsorption/desorption studies had been made with both model solutions and fermentation substrates and broths on analytical supports, where the capacity using different mobile phases was investigated both on-line<sup>36</sup> and off-line.<sup>44</sup> The model compounds were mostly phenols and phenolic derivatives, i.e., breakdown products from lignin in fermentation substrates and broths. The experience gained from these studies became the basis for the inclusion of the precolumn in our system.

After passing the sample through the membrane of the sampling unit, an efficient removal of particles and large molecules present in the broth, e.g., cells, extracellular proteins, and membranes, was obtained. These were mainly excluded on the basis of the cutoff size of the membrane. However, additional cleanup was found to be necessary. To obtain chromatographic separations that could be evaluated quantitatively and qualitatively, interfering components in the fermentation broths needed to be selectively excluded.<sup>45,46</sup> It was shown by Marko-Varga et al. that an efficient cleanup may reduce the level of interfering compounds by more than 2 orders of magnitude, as measured by diode array UV detection.<sup>23,47</sup>

By introducing a SPE cleanup step in this system, the lifetime of the analytical column was extended, if the capacity of the SPE step is large enough. Therefore, breakthrough experiments were performed using a mixture of cation ( $\text{SO}_4^{2-}$ ) and anion [ $\text{N}(\text{CH}_3)^{3+}$ ] exchange polymer supports and SSL as the sample for capacity determinations of these materials. The experiments were performed in a single-flow system with the SPE column mounted on a six-port switch valve. Best cleanup performance was achieved using a 1:1 (w/w) mixture of these polymer supports, slurry-packed in the precolumn. Although a thorough capacity investigation of the two supports was not conducted, the capacities were found to be sufficient. This conclusion was drawn because no deterioration of the performance of the analytical column was seen after 24 h and some 70 injections. Similar sample cleanup efficiencies were found for the SPE system as described above.<sup>23,47</sup>

**CLC Separation.** Column liquid chromatography using a strong cation ligand-exchange column is nowadays a well-established technique for quantitative carbohydrate determinations.<sup>48-50</sup> It has been shown that  $\text{Pb}^{2+}$ -loaded supports have the best chromatographic characteristics of the phases available for carbohydrate separations.<sup>51</sup> A column of this type is able to separate cellobiose, glucose, xylose, arabinose, galactose, and mannose, although no complete separation of arabinose and mannose is achieved. Although the stability of this type of column was found to reach certain

(40) McDowall, R. D. *J. Chromatogr.* 1989, 492, 3-58.

(41) Brinkman, U. A. Th.; Frei, R. W.; Lingeman, H. J. *J. Chromatogr.* 1989, 492, 251-98.

(42) Irth, H.; de Jong, G. J.; Brinkman, U. A. Th. *Anal. Chim. Acta* 1990, 236, 165-72.

(43) Lipschitz, C.; Irth, H.; de Jong, G. J.; Brinkman, U. A. Th.; Frei, R. W. *J. Chromatogr.* 1989, 471, 321-34.

(44) Marko-Varga, G.; Domínguez, E.; Persson, L.-L.; Gorton, L. *Lab. Rob. Autom.* 1993, 5, 11-22.

(45) Marko-Varga, G.; Domínguez, E.; Gorton, L.; Barceló, D. *Chromatographia* 1993, 36, 381-98.

(46) Buttler, T.; Marko-Varga, G.; Gorton, L., University of Lund, Lund, Sweden, unpublished work, 1991-1992.

(47) Marko-Varga, G.; Domínguez, E.; Hahn-Hägerdal, B.; Gorton, L. *Chromatographia* 1990, 30, 591-4.

(48) Marko-Varga, G. Doctoral Thesis, University of Lund, Lund, 1988.

(49) Skoog, K. Doctoral Thesis, University of Lund, Lund, 1992.

(50) Lindén, T. Doctoral Thesis, University of Lund, Lund, 1992.

(51) Marko-Varga, G.; Domínguez, E.; Hahn-Hägerdal, B.; Gorton, L. *J. Chromatogr.* 1990, 506, 423-41.

(38) Liaska, I.; Krupcik, J.; Leclercq, P. A. *J. High Resolut. Chromatogr.* 1989, 12, 577-90.

(39) Nielsen, M. W. F.; van Ingen, H. E.; Valk, A. J.; Frei, R. W.; Brinkman, U. A. Th. *J. Liq. Chromatogr.* 1987, 10, 617-33.

**Table I. Effect of Injection Volume on Column Dilution and Column Efficiency (N)**

injection vol ( $\mu$ L)	retention time (min)	peak ht (mm)	peak width at half-ht (mm)	N	peak vol (mL)	dilution factor
1	10.1	73.5	2.5	2300	0.96	960
2	10.0	76.0	2.5	2200	1.32	660
	10.0	75.0	2.5	2200	1.08	540
5	10.0	55.0	2.5	2200	0.96	190
	10.0	50.0	2.5	2200	0.96	190
10	10.0	46.0	2.5	2200	0.96	100
	10.0	46.0	2.5	2200	0.96	100
20	10.0	90.5	2.5	2200	0.96	50
	10.0	92.5	2.5	2600	1.08	50

limitations in comparison with other ligand-exchange phases, e.g.,  $\text{Na}^+$  or  $\text{Ca}^{2+}$ , the lead column was chosen due to its better selectivity. Heating the column makes the ligand-exchange process more rapid, which results in peak shape improvements and more accurate quantitative determinations. Anion-exchange chromatography at high pH with pulsed amperometric detection is a technique yielding a higher selectivity, at least for pure carbohydrate solutions. However, a complicated matrix can make the interpretation of chromatograms difficult. Whether or not this technique offers an advantage over ligand-exchange chromatography in these applications is a subject for further investigation. The repeatability of the chromatographic system is very good. Seven repetitive injections of solutions containing 10 mM each of glucose and xylose gave RSD values in peak height of 0.49% and 0.83%, respectively. The reproducibility for standard solutions of carbohydrates was found to give RSD values in the same range.

It would be very convenient if the filtrated sample could be directly injected into the CLC system. But 20  $\mu$ L, a normal injection volume, was found to deactivate the analytical column faster due to the high amount of interferents still present in the sample.<sup>23</sup> Anions and chelating agents may strip the column of its metal ions bound to the stationary phase, forming precipitates or soluble complexes that will be washed out with the mobile phase. Other cations may cause ion-exchange reactions. The presence of such interfering compounds will deteriorate the column performance and alter its selectivity. Dilution is the simplest and one of the best ways of lowering the level of interferents, but is feasible only if the concentration of the analyte is high enough. However, in the chromatographic column, there is a natural dilution of a sample, which results in a broadening of the peak. This band broadening is dependent on the injection volume. Therefore, the effect of the injection volume on sample dilution was studied. In Table I the results obtained are shown, and as can be seen, all peak volumes are around 1 mL. This means that an injection volume of 1  $\mu$ L is dispersed ~1000 times while an injection volume of 20  $\mu$ L is dispersed 50 times, calculated as the peak volume of the test substance (1 mM cellobiose solution) divided by the injection volume. The retention times, which may vary slightly between different amounts of a sample, were found to be constant for the investigated injection volumes (see Table I). The number of theoretical plates,  $N$ , does not vary drastically and was found to be ~2200 for almost all injection volumes studied. The greatest impact on the separations going from 20- to 1- $\mu$ L injection volume was the sensitivity using peak height measurements. A signal response obtained by lowering the injection volume was 22% lower but resulted in an increased stability of the analytical column by a factor of at least 20. The peak height values for 5- and 10- $\mu$ L injection volumes were somewhat lower than expected; the explanation is still not clear.

In summary, a very small injection volume will be diluted so that the column performance does not deteriorate. The collected sample will also be diluted 2-fold during the transport from valve II to valve IV (see Figure 1), which includes the dilution in the SPE column. In combination with a cleanup column, it is possible to directly inject a filtered sample from the fermenter without further dilution and without loss in efficiency.

**Detection Systems.** Two different detection principles, one electrochemical using an amperometric biosensor and one photometrical, RI, were used for monitoring the production of short-chained alcohols and the consumption of carbohydrates, respectively. Selective and sensitive detection in FI and CLC of aliphatic alcohols can be achieved by use of immobilized alcohol oxidase (AOD)<sup>30,37,52,53</sup> or alcohol dehydrogenase (ADH).<sup>54-56</sup> Several solutions have been chosen to investigate these two enzymes in the analysis of ethanol. AODs from different species have been used in immobilized enzyme reactors using both silica and polymer-based supports, and in one case immobilized directly into a carbon paste electrode material.<sup>30,37</sup> AOD is generally considered as an unstable enzyme.<sup>57</sup> We found that this lack of stability could be circumvented by immobilizing the enzyme into a modified carbon paste electrode.<sup>30</sup> The paste comprised a polymer (polyethyleneimine) that acted as a promoter and a stabilizer<sup>30,37,58</sup> and was prepared as described in the Experimental Section. The alcohol sensor was optimized with respect to sensitivity, selectivity, and long-term stability, with the ultimate goal being the analysis of complicated fermentation samples. These optimizations were made separately, first in a FI system where repetitive injections of crude biotechnological samples were analyzed. This approach was found to be less successful since the response signal of the biosensor dropped after less than 10 injections. These fermentation substrates and broth samples were therefore subjected to a SPE step in an off-line mode before injection into the single-line CLC system.<sup>37</sup> Thus, the recovery of these determinations was low (~50%) using a mixed SPE phase. The stability of the alcohol sensor was improved but still inadequate for continuous on-line analysis purposes. Therefore, the biosensor was covered by two types of membranes (see Experimental Section). The combination of an electropolymerized layer of *o*-phenylenediamine and the Eastman AQ membrane resulted in an improved operational stability, where repetitive injections could be made with RSD values below 4% ( $n = 20$ ). The results obtained, using a SPE step prior to injection and the protective membranes on the electrode surface, meet the criteria and needs of an on-line detection unit.

Several detection systems for carbohydrates in biotechnological samples exist today. Carbohydrates show weak absorbance in the low-UV region (190 nm). The advantages and disadvantages of using UV detection in fermentation process monitoring have been discussed previously.<sup>27,38,60</sup>

(52) Tagliaro, F.; Dorizzi, R.; Ghielmi, S.; Marigo, M. *J. Chromatogr.* **1991**, *566*, 333-9.

(53) Kulya, J.; Bilitewski, U.; Schmid, R. D. *Sens. Actuators* **1991**, *3*, 227-34.

(54) Gorton, L.; Domínguez, E.; Marko-Varga, G.; Persson, B.; Jönsson-Pettersson, G.; Csöregi, E.; Johansson, K.; Narasiah, D.; Ghobadi, S.; Kacaniklik, V.; Skotheim, T.; Hale, P.; Okamoto, Y.; Lan, H.-L. In *Bioelectroanalysis*; Pungor, E., Ed.; Akadémiai Kiadó: Budapest, 1993; Vol. 2, pp 33-52.

(55) Aizawa, M. *Anal. Chim. Acta* **1991**, *250*, 249-56.

(56) Kitagawa, Y.; Kitabatake, K.; Sua, M.; Muramatsu, H.; Ataka, T.; Mori, A.; Tamaiya, E.; Karube, I. *Anal. Chem.* **1991**, *63*, 2391-3.

(57) Gibson, T. D.; Higgins, I. J.; Woodward, J. R. *Analyst* **1992**, *117*, 1293-7.

(58) Marko-Varga, G.; Johansson, K.; Gorton, L. In *Bioelectroanalysis*; Pungor, E., Ed.; Akadémiai Kiadó: Budapest, 1993; Vol. 2, pp 377-87.

(59) Johnson, D. C.; LaCourse, W. R. *Electroanalysis* **1992**, *4*, 367-80.

**Table II. Valve Sequences for On-Line Sampling, Pretreatment, and Analysis of Carbohydrates**

time (min)	valves				comments
	I	II	III	IV	
0	open	load	inject	load	initial position. Sample/std line is open
1.0	closed	inject	inject	load	sample/std line is closed. The content of the sampling loop is transported through the cleanup column to the analytical loop
1.92	closed	inject	inject	inject	the content of the analytical loop is injected into the CLC system

Detection improvements are made by pre- and postcolumn derivatization techniques using soluble chemical reagents.<sup>36,61-63</sup> Refractive index is the most commonly used detection principle in carbohydrate analysis in CLC. Pulsed amperometric detection (PAD), first described by Johnson et al. has also gained much attention and is now widely used.<sup>59</sup>

Several catalytic reaction detection systems utilizing immobilized enzymes on solid supports in combination with electrochemical, fluorometric, or UV detection have also been developed lately.<sup>32,64,65</sup> Since RI is nonspecific, the high levels of interfering compounds will disturb the sugar analysis in several ways. First, interferences may coelute with some analyte of interest, causing quantification errors. This has been shown using mass spectrometry or in comparison with PAD.<sup>46</sup> Also, analyte peaks may be distorted due to the high background level, making quantification more difficult. However, with the two cleanup steps used here (tangential flow filtration and SPE) and with samples comprising high levels of sugar, RI detection was considered applicable for these substrate monitoring studies.

**On-Line Coupling.** After all parts (sampling, SPE, separation, and detection) had been optimized separately, they were coupled together into an on-line flow system. The four computer-controlled valves are important parts. By programming event sequences, coupled together into cycles, the valves are put in either a load or inject position. For the internal valve (valve I, Figure 1), this corresponds to an open or closed position. In the open position, the filtrate line is kept open allowing samples to be taken from the sampling unit. By switching this valve into the closed position, manual injections can be made for calibration purposes. Table II shows the programmed sequence for the various steps in carbohydrate analysis and Figure 2 the corresponding positions of valves II-IV during one cycle of operation.

At time zero, valve I is opened and valve II is put in load position (A in Figure 2). The filtrate from the FAM unit is then guided to the sampling loop (volume 100  $\mu$ L, placed on valve II), where it is trapped and eluted to waste. To exclude memory effects in the sampling loop, since the dead volume from the filtration module to the sampling loop was ca. 200  $\mu$ L, there is a 2-3-fold washing of the loop on each sampling occasion. After 60 s, valve I is closed and valve II is put into its injection position (B in Figure 2). The content of the sampling loop is then transferred to the cleanup column, positioned on valve III, to eliminate interfering components. When the SPE column is not in use, the valve may be switched to load position, the flow will pass by, and the ion-exchange material may be regenerated manually if necessary. This is illustrated by the syringe in Figure 2.

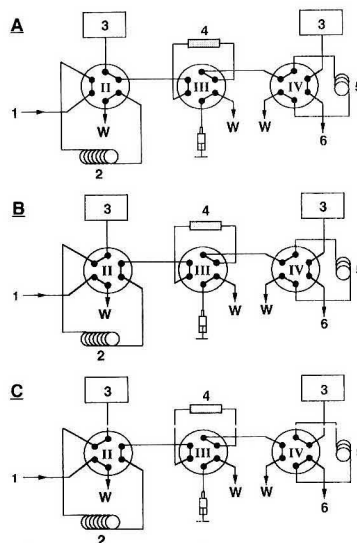


**Figure 2.** Valve sequences for on-line sampling, pretreatment and analysis: (A) Loading of sampling loop with filtrate or standard; (B) cleanup of sampling loop content and trapping in analytical loop; (C) injection into the chromatographic system. (1) sampling line, (2) sampling loop, (3) LC pump, (4) cleanup column, (5) analytical loop, (6) to analytical column and detector, and (W) waste.

After the precolumn, the sample is eluted into the analytical loop (volume ca. 1  $\mu$ L) placed on the fourth valve, where a heart cut of the sample plug is made. This step was optimized separately. When the content of the sampling loop is transferred to the analytical loop, a sample plug develops in the tubings. The plug profile is dependent upon several parameters, e.g., flow rate and inner diameter of the tubing.<sup>11</sup> When this plug reaches the analytical loop, a characteristic band profile is established. To obtain maximum sensitivity, valve IV should be switched to the inject position when the part of the plug profile containing the highest sample concentration passes the analytical loop.

The window (height and width) for two flow rates, 0.4 and 0.3 mL/min, was investigated. A 10% higher peak height was found for 0.4 mL/min; however, a much broader maximum was obtained for 0.3 mL/min. The lower flow rate was chosen since it is less sensitive to small changes in the flow system. Changing the heart cut by 2 s results in a decrease in peak height with 1.5% and 8.2% for 0.3 and 0.4 mL/min, respectively. On the basis of these experiments (data not shown), the content of the analytical loop is determined to be injected into the CLC system 115.2 s after opening valve I (C in Figure 2).

Simultaneously, a signal is sent to the chromatography data station to start collecting data. After a total analysis time of 24 min, data collection will stop and 1 min later the sequence will start over from the beginning (or zero). The

(60) Weigang, F.; Reiter, M.; Jungbauer, A.; Kättinger, H. *J. Chromatogr.* 1989, 497, 59-68.

(61) Krämer, M.; Engelhardt, H. *J. High. Resolut. Chromatogr.* 1992, 15, 24-9.

(62) Maness, N. O.; Miranda, E. T.; Mort, A. *J. J. Chromatogr.* 1991, 587, 177-83.

(63) Watanabe, N.; Inoue, M. *Anal. Chem.* 1983, 55, 1016-9.

(64) Gorton, L.; Csöregi, E.; Domínguez, E.; Ennéus, J.; Jönsson-Pettersson, G.; Marko-Varga, G.; Persson, B. *Anal. Chim. Acta* 1991, 250, 203-48.

(65) Yao, T. In *Applied Biosensors*; Wise, D. L., Ed.; Butterworths: London, 1989; p 321.

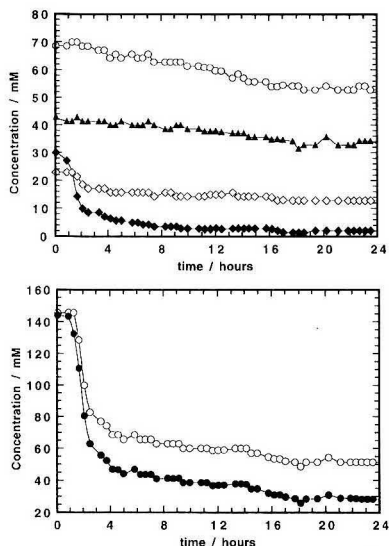


**Figure 3.** (a, top) Variation in concentration of glucose (◆), xylose (○), galactose (▲), and arabinose (◇) during the fermentation. (b, bottom) Variation in mannose concentration during the fermentation: (○) uncorrected; (●) recalculated. For details, see text.

sequence is then repeated four more times (four samples). When five filtrate samples have been taken and the sixth sequence starts, valve I remains closed, which provides an opportunity to inject a standard solution. If this is not done, mobile phase (pure water) will be injected into the flow system instead. This 2.5-h event cycle containing the six sequences are then repeated until a manual stop. The flexibility of this system is high; for example, it is very easy to exclude manual injections from the event cycle. A similar program (event cycle) was used for ethanol analysis. Since the residence time for the sample in the polymer column is much shorter than in the carbohydrate column, samples were taken every 10 min during the first 4.5 h. Thereafter, when the change in ethanol concentration is small, samples were drawn every 30 min.

**On-Line Monitoring of Ethanol Fermentations. Carbohydrate Analysis.** Based on the results of the on-line coupling described above, an automated system for on-line sampling, pretreatment, separation, and detection of carbohydrates was accomplished. The five sugars (glucose, xylose, galactose, arabinose, and mannose) in the technical substrate were monitored over a period of 24 h. The automated analysis was performed according to the sequence described above. An injection of a standard carbohydrate mixture, as above, was made every sixth sample. This was done to control the variation of the chromatographic separation. The variation of the sugars was found to be 5–6% (RSD,  $n = 7$ ) over a 24-h period of operation. These values were found to be of the order where normalization of the data could be easily made.

Figure 3 shows the concentration of the five sugars in SSL during the fermentation. The time when the yeast was added to the substrate is defined as  $t = 0$ . The concentrations of glucose, xylose, arabinose, and galactose are shown in Figure 3a, and that of mannose in 3b. The difference between the two lines in Figure 3b is discussed below. Initially, the concentration of glucose, xylose, galactose, arabinose, and mannose is 30, 68, 42, 22 and 144 mM, respectively. Glucose and mannose are the most preferred carbohydrates of the

five for ethanol production using *S. cerevisiae*. This is in agreement with results found by others.<sup>50</sup> It seems that glucose is the preferred sugar down to a concentration of about 10–15 mM. During the first hour, the level of mannose appears constant. However, due to coelution with ethanol (the retention times of ethanol and mannose are 16.4 and 16.8 min, respectively), this is probably not the case. This can be concluded from the first part of the ethanol production figure (see Figure 5) where only the ethanol was detected by the alcohol biosensor. It is assumed that the increase in ethanol concentration during this period has to correspond to a decrease in mannose concentration. This gives rise to the constant mannose level in the upper line (open circles) in Figure 3b.

The values for mannose were then corrected by taking the coeluting ethanol into consideration. The data were recalculated using the RI factors of mannose and ethanol, and the result is shown in Figure 3b as the lower line (filled circles). One important assumption made in these calculations is that the two fermentations carried out for carbohydrate and ethanol monitoring are identical. The steep decrease in mannose concentration after 1.5 h is due to the fast consumption of this sugar. As the glucose concentration approaches zero, the calculated mannose level stabilizes at 28 mM after 16 h.

Evaluation of these data has to include a careful treatment of differences in RI factors for mannose, arabinose, and ethanol. Arabinose is a pentose sugar that does not take part in the production of ethanol. However, as it elutes close to the mannose peak, with no baseline separation, the evaluation will be difficult. Still, the variation in the mannose/ethanol ratio will not affect the resolution ( $R_s$ ) between the peak containing both mannose and ethanol, and arabinose.

The third hexose present, galactose, was under the employed conditions not a good substrate for the yeast, which is reflected in the (somewhat decreasing) horizontal line during the fermentation. Although arabinose not yet has been reported as a substrate for *S. cerevisiae*, an initial decrease in its concentration is found. One explanation may be its conversion from sugar to the corresponding sugar alcohol, arabitol. The initial xylose concentration is ~70 mM, and as can be seen, this five-carbon sugar is not fermented by this microorganism. During the 24-h fermentation, the level fluctuates to some extent. It should be emphasized, though, that this variation is not due to the chromatographic system but rather to the reactions in the bioprocess itself.

In Figure 4, two typical chromatograms of the fermentation broth are shown. The first is acquired at an early stage (after 1 h), where the broth composition resembles the composition of the substrate. The second illustrates the composition after 24 h of fermentation. At this stage, the physical properties of the broth have become more hydrophobic, which in turn results in an increase of dissolved apolar components. By comparing the two chromatograms, it can be noted that there is a buildup of matrix components with time. It is seen as a hump eluting between the front and the fourth sugar. These compounds may disturb or at least interfere with the detection of carbohydrates, although both membrane filtration and SPE have been used.

The total elution time is 17 min for the sugars. Unknown compounds continued to elute for at least 5 min. To avoid coelution of these late-eluting substances with the next sample, sampling was made every 25 min.

**Ethanol Analysis.** At the time the experiments were conducted, it was not possible to analyze both carbohydrates and ethanol simultaneously during the same fermentation. It was therefore necessary to perform two fermentations. However, to be able to compare data and results, we did our



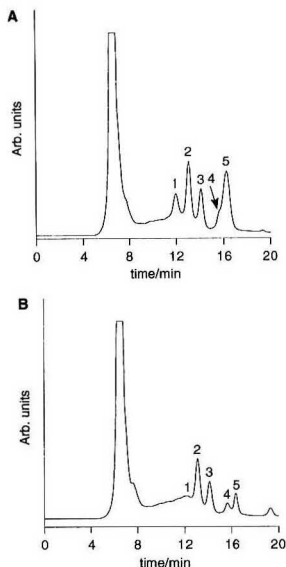


**Figure 4.** Chromatograms of the fermentation broth using the carbohydrate analysis setup in Figure 1. (A) shows a separation after 1 h of fermentation and (B) after 24 h: (1) glucose, (2) xylose, (3) galactose, (4) arabinose, and (5) mannose; detector, RI (Att 32); injection volume, 1  $\mu$ L. For further details, see text.

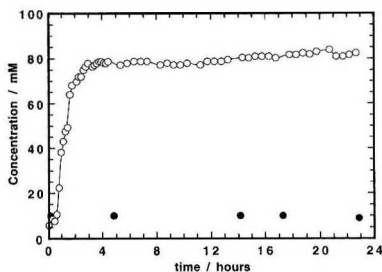


**Figure 5.** Production of ethanol during the fermentation: (O) ethanol; (●) standard injection (10 mM).

utmost to use conditions as identical as possible. To selectively determine the ethanol produced, the alcohol biosensor described above was used instead of RI detection. The concentration of ethanol during the fermentation is shown in Figure 5. Also shown are five standard injections of a 10 mM ethanol solution. Evidently, the response of the sensor is not altered even after 24 h and some 75 injections. The ethanol concentration is initially  $\sim 5$  mM. After the addition of yeast it rises rather quickly to  $\sim 80$  mM, and after 4 h it is approximately constant. Two chromatograms are shown in Figure 6 acquired after 1 and 23 h of fermentation. The chromatograms contain only three peaks, where the first two are matrix components and the third is ethanol. As can be seen, the elution time is only  $\sim 3$  min, which together with a sampling and pretreatment time of  $\sim 2$  min gives a total time of analysis of 5 min. These fast CLC separations for the determination of ethanol are comparable with an FI monitoring system. The ethanol CLC system gave dilution factors of  $\sim 600$ , which make the high levels of ethanol fall within the linear response range of the sensor.<sup>37</sup>

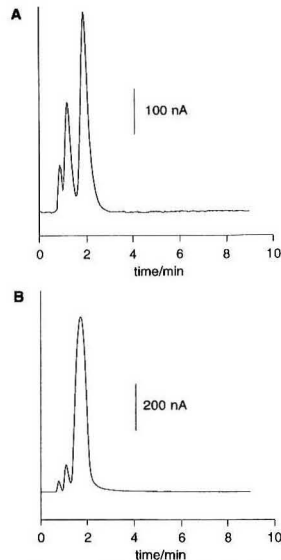


**Figure 6.** Chromatograms of the fermentation broth using the ethanol analysis setup in Figure 1. (A) is acquired after 1 h and (B) after 23 h. Note the different scales on the y axes: detector, alcohol biosensor; injection volume, 1  $\mu$ L. For further details, see text.

The theoretical yield of this process is 0.51, and under optimal conditions, maximum experimental yields of  $\sim 0.45$  have been reported.<sup>2</sup> The total production of ethanol was found to be 85 mM, which corresponds to much a lower experimental yield of 0.18. The reason for this decreased yield is that the fermentation runs made in our laboratory were as close as possible to the real conditions followed in an ethanol fermentation plant, where waste water from pulp industry is used as the technical substrate. No fine tuning (giving yields above 0.40) of the process is made in these plant processes, such as feedback control of pH and oxygen. The absence of pH control also results in a pH drop during the fermentation. Lowering the pH means slowing down and finally inhibiting the metabolism of the yeast. Consequently, mannose and galactose were not fully utilized, as can be seen in Figure 3.

## CONCLUSIONS

An analytical system for on-line fermentation monitoring has been described in which a discontinuous sampling mode was developed for small-volume ethanol fermentation processes. Unattended operation of the system including sampling, sample pretreatment, CLC separation, detection, and data acquisition was performed during the 24-h processes. After more than 130 injections of pretreated spent sulfite liquor, no deterioration of the performance of the precolumns and analytical columns could be noticed. The discontinuous mode of sampling, for low bioreactor volumes, is a mode of operation which was found to operate well without the need to pump the filtrate back to the fermenter, as in the continuous mode, thereby eliminating a major risk of contamination. The qualitative and quantitative evaluation that can be made with RI detection is a weak link in the present setup. Nevertheless, it is by far the most commonly used detection principle for carbohydrates in biotechnological samples. We are therefore currently developing an enzyme-based detector for the carbohydrates for increased selectivity. Comparisons

of the results obtained by RI detection will be made with those from the carbohydrate biosensor. Some promising preliminary studies have been made for the development of carbon past biosensors for the types of carbohydrates present in these fermentation substrates and broths. We have also recently shown the use of microdialysis as a possible sampling device in these complex fermentation processes.<sup>66</sup> Currently, we are focusing on the characterization and optimization of the dialysis unit with respect to membrane types and dialysis mechanisms. The combination of microdialysis and biosensors is also under investigation, with some very promising results.<sup>67</sup> This coupling will likely eliminate the need for a SPE step and thereby simplify the entire setup.

(66) Marko-Varga, G.; Buttler, T.; Gorton, L.; Grönsterwall, C. *Chromatographia* 1993, 35, 285-9.

(67) Buttler, T.; Gorton, L.; Jarskog, H.; Marko-Varga, G.; Hahn-Hägerdal, B.; Meinander, N.; Olsson, L., manuscript in preparation.

## ACKNOWLEDGMENT

The authors thank Dr. W. Waeny, Eastman Chemical International AG, Zug, Switzerland, for the gift of the Eastman AQ-29D preparation and Mr. Ingolf Elmhammar (Waters Division of Millipore in Sweden) and Dr. George Vella (Millipore, Milford, MA) for continuous support during this project. Financial support from the Swedish Natural Science Research Council (NFR) and the Swedish National Board for Technical and Industrial Development (NUTEK) is gratefully acknowledged. Finally, we also thank MoDo for the gift of the spent sulfite liquor.

RECEIVED for review February 24, 1993. Accepted June 16, 1993.

# Glass Chips for High-Speed Capillary Electrophoresis Separations with Submicrometer Plate Heights

Carlo S. Effenhauser,\* Andreas Manz, and H. Michael Widmer

Corporate Analytical Research, Ciba-Geigy Ltd., CH-4002 Basel, Switzerland

Micromachined capillary electrophoresis systems with integrated sample injection have been fabricated on glass chips using standard photolithographic and etching techniques. The injector permits volume-defined electrokinetic sample injection without sample biasing. Utilization of short separation capillaries and high field strengths in combination with a small sample plug length results in both fast and efficient separations of fluorescein isothiocyanate- (FITC-) labeled amino acids. Analysis times range from a few seconds to a few tens of seconds with corresponding plate numbers of 5800–160 000, respectively. Plate heights down to 0.3  $\mu\text{m}$  have been obtained using a separation length of 24 mm and an electric field of 1 kV/cm. As it turns out, a maximum separation efficiency has been reached, limited only by diffusion and the effects of both injection and detection. Automated repetitive sample injection and separation on a time scale of seconds is demonstrated and provides a route to quasi-continuous on-line monitoring of chemical species in a sensorlike fashion.

## 1. INTRODUCTION

In a recent line of development, capillary electrophoresis (CE) and other separation techniques have been successfully integrated into the concept of so-called Total chemical Analysis Systems (TAS).<sup>1–3</sup> The combination of all sample handling and measurement steps into a single package incorporating a high level of automation makes the TAS an ideal approach for continuous monitoring of chemical concentrations in industrial chemical and biochemical processes. As such, the TAS concept has many potential applications in biotechnology,<sup>4,5</sup> process control,<sup>3,6</sup> and the environmental<sup>7,8</sup> and medical sciences,<sup>9,10</sup> fields in which continuous monitoring has become increasingly important. The TAS user is provided with chemical information in the form of electronic data at short, regularly spaced intervals. The elimination of the dependence on external laboratory analyses should have an

enormous impact on the way chemical and biochemical processes are monitored and controlled. Among several examples of TAS that have appeared in the recent literature are a gas chromatograph-based monitor for trace analysis in air,<sup>2</sup> an on-line glucose analyzer for bioprocess control,<sup>11</sup> a supercritical fluid chromatograph-based monitor for process control,<sup>12</sup> and high-speed capillary electrophoresis as a detection method for HPLC.<sup>13</sup>

A logical extension of the TAS concept is miniaturization of these systems, to yield miniaturized TAS, or  $\mu$ -TAS.<sup>14</sup> With sample handling, separation, and detection methods incorporated into a single, small probe, the  $\mu$ -TAS would resemble a sensor in many regards, although each function could be under the dynamic control of the user. All sample-handling steps are carried out extremely close to the location where initial sampling takes place. In order to compete with chemical sensors, the total cycle time from sample injection to the generation of an electronic signal proportional to the concentration of a certain chemical species would have to be about as long as the response time of a typical sensor, i.e., in the range from some seconds to at most a few minutes. This would provide a means to circumvent the severe selectivity and lifetime requirements of "conventional" chemical sensors by incorporation of a separation step in the analysis procedure.

The fact that electric field-driven separations can be very rapid and at the same time exhibit excellent resolution performance was demonstrated by Schumacher in 1962. In these experiments, he showed that isoelectric focusing separations of  $\text{Ce}^{3+}$  and  $\text{Ce}^{4+}$  can be achieved in less than 90 s.<sup>15</sup> Recently, Monnig and Jorgenson<sup>16</sup> reported amino acid separations on a time scale of seconds using CE. In their experiment, small sample plugs were introduced into a short separation capillary by means of a gated laser-induced photolysis technique. Even though this method is well-suited to generating very small sample plugs, its general use is restricted by the complexity of the experiment. Furthermore, this technique leads to plugs having compositions which are not representative of the actual sample, since the individual plug lengths depend on the differing electrokinetic mobilities of these components. Pawliszyn and Wu<sup>17</sup> have demonstrated that rapid sample separations in less than 30 s can be achieved using moving boundary CE, which also provides discrimination-free sample injection. In another study, an integrated electrokinetically driven separation system was used to separate a mixture of laser dyes in 35 s, although at the expense of separation efficiency.<sup>18</sup>

\* Author to whom correspondence should be addressed.  
(1) Widmer, H. M. *Trends Anal. Chem.* 1983, 2, 8.  
(2) Widmer, H. M.; Erard, J.-F.; Grass, G. *Int. J. Environ. Anal. Chem.* 1984, 18, 1.  
(3) Graber, N.; Lüdi, H.; Widmer, H. M. *Sens. Actuators* 1990, B1, 239.  
(4) Lüdi, H.; Garn, M. B.; Bataillard, P.; Widmer, H. M. *J. Biotechnol.* 1990, 14, 71.  
(5) Fillipini, C.; Sonleitner, B.; Fiechter, A.; Bradley, J.; Schmid, R. *J. Biotechnol.* 1991, 18, 153.  
(6) Tschulena, G. *Phys. Scr.* 1988, T23, 293.  
(7) Guibault, G. G. *Anal. Chem. Symp. Ser.* 1983, 17, 637.  
(8) Edmonds, T. E. *Trends Anal. Chem.* 1985, 4, 220.  
(9) Shapiro, B. A.; Harrison, R. A.; Cane, R. D.; Kozlowsky-Templin, R. *Clinical Application of Blood Gases*; Year Book Medical Publishers Inc.: Chicago, 1989.  
(10) Stinshoff, K. E.; Freytag, J. W.; Laska, P. F.; Gill-Pazaris, L. *Anal. Chem.* 1985, 57, 114R.

(11) Garn, M. B.; Cevey, P.; Gisin, M.; Thommen, C. *Biotechnol. Bioeng.* 1989, 34, 423.  
(12) Giorgetti, A.; Pericls, N.; Widmer, H. M.; Anton, K.; Dätwyler, P. *J. Chromatogr. Sci.* 1989, 27, 318.  
(13) Bushey, M. M.; Jorgenson, J. W. *Anal. Chem.* 1990, 62, 978.  
(14) Manz, A.; Graber, N.; Widmer, H. M. *Sens. Actuators* 1990, B1, 244.  
(15) Schumacher, E. J. *Lawrence Radiation Lab. [Rep.] UCRL* 1962, UCRL-10624, 210.  
(16) Monnig, C. A.; Jorgenson, J. W. *Anal. Chem.* 1991, 63, 802.  
(17) Pawliszyn, J.; Wu, J. J. *J. Chromatogr.* 1991, 559, 111.  
(18) de Bokx, P. K.; Gillissen, E. E. A.; van de Weijer, P.; Bekkers, M. H. J.; van Bommel, C. H. M.; Janssen, H.-G. *J. Chromatogr.* 1992, 598, 115.

Microfabrication technologies using photolithographic patterning processes were used by Terry et al. in 1975 for the integration of a gas chromatograph onto an entire silicon wafer.<sup>19,20</sup> This important work went unrecognized for over a decade before the fabrication by Hitachi (Japan) of a liquid chromatographic chip containing a capillary column with an electrochemical detector, in 1987 (published in 1990<sup>21</sup>). Since then, the integration of capillary electrophoresis channels into silicon and glass microstructures has been proposed<sup>22-24</sup> and experimentally demonstrated.<sup>25-28</sup> The photolithographic fabrication process allows for the formation of channels of almost any shape, for branched channel systems and for integration of sample preparation, injection, postcolumn reactions, and detector cells (for a review, see ref 29). Recently, optical absorbance detector cells,<sup>30,31</sup> rapid CE separations,<sup>32,33</sup> and a column-switching technique called "synchronized cyclic CE"<sup>34,35</sup> have been evaluated.

The present work reports on both fast and efficient separations of amino acids carried out on a micromachined CE device. An integrated sample injector allows electrokinetic injection of small sample volumes in a volume-defined injection scheme. The capillary system was formed in the surface of a glass plate using standard photolithographic and glass-etching techniques, which provide an elegant and versatile route to branched capillary manifolds with virtually no dead volumes.<sup>27</sup> The first demonstration of the volume-defined injection principle to prevent sample biasing was given by Verheggen et al.<sup>36</sup> These authors constructed a special sampling device capable of injecting sample volumes in the microliter range and plug lengths of several centimeters. In our device, this injection scheme has been miniaturized and electrokinetic pumping has been employed. This way, small sample aliquots of 100 pL with a plug length of 150  $\mu\text{m}$  can be introduced into the separation capillary without utilization of external pumps and valves. Although electrokinetic sample transport is employed, sample can be injected in a nonbiased manner, as will be described in the following section.

It is clear that in order to increase the speed of analysis in CE, shorter capillaries should be used in combination with

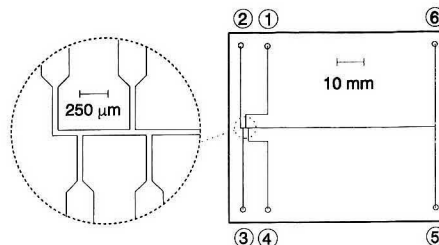


**Figure 1.** Layout of the glass chip with integrated sample injection; chip dimensions 80  $\times$  70  $\times$  3 mm. The horizontal channel was used as separation channel. The inset shows details of the channel geometry in the injection region. Reservoir numbers are indicated.

higher electric field strengths. Optimum efficiency depends on minimization of all unavoidable sources causing band broadening (longitudinal diffusion, finite length of injected sample plug, etc.) and the elimination of all nonideal effects like Joule heating and adsorption on capillary walls. This means that the short separation length imposes strict limits on the contributions of injection and detection to the total variance, if both objectives are to be obtained simultaneously. The use of a high field strength, although of vital importance for short analysis times, can be detrimental to efficiency due to Joule heating effects. Fortunately, it turned out that the high electric field strengths do not limit the efficiency attainable in our experiments, due in part to the good power dissipation capability of rectangular-shaped capillaries of small cross section etched in a glass matrix.<sup>22</sup>

## 2. EXPERIMENTAL SECTION

**Glass Chips.** The layout of the glass chips used in this work is shown in Figure 1. The capillary manifold was formed into the surface of a glass plate (Hoya SLW) by a standard photolithographic procedure<sup>37</sup> including a wet chemical etching step. This was performed under contract by Baumer IMT Industrielle Messtechnik AG, CH-8606 Greifensee, Switzerland, using their proprietary process. Briefly, this process involves deposition of separate metal and photoresist layers onto the glass substrate, followed by illumination of the substrate through a metal mask containing the capillary pattern. After the photoresist is developed, a HF-based solution is used in order to etch the capillary manifold into the substrate, and the metal layer is finally removed. The dimensions of the glass plate are 80  $\times$  70  $\times$  3 mm. In order to seal the capillary system, a second glass plate of the same dimensions was thermally bonded (4 h, 620  $^{\circ}\text{C}$ ) on top of the plate containing the microstructures.<sup>27</sup> Holes (diameter 2 mm) in the cover plate provide access to the capillaries; pipet tips glued into these holes serve as reservoirs. All channels have been etched to a depth of 12  $\mu\text{m}$  and a width of 50  $\mu\text{m}$ , except for the four capillaries in the left part of the glass chip (250- $\mu\text{m}$  width), as is shown in the inset in Figure 1. The smoothness of the channel walls, the precision of the fabrication process, and the shape of the channel cross section are clearly shown on the electron micrograph displayed in Figure 2.

**Sample Injection.** Initially, one of the reservoirs was filled with buffer solution by use of a microsyringe. The capillary system was then flushed with buffer solution by applying pressure to this reservoir. In order to ensure equal hydrostatic pressure, the remaining reservoirs, except reservoir 1, were carefully filled with 50  $\mu\text{L}$  of buffer solution using a microsyringe to prevent the formation of air bubbles in the reservoirs. In the same way, 50  $\mu\text{L}$  of sample solution was added into reservoir 1. Applying a voltage between reservoirs 1 (+2 kV) and 4 (ground) causes sample solution to be pumped electroosmotically from 1 to 4, thereby filling the 150- $\mu\text{m}$  section (sample loop) of the separation capillary (horizontal channel in Figure 1). After a delay time of 1 s, the separation voltage is applied between reservoirs 2 (positive) and

(19) Terry, S. C. A gas chromatography system fabricated on a silicon wafer using integrated circuit technology. Ph.D. Dissertation, Stanford University, 1976.

(20) Terry, S. C.; Jerman, J. H.; Angell, J. B. *IEEE Trans. Electron Devices* 1979, ED-26, 1880.

(21) Manz, A.; Miyahara, Y.; Miura, J.; Watanabe, Y.; Miyagi, H.; Sato, K. *Sens. Actuators* 1990, B1, 249.

(22) Jansson, M.; Emmer, A.; Roeraade, J. *J. High Resolut. Chromatogr.* 1989, 12, 797.

(23) Manz, A.; Fetting, J. C.; Verpoorte, E.; Lüdi, H.; Widmer, H. M.; Harrison, D. J. *Trends Anal. Chem.* 1991, 10, 144.

(24) Harrison, D. J.; Glavina, P. G.; Manz, A. *Sens. Actuators* 1993, B10, 107.

(25) Harrison, D. J.; Manz, A.; Glavina, P. G. *Transducers '91, Digest of Technical Papers*; IEEE: New York, 1991, 91CH2817-5, 792.

(26) Manz, A.; Harrison, D. J.; Verpoorte, E.; Fetting, J. C.; Lüdi, H.; Widmer, H. M. *J. Chromatogr.* 1992, 593, 253.

(27) Hännel, D. J.; Manz, A.; Fan, Z.; Lüdi, H.; Widmer, H. M. *Anal. Chem.* 1992, 64, 1926.

(28) Seiler, K.; Harrison, D. J.; Manz, A. *Anal. Chem.*, in press.

(29) Manz, A.; Harrison, D. J.; Verpoorte, E.; Widmer, H. M. *Adv. Chromatogr.*, in press.

(30) Verpoorte, E.; Manz, A.; Lüdi, H.; Widmer, H. M. *Transducers '91, Digest of Technical Papers*; IEEE: New York, 1991, 91CH2817-5, 796.

(31) Verpoorte, E.; Manz, A.; Lüdi, H.; Bruno, A. E.; Maystre, F.; Krattiger, B.; Widmer, H. M.; van der Schoot, B. H.; de Rooij, N. F. *Sens. Actuators* 1992, B6, 66.

(32) Harrison, D. J.; Fan, Z.; Seiler, K.; Manz, A.; Widmer, H. M. *Anal. Chim. Acta*, in press.

(33) Manz, A.; Verpoorte, E.; Effenhauser, C. S.; Burggraf, N.; Raymond, D. E.; Harrison, D. J.; Widmer, H. M. *J. High Resolut. Chromatogr.*, in press.

(34) Burggraf, N.; Manz, A.; de Rooij, N. F.; Widmer, H. M. *Anal. Methods Instrum.*, in press.

(35) Burggraf, N.; Manz, A.; Effenhauser, C. S.; Verpoorte, E.; de Rooij, N. F.; Widmer, H. M. *J. High Resolut. Chromatogr.*, in press.

(36) Verheggen, T. P. E. M.; Beckers, J. L.; Everaerts, F. M. *J. Chromatogr.* 1988, 452, 615.

(37) See, for example: Middelhoek, S.; Audet, S. A. *Silicon Sensors*; Academic Press: London, 1989; Chapter 7, and literature cited therein.



**Figure 2.** Electron micrograph displaying details of the injection volume. The horizontal capillary represents the separation channel; the vertical channels in the left and right parts of the micrograph are connected to reservoirs 1 and 4, respectively. The distance between the outside walls of the injection channels defining the plug length is 150  $\mu\text{m}$ .

5 (ground), inducing flow of buffer solution from 2 to 5 and carrying the sample plug into the separation channel. In this manner, geometrically well-defined sample plugs of about 100-pL volume can be reproducibly injected. An additional capillary leading to reservoir 3 allows injection of two additional plug sizes (injection from 1 to 3, 300  $\mu\text{m}$ ; from 3 to 4, 400  $\mu\text{m}$ ).

If the injection voltage is applied for a long enough time, the injection volume will be completely filled with even the sample component possessing the lowest net mobility. The sample composition in the injection volume will thus be the same as in the sample reservoir. Although the concentration of each component in the reservoir will change slightly depending on its mobility, this effect is negligible due to the large difference in volume between the sample reservoir and the injection capillary, provided the accumulated injection time for repetitive injections is not too long ( $\leq 1000$  s). This is in contrast to the conventional electrokinetic injection procedure, which produces a strongly biased sample plug due to differences in sample mobilities.

For sample injection and sample separation, Models HCN 2000 (0–2 kV) and HCN 12500 (0–12.5 kV) power supplies (FUG Elektronik GmbH, D-8200 Rosenheim, Germany), respectively, were employed. Repetitive sample injection was controlled with a programmable timer clock (Alphatronic, D-7513 Stutensee, Germany). Current was monitored during separation by means of a Keithley picoammeter (Model 485). A measurement of the current as a function of voltage applied between reservoirs 2 and 5 showed a perfectly linear behavior up to a maximum voltage of 11.25 kV (corresponding current 1.0  $\mu\text{A}$ ). This limitation is caused by the breakthrough voltage of the high-voltage relays used for switching the potentials in our experiment.

**Laser-Induced Fluorescence Detection.** The detection setup used in the experiments described here was similar to the one described in ref 28. The 488-nm line of an Ar<sup>+</sup>-ion laser (Omnichrome, Model 532 AP) was coupled into a 600- $\mu\text{m}$ -diameter optical fiber and used as excitation source. The unfocused output (4 mW) of the fiber was positioned to illuminate a portion of the separation capillary under an angle of about 45°. Fluorescence was collected perpendicular to the surface of the glass chip by means of a microscope objective (Leitz NPL Fluotar L, 25 $\times$ , N.A. 0.35, working distance 17 mm) mounted on a homemade microscope body. After passing a 514-nm interference filter (Spindler & Hoyer GmbH, Göttingen, Germany, fwhm 11.5 nm) and a pinhole placed in the focal plane of the objective (diameter 1 mm), fluorescence radiation was detected with a Hamamatsu R1477 photomultiplier tube (PMT). The 40- $\mu\text{m}$  diameter of the viewing window of the PMT is given by the pinhole diameter divided by the magnification of the objective. In our experiment, the corresponding detection volume amounts to about 15 pL. The PMT was mounted in an integrated detection module (SMT, D-8031 Seefeld, Germany, Model NV 30-1) including HV power supply, voltage divider, and amplifier. The amplifier output was smoothed with a low-pass filter (Avens Signal Equipment Corp., Elmhurst, NY, Model AP-255-5) set at 100 Hz and finally recorded using a digital storage oscilloscope

(LeCroy 9310). The whole fluorescence detector is mounted on an X–Y translational stage (Spindler & Hoyer, Göttingen, Germany) in order to allow variation of the location of the detection volume in the separation capillary.

**Solutions and Labeling Procedure.** Amino acids were labeled by adding 100  $\mu\text{L}$  of a 1 mM solution of fluorescein isothiocyanate (FITC) in acetone (with a drop of pyridine added to the stock solution) to 1 mL of a 1 mM solution of each amino acid dissolved in buffer. After standing in the dark overnight, each solution was diluted to a formal concentration of 10  $\mu\text{M}$  with respect to FITC. A pH 9.0 buffer [20 mM boric acid–100 mM tris(hydroxymethyl)aminomethane (Tris)] was used in all experiments. All solutions were filtered through 0.2- $\mu\text{m}$  filters (Gelman Sciences, Ann Arbor, MI) before use. All chemicals were analytical grade and were purchased from Fluka AG, CH-9470 Buchs, Switzerland.

### 3. RESULTS AND DISCUSSION

**General Remarks.** Recently, several authors have investigated the influence of sample injection on resolution and quantitation in CE in great detail, pointing out the crucial role it plays for the performance of CE.<sup>38–41</sup> Since the experiments presented here have been carried out using unusually short separation capillaries and a novel sample injection scheme, a few general remarks concerning analysis time and separation efficiency in CE might be helpful in order to simplify the discussion of the results in the following two sections.

The analysis time  $t$  in CE (migration time of the slowest detectable sample constituent  $i$ ) can be calculated from the relationship<sup>42</sup>

$$t = L/\mu_i E = L^2/\mu_i V_{\text{sep}} \quad (1)$$

where  $L$  denotes the distance between the injection and detection points,  $\mu_i$  the sum of the electroosmotic ( $\mu_{\text{eo}}$ ) and electrophoretic ( $\mu_{\text{ep}}$ ) mobilities of component  $i$ ,  $E$  the absolute value of the electric field strength in the separation capillary, and  $V_{\text{sep}}$  the potential drop across  $L$ . Short analysis times are basically favored when short separation capillaries are employed in combination with high field strengths or high voltages, respectively.

From the experimental point of view, the ultimate limit of the separation efficiency in CE is governed by three principally unavoidable sources of band broadening, namely, longitudinal diffusion and the effects of both injection and detection. If the separation efficiency is expressed in terms of the number of theoretical plates  $N$ , the ultimate upper limit  $N_{\text{max}}$  is given by eqs 2 and 3

$$\sigma^2 = \sigma_{\text{diff}}^2 + \sigma_{\text{inj}}^2 + \sigma_{\text{det}}^2 = 2D_i t + \sigma_{\text{id}}^2 \quad (2)$$

$$N_{\text{max}} = \frac{L^2}{\sigma^2} = \left( \frac{2D_i}{\mu_i E L} + \frac{\sigma_{\text{id}}^2}{L^2} \right)^{-1} \quad (3)$$

where  $D_i$  denotes the molecular diffusion coefficient of the component  $i$ ,  $\sigma_{\text{diff}}^2$ ,  $\sigma_{\text{inj}}^2$ , and  $\sigma_{\text{det}}^2$  denote the variances due to diffusion, injection, and detection, respectively, and  $\sigma_{\text{id}}^2$  denotes the sum of the injection and detection variances. This theoretical upper limit represents the best separation efficiency that can be attained with any CE apparatus.

Alternatively, the plate height  $H$  can be used as a measure of efficiency per unit separation length with an ultimate lower limit given by eq 4

$$H_{\text{min}} = 2D_i/\mu_i E + \sigma_{\text{id}}^2/L \quad (4)$$

The variances  $\sigma_{\text{inj}}^2$  and  $\sigma_{\text{det}}^2$  can be written in more detail as

(38) Dose, E. V.; Guiochon, G. *Anal. Chem.* 1992, 64, 123.

(39) Lee, T. T.; Yeung, E. S. *Anal. Chem.* 1992, 64, 1226.

(40) Delinger, S. L.; Davis, J. M. *Anal. Chem.* 1992, 64, 1947.

(41) Huang, X.; Coleman, W. F.; Zare, R. N. *J. Chromatogr.* 1989, 480, 95.

(42) Jorgenson, J. W.; Lukacs, K. D. *Anal. Chem.* 1981, 53, 1298.



**Table I. Experimentally Determined Diffusion Coefficients  $D$ , Electrophoretic Mobilities  $\mu_{ep}$ , and Effective Charges  $z$** 

	$D/(10^{-6} \text{ cm}^2/\text{s})$	$\mu_{ep}/(10^{-4} \text{ cm}^2/\text{Vs})^a$	$z/e$
Arg-FITC	$3.9 \pm 0.4$	$-2.6 \pm 0.2$	$-1.7 \pm 0.2$
Gln-FITC	$3.0 \pm 0.3$	$-3.0 \pm 0.2$	$-2.5 \pm 0.3$
Phe-FITC	$3.4 \pm 0.3$	$-3.5 \pm 0.2$	$-2.6 \pm 0.3$
Gly-FITC	$3.7 \pm 0.4$	$-3.7 \pm 0.2$	$-2.6 \pm 0.3$

<sup>a</sup>  $\mu_{ep} = \mu - \mu_{eoi}$ ;  $\mu_{eoi} = 5.4 \pm 0.2 \times 10^{-4} \text{ cm}^2/\text{Vs}$ . Note that the precision of the experimental determination of the total mobilities  $\mu$  was better than 1%.

$$\sigma_{inj}^2 = l_{inj}^2/12 + 2D_i(t_{inj} + t_{dl}) \quad (5)$$

$$\sigma_{det}^2 = l_{det}^2/12 + \sigma_{el}^2 = l_{det}^2/12 + (\mu_i E \tau)^2 \quad (6)$$

where the injected plug length has been abbreviated to  $l_{inj}$ , the length of the detector volume to  $l_{det}$ , and the variance introduced by the detection electronics to  $\sigma_{el}^2$ . The time during which the sample plug is subject to diffusion in the separation capillary is the sum of the actual injection time  $t_{inj}$  and the time delay  $t_{dl}$  between the termination of sample injection and the start of the separation. In the formulation of eqs 5 and 6 it has been assumed that both the injection and detection volumes have a rectangular-shaped profile along the capillary axis.<sup>43</sup> The time constant of the detection system is denoted  $\tau$ . The variances caused by the finite length of the injection and detection volumes can be calculated to  $l_{inj}^2/12 = 1.88 \times 10^{-5} \text{ cm}^2$  (49%), and  $l_{det}^2/12 = 0.13 \times 10^{-5} \text{ cm}^2$  (3%) (see also Experimental Section; the figures in brackets are fractions of  $\sigma_{id}^2$ ). A delay time  $t_{dl}$  of 1 s and an injection time of 2 s are typically used in the experiments, which together with the typical diffusion coefficients listed in Table I lead to a numerical value of  $2D_i(t_{inj} + t_{dl}) = 1.80 \times 10^{-5} \text{ cm}^2$  (47%). With the low-pass filter set at  $f = 100 \text{ Hz}$ , the time constant of the detector can be determined to be  $\tau = 1/(2\pi f) = 1.6 \text{ ms}$ . For the fastest component detected in our experiment (Arg-FITC), this results in  $\sigma_{el}^2 = 2.2 \times 10^{-7} \text{ cm}^2$  (<1%) according to eq 6.<sup>43</sup> The total variance of the sum of all injection and detection effects amounts to  $\sigma_{id}^2 = 3.8 \times 10^{-5} \text{ cm}^2$ .

It should be emphasized at this point that the length of the volume-defined sample plug and diffusion effects during injection dominate  $\sigma_{id}^2$  and are of equal importance under our experimental conditions. A further reduction of the geometrically defined plug length will only lead to a significant gain in efficiency for small values of  $L$  if diffusional band broadening during injection can also be reduced at the same time. We believe that the combined injection and delay time of a few seconds in our experiment is already close to the lower limit and cannot be significantly improved, if good reproducibility is to be retained. For this reason, as far as analysis speed and separation efficiency are concerned, the experiments described here might already be close to the maximum performance achievable with this kind of analysis device.

Equations 1 and 3 can be combined to yield  $N/t$  as an index of separation speed<sup>44</sup> with an upper limit given by

$$\left(\frac{N}{t}\right)_{\max} = \frac{\mu_i^2 E^2}{2D_i + \mu_i E(\sigma_{id}^2/L)} \quad (7)$$

i.e.,  $N/t$  can be optimized by employing high field strengths  $E$  while at the same time keeping the ratio  $\sigma_{id}^2/L$  as low as possible. If the experimental parameters found for Gln-FITC (see Table I) are inserted in this equation, the second term of the denominator represents 89%, 59%, and 39% of its total numerical value at  $L = 5, 24$ , and  $50 \text{ mm}$ , respectively. Despite the fact that band broadening due to injection and

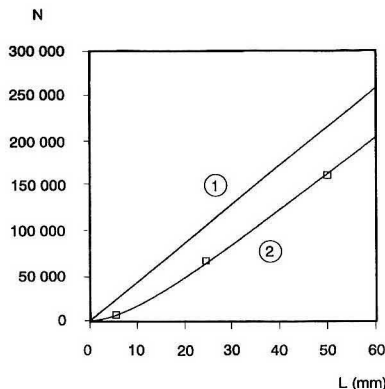


**Figure 3.** Number of theoretical plates  $N$  vs length of separation capillary  $L$ . The electric field strength is fixed at the value  $E = 1060 \text{ V/cm}$  used in the experiments. Curve 1 applies to a situation where longitudinal diffusion is the only source of band broadening, i.e.,  $N = \mu_i E L / 2D_i$ . The parameters  $\mu_i$  and  $D_i$  are drawn from experiment and refer to Gln-FITC (see Table I). Curve 2 additionally takes into account band broadening due to injection and detection (eq 3). The squares represent experimentally determined  $N$  values for Gln-FITC at  $L = 5, 24$ , and  $50 \text{ mm}$  (see text).

detection can be kept at very low level in our experiment, these effects still are of crucial importance when the maximum separation speed obtainable is being considered.

A plot of  $N$  vs  $L$  according to eq 3 is depicted in Figure 3. Curve 1 represents the limiting case  $\sigma_{id}^2 = 0$ ; i.e., longitudinal diffusion is considered to be the only source of band broadening, whereas curve 2 explicitly takes into account the variances of injection and detection. Again, the parameters  $\mu_i$  and  $D_i$  for both curves were taken from the experimental data obtained for glutamine-FITC (see Table I). As can be inferred from this figure, decreasing the separation length  $L$  at constant  $E$  means that the variance  $\sigma_{id}^2$  becomes a more and more important contribution to  $\sigma^2$ . This effect is even more pronounced by the fact that  $\sigma_{diff}^2 = 2D_i t$  is decreasing at the same time due to the increasing speed of the analysis (eq 1).

**Amino Acid Separations.** The results of the separation of a mixture of the six FITC-labeled amino acids arginine (Arg), glutamine (Gln), phenylalanine (Phe), asparagine (Asn), serine (Ser), and glycine (Gly) using the injection scheme outlined in the Experimental Section are depicted in Figure 4a,b. Both electropherograms were recorded at an electric field strength of  $1060 \text{ V/cm}$  (11 250 V applied between reservoirs 2 and 5). The assignment of the various peaks is based on single runs of each of the six amino acids.

Data depicted in Figure 4a were measured by positioning the fluorescence detector at  $L = 24 \text{ mm}$  downstream from the injection section, corresponding to a separation potential of  $V_{sep} = 2540 \text{ V}$ . As can be seen, even five "neutral" amino acids (Gln, Phe, Asp, Ser, Gly) with similar isoelectric points could be separated within an analysis time of about 14 s. The plate numbers attained range from 45 000 for Gly-FITC to 75 000 for Gln-FITC with associated plate heights of  $0.5$  and  $0.3 \mu\text{m}$ , respectively.

The limit of detection can be estimated from the data shown in Figure 4a and yields a value of about  $200 \text{ nM}$  in terms of sample concentration or  $20 \text{ amol}$  in terms of amount of injected substance ( $S/N = 3$ , injection volume  $100 \text{ pL}$ ). It should be noted, however, that the setup of the fluorescence detector in our experiment has not been optimized with respect to sensitivity.

(43) Sternberg, J. C. *Adv. Chromatogr.* 1966, 2, 206.

(44) Giddings, J. C. *Sep. Sci.* 1969, 4, 181.

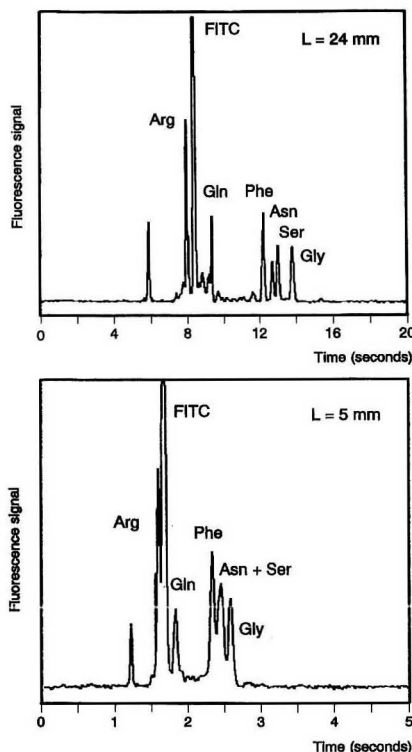


**Figure 4.** Electropherograms of a mixture of six FITC-labeled amino acids recorded at separation lengths of (a, top)  $L = 24$  mm and (b, bottom)  $L = 5$  mm. Electric field strength in both cases was 1060 V/cm. Formal concentration of each amino acid 10  $\mu$ M. Buffer solution 20 mM boric acid–100 mM Tris buffer (pH 9.0).

A very fast separation is shown in Figure 4b. By employing a separation length of only 5 mm ( $V_{sep} = 530$  V), most of the amino acids could still be resolved within an analysis time of only 2.5 s. The plate numbers obtained still range up to 5800 for Gln-FITC.

The diffusion coefficients have been experimentally determined by recording electropherograms at various values of the electric field strength ranging from 236 to 1060 V/cm. The separation length was held constant ( $L = 24$  mm). A simple rearrangement of eq 3 yields

$$N^{-1} = \sigma_{id}^2/L^2 + (2D_i/L^2)t \quad (8)$$

In general, however,  $D$  does not necessarily represent the molecular diffusion coefficient, as has been tacitly assumed in the previous section, but rather a collective term which takes into account all kinds of experimental nonideal effects.<sup>46</sup> The  $D$  parameters calculated from a least-squares fit of  $N^{-1}$  vs  $t$  for various FITC-amino acids are summarized in Table I. In an independent experimental determination of the molecular diffusion coefficient of fluorescein, Harrison et al.<sup>27</sup> found a value of  $D = (3.4 \pm 0.3) \times 10^{-6}$  cm<sup>2</sup>/s. All values of  $D$  listed in Table I are found to be in very good agreement with this molecular diffusion coefficient within the experimental standard deviations of both determinations. Since the comparatively large fluorescein label can be expected to

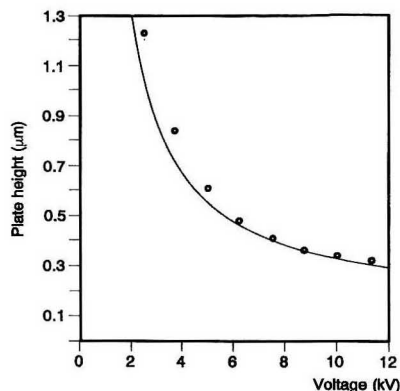


**Figure 5.** Plate height  $H$  vs potential applied between reservoirs 2 and 5. The separation length was held constant at  $L = 24$  mm. Circles, experimental plate heights for Gln-FITC. The curve represents the lower limit of  $H$  calculated according to eq 4. The parameters  $D_i$  and  $\mu_i$  refer to the experimental values for Gln-FITC (see Table I);  $E = 1060$  V/cm.

dominate the diffusion behavior of the FITC-labeled amino acids, all  $D$  parameters listed in Table I can be regarded as representing molecular diffusion coefficients. (i.e.,  $\theta = D_i/D = 1$  in the notation of Giddings<sup>44</sup>.)

The experimental plate numbers obtained for Gln-FITC for three different separation lengths  $L$  are shown in Figure 3 and are found to be in excellent agreement with the ultimate limit imposed by  $\sigma_{id}^2$  and longitudinal diffusion (curve 2). The variation of the plate height  $H$  as a function of the separation voltage applied is depicted in Figure 5. Again, the experimental values are in very good agreement with the theoretical limit given by eq 4. The theoretical upper limit of the separation speed index ( $N/t$ ) calculated according to eq 7 amounts to  $(N/t)_{max} = 8500$  s<sup>-1</sup> for Gln-FITC and is also in good agreement with the figure  $N/t = 8300$  s<sup>-1</sup> drawn from experiment.

The electroosmotic mobility  $\mu_{eo}$  under our experimental conditions has been measured according to a method first described by Huang et al.<sup>46</sup> This technique is based on monitoring the temporal change of the electric current after the buffer reservoir at the positive electrode has been diluted with water by 5–10%. The value of  $\mu_{eo} = (5.4 \pm 0.2) \times 10^{-4}$  cm<sup>2</sup>/Vs thus determined was subtracted from the measured overall mobilities in order to obtain the electrophoretic mobilities of the FITC-amino acids listed in Table I. Also included in Table I are the effective charges of the labeled amino acids which have been calculated according to the Nernst–Einstein equation<sup>47</sup>

$$\mu_{ep,i}/D_i = z_i e/k_B T \quad (9)$$

where  $z_i$  is the net effective charge of species  $i$  in proton units,  $e$  is the proton charge,  $k_B$  is Boltzmann's constant, and  $T$  is temperature. On the basis of the chemical structure of the FITC-labeled amino acids at pH 9, one would expect a total charge of  $-2$  for Arg-FITC (Arg amino group coupled to FITC, guanidine group positively charged) and  $-3$  for all "neutral" FITC-labeled amino acids. The experimentally determined values of  $-1.7$  for Arg-FITC and  $-2.5$  to  $-2.6$  for the other amino acids are in reasonable agreement with the figures given above, if one takes into account the formation of a diffuse double layer of counterions, which makes the effective charge

(45) Wieme, R. J. In *Chromatography*, 3rd ed.; Heftmann, E., Ed.; Van Nostrand Reinhold: New York, 1975.

(46) Huang, X.; Gordon, M. J.; Zare, R. N. *Anal. Chem.* 1988, 60, 1837.

(47) See, for example: Bockris, J. O'M.; Reddy, A. K. *Modern Electrochemistry*; Plenum Press: New York, 1970.

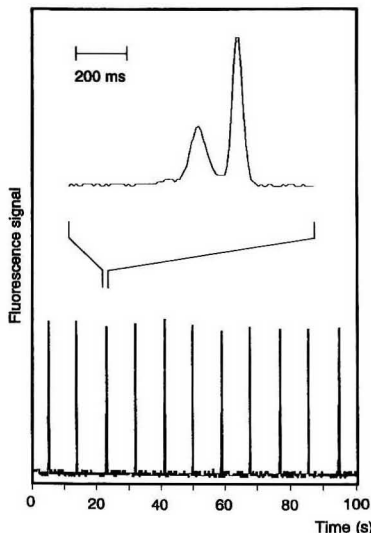


**Figure 6.** Automated repetitive sample injection. Sample, 100  $\mu$ M FITC in pH 9 buffer solution. Cycle composition: injection (3 s), dead time (1 s), separation (4 s), dead time (1 s); total cycle time 9 s. Timing was controlled with a programmable timer clock. The inset shows one selected sample separation event on a time scale expanded by a factor of 100.

more positive than the total charge. A detailed discussion of these effects is beyond the scope of this work and may be found, for example, in ref 48.

**Repetitive Sample Injection.** As has already been mentioned in the Introduction, micromachined integrated CE systems are one kind of realization of the general concept of miniaturized total analysis systems ( $\mu$ -TAS). Besides showing that a chemical analysis can be done on the time scale of the response time of chemical sensors, it is also very desirable to demonstrate that complete injection/separation cycles can be performed on this time scale in a reproducible way, for this would provide access to the field of quasi-continuous on-line monitoring of chemical species.

The data depicted in Figure 6 showing 11 successive injection/separation cycles within 100 s demonstrate that this can indeed be achieved with planar CE devices. A 100  $\mu$ M solution of FITC in pH 9.0 buffer was used as sample and gave rise to two closely spaced signals in the electropherogram, as can be seen in the inset in Figure 6. These two peaks originate either from the two isomers (NCS group in 5- and 6-position) and/or from FITC and its hydrolysis product. The whole analysis cycle was composed of a 3-s injection time, 1-s dead time (allowing the high voltage potentials to "settle"), followed by 4-s separation time and another 1-s dead time. One complete cycle lasted 9 s. Due to the large difference of the separation and cycle time scales involved (peak separation 170 ms; total time needed for 11 cycles 99 s), it is not possible to demonstrate both separation and repetition on a single time scale. For this reason, separation efficiency is shown only for one cycle in the inset of Figure 6. Data have been recorded using a digital storage oscilloscope with a (maximum) number of 10 000 channels and 10-ms channel width. Surprisingly, the temporal distance of the peaks between two successive cycles was found to be exactly 9.00 s for all 10

spacings measured except one (9.01 s). Since this single deviation is likely to be caused by the finite width of the time increments, we cannot calculate a reasonable standard deviation for the reproducibility of the migration time, but only claim that it is better than 0.1% over the 100-s time interval.

Unfortunately, due to the limited 8-bit vertical resolution of the oscilloscope and to the fact that the sampling rate of 100 Hz does not allow a reliable characterization of the peak maximum [full width at half maximum (fwhm) of signal 60 ms], the peak-to-peak reproducibility cannot be properly exhibited in Figure 6. The estimation of the peak areas with a simple algorithm yielded a standard deviation of peak area reproducibility of 2%. This figure certainly includes some error due to the rather coarse discrete horizontal and vertical grids of the data acquisition and can therefore be regarded as an upper limit.

#### 4. CONCLUSIONS

The data presented here clearly demonstrate that performance of CE close to the theoretical limit can be achieved by means of micromachined capillary manifolds on planar glass substrates. Complete analysis with high separation efficiency can be attained on a time scale of seconds. Plate numbers of 75 000 and 160 000 have been obtained for Gln-FITC in migration times of 10 and 20 s, respectively, with associated plate heights of 0.3  $\mu$ m. These analysis times are 50–100 times shorter than those of conventional CE separations of similar efficiencies and compare favorably with the response times of chemical sensors and biosensors.

Integration of a sample injector based on a volume-defined injection scheme allows reproducible introduction of very small sample volumes of about 100 pL without sample biasing. Reproducibility of the migration times and the peak areas is reasonably good.

Fluid flow can be effectively controlled on these devices by simple switching of electric potentials. The fact that no external pumps and valves are required makes this technique particularly suitable to automation and miniaturization. Furthermore, photolithographic definition of the channel pattern also provides an elegant route to more and more densely integrated functional components such as sample pretreatment or postcolumn derivatization on the same glass structure. Miniaturization and integration of other components, especially suitable detection systems, is another very desirable goal for future developments. The advantages of such planar microflow systems are many, ranging from quasi-continuous monitoring of chemical and biochemical species in miniaturized total analysis systems to highly reproducible and efficient separations in the "classical" field of CE.

In the authors' opinion, the experimental data presented here will lead to significant improvements in future generations of instruments, including benchtop CE instruments for laboratory analysis, but also for the integration of CE into on-line at-site monitors according to the  $\mu$ -TAS concept.

#### ACKNOWLEDGMENT

We thank Prof. D. J. Harrison (University of Alberta, Canada) and Dr. S. E. Wouters (Ciba-Geigy) for helpful discussions, Dr. E. Verpoorte (Ciba-Geigy) for critical reading of the manuscript, and Dr. J.-M. Bochat and Mr. D. Merian (Ciba-Geigy) for providing the electron micrograph.

Received for review April 19, 1993. Accepted June 23, 1993.\*

(48) Saville, D. A. In *The Dynamics of Electrophoresis*; Mosher, R. A., Saville, D. A., Thormann, W., Eds.; VCH Verlagsgesellschaft: Weinheim, Germany, 1992; and literature cited therein.

\* Abstract published in *Advance ACS Abstracts*, August 15, 1993.

# New Parameters for the Characterization of Relationship between Gas Chromatographic Retention and Temperature

M. de Frutos, J. Sanz,\* I. Martinez-Castro, and M. I. Jiménez

Instituto de Química Orgánica General (CSIC), Juan de la Cierva, 3, 28006 Madrid, Spain

Estimation of the gas chromatographic retention at different temperatures can be carried out by calculation of the parameters relating capacity ratio ( $k$ ) and temperature; these parameters can also be used in the optimization of separations. However, their use in the characterization of gas chromatographic retention requires precise measures, since they are very sensitive to experimental errors. We propose in this study the use of the parameters  $T_{ik}$  (defined as the isothermal column temperature at which a compound  $i$  has a capacity ratio  $k$ ) and of other parameters derived from them by principal component analysis, in order to characterize, in several approximation levels, the relationship between  $k$  and  $T$  for any compound/column pair, and as a starting point for the calculation of gas chromatographic retention and the optimization of separations.

## INTRODUCTION

The dependence between capacity ratio ( $k$ ) and temperature has been used by several authors in order to determine the thermodynamic properties of a gas chromatographic system.<sup>1–7</sup> Also, a number of workers interested in the practical aspects of gas chromatography have used this dependence in the calculation of gas chromatographic retention behavior<sup>8–13</sup> and in the optimization of gas chromatographic separations.<sup>14–20</sup>

The first approach requires of an accurate calculation method to compute, from experimental data, the thermo-

dynamic magnitudes of interest. A first objective in the second approach is the calculation of retention times or retention indexes under different conditions, including temperature programming. In both cases, the parameters that express the relationship between  $k$  and  $T$  could be used to characterize, in a quantitative way, the retention of a compound in a gas chromatographic system. However, their values are very sensitive to experimental errors, and very precise measures are necessary for their calculation.

The objective of the present study is the development of new parameters for the empiric characterization of the dependence between  $k$  and  $T$ . We propose the parameters  $T_{ik}$ , defined as the isothermal column temperature at which a compound  $i$  has a capacity ratio  $k$  in a given column, and other parameters derived from them by principal component analysis. These parameters allow the calculation of gas chromatographic retentions and also the optimization of separations.

## THEORY

The basic equation for the retention time ( $t_r$ ) is

$$t_r = t_0(1 + k) \quad (1)$$

In open tubular columns, dead time ( $t_0$ ) can be calculated from column geometry (length  $L$  and radius  $r$ ) and inlet ( $P_i$ ) and outlet ( $P_o$ ) pressures by using

$$t_0 = \frac{L^2 \eta 16}{r^2 j (P_o^2 (P_i^2 - P_o^2))} \quad (2)$$

where  $j$ , the mobile-phase compressibility factor, depends on  $P_o$  and  $P_i$ . Carrier gas viscosity ( $\eta$ ) is related to temperature  $T$  and must be taken from tabulated values.

For a given column, if  $P_i$  and  $P_o$  are constant, eq 2 can be rewritten as  $t_0 = (\text{constant})\eta$ . Ettre<sup>21</sup> proposed relating carrier gas viscosity and temperature by  $\eta = A(T/273)^B$ . Equation 2 then becomes

$$t_0 = A_t(T)^{B_t} \quad (3)$$

From experimental  $t_0$  values measured at a given pressure and different temperatures,  $A_t$  and  $B_t$  can be calculated by regression and then used to calculate dead time at any temperature.

The influence of stationary phase on the retention is expressed in eq 1 by the capacity ratio ( $k$ ). The partition coefficient  $K$  is related to  $k$  through the phase ratio  $\beta$ :

$$k = K/\beta \quad (4)$$

For a given solute in a given stationary phase  $K$  only depends on the temperature according to eq 5, where  $R$  is the gas

$$\ln K = -\Delta G^\circ/RT \quad (5)$$

constant and  $\Delta G^\circ$  the change in the Gibbs free energy for the

- (1) Podmaniczky, L.; Szepeszy, L.; Lakszner, K.; Schomburg, G. *Chromatographia* 1986, 21, 91–94.
- (2) Bincheng, L.; Binchang, L.; Koppenhoefer, B. *Anal. Chem.* 1988, 60, 2135–2137.
- (3) Guan, Y.; Kiraly, J.; Rijks, J. A. *J. Chromatogr.* 1989, 472, 129–143.
- (4) Dose, E. V. *Anal. Chem.* 1987, 59, 2414–2419.
- (5) Podmaniczky, L.; Szepeszy, L.; Lakszner, K.; Schomburg, G. *Chromatographia* 1985, 20, 591–595.
- (6) Castells, R. C.; Arancibia, E. L.; Nardillo, A. M. *J. Chromatogr.* 1990, 504, 45–53.
- (7) Comor, J. J.; Kopecki, M. M. *Anal. Chem.* 1990, 62, 991–994.
- (8) Shrotri, P. Y.; Mckashi, A.; Mukesh, D. *J. Chromatogr.* 1987, 387, 399–403.
- (9) Bautz, D. E.; Dolan, J. W.; Snyder, L. R. *J. Chromatogr.* 1991, 541, 1–19.
- (10) Dolan, J. W.; Snyder, L. R.; Bautz, D. E. *J. Chromatogr.* 1991, 541, 21–34.
- (11) Snyder, L. R.; Bautz, D. E.; Dolan, J. W. *J. Chromatogr.* 1991, 541, 35–58.
- (12) Wright, L. H.; Walling, J. F. *J. Chromatogr.* 1991, 540, 311–322.
- (13) Bautz, D. E.; Dolan, J. W.; Raddatz, W. D.; Snyder, L. R. *Anal. Chem.* 1990, 62, 1560–1567.
- (14) Bártu, V. *J. Chromatogr.* 1983, 260, 255–264.
- (15) Bártu, V.; Wicar, S. *Anal. Chim. Acta* 1983, 150, 245–252.
- (16) Sanz, J.; Martínez-Castro, I.; Reglero, G.; Cabezu, M. D. *Anal. Chim. Acta* 1987, 194, 91–98.
- (17) Lanin, S. N.; Lysko, O. V.; Nikitin, Y. S. *Chromatographia* 1988, 26, 63–69.
- (18) Peichang, L.; Bingcheng, L.; Xinhua, C.; Chunrong, L.; Guangda, L.; Haochun, L. *HRC & CC, J. High Resolut. Chromatogr. Chromatogr. Commun.* 1986, 9, 702–707.
- (19) Akporhonor, E. E.; Le Vent, S.; Taylor, D. R. *J. Chromatogr.* 1987, 405, 67–76.

- (20) Akporhonor, E. E.; Le Vent, S.; Taylor, D. R. *J. Chromatogr.* 1990, 504, 269–278.
- (21) Ettre, L. S. *Chromatographia* 1984, 19, 243.

**Table I. Capillary Columns Used in the Experimental Determinations**

column	stationary phase	length (m)	i.d. (mm)	d <sub>f</sub> (μm)	supplier
A	OV-1	20	0.2	0.5	homemade
B	OV-1	22	0.22	0.14	homemade
C	SP-1000	25	0.22	0.25	Perkin-Elmer
D	OV-1	22	0.22	0.14	homemade

**Table II. Compounds Used in the Determination of *k* Values at Several Temperatures in Columns A-D and Temperature Ranges for Each Compound Class<sup>a</sup>**

column	compounds	carbon no.	temp range (°C)
A (OV-1)	<i>n</i> -alkanes	(9-19)	100-240
B (OV-1)	methyl esters	(5-12)	60-200
	<i>n</i> -acids	(6-12,14,16,18)	75-250
	2-ketones	(8-13,15,17,19)	80-225
	ethyl esters	(6-12,14,16)	75-250
C (SP-1000)	<i>n</i> -alkanes	(10-20,22,24)	75-270
	methyl esters	(5-11)	80-180
	<i>n</i> -acids	(5-8)	120-180
	2-ketones	(8-13)	80-180
	ethyl esters	(4-12)	80-180
D (OV-1)	<i>n</i> -alkanes	(14-20)	80-180
	<i>n</i> -tetradeceane		80-250

<sup>a</sup> Numbers in parentheses indicate carbon chain length.

evaporation of the solute from the stationary phase. Then, for a given compound and phase, capacity ratio depends only on the phase ratio (eq 4) and on the temperature (eq 5, where  $\Delta G^\circ$  also depends on the temperature).

The temperature of gas chromatographic separations is usually selected in order to obtain suitable *k* values; frequently a temperature program is used when the volatility of sample components covers a wide range.

In the temperature-programmed mode, the speed of the chromatographic band changes continuously, since both gas velocity and capacity ratio depend on the temperature.<sup>22</sup> Retention time can be calculated<sup>16</sup> by a numerical procedure, supposing that band movement is decomposed in steps corresponding to small time intervals:

$$\sum_{t=t_0}^{t=t_f} \frac{t}{t_0(1+k_t)} = 1 \quad (6)$$

where  $k_t$  and  $t_0$  are the values of capacity ratio and dead time in the isothermal mode at the mean temperature in the time interval  $t$ .

## EXPERIMENTAL SECTION

Retention times were determined, using the capillary columns listed in Table I, in a Hewlett-Packard 5890 gas chromatograph equipped with a flame ionization detector and a split/splitless injector. Nitrogen was used as carrier gas. Inlet pressure was usually selected in order to obtain a flow rate near the Van Deemter optimum for each column; different flow rates were selected in some determinations. Chromatograms were recorded in a Spectra Physics SP-4270 integrator.

Table II lists the compounds whose *k* values were determined at four to six different temperatures in the range 80-240 °C in columns A-C. Column D was used in the determination of *k* values for *n*-tetradeceane at 11 different temperatures between 80 and 250 °C. The compounds are members of several homologous series; their carbon chain lengths are listed in parentheses. Oven temperatures were chosen for each compound in order to obtain *k* values in the usual range for gas chroma-

**Table III. Equations Used for Correlating *k* and *T* Values<sup>a</sup>**

code	equation	mean square residuals <sup>b</sup> ( $\sum (k_{exp} - k_{calc})^2 / nt$ ) <sup>1/2</sup>			
		A	B	C	D
E1	$k = p_1 T e^{p_2/T}$	0.026	0.039	0.048	0.104
E2	$k = p_1 e^{p_2/T}$	0.028	0.041	0.054	0.112
E3	$k = p_1 T^{p_2}$	0.046	0.082	0.136	0.229
E4	$k = p_1(p_2 + T)^{p_3}$	0.022	0.019	0.013	0.019
E5	$k = p_1 e^{p_2/T} + p_3$	0.031	0.023	0.013	0.090
E6	$k = p_1 T^{p_2} e^{p_3/T}$	0.033	0.022	0.029	0.034

Other Equations Showing Less Quality of Fit

$$\begin{aligned} k &= p_1/T^{p_2} + p_3 & k &= p_1 p_2^{p_3 T} & k &= (p_1 + T)/(p_2 T + p_3) \\ k &= p_1 p_2^T + p_3 & k &= p_1 T^2 + p_2 T + p_3 & k &= (p_1 + T)/(p_2 T^2 + p_3) \\ k &= 1/(p_1 T + p_2) & k &= 1/(p_1 \log T + p_2) & k &= p_1 + p_2/T \\ k &= 1/(p_1 T + p_2) & k &= p_1 + p_2^T \end{aligned}$$

<sup>a</sup> Quality of fit (mean square residual) is given for the best equations. *nt*, total number of *k* pairs in each data set. <sup>b</sup> For data sets A-D.

tography (between 1 and 20): *k* was calculated as the mean value from several measures. Dead time was always determined by the injection of methane; dependence of dead time with *T* was characterized for each column by the *A<sub>t</sub>* and *B<sub>t</sub>* values obtained from experimental data at different temperatures using eq 3.

Calculations were carried out in an M-20 Olivetti and in an Amstrad PC 1640 microcomputers. Programs were written in Basic and QuickBasic.

## RESULTS AND DISCUSSION

***k*-*T* Dependence through *p<sub>i</sub>* Parameters.** The dependence of *k* on the temperature for a given compound *i* and a column *c* can be written

$$k_{i,c} = f(p_1, \dots, p_r, \dots, T) \quad (7)$$

where the value of the parameters *p<sub>i</sub>* depends on compound and stationary phase, but also on the column phase ratio. The different retention behavior of the compounds should be reflected in their different *p<sub>i</sub>* values.

In a first approximation, it could be supposed that only one parameter *p<sub>i</sub>* would be enough to describe the variation of *k* with *T*. This would mean that compounds having the same *k* at a given *T* would also coelute at other temperatures. Although this can be true for compounds having a similar chemical structure, many cases are known of different retention behavior and even of elution order inversion in the elution of pairs of components when the column temperature is changed.<sup>23-25</sup> Then, at least two parameters seem to be necessary for characterizing the capacity ratio of a compound in a column.

In order to describe the variation of *k* with *T*, we have empirically selected 17 different equations based in eq 7, using two or three parameters *p<sub>i</sub>* (see Table III). Equations E1, E2, and E5 had been previously used.<sup>4,6,12,14-16,19</sup> Since eq E2 can be deduced from eqs 4 and 5 (see Theory section), its *p<sub>i</sub>* parameters<sup>5,12,19</sup> have a physical significance.

The *k*-*T* data pairs for columns A-D (data sets A-D in Table II) were submitted to nonlinear regression calculations<sup>26</sup> in order to determine the *p<sub>i</sub>* parameters and the quality of fit for the 17 equations. Table III lists the average quality

(23) Saha, N. C.; Mitra, G. D. *J. Chromatogr. Sci.* 1970, 8, 84-90.(24) Saxton, W. L. *J. Chromatogr.* 1986, 357, 1-10.(25) Pell, R. J.; Gearhart, H. L. *HRC & CC, J. High Resolut. Chromatogr. Chromatogr. Commun.* 1987, 10, 388-391.(26) Draper, N. R.; Smith, H. *Applied Regression Analysis*; John Wiley & Sons: New York, 1980; Chapter 10.(22) Harris, W. E.; Habgood, H. W. *Programmed Temperature Gas Chromatography*; John Wiley & Sons: New York, 1966.



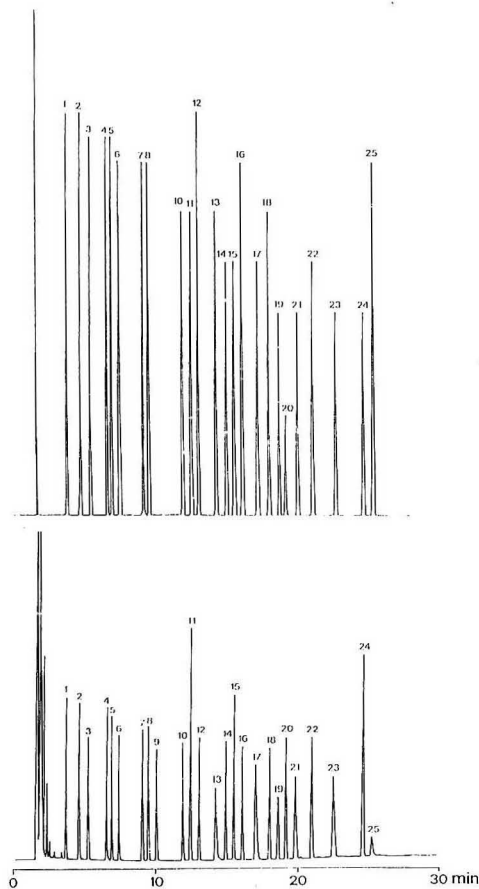


**Figure 1.** Chromatograms of a standard mixture of compounds usually present in cheese volatile fractions. Upper plot: calculated chromatogram. Lower plot: real chromatogram. Column characteristics: 21 m  $\times$  0.25 mm i.d., stationary phase 43% FFAP/57% OV-1. Peak identification: 1, methyl hexanoate; 2, ethyl hexanoate; 3, methyl heptanoate; 4, ethyl heptanoate; 5, 2-nonanone; 6, methyl octanoate; 7, ethyl octanoate; 8, 2-decanone; 9, methyl nonanoate; 10, ethyl nonanoate; 11, 2-undecanone; 12, methyl decanoate; 13, hexanoic acid; 14, ethyl decanoate; 15, 2-dodecanone; 16, methyl undecanoate; 17, heptanoic acid; 18, ethyl undecanoate; 19, 2-tridecanone; 20, methyl dodecanoate; 21, octanoic acid; 22, ethyl dodecanoate; 23, nonanoic acid; 24, 2-pentadecanone; 25, decanoic acid. See ref 27 for details.

of fit for the three "best" two-parameter and three-parameter equations, expressed as the mean square residual:

$$\left( \sum (k_{\text{exp}} - k_{\text{calc}})^2 / nt \right)^{1/2} \quad (8)$$

where  $k_{\text{exp}}$  is the experimental  $k$  value,  $k_{\text{calc}}$  is calculated by nonlinear least squares regression, and the mean is extended to the total number ( $nt$ ) of  $k$ - $T$  determinations in each data set.

A study of the residuals ( $k_{\text{exp}} - k_{\text{calc}}$ ) shows the presence of systematic deviations in small and high  $k$  values. The presence of this kind of errors indicates that great care should be taken when these equations are used in extrapolation.

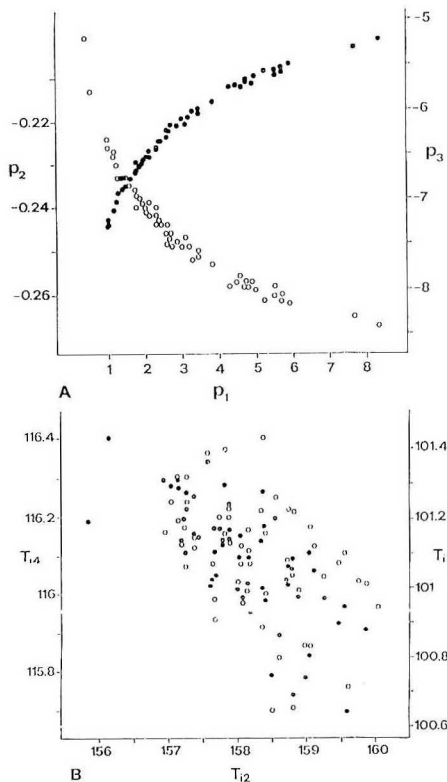


**Figure 2.** (A)  $p_i$  values in eq E4 calculated for 60  $k$ - $T$  data pairs obtained by random modification of data set D.  $p_2$  (○) and  $p_3$  (●) are plotted against  $p_1$ . (B)  $T_k$  values calculated from the same  $k$ - $T$  data pairs.  $T_4$  (○) and  $T_6$  (●) are plotted against  $T_2$ .

When a data set covering a wider  $k$  range ( $n$ -tetradecane at 11 different temperatures in column D) was used, the same kind of error appeared. The use of the best three-parameter equation (eq E4 in Table III) reduces the error. However, the quality of fit of the two-parameter eqs E1 and E2 is enough for several practical purposes; for instance, they can be used in the optimization of chromatographic separations.

**Optimization of the Resolution.** Determination of the resolution requires the calculation of both  $t_r$  and peak width ( $w$ ) values. According to eq 1 (isotherm operation) or eq 6 (programmed temperature operation),  $t_r$  can be calculated from  $t_0$  (related to  $T$  through eq 3) and  $k$ . Peak width mainly depends on flow rate and  $k$ ; the influence of column efficiency in  $w$  presents an additional problem. Data sets B and C were used to design a mixed-phase column optimized for the separation of 24 volatile constituents of cheese.<sup>27</sup> Equation E1 was chosen for the determination of  $p_i$  parameters. Optimization was carried out by calculation of retention time and peak width for different column composition (OV-1/FFAP ratio and film thickness  $d_f$ ) and operating conditions (initial temperature and programming rate); the worst resolution between pairs of components was taken as the resolution of the mixture, and the variables maximizing this value were selected. The highest resolution was obtained for a column

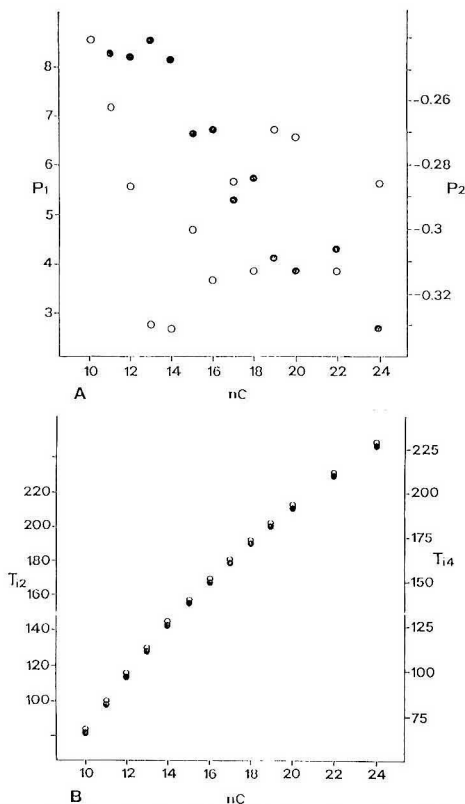


**Figure 3.** (A)  $p_1$  values in eq E4 calculated from the  $n$ -alkanes in data set B.  $p_1$  (O) and  $p_2$  (●) are plotted against carbon number. (B)  $T_k$  values calculated from the same data.  $T_{12}$  (O) and  $T_{14}$  (●) are plotted against carbon number.

having 43% FFAP and 57% OV-1, using 80 °C as initial temperature and a program rate of 4 °C/min. More details are given elsewhere.<sup>27</sup> Figure 1 shows (lower plot) the real chromatogram of a mixture of standards in the mixed-phase column, prepared according to the above results and (upper plot) the calculated chromatogram for the optimal separation.

**Characterization of the Retention Behavior.** The use of both two- and three-parameter equations presents a problem, which appears in nonlinear estimation in some ill-conditioned cases:<sup>28</sup> the parameters are highly correlated and the error of  $p_1$  values can become very high, especially when there are few data points or the experimental error in their determination is high. The error also depends on the least squares criterion used in the fit (i.e., fitting by nonlinear regression or by linear regression after a logarithmic transformation, in eq E2) or on the weights that can be associated with data in the calculations.

As an example, 60 sets of  $p_i$  coefficients were calculated after adding a random error to the experimental  $k$  values in column D data set in order to obtain a 1% variation coefficient in the simulated  $k$  values. Variation coefficients obtained for  $p_1$  and  $p_2$  values in eq E1 were 17.8% and 0.9%, respectively.

The problem is worse in the three-parameter equations.  $p_1$ ,  $p_2$ , and  $p_3$  parameters in eq E4 were calculated from the

**Table IV.**  $T_{ik}$  Parameters for the Homologous Series Compounds in Data Set B

compd codes <sup>a</sup>	$T_{ik}$ (°C) for $k$						
	0.5	1	2	4	5	8	10
M5	82.78	63.87	46.02	29.17	23.94	13.25	8.31
M6	103.66	83.52	66.09	51.01	46.60	37.95	34.14
M7	122.74	102.12	83.98	68.02	63.30	53.97	49.82
M8	140.09	119.27	100.73	84.24	79.32	69.56	65.19
M10	172.81	150.39	130.67	113.33	108.20	98.08	93.57
M11	187.06	164.54	144.54	126.79	121.51	111.03	106.34
M12	200.13	177.67	157.56	139.57	134.19	123.46	118.64
A6	111.47	93.65	78.87	66.60	63.12	56.43	53.54
A7	129.44	110.29	94.03	80.23	76.25	68.52	65.14
A8	146.06	125.82	108.42	93.46	89.11	80.60	76.86
A9	161.88	141.45	123.42	107.51	102.79	93.47	89.31
A10	176.31	155.49	136.99	120.55	115.66	105.94	101.60
A11	190.73	168.53	149.33	132.71	127.86	118.34	114.13
A12	204.20	181.50	161.68	144.37	139.28	129.26	124.81
A14	228.58	205.48	185.00	166.84	161.44	150.73	145.94
A16	251.18	227.17	206.01	187.35	181.82	170.89	166.02
A18	271.16	247.04	225.55	206.41	200.71	189.36	184.28
K8	116.96	96.05	77.63	61.40	56.60	47.10	42.87
K9	135.11	113.68	94.93	78.50	73.67	64.13	59.89
K10	152.10	130.34	111.12	94.12	89.08	79.10	74.64
K11	167.77	145.84	126.30	108.87	103.68	93.34	88.71
K12	183.31	160.54	140.39	122.57	117.28	106.81	102.13
K13	196.92	174.17	153.87	135.74	130.33	119.55	114.72
K15	222.61	199.29	178.44	159.78	154.20	143.09	138.10
K17	245.81	221.94	200.58	181.47	175.75	164.36	159.25
K19	266.80	242.50	220.73	201.24	195.41	183.78	178.56
E6	118.09	97.43	79.56	64.10	59.58	50.73	46.82
E7	135.85	114.83	96.35	80.11	75.31	65.84	61.62
E8	152.13	130.92	112.08	95.35	90.37	80.49	76.07
E9	167.64	145.98	126.75	109.67	104.59	94.51	89.99
E10	181.93	160.09	140.58	123.17	117.97	107.61	102.97
E11	196.34	173.56	153.49	135.81	130.58	120.23	115.62
E12	209.30	186.35	165.97	147.89	142.51	131.83	127.05
E14	234.00	210.15	189.03	170.32	164.76	153.75	148.83
E16	255.77	231.50	209.95	190.81	185.11	173.81	168.76
C10	121.96	100.74	82.48	66.77	62.20	53.26	49.33
C11	140.10	118.26	99.27	82.77	77.93	68.42	64.21
C12	156.92	134.70	115.17	98.01	92.94	82.93	78.47
C13	170.60	149.01	129.73	112.51	107.37	97.14	92.55
C14	184.95	163.08	143.50	125.95	120.70	110.24	105.54
C15	199.41	176.67	156.49	138.58	133.26	122.70	117.97
C16	211.87	189.09	168.73	150.52	145.08	134.25	129.38
C17	224.30	200.93	180.22	161.86	156.41	145.59	140.76
C18	235.54	212.31	191.49	172.84	167.26	156.12	151.12
C19	247.13	223.12	201.85	183.01	177.42	166.33	161.37
C20	257.77	233.53	212.0	192.88	187.19	175.89	170.84
C22	276.31	252.43	230.90	211.50	205.67	194.01	188.75
C24	294.82	270.21	248.17	228.42	222.52	210.74	205.44

<sup>a</sup> M, methyl esters; A,  $n$ -acids; K, 2-ketones; E, ethyl esters; C,  $n$ -alkanes. Numbers in codes indicate carbon chain length.

same simulated data; their variation coefficients are 59.4%, 5.4%, and 9.9%, respectively. Figure 2A plots the  $p_1$ ,  $p_2$ , and  $p_3$  calculated values; it can be seen that the changes in their values caused by the added error are related.

These  $p_i$  coefficients can be used without problem to calculate  $k$  values at different temperatures. However, their use in the characterization of chromatographic behavior or the interpretation of their possible physical significance is very dangerous unless special care in the experimental determinations and calculations is taken. As an example,  $p_1$  and  $p_2$  values in eq E4 calculated for the  $n$ -alkanes in column C are plotted against carbon number in Figure 3A. The expected regular behavior is masked by the high relative error.

**Parameters  $T_{ik}$ .** An ideal set of parameters for the characterization of chromatographic retention behavior should be easily calculated from experimental data for a compound and column, should show small variation with experimental error, and should also easily allow the calculation of  $k$  at any temperature.

We propose to characterize the retention of a compound  $i$  in a given column from its parameters  $T_{ik}$ , defined as the isothermal column temperature at which the compound has a capacity ratio  $k$ .

When an equation from those listed in Table III can be written as  $T = f(k, p_i)$ ,  $T_{ik}$  can be easily calculated from  $k$  and  $p_i$  parameters. In the other cases, they can be obtained iteratively by the Newton-Raphson method.<sup>28</sup>

Since many values of  $k$  can be chosen, any number of  $T_{ik}$  parameters can be used in the characterization; it seems reasonable to choose  $k$  values in the usual chromatographic range. Table IV shows  $T_{ik}$  values for the compounds in data set B for  $k = 0.5, 1, 2, 4, 5, 8$ , and  $10$ ; values for other  $k$  can be easily calculated.

When the simulated  $k$  values with random error are used as experimental data, the variation coefficient for calculated  $T_{ik}$  values range only from 0.9% to 0.1% ( $k$  between 0.5 and 10). Figure 2B shows a plot of  $T_{i4}$  and  $T_{i5}$  against  $T_{i2}$ . While in Figure 2A the errors in parameters  $p_1$  and  $p_2$  are systematically related, no trends are observed in the simulated errors in Figure 2B.

In Figure 3B,  $T_{i2}$  and  $T_{i4}$  calculated for the  $n$ -alkanes in data set B are plotted against carbon number. The regular behavior (compare with Figure 3A) is expected for a homologous series.

$k$  values at any temperature can be calculated from  $T_{ik}$  parameters, which are used as starting data for a nonlinear regression. In a first step the  $p_i$  coefficients of a given  $k$ - $T$  equation are obtained, then the equation can be used to calculate  $k$  values at any temperature.

Although in the example of Table IV each compound is characterized by seven values, it can be seen that there is a high correlation among the values corresponding to the different columns of the table. For instance, if we take  $T_{i2}$  ( $k = 2$ ) as the independent variable, the other  $T_{ik}$  in Table IV can be calculated using a single linear regression ( $T_{ik} = aT_{i2} + b$ ) with a good quality of fit ( $r$  between 0.9991 and 0.9999). That means that most of the information contained in them is redundant: the number of  $T_{ik}$  values used in the characterization could then be reduced. A way to do it is principal component analysis.

**New Parameters Calculated by Principal Component Analysis.** Principal component analysis<sup>29</sup> can be used to study the structure of a data matrix and the correlations among its variables. The principal component model decomposes a data matrix into the product of a row matrix and a column matrix. Row ( $r_{ij}$ ) and column ( $c_{ij}$ ) matrix values are calculated in order to reproduce the data ( $d_{ij}$ ) with the highest possible accuracy for each value of  $n$  (components):

$$d_{ij} = \sum_{l=1}^n r_{il}c_{lj} \quad (9)$$

A set of values (eigenvalues) which measure the amount of variance in the original data explained by each component is also calculated.<sup>30</sup>

A study by principal component analysis of the  $T_{ik}$  values calculated from data set B (Table IV) shows the results summarized in Table V. A 99.80% of total variance is associated with the first component, while the second component explains 0.18%.  $r_{il}$  and  $c_{lj}$  coefficients are also shown in the table. The mean error in the recalculation of

**Table V. Results of Principal Component Analysis of Data Set B<sup>a</sup>**

$l$	$c_{lj}$ coeff ( $k = 0.5-10$ )						
	0.5	1	2	4	5	8	10
1	0.49	0.44	0.39	0.35	0.33	0.31	0.30
2	-0.61	-0.30	-0.03	0.21	0.28	0.42	0.48
3	-0.52	0.27	0.51	0.29	0.16	-0.24	-0.48

	$r_{il}$ coeff ( $l = 1-3$ )		
	1	2	3
M5	111.29	-48.24	2.98
M6	168.39	-33.43	-0.57
M7	213.94	-28.42	-0.03
M8	256.84	-22.58	0.37
M10	335.15	-12.53	-0.22
M11	370.66	-7.56	0.14
M12	404.04	-2.30	0.45
A6	204.01	-16.40	-1.88
A7	242.31	-15.41	-1.33
A8	278.97	-13.35	-1.00
A9	316.53	-9.77	-0.09
A10	351.37	-5.51	0.15
A11	384.81	-1.21	-0.97
A12	416.31	1.85	-0.64
A14	475.95	9.52	-0.06
A16	530.83	17.03	-0.39
A18	581.00	24.41	0.01
K8	197.26	-32.47	0.06
K9	242.57	-25.40	-0.26
K10	284.07	-20.04	0.07
K11	323.03	-14.56	0.38
K12	360.02	-9.87	0.01
K13	394.51	-4.65	0.36
K15	458.21	4.61	0.37
K17	515.70	13.02	0.32
K19	568.00	20.83	0.30
E6	203.39	-28.77	-0.65
E7	246.14	-23.87	-0.11
E8	286.42	-18.35	0.25
E9	324.52	-12.99	0.20
E10	360.15	-7.83	0.39
E11	394.40	-3.31	-0.22
E12	426.37	1.00	0.06
E14	486.34	9.06	-0.11
E16	540.53	17.05	-0.07
C10	211.21	-28.61	-0.89
C11	254.22	-23.91	-0.57
C12	294.88	-19.00	-0.18
C13	331.94	-12.04	0.42
C14	367.53	-6.93	0.51
C15	401.75	-2.65	0.07
C16	433.12	1.98	0.37
C17	463.47	6.46	-0.06
C18	492.11	10.76	0.40
C19	519.69	14.48	-0.16
C20	545.87	18.09	-0.07
C22	594.15	26.12	0.55
C24	639.36	32.55	0.21

<sup>a</sup>  $l$ , number of components (1-3);  $i$ , compounds (code names as in Table IV);  $j$ ,  $k$  values.

$T_{ik}$  values is 4.68, 0.15, and 0.004 °C when, respectively, one, two, or three components are used; the rest of the components do not have practical significance.

When the same calculations are carried out using the experimental data set from column C, 99.77% and 0.22% of variance are associated respectively with first and second components and 5.15, 0.15, and 0.003 °C are the mean errors in the recalculation of  $T_{ik}$  with one, two, and three components. Figure 4 plots  $c_{lj}$  ( $l = 1, 2, 3$ ) against  $k$  for data sets B and C;  $c_{lj}$  values are surprisingly similar for the two data sets.

Since in both cases components higher than 3 have no relevance, three approximation levels using one, two, and

(28) Press, W. H.; Flannery, B. P.; Teukolsky, S. D.; Vetterling, W. T. *Numerical Recipes*; Cambridge University Press: Cambridge, UK, 1986; Chapter 9.

(29) Malinowski, E. R.; Howery, D. G. *Factor Analysis in Chemistry*; John Wiley & Sons: New York, 1980.

(30) Wolff, D. D.; Parsons, M. L. *Pattern Recognition Approach to Data Identification*; Plenum Press: New York, 1983.

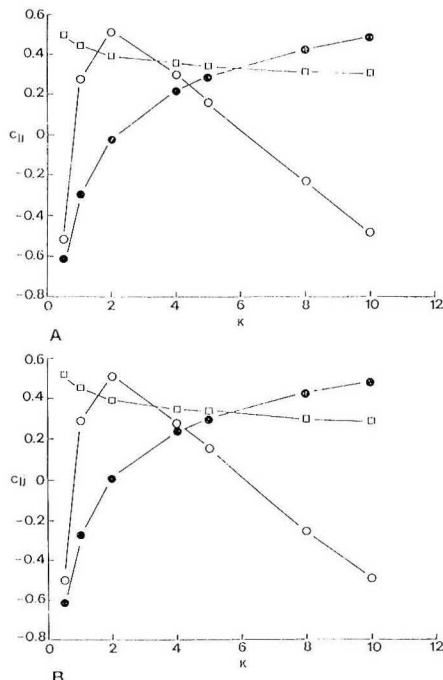


Figure 4. Column coefficients  $c_{ij}$  obtained by principal component analysis of the  $T_{ik}$  matrix: (A) data set B; (B) data set C. (□) first component; (●) second component; (○) third component.  $c_{ij}$  values are plotted against  $k$ .

three components can be defined in order to describe the data ( $n = 1, 2$ , or  $3$  in eq 9). Column coefficients  $c_{ij}$  are related to the  $k$  values used to calculate the matrix, while row coefficients  $r_{ij}$  are characteristic of the compounds.

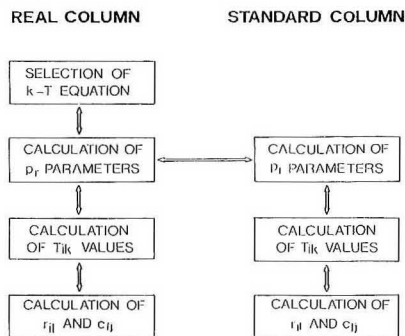
In the first level,  $T_{ik}$  can be calculated as the product  $r_{ij}c_{ij}$ . Row coefficient  $r_{ij}$  is highly correlated with  $T_{ik}$  ( $r = 0.9994$ – $0.9999$ ) and has the meaning of an "average" retention. Since each compound is characterized by a single number, the elution order for a series of compounds would be the same regardless of temperature.

The second approximation level uses the second component to take into account the different variation of retention with temperature for different compounds. Since  $c_{2j}$  coefficients are negative for low  $k$  values and positive for high  $k$  values, compounds with  $r_{12}$  positive will be more retained than an average compound at low temperatures and less at high temperatures. For instance,  $r_{12}$  for ethyl hexadecanoate in column C is 17.05. While the first approximation (first component) indicates that it would need a temperature of 210.43 °C to elute with  $k = 2$ , and 160.49 °C for  $k = 10$ , the corrected temperatures using the second component coefficients are 210.00 and 168.71 °C, respectively.

The third level introduces a further approximation, described by the values  $c_{3j}$ . Calculated  $T_{12}$  and  $T_{110}$  for ethyl hexadecanoate, corrected using the third component, are 209.96 and 168.74 °C ( $T_{12}$  and  $T_{110}$  values in Table IV are 209.95 and 168.76 °C).

The existence of three levels agrees with the results of Hawkes<sup>31</sup> about the relation between retention index  $I$  and

#### Scheme I



$T$ . The use of our first approximation level supposes that  $I$  is constant; the second level is approximately related to the linear dependence between  $I$  and  $T$  while the third level could explain the small deviations from linearity.

**Characterization Scheme.** In the proposed scheme, the characterization of retention includes parameters related to column and compound behavior. The calculation of these parameters from experimental  $k$ – $T$  data for several compounds (including a set of "standard" compounds, in our case,  $n$ -alkanes) is summarized in the left side of Scheme I and can be carried out in the following steps:

(1) A suitable equation based on eq 7 relating  $k$  and  $T$  is selected (eq E4 seems to be advisable when data at four temperatures at least are available).

(2) The  $p_i$  parameters in the equation are calculated for each compound using nonlinear regression.

(3) Several  $k$  values, in the same range that those experimentally obtained, are selected.  $T_{ik}$  are calculated for each compound and  $k$  value.

(4) Principal component analysis is performed over the  $T_{ik}$  data matrix. Row and column matrices as in Table V are obtained.

While the retention behavior of the chromatographic column is characterized by the matrix column values  $c_{ij}$ , compounds are characterized by their row values  $r_{ij}$ . If  $T_{ik}$  values of new compounds are available, their  $r_{ij}$  values can be calculated by regression from  $T_{ik}$  and  $c_{ij}$  data.

**Calculation of  $k$  Values.** Capacity ratio values at any temperature for a given column and compound can be easily calculated from  $r_{ij}$  and  $c_{ij}$  values (Scheme I). In a first step, the number of parameters ( $l = 1, 2$ , or  $3$ ) is selected according to the necessary precision level.  $T_{ik}$  matrix is then calculated by the Newton–Raphson method. A suitable equation (i.e., eq E1 or eq E4 in the Table III) relating  $k$  and  $T$  is then selected and its parameters ( $p_i$ ) are calculated by regression from  $T_{ik}$  data. The equation can be used in the calculation of  $k$  at any  $T$ .

**Extension to Stationary-Phase Characterization.** When the equations based on eq 7 are written

$$k_{i,c} = p_l f(\dots, p_l, \dots, T) \quad (10)$$

from eq 4 we have

$$K_{i,c} = (\beta p_l) f(\dots, p_l, \dots, T) \quad (11)$$

where  $\beta$  is the phase ratio. In this way parameters independent from column geometry can be calculated; according to the equation selected, they can have thermodynamic significance from their relationship with partition coefficient  $K$ . Although these parameters could be used in the char-

(31) Hawkes, S. J. *Anal. Chem.* 1989, 61, 88–90.

acterization of the stationary-phase behavior, they would present the same problems previously mentioned.

A more practical approach could be the use of a hypothetical "standard" chromatographic column. For instance, such column can be defined as having 0.25-mm i.d. and 0.25- $\mu$ m  $d_t$  ( $\beta_s = 250$ )

$$k_{s,c} = k_{i,c} (\beta_i/\beta_s) = p_1(\beta_i/250)f(\dots, p_r, \dots, T) \quad (12)$$

where  $k_i$  and  $\beta_i$  are capacity ratio and phase ratio in any column and  $k_s$  is the capacity ratio in the standard column.  $p_r$  parameters in any column can be easily referred to the standard column: only the  $p_1$  parameter needs to be changed.

$T_{ik}$  and related parameters  $r_{il}$  and  $c_{ij}$  in the standard column can be calculated and used to characterize the chromatographic interactions of a given compound and a given stationary phase in the steps summarized in the right side of Scheme I.

## CONCLUSIONS

Scheme I shows that it is possible to characterize the variation of  $k$  with  $T$  using different types of parameters.

(a)  **$p_r$  Parameters.** They can be easily calculated for many expressions relating  $k$  with  $T$ . Table III shows the equations that we have found to give the best quality of fit. According to the equation selected,  $p_r$  parameters can have physical significance, but great care in their determination is needed to avoid errors in their absolute values caused by correlation between parameters. The calculation of  $p_r$  on the basis of structural considerations (i.e., in a homologous series) seems to be very difficult. However, they can be used in the optimization of chromatographic separations, as shown in Figure 1.

(b)  **$T_{ik}$  Parameters.** Their calculation can be carried out from any set of  $p_r$  parameters. The use of their values in the characterization of the gas chromatographic relation between retention and temperature presents several advantages:

(1) Their values are less sensible to experimental errors than those of  $p_r$  (see Figure 3A,B).

(2) They have an easy chromatographic interpretation since they represent the temperature necessary to elute a compound with a given  $k$  value. Their values are then always included in the usual gas chromatographic temperature range.

(3)  $T_{ik}$  values for a fixed  $k$  can be considered as a sort of retention scale and can be used to determine elution order.

(4) Their estimation using interpolation seems to be possible for compounds in homologous series.

Although they must be calculated from the  $p_r$  parameters, and their use in optimization requires a previous conversion to them, the calculations involved can be easily carried out with a microcomputer.

The characterization of the elution order inversion behavior requires, however, the use of several  $T_{ik}$  values at different  $k$  for each compound. Their values are highly correlated, making difficult their precise interpretation.

(c)  **$r_{il}$  and  $c_{ij}$  Parameters.** The redundancy introduced by choosing many correlated  $T_{ik}$  values can be eliminated by using the  $r_{il}$  and  $c_{ij}$  parameters. Three levels of precision can be attained ( $l = 1, 2$ , or  $3$ ).  $r_{il}$  does not depend on  $k$  and its chromatographic significance is similar to that of  $T_{ik}$ , while  $r_{i2}$  and  $r_{i3}$  describe quantitatively the difference in the variation of  $k$  with  $T$  for different compounds.

The main disadvantage of these parameters is the possible dependence of  $c_{ij}$  on the data set used in the calculations. The two data sets analyzed show that the retention behavior of their compounds can be accurately described with three parameters and that the distribution of  $c_{ij}$  values is surprisingly similar for the two columns. However, the retention of compounds with different chemical structures in columns with other stationary phases must be studied to confirm whether the behavior observed in this work is really representative of the gas chromatographic retention.

The selection of the type of parameter depends on the aspect of the chromatographic retention behavior which must be studied. While  $T_{ik}$ ,  $r_{il}$ , and  $c_{ij}$  parameters are useful for characterization purposes, the use of  $p_r$  values allows the optimization of gas chromatographic separations in different conditions, including mixed phases, serially coupled columns, and any kind of temperature programming. The possibility, shown in Scheme I, of using any of these parameters in the calculation of the others, even for another chromatographic column of the same phase, allows a flexible way for the characterization of both columns and stationary phases.

## ACKNOWLEDGMENT

This work was supported by the Comisión Interministerial de Investigación Científica y Técnica (Projects PB88-034 and PB91-0077).

RECEIVED for review May 14, 1993. Accepted June 10, 1993.



# Separation and Identification of Higher Molecular Weight Fullerenes by High-Performance Liquid Chromatography with Monomeric and Polymeric Octadecylsilica Bonded Phases

Kiyokatsu Jinno,\* Takashi Uemura, Hatsuichi Ohta, Hideo Nagashima, and Kenji Itoh

School of Materials Science, Toyohashi University of Technology, Toyohashi 441, Japan

The separation of fullerenes with monomeric and polymeric octadecylsilica (ODS) bonded phases has been studied and the existence of three  $C_{78}$  isomers confirmed. It has been found that the elution order of higher fullerenes is controlled by their molecular size and shape and that polymeric ODS resolves three  $C_{78}$  isomers, one being eluted faster than  $C_{76}$ . Monomeric ODS cannot resolve two of the  $C_{78}$  isomers, although a lower column temperature of 10 °C gives its partial separation. UV-visible spectral assignments were confirmed by FAB-MS measurements of the fractionated samples.

## INTRODUCTION

Separation of fullerenes in the soot extract is an important analytical problem, considering the increasing attention paid to these new compounds of potential importance in materials science, superconductivity, and other related technologies. Liquid chromatographic approaches have been reported to separate typical fullerenes such as  $C_{60}$  and  $C_{70}$  and other higher molecular weight fullerenes.<sup>1-6</sup> Stationary phases which have had some success in separating fullerenes, such as Pirkle-type,<sup>6</sup> multilegged phenyl bonded phase,<sup>7</sup> and multi-methoxyphenylpropyl phases<sup>8</sup> indicate the need to study in more detail the retention mechanism of fullerene LC separations as based on molecular recognition. However, those approaches still need development before they could be useful for industrial or large laboratory-scale separations. Therefore, the main approach at present for separation of various sizes of fullerenes is to use octadecylsilica (ODS) bonded phases with toluene-based mobile-phase systems, which increase the solubility of fullerenes in the mobile phase and hence the amount injectable into the separation system. Although several investigators have reported the use of ODS stationary phases for this analysis,<sup>9-18</sup> basic discussions on whether

polymeric-type or monomeric-type phases are a better choice have not appeared in the literature. In this paper, we investigate which is the better stationary phase for fullerene separation, monomeric or polymeric, focusing on isomer resolution. It has been found that monomeric ODS phase is the more powerful stationary phase for the isomer separations, based on the difference in their molecular weights, but polymeric ODS is better for the separation based on molecular shape difference.

## EXPERIMENTAL SECTION

**Instrumentation.** The mass spectrometer (MS) used in this work was a JEOL JMS-SX102 A (Akishima, Japan). The ionization was performed by fast atom bombardment (FAB) using Xe (5 kV) as the primary beam and *m*-nitrobenzyl alcohol (*m*-NBA) plus 1% toluene as the matrix. The samples were introduced into the MS system using a flow injection method.

Basic studies on LC separations were performed using a 880 PU LC pump (Jasco, Hachioji, Japan) combined with a UV detector (Shodex M315, Showa Denko, Tokyo, Japan) set at 320 nm or a Jasco MD-920 UV-visible photodiode array detector. Mobile phases were toluene-methanol and toluene-acetonitrile mixtures. A 4.6 mm i.d. × 250 mm Develosil ODS-5 column (monomeric ODS, 5  $\mu$ m, Nomura Chemicals, Seto, Japan) and the same size Wakosil II 5C18AR column (polymeric ODS, 5  $\mu$ m, Wako Chemicals, Tokyo, Japan) were used in the evaluation. The flow rate of the mobile phases was always 1 mL/min. The same Develosil ODS-5 stationary phase packed into a 20 mm i.d. × 250 mm column was used for the semipreparative-scale separations together with a Jasco 880 PU pump connected to a Jasco 880 UV detector. The mobile phase for the sample fraction collection process was a toluene-methanol mixture which was optimized using an analytical-scale column with a flow rate of 10 mL/min. Column temperature was controlled by a LAB-Thermo Model LH-1000E (Toyo Seisakusho, Tokyo, Japan) and Tosoh RE-8000 oven (Tokyo, Japan).

**Sample Preparation.** Carbon soot was produced by an arc discharge in an inert gas environment. The soot was first extracted with toluene (fraction A in Figure 1, where the sample preparation process is schematically summarized), and then the residue was extracted with trichlorobenzene in order to obtain

(1) Ajie, H.; Alvarez, M. M.; Anz, S. J.; Beck, R. D.; Diederich, F.; Fostiropoulos, K.; Huffman, D. R.; Kraetschmer, W.; Rubin, Y.; Schriver, K. E.; Sensharma, D.; Whetten, R. L. *J. Phys. Chem.* 1990, 94, 8630-8633.

(2) Taylor, R.; Hare, J. P.; Abdul-Sada, A. K.; Kroto, H. W. *J. Chem. Soc., Chem. Commun.* 1990, 1423-1425.

(3) Hawkins, J. M.; Lewis, T. A.; Loren, S. D.; Meyer, A.; Heath, J. R.; Shihato, Y.; Smalley, R. E. *J. Org. Chem.* 1990, 55, 6250-6252.

(4) Kikuchi, K.; Nakahara, N.; Honda, M.; Suzuki, S.; Saito, K.; Shimomaru, H.; Yamachi, K.; Ikemoto, I.; Kuromochi, T.; Hino, S.; Achiba, Y. *Chem. Lett.* 1991, 1607-1610.

(5) Bethune, D. S.; Meijer, G.; Tang, W. C.; Rosen, T. H.; Golden, W. G.; Seki, H.; Brown, C. A.; de Vries, M. S. *Chem. Phys. Lett.* 1991, 179, 181-186.

(6) Welch, C. J.; Pirkle, W. H. *J. Chromatogr.* 1992, 609, 89-102.

(7) Jinno, K.; Yamamoto, K.; Ueda, T.; Nagashima, H.; Itoh, K. *J. Chromatogr.* 1992, 594, 105-109.

(8) Jinno, K.; Saito, Y.; Chen, Y.-L.; Luehr, G.; Archer, J.; Fetzer, J. C.; Biggs, W. R. *J. Microcolumn Sep.* 1993, 5, 135-139.

(9) Fetzer, J. C.; Biggs, W. R. *Polycyclic Aromat. Compd.* 1992, 2, 245-251.

(10) Diack, M.; Hettich, R. L.; Compton, R. N.; Guiochon, G. *Anal. Chem.* 1992, 64, 2143-2148.

(11) Klute, R. C.; Dorn, H. C.; McNair, H. M. *J. Chromatogr. Sci.* 1992, 30, 438-442.

(12) Jinno, K.; Uemura, T.; Nagashima, H.; Itoh, K. *Chromatographia* 1993, 35, 38-44.

(13) Jinno, K.; Ohta, H.; Saito, Y.; Uemura, T.; Nagashima, H.; Itoh, K.; Chen, Y. L.; Luehr, G.; Archer, J.; Fetzer, J. C.; Biggs, W. R. *J. Chromatogr.*, in press.

(14) Jinno, K.; Uemura, T.; Nagashima, H.; Itoh, K. *J. High Resolut. Chromatogr.* 1992, 15, 627-628.

(15) Hirsch, A.; Soi, A.; Karfunkel, H. R. *Angew. Chem.* 1992, 104, 808-810.

(16) Elemes, Y.; Silverman, S. K.; Sheu, C.; Kao, M.; Foote, C. S.; Alvarez, M. M.; Whetten, R. L. *Angew. Chem.* 1992, 104, 364-366.

(17) Mittelbach, A.; Honle, W.; von Schnering, H. G.; Carlsen, J.; Janiak, R.; Quast, H. *Angew. Chem.* 1992, 104, 1681-1683.

(18) Cui, Y.; Lee, S. T.; Olesik, S. V.; Flory, W.; Mearini, M. *J. Chromatogr.* 1992, 625, 131-140.

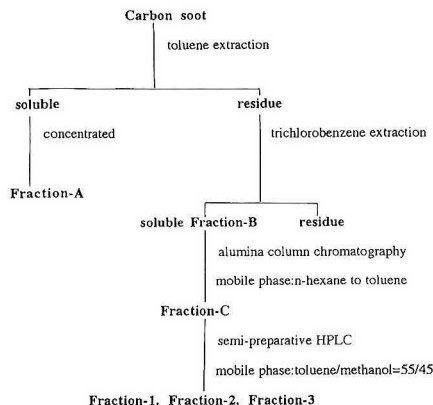


Figure 1. Schematic diagram of the sample preparation process.

a high concentration of fullerenes larger than  $C_{70}$  (fraction B in Figure 1). The remaining  $C_{60}$  and  $C_{70}$  in fraction B was eliminated by passing through an alumina column with an *n*-hexane and toluene gradient elution, fraction C in Figure 1. Fraction C was used as the sample for the MS measurements after preparative-scale LC separation and fractionation (Fractions 1–3). Those several fractions were evaporated to dryness and then dissolved again in toluene as samples for the investigation. The analytical-scale LC separations were performed by injecting 10  $\mu$ L of these samples and the semipreparative scale LC separations by injecting 1 mL of the sample into each separation system.

## RESULTS AND DISCUSSION

**Mobile-Phase Selection.** In order to separate higher fullerenes by LC, the first task is to find the optimum mobile-phase composition. *n*-Hexane is common in several previous publications with ODS stationary phases,<sup>9–14</sup> but the low solubility of higher fullerenes limits its use. A toluene-based mobile phase should be useful in this context and toluene-methanol and toluene-acetonitrile were, therefore, evaluated as candidates.

With Develosil ODS-5, the monomeric ODS, two mobile phases were examined and the results are shown in Figure 2 [toluene-acetonitrile (A) and toluene-methanol (B)]. Although solvent strength of both solvents does not explain the elution if the retention is induced by a typical reversed-phase mechanism, both give relatively good separations for fullerenes higher than  $C_{70}$ . One can choose the countercurrent in toluene on the following bases: (1) if a better separation for higher fullerenes is desired, acetonitrile is the choice; (2) if faster analysis with a high-resolution column is required, methanol should be used. As this investigation was using conventional-size columns for analytical separation, toluene-acetonitrile was preferred. Experiments to find the optimum composition of toluene and acetonitrile in the mobile phase showed 40–60% acetonitrile in toluene to give the best compromise in resolution, analysis time, and solubility of the samples.

**Comparison of Monomeric and Polymeric ODS Phases for Higher Fullerene Separation.** Figure 3 illustrates the chromatogram of fraction A with the monomeric ODS, several peaks later than  $C_{70}$  retention time being seen. The UV-visible spectra of these peaks are summarized in Figure 4. The peak assignments are tentatively made by reference to published spectra.<sup>19–22</sup> The results are as follows: (A)  $C_{60}$ , (B)  $C_{70}$ , (C)  $C_{76}$ , (D)  $C_{78} C_{20'}$ , (E)  $C_{78} C_{20'}$ , (F) no reference data

(19) Diederich, F.; Whetten, R. L. *Acc. Chem. Res.* **1992**, *25*, 119–126.

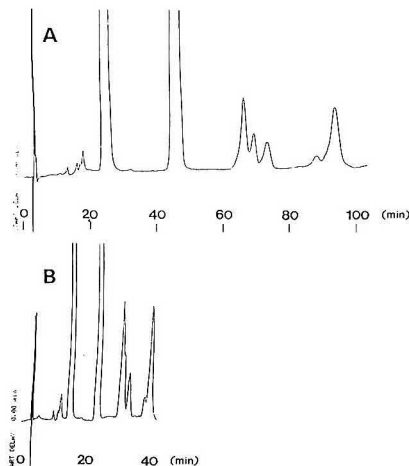


Figure 2. Chromatograms of fraction A with toluene-acetonitrile and toluene-methanol mobile-phase systems: (A) toluene/acetonitrile = 50/50; (B) toluene/methanol = 50/50. Column, Develosil ODS-5; temperature, room temperature (ca. 15–20 °C), mobile-phase flow rate, 1 mL/min; detector, UV at 325 nm.

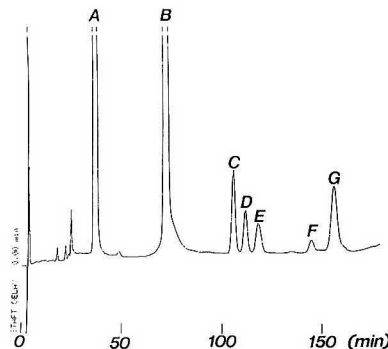


Figure 3. Chromatogram of fraction A with the monomeric ODS: mobile phase, toluene/acetonitrile = 45/55; flow rate, 1 mL/min; detection, UV at 325 nm; temperature, room temperature.

found but probably  $C_{82}$ , and (G)  $C_{84}$ . More accurate identification is made later by FAB-MS measurements.

For the comparative study of monomeric and polymeric ODS phases, similar experiments were performed with the Wakosil ODS polymeric phase and the chromatogram is shown in Figure 5. The UV-visible spectra of the peaks are summarized in Figure 6. It was confirmed that peaks J, K, L, and N are assigned to the same solutes of peaks D, C, E, and G, respectively, in Figure 3. This means that the elution order of  $C_{76}$  and  $C_{78} C_{20'}$  for the monomeric ODS is reversed with the polymeric ODS phase using the same mobile phase. It is also noted that the solute in peak M in Figure 5 cannot be seen in Figure 3, and its spectrum is very similar to that

(20) Diederich, F.; Whetten, R. L.; Thilgen, C.; Etti, R.; Chao, I.; Alvarez, M. M. *Science* **1991**, *254*, 1768–1770.

(21) Diederich, F.; Etti, R.; Rubin, Y.; Whetten, R. L.; Beck, R.; Alvarez, M. M.; Ans, S.; Sensharma, D.; Wudl, F.; Khemani, K. C.; Koch, A. *Science* **1991**, *252*, 548–549.

(22) Kikuchi, K.; Nakahara, Y.; Suzuki, S.; Saito, K.; Ikemoto, I.; Achiba, Y. *Proceedings of the 3rd C<sub>60</sub> Symposium*, July 14–15, Tokyo, 1992; p 23.

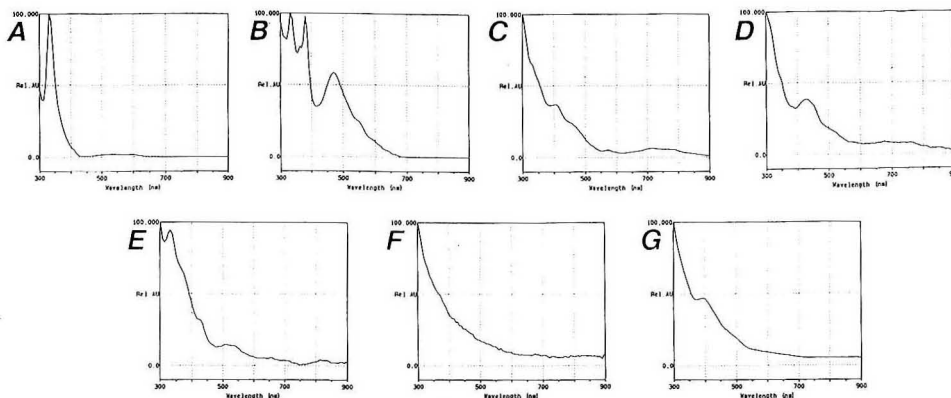


Figure 4. UV-visible spectra of the peaks in the chromatogram in Figure 3. Alphabetical order corresponds to these peaks in the chromatogram.

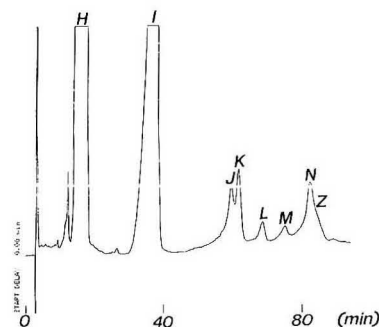


Figure 5. Chromatogram of fraction A with the polymeric ODS: mobile phase, toluene/acetonitrile = 45/55; flow rate, 1 mL/min; detection, UV at 325 nm; temperature, room temperature.

of  $C_{78}D_3$  as observed by Kikuchi et al.<sup>22</sup> The right shoulder of peak N (Z in the figure) gives a spectrum similar to peak F in Figure 3, although some overlapping of their elution distorts its spectrum. The results indicate that the polymeric ODS phase gives a different elution order compared to that with the monomeric ODS phase; such differences have also been found in the study of elution characteristics of planar and nonplanar polycyclic aromatic hydrocarbons (PAHs) by Wise and Sander<sup>23,24</sup> and by Jinno et al.<sup>25-27</sup> The results can be explained by the supposition that the polymeric phase has higher molecular planarity recognition capability than the monomeric ODS phase. Consideration of the shape of the isomers of the higher fullerenes can explain the retention differences. For the isomers of  $C_{78}$ ,  $C_{78}C_{2v}$  has the longest of the shorter diameter (most bulky),  $C_{78}C_{2v}$  has a little different symmetry, and  $D_3$  has a narrower shape than the other two isomers. The polymeric ODS elutes bulkier  $C_{2v}$  first and the more cylindrical  $D_3$  late by virtue of its planarity recognition capability. The reversed elution order of  $C_{84}$  and  $C_{82}$  with the polymeric ODS [as tentatively assigned, peak F

in Figure 3 and the right shoulder of peak N (Z in Figure 5)] can be also explained the same way. The  $C_{82}$  shape is considered to be longer and narrower than  $C_{84}$  (although there are possibilities for at least three isomers of this fullerene to exist<sup>28</sup>), and this difference can induce such an elution order with the polymeric phase because of its planarity recognition capability. However, the problem remained as to why the  $D_3$  isomer of  $C_{78}$  could not be found with the monomeric ODS phase. The following investigation of temperature effects addresses this question.

**Temperature Effects in Separation of Higher Fullerenes.** The temperature effect on the separation of higher fullerenes has been investigated, the results being summarized in Figure 7 and 8 for the monomeric and the polymeric phases, respectively.

In Figure 7, four chromatograms with the monomeric ODS are illustrated at column temperatures from 10 (D) to 70 °C (A). High temperature does not give good resolution, and decreasing the temperature increases the resolution. At 30 °C, five clear peaks are seen in the chromatogram (C in Figure 7) and the UV-visible spectra of each peak assign the solutes in the order of  $C_{78}$ ,  $C_{78}C_{2v}$ ,  $C_{78}C_{2v}$ ,  $C_{82}$ , and  $C_{84}$ , respectively. However, the peak for  $C_{78}D_3$ , the existence of which has been confirmed by separation with the polymeric phase as shown in Figures 5 and 6, is not found. When the temperature is decreased to 10 °C with the monomeric phase, the fifth peak in chromatogram D in Figure 7 appears to include at least two components, as indicated by the asterisk in the figure. UV-visible spectral matching for the left side and the right side of this peak assigns the former as  $C_{78}C_{2v}$  and the latter as  $C_{78}D_3$ . It is also interesting that this peak seems to have other components coeluted (as shown by the two asterisks in the chromatogram), and this might be assigned as the second isomer of  $C_{84}$ ; further confirmation is required by increasing the column efficiency or decreasing the temperature to 0 °C or below.

In Figure 8, four chromatograms with the polymeric ODS are shown with changing column temperature from 10 to 70 °C at 20 °C intervals. Focusing on the elution profiles for the  $C_{78}$ ,  $C_{78}$ ,  $C_{82}$ , and  $C_{84}$  isomers, resolution for those isomers is also improved upon decreasing the temperature. At 70 °C, only two major peaks are found and the higher fullerenes are eluted at the shoulder of the second peak; however, at 50 °C, four major peaks are seen. At 30 °C, clear peaks for the higher

(23) Sander, L. C.; Wise, S. A. *Anal. Chem.* 1987, 59, 2309-2313.

(24) Sander, L. C.; Wise, S. A. *LC-GC* 1990, 8, 378-390.

(25) Jinno, K.; Ibuki, T.; Tanaka, N.; Okamoto, M.; Fetzer, J. C.; Biggs, W. R.; Griffiths, P. R.; Olinger, J. M. *J. Chromatogr.* 1989, 461, 209-227.

(26) Jinno, K.; Saito, Y.; Malhan nee Chopra, R.; Pesek, J. J.; Fetzer, J. C.; Biggs, W. R. *J. Chromatogr.* 1991, 557, 459-468.

(27) Jinno, K.; Yamamoto, K.; Kuwamoto, T.; Nagashima, H.; Ueda, T.; Tajima, S.; Kimura, E.; Itoh, K.; Fetzer, J. C.; Biggs, W. R. *Chromatographia* 1992, 34, 381-385.

(28) Wakabayashi, T.; Kikuchi, K.; Nakajima, Y.; Shiromaru, H.; Suzuki, S.; Achiba, Y. *Proceedings of the 4th C<sub>60</sub> Symposium*, January 26-27, Toyohashi, 1993, p 144.

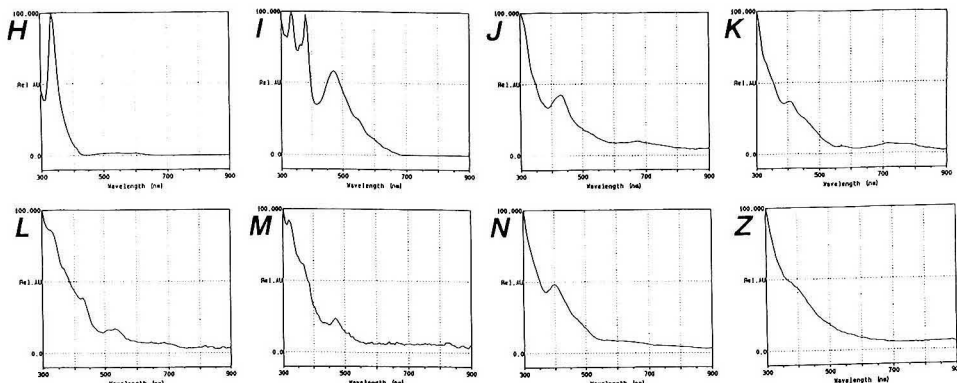


Figure 6. UV-visible spectra of the peaks in the chromatogram in Figure 5. Alphabetical order corresponds to these peaks in the chromatogram.

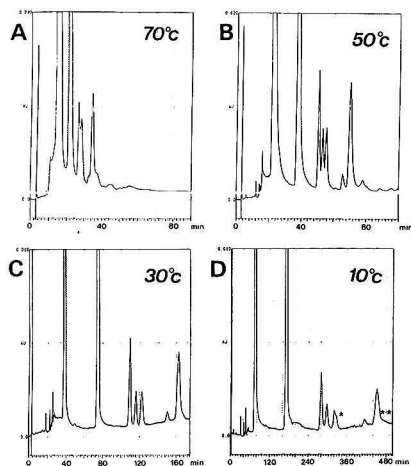


Figure 7. Chromatograms of fraction A with the monomeric ODS at different column temperatures: (A) 70, (B) 50, (C) 30, and (D) 10 °C. Mobile phase, toluene/acetonitrile = 45/55; flow rate, 1 mL/min; detection, UV at 325 nm.

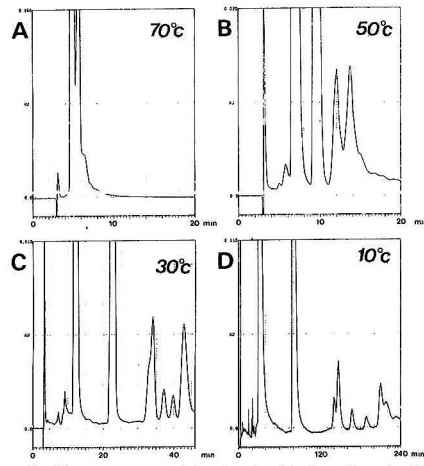
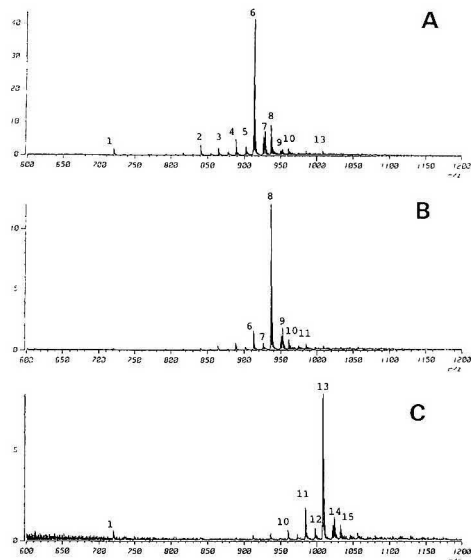


Figure 8. Chromatograms of fraction A with the polymeric ODS at different column temperatures: (A) 70, (B) 50, (C) 30, and (D) 10 °C. Mobile phase, toluene/acetonitrile = 45/55; flow rate, 1 mL/min; detection, UV at 325 nm.

fullerene isomers are found, and eight peaks are resolved at 10 °C. The elution order at 10 °C can be defined by the UV-visible spectral measurements and that is  $C_{78} C_{82}$ , first,  $C_{76}$ ,  $C_{78} C_{20}$ ,  $C_{78} D_3$ ,  $C_{84}$ , and probably  $C_{82}$ , over an elution range from 120 to 240 min. The peak in Figure 8 at a retention time of 220 min can be assigned to the same solute as in the right shoulder of peak N (Z) in Figure 5. The polymeric ODS phase is more rigid at a temperature range lower than its critical temperature, which is generally between 40 and 50 °C.<sup>25</sup> The rigid situation of the alkyl chains at the lower temperature induces much higher molecular planarity recognition capability, and hence, the resolution among these higher fullerene isomers can be improved, based on the difference of the shape of those molecules.

**FAB-MS Identification of Higher Fullerenes.** In order to confirm the tentative identification by UV-visible spectra, FAB-MS measurements have been performed for the samples fractionated by the semipreparative-scale LC procedure. For this purpose, a highly concentrated fraction of higher fullerenes is required as shown in Figure 1, where fraction B

includes a greater concentration of higher fullerenes than fraction A because of their higher solubility in trichlorobenzene. This process has been established previously.<sup>12</sup> Three fractions, 1–3 for  $C_{76}$ ,  $C_{78}$ , and  $C_{84}$  isomers, respectively, were collected, since the resolution between the three  $C_{78}$  isomers and between the  $C_{82}$  and  $C_{84}$  isomers was not adequate under the conditions used in the semipreparative scale LC separation. Those three fractions were analyzed by FAB-MS negative ion measurements, and the MS spectra obtained are illustrated in Figure 9. As can be seen, the existence of several isomers in these fractions is confirmed as mainly  $C_{78}$  and  $C_{78}$  in fraction 1,  $C_{78}$  and small amounts of  $C_{76}$  in fraction 2, and  $C_{82}$  and  $C_{84}$  in fraction 3. There are some signals caused by isomer oxides whose existence can be explained by two major reasons: (1) they may be produced in the ionization process of the FAB-MS measurements, and (2) it is well-known that if fullerenes are left in a solution which is exposed to air, oxidation of these materials occurs. The assignments by UV-visible spectral measurements are now confirmed. The UV-visible spectra of peak F in Figure 3 and the right shoulder



**Figure 9.** FAB-MS spectra for three fractions: (A) fraction 1, (B) fraction 2, and (C) fraction 3. Mass number tentative assignments: (1)  $C_{60}$ , (2)  $C_{70}$ , (3)  $C_{72}$ , (4)  $C_{74}$ , (5)  $C_{76}O$ , (6)  $C_{76}$ , (7)  $C_{78}O$ , (8)  $C_{78}$ , (9)  $C_{78}O$ , (10)  $C_{80}$ , (11)  $C_{82}$ , (12)  $C_{82}O$ , (13)  $C_{84}$ , (14)  $C_{84}O$ , and (15)  $C_{86}$ .

of peak N (Z) were thus confirmed as  $C_{82}$ , because  $C_{82}$  signals are clearly seen in the mass spectrum of fraction 3.

## CONCLUSION

The elution characteristics of higher fullerenes with monomeric and the polymeric ODS phases have been investigated, and the results clearly indicate that shape recognition capability controls the retention order of higher fullerenes. The polymeric phase has higher molecular shape recognition capability and elution order is determined by the shape of the molecules, but the monomeric phase has a lower such capability and elutes higher fullerenes in the order of their molecular size (molecular weight) with the toluene-acetonitrile mobile phase. Three  $C_{78}$  isomers are resolved with the polymeric phase, and the lower resolution of those solutes with the monomeric phase has been improved at a lower temperature.  $C_{82}$  elutes later than  $C_{84}$  with the polymeric phase, but the order was reversed with the monomeric phase. These findings can be explained as previously proposed by the authors<sup>26-27</sup> and Wise et al.<sup>28,24</sup> for PAH separations. The UV-visible spectra obtained can be identified by FAB-MS measurements after a preparative-LC sample fractionation process.

## ACKNOWLEDGMENT

The authors show their sincere thanks to Mr. Matsuura, JEOL, Akishima, Japan, for his help in FAB-MS measurements. Useful discussions with Dr. J. C. Fetzer and Dr. W. R. Biggs of Chevron Research and Technology Co., Richmond, CA, are also acknowledged.

RECEIVED for review February 16, 1993. Accepted July 8, 1993.\*

\* Abstract published in *Advance ACS Abstracts*, August 15, 1993.



# Mathematical Treatment of Electrophoretically Mediated Microanalysis

Bryan J. Harmon, Dale H. Patterson, and Fred E. Regnier\*

Purdue University, Department of Chemistry, West Lafayette, Indiana 47907-1393

A new concept in reaction-based chemical analysis is introduced and theoretically described. By utilization of the variability in electrophoretic mobilities among charged species, spatially distinct zones of chemical reagents can be electrophoretically merged under the influence of an applied electric field. *Electrophoretically mediated microanalysis* (EMMA) exploits this phenomenon as a basis for chemical analysis utilizing capillary electrophoretic systems. EMMA is described in terms of the four stages required for reaction-based analysis: (1) analyte and analytical reagent metering; (2) initiation of reaction; (3) control of reaction conditions and product formation; (4) detection of species whose production or depletion is indicative of the concentration or quantity of the analyte of interest. The method is illustrated by the enzymatic oxidation of ethanol to acetaldehyde by alcohol dehydrogenase with the concurrent reduction of  $\text{NAD}^+$  to NADH monitored at 340 nm. Experimental results for both substrate and enzyme determinations are shown to agree with the presented theory.

## INTRODUCTION

Analytical determinations are frequently based upon direct instrumental measurements of analytes. When interfering substances preclude direct analysis, a separation method or a chemical reaction is often added to increase detection specificity. Combinations of separation methods and specific chemical reactions provide maximal specificity. This paper will focus on the use of specific chemical reactions in conjunction with electrophoresis for analytical determinations.

Electrophoresis is the migration of charged species under the influence of an electric field.<sup>1</sup> The electrophoretic mobility  $\mu_{ep}$  of an ionic species is described by the equation

$$\mu_{ep} = \frac{Ze}{6\pi\eta a} \quad (1)$$

where  $Z$  is the effective net charge of the species,  $e$  is the electrical charge,  $\eta$  is the solution viscosity, and  $a$  is the hydrodynamic radius of the species. The electrophoretic velocity with which the species migrates through a solution under the influence of an applied electric field is the product of the electrophoretic mobility and the electric field strength  $E$

$$v_{ep} = \mu_{ep}E \quad (2)$$

When capillary electrophoresis (CE) is performed in fused silica capillaries, negative charges at the capillary wall cause the formation of an ionic double layer which electrophoret-

ically migrates toward the negative electrode under the influence of an electric field. Bulk liquid in the capillary is pulled along by a phenomenon known as electroosmosis.<sup>2</sup> The resulting migration velocity  $v_m$  of any substance in a CE system is the sum of both the electrophoretic  $v_{ep}$  and electroosmotic  $v_{eo}$  transport velocities

$$v_m = v_{ep} + v_{eo} = (\mu_{ep} + \mu_{eo})E \quad (3)$$

where  $\mu_{eo}$  is the specific transport mobility due to electroosmotic flow.

Because the electroosmotic component is equal for all substances, differences in transport velocity in a CE medium must be imparted by variations in electrophoretic mobility among charged substances. Cations in a fused silica capillary migrate with a positive electrophoretic velocity in the same direction as the electroosmotically induced flow. In contrast, anions migrate against the bulk flow with a negative electrophoretic velocity. Differences in electrophoretic mobility among charged species have been widely used in electrophoresis as a separation technique.<sup>3,4</sup>

It will be shown in this paper that exploitation of differential transport velocities is equally useful as a mixing technique. Spatially distinct zones of chemical reagents of different electrophoretic mobility can be made to interpenetrate under the influence of an applied electric field as shown in Figure 1. Based upon this observation, electrophoretic methods will be used to initiate chemical reactions by mixing analyte and analytical reagents, control reagent contact time, separate the reactants and detectable product, and transport the detectable product to a detector. This technique is termed *electrophoretically mediated microanalysis* (EMMA). Preliminary studies by Bao and Regnier<sup>5</sup> reported the assay of glucose-6-phosphate dehydrogenase in a CE system via its enzymatic reaction with glucose 6-phosphate and nicotinamide adenine dinucleotide phosphate (NADP) to produce 6-phosphogluconate and reduced nicotinamide adenine dinucleotide phosphate (NADPH). NADPH exhibits a unique absorbance at 340 nm, thereby serving as an indicator of the extent of the reaction and, consequently, the quantity of glucose-6-phosphate dehydrogenase injected. The purpose of the work presented here is to identify by theory and experimentation those variables that mediate such chemical analyses in a CE system.

## MATERIALS AND METHODS

**Instrumentation.** All experiments were performed using a CE system built in-house. Polyimide-coated, fused silica capillaries (Polymicro Technologies, Phoenix, AZ) of 75  $\mu\text{m}$  inner diameter and 360  $\mu\text{m}$  outer diameter were utilized. The capillaries were of 40 cm total length with separation lengths (distance from injection to detection position) of 25 and 15 cm for the ethanol and ADH determinations, respectively. Electric fields were applied with a Spellman (Plainville, NY) Model FHR 30P 60/EI

(2) Rice, C. L.; Whitehead, R. *J. Phys. Chem.* 1965, 11, 4017.

(3) Jorgenson, J. W.; Lukacs, K. D. *Anal. Chem.* 1981, 53, 1298.

(4) Wallingford, R. A.; Ewing, A. G. *Adv. Chromatogr.* 1989, 29, 1.

(5) Bao, J.; Regnier, F. E. *J. Chromatogr.* 1992, 608, 217.

(1) Tiselius, A. *Trans. Faraday Soc.* 1937, 33, 524.

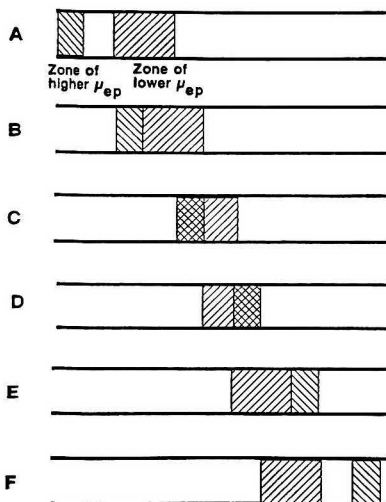


**Figure 1.** An illustration of electrophoretic mixing of two zones. Spatially distinct zones (A), beginning engagement (B), fully interpenetrated (C), beginning disengagement (D), fully disengaged (E), and continuing to traverse the capillary (F). The zone of higher electrophoretic mobility ( $\mu_{ep}$ ) is half the width of the zone of lower  $\mu_{ep}$  and migrates with twice the transport velocity.

power supply. Detection was achieved using an ISCO (Lincoln, NE) CV4 CE variable-wavelength absorbance detector. NADH, proteins, and mesityl oxide were monitored at 340, 200, and 254 nm, respectively. Data were collected either by a Linear (Reno, NV) 1200 strip-chart recorder or an i486 personal computer interfaced with a PC-LPM-16 I/O board and NI-DAQ DOS software (National Instruments Corp., Austin, TX).

**Reagents.** Yeast alcohol dehydrogenase (YADH), nicotinamide adenine dinucleotide ( $NAD^+$ ), reduced nicotinamide adenine dinucleotide (NADH), glycine buffer solution (0.5 M, pH 9.0), tris[hydroxymethyl]aminomethane, and tris[hydroxymethyl]aminomethane hydrochloride were purchased from Sigma Chemical Co. (St. Louis, MO). Absolute ethanol and mesityl oxide were purchased from Midwest Solvents Co. of Illinois (Pekin, IL) and Aldrich Chemical Co. (Milwaukee, WI), respectively. For the determination of ethanol, 50 mM glycine CE running buffer was prepared by diluting the glycine buffer solution with degassed, double-distilled, deionized water. A 50 mM Trizma CE running buffer solution for the determination of ADH was made by dissolving tris[hydroxymethyl]aminomethane and tris[hydroxymethyl]aminomethane hydrochloride in degassed, double-distilled, deionized water. The CE running buffers were adjusted to pH 9.0 with either 1.0 M HCl or 1.0 M NaOH. The analytical reagent solutions were prepared by dissolving the appropriate analytical reagents (8 units/mL YADH and 10 mM  $NAD^+$  for determinations of ethanol depicted in Figures 2 and 3; 75 units/mL YADH and 10 mM  $NAD^+$  for the ethanol determination depicted in Figure 4; 50 mM ethanol and 10 mM  $NAD^+$  for the determination of ADH shown in Figure 5) in the appropriate running buffer solutions.

**Electrophoresis Procedures.** The capillaries were treated with 1 M NaOH for 10 min and then rinsed with buffer solution for 10 min prior to use. The capillary and buffer reservoirs were filled by vacuum with the appropriate analytical reagent/running buffer solution. A plug of analyte solution was then hydrodynamically injected by manually placing the anodic end of the capillary into the sample vial and raising for a fixed height and time (typically 5–10 cm for 2–5 s). The assay was effected by applying an electric field strength of 125 V/cm and monitoring the absorbance electropherogram of NADH at 340 nm. All assays were performed either under the influence of a constant potential or with an intermittent time period at zero potential. Electro-

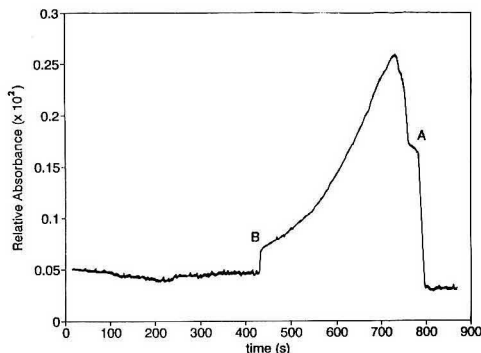


**Figure 2.** An electropherogram of an EMMA determination of a 0.5 g/L sample of ethanol. A shows the formation of NADH at the reagent interfaces prior to the application of potential while B indicates truncation of the NADH concentration profile as unreacted ethanol migrates past the detection window. Experimental conditions stated in text.

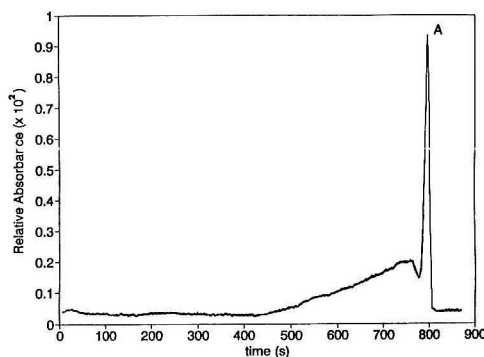


**Figure 3.** An electropherogram of an EMMA determination of a 0.5 g/L sample of ethanol. A indicates the accumulation of NADH at the reagent interfaces as the injected plug of ethanol is allowed to incubate for 120 s prior to the application of electric field. Experimental conditions are stated in the text.

phoretic mobilities were determined by injecting the species of interest along with a neutral marker (mesityl oxide) and monitoring the migration times of the two species. Electrophoretic mobility was calculated as

$$\mu_{ep} = \frac{(t_{MO} - t_A)l}{t_A t_{MO} E} \quad (4)$$

where  $t_{MO}$  and  $t_A$  are the migration times of the analyte and mesityl oxide, respectively, and  $l$  is the separation length of the capillary.

## RESULTS AND DISCUSSION

The reaction-based determination of an analyte requires four operations: (1) *analyte and analytical reagent metering*; (2) *initiation of reaction*; (3) *control of reaction conditions and product formation*; (4) *detection of species whose production or depletion is indicative of the concentration or quantity of the analyte of interest*. This paper demonstrates that CE systems, as employed by EMMA, are capable of performing each of these tasks.

The chemical system employed in a reaction-based determination typically involves the reaction of an analyte A with one or more analytical reagents R to produce or deplete a

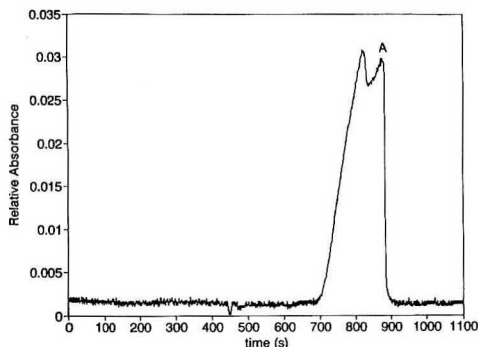


**Figure 4.** An EMMA determination of ethanol utilizing elevated concentrations of analytical reagents (75 units/mL YADH; 10 mM NAD<sup>+</sup>) relative to those of Figure 2 (8 units/mL YADH; 10 mM NAD<sup>+</sup>). No truncation of the NADH profile is observed. A indicates NADH production at the reagent interfaces prior to the application of the electric field. Experimental conditions stated in text.

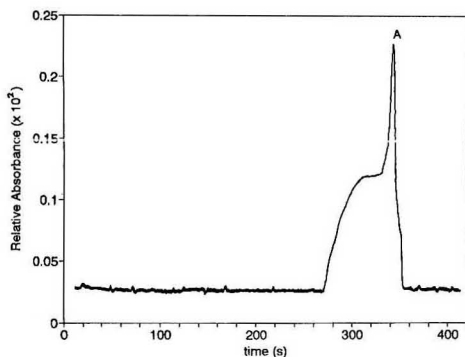
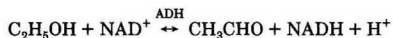


**Figure 5.** An EMMA determination of 5 units/mL sample of YADH. A indicates NADH accumulation at the reagent interfaces prior to the application of the electric field. Experimental conditions are stated in the text.

detectable species D which is stoichiometrically indicative of the quantity or concentration of the analyte present in the sample. This reaction may be depicted simplistically as



The chemical system chosen for this study is the enzymatic reaction of alcohol dehydrogenase (ADH; alcohol:NAD oxidoreductase, EC 1.1.1.1), which reversibly catalyzes the oxidation of ethanol to acetaldehyde:



The concurrent reduction of coenzyme NAD<sup>+</sup> to NADH can be directly monitored by the increase in absorbance at 340 nm as a measure of the extent of reaction.

Two modes of analysis are possible utilizing this enzymatic system: (1) the determination of ethanol in which ethanol serves as the analyte, ADH and NAD<sup>+</sup> as the analytical reagents, and NADH as the detectable species; (2) the determination of ADH in which ADH serves as the analyte, ethanol and NAD<sup>+</sup> as the analytical reagents, and NADH as the detectable species. Figures 2, 3, and 4 illustrate experimental EMMA determinations of ethanol while Figure 5 shows an EMMA ADH determination. The methodologies

chosen here for the analysis of both ethanol and ADH require a forward reaction. The equilibrium, which lies far to the left at neutral pH, can be forced to the right by buffering at pH 9 and by trapping the acetaldehyde with an agent, such as hydrazine, thereby inhibiting the reverse reaction.<sup>6</sup> The following sections describe the EMMA procedures in terms of the stated four required steps in a chemical analysis.

**1. Analyte and Analytical Reagent Metering.** The EMMA methodology requires that the analyte and analytical reagents be sequentially introduced into the capillary. There are numerous potential metering modes varying both by their method of introduction (*e.g.* hydrodynamic, electrokinetic, and vacuum methods) and the size (*i.e.* plug width) of the reagent regions. The initial spatial positioning of the analyte and analytical reagent zones in the capillary is determined by the sign and magnitude of the electrophoretic mobilities of the various species involved so that the appropriate reagents approach and engage each other under the influence of an applied electric field. In the methodologies chosen for the determinations of both ethanol and ADH, the capillary is filled by vacuum with the analytical reagents contained in the CE running buffer. The analytical reagent solution is also maintained in the cathodic and anodic buffer reservoirs. The sample containing the analyte is then injected into the anodic end of the capillary via a hydrodynamic injection. In the analysis of ethanol, since the neutral ethanol has a greater transport velocity than either the negatively-charged ADH or NAD<sup>+</sup>, the analyte must be positioned "behind" the analytical reagent zone contained in the filled capillary and cathodic buffer reservoir so that interpenetration of the zones occurs upon application of an electric field. In the determination of ADH, the ADH has a lower transport velocity than either the ethanol or NAD<sup>+</sup>. Consequently, the analyte must be positioned "in front" of the analytical reagents contained in the anodic buffer reservoir so that the reagent zones merge upon the application of an electric field.

As described, both the ethanol and ADH determinations employ what may be termed the "reagent filled capillary" approach in which the capillary and buffer reservoirs are initially filled with reagents. Since the analytical reagent solution is maintained as a continuous stream within the CE system, upon electrophoretic mixing the analyte remains engaged with the analytical reagent zone throughout its traversal of the capillary. This strategy permits an analyte to encounter a maximal volume of analytical reagents and allows for the logistically simplest method of analytical reagent metering. Prior to each assay, the capillary is simply refilled with the analytical reagent solution. Conversely, one or more zones of analytical reagent(s) of finite width may be introduced into the capillary. The analyte encounters analytical reagent only during the time period in which the two regions are merged. The width of reagent zones introduced depends upon the desired reagent contact time as described in the next section. This approach allows for minimal consumption of analytical reagents.

Analytes are typically introduced in EMMA as a zone of finite width employing traditional CE injection methods, including hydrodynamic,<sup>7,8</sup> electrokinetic,<sup>3,7,9</sup> and microinjection techniques.<sup>10,11</sup> As determined by the Poiseuille equation,<sup>11</sup> approximately 2 nL of sample was injected for the determinations illustrated in Figures 2, 3, and 5. The

(6) Blanke, R. V.; Decker, W. J. In *Textbook of Clinical Chemistry*; Tietz, N. W., Ed.; W.B. Saunders: Philadelphia, PA, 1986; pp 1670-1744.

(7) Fujiwara, S.; Honda, S. *Anal. Chem.* 1987, 59, 487.

(8) Rose, J. D.; Jorgenson, J. W. *Anal. Chem.* 1988, 60, 642.

(9) Jorgenson, J. W.; Lukacs, K. D. *J. Chromatogr.* 1981, 218, 209.

(10) Wallingford, R. A.; Ewing, A. G. *Anal. Chem.* 1987, 59, 678.

(11) Wallingford, R. A.; Ewing, A. G. *Anal. Chem.* 1988, 60, 1972.

(12) Lamb, H. *Hydrodynamics*; Dover: New York, 1932; pp 585-586.

analysis depicted in Figure 4 utilized approximately a 10-nL analyte injection volume. Depending upon the sensitivity of a particular assay and the physical dimensions of the CE system employed (*i.e.* capillary diameter), typical injection volumes in EMMA can range from 0.1 to 20 nL.

The small dimensions of the CE systems utilized are a primary advantage of the EMMA methodology. The ultra-microinjection volumes allow for the determination of microsamples, such as those encountered in the analysis of interstitial fluids or the intracellular fluids of a single cell. Furthermore, EMMA consumes small volumes of analytical reagents. The consumption of analytical reagent per assay depends upon the width of the analytical reagent plug used. However, the limiting case of maximal consumption of analytical reagent solution, in which the analytical reagents are maintained in the running buffer, is equal to the volumetric flow rate of the bulk buffer solution  $V_f$

$$V_f = \pi r^2 \mu_{\text{oe}} E \quad (5)$$

where  $r$  is the radius of the capillary. Depending upon the electroosmotic flow and the radius of the capillary employed, typical volumetric flow rates are on the order of a few microliters per hour.

Due to their electrophoretic mobility, charged reagent species are selectively depleted from buffer reservoirs. Consequently, reagent concentrations can change significantly over time for species with large positive or negative electrophoretic mobilities if relatively small buffer reservoirs are employed. Based upon the experimental capillary diameter of 75  $\mu\text{m}$  and an electric field strength of 125 V/cm, the ethanol and ADH determinations depicted in Figures 2 and 5, respectively, consume the analytical reagent/running buffer solutions at rates of approximately 9.5 and 12  $\mu\text{L/h}$ , respectively, as calculated by eq 5. A single ethanol assay as depicted in Figure 2 requires 13 min, thereby consuming approximately 2.1  $\mu\text{L}$  of analytical reagent/running buffer solution, 16 mmol of  $\text{NAD}^+$ , and 0.01 unit of ADH. The 6-min ADH determination shown in Figure 5 consumes approximately 1.2  $\mu\text{L}$  of analytical reagent/running buffer solution, 60 nmol of ethanol, and 9 nmol of  $\text{NAD}^+$  per assay. The minimal reagent requirements of EMMA diminish the frequent concerns over cost and disposal of analytical reagents in chemical analysis.

**2. Initiation of Reaction.** Chemical reactions are generally initiated in traditional methods by blending solutions containing the analyte and the analytical reagents in an active process involving turbulent mixing. Mixing bulk solutions by turbulent methods inherently dilutes the reagents, disperses the reactants and products (as in flow injection analysis), and diminishes the sensitivity of detection by diluting the detectable species.<sup>13,14</sup> The mixing of the analyte and analytical reagents is accomplished in EMMA by exploiting the variability in transport velocity among the chemical species in the chosen electrophoretic medium. In the free zonal CE medium chosen for this study, each of the reagent species has a different electrophoretic mobility due to their variable charge densities as dictated by eq 1.

Following the metering of the reagents into the capillary in appropriate positions, electrophoretic mixing is initiated by the application of an electrical field. The reagent zones migrate at a differential rate dependent upon the deviation in electrophoretic mobility between the two components of interest  $\Delta\mu_{\text{ep}}$  and the applied electric field strength

$$v_{\text{diff}} = \Delta\mu_{\text{ep}} E \quad (6)$$

Ignoring the effects of diffusional broadening of the reagent

zones, the time required for two spatially separated reagent bands to initiate contact  $t_{\text{contact}}$  (Figure 1B) can be estimated as

$$t_{\text{contact}} = d/\Delta\mu_{\text{ep}} E \quad (7)$$

where  $d$  is the distance between the leading edge (toward direction defined as positive mobility) of the zone of greater transport velocity and trailing edge (away from direction defined as positive mobility) of the zone of lesser transport velocity. If the reagent zones are metered adjacently (*i.e.*  $d = 0$ ), interpenetration of the zones occurs immediately upon the application of the electric field. The interpenetration of the zones continues as the potential is maintained, and the substance of greater transport velocity migrates through that of lower transport velocity.

Equation 7 can be used to estimate the time required for the two zones to fully interpenetrate (*i.e.* the narrower zone is completely merged within the wider zone; Figure 1C) if  $d$  is defined as the shorter distance of that between the two leading edges or the two trailing edges of the respective zones. In the frequently encountered situation in which a relatively narrow reagent plug of width  $w$  is injected adjacent to a broad (*i.e.* capillary-filling) reagent zone, the time required to fully electrophoretically mix the two regions  $t_{\text{mix}}$  can be estimated as

$$t_{\text{mix}} = w/\Delta\mu_{\text{ep}} E \quad (8)$$

The complete immersion of the narrower zone within the wider zone continues until that time at which disengagement of the regions begins. The time at which this full interpenetration of the narrower zone within the wider zone ends (Figure 1D) can be estimated from eq 7 if  $d$  is defined as the greater distance of that between the two leading edges or the two trailing edges of the respective zones. If a reagent is maintained in an appropriate running buffer reservoir, as in the ethanol and ADH determinations described in this paper, its zonal width may be viewed as infinite, and the reagent zones will remain engaged throughout the remainder of the experiment.

Ignoring the effects of diffusional broadening and reaction-induced depletion of the reagent zones, the time interval during which total merging of the narrower zone within the wider zone is experienced  $\Delta t_{\text{merge}}$  can be estimated as

$$\Delta t_{\text{merge}} = \frac{\Delta w}{\Delta\mu_{\text{ep}} E} \quad (9)$$

where  $\Delta w$  is the difference in widths of the two zones. Zonal engagement ceases as the two zones completely pass each other.

The time at which the two zones fully disengage (Figure 1E) can be estimated from eq 7 when  $d$  is defined as the distance from the trailing edge of the zone of greater transport velocity to the leading edge of the zone of lesser transport velocity. While eqs 7, 8, and 9 neglect contributions of diffusion and reaction-induced depletion of reagents to zonal width, each illustrates the critical roles of differential electrophoretic mobility, the magnitude and duration of the electric field strength, and the widths and positioning of the respective reagent zones in the zonal engagement and disengagement processes.

In the determination of ethanol, neutral ethanol ( $\mu_{\text{ep}} = 0 \text{ cm}^2/\text{V s}$ ) is transported with the electroosmotic flow toward the negative electrode. ADH ( $\mu_{\text{ep}} = -1.6 \times 10^{-4} \text{ cm}^2/\text{V s}$ ) and  $\text{NAD}^+$  ( $\mu_{\text{ep}} = -1.2 \times 10^{-4} \text{ cm}^2/\text{V s}$ ) are each negatively charged at pH 9 and electrophorese against the electroosmotic flow, thereby allowing each to interpenetrate the ethanol zone under the influence of an applied electric field. Since electroosmotic flow is of greater magnitude than either reagent's electro-

(13) Panton, C. C.; Mottola, H. A. *Anal. Chim. Acta* 1983, 154, 1.  
(14) Wada, H.; Hirakawa, S.; Yuchi, A.; Nakagawa, G. *Anal. Chim. Acta* 1986, 179, 181.

phoretic mobility, ADH and NAD<sup>+</sup> each travel toward the negative electrode and the detection window. At an experimental electric field strength of 125 V/cm, it may be calculated from eq 8 that a 0.5 mm wide injected plug of ethanol, such as that estimated by the Poiseuille equation for the determination illustrated in Figure 2, is fully interpenetrated by adjacent ADH and NAD<sup>+</sup> zones in approximately 2.5 and 3.3 s, respectively, based upon the experimental differential values of electrophoretic mobility for the reagent species ( $\Delta\mu_{\text{ep,ethanol-ADH}} = 1.6 \times 10^{-4} \text{ cm}^2/\text{V}\cdot\text{s}$ ;  $\Delta\mu_{\text{ep,ethanol-NAD}} = 1.2 \times 10^{-4} \text{ cm}^2/\text{V}\cdot\text{s}$ ). In the determination of ADH, such as that depicted in Figure 5, an adjacent zone of ethanol fully merges with a 0.5 mm wide plug of ADH in only 2.5 s at an experimental electric field strength of 125 V/cm. In contrast, an adjacent zone of NAD<sup>+</sup> requires 10 s to fully interpenetrate the ADH zone due to the relatively similar values of electrophoretic mobility for ADH and NAD<sup>+</sup> ( $\Delta\mu_{\text{ep,ADH-NAD}} = 4 \times 10^{-5} \text{ cm}^2/\text{V}\cdot\text{s}$ ).

If the analyte and analytical reagents are metered into the capillary adjacent to each other, mixing will occur immediately upon the application of the potential, as previously noted. However, diffusional broadening of the reagent zones can allow interpenetration and concurrent reaction at the interfaces between the reagents to occur prior to the application of the electric field. This phenomenon is shown as the product formations designated by A in the determinations of ethanol in Figures 2 and 4 and ADH in Figure 5. This NADH accumulation occurs as the adjacent analyte and analytical reagent zones diffusively interpenetrate and react during the approximately 5–10 s period that the analyte is being injected, and the electric field is being applied. This effect is confirmed by the large NADH accumulation indicated by peak A in Figure 3 in which the reaction is allowed to occur at the reagent interfaces for 120 s prior to the application of the electric field. This phenomenon can be eliminated by injecting "spacer" plugs between the reagent zones. These spacers contain only buffer and must be sufficiently broad to prevent diffusional interpenetration of the reagent zones prior to the application of the electric field.

There are numerous advantages to the electrophoretic mixing utilized in EMMA relative to the traditional methods of mixing of bulk solutions. As species electrophorese essentially independently of the bulk solution, electrophoretic mixing merges two or more zones of varying electrophoretic mobility without a concurrent change in volume and, therefore, dilution of the zones. In an EMMA system for which Joule heating does not cause substantial band spreading, lateral diffusion is often the only significant factor causing dilution<sup>3,16</sup> of the reagent zones other than reaction-induced depletion. When the electrophoretic mobilities of two reagents vary substantially, full interpenetration can be achieved in several milliseconds by the application of high electric field strengths. Furthermore, theoretical and experimental design considerations are much simpler when turbulent mixing does not have to be built into the analytical apparatus. A typical CE system is capable of performing numerous EMMA analyses of various modes.

**3. Control of Reaction Conditions and Product Formation.** The production of detectable species in an EMMA system is dictated by the kinetics of the chosen chemical system, the concentrations of the overlapping reagent zones, the duration of the zonal engagement, and the electrophoretic properties of the species involved. The concentration profile of the detectable species can be estimated based upon these factors. The following discussion illustrates the effects of kinetics upon the production of detectable species in the determinations of ethanol and ADH described in this study.

The mechanism and kinetic parameters of YADH are well characterized.<sup>16,17</sup> At pH between 8 and 9, YADH exhibits a catalysis mechanism described as an ordered bi-bi model.<sup>16</sup> The kinetic constants of YADH at 25 °C and pH 8.9 have been experimentally determined by Dickenson and Dickinson.<sup>17</sup> To simplify the kinetic considerations, the reaction may be viewed as irreversible. In the determination of ethanol or ADH, the product NADH ( $\mu_{\text{ep}} = -2.3 \times 10^{-4} \text{ cm}^2/\text{V}\cdot\text{s}$ ), which inherently differs in electrophoretic mobility from either analyte, is electrophoresed away from the vicinity of the reaction. This separation inhibits the reverse reaction. The use of positively-charged hydrazine to complex the other product, acetaldehyde, further inhibits the reverse reaction both by trapping the acetaldehyde and by imparting a positive electrophoretic mobility upon neutral acetaldehyde. Acetaldehyde is consequently electrophoresed from the vicinity of the neutral ethanol under the influence of an applied electric field.

When the reaction is irreversible, the kinetics simplify to the initial rate expression

$$\frac{[\text{ADH}]}{v} = \phi_0 + \frac{\phi_{\text{NAD}}}{[\text{NAD}]} + \frac{\phi_{\text{EtOH}}}{[\text{EtOH}]} + \frac{\phi_{\text{NAD-EtOH}}}{[\text{NAD}][\text{EtOH}]} \quad (10)$$

where  $v$  is the velocity of the reaction and  $\phi_0$ ,  $\phi_{\text{NAD}}$ ,  $\phi_{\text{EtOH}}$ , and  $\phi_{\text{NAD-EtOH}}$  are kinetic constants.<sup>17</sup> The kinetic considerations can be further simplified if the experimental concentration of NAD<sup>+</sup> is chosen to be sufficiently high so that the YADH encounters enzyme-saturating concentrations of NAD<sup>+</sup>, and insignificant depletion of NAD<sup>+</sup> occurs during the analyte zone's traversal of the NAD<sup>+</sup> region. Under these conditions, eq 10 simplifies to a pseudo-Michaelis-Menten model:

$$v = \frac{V_{\text{max}}[\text{EtOH}]}{K_{\text{M,EtOH}} + [\text{EtOH}]} \quad (11)$$

where  $V_{\text{max}}$  is the maximal rate of the reaction (equal to  $[\text{ADH}]/\phi_0$ ) and  $K_{\text{M,EtOH}}$  is the Michaelis-Menten constant for ethanol (equal to  $\phi_{\text{EtOH}}/\phi_0$ ). Equation 11 reveals that at high ethanol concentrations ( $[\text{EtOH}] \gg K_{\text{M,EtOH}}$ ), the ADH is saturated with substrate, and the velocity of the reaction approaches  $V_{\text{max}}$ . The reaction rate will remain relatively constant until the substrate is depleted or product accumulation produces inhibition. At low ethanol concentration ( $[\text{EtOH}] \ll K_{\text{M,EtOH}}$ ), the reaction rate is directly proportional to the substrate concentration. The rate of product of detectable NADH is clearly dependent upon the concentration of the overlapping reagent zones.

In the determination of ethanol, as depicted in Figures 2, 3, and 4, the reaction rate and, therefore, production of NADH at high substrate concentrations is relatively constant and independent of ethanol concentration. Therefore, purely enzyme-saturating concentrations of substrate are of little analytical value in the determination of ethanol. However, as the ethanol zone is depleted, so that enzyme-saturating conditions no longer exist, the rate of the reaction and, therefore, production of NADH decrease until they are directly proportional to the substrate concentration. Consequently, the plug of ethanol is depleted as it passes through the zones containing ADH and enzyme-saturating concentrations of NAD<sup>+</sup>, and the rate of the reaction lessens as illustrated by Figure 6A. This figure depicts the time dependence of the reaction velocity due to ethanol depletion as predicted by eq 10 utilizing the kinetic constants of Dickenson and Dickinson<sup>17</sup> and a constant enzyme-saturating concentration of NAD<sup>+</sup>.

(16) Wratten, C. C.; Cleland, W. W. *Biochemistry* 1963, 2, 935.

(17) Dickenson, C. J.; Dickinson, F. M. *Biochem. J.* 1975, 147, 303.

(15) Jorgenson, J. W.; Lukacs, K. D. *Science* 1983, 222, 266.



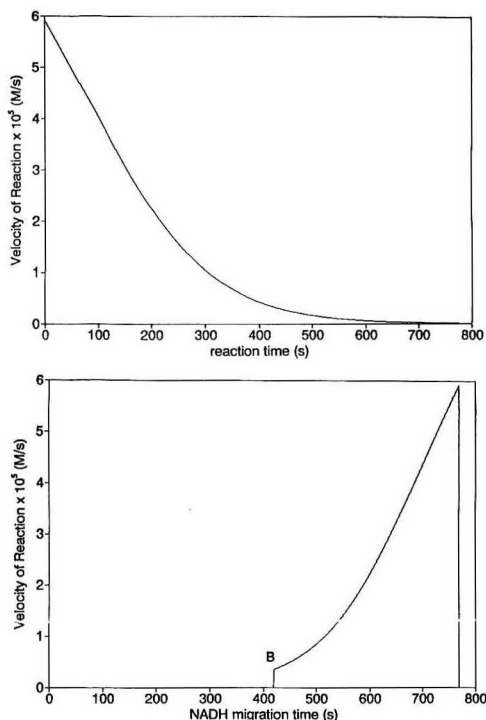


**Figure 6.** (A) Reaction velocity for the enzymatic oxidation of 0.5 g/L ethanol as a function of time as determined by eq 10. Kinetic constants are those of Dickenson and Dickinson<sup>18</sup> for YADH at pH 8.9 and 25 °C ( $\phi_0 = 0.0019 \text{ s}^{-1}$ ;  $\phi_{\text{NAD}} = 0.26 \mu\text{M s}$ ;  $\phi_{\text{ethanol}} \sim 23 \mu\text{M s}$ ;  $\phi_{\text{NAD-ethanol}} = 19700 \mu\text{M}^2 \text{ s}$ ). YADH and  $\text{NAD}^+$  concentrations are those of experimental determination depicted in Figure 2 (8 units/mL and 10 mM, respectively). (B) Theoretical electropherogram for an EMMA determination of 0.5 g/L ethanol obtained by converting the reaction times of Figure 6A to migration times by eq 17. Instrumental parameters are those of experimental determination depicted in Figure 2 ( $E = 125 \text{ V/cm}$ ;  $l = 25 \text{ cm}$ ). Electrophoretic properties are stated in the text. B designates expected truncation of NADH concentration profile due to incomplete depletion of the ethanol zone as it migrates past the detection position.

The kinetics are very different for the determination of ADH as depicted in Figure 5. As the enzyme plug passes through the ethanol and  $\text{NAD}^+$  regions, ADH is not depleted. If enzyme-saturating concentrations of both ethanol and  $\text{NAD}^+$  are maintained, the rate of the reaction is relatively constant and directly proportional to the concentration of ADH:

$$v = V_{\text{max}} = [\text{ADH}]/\phi_0 \quad (12)$$

Furthermore, the velocity of the reaction is directly proportional to the turnover number (defined as the reciprocal of  $\phi_0$ ) of the enzyme. However, if sufficient depletion of one or more substrates occurs, so that enzyme-saturating conditions do not prevail, the velocity of the reaction is dependent upon the concentrations of substrate as dictated by eq 10 and is no longer directly proportional to the concentration of enzyme.

The reaction phase may be performed in a constant or zero potential mode. In the constant potential mode, as utilized in the determinations illustrated in this paper, two or more reagent zones, which have been previously electrophoretically mixed, continually electrophorese through each other under

the influence of an applied electric field as the reaction progresses. A zone of analyte can be made to engage many times its own volume in analytical reagents by allowing a small zone of the analyte to migrate through a larger plug of the analytical reagent. Maximal analytical reagent is contacted when the analyte is metered adjacent to a continuous stream of analytical reagents (i.e. capillary and buffer reservoirs filled with analytical reagent solution as in this study) so that the analyte zone encounters analytical reagent throughout its traversal from injection until migrating past the detection position. In this mode,  $R_{\text{vol}}$  (defined as the ratio of analytical reagent volume encountered to analyte volume) depends upon the difference in electrophoretic mobility between the analyte and analytical reagent species  $\Delta\mu_{\text{ep,A-R}}$ , capillary distance from injection to detection, electrophoretic mobility of the analyte  $\mu_{\text{ep,A}}$ , electroosmotic flow, and the width of the injected analyte zone

$$R_{\text{vol}} = \frac{\Delta\mu_{\text{ep,A-R}} l}{(\mu_{\text{ep,A}} + \mu_{\text{eo}})w} \quad (13)$$

In the determination of ethanol depicted in Figure 2, eq 13 estimates that a 0.5-mm plug of analyte encounters approximately 170 times its volume in ADH and 120 times its volume in  $\text{NAD}^+$ . In the ADH assay depicted in Figure 5, a 0.5-mm zone of analyte interpenetrates about 110 and 30 times its own volume in ethanol and  $\text{NAD}^+$ , respectively, prior to passing by the detection position. Reaction under the influence of an applied electric field allows fresh analytical reagents to be transported to the analyte throughout the reaction without the concurrent dilution experienced in the mixing of bulk solutions.

Reactions in the zero potential mode are quite different. At zero potential, two or more reagent zones, which have been electrophoretically mixed by the previous application of an electric field, are allowed to incubate in the absence of an electric field in order to allow the detectable effects of the reaction (e.g. production or depletion of detectable species) to accumulate for a fixed period of time as previously described.<sup>5</sup> Following the zero potential time period, the potential is again applied to transport the detectable species to the detector.

If the analyte and detectable species differ in electrophoretic mobility, and the reaction proceeds under the influence of an applied electric field, the detectable species is continually transported away from the analyte region throughout the duration of the reaction. This separation occurs at a rate  $v_{\text{disengagement}}$  which is dependent upon the difference in electrophoretic mobility between the analyte and the detectable species  $\Delta\mu_{\text{ep,A-D}}$  and the applied electric field strength

$$v_{\text{disengagement}} = \Delta\mu_{\text{ep,A-D}} E \quad (14)$$

Consequently, the concentration profile of the detectable species is broadened relative to the zone width of the analyte. Minimum band broadening and maximum sensitivity are obtained in the constant potential mode when the two species differ little in electrophoretic mobility and at low electric field strengths. Under these conditions, the detectable species is allowed to accumulate in the vicinity of the reaction.<sup>5</sup> Optimum sensitivity is obtained in the zero potential mode because the detectable species is not separated from the vicinity of the analyte. This effect allows maximum accumulation of product. As no electrophoretic separation occurs in the absence of an applied electric field, the difference in electrophoretic mobility of the analyte and detectable species is not important in the zero potential mode. Sensitivity in this case is limited by diffusional band broadening of the accumulating detectable species, production inhibition, and depletion of the analytical reagents. The zero potential mode

is of particular value in those determinations for which maximum sensitivity is desired, such as the analysis of dilute analytes and in those cases for which the kinetics are slow (*i.e.* low turnover number enzymes).

**4. Detection.** Detection in EMMA is generally performed by electrophoretically transporting the detectable species to the detection system. The rate of transport is dependent upon the detectable species' electrophoretic mobility and the electroosmotic flow. In both the determination of ethanol and ADH, NADH has a lower transport velocity than either analyte. Therefore, the first NADH formed is the last to be detected. The first NADH which can be detected is that which last forms before the analyte zone (ADH or unreacted ethanol) migrates past the detection position. Therefore, there is a detection "time window"  $t_{\text{det}}$  during which NADH can be observed as defined by the apparent mobilities of the analyte and the detected product

$$\frac{l}{(\mu_{\text{ep,A}} + \mu_{\text{eo}})E} \leq t_{\text{det}} \leq \frac{l}{(\mu_{\text{ep,D}} + \mu_{\text{eo}})E} \quad (15)$$

The detection time window for the ethanol assay described in Figure 2 corresponds to NADH detection times of 420–770 s based upon the experimental values of electrophoretic mobility and electroosmotic flow. In contrast, the detection window for the ADH determination in Figure 5 spans from approximately 270 to 350 s. In an EMMA assay for which the detectable species has a greater transport velocity than the analyte, the first detectable species formed is the first to be detected, and the last detectable species which can be detected is that which forms as the analyte zone passes by the detection position. In this case, the detection window is defined as

$$\frac{l}{(\mu_{\text{ep,D}} + \mu_{\text{eo}})E} \leq t_{\text{det}} \leq \frac{l}{(\mu_{\text{ep,A}} + \mu_{\text{eo}})E} \quad (16)$$

Since the quantity of detectable species produced or depleted at a given time is dependent upon the rate of the reaction, and the detectable species is electrophoresed away from the vicinity of the reacting analyte at a rate indicated by eq 14, the resulting peak in the electropherogram provides a profile of the velocity of the reaction as the analyte traverses the capillary. When the assay is performed at constant applied potential, the total time required for the observed detectable species to migrate to the detector  $t_{\text{mig}}$  is the sum of the time  $t_A$  prior to the reaction during which the analyte moves with its electrophoretic mobility  $\mu_{\text{ep,A}}$  a certain distance  $d$  from the point of injection and the time  $t_D$  required following the reaction for the resulting detectable species to traverse the remaining distance  $(l - d)$  to the detector position with its unique electrophoretic mobility  $\mu_{\text{ep,D}}$

$$t_{\text{mig}} = t_A + t_D = \frac{l + (t_A \Delta\mu_{\text{ep,D-A}}E)}{(\mu_{\text{ep,D}} + \mu_{\text{eo}})E} \quad (17)$$

where  $\Delta\mu_{\text{ep,D-A}}$  is the difference in electrophoretic mobility between the detectable species and the analyte. The correlation between  $t_A$  and  $t_{\text{mig}}$  allows for the estimation of the time at which a given observed detectable species was formed in the assay

$$t_A = \frac{[t_{\text{mig}}(\mu_{\text{ep,D}} + \mu_{\text{eo}})E] - l}{\Delta\mu_{\text{ep,D-A}}E} \quad (18)$$

where  $t_A$  includes the time required to electrophoretically engage the analytical reagent zones and the reaction time following mixing. If electrophoretic mixing occurs rapidly,  $t_A$  approximates the time of reaction as dictated by the kinetics of the chemical system. Therefore, it is often possible to estimate the resultant electropherogram depicting the con-

centration profile of the detectable species based upon knowledge of the electrophoretic properties and kinetics of the system. Utilizing the same kinetic parameters as in Figure 6A and the experimental values of electrophoretic mobility and electroosmotic flow and the instrumental parameters of Figure 2, Figure 6B illustrates a theoretical NADH profile obtained by converting the reaction times of Figure 6A to electrophoretic migration times (*i.e.* NADH detection times) as dictated by eq 17. There is a definite similarity in appearance between the theoretical and experimental concentration profiles of Figures 2 and 6B, respectively, thereby verifying the stated kinetic and electrophoretic effects upon peak shape. The experimental NADH peak of Figure 2 is convoluted by other factors, including the interfacial accumulation described previously, diffusion of the reagent and product zones, the width of the injected analyte zone, and uneven depletion of the analyte zone due to the time required for electrophoretic mixing, which are not considered in the simple model depicted in Figure 6B.

Clinical substrate assays are often based on an end-point method in which the reaction is allowed to essentially reach completion prior to taking a spectrophotometric reading. An EMMA end-point determination of ethanol requires all of the substrate to react prior to passing the detection window. As a result, the area of the NADH peak is directly proportional to the quantity of ethanol injected. The total reaction time  $t_{\text{rxn}}$  available to fully deplete the substrate is equal to the time required for the ethanol to migrate from the injection point to the detection window

$$t_{\text{rxn}} = \frac{l}{(\mu_{\text{ep,A}} + \mu_{\text{eo}})E} \quad (19)$$

When the reaction is not completed prior to passing the detection window, the peak is abruptly truncated as NADH produced beyond this point is not observed by the detector. This phenomenon is illustrated in Figure 2 as the truncation of the NADH profile at position B as the approximately 420-s migration time of the ethanol zone through the analytical reagents' zone is insufficient to fully react the 1 ng (2 nL, as estimated by the Poiseuille equation, of 0.5 g/L sample) of ethanol injected. The theoretical NADH concentration profile of Figure 6B predicts this truncation based upon the expected detection window determined by eq 15. This truncation effect places the upper limit on the linear range of the technique as the area contained within the peak is no longer indicative of the quantity of substrate injected. The linear range can be extended either by increasing the available reaction time or by increasing the rate of the reaction. The available reaction time may be increased by operating at lower electric field strengths or by increasing the effective plug width of analytical reagents encountered by the analyte zone. In the reagent filled capillary mode, the latter effect can be accomplished by increasing the separation length of the capillary. However, elevating the available reaction time by decreasing the electric field strength or increasing the separation length concurrently lengthens the analysis time as dictated by the upper limits of eqs 15 and 16. The linear range may be extended without adversely affecting the analysis time by increasing the rate of the reaction by elevating the concentrations of analytical reagents. Although the turnover number of an individual enzyme is not altered, raising the concentration of the ADH proportionally increases the value of  $V_{\text{max}}$  by raising the number of enzyme molecules capable of operating at a given turnover number. This effect is shown in the ethanol determination of Figure 4 in which the concentration of ADH is increased from approximately 8 to 75 units/mL relative to the assay depicted in Figure 2. A 5-ng (10 nL, as estimated by the Poiseuille equation, of 0.5

g/L) sample of ethanol does not experience truncation as does the 1-ng sample of Figure 2. The NADH profile returns to the baseline at a migration time of 690 s, corresponding to a required reaction time of approximately 180 s as estimated by eq 18.

In the determination of an enzyme performed at constant potential and enzyme-saturating concentrations of substrates, such as that depicted for ADH in Figure 5, the rate of production and separation of detectable species is relatively constant as indicated by eqs 12 and 14, respectively. Therefore, the resulting concentration profile of detectable species is a plateau as previously described.<sup>5</sup> The width of the plateau is dependent upon the relative electrophoretic mobilities of the analyte and detectable species and the applied electric field strength as dictated by eq 15 or 16. The height of the plateau and, therefore, the sensitivity of the technique can be approximated by

$$h = \frac{\epsilon b k_3 [\text{enzyme}] w}{\Delta \mu_{\text{ep,A-D}} E} \quad (20)$$

where  $h$  is the height of the plateau in absorbance units,  $\epsilon$  is the molar absorptivity of the detectable species,  $b$  is the cell path length,  $k_3$  is the turnover number of the enzyme, and  $w$  is the injected plug width of the enzyme. Consequently, the height of the plateau is directly proportional to the quantity of enzyme injected, and the sensitivity of the method is directly proportional to the turnover number of the enzyme and inversely proportional to the rate of separation of the detectable species from the analyte.

In the zero potential mode, the detectable species accumulated in the absence of an electric field appears as a peak superimposed upon a plateau. The plateau results from the applied potential intervals which are required to electrophoretically mix the reagents prior to the zero potential period and to transport the detectable species to the detector position following the zero potential interval. The applied potential migration time of the zero potential peak can be estimated by eq 17 if  $t_A$  is defined as the time prior to the zero potential interval during which constant potential is maintained.

The lower limits of detection (LLD) observed using EMMA vary widely depending upon the chemical nature of the analysis and the detection system. In the determination of substrates, if sufficiently high concentrations of analytical reagents are utilized so that the reaction is nearly instantaneous and insignificant band broadening occurs due to the kinetic effects previously described, the LLD for the assay corresponds closely to that observed for a normal injection of the detectable species. For the EMMA determination of ethanol, we have reported a LLD of  $1 \times 10^{-4}$  M corresponding to the detection of approximately  $3 \times 10^{-13}$  mol of ethanol by

UV absorption.<sup>18</sup> EMMA determinations of enzymes offer much lower LLDs than those encountered with substrates due to the amplifying nature of the enzymatic reaction. Wu and Regnier,<sup>19</sup> utilizing the zero potential mode and gel-filled capillaries to minimize diffusional band broadening, have reported the detection of  $7.6 \times 10^{-12}$  M ( $5 \times 10^{-20}$  mol) alkaline phosphatase by the VIS absorption of the *p*-nitrophenol reaction product. The LLD can be further lowered by the use of more sensitive detection methods. Detecting reaction product 4-methoxy- $\beta$ -naphthylamine by time-resolved laser-induced fluorescence, Miller *et al.*<sup>20</sup> have reported the determination of  $6 \times 10^{-13}$  M ( $7 \times 10^{-22}$  mol) leucine aminopeptidase by the zero potential mode in free solution.

## CONCLUSIONS

EMMA offers numerous advantages to traditional chemical methods of analysis. The use of electrophoretic mixing allows reagent zones to be merged without the concurrent dilution experienced in bulk methods, does not require turbulence and the resulting band spreading, and allows an analyte to encounter many times its own volume in analytical reagents. The small dimensions of the CE systems employed in EMMA allow analyses to be performed on ultramicrosamples with minimal consumption of analytical reagents. While this paper has focused on the use of electrophoresis as a means for mixing and transport in chemical analysis, EMMA will become most powerful when this capability is combined with the intrinsic separative capacity of electrophoresis. Present day chemical analyses often require that the detectable species possess a unique detection characteristic such that the reaction may be monitored free of interferences from the other chemical species involved in the reaction. This necessity can often force the experimenter to couple the analytical reaction to one or more secondary reactions in order to produce a substance with unique detection characteristics. The separative capability of EMMA can allow a species produced in the analytical reaction with similar detection characteristics but unique electrophoretic properties to serve as the monitored species without the need to couple it to a secondary reaction. Furthermore, the separative capability of CE can allow simultaneous analyses to be performed as either analytes or monitored species which differ in electrophoretic mobility can be separated prior to or following the analytical reactions.

## ACKNOWLEDGMENT

We gratefully acknowledge the generous loan of the capillary electrophoresis CV<sup>4</sup> variable wavelength absorbance detector from ISCO. Financial support was received in part from the National Institutes of Health (Grant No. GM 25431) and from the Purdue Research Foundation.

RECEIVED for review April 20, 1993. Accepted June 29, 1993.\*

(18) Harmon, B. J.; Patterson, D. H.; Regnier, F. E. Submitted for publication in *J. Chromatogr.*

(19) Wu, D.; Regnier, F. E. *Anal. Chem.*, in press.

(20) Miller, K. J.; Leesong, L.; Bao, J.; Regnier, F. E.; Lytle, F. E. Submitted for publication in *Anal. Chem.*

\* Abstract published in *Advance ACS Abstracts*, August 15, 1993.

# Axial Thermal Gradient Microbore Liquid Chromatography by Flow Programming

Leslie K. Moore and Robert E. Synovec\*

Center for Process Analytical Chemistry, Department of Chemistry, BG-10, University of Washington, Seattle, Washington 98195

A novel thermal gradient technique that combines flow and temperature programming has been developed for high-performance microbore liquid chromatography ( $\mu$ LC). Axial thermal gradient  $\mu$ LC (AxTG- $\mu$ LC) modulates column temperature and changes analyte retention by introducing heated solvent into the column. The column, at ambient temperature, acts as a heat sink. Flow programming the mobile phase increases the rate of heat provided to the column and raises the average column temperature with time. For example, when introducing heated eluent at 100 °C into a 1 mm  $\times$  5 cm reversed-phase column made of PEEK, the average column temperature is 40 °C at 25  $\mu$ L/min and 87 °C at 400  $\mu$ L/min. Thermal losses of the mobile phase down the length of the column were modeled with a two-dimensional distributed parameter model for a cylindrical packed bed. The change in average column temperature with flow rate was calculated and compared to chromatographic data. The AxTG- $\mu$ LC technique maintains low column back pressure and peak resolution at high linear flow velocities. This results in good separation efficiency with reduced analysis time. Run-to-run cycle time is potentially reduced when compared to radially heating the column as the column is heated and cooled using the mobile phase.

## INTRODUCTION

Gradient elution is a well-established technique for high-performance liquid chromatography (LC). Traditionally, mobile phase gradients have been more commonly used than thermal gradients due, in part, to problems associated with adequately heating conventional sized columns. A growing acceptance of microbore and capillary columns for standard analysis has renewed interest in temperature programming for LC.<sup>1</sup> Problems, such as radial temperature gradients, are reduced with small volume columns. For example, Poppe and co-workers calculated the radial temperature profiles associated with introducing room temperature solvent into heated conventional and preparatory sized columns.<sup>2</sup> The authors found the magnitude of the radial temperature profile in the column to be related to the square of the column radius. In another study, Bowermaster and McNair compared the response time of heating conventional (4.6 mm i.d.) and microbore (1.0 mm i.d.) columns with a temperature step

change.<sup>3</sup> The authors concluded that both the smaller internal volume and total mass of microbore columns enable them to respond quickly to changes in temperature.

From an instrumental point of view, thermal gradients are easier to engineer than mobile phase gradients for small diameter columns. Thermal gradient LC requires only one solvent pump, one solvent reservoir, and a heating device. Whereas mobile phase gradient generation normally requires two pumps, two solvent reservoirs, and mixing chambers.<sup>4</sup> The low column back pressures associated with thermal gradient LC separations reduce the likelihood of pump seal failure.<sup>5</sup> Thus, low pressure thermal gradient LC systems require less maintenance and are more reliable than mobile phase gradient systems.

In previous work, thermal gradient microbore LC (TG- $\mu$ LC) has been demonstrated by radially heating the whole column much like temperature programming for gas chromatography.<sup>6</sup> In this work we demonstrate a novel gradient technique that uses the mobile phase to heat and cool a microbore LC column. The axial thermal gradient (AxTG) technique modulates column temperature and changes analyte retention times by heating only the mobile phase immediately before it enters the column. The axial dimension refers to the column length. Figure 1A shows the instrument schematic, where the column, at ambient temperature, acts as a heat sink. Relatively short (5 cm) microbore columns are used to minimize thermal losses. Increasing the flow rate increases the temperature of the column stationary phase and mobile phase and, to an extent, the column itself. Flow programming the mobile phase modulates the column temperature without additional heating or cooling mechanisms. By combining flow and temperature programming, AxTG- $\mu$ LC overcomes many of the traditional obstacles of flow programming for LC such as band broadening and increased column back pressure. In addition, the technique potentially reduces run-to-run cycle time because the column is heated and cooled using the mobile phase rather than being in direct contact with the heating element. A number of authors have reported using short columns for high-speed analysis.<sup>7</sup> Regnier performed rapid mobile phase gradient separations on short columns to monitor eluting peaks from a preparatory sized column.<sup>8</sup> Kinkel and co-workers used 5 cm long columns packed with 1–2  $\mu$ m particles to separate low molecular weight compounds in 30 s.<sup>9</sup> AxTG- $\mu$ LC is an alternative technique that utilizes short column technology for rapid LC analysis.

(3) Bowermaster, J.; McNair, H. M. *J. Chromatogr. Sci.* 1981, 22, 165–170.

(4) Powley, C. R.; Howard, W. A.; Rogers, L. B. *J. Chromatogr.* 1984, 299, 43.

(5) Berry, V. *Crit. Rev. Anal. Chem.* 1989, 21, 115–191.

(6) Renn, C. N.; Synovec, R. E. *Anal. Chem.* 1991, 63, 568–574.

(7) Dunphy, D. R.; Synovec, R. E. *Talanta* 1993, 40, 775–780.

(8) Thevenon-Emeric, G.; Regnier, F. E. *Anal. Chem.* 1991, 63, 1114–1118.

(9) Giesche, H.; Unger, K. K.; Esser, U.; Eray, B.; Trudinger, U.; Kinkel, J. N. *J. Chromatogr.* 1989, 465, 39–67.

(1) McNair, H. M.; Bowermaster, J. *HRC CC, J. High Resolut. Chromatogr. Chromatogr. Commun.* 1987, 10, 27–31.

(2) Poppe, H.; Kraak, J. C.; Huber, J. F. K.; van den Berg, J. H. M. *Chromatographia* 1981, 14, 515–523.

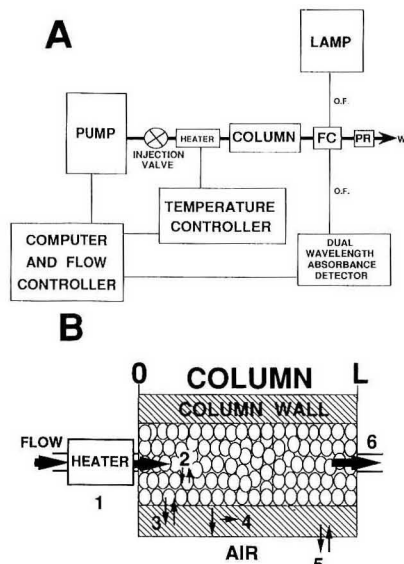


**Figure 1.** (A) Schematic diagram for AxTG- $\mu$ LC with the single fiber optic dual wavelength absorbance detector: OF, optical fiber; FC, flow cell; PR, pressure restrictor. (B) Close up view of the heater and chromatographic column highlighting primary heat exchange processes: 1, heat exchange region where the mobile phase is heated by contact with the tubing wall; 2, heat transfer of the mobile phase with the packing material; 3, heat transfer between the mobile phase and the column wall; 4, conduction of heat through the column wall; 5, heat transfer between column and ambient air surrounding the column; 6, heat exiting the column in the mobile phase; L, column length.

This work introduces AxTG- $\mu$ LC by flow programming as a gradient technique for LC. We will delineate the heat transfer processes for the system and calculate the thermal losses expected for a microbore column using a two-dimensional model for a cylindrical packed bed. The calculations will show an axial temperature profile down the column and a change in overall column temperature with mobile phase flow rate. We will compare the calculations with AxTG chromatographic data. In view of these results, we will demonstrate AxTG- $\mu$ LC by flow programming with a separation of aldehyde dinitrophenylhydrazine (DNPH) derivatives. The benefits of flow programming with an AxTG for LC will be discussed with respect to minimizing column back pressure and chromatographic band broadening. Finally, we will examine the of run-to-run cycle time for the AxTG system.

## THEORY

Thermally modulating a liquid chromatographic column by heating the solvent before the column is a balance between the rate of heat input to the mobile phase and the rate of thermal loss to the column and to the surroundings. Figure 1B illustrates the energy distribution. Heat input to the mobile phase (1) is distributed to the column packing material (2), into and out of the column wall (3–5) and a certain proportion exits the column in the mobile phase (6). The energy balance equation for the system is

$$q_{in} = q_{bed} + q_{wall} + q_{mp} \quad (1)$$

where  $q_{in}$  is the rate at which heat is introduced to the mobile phase by the heater,  $q_{bed}$  is the rate of heat loss to the packing material,  $q_{wall}$  is the rate of heat loss to the column wall, and

$q_{mp}$  is the rate at which heat exits the column in the mobile phase. It is assumed, for these calculations, that no heat is lost as the mobile phase passes from heater to column. Each component of eq 1 varies as a function of system dimension and separation conditions.

To illustrate the axial thermal gradient temperature profile, simulations of thermal losses from a chromatographic column were developed using a two-dimensional distributed parameter model for a cylindrical packed bed by Finlayson et al.<sup>10</sup> The program establishes temperature profiles in the axial and radial directions using an orthogonal collocation method to solve the partial differential equation

$$\rho u C_{mp} \frac{\delta T^v}{\delta L} = \frac{k_{eff}}{r} \frac{\delta}{\delta r} \left( r' \frac{dT^v}{dr'} \right) \quad (2)$$

with the boundary conditions

$$T^v = T'_i \text{ at } L' = 0 \quad dT/dr' = 0 \text{ at } r' = 0$$

where  $k_{eff}$  is the effective thermal conductivity of the packed bed,  $r$  is a radial position in the column, and  $T^v$  is the temperature at a given axial and radial positions. The program embodies the convective and conductive heat transfer processes shown in the Appendix. A plug flow distribution across the packed bed was assumed resulting in a constant value for  $k_{eff}$ .<sup>11</sup> The center of the packed bed was defined as  $r = 0$ .

It was of interest to compare simulated column temperature profiles, with average column temperature as predicted by AxTG chromatography data. This can be done by considering the relationship between analyte retention and column temperature. The fundamental relationship between temperature and analyte retention is expressed by a variation of van't Hoff's equation

$$\ln k' = \frac{\Delta H}{RT} + \frac{\Delta S}{R} + \ln f \quad (3)$$

where  $k'$  is the capacity factor of an analyte,  $\Delta H$  and  $\Delta S$  are enthalpy and entropy of an analyte partitioning from the stationary phase to the mobile phase,  $R$  is the gas constant, and  $f$  is the phase volume ratio of the stationary phase to the mobile phase.<sup>12</sup> The capacity factor of the analyte is a measure of analyte retention and is defined as

$$k' = \frac{V_r - V_0}{V_0} \quad (4)$$

where  $V_r$  is the retention volume of the analyte and  $V_0$  is the void volume of the column. Each analyte has a unique relationship between retention and temperature for a given stationary phase and mobile phase composition, and this relationship can be determined empirically. Because capacity factor varies logarithmically with temperature, eq 3, the average column temperature experienced by an analyte cannot be predicted by simply averaging the column temperature profile for a given flow rate. To accurately estimate the average column temperature experienced by an analyte, the column can be considered to be a series of temperature segments. For a given analyte, each segment can be assigned a capacity factor,  $k'_i$ , based on the average temperature of that segment. Capacity factor is calculated at a given temperature by rearranging eq 3

$$k'_i = \exp \left( \frac{A}{T_{avg_i}} + B \right) \quad (5)$$

where  $A$  is  $(\Delta H/R)$ ,  $B$  is  $(\Delta S/R) + \ln f$ , and  $T_{avg_i}$  is the average

(10) Finlayson, B. A. *Chem. Eng. Sci.* 1971, 26, 1081–1091.

(11) Kuni, D.; Smith, J. M. *AIChE J.* 1960, 6, 71–78.

(12) Tchaplai, A.; Heron, S.; Colin, H.; Guiochon, G. *Anal. Chem.* 1988, 60, 1443–1448.



column temperature for a given column segment. The average capacity factor at which an analyte elutes,  $k'_{avg}$ , is calculated by summing the capacity factor contributions,  $k'_i$ :

$$k'_{avg} = \sum_{i=1}^n k'_i \quad (6)$$

By use of eq 3 and  $k'_{avg}$ , the average temperature,  $T_{avg}$ , can now be calculated for an analyte under a given set of conditions.

## EXPERIMENTAL SECTION

**Chromatographic System.** Figure 1 illustrates the axial thermal gradient system. A syringe pump (ISCO, LC-2500, Lincoln, NE) delivered the mobile phase. The flow programs for Figure 7 were accomplished by a manual step adjustment of the flow rate. The cycle time study required interfacing the syringe pump and the injection valve to a personal computer (Leading Edge, Model D, Canton, MA). The computer was equipped with a 12-bit analog to digital converter (DACA, IBM, Boca Raton, FL). The control software was written in house using Quick Basic (Microsoft, Redmond, WA). A pneumatically driven microbore injection valve (Rheodyne 7520, Cotati, CA) accomplished the injections of 1  $\mu$ L. For the axial thermal gradient experiments, a 127  $\mu$ m  $\times$  3 cm length stainless steel union (Upchurch, Oak Harbor, WA) was thermostated by resting it on a heat strip (Wellman, SS2181, Shelbyville, IN). Covering the union with a heat sink compound (Rawn Co., Spooner, WI) and wrapping it in Fiberglass insulation promoted uniform heating. A temperature control unit (FIATron Lab Systems, TC-55, Oconomowoc, WI) controlled the heat strip with feedback from a 1000- $\Omega$ , thin film platinum resistance temperature detector (RTD, Omega Engineering, Stamford, CT). The controller regulates the heat strip temperature within  $\pm 0.01$   $^{\circ}$ C of the set point temperature. The union joined short sections 127  $\mu$ m i.d. PEEK tubing (Upchurch) connecting the injection valve to the column. Radially heated isothermal separations were accomplished by placing the entire column on the heat strip. Aluminum blocks allowed every part of the column to be in thermal contact with the heat strip. The column and aluminum blocks were covered with heat sink compound and insulated to promote uniform heating. A thermocouple, made in house, measured the column outer wall temperature and provided feedback to the controller. Comparing thermocouple and RTD readings for a heated surface enabled calibration of the thermocouple. The axial thermal gradients were performed on a 1 mm  $\times$  5 cm, 9  $\mu$ m, C18 derivatized poly(vinyl alcohol) copolymer reversed-phase column made of PEEK (Keystone Scientific, Bellefonte, PA). The high-temperature, isothermal, data were obtained on a 1 mm  $\times$  5 cm, 5  $\mu$ m, C18 derivatized poly(vinyl alcohol) copolymer reversed-phase column made of stainless steel (Keystone Scientific). The polymer based packing materials exhibits thermal stability up to 150  $^{\circ}$ C. A 100 psi pressure restrictor (Upchurch) was necessary to maintain the eluent in a liquid phase at all times.

**Detection and Data Collection.** Previous reports describe the lamp, flow cell, optical fibers, monochromator, and position sensitive detector (PSD).<sup>13,14</sup> All detection specifications are the same as reported except the flow cell was constructed from PEEK, and the PSD was configured with 5  $\times$  10<sup>7</sup> V/A resistors at the outputs A and B. In all cases, the analysis of aldehyde-DNPH derivatives occurred at wavelengths of 365 and 615 nm. A personal computer (Leading Edge, Model D) equipped with a 12-bit analog to digital converter (DACA, IBM) recorded the amplified signal. The data acquisition software was written in house using Quick Basic (Microsoft). In these experiments the signal was averaged from 100 points to 1 point on the fly. Data were collected at 1 point/s.

**Reagents.** The mobile phase consisted of high-purity acetonitrile (Burdick and Jackson UV grade, Muskegon, MI) and water (distilled, deionized with a 18 M $\Omega$  Milli-Q water system, Millipore Corp., Bedford, MA). The aldehyde DNPH derivatives

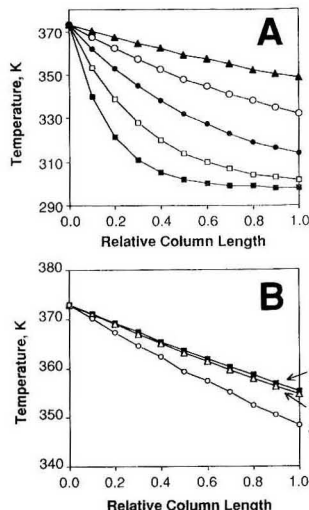


**Figure 2.** (A) Temperature as a function of column length at various flow rates calculated for an AxTG profile in cylindrical packed bed using eq 2. Column conditions: internal diameter, 1.0 mm; external diameter, 8.7 mm; length, 5 cm; stationary phase, 9- $\mu$ m, C18 derivatized poly(vinyl alcohol) copolymer; mobile phase, acetonitrile-water (50:50) (v/v); column inlet temperature, 100  $^{\circ}$ C;  $\blacksquare$ , 25  $\mu$ L/min;  $\square$ , 50  $\mu$ L/min;  $\bullet$ , 100  $\mu$ L/min;  $\circ$ , 200  $\mu$ L/min;  $\blacktriangle$ , 400  $\mu$ L/min. (B) Temperature as a function of column length for different column geometries and column wall compositions calculated using eq 2: chromatographic conditions are the same as Figure 2A; mobile phase flow rate, 400  $\mu$ L/min;  $\blacksquare$ , stainless steel column with internal diameter (i.d.) 1.0 mm, outer diameter (o.d.) 1.7 mm;  $\Delta$ , PEEK column with 1.0 mm i.d., 1.7 mm o.d.;  $\circ$ , PEEK column with 1.0 mm i.d., 8.7 mm o.d.

were a gift from Dr. William Zoller, University of Washington. Primary standards were dissolved in acetonitrile. Working standards were diluted in the mobile phase from the primary standard solutions and were filtered with a 0.02- $\mu$ m syringe filter (Anatop syringe filters, Alltech, Deerfield, IL) before injection.

## RESULTS AND DISCUSSION

We will now examine the theory to understand and predict the AxTG column profile with respect to eluent flow rate and column dimension. Figure 2A illustrates the application of eq 2, and demonstrates an increase in temperature throughout the column with eluent flow rate. Column temperature changes result from thermal losses of the mobile phase to the surroundings. Calculations for a 1 mm  $\times$  5 cm reversed-phase column composed of poly(ether ether ketone) (PEEK), with an inlet temperature of 100  $^{\circ}$ C, result in an average column temperature of 40  $^{\circ}$ C at 25  $\mu$ L/min and 87  $^{\circ}$ C at 400  $\mu$ L/min. This is expected as the rate of heat input into the column by the mobile phase is linear with linear flow velocity,  $u$ , while rate of heat dissipation through the column wall has a  $(u)^{0.8}/[1 + (u)^{0.8}]$  relationship (see Appendix). The AxTG simulation also indicated a flow-dependent radial temperature profile, from the center of the column to the column wall. For the results shown in Figure 2A, the radial temperature gradient was  $\leq 1$   $^{\circ}$ C for flow rates up to 50  $\mu$ L/min and 4  $^{\circ}$ C for the fastest flow rate of 400  $\mu$ L/min.

Figure 2B illustrates the column temperature dependence on column wall geometry and wall composition. Temperature as a function of relative column length is higher for thin-walled column walls where heat loss is dominated by convective heat transfer from the column wall to ambient air.

(13) Renn, C. N.; Synovec, R. E. *Anal. Chem.* **1990**, *62*, 558-564.

(14) Synovec, R. E.; Renn, C. N.; Moore, L. K. *Proc. SPIE—Int. Soc. Opt. Eng.* **1989**, *1172*, 49-59.

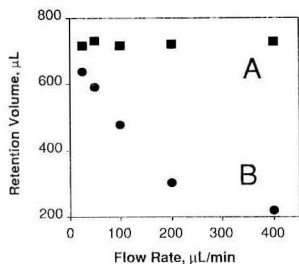


**Figure 3.** Retention volume as a function of flow rate for isothermal and AxTG elution of B-DNPH: (A) Isothermal elution at 25 °C; (B) AxTG elution with heater in Figure 1 held constant at 150 °C. Chromatographic conditions were the same as in Figure 2.

The figure shows that, for a given outer column diameter, the average column temperature is slightly greater for a column wall composed of stainless steel, Figure 2B(A), than for a column made of PEEK, Figure 2B(B). This is due to the fact that stainless steel is approximately 120 times more thermally conductive than PEEK.<sup>15,16</sup> In practice the effect of column wall composition on average column temperature is small when compared to the effect of column wall thickness. Figure 2B(C) shows the average column temperature decreases for a PEEK column when the outer diameter is increased. A large outer column diameter conducts more heat in the column wall. Heat loss increases with column wall thickness resulting in small changes in average column temperatures with flow rate.

The separation of aldehyde-DNPH derivatives provided data to demonstrate AxTG-μLC. To demonstrate a change in average column temperature with mobile phase flow rate, benzaldehyde-DNPH (B-DNPH) was eluted at different flow rates, both with and without an AxTG. Figure 3 shows retention volume is independent of flow rate with isothermal elution (A) but is reduced by an approximate factor of 4 for the AxTG elution (B) with a 16-fold flow rate change from 25 to 400 μL/min. The results support calculations predicting an overall increase in column temperature with an increase in the rate of heat input to the column. To show the axial temperature profile in the column, thermocouple measurements were made along the outer wall of a stainless steel column. Figure 4 compares a temperature profile, calculated using eq 2, for an 1 mm × 5 cm stainless steel column with an inlet temperature of 100 °C (A), to the temperature profile for an identical column determined from thermocouple measurement on the outer column wall (B). The figures show an axial temperature profile with column length resulting from thermal losses of the mobile phase. The figures also show the overall increase in column temperature with increased flow rate. Variations between measured and calculated profiles can be attributed to imperfect contact of the thermocouple with the column wall surface, as well as thermal losses to the tubing between the heated region before the column and the column itself.

Since it is difficult to measure the internal column temperature at various positions, the average internal column temperature was determined from chromatographic data. Retention volume provides a means of monitoring the internal temperature of a packed bed as it reflects the average temperature experienced by the analyte as it elutes from the column. To determine the average internal column tem-

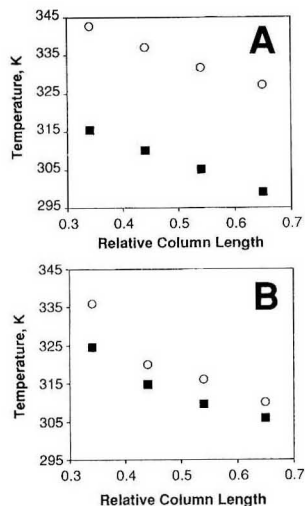


**Figure 4.** (A) Temperature as a function of column length at two flow rates for an AxTG profile calculated using eq 2: O, 75 μL/min; ■, 25 μL/min. Stainless steel column with 1.0 mm i.d. and 1.7 mm o.d. Chromatographic conditions were the same as in Figure 2. Heater held constant at 150 °C. (B) Temperature as a function of length as determined from thermocouple measurements on the outer column wall: O, 75 μL/min; ■, 25 μL/min. Chromatographic conditions were the same as Figure 4A.

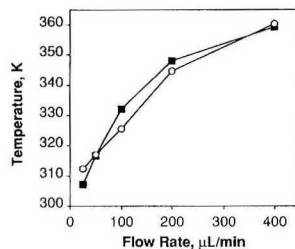


**Figure 5.** Average column temperature as a function of flow rate: O, calculated using chromatographic data and eqs 3-4; ■, calculated from simulations of an AxTG profile for the same chromatographic conditions (see Figure 2A, eq 2, text).

perature, experiments were performed to evaluate the relationship between retention volume and column temperature for B-DNPH eluted from a polymer-based C18 column, eq 3. Isothermal elution of B-DNPH at several temperatures provided data for a best fit linear regression of  $\ln k' = (2804/T) - 5.461$ .  $T_{avg}$  for AxTG elution of B-DNPH was then determined by measuring the capacity factor of the analyte with data shown in Figure 3B. As a result, Figure 5 compares the average column temperature at various flow rates as determined from chromatographic data, to column temperature calculated using eqs 2-6. Calculations were performed for a column of the same dimension and composition, and an inlet temperature of 100 °C. The calculated and simulated values are close in value with a correlation coefficient of  $R = 0.973$ . The close fit of the modeled to the chromatographic data indicates that while the heater before the column was set to 150 °C, the column inlet temperature was actually close to 100 °C. Thermal losses between the heater and the tubing wall of the heat exchange region combined with thermal losses

(15) Weast, R. C.; Astle, M. J., Eds. *CRC Handbook of Chemistry and Physics*, 73rd ed.; CRC Press: Boca Raton, FL, 1992.

(16) Scheffler, W., Greentweed Engineering and Plastics, personal communication, Dec 1991.

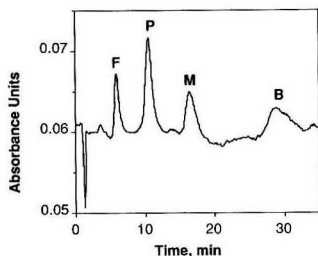


**Figure 6.** Isocratic, room temperature separation of four aldehyde-DNPH derivatives: F, formaldehyde-DNPH; P, propanal-DNPH; M, methacrolein-DNPH; B, benzaldehyde-DNPH. Chromatographic conditions were the same as in Figure 2. Flow rate = 25  $\mu\text{L}/\text{min}$ .  $P = 60$  psi.

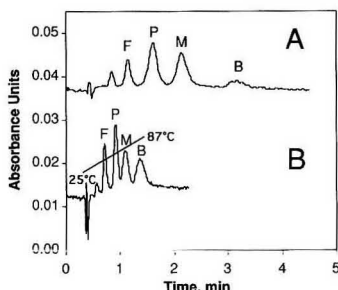


**Figure 7.** Room temperature (A) and AxtG (B) separations of four aldehyde-DNPH derivatives by flow programming. Flow program = 25 to 400  $\mu\text{L}/\text{min}$  in 1.5 min. Column conditions and analytes were the same as in Figure 6. Heater was held constant at 150  $^{\circ}\text{C}$  for the AxtG elution. The final pressure is 950 psi for the room temperature program (A) and 380 psi with the AxtG (B).

of the mobile phase in the connecting tubing before the column could account for much of the discrepancy.

Mobile phase flow programming was applied to the separation of four aldehyde-DNPH derivatives to demonstrate how an AxtG changes the overall column temperature with time. Flow programming is a technique where the mobile phase flow rate is systematically changed during a chromatographic run.<sup>17</sup> The technique can solve the general elution problem by eluting strongly retained peaks quickly. AxtG separations by flow programming simultaneously increase both mobile phase flow rate and overall column temperature. Figure 6 shows an isocratic, isothermal separation of four aldehyde-DNPH derivatives on a polymer-based C18 column. The separation is well resolved; however the run time is about 30 min. Figure 7B shows a separation of the four derivatives in the same eluent with an AxtG. The analytes are separated in 1.5 min. The average column temperature was modulated by flow programming the heated mobile phase from 25 to 400  $\mu\text{L}/\text{min}$  in 1.5 min. The AxtG separation shows resolutions  $\geq 1.0$  for the four analytes in 1/20th the time. The effect of flow programming without elevating the temperature can be seen in Figure 7A. Retention times and column back pressure are lower for the AxtG separation, reflecting the overall increase in column temperature with increasing flow rate. Flow programming is not generally applied to liquid chromatography for several reasons. Primarily, instrumentation failure due to high column back pressure prohibits room temperature, high-speed separations.

(17) Nygren, S. *HRC CC, J. High Resolut. Chromatogr. Chromatogr. Column* 1979, 2, 319-323.

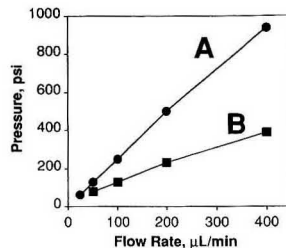


**Figure 8.** Pressure vs flow rate for room temperature (A) and AxtG (B) elutions. Column and mobile phase condition are the same as Figure 2. Heater held constant at 150  $^{\circ}\text{C}$  for AxtG elutions.

Figure 8 shows how an AxtG minimizes pressure with mobile phase flow rate. At room temperature, Figure 8A, a change in mobile phase flow from 25 to 400  $\mu\text{L}/\text{min}$  produced a 16-fold increase in pressure. However, the same flow program with an AxtG, Figure 8B, shows only a 6-fold increase in pressure. The increase in the mobile phase temperature with the AxtG reduces the mobile phase viscosity and column back pressure. These pressure data correspond to the chromatograms shown in Figure 7.

Column back pressure can be used as a second method of calculating average column temperature. Darcy's law relates column back pressure to linear flow velocity,  $u$ , and mobile phase viscosity,  $\eta_{\text{mp}}$ ,

$$P \propto \eta_{\text{mp}} u \quad (7)$$

Viscosity is related to temperature by

$$\eta_{\text{mp}} = A' \exp\left(\frac{B'}{T}\right) \quad (8)$$

where  $A'$  and  $B'$  are empirically determined constants.<sup>18</sup> Rearranging and ratioing eq 8 at two temperatures gives

$$\ln\left(\frac{\eta_2}{\eta_1}\right) = B' \left( \frac{1}{T_2} - \frac{1}{T_1} \right) \quad (9)$$

The pressure data in Figure 8 were used to calculate average column temperature as a function of flow rate. The results agreed closely with those plotted in Figure 5 but are not shown for brevity.

Band broadening is another concern in the application of flow programming to liquid chromatography. Chromatographic separation efficiency is defined by a combination of mobile phase flow properties and analyte diffusion characteristics. It is defined by the van Deemter equation and is measured in terms of the height of one theoretical plate,  $H$ .<sup>19</sup> For liquid chromatography with porous packing materials, the van Deemter equation is dominated by slow analyte mass transport and is expressed as

$$H = A + \frac{qk'd_p^2 u}{(1 + k')^2 D_s} \quad (10)$$

where  $A$  is the multipath term,  $D_s$  is the diffusion coefficient for the analyte in the stagnant mobile phase within the pores, and  $q$  is a constant based on the shape of the packing material.<sup>20</sup> To evaluate the effect of temperature on analyte diffusion,  $H$  was normalized for changes in  $k'$  due to temperature. The result is an expression for band broadening

(18) Anita, F. D.; Horvath, C. *J. Chromatogr.* 1988, 435, 1-15.

(19) Giddings, J. C. *Dynamics of Chromatography, Part 1*; John Wiley: New York, 1973; Chapter 2.

(20) Karger, B. L.; Snyder, L. R.; Horvath, C. *Introduction to Separation Science*; John Wiley: New York, 1973; Chapter 5.

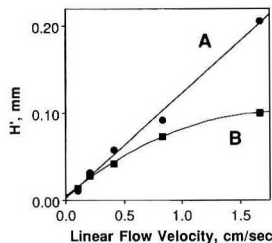


Figure 9. Separation efficiency as a function of flow rate for room temperature (A) and AxTG (B) elution of B-DNPH. Chromatographic conditions were the same as in Figure 2.  $H'$  (eq 11) represents theoretical plate height normalized for changes in capacity factor. Heater held constant at 150 °C for AxTG elutions.

in terms of linear flow velocity and analyte diffusivity

$$H' = \frac{(H - A)(1 + k')^2}{k'} = \frac{q d_p^2 u}{D_s} \quad (11)$$

Figure 9 compares  $H'$  for room temperature and AxTG elution of B-DNPH from a polymer-based C18 column. The band broadening data under room temperature conditions (A) is linear with linear flow velocity as predicted by eq 6. However the band broadening data under AxTG conditions (B) is minimized with linear flow velocity. In previous work, high temperature separations have been shown to improve analyte resolution by decreasing mobile phase viscosity, thus increasing mass transfer of the analyte to the stationary phase.<sup>21</sup> The temperature dependence of analyte diffusivity,  $D_s$ , can be represented by

$$\frac{D_{s2}}{D_{s1}} = \left( \frac{T_2 \eta_1}{T_1 \eta_2} \right) \quad (12)$$

where  $D_{s2}/D_{s1}$  is the ratio of two analyte diffusion coefficients at room temperatures.<sup>22</sup> This ratio indicates the theoretical improvement in separation efficiency due to temperature.

The theoretical increase in column efficiency due to temperature was calculated for the AxTG system using eq 12. The ratio of eluent viscosity at room temperature, and with an axial thermal gradient, was determined using eq 7 and the pressure data in Figure 8. The average column temperature for the AxTG profile at 400  $\mu\text{L}/\text{min}$  is 87 °C, Figure 5. Thus, the theoretical increase in column efficiency due to temperature is 3-fold or 300%. Figure 9 shows a 2-fold increase in the  $D_s$  for the AxTG elution of B-DNPH at 400  $\mu\text{L}/\text{min}$  when compared to room temperature conditions. Radial temperature gradients in the column can diminish the improvement in column efficiency due to temperature. Horvath as well as other authors report a marked decrease in column efficiency in the presence of radial temperature profiles.<sup>23,24</sup> For example, Schrenker reported up to a 90% decrease in column efficiency, for a 4.6 mm i.d. column thermostated at 80 °C, when compared to the same separation with solvent preheating.<sup>25</sup> Heat transfer calculations, eq 2, predict a maximum radial temperature profile of 4 °C. The band broadening expected from a 4 °C radial gradient for the AxTG elution of B-DNPH at 400  $\mu\text{L}/\text{min}$  can be calculated using eqs 3 and 4 and the on-column definition of column

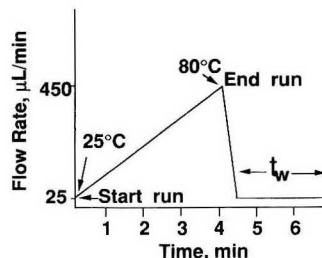


Figure 10. Automated AxTG flow program to establish the retention time reproducibility as a function of wait time,  $t_w$ .

efficiency

$$H = \left( \frac{\sigma_L^2}{L} \right) \quad (13)$$

where  $\sigma_L^2$  is the variance of the peak in length.<sup>22</sup> The result is a decrease in column efficiency of 17%. Since the temperature benefit for the analyte is a increase in column efficiency of theoretically 300%, the presence of a slight radial temperature gradient proves to be insignificant.

We will now consider the advantages of the present AxTG- $\mu\text{LC}$  method over radial temperature programming and mobile phase gradient elution in terms of equilibration time. Run-to-run analysis time is dictated by analyte elution time plus the time required to reequilibrate the column. Dorsey and others recommend passing 15–20 column volumes through a column to reequilibrate after a mobile phase gradient elution.<sup>26</sup> For a 1 mm  $\times$  5 cm ( $V_0 = 20 \mu\text{L}$ ) column operated at 25  $\mu\text{L}/\text{min}$ , the column will take 16 min to equilibrate. An observation in our laboratory has shown that the equilibration time period to cool a 1 mm  $\times$  5 cm radially heated stainless steel column from 80 to 24 °C, using natural convection and a flow rate of 25  $\mu\text{L}/\text{min}$ , was about 30 min. The equilibration time required to cool an AxTG from 80 to 24 °C at a flow rate of 25  $\mu\text{L}/\text{min}$  was 10 min, although it will be shown that a cooling time of 5.5 min can be applied with good results.

To evaluate the equilibration time of the AxTG device, five replicate chromatographic runs were performed at various reequilibration times. Figure 10 shows the experimental AxTG flow rate program. The column temperature was calculated to have changed from 24 to 80 °C over the 4-min run. At the end of the chromatogram, the flow rate was reduced to 25  $\mu\text{L}/\text{min}$  and held at that flow rate for a given wait time,  $t_w$ . The retention times of the analytes were monitored. It is expected, from eq 3, that the later eluting peak would be the most sensitive to the thermal equilibration of the column. On the other hand, the earliest eluting peak should be the most sensitive to flow rate equilibration. These trends were found to be true. Figure 11 shows the retention times for repetitive runs of F-DNPH as a function of wait time. At short wait times the retention time of the second run is considerably less than that of the first, indicating the system temperature and flow rate have not equilibrated. As the wait time for the system is extended, the retention times converge, indicating the system is equilibrated. At a wait time of 10 min, the retention times of F-DNPH for runs 1 and 2 are within a relative standard deviation (RSD) of 3.5%. However, the wait time necessary to achieve a retention time RSD of 3.5% for B-DNPH, the last peak to elute, was only 5.0 min. This suggests thermal equilibration of the column occurs more rapidly than equilibration of the eluent flow. For both F-DNPH and B-DNPH, retention time differences were

(21) Perchalski, R. J.; Wilder, B. J. *Anal. Chem.* 1979, 51, 774–776.  
(22) Cantor, C. R.; Schimmel, P. R. *Biophysical Chemistry*; W. H. Freeman: San Francisco, CA, 1980; Vol. 2, p 584.

(23) Horvath, C.; Lin, H. J. *Chromatogr.* 1978, 149, 43–70.

(24) Abbott, S.; Achener, P.; Simpson, R.; Klink, F. J. *Chromatogr.* 1981, 218, 123–135.

(25) Schrenker, H. J. *Chromatogr.* 1981, 213, 243–252.

(26) Cole, L. A.; Dorsey, J. G. *Anal. Chem.* 1990, 62, 16–21.

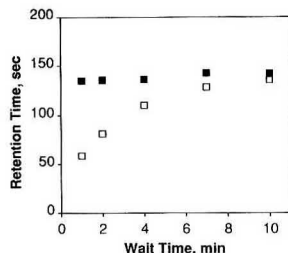


**Figure 11.** Retention time vs wait time for F-DNPH: ■, run 1; □, run 2. Column conditions: 1.0 mm i.d.; 4.0 mm o.d.; length, 5 cm. Column stationary phase was the same as in Figure 2. Mobile phase was acetonitrile–water (60:40) (v/v).

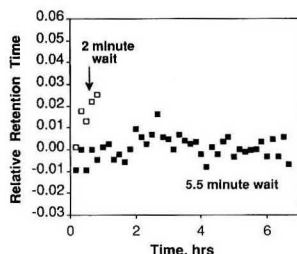


**Figure 12.** Relative retention time variation as a function of time for the AxTG reproducibility study: ■, relative retention time for M-DNPH at a wait time of 5.5 min; □, relative retention time for M-DNPH at a wait time of 2.0 min. Flow program and conditions were the same as in Figures 10 and 11.

greatest between the first and second runs and were reproducible for runs 2 through 5. The RSD for F-DNPH was less than 1.0% for runs 2 through 5 at a wait time of 1 min suggesting the system achieves a state of pseudoequilibrium at very short wait times. The run-to-run cycle time associated with flow programming alone was determined by conducting the same experiment without heating the mobile phase. The retention time differences between runs 1 and 2 for all the analytes were on average 40% less than the differences associated with the AxTG. It was observed during the course of the experiment that flow rate equilibration time was minimized at low column back pressure.

To evaluate analyte retention time reproducibility for the AxTG at relatively short wait times, a study was conducted using the gradient shown in Figure 10. Forty-one repetitive runs were performed with a wait time of 5.5 min and again at a wait time of 2.0 min. Figure 12 shows the relative retention time for M-DNPH as a function of time for runs 2 through 41. The reproducibility was good for the wait time of 5.5 min demonstrating a retention time RSD of 0.54%, and a drift of 0.02%/h. Figure 12 also shows poor reproducibility for a wait time of 2.0 min, with a retention time RSD of almost 3.0% at the end of six runs. As expected, retention time variations were largest for the earliest eluting peak, F-DNPH, not shown for brevity. A wait time of 5.5 min produced a retention time reproducibility of 0.64% with a drift of 0.74%/h, or a retention time drift of 5.0% over the 7-h study. The long-term study showed the run-to-run cycle time for the AxTG can be reduced if a slight systematic retention time drift for some analytes can be tolerated. Reproducibility and run-to-run cycle time may be improved by applying forced convection to the outer column surface.<sup>27</sup> It is expected that the air will not substantially cool the column but will provide a stable environment in which the AxTG can operate.

Furthermore, the equilibration time due to temperature could be minimized by employing columns made of perfectly insulating materials. Equilibration time due to changes in flow may be minimized by employing very low pressure chromatography columns.

The AxTG system is well suited for on-line chromatography because of its relatively simple instrumentation and rapid run-to-run cycle time. It is of interest to apply the AxTG to novel stationary phases designed for high-speed separations. Such materials may include perfusion particles.<sup>28</sup> The AxTG may improve the performance of such stationary phases. Additional applications include using the AxTG as a way to desorb analytes from the surface of a chemical sensor. The technique is ideal for sensors constructed from thermally insulated materials.

## ACKNOWLEDGMENT

The authors thank J. W. Rogers and B. A. Finlayson for their helpful discussions on heat transfer and Brigitte Rosendall for her technical assistance in setting up the Fortran program. We also appreciate the financial support of the Center for Process Analytical Chemistry.

## APPENDIX

### Heat Transfer Processes for the AxTG-μLC System.

The design of an efficient AxTG system requires an understanding of the systems heat transfer processes. Heat is introduced into the system by passing the eluent through heated tubing. Heat transfer from a heated surface to a flowing liquid,  $q_{in}$ , is a function of the mobile phase density, specific heat and flow rate, the surface area of the heat exchange region, and the temperature difference between the heated surface and the fluid. For fluid flowing through a heated tube, the total heat transfer rate is described by

$$q_{in} = \rho \pi d u C_{mp} (T_2 - T_1) \quad (A1)$$

where  $\rho$  is the density of the mobile phase,  $d$  is the diameter of the tubing being heated,  $z$  is the length of the heat exchange region,  $u$  is the average linear flow velocity of the mobile phase,  $C_{mp}$  is the specific heat of the mobile phase, and  $T_1$  and  $T_2$  are the temperatures of the mobile phase entering and exiting the heated section of tubing, respectively.<sup>29</sup> Furthermore, when the tubing has a fixed wall temperature, the rate of heat transfer to the fluid is described by

$$q_{in} = h_{in} \pi d z \left( \frac{(T_2 - T_1)}{\ln \left( \frac{T_w - T_1}{T_w - T_2} \right)} \right) \quad (A2)$$

where  $h_{in}$  is the average local heat transfer coefficient at the wall surface and  $T_w$  is the temperature of the tube wall. The heat transfer coefficient can be thought of as the slope of the fluids temperature distribution at the tubing surface. It is defined as

$$h_{in} = \frac{(N_{nu} k_{mp})}{d} \quad (A3)$$

where  $N_{nu}$  is the dimensionless heat transfer coefficient, or the Nusselt number, and  $k_{mp}$  is the thermal conductivity of the mobile phase. An empirical correlation defines the Nusselt number in the case of laminar flow in a circular tube with

(27) Incropera, F. P.; DeWitt, D. P. *Fundamentals of Heat Transfer*; John Wiley: New York, 1981; Chapter 9.

(28) Afeyan, N. B.; Regnier, F. E.; et al. *J. Chromatogr.* **1990**, 519, 1–29.

(29) Giedt, W. H. *Principles of Engineering Heat Transfer*; Van Nostrand: New York, 1957; Chapter 16.



constant wall temperature

$$N_{\text{nu}} = 3.65 + \frac{0.06 (d/z) \text{Re} \text{Pr}}{1 + 0.04 (d/z \text{Re} \text{Pr})^{2/3}} \quad (\text{A4})$$

where Re is the Reynolds number ( $\text{Re} = rud/\eta_{\text{mp}}$ ),  $\eta_{\text{mp}}$  is the viscosity of the mobile phase, and Pr is the Prandtl number ( $\text{Pr} = C_{\text{mp}}\eta_{\text{mp}}/k_{\text{mp}}$ ).<sup>30</sup> Though  $N_{\text{au}}$  has a mobile phase flow rate dependency, it is assumed constant when the heat exchange region has a small diameter to length ratio. Under these conditions, the Nusselt number for a cylindrical heat exchange region is 3.66. Thus, the rate of heat transfer into the fluid can be expressed as follows:

$$q_{\text{in}} = 3.66k_{\text{mp}}\pi z \left( \frac{T_2 - T_1}{\ln\left(\frac{T_w - T_1}{T_w - T_2}\right)} \right) \quad (\text{A5})$$

Using eqs A1 and A5, the temperature of the heated mobile phase,  $T_2$ , can be determined. Calculations indicate that for small volume systems there is little change in heat transfer to the mobile phase with flow rate. For example, if a 3 cm length of 0.005 in. i.d. tubing has a constant wall temperature of 150 °C, calculations indicate  $T_2$  for a 50:50 (v/v) water, acetonitrile eluent would be within 1 °C of the wall temperature for flow rates from 25 to 400  $\mu\text{L}/\text{min}$ .

As illustrated in Figure 1B, heat is lost to the column bed and through the column wall. The rate of heat loss to the column bed is described by

$$q_{\text{bed}} = h_{\text{bed}}\alpha V_b(T_f - T_b) \quad (\text{A6})$$

where  $h_{\text{bed}}$  is the heat transfer coefficient for the bed,  $\alpha$  is the particle surface area per bed volume,  $V_b$  is the packed bed volume,  $T_f$  is the temperature of the fluid, and  $T_b$  is the temperature of the bed.<sup>31</sup> Calculations for a C18 derivative poly(vinyl alcohol) microbore column, with 9- $\mu\text{m}$  particles, and an eluent of 50:50 (v/v) water/acetonitrile, indicate  $h_{\text{bed}}$  is on the order of  $10^4 \text{ W}/(\text{m}^2 \text{ K})$ . This means the particles and mobile phase rapidly equilibrate and there is minimal heat loss from the fluid to the bed. The rate of heat loss to the wall,  $q_{\text{wall}}$ , is defined as the sum of three heat transfer processes: heat transfer from the mobile phase to the inside

column wall, conduction through the column wall, and heat transfer from the column wall to the ambient air. The expression for convective heat lost to the column wall is of the same form as above

$$q_{\text{wall}} = U\pi D_i L(T_0 - T_{\text{rt}}) \quad (\text{A7})$$

where  $U$  is the overall heat transfer coefficient,  $D_i$  is the inside diameter of the column,  $L$  is the length of the column,  $T_0$  is the temperature at the center of the column, and  $T_{\text{rt}}$  is the ambient room temperature. The overall heat transfer coefficient can be expressed as

$$\frac{1}{U} = \pi D_i L \left( \frac{1}{h_w \pi D_i L} + \frac{\ln(D_i/D_0)}{2\pi k_{\text{wall}} L} + \frac{1}{h_0 \pi D_0 L} \right) \quad (\text{A8})$$

where  $h_w$  is the heat transfer coefficient for transfer from the mobile phase to the wall,  $k_{\text{wall}}$  is the thermal conductivity of the column wall,  $D_0$  is the external diameter of the column, and  $h_0$  is the heat transfer coefficient for heat transferred from the column wall to the ambient air.<sup>27</sup> The heat transfer coefficient for heat transfer between the mobile phase and the interior column wall,  $h_w$ , is defined as

$$h_w = \frac{k_{\text{mp}}}{d_p} 0.17 \left( \frac{\rho_{\text{mp}} u d_p}{\eta_{\text{mp}}} \right)^{0.79} \left( \frac{C_{\text{mp}} \eta_{\text{mp}}}{0.7 k_{\text{mp}}} \right)^{0.38} \quad (\text{A9})$$

where  $d_p$  is the particle diameter.<sup>32</sup> The heat transfer coefficient for heat transfer from the outer wall to ambient air,  $h_0$ , is defined as

$$h_0 = \frac{k_{\text{air}}}{D_0} 1.02 \left( \frac{g\beta(T_0 - T_{\text{rt}})D_0^3}{\nu \alpha} \right)^{0.148} \quad (\text{A10})$$

where  $k_{\text{air}}$  is the thermal conductivity of air,  $g$  is the force of gravity,  $\beta$  is the volumetric thermal expansion coefficient of air,  $\nu$  is the kinematic viscosity of air, and  $\alpha$  is the thermal diffusivity of air.<sup>27</sup> Calculations indicate  $h_0 \ll h_w$ ; thus it is convective heat transfer from the column wall to the ambient air that regulates the heat loss from the column. Heat loss by conduction through the column wall becomes significant as column outer diameter is increased.

RECEIVED for review January 4, 1993. Accepted June 29, 1993.\*

(30) Giedt, W. H. *Principles of Engineering Heat Transfer*; Van Nostrand: New York, 1957; Chapter 7.

(31) Bird, R. B.; Stewart, W. E.; Lightfoot, E. N. *Transport Phenomena*; John Wiley: New York, 1960; Chapter 13.

(32) Li, C.; Finlayson, B. A. *Chem. Eng. Sci.* 1977, 32, 1055-1066.

\* Abstract published in *Advance ACS Abstracts*, August 15, 1993.

# Affinity of Antifluorescein Antibodies Encapsulated within a Transparent Sol-Gel Glass

Run Wang, Upvan Narang, Paras N. Prasad,\* and Frank V. Bright\*

Acheson Hall, Department of Chemistry and Photonics Research Laboratory, State University of New York at Buffalo, Buffalo, New York 14214

Low temperature processed, porous sol-gel glasses represent a new class of materials for immobilization of biomolecules. The ability to form these materials into films, monoliths, and fibers to produce high-purity, porous glasses and the fact that they are optically transparent and chemically inert make them an intriguing platform for the development of chemical biosensors. In this paper, we report on the first attempt to encapsulate an intact antibody in a sol-gel glass matrix. Specifically, we present results on the affinity of sol-gel-encapsulated polyclonal antifluorescein. The results demonstrate that the sol-gel-encapsulated antibody retains an affinity for fluorescein; the affinity constant ( $K_f$ ) for antibody-hapten complex is on the order of  $10^7 \text{ M}^{-1}$ . The encapsulation process decreases  $K_f$  by about 2 orders of magnitude compared to the native system in buffer solution. The effect of aging and drying on the  $K_f$  for sol-gel-encapsulated antifluorescein is reported. Finally, we demonstrate that the intact antibody affinity can be maintained using simple storage protocols.

## INTRODUCTION

The selectivity of antibodies has been widely used for the development of antibody-based biosensors.<sup>1-6</sup> In these schemes, an immobilized antibody (or fragment) serves to recognize selectively the target analyte, and the binding process leads to an optical, mass, or electrochemical response related to the concentration of analyte in the sample.<sup>1-7</sup>

Of course, one must recognize that there are many steps associated with the actual development of any real antibody-based biosensor.<sup>1-7</sup> For example, one initially selects an appropriate target analyte-antibody pair and then "immobilizes" the antibody<sup>7</sup> such that it retains its affinity and is stable over time. Thus, protein immobilization technology represents one of the key aspects in biosensor development.<sup>1-7</sup> The most common methods of immobilization involve non-

covalent (entrapment and adsorption) or covalent schemes.<sup>8</sup> However, these immobilization procedures can be nontrivial and the immobilized antibodies are often unstable or lose a significant portion of their affinity with time.<sup>8,9</sup> Therefore, it should be obvious that biosensor development is limited somewhat by the lack of a simple, generic immobilization protocol. As a result, a simple (ideally one-step) method to immobilize and stabilize active antibodies such that they can be located at sensor or transducer interfaces would offer many advantages.

Recently, ambient condition sol-gel methods have yielded a new way to immobilize (i.e., encapsulate) proteins within porous, optically transparent glasses.<sup>10-15</sup> Because of the mild conditions associated with the sol-gel glass processing, encapsulated biomolecules have shown some degree of function/activity.<sup>10-15</sup> This approach is unique compared to the conventional methods involving adsorption on glass surfaces, entrapment in polymer matrices, or impregnation of porous glass powders<sup>9</sup> because encapsulation is based on the growing of siloxane polymer chains around the biomolecule within an inorganic oxide network. These encapsulated biomolecules do not leach from the matrix even under harsh washing conditions.<sup>11</sup> Further, because of the porous nature of the sol-gel network, a certain subpopulation remains accessible and can react with external chemical species (e.g., analytes). In addition, one can, in principle, control the mean pore size within the sol-gel matrix<sup>16</sup> and use this to improve selectivity further.

There are an increasing number of reports on the encapsulation of organic molecular and biomolecules within sol-gel glasses.<sup>10-15</sup> For example, *o*-phenanthroline has been doped into a porous sol-gel glass and used for the quantification of  $\text{Fe}^{2+}$  in water.<sup>17</sup> Detection limits were reported to be 100 ppt. The enzyme alkaline phosphatase was reported to retain its activity for 2 months at room temperature when encapsulated in a hydrated sol-gel glass.<sup>14</sup> Copper-zinc superoxide dismutase encapsulated in a porous silica glass matrix under mild conditions exhibits the characteristic reactivities and

\* Authors to whom correspondence should be sent.

(1) Janata, J. *Principles of Chemical Sensors*; Plenum Press: New York, 1989; pp 241-283.

(2) *Fiber Optic Chemical Sensors and Biosensors*; Wolfbeis, O. S., Ed.; CRC Press: Boca Raton, FL, 1991; Vols. I and II.

(3) Wise, D. L.; Wingard, C. B., Jr. *Biosensors with Fiber Optics*; Humana Press: Clifton, NJ, 1991.

(4) Tromberg, B. J.; Sepaniak, M. J.; Vo-Dinh, T.; Griffin, G. D. *Anal. Chem.* 1987, 59, 1226-1230.

(5) Bright, F. V.; Betts, T. A.; Litwiler, K. S. *Anal. Chem.* 1990, 62, 1065-1069.

(6) Bright, F. V.; Litwiler, K. S.; Vargo, T. G.; Gardella, J. A., Jr. *Anal. Chim. Acta* 1992, 262, 323-330.

(7) Thompson, M.; Krull, U. J. *Anal. Chem.* 1991, 63 (7), 393A-405A.

(8) Taylor, R. F. *Protein Immobilization: Fundamentals and Applications*; Marcel Dekker, Inc.: New York, 1991; Chapter 8, pp 263-303.

(9) Weetall, H. H. *Immobilized Enzymes, Antigens, Antibodies, and Peptides: Preparation and Characterization*; Marcel Dekker, Inc.: New York, 1975; Chapter 6, pp 246-292, and Chapter 8, pp 419-497.

(10) Ellerby, L. M.; Nishida, C. R.; Nishida, F.; Yamanaka, S. A.; Dunn, B.; Valentine, J. S.; Zink, J. I. *Science* 1992, 225, 1113-1115.

(11) Shtelzer, S.; Rappoport, S.; Avnir, D.; Ottolenghi, M.; Braun, S. *Biotechnol. Appl. Biochem.* 1992, 15, 227-235.

(12) Wu, S.; Ellerby, L. M.; Cohen, J. S.; Dunn, B.; El-Sayed, A.; Valentine, J. S.; Zink, J. I. *Chem. Mater.* 1993, 5, 115-120.

(13) Tatsu, Y.; Yamashita, K.; Yamaguchi, M.; Yamamura, S.; Yamamoto, H.; Yoshikawa, S. *Chem. Lett.* 1992, 11, 1615-1618.

(14) Braun, S.; Rappoport, S.; Zusman, R.; Avnir, D.; Ottolenghi, M. *Mater. Lett.* 1990, 10, 1-5.

(15) Yamanaka, S. A.; Nishida, F.; Ellerby, L. M.; Nishida, C. R.; Dunn, B.; Valentine, J. S.; Zink, J. I. *Chem. Mater.* 1992, 4, 495-497.

(16) Brinker, C. J.; Smith, D. M.; Deshpande, R.; Davis, P. M.; Hietala, S.; Frye, G. C.; Ashley, C. S.; Assink, R. A. *Catal. Today* 1992, 14, 155-163.

(17) Lev, O.; Kuyavskaya, B. I.; Gigozin, I.; Ottolenghi, M.; Avnir, D. *Fresenius J. Anal. Chem.* 1992, 343, 370-372.

spectroscopic properties observed in aqueous solution.<sup>10</sup> We previously reported that sol-gel-processed films doped with the artificial receptor dansylglycine- $\beta$ -cyclodextrin can be used as a reversible sensor platform for quantification of borneol.<sup>18</sup> Unfortunately, in spite of all this success and apparent suitability of the sol-gel method, there is a lack of quantitative information on sol-gel-encapsulated biomolecules as a function of aging, drying, and storage conditions.<sup>10-15</sup>

In this paper, we report (1) the first attempt to encapsulate intact antibodies in a sol-gel glass, (2) the affinity of the sol-gel-encapsulated antibody for its hapten, and (3) the effects of sol-gel aging, drying, and storage time on the affinity of the encapsulated antibody. Antifluorescein was used as our model antibody because (1) it is available commercially, (2) the affinity of antifluorescein to fluorescein has been studied extensively in aqueous solution,<sup>19-21</sup> (3) the fluorescence (temporal and spectral) characteristics of fluorescein change upon binding to antifluorescein, and (4) the excitation and emission are in the visible spectral region.

## EXPERIMENTAL SECTION

**Materials.** The following chemicals were used: tetramethoxysilane (TMOS) (Aldrich Chemical Co.); HCl, Na<sub>2</sub>HPO<sub>4</sub>, NaH<sub>2</sub>PO<sub>4</sub>·2H<sub>2</sub>O (Fisher Scientific Co.); fluorescein, polyclonal antifluorescein antibodies (Molecular Probes, Inc.); and ethanol (Quantum Chemical Corp.). All reagents were used as received without further purification. All aqueous solutions were prepared in doubly distilled-deionized water. Unless otherwise noted, freshly made samples were used for all steady-state and dynamic fluorescence measurements.

**Quantification of Antibody Binding Sites.** To determine the analytical concentration of antibody, a known concentration of fluorescein in 0.20 M phosphate buffer (pH 8.0) was titrated with the antifluorescein stock solution. The observed fluorescence intensity decreases as antifluorescein is added and plateaus after all available fluorescein becomes antibody bound. It is known that a single antifluorescein antibody possesses two identical binding sites, and each can accommodate a single fluorescein molecule.<sup>22</sup> Therefore, from the equivalence point, where the number of antibody binding sites equals the total amount of fluorescein in the solution, one is able to determine the concentration of the antibody binding sites.<sup>22</sup> The recovered concentration of the binding sites for our antifluorescein (as prepared following Molecular Probes' recommendations) is  $5.6 \pm 0.1 \mu\text{M}$  ( $2.8 \pm 0.1 \mu\text{M}$  of active antifluorescein antibody).

**Encapsulation of Antifluorescein in Sol-Gel Glass.** The silica sol was prepared following the procedure described by Ellerby et al.<sup>10</sup> Briefly, 7.00 g of TMOS, 1.50 g of deionized water, and 0.40 g of 0.04 M HCl were mixed with stirring and then sonicated for 30 min to obtain a silica sol. In a disposable polystyrene cuvette, a 0.5-mL aliquot of the silica sol was rapidly mixed with a known (0–40  $\mu\text{L}$ ) amount of the antifluorescein stock solution (2.8  $\mu\text{M}$ ) containing 0 or 90 nM fluorescein. After mixing, 0.5 mL of phosphate buffer (0.02 M, pH 8.0) was immediately added to the cuvette and gelation occurred within 2 min. (The total time the antibody was kept in the unbuffered solutions was less than 10 s and the final pH was very near 8.) The antibody-doped sol-gel glass samples were then stored (*vide infra*) at 4 °C for all subsequent studies.

**Fluorescence Measurements.** All steady-state fluorescence measurements were performed with an SLM 48000 MHF spectrofluorometer using a Xe arc lamp as the excitation source. All emission spectra were background subtracted.

Time-resolved decay data were acquired in the frequency domain using an SLM 48000 MHF multifrequency phase-

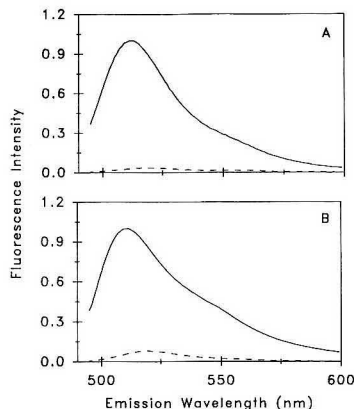


**Figure 1.** Emission spectra of fluorescein without (—) or with (---) antifluorescein: (panel A) in solution; (panel B) in a sol-gel glass matrix.

modulation fluorometer. An argon ion laser (Coherent, Model Innova 90-6) operating at 476 nm was used as the excitation source. A  $480 \pm 10$  nm band-pass filter (Oriel) was used to eliminate extraneous plasma discharge. Emission was observed through a 495-nm long-pass filter (Oriel). Magic angle polarization was used for all sample lifetime measurements.<sup>23</sup> Fluorescein in 0.01 M NaOH was used as the reference lifetime standard. Its lifetime was assigned a value of 4.00 ns. Inert gas was not used to eliminate molecular oxygen. The multifrequency data were acquired as described elsewhere.<sup>24,25</sup> For all experiments, the Pockels cell modulator was operated at a repetition rate of 5 MHz. Typically, data were acquired for 60 s from 5 to 125 MHz (25 frequencies) and analyzed using a global analysis approach.<sup>26</sup> To improve the precision and accuracy of the recovered kinetic parameters, multiple sets of frequency-domain data were linked<sup>26</sup> (when possible) together. The average experimental phase variances were used for minimization of the  $\chi^2$  function.<sup>25,26</sup>

## RESULTS AND DISCUSSION

**Affinity of Encapsulated Antifluorescein for Fluorescein.** Fluorescein is one of the most extensively characterized and widely used fluorescent probes.<sup>27</sup> In basic media, it exhibits a quantum yield close to unity and is strongly fluorescent. The antifluorescein antibody has a very high affinity for fluorescein in aqueous solution,<sup>19-21</sup> and when fluorescein becomes antibody bound, its fluorescence decreases and the emission spectrum red shifts. The decrease in fluorescence and red shift can be used directly to quantify the antifluorescein affinity.<sup>19-21</sup>

The primary issue for the sol-gel-entrapped antifluorescein is whether it retains any affinity for fluorescein. Figure 1 presents the emission spectra of fluorescein with (---) and without (—) antifluorescein in pH 8.0 buffer solution (panel A) and when encapsulated in a transparent sol-gel glass monolith (panel B). Several points are readily apparent and merit additional discussion. First, as fluorescein binds to antifluorescein in solution, the emission is red shifted and the fluorescence decreases significantly (Figure 1A).<sup>19-21</sup> Second, an identical trend is observed for the sol-gel-

(18) Narang, U.; Dunbar, R. A.; Bright, F. V.; Prasad, P. N. *Appl. Spectrosc.*, in press.

(19) Watt, R. M.; Herron, J. N.; Voss, E. W., Jr. *Mol. Immunol.* **1980**, *17*, 1237–1243.

(20) Kranz, D. M.; Herron, J. N.; Giannis, D. E.; Voss, E. W., Jr. *J. Biol. Chem.* **1981**, *256*, 4433–4438.

(21) Reinitz, D. M.; Voss, E. W., Jr. *J. Immunol.* **1985**, *135*, 3365–3371.

(22) Blake, C. C. *Nature* **1975**, *253*, 158.

(23) Spencer, R. D.; Weber, G. *J. Chem. Phys.* **1970**, *52*, 1654–1663.

(24) Feddersen, B. A.; Piston, D. W.; Gratton, E. *Rev. Sci. Instrum.* **1989**, *60*, 2929–2936.

(25) Bright, F. V.; Betts, T. A.; Litwiler, K. S. *CRC Crit. Rev. Anal. Chem.* **1990**, *21*, 389–405.

(26) Beechem, J. M.; Gratton, E. *Proc. SPIE* **1988**, *909*, 70–81.

(27) Haugland, R. G. *Handbook of Fluorescence Probes and Research Chemicals*; Molecular Probes, Inc.: Eugene, OR, 1992; pp 81–88.

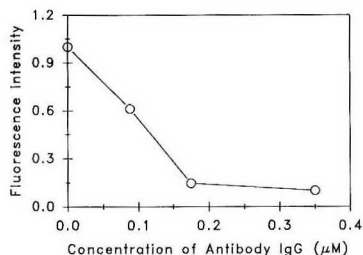


**Figure 2.** Observed fluorescence from sol-gels doped with fluorescein (90 nM) and antifluorescein as a function of added antifluorescein.

encapsulated system (Figure 1B), indicating that the anti-fluorescein-fluorescein complex still forms within the porous sol-gel glass matrix. Finally, the emission spectra for the native and sol-gel-encapsulated systems are very similar. This is consistent with sol-gel entrapment not affecting the basic fluorescein photophysics (*vide infra*).

The observed fluorescence from fluorescein decreases as the concentration of antifluorescein encapsulated in the sol-gel glass matrix increases and plateaus once all the fluorescein becomes antibody bound (Figure 2). When all the fluorescein molecules are bound to antifluorescein, the fluorescence intensity is about 10% that of free fluorescein; it is quenched by about 90%. These results are very similar to those seen in solution.<sup>19-21</sup>

Confident that the antifluorescein retained a portion of its affinity, we next questioned if fluorescein could diffuse into the porous sol-gel matrix and bind selectively to the encapsulated antifluorescein. To address this issue, we prepared two identical sol-gel monoliths with and without antifluorescein and immersed these (overnight) in aqueous solutions containing the same concentration of fluorescein (90 nM). After incubation we acquired the emission spectra for both monoliths. We noted a significant decrease in intensity and red shift in the fluorescein emission spectrum for the sample that was doped with antibody. For all practical purposes these spectra are indistinguishable from those presented in Figure 1B, demonstrating that fluorescein can diffuse into the sol-gel network and bind selectively to the sol-gel-encapsulated antifluorescein.

On the basis of the previous experiments we set out to determine how sol-gel aging, drying, and storage conditions affected the encapsulated antifluorescein antibody affinity. For the remaining discussion, the term "aging" reflects change(s) in structure and properties of the sol-gel matrix after gelation.<sup>28</sup> "Drying" denotes the removal of solvent molecules from the sol-gel network. However, because aging and drying normally occur simultaneously and are accompanied by shrinkage of the gel,<sup>28</sup> they are somewhat difficult to decouple. In an effort to understand these effects we prepared a set of sol-gel samples, doped with identical amounts of fluorescein with or without antifluorescein, and stored them desiccated at 4 °C. These samples were removed from the desiccator every few days and their emission spectra recorded. Under our experimental conditions, fresh sol-gel samples weighed  $1.14 \pm 0.02$  g and those stored for 3 weeks weighed  $0.32 \pm 0.04$  g.

Figure 3 illustrates the effects of storage conditions and storage time on the fluorescein emission. Panels A and B of Figure 3 show that the fluorescein fluorescence decreases by about 90% due to antifluorescein complexation for 1-week-

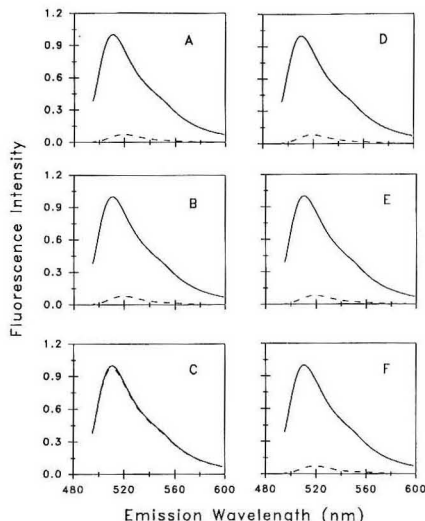


**Figure 3.** Effects of storage conditions and storage time on the emission spectra of 90 nM fluorescein without (—) or with (---) antifluorescein within a sol-gel matrix. Panels A, B, and C show the spectra for monoliths that were kept desiccated (4 °C) for 2, 3, and 4 weeks, respectively. Panels D, E, and F show the spectra for monoliths on aging identically prepared samples that were stored in water immediately on gelation after 2, 3, and 5 weeks, respectively.

old (panel A) and 3-week-old (panel B) samples. This trend is not seen when the sol-gel-encapsulated antifluorescein samples were stored for 4 weeks (Figure 3C), indicating that the antifluorescein-fluorescein complex is completely disrupted after 4 weeks of storage. Also, it is important to recognize that after 3 weeks of desiccated storage, all water has been removed from our sol-gel monoliths.<sup>10,28</sup> Thus, there are two possible explanations for the decrease in antifluorescein-fluorescein binding: (1) antifluorescein-fluorescein binding requires the presence of water and/or (2) drying denatures the sol-gel-encapsulated antifluorescein to the point that its affinity for fluorescein is lost.

To discriminate between these possible scenarios, we carried out a set of simple experiments. First, we gradually added water (pH 8.0 buffer) to a sol-gel monolith that had been stored desiccated for 4 weeks. The water was added slowly to prevent the monolith from cracking. The recovered fluorescence spectra before and after "rehydration" were effectively identical to that shown in Figure 3C. Therefore, rehydration of the dried sol-gel does not lead to recovery of the antifluorescein-fluorescein binding. This suggests that (1) shrinkage of sol-gel "squeezes" antifluorescein to the point that its conformation is altered or its binding site shielded and it cannot bind fluorescein and (2) conformational changes of sol-gel-encapsulated antifluorescein are apparently irreversible.

In an effort to overcome this storage problem we investigated the effect of storing the samples (after gelation) in water. That is, a series of samples were prepared as described above, and immediately after gelation was complete, they were stored in water at 4 °C. Panels D-F of Figure 3 summarize the results from these samples and show that the sol-gel-encapsulated antifluorescein molecules remained active for at least 5 weeks. On the basis of these results we can conclude that sol-gel-entrapped antifluorescein retains its

(28) Brinker, C. J.; Scherer, G. W. *Sol-Gel Science, The Physics and Chemistry of Sol-Gel Processing*; Academic Press, Inc.: San Diego, 1990; pp 1-18.

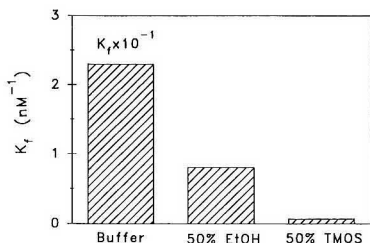
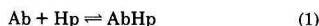


**Figure 4.** Recovered affinity constant ( $K_f$ ) for anti-fluorescein complexation with fluorescein in buffer, in 50% ethanol–buffer mixture, or in 50% TMOS–buffer mixture. Buffer is 0.1 M phosphate (pH 8.0).

affinity for fluorescein if stored in water after the gelation step.

**Effects of Medium and Storage Conditions on Anti-fluorescein Affinity Constant.** The anti-fluorescein antibody has two identical binding sites.<sup>22</sup> Therefore, the binding affinity of anti-fluorescein to fluorescein is described by the formation constant ( $K_f$ ):



$$K_f = \frac{[\text{AbHp}]}{[\text{Ab}][\text{Hp}]} \quad (2)$$

where  $[\text{Ab}]$  and  $[\text{Hp}]$  denote the equilibrium concentrations of antibody binding sites and free fluorescein, respectively.  $[\text{AbHp}]$  represents the equilibrium concentration of the anti-fluorescein–fluorescein complex. The equilibrium concentration for each of the species in the antibody–hapten complexation (eq 1) can be calculated using the following expressions:

$$[\text{AbHp}] = \frac{\Delta I}{\Delta I_{\max}} [\text{Hp}]_0 \quad (3)$$

$$[\text{Ab}] = [\text{Ab}]_0 - [\text{AbHp}] \quad (4)$$

$$[\text{Hp}] = [\text{Hp}]_0 - [\text{AbHp}] \quad (5)$$

in which the subscript zero denotes the analytical concentrations and  $\Delta I$  is the observed intensity decrease associated with the complexation of fluorescein to anti-fluorescein. The formation constant can be calculated using eqs 2–5.

We determined  $K_f$  for the anti-fluorescein–fluorescein complex in buffer, in 50% ethanol plus buffer, and in a TMOS–buffer mixture. (In all cases, the affinity constant was determined immediately after antibody was added to the solutions and the buffer was 0.1 M phosphate at pH 8.0.) Ethanol was chosen because it has been used in many sol-gel processing schemes<sup>28</sup> and we were curious how it would affect the antibody affinity. Figure 4 summarizes the results of these experiments and shows that aqueous solutions of ethanol or TMOS lead to a significant decrease in the anti-fluorescein affinity. This was one of the main reasons behind our choosing the modified<sup>10</sup> (no alcohol) sol-gel process for anti-fluorescein encapsulation.

Figure 5 shows the effect of aging time and storage conditions on the  $K_f$  of sol-gel-encapsulated anti-fluorescein. Results for samples stored in a desiccator (○) and those allowed to gel and then kept in water (■) are shown. Several points merit further discussion. First, the initial  $K_f$  for anti-fluorescein encapsulated within the TMOS sol-gel matrix is on the order of  $7 \times 10^7 \text{ M}^{-1}$ . The native antibody (Figure 4) in buffer is on the order of  $2.3 \times 10^{10} \text{ M}^{-1}$ . Thus, there is a loss in affinity (2 orders of magnitude) on encapsulation in the sol-gel matrix. Second, during the first 2 weeks, there is no significant change or difference in the  $K_f$  for samples stored

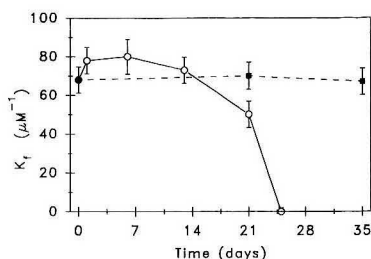


**Figure 5.** Recovered affinity constant ( $K_f$ ) for sol-gel-encapsulated anti-fluorescein as a function of storage time: (○) samples stored at 4 °C and kept in a desiccator; (■) samples stored in water at 4 °C immediately on gelation.

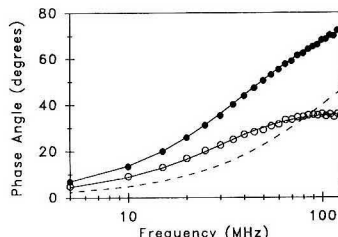


**Figure 6.** Multifrequency phase trace for fluorescein (●) and anti-fluorescein plus fluorescein (○) encapsulated in a sol-gel matrix. The solid lines denote the best fits to the experimental data. The experimental data without antibody are best described by a single-exponential decay law (—), whereas the samples with antibody are best modeled by a double-exponential decay law (---). The dashed curve is the best single-exponential fit to the experimental data with antibody (---).

desiccated or kept wet. Third, after 2 weeks,  $K_f$  decreases rapidly for the desiccated samples, and after 4 weeks the affinity is effectively zero. That is, after prolonged storage under dry conditions the encapsulated antibody no longer binds fluorescein. Finally,  $K_f$  for the samples that were allowed to gel and then kept stored in water remained constant for up to 5 weeks.

**Time-Resolved Fluorescence.** Steady-state fluorescence provides information on the average emission from all fluorescing species in the system. Unfortunately, it cannot generally provide insight into the origin of the emitting species. To obtain more information on the anti-fluorescein–fluorescein complexation and fluorescein speciation, we carried out a series of multifrequency fluorescence experiments.<sup>25</sup>

Figure 6 shows a typical set of multifrequency phase angle data for sol-gel-encapsulated fluorescein (●) and anti-fluorescein plus fluorescein (○) for a 3-week-old sample (desiccated). (Phase data alone are reported because of the difficulties associated with making accurate modulation measurements from irregularly shaped solid samples when liquids are used as the reference lifetime standards.<sup>29</sup>) A single-exponential decay law best models the fluorescein data (—), and the recovered lifetime is 3.9 ns. In contrast, a single-exponential decay law (---) cannot describe the sample containing anti-fluorescein and fluorescein; it is best modeled with a double-exponential decay law (—). These results argue that there are two subpopulations contributing to the total fluorescence. We also note that the recovered decay times are very similar ( $\pm 0.07 \text{ ns}$ ) to those recovered for free

(29) Litwiler, K. S. Ph.D. Thesis, State University of New York at Buffalo, Buffalo, NY, 1991, p 50.



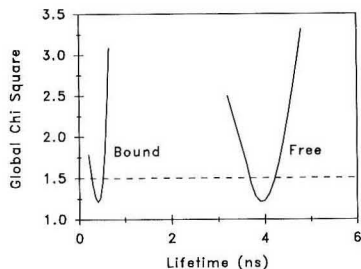


**Figure 7.** Recovered  $\chi^2$  surfaces for the anti fluorescein–fluorescein data in Figure 6. The horizontal dashed line indicates the 2 standard deviation (95%) confidence level.

fluorescein and anti fluorescein-bound fluorescein in solution,<sup>30</sup> confirming that the sol-gel matrix does not alter the fluorescein photophysics.

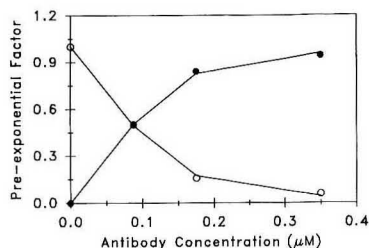
Prior to beginning a detailed interpretation of these multifrequency data, it is important to determine the precision in the recovered kinetic parameters. To address this issue, confidence interval analysis was performed. In this approach, one fixes a particular decay parameter (e.g.,  $\tau_1$ ) at a predetermined value, refits the entire data set (adjusting all floating parameters), and calculates a new  $\chi^2$ . This process is repeated over a range of  $\tau_1$  values and the  $\chi^2$  vs  $\tau_1$  yields a convenient measure of the imprecision in  $\tau_1$ . Further, because one investigates each parameter separately, any correlation between terms is compensated.

Figure 7 presents the confidence interval results ( $\chi^2$  surfaces) for the anti fluorescein–fluorescein data presented in Figure 6. The dashed horizontal line represents the 2 standard deviation limit, and its position indicates the imprecision (measured from the points where the curves intersect the dashed line) in the parameters. These results show that the decay times are easily resolved from one another and are moderately precise. They also show that one of the decay times is near 3.9 ns, corresponding well to free fluorescein.<sup>30</sup> The other, shorter-lived species represents anti fluorescein-bound fluorescein (0.571 vs 0.501 ns). These results are consistent with the complexation equilibria represented by eq 1.

Using the recovered time-resolved parameters, one can determine  $K_f$  for the sol-gel-entrapped anti fluorescein–fluorescein complex. In this approach, the preexponential factors ( $\alpha_i$ ) are used as a direct measure of the equilibrium distribution of free and anti fluorescein-bound fluorescein.<sup>31</sup> In the current case, the preexponential factor ( $\alpha_{free}$ ) for the longer lifetime component represents the mole fraction of free fluorescein, and  $\alpha_{bound}$  ( $=1 - \alpha_{free}$ ) denotes the mole fraction of anti fluorescein-bound fluorescein. Therefore, based on the time-resolved data, the affinity constant can be written

$$K_f = \frac{\alpha_{bound}/\alpha_{free}}{[Ab]_0 - \alpha_{bound}[Hp]_0} \quad (6)$$

Figure 8 shows the recovered preexponential factors ( $\alpha$ 's) versus the analytical concentration of anti fluorescein within the sol-gel matrix. We note that the amount of fluorescein bound to anti fluorescein (●) increases as we increase the



**Figure 8.** Recovered preexponential factor for the short-lived (●) and long-lived (○) fluorescein species as a function of added anti fluorescein. The solid traces are the calculated preexponential factors predicted based on a simple equilibrium (eq 1) and a  $K_f$  of 56  $\mu\text{M}$ .

amount of antibody, and a concomitant decrease in the amount of free fluorescein (○) is observed. This is again consistent with a simple complexation scheme (eq 1). By using the recovered preexponential factors for free and antibody-bound fluorescein, an affinity constant of  $56 \pm 4 \mu\text{M}^{-1}$  was recovered for a 3-week-old preparation of anti fluorescein entrapped in a sol-gel matrix. (The solid line in Figure 8 is the fit of the data to a  $K_f$  of 56  $\mu\text{M}^{-1}$ .) This  $K_f$  value is consistent with the value recovered from the steady-state measurements ( $51 \pm 7 \mu\text{M}^{-1}$ ) (Figure 5).

## CONCLUSIONS

In this report, steady-state fluorescence spectroscopy and time-resolved fluorescence spectroscopy were used to investigate the affinity of sol-gel-encapsulated anti fluorescein. Several points should be highlighted. (1) The form of the anti fluorescein–fluorescein equilibrium remains unchanged upon encapsulation in a sol-gel matrix. (2) Storage time and conditions affect the affinity of the encapsulated antibody significantly. (3) The affinity of the sol-gel-encapsulated anti fluorescein antibody is retained if the samples are allowed to first gel and are then stored in water at 4 °C. (4) In the best case, encapsulation leads to a 2 order of magnitude decrease in affinity; however,  $K_f$  remains well over  $10^7 \text{ M}^{-1}$ .

The ability to easily encapsulate and retain the affinity of antibodies within a sol-gel matrix should find many applications in biosensor technology. We are currently focusing on the effects of pore structure (size)<sup>16,28</sup> and other physicochemical aspects of the sol-gel matrix on the behavior of encapsulated antibodies.

## ACKNOWLEDGMENT

This work was generously supported by the National Science Foundation (Grant CHE-9300694) and by an SBIR subcontract (DOE Award No. DE-FG02-92ER81408) from Laser Photonics Technology, Inc. The work at the Photonics Research Laboratory was supported by the Office of Innovative Science and Technology of the Strategic Defense Initiative Organization and the Air Force Office of Scientific Research, Directorate of Chemistry and Materials Science, through Contract No. F49620-90-C-0053.

RECEIVED for review April 15, 1993. Accepted June 29, 1993.\*

(30) A separate set of experiments using native anti fluorescein and fluorescein in buffer (0.1 M phosphate (pH 8.0)) recovered lifetimes of 3.92 (free fluorescein) and 0.501 ns (antibody-bound fluorescein).

(31) This simple expression holds only if the molar absorptivities of the free and bound forms of fluorescein do not change significantly upon binding. Under our illumination conditions this is the case.

\* Abstract published in *Advance ACS Abstracts*, August 15, 1993.

# Engineering Protein Orientation at Surfaces To Control Macromolecular Recognition Events

Mark A. McLean, Patrick S. Stayton, and Stephen G. Sligar\*

Beckman Institute of Advanced Science and Technology, 405 North Mathews Street, Urbana, Illinois 61801

**In this report we demonstrate that heterologous protein-protein interactions can be controlled at an immobilization surface by genetically engineering an appropriately de novo designed attachment point on the protein surface.**

## INTRODUCTION

Surface-immobilized proteins have had a great impact in many fields of basic research and in many industrial and medical technologies.<sup>1,2</sup> Most research in this area has been directed toward controlling the overall activity of the hybrid biomaterials, for example, through reversibly affecting the surrounding matrix properties<sup>3</sup> or by immobilizing related proteins in close proximity to provide multistep enzyme processing.<sup>4</sup> In principle, a great leap in biotechnological potential would be realized if the immobilization process itself specified self-assembly and regulated function, but very little research has been aimed at selectively controlling molecular recognition events at the protein-substrate interface.<sup>5,6</sup> Because many molecular recognition processes are controlled through specificity in complementary reactive surfaces, controlling the orientation of immobilized proteins is perhaps the most straightforward means toward manipulating assembly and function in this manner. We have recently demonstrated that proteins in monolayer assemblies can be differentially oriented on planar surfaces by genetically engineering unique attachment sites,<sup>7</sup> and here we show that protein-protein interactions can be controlled at an immobilization interface by similarly controlling the orientation of the protein binding surface. Protein-protein interactions are crucial to important biological and biotechnological processes such as antibody-based diagnostics, affinity chromatography, electron transfer, and vectoral proton transfer. Manipulating macromolecular specificity at interfaces is thus an important step toward controlling function and self-assembly in a wide variety of immobilized protein systems.

One of the best studied protein-protein complexes is the cytochrome *b<sub>5</sub>*/cytochrome *c* electron-transfer pair. Extensive biochemical, biophysical, theoretical, and genetic investigations have provided a detailed understanding of the interaction surfaces for both cytochromes *b<sub>5</sub>* and *c*.<sup>8-12</sup> Computer

modeling studies generated from the isolated X-ray crystal structures first noted the striking electrostatic complementarity of charged amino acids surrounding the exposed heme edges of both proteins.<sup>13</sup> The basic tenants of the computer model have been largely confirmed through chemical modification and genetic engineering studies.<sup>14,15</sup> The complementary binding interface places the two heme edges in close proximity for fast electron transfer between the redox centers.<sup>16,17</sup>

Genetic engineering techniques have been utilized to independently place a unique thiol side chain at amino acid positions 65 and 8.<sup>18</sup> Position 65 was chosen to provide an attachment site close to the proposed cytochrome *b<sub>5</sub>*/cytochrome *c* binding interface, yet spatially distinct enough to prevent steric interference. In solution, labeling this site with the fluorophore acrylodan permits an independent measurement of the equilibrium constant,<sup>18</sup> which closely agrees with absorption difference titrations.<sup>19</sup> This finding, and a separate study utilizing the T65C mutant as a labeling site for a ruthenium redox center used to photoinitiate electron transfer from cytochrome *b<sub>5</sub>* to cytochrome *c*,<sup>17</sup> strongly support the hypothesis that labeling this position does not sterically inhibit complex formation. The T8C mutant positions the unique cysteine residue on the surface opposite the exposed heme edge, at a site diametrically opposite the binding interface. These two mutants have been used to build monolayer protein assemblies on functionalized glass substrates. Linear dichroism measurements of the prosthetic heme group orientation demonstrate that T65C and T8C are differentially oriented at the substrate interface.<sup>7</sup> These results suggested that designed attachment sites could be used to control the orientation of the cytochrome *b<sub>5</sub>* binding surface relative to a stationary support. Here we report the control of macromolecular recognition between cytochrome *b<sub>5</sub>* and cytochrome *c* through specific orientation on a chromatography support.

## MATERIALS AND METHODS

**Site-Directed Mutagenesis.** The cytochrome *b<sub>5</sub>* T8C and T65C mutations were generated as previously described<sup>18</sup> and

\* Address correspondence to this author.

(1) *Methods in Enzymology*; Mosbach, K., Ed.; Academic Press: New York, 1976; Vol. 44.

(2) Langer, R. *Science* 1990, 249, 1527.

(3) Hoffman, A. S. *MRS Bull.* 1991, 16, 42-46.

(4) Mosbach, K.; Mattiasson, B. In *Methods in Enzymology*; Mosbach, K., Ed.; Academic Press: New York, 1976; Vol. 44, pp 453-478.

(5) Whitesides, G. M.; Mathias, J. P.; Seto, C. T. *Science* 1991, 254, 1312-1319.

(6) Prime, K. L.; Whitesides, G. M. *Science* 1991, 252, 1164-1167.

(7) Stayton, P. S.; Olinger, J. M.; Bohn, P. W.; Sligar, S. G. *J. Am. Chem. Soc.* 1992, 114, 9298-9299.

(8) Rodgers, K. K.; Pochapsky, T. C.; Sligar, S. G. *Science* 1988, 240, 1657-1659.

(9) Ferguson-Miller, S.; Brautigan, D. L.; Margoliash, E. *J. Biol. Chem.* 1978, 253, 149-159.

(10) Dailey, H. A.; Strittmatter, P. *J. Biol. Chem.* 1979, 254, 5388-5396.

(11) Wendoloski, J. J.; Matthew, J. B.; Weber, P. C.; Salemme, F. R. *Science* 1987, 238, 794-797.

(12) Hazzard, J. T.; McLendon, G.; Cusanovich, M. A.; Das, G.; Sherman, F.; Tollin, G. *Biochemistry* 1988, 27, 4445-4451.

(13) Salemme, F. R. *J. Mol. Biol.* 1976, 102, 563-568.

(14) Kang, C. H.; Brautigan, D. L.; Osheroff, N.; Margoliash, E. *J. Biol. Chem.* 1978, 253, 6502-6510.

(15) Rodgers, K. K.; Sligar, S. G. *J. Mol. Biol.* 1991, 221, 1453-1460.

(16) McLendon, G.; Miller, J. R. *J. Am. Chem. Soc.* 1985, 107, 7811-7816.

(17) Willie, A.; Stayton, P. S.; Durham, B.; Sligar, S. G.; Millet, F. *Biochemistry* 1992, 31, 7237-7243.

(18) Stayton, P. S.; Fisher, M. T.; Sligar, S. G. *J. Biol. Chem.* 1988, 263, 13544-13548.

(19) Mauk, M. R.; Reid, L. S.; Mauk, A. G. *Biochemistry* 1982, 21, 1843-1846.

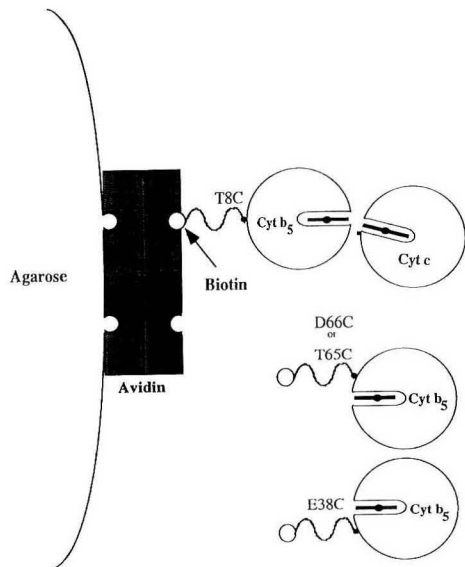


Figure 1. Schematic of cytochrome  $b_5$  immobilization system.

purified as described by von Bodman et al.<sup>19</sup> In addition to the T8C and T65C mutant proteins, a double mutant with attachment sites on either side of the heme edge was constructed (D66C/E38C) using a protocol slightly modified from the method of Sligar et al.<sup>21</sup> Briefly, two oligonucleotide primers encoding the position 66 mutation and the position 38 mutation were used to amplify the gene segment between the mutation sites. This product was then utilized as a primer with the universal sequencing primer to amplify the 3'-end of the mutated gene. Finally, this secondary product was used with the reverse sequencing primer to amplify the entire gene. This mutant, like T65C, places the attachment sites relatively close to, yet sterically distinct from, the binding interface. The double mutant has two free thiols for immobilization, although the percentage of protein linked at both sites is undetermined.

**Preparation of Cytochrome  $b_5$  Affinity Resin.** Specific sulfhydryl mutations, T8C, T65C, D66C/E38C, of cytochrome  $b_5$  were reduced for 10 min with a 1:1 ratio dithiothreitol in 100 mM NaPi, pH 7.8. The proteins were labeled by adding iodoacetyl-LC-biotin obtained from Pierce at a 2:1 ratio of biotin to protein. The reaction was allowed to proceed overnight. Excess biotin label was removed by passing the sample over a Sephadex G-25 column equilibrated in 100 mM NaPi, pH 7. Aliquots of the biotinylated sample(s) were slowly added to a slurry of avidin-Sepharose 6B resin obtained from Pierce. After washing extensively with buffer, the concentrations of the cytochrome  $b_5$  on the column were measured by taking the absorbance of a 10–20% slurry in a Hitachi 3800 spectrophotometer equipped with an integrating sphere. The slurry was stirred and a spectrum was taken before an appreciable amount of settling could occur. The concentration was determined by using an extinction coefficient of  $130 \text{ mM}^{-1}$  at 412 nm.<sup>20</sup> Since the active protein has the heme incorporated, we can take the 412-nm absorbance as a representation of the amount of active cytochrome  $b_5$  bound to the solid support. A schematic representation of the chromatographic supports that were constructed is shown in Figure 1.

(20) Beck von Bodman, S.; Schuler, M. A.; Jollie, D. R.; Sligar, S. G. *Proc. Natl. Acad. Sci. U.S.A.* **1986**, *83*, 9443–9447.

(21) Sligar, S. G.; Filipovic, D.; Stayton, P. S. In *Methods in Enzymology*; Waterman, M. R.; Johnson, E. F., Eds.; Academic Press: New York, 1992; Vol. 206, pp 31–49.

(22) Margoliash, E.; Frowhrt, N. *Biochem. J.* **1959**, *71*, 570–572.

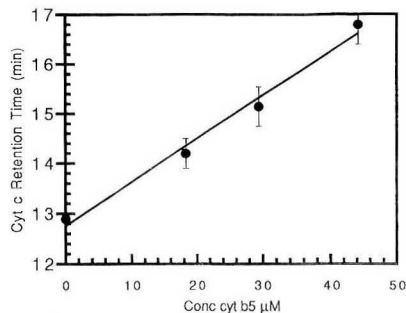


Figure 2. Cytochrome  $c$  column retention times as a function of cytochrome  $b_5$ -T8C concentration on the immobilized support.

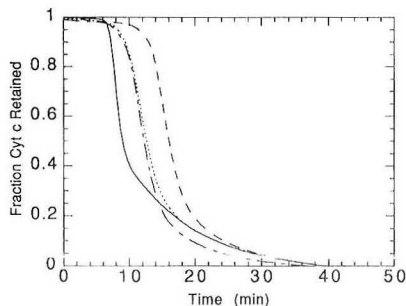


Figure 3. Orientation-specific equilibrium binding isotherms. Equilibrium binding isotherms were determined from the elution profiles generated with linear ionic strength gradients: (---) T8C, (- · -) T65C, (···) D66C/E38C, and (—) avidin control.

**Affinity Chromatography of Cytochrome  $c$ .** Horse heart cytochrome  $c$ , Type VI, obtained from Sigma was used without further purification. A 206  $\mu\text{M}$  solution of cytochrome  $c$  was prepared in 1 mM NaPi, pH 7.4. The affinity columns were packed into a Pharmacia HR/5 column in which the total volume was 0.8 mL. The column was connected to a Pharmacia FPLC pump system and equilibrated in 1 mM NaPi, pH 7.4, by passing seven column volumes through at 0.5 mL/min. A 50- $\mu\text{L}$  aliquot of the cytochrome  $c$  solution was loaded onto the column, and the column was washed with one column volume of buffer. A gradient was run from 1 mM NaPi, pH 7.4, to 1 mM NaPi/100 mM NaCl, pH 7.4, over a total volume of 30 mL with a flow rate of 0.5 mL/min. The elution of cytochrome  $c$  was monitored by the absorbance at 405 nm. The T8C cytochrome  $b_5$  concentration dependence was determined in order to correct for the differences in concentration between the columns containing the mutant cytochrome  $b_5$ . It is expected that there would be a linear relationship in the differences in retention times of cytochrome  $c$  vs cytochrome  $b_5$  concentration, and the slope of this line will be proportional to the binding constant between cytochrome  $b_5$  and cytochrome  $c$ .<sup>23,24</sup> We can thus correct for the concentration differences in the columns. The T8C mutation was used to derive the correction factor because its reactive surface is oriented away from the solid support and exhibits the longest retention time. The retention times of mutant binding isotherms are corrected to represent a concentration that is equal to that of the T8C column. The binding isotherms were generated by integrating the elution profile over time and normalizing them to the total area. This curve was then subtracted from 1 to get the fraction of cytochrome  $c$  retained on the column.

(23) Hethcote, H. W.; Delisi, C. J. *Chromatogr.* **1982**, *248*, 183–202.

(24) Delisi, C.; Hethcote, H. W. *Affinity Chromatography and Related Techniques*; Anal. Chem. Symp. Ser. **1982**, *9*, 63–78.

## RESULTS

The binding isotherms for the T65C, T8C, and D66C/E38C mutants are shown in Figure 3. The striking dependence of cytochrome *c* affinity on a cytochrome *b<sub>5</sub>* attachment site is readily observed. Consistent with the previous measurement of differential T8C and T65C orientations at surface immobilization sites, these mutants display distinct binding isotherms. Further, the reduction in cytochrome *c* affinity with the T65C and D66C/E38C mutants is in the direction expected for orienting the cytochrome *b<sub>5</sub>* binding surface toward the immobilization interface and inhibiting interaction with the process stream, while the T8C data are consistent with an orientation allowing for substantial cytochrome *c* interaction. Control measurements of the binding isotherm for cytochrome *c*-avidin interactions show that the T65C and D66C/E38C association constants are higher than any non-specific background, indicating that a majority of the cytochrome *b<sub>5</sub>*/cytochrome *c* interactions are retained. These results, in combination with the previous documentation indicating cytochrome *c* binds close to, but sterically distinct

from, the T65C and D66C/E38C positions, strongly suggests that orientation-dependent molecular recognition has been achieved in this immobilized protein system.

Orientational control of protein-protein molecular recognition at interfaces will be important in two crucial and interrelated aspects of process design: protein function and molecular assembly. Protein function is often exquisitely sensitive to the spatial relationships of subunits and partner proteins.<sup>25</sup> This work demonstrates the ability to control molecular orientation of individual protein molecules, allowing for the possibility of constructing patterned multilayer protein assemblies where function is controlled by the molecular architecture specified in the availability of reactive surfaces.

## ACKNOWLEDGMENT

Supported by NIH Grants GM 31756 and GM 33775 and the Biotechnology Research and Development Corp.

(25) Fersht, A. *Enzyme Structure and Mechanism*, 2nd ed.; W. H. Freeman and Co.: New York, 1985; Chapter 10.

RECEIVED for review June 1, 1993. Accepted June 25, 1993.

# Purification and Analysis of Drug Residues in Urine Samples by On-Line Immunoaffinity Chromatography/High-Performance Liquid Chromatography/Continuous-Flow Fast Atom Bombardment Mass Spectrometry

Enrico Davoli, Roberto Fanelli, and Renzo Bagnati\*

Istituto di Ricerche Farmacologiche "Mario Negri", via Eritrea 62, 20157 Milano, Italy

An automatic system for the on-line extraction and analysis of diethylstilbestrol in the urine of rats and calves is described. Extraction was done by injecting samples directly into an immunoaffinity column containing anti-diethylstilbestrol antibodies bound to a Sepharose matrix, and analysis was done by on-line high-performance liquid chromatography with ultraviolet and continuous-flow fast atom bombardment mass spectrometry detectors. The system, consisting of one injector, two switching valves, and three pumps, was operated under computer control and allowed to perform a complete analysis of a sample in 28 min. An accurate quantitation by isotope dilution was also possible, by the use of deuterated diethylstilbestrol as internal standard. The sensitivity of the method, using selected-ion monitoring of the molecular ion of diethylstilbestrol, was 2 ng/mL, injecting 1 mL of urine sample. Results obtained from analyzing the urine of rats and calves treated with diethylstilbestrol are presented.

## INTRODUCTION

The recent development of new mass spectrometric techniques able to give fine structural information on high molecular weight biological molecules has opened the way to a potential rapid increase in the use of mass spectrometry for the solution of real research problems in the biomedical laboratory.<sup>1,2</sup> The success of joint ventures between mass spectrometry and the clinical/biochemical laboratory is often bound to the mutual solution of the common problem of transforming the biological sample (blood, urine, tissue cell cultures, etc.) into a form which is suitable to be analyzed by mass spectrometry; this objective is not simple to achieve and, if underestimated, can be responsible for the failure of the entire investigation.

Among all the possible choices to separate molecules to be analyzed from the rest of the biological matrix, affinity chromatography techniques deserve a special place, since the high specificity that can be achieved in the binding of the analytes to the affinity supports often results in a "mass spectrometry grade" purified sample, ready for analysis.<sup>3,4</sup>

In our hands affinity chromatography, using immobilized antibodies as a stationary phase (immunoaffinity chroma-

tography), has proved to be an excellent tool for the off-line step preparation of biological samples for mass spectrometric analysis of a variety of biomedical compounds.<sup>5-8</sup> Recently, some papers have described the automated on-line use of this technique for sample preparation and analysis.<sup>9-13</sup> The advantages of an on-line method are evident: time saving, high sample throughput, and better reproducibility and reliability.

In this paper we report the feasibility and the performances of an on-line automated system for the direct extraction/purification/analysis of diethylstilbestrol (DES), in urine of treated animals, by immunoaffinity chromatography/HPLC/continuous-flow fast atom bombardment mass spectrometry (IACH-HPLC-cf-FAB-MS). An on-line direct coupling of a liquid chromatography/mass spectrometry system for FAB ionization has been done since 1981, with a moving belt HPLC interface,<sup>14</sup> and since 1985, with a capillary tubing interface.<sup>15</sup> The first application of cf-FAB on biological samples, with an on-line microdialysis system, was reported in 1988.<sup>16</sup> Recently it has been also shown that reduction in the matrix concentration, in cf-FAB operations, leads to drastic improvements of the signal-to-noise ratio, with the achievement of lower detection limits, down to the picomole region.<sup>17,18</sup>

The system here described is based on the use of a small immunoaffinity column, containing immobilized anti-DES antibodies, which separates the drug from urine components and is connected directly to an HPLC-cf-FAB analytical system.

## EXPERIMENTAL SECTION

**Materials.**  $\beta$ -Glucuronidase/arylsulfatase, from *Helix Pomatia*, was obtained from Boehringer (Mannheim, Germany).

(5) Bonfanti, M.; Magagnotti, C.; Galli, A.; Bagnati, R.; Moret, M.; Gariboldi, P.; Fanelli, R.; Airoldi, L. *Cancer Res.* 1990, 50, 6870-6875.

(6) Chiabrando, C.; Benigni, A.; Piccinelli, A.; Carminati, C.; Cozzi, E.; Remuzzi, G.; Fanelli, R. *Anal. Biochem.* 1987, 163, 255-262.

(7) Bagnati, R.; Castelli, M. G.; Airoldi, L.; Paleologo Oriundi, M.; Ubaldi, A.; Fanelli, R. *J. Chromatogr.* 1990, 527, 267-278.

(8) Bagnati, R.; Paleologo Oriundi, M.; Russo, V.; Danese, M.; Berti, F.; Fanelli, R. *J. Chromatogr.* 1991, 564, 493-502.

(9) Haasnoot, W.; Ploun, M. E.; Paulussen, R. J. A.; Schilt, R.; Huf, F. A. *J. Chromatogr.* 1990, 519, 323-335.

(10) Sharman, M.; Gilbert, J. J. *J. Chromatogr.* 1991, 543, 220-225.

(11) Farjam, A.; Brugman, A. E.; Lingeman, H.; Brinkman, U. A. *Analyst* 1991, 116, 891-896.

(12) Rule, G. S.; Henion, J. D. *J. Chromatogr.* 1992, 582, 103-112.

(13) de Frutos, M.; Regnier, F. E. *Anal. Chem.* 1993, 65, 17A-25A.

(14) Smith, R. D.; Burger, J. E.; Johnson, A. L. *Anal. Chem.* 1981, 53, 1603-1611.

(15) Ito, Y.; Takeuchi, T.; Ishii, D.; Goto, M. *J. Chromatogr.* 1985, 346, 161-166.

(16) Lin, S. N.; Caprioli, R. M. *Proceedings of the 36th ASMS Conference on Mass Spectrometry and Allied Topics*, San Francisco, CA, June 5-10, 1988; pp 1000-1001.

(17) Caprioli, R. M.; Fan, T.; Cottrel, J. S. *Anal. Chem.* 1986, 58, 2949-2954.

(18) Moseley, M. A.; Deterding, L. J.; Tomer, K. B.; Jorgenson, J. W. *Anal. Chem.* 1991, 63, 1467-1473.

(1) Carr, S. A.; Hemling, M. E.; Bean, M. F.; Roberts, G. D. *Anal. Chem.* 1991, 63, 2802-2824.

(2) Burlingame, A. L.; Baillie, T. A.; Russel, D. H. *Anal. Chem.* 1992, 64, 467R-502R.

(3) Gaskell, S. J.; Brownsey, B. G. *Clin. Chem.* 1983, 29, 677-680.

(4) van Ginkel, L. A. *J. Chromatogr.* 1991, 564, 363-384.



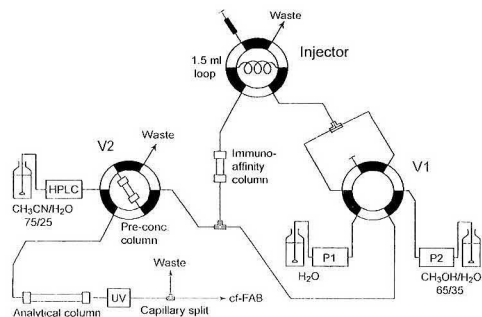


**Figure 1.** Scheme of the IAC-HPLC-cf-FAB system described in the Experimental Section. The three valves indicated in the figure are six-way HPLC switching valves. Each one has two positions ("white" and "black", corresponding to the schematized parts) which allow selection of the path of the sample and eluents through the system. Operating steps of the system are summarized in Table I.

CNBr-Sepharose 4B was obtained from Pharmacia (Uppsala, Sweden). HPLC grade solvents (acetonitrile and methanol) and glycerol were obtained from Merck (Darmstadt, Germany). HPLC grade water was prepared by using a Milli-Q purification system (Millipore, Bedford, MA). Diethylstilbestrol (pure trans isomer, *trans*-DES) was obtained from Aldrich (Milwaukee, WI). Octadeuteriodiethylstilbestrol (DES<sub>8</sub>), a mixture of *cis* and *trans* isomers, containing an impurity of *cis*-octadeuterio-3,4-bis(*p*-hydroxyphenyl)-2-hexene ( $\psi$ -DES<sub>8</sub>), was synthesized from unlabeled DES as already described.<sup>14,19</sup> Stock (1 mg/mL) and other diluted solutions of DES and DES<sub>8</sub> were made in acetonitrile and stored at -20 °C in the dark; water or buffer solutions of the same substances were made by dilution of the standards in acetonitrile, with a final percentage of solvent equal or less than 2%, and stored for no more than 1 week at 4 °C in the dark.

**Apparatus.** The scheme of the IAC-HPLC-cf-FAB-MS system is shown in Figure 1. The HPLC was a Beckman System Gold (Beckman Instruments Inc., San Ramon, CA), consisting of a Model 126 programmable solvent module, a Model 166 programmable UV detector module, and a NEC PC-8300 computer. The mobile phase delivered by the HPLC pumps was acetonitrile/water (75:25, v/v, isocratic), containing 0.8% (w/v) glycerol, at a constant flow rate of 200  $\mu$ L/min. Other pumps were as follows: pump 1 (P1), a Eldex Model B-100-S2 pump (Eldex Lab., San Carlos, CA), delivering water at a flow rate of 1 mL/min and pump 2 (P2), a Laboratory Data Control single-piston pump, delivering methanol/water (65:35, v/v) at a flow rate of 200  $\mu$ L/min. Both P1 and P2 were equipped with a pulse dampener and with a manometer for pressure measurement. The injector was a Beckman 210A sampling valve, equipped with a 1.5-mL loop which was made by using  $1/16$ -in. stainless steel tubing with 1-mm internal diameter (i.d.). The V1 and V2 valves (Model 7010; Rheodyne, Cotati, CA) were part of an electrical valve actuator (MUST; Chrompack, Middelburg, The Netherlands) which was controlled by the HPLC computer. The immunoaffinity column (IAC) was a Chromsep HPLC cartridge (Chrompack), 75 mm  $\times$  2 mm i.d., filled with immunosorbent (160  $\mu$ L) and equipped with 5- $\mu$ m stainless steel filters and Teflon rings for immobilization in the cartridge holder. The preconcentration column was a reversed-phase (C<sub>18</sub>) cartridge 10 mm  $\times$  2 mm i.d. (Chrompack), containing 40- $\mu$ m particles. The analytical column was a 5- $\mu$ m-particle Chromospher C<sub>18</sub>, 200 mm  $\times$  3 mm i.d. (Chrompack), consisting of two 100-mm glass cartridges and of a 10 mm  $\times$  2 mm i.d. precolumn, held together by a cartridge holder. All connections between the components of the system were made with  $1/16$ -in. stainless steel tubing until the inlet of the UV detector. At the exit of the detector cell a 50 cm length  $\times$  150  $\mu$ m i.d. uncoated, deactivated fused-silica capillary was assuring the necessary back pressure.

The interface between the HPLC and the mass spectrometer was a "capillary split connection" and was made as follows: the capillary from the UV detector was connected to a zero-dead volume T-connector for HPLC (Valco Instruments Co. Inc., Houston, TX), to which were also connected the fused-silica capillary from the cf-FAB probe (160 cm  $\times$  50  $\mu$ m i.d.) and another capillary (150  $\mu$ m i.d.), leading directly to waste and which was used for the regulation of the split ratio. The length of this last capillary determined the split ratio of the interface and also produced a small head pressure in the cf-FAB capillary which stabilized the flow and the operations of the FAB probe.

The cf-FAB probe (ending with a domed stainless steel tip) and the cf-FAB source were standard VG components (VG Analytical, Manchester, U.K.) used with no modifications. The mass spectrometer was a fully computerized VG 70-250 double-focusing (EB optics) instrument, equipped with a saddle field FAB gun (Ion Tech Ltd., Teddington, U.K.) which was operated with xenon at 8 kV and with 1.5-mA discharge current. The original VG data system (M1 version, PDP 11-24 based) was completely replaced with a general purpose Teknivent Vector One data system (Teknivent Corp., St. Louis, MO), directly connected to the VG 70-250 test box. Full-scan and selected-ion monitoring (SIM) experiments were performed with the accelerating voltage fixed at 6 kV and scanning the magnetic field with a 0-10 V ramp, generated from the Vector One data system. The magnetic field was controlled with the standard VG Hall effect probe, back feeding the magnet power supply unit.

Optimization of chromatographic conditions for DES and injections of reference standards for recovery calculations were made by disconnecting the IAC from V2 and by substituting the preconcentration column in the same valve with a 20- $\mu$ L loop. Standards of DES and DES<sub>8</sub> were injected into the analytical column through V2 using an injector adapter (Rheodyne Model 7012) inserted in the place of the previous IAC connection.

**Procedures.** *Production of the Antiserum and of the Immunoaffinity Column.* The production of the anti-DES antiserum and the purification of immunoglobulins (IgG) and their coupling to Sepharose have been already described.<sup>7</sup> Briefly, IgG were obtained from sera of rabbits immunized with a conjugate of DES-monocarboxymethyl ether with bovine serum albumin (DES-BSA) and were purified with protein A affinity columns. Purified IgGs were then coupled to CNBr-Sepharose 4B (5 mg of IgG/mL of gel) following the manufacturer's recommended procedure.

The immunosorbent obtained had a capacity of ~700 ng of DES/mL of gel; thus the IAC used in this study had a total capacity of ~110 ng of DES. The column was prepared by filling the cartridge from one end with a suspension of the Sepharose gel in distilled water and packing it by vacuum suction from the other end. A slight compression of the gel resulted after using the column for the first extractions, due to the moderate operating pressures of pumps P1 and P2 (ca. 250 psi); the consequent small dead volume in the head of the column did not affect seriously the performances of the system and it could be easily filled with additional gel. The column was stored in methanol/water (65:35) at room temperature when not in use.

**Animal Experiments.** Animal treatments were done by subcutaneous injections of DES in corn oil. Procedures involving animals and their care were conducted in conformity with the institutional guidelines that are in compliance with national and international laws and policies (EEC Council Directive 86/609, OJ L 358, 1, December 12, 1987; NIH Guide for the Care and Use of Laboratory Animals, NIH Publication No. 85-23, 1985).

Three male CD rats (Charles River, Calco, Como, Italy), weighing  $280 \pm 20$  g, were treated with single subcutaneous injections of 0, 0.25, and 2 mg of DES, respectively. Urine samples were entirely collected every 24 h for 4 days and frozen at -20 °C until analysis.

Two calves were treated two times, with an interval from injections of 10 days, with 4 mg of DES. Urine samples were collected every 3 days for 22 days and frozen at -20 °C until analysis.

**Sample Pretreatments.** Urine samples coming from treated rats and calves were analyzed without and after enzymatic hydrolysis with  $\beta$ -glucuronidase/arylsulfatase. Urine samples to be hydrolyzed were first centrifuged and spiked with internal

(19) Liehr, J. G.; Ballatore, A. M. *Steroids* 1982, 40, 713-722.

**Table I. Sequential Steps of the On-Line IAC-HPLC-cf-FAB System of Figure 1, As Implemented in the Program of the Computer Which Controls Pump and Valve Operations**

start time (min)	type of operation	valve	valve position <sup>a</sup>
	sample loading (manual)	injector	white
		V1	black
		V2	white
0	sample injection into the immunoaffinity column and subsequent washing of the column with water, by using pump P1	injector	black
		V1	black
		V2	white
5	elution of the immunoaffinity column with methanol/water (65:35, v/v), by using pump P2	injector	black
		V1	white
		V2	white
11	trapping of the immunosorbed substances into the preconcentration column, by using pump P1 and pump P2	injector	black
		V1	white
		V2	black
20	injection of the trapped substances into the analytical column, by using HPLC pumps, and start of HPLC-cf-FAB analysis	injector	black
		V1	white
		V2	white
24	reconditioning of the immunoaffinity column with water, by using pump P1	injector	black
		V1	black
		V2	white
28	end of cycle	injector	white
		V1	black
		V2	white

<sup>a</sup> With reference to Figure 1, the position "black" stands for eluents flowing through the black parts of the schematized valves, and "white" through the white parts

standard (to a concentration of 20 ng/mL *trans*-DESD<sub>8</sub>, 15 ng/mL *ψ*-DESD<sub>8</sub>, and 8 ng/mL *cis*-DESD<sub>8</sub>), diluted with 0.25 M acetate buffer, pH 4.8 (0.2 mL/mL of urine) and, after adding enzyme solution (5  $\mu$ L/mL of urine), were incubated overnight at 37 °C. Finally they were diluted with 0.25 M phosphate buffer, pH 7.4 (0.3 mL/mL of urine) and loaded directly into the injector loop. When enzymatic hydrolysis was not required, urines were only spiked with the same amount of internal standard and diluted with 0.5 mL of phosphate buffer/mL of urine.

**On-Line Extraction by Immunoaffinity Chromatography.** The on-line analysis of samples, with the system shown in Figure 1, was performed by following the steps summarized in Table I. After the sample was manually loaded into the loop, the IAC-HPLC operations of the system were executed automatically under computer control. P1 and P2 pumps were both maintained in continuous operation during the analyses, using HPLC valves to select the paths of their respective eluents through the system. During the first 5 min the diluted urine sample (1.5 mL, corresponding to 1 mL of undiluted urine) was pumped at 1 mL/min by P1 through the IAC, followed by water (3.5 mL) as washing solvent. At 5 min valve V1 was switched, so that methanol/water from P2 began to flow through the injection loop. At the flow rate of P2 (200  $\mu$ L/min), the time required to fill the loop and to begin eluting the IAC was 7.5 min. Some time before, at 11 min from the start of analysis, valve V2 was switched, to connect the preconcentration column to the exit of the IAC. Under these conditions, while P2 pumped the methanol/water eluent through the IAC, P1 was used to dilute with water the same eluent after the IAC (final percentage of methanol was ca. 10%) to allow reconcentration of immunodesorbed substances into the preconcentration column. At 20 min, elution and trapping were complete and the preconcentration column was connected, by again switching valve V2, to the analytical column. HPLC and cf-FAB analysis started at this time. The IAC remained under solvent washing until 24 min and then was reconditioned with water by P1. After 28 min the system was ready for another analysis.

**HPLC Separation and cf-FAB Analysis.** HPLC separation was performed with an isocratic eluent [acetonitrile/water

(75:25, v/v) containing 0.8% glycerol as FAB matrix], with a flow rate of 200  $\mu$ L/min. The eluate of the HPLC, after the UV detector ( $\lambda$  = 276 nm), was directly transferred to the mass spectrometer through the capillary split connection described before.

During cf-FAB analysis of samples, mass spectrometric conditions were as follows: source temperature, 60 °C; acquisition method, selected-ion monitoring (SIM) of  $m/z$  268 and 276 (dwell time, 0.8 s each), corresponding to the molecular cations of DES and DESD<sub>8</sub> isomers, respectively.

Full-scan spectra of standard solutions of different compounds were recorded from  $m/z$  = 40 to 400 (positive ions), with a 4-s/decade scan speed.

## RESULTS AND DISCUSSION

An immunoaffinity gel containing antibodies raised in rabbits against DES has been characterized and used in a previous study for the manual extraction of urine and plasma samples.<sup>7</sup> The same immunosorbent was used to prepare the IAC of the present study. The principal steps in the analytical procedure which used this column as part of the automated system described in the previous sections, are the following: immunoaffinity extraction of analytes and reconcentration of the same analytes in the small preconcentration column; HPLC separation; cf-FAB-MS detection.

**Immunoaffinity Extraction and Reconcentration of Analytes.** Urine samples were pumped through the IAC at a relatively high flow rate (1 mL/min), with respect to manual procedures, in which samples are even left in contact to the gel for some minutes.<sup>5-8</sup> This did not significantly affect the performances of the on-line system.

The percent recoveries were calculated by injecting blank urine samples spiked with known amounts of DESD<sub>8</sub> mixture and comparing the peak areas obtained with the UV detector with those of pure DESD<sub>8</sub> standards injected directly into the analytical HPLC column. The recoveries obtained were  $87 \pm 13\%$  for *trans*-DESD<sub>8</sub>,  $51 \pm 15\%$  for *cis*-DESD<sub>8</sub>, and  $31 \pm 12\%$  for *ψ*-DESD<sub>8</sub> (mean  $\pm$  SD,  $n$  = 13). The recoveries calculated in this way also account for the precolumn reconcentration step. No difference was found when phosphate buffer was used, instead of water, as the washing solvent delivered by pump P1 and by increasing the washing time. Water was chosen as the washing solvent because of simplicity of use, also with regard to its contemporary use as diluting agent of the IAC elution solvent. The composition of the IAC elution solvent (methanol/water 65:35) and the flow rates of pump P1 and P2 were optimized also on account of the subsequent reconcentration step. This step was necessary because the IAC could not be connected directly to the analytical HPLC column, whose operating pressure was too high for the immunoaffinity gel. During the reconcentration, the final methanol content (ca. 10%) flowing through the preconcentration column was sufficiently low to allow trapping of DES isomers with almost quantitative recovery. All the switching times of valves V1 and V2 were optimized, taking account of dead volumes and flow rates, to obtain maximum recovery and sample purity. The size of the preconcentration column was small enough to allow a subsequent fast elution by the HPLC eluent and to avoid broadening or tailing of the peaks during the HPLC separation.

It may be noted that the IAC, which was made with an antiserum raised mainly against the *trans* isomer of DES, could also recover the other isomers (*cis*-DESD<sub>8</sub> and *ψ*-DESD<sub>8</sub>), although with lesser and more variable results. This was due to the use of polyclonal antibodies which contained several IgG subpopulations.

The IAC used for this study did not show an apparent decrease in the performance after repeated injections of standards and samples: more than 100 injections were made without decrease of the recoveries. The only maintenance

**Table II. HPLC Retention Times of DES and DESD<sub>8</sub> Isomers As Measured by UV and by cf-FAB Detection, Using the System Described in Figure 1<sup>a</sup>**

substance	retention time (min)	
	HPLC/UV	HPLC-cf-FAB
<i>trans</i> -DESD <sub>8</sub>	5.3	7.1
<i>trans</i> -DES	5.4	7.2
<i>ψ</i> -DESD <sub>8</sub>	6.5	8.3
<i>cis</i> -DESD <sub>8</sub>	7.3	9.1
<i>cis</i> -DES	7.4	9.2

<sup>a</sup> The delay obtained with cf-FAB detection is due to the time necessary for the substances to flow through the capillary leading to the cf-FAB source.

**Table III. *trans*-DES and *cis*-DES Levels Found in Urine of Rats Treated Subcutaneously with 0.25 and 2 mg of *trans*-DES, without and after Hydrolysis with β-Glucuronidase/arylsulfatase<sup>a</sup>**

day	without hydrolysis with β-glucuronidase/arylsulfatase		after hydrolysis with β-glucuronidase/arylsulfatase	
	<i>trans</i> -DES (ng/mL)	<i>cis</i> -DES (ng/mL)	<i>trans</i> -DES (ng/mL)	<i>cis</i> -DES (ng/mL)
Rat 1 (0.25 mg of DES)				
1	2.5	2.4	2.5	4.0
2	3.6	4.8	4.4	8.1
3	2.1	2.8	2.1	3.1
4	<2	<2	<2	<2
Rat 2 (2 mg of DES)				
1	8.1	10.9	15.8	15.6
2	6.9	8.1	10.5	9.2
3	4.4	5.0	6.4	7.0
4	2.9	3.1	3.0	3.4

<sup>a</sup> Complete urine samples were collected every day for 4 days and analyzed with the IACHR-HPLC-cf-FAB method described in the Experimental Section.

operation required was the substitution of the inlet stainless steel filter when it began to become obstructed. The frequency of this operation depended on the cleanliness of the samples injected: in our case, urine samples (which were centrifuged but not prefiltered, because of adsorption problems of DES on some filter membranes) caused partial obstruction of the filter (revealed by an increase of pump P1 operating pressure) after about 40–50 samples.

On-line IAC seem to last more than columns used manually, probably because of more controlled and standardized operating procedures.

**HPLC Separation and UV Detection.** HPLC separation was made isocratically using a reduced eluent flow rate (200 μL/min) with respect to that indicated by the manufacturer to be the optimal one (400–600 μL/min) for the type of HPLC column employed. This choice was made exclusively in consideration of optimal performances of the cf-FAB interface and not of chromatographic performances, which in fact could have been increased with higher eluent flow rates. The eluent contained also glycerol, necessary to FAB ionization, in a percentage (0.8%) that did not affect chromatographic separation.

The two isomers of DES or DESD<sub>8</sub> were well separated with the HPLC conditions described, as well as the related impurity of the deuterated standard mixture (*ψ*-DESD<sub>8</sub>). The deuterated analogs (*trans*-DESD<sub>8</sub> and *cis*-DESD<sub>8</sub>) had slightly lower retention times with respect to the corresponding nondeuterated substances (Table II), but when injected together, their respective peaks could not be distinguished using the UV detector. This behavior is similar to that of the same or other deuterated analogs during analyses by gas chromatography.

**Table IV. *trans*-DES and *cis*-DES Levels Found in Urine of Calves Treated Two Times Subcutaneously with 4 mg of *trans*-DES<sup>a</sup>**

day	IACHR-HPLC-cf-FAB method		GC/MS method	
	<i>trans</i> -DES (ng/mL)	<i>cis</i> -DES (ng/mL)	<i>trans</i> -DES (ng/mL)	<i>cis</i> -DES (ng/mL)
Calf 1 (Female)				
1 <sup>b</sup>	<2	<2	<0.02	<0.02
5	17.3	21.7	14.1	14.0
8	11.5	13.0	9.8	7.0
12 <sup>b</sup>	4.0	7.5	2.5	2.1
15	16.3	8.3	9.0	4.8
19	<2	<2	2.0	0.82
22	<2	<2	0.55	0.24
Calf 2 (Male)				
1 <sup>b</sup>	<2	<2	<0.02	<0.02
5	7.9	12.3	6.2	7.0
8	8.6	11.7	12.1	8.2
12 <sup>b</sup>	3.5	2.4	1.2	0.8
15	4.6	6.3	3.5	3.8
19	<2	2.1	1.3	1.0
22	<2	<2	0.80	0.56

<sup>a</sup> Urine samples were collected every 4 days and analyzed with the IACHR-HPLC-cf-FAB method described in the Experimental Section and with a GC/MS method, also involving the use of immunoaffinity extraction. All samples were treated with β-glucuronidase/arylsulfatase to hydrolyze the DES-glucuronide present in the urine. See text for other explanations. <sup>b</sup> Days in which treatments with DES were done (urine samples in these days were collected before treatments).

UV chromatograms of a standard and of a urine spiked with DES and DESD<sub>8</sub> are shown in Figure 2, together with cf-FAB traces of the molecular ions of the two substances. The UV chromatograms are sufficiently clean, but quantitation with respect to the deuterated internal standard is not possible. The same is true for real urine samples, where in some cases more interfering peaks were present (see Analytical Data section).

**cf-FAB Detection.** The capillary split connection employed in this work assured a split ratio of about 1:115, when the length of the third "waste" capillary of the T-connection was 50 cm. The flow rate of the mobile phase introduced in the mass spectrometer was 1.75 μL/min. This flow in the 50-μm capillary which was feeding the cf-FAB source was calculated from the 1.8-min time delay of the peaks eluting from the HPLC, considering nonsignificant the amount of time necessary for the eluent to reach the interface. Under these experimental conditions, assuming that the baseline intensity reflects the flow stability, the flow has been very stable for periods as long as a working day. Moreover, the little amounts of glycerol supplied (14 ng/min) did not cause matrix buildup on the FAB probe tip and the chemical noise was maintained at a minimum.

In Figure 3 full-scan spectra of *trans*-DES (without and with background subtraction) and of *trans*-DESD<sub>8</sub> and *ψ*-DESD<sub>8</sub> (with background subtraction), in the mobile phase, are shown. The spectra of the *cis* isomers were identical to those of the *trans* isomers. The molecular cation is present in the mass spectra of all compounds and no protonation occurred in our experimental conditions. This unusual behavior of DES isomers with cf-FAB ionization (which normally gives protonated molecular cations) was confirmed by static FAB experiments and also by obtaining, in the same cf-FAB conditions, similar mass spectra from other compounds, such as estradiol and dienestrol, which also have a chemical structure bearing only phenolic or alcoholic groups, which cannot be easily protonated. However, with compounds containing other chemical groups, such as zanol (carboxylic

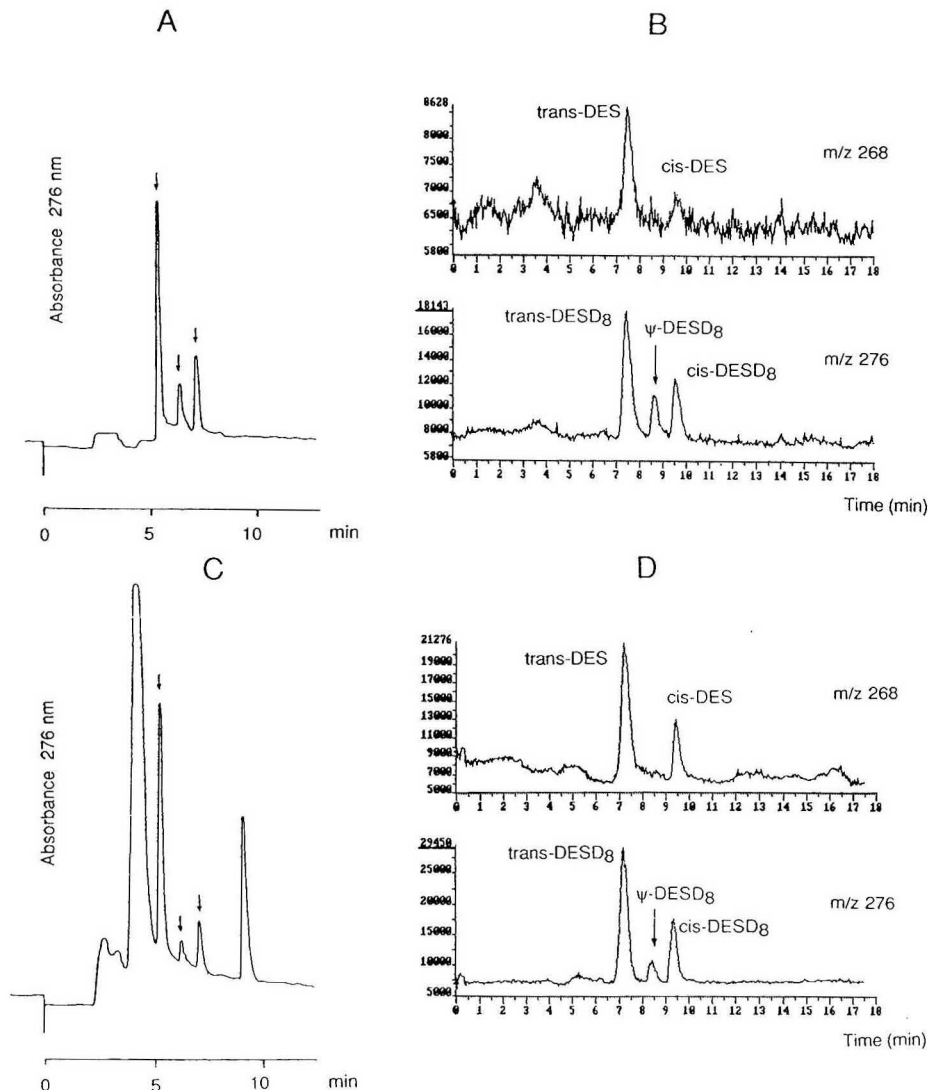


**Figure 2.** UV (A) and selected-ion monitoring (B) liquid chromatograms of a standard solution in water, containing *trans*-DES (4 ng/mL) and a deuterated DES mixture (20 ng/mL *trans*-DESD<sub>8</sub>, 15 ng/mL  $\psi$ -DESD<sub>8</sub>, and 8 ng/mL *cis*-DESD<sub>8</sub>) and of a blank urine sample (C and D) spiked with 10 ng/mL *trans*-DES and with a deuterated DES mixture (in the same amount as in the standard solution above). Chromatograms were obtained with the system described in Figure 1 and Table I. Arrows in the UV traces indicate, in order of elution, the peaks of *trans*,  $\psi$ , and *cis* isomers of DES and DESD<sub>8</sub>.

ester), testosterone (keto group), and stanozolol (pyrazole group), the *cf*-FAB source produced the usual protonated molecular cations.

In the *cf*-FAB mass spectra of DES isomers, fragment ions are evident after background subtraction. By comparison with deuterated standards, the structure of the most intense ions of *trans*-DES could be determined:  $m/z$ , 268 [M]<sup>+</sup>, 253 [M - CH<sub>3</sub>]<sup>+</sup>, 239 [M - CH<sub>2</sub>CH<sub>3</sub>]<sup>+</sup>, 175 [M - C<sub>6</sub>H<sub>4</sub>OH]<sup>+</sup>, 135 [CH<sub>3</sub>CH<sub>2</sub>CHC<sub>6</sub>H<sub>4</sub>OH]<sup>+</sup>, 107 [C<sub>7</sub>H<sub>6</sub>OH]<sup>+</sup>.

**Analytical Data.** Urine samples of treated rats and calves were analyzed by the method described and gave the results

shown in Table III. Both treated rats gave measurable values of DES concentration in the urine, except in the fourth day for the rat treated with the lower dose (0.25 mg). The moderate difference between the levels of *cis*- and *trans*-DES without and after hydrolysis with  $\beta$ -glucuronidase/arylsulfatase indicates that DES was excreted in rat urine mainly as the unchanged drug, with low levels of DES-glucuronide.

Urines of treated calves were analyzed only after hydrolysis with  $\beta$ -glucuronidase/arylsulfatase, because the urinary excretion of DES in calves has been shown to be mainly as the

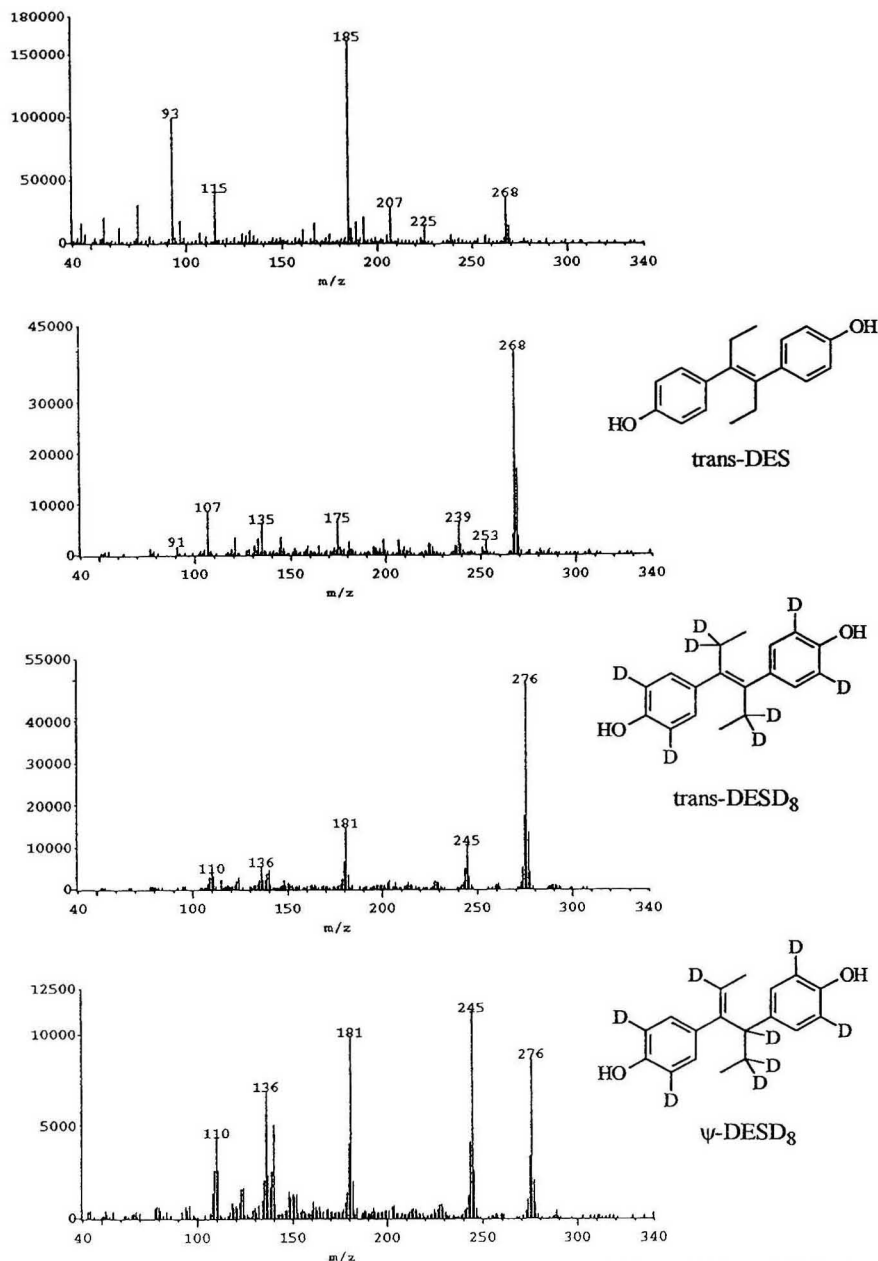


**Figure 3.** cf-FAB mass spectra of *trans*-DES without background subtraction (top) and of *trans*-DES, *trans*-DESD<sub>8</sub>, and  $\psi$ -DESD<sub>8</sub> after background subtraction (indicated by their relative structures and names). Spectra were taken after injecting 400 ng of each substance directly into an analytical HPLC column and using the capillary split connection described in the Experimental Section to interface the HPLC and the cf-FAB probe. Background ions are generated by the glycerol matrix present in the HPLC eluting solvent (0.8% w/v).

DES-glucuronide.<sup>7</sup> The same urine samples were also analyzed by off-line IACr-GC/MS, with a method already described<sup>7</sup> and the results are shown in Table IV. The agreement of the data obtained with the two methods may

be considered good, considering the problem of the isomerization of DES, which is a phenomenon not easily controllable and not yet clearly understood.<sup>7,20</sup> In fact, cis-trans isomerization may be influenced by temperature, matrix compo-



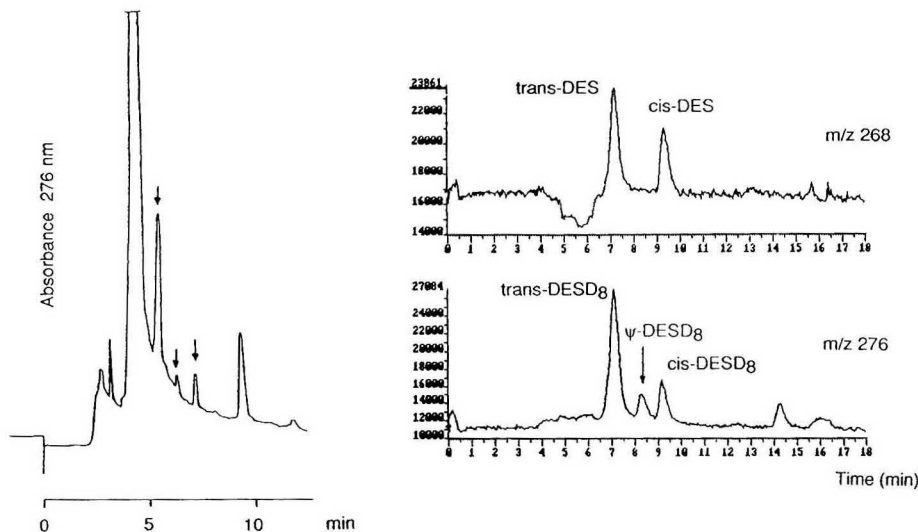


**Figure 4.** UV (left) and selected-ion monitoring (right) chromatograms of a calf urine sample spiked with a deuterated DES mixture (20 ng/mL *trans*-DESD<sub>8</sub>, 15 ng/mL *ψ*-DESD<sub>8</sub>, and 8 ng/mL *cis*-DESD<sub>8</sub>) as internal standard. Chromatograms were obtained with the system described in Figure 1 and Table I. Arrows in the UV traces indicate, in order of elution, the peaks of *trans*, *ψ*, and *cis* isomers of DES and DESD<sub>8</sub>.

sition, enzymatic reactions, and light. Some additional isomerization may have been present during the derivatization step required for the GC/MS procedure, while the HPLC/MS method did not introduce a similar possibility.

Quantitation of samples with the IACr-HPLC-cf-FAB method was made by an isotope dilution method, using calibration curves obtained by injecting standards containing known amounts of DES (2, 4, 10, 20, and 40 ng/mL) and a constant amount of internal standard (20 ng/mL *trans*-DESD<sub>8</sub>, 15 ng/mL *ψ*-DESD<sub>8</sub> and 8 ng/mL *cis*-DESD<sub>8</sub>). The *trans*-DES/*trans*-DESD<sub>8</sub> and *cis*-DES/*cis*-DESD<sub>8</sub> peak area ratios were plotted against the concentrations of *trans*-DES and *cis*-DES, respectively, in standard solutions and the linear regression curves obtained were used to quantitate samples. Standard errors of 4.6% and 11.2% were obtained for *trans*-DES and *cis*-DES, respectively.

Chromatograms of the *m/z* 268 and 276 ions and of a UV trace of a calf urine sample are shown in Figure 4. The SIM tracings are very clean and show a minimal loss of chromatographic resolution, with respect to the UV trace.

The repeatability of the procedure was measured by injecting, four times, a urine sample containing about 10 ng/mL *trans*-DES and *cis*-DES and was of 8% and 18%, respectively, for the two isomers. The sensitivity of the method was ca. 2 ng/mL for each isomer of DES, when 1.5 mL of diluted sample was injected.

## CONCLUSIONS

We have shown that the analytical system illustrated in this paper has been able to give fast quantitative and structural information on the small molecular weight compounds (*trans*-DES and other cross-reacting isomers) present at ppb levels in a complex biological matrix. The system may be adapted for the analysis of other molecules, provided the relative antisera are available. Different antisera may also be used in combination in the same IAC, or a single antiserum may be used to extract several molecules bearing a common cross-reacting group.

As a final consideration, we can say that the possibility here presented of introducing on-line into the mass spectrometer purified molecules selected on the basis of their interaction with immobilized ligands, coupled with the present capabilities of mass spectrometry to give structural information on high molecular weight macromolecules, opens promising routes to address priority biological problems involving the identification of endogenous ligands.

## ACKNOWLEDGMENT

This work was done with the support of Chrompack International and Chrompack Italia, which kindly supplied HPLC materials.

(20) Derks, H. J. G. M.; Freudenthal, J.; Litjens, J. L. M.; Klaassen, R.; Gramberg, L. G.; Borrias-van Tongeren, V. *Biomed. Mass Spectrom.* 1983, 10, 209-214.

RECEIVED for review April 15, 1993. Accepted June 25, 1993.

## CORRESPONDENCE

# Molecular Basis of Peak Width in Capillary Gas Chromatography under High Column Pressure Drop

Leonid M. Blumberg\* and Terry A. Berger

Hewlett-Packard Co., 2850 Centerville Road, Wilmington, Delaware 19808

Under normal conditions in GC (gas chromatography), the first peaks in the run are the narrowest and pose the highest demand for avoidance of extra column peak broadening effects by detector volumes, time constants of detector electronics, etc. Furthermore, the widths of all the peaks in a chromatographic run are predetermined by the width of the unretained peak. Therefore, the width of the unretained peak can serve as an indicator of the speed of the entire analysis. In view of this, we made an attempt to derive a relation for the width of unretained peaks based on column dimensions and its operational conditions. We came to the unexpected and previously unknown conclusion that under high inlet-to-outlet pressure drop, the width of an unretained peak does not depend on the column diameter, but only on the column length and molecular properties of the carrier gas and the solute.

A more accurate formulation of that result as well as its derivation and discussion is the subject of this report.

## THEORY

**Conditions for the Analysis.** Typically, high-speed capillary GC is associated with small column diameters which frequency require high pressure drop, i.e.

$$P_{\text{in}} \gg P_{\text{out}} \quad (1)$$

That along with conditions

$$M_s \gg M_m \quad (2)$$

$$\nu_{\text{out}} \geq \nu_{\text{out,opt}} \quad (3)$$

constitutes the boundaries of analysis in this paper. In the latter inequalities,  $M_s$  and  $M_m$  are molecular weights of, respectively, the solute and the mobile phase while  $\nu_{\text{out}}$  and  $\nu_{\text{out,opt}}$  are, respectively, carrier gas outlet linear velocity and its Van Deemter optimum.<sup>1,2</sup>

Also, in the analysis, a carrier gas is assumed to be ideal, and, when retained peaks are considered, the affect of the stationary phase film thickness on the plate height is ignored. The latter means that, in cases of a solute retention, thin film columns are assumed. Special attention in the analysis is given to overoptimized columns where

$$\nu_{\text{out}} \gg \nu_{\text{out,opt}} \quad (4)$$

The optimized columns, i.e.

$$\nu_{\text{out}} = \nu_{\text{out,opt}} \quad (5)$$

are also considered.

**Variance of a Peak.** In thin film capillary GC, under the condition in eq 1, the variance of a peak can be expressed (see Appendix) as

$$\tau^2 = \frac{\eta L^2 G(k)}{3 D_{\text{out}} P_{\text{out}}} \left( 1 + \left( \frac{\nu_{\text{out,opt}}}{\nu_{\text{out}}} \right)^2 \right) \quad (6)$$

$$G(k) = 1 + 6k + 11k^2$$

In eq 6, while  $\eta$  is a property of only the mobile phase,  $D_{\text{out}}$  depends on the phase and on the solute. Substitution

$$D_r = D_{\text{out}}/D_{m,\text{out}} \quad (7)$$

where  $D_{m,\text{out}}$  is coefficient of self-diffusion of the mobile phase at the column outlet conditions, allows the properties of the mobile phase,  $\eta$  and  $D_{m,\text{out}}$ , to be separated from the property of the mixture. Equation 6 becomes

$$\tau^2 = \frac{\eta L^2 G(k)}{3 D_r D_{m,\text{out}} P_{\text{out}}} \left( 1 + \left( \frac{\nu_{\text{out,opt}}}{\nu_{\text{out}}} \right)^2 \right) \quad (8)$$

**Reduced Diffusivity of a Solute.** Ratio  $D_r$ , in eq 7, can be viewed as the reduced diffusivity of a solute in the mobile phase. It can be expressed via molecular properties of the mobile phase and the solute<sup>3,4</sup>

$$D_r = D_{\text{out}} \frac{1}{D_{m,\text{out}}} = \frac{(1/M_m + 1/M_s)^{1/2}}{(d_m + d_s)^2} \frac{(2d_m)^2}{(2/M_m)^{1/2}} \quad (9)$$

Typically in GC, the solutes have much larger molecular weights compared to the carrier gas, eq 2. Equation 9 yields

$$D_r = \frac{2(2)^{1/2}}{(1 + d_s/d_m)^2} \quad (10)$$

**Peak Width and Molecular Properties of Carrier Gases and Solutes.** Assuming ideal gas conditions, the combination  $\eta/(D_{m,\text{out}} P_{\text{out}})$  in eq 8 can be further reduced. Due to the relations  $\rho D = 1.2\eta$  and  $\mu^2 = 3RT/M = 3P/\rho$  known from the kinetic theory of ideal gases,<sup>5</sup> one has

$$\frac{\eta}{3 D_{m,\text{out}} P_{\text{out}}} = \frac{\rho_{m,\text{out}}}{3.6 P_{\text{out}}} = \frac{M_m}{3.6 RT}$$

(1) Van Deemter, J. J.; Zuiderweg, F. J.; Klinkenberg, A. *Chem. Eng. Sci.* 1956, 5, 271-289.

(2) Golay, M. J. E. *Gas Chromatography*; Desty, D. H., Ed.; Butterworth: London, 1958; pp 36-55.

(3) Fuller, E. N.; Giddings, J. C. *J. Gas Chromatogr.* 1965, 3, 222-227.

(4) Fuller, E. N.; Schettler, P. D.; Giddings, J. C. *Ind. Eng. Chem.* 1966, 58 (5), 19-27.

(5) Moore, W. J. *Physical Chemistry*, Prentice-Hall: Englewood Cliffs, NJ, 1972.

and eq 8 becomes

$$\tau^2 = \frac{L^2 M_m G(k)}{3.6 D_r R T} \left( 1 + \left( \frac{v_{\text{out,opt}}}{v_{\text{out}}} \right)^2 \right) = \frac{L^2 G(k)}{1.2 D_r \mu_m^2} \left( 1 + \left( \frac{v_{\text{out,opt}}}{v_{\text{out}}} \right)^2 \right) \quad (11)$$

**Lower Bounds for Peak Widths.** When the condition in eq 4 is met a column is overoptimized and eq 11 becomes

$$\tau_{\min} = \tau_{\min}(D_r, k) = L \left( \frac{G(k) M_m}{3.6 D_r R T} \right)^{1/2} = \left( \frac{G(k)}{1.2 D_r} \right)^{1/2} \frac{L}{\mu_m} \quad (12)$$

Quantity  $\tau_{\min}$  represents the *solute-specific lower bound* for standard deviation of peaks. The solute dependence is represented by capacity ratio,  $k$ , for the solute and by its reduced diffusivity  $D_r$ , eq 7. Consider the quantity

$$\tau_{\min, \text{abe}} = L \left( \frac{M_m}{3.6 R T} \right)^{1/2} = \frac{L}{1.2^{1/2} \mu_m} \quad (13)$$

It follows from eq 6 that  $G(k) \geq G(0) = 1$ . Also from eq 7 and refs 3 and 4 under the condition of eq 2, it follows that  $D_r < 1$ . Therefore,  $\tau_{\min, \text{abe}} < \tau_{\min}$  and quantity  $\tau_{\min, \text{abe}}$  represents the *absolute lower bound* for the standard deviation of unretained peaks. In a given carrier gas, no peak can have standard deviation below  $\tau_{\min, \text{abe}}$ . Comparison of eqs 12 and 13 indicates that

$$\tau_{\min} = \tau_{\min}(D_r, k) = \left( \frac{G(k)}{D_r} \right)^{1/2} \tau_{\min, \text{abe}} \quad (14)$$

Also from eqs 5, 11, and 12, one has

$$\tau_{\text{opt}} = \tau_{\text{opt}}(D_r, k) = 2^{1/2} \tau_{\min} = \left( \frac{2G(k)}{D_r} \right)^{1/2} \tau_{\min, \text{abe}} \quad (15)$$

Due to the discussion following eq 13, the last three quantities relate as

$$\tau_{\min, \text{abe}} < \tau_{\min} < \tau_{\text{opt}} \quad (16)$$

## DISCUSSION

**Peak Width and Column Diameter.** The most important results of the theory are expressed in eqs 11 and 13–16. Equation 11 gives a general formula for the peak width (expressed via the peak's standard deviation) under high pressure drop. It shows how the peak width relates to the molecular properties of the carrier gas and the solute at a given temperature. Equations 13–16 deal with special cases. The peak width also depends on column length but, interestingly (and unexpectedly), **does not depend on column diameter**. Below, we provide a more detailed discussion of this conclusion.

A GC analysis depends on the combination of many conditions which, in this discussion, are assumed to remain constant (isothermal, isobaric, etc.) during a given run. One such condition is carrier gas flow. Increase in the flow, when all other conditions remain the same, can reduce peak widths and analysis time.<sup>6,7</sup> However, there is a limit to the peak width reduction achievable via flow increase. In a capillary column, when the column flow gets larger and larger the outlet carrier gas velocity,  $v_{\text{out}}$ , will, eventually, exceed its optimum  $v_{\text{out,opt}}$  and further reduction in the peak width will no longer be available, as eq 11, suggests. In other words, the *lower bounds* for the peak widths will be reached.

Two lower bounds,  $\tau_{\min, \text{abe}}$  and  $\tau_{\min}$ , eqs 13 and 14 (see also eq 16 for their relations), can be recognized.

Equation 13 gives an absolute lower bound,  $\tau_{\min, \text{abe}}$ , of the peak width. For a given column length and carrier gas, no peak in a GC run can be narrower than the absolute lower bound,  $\tau_{\min, \text{abe}}$ , which **does not depend on the column diameter, the nature of the solute in the peak, or its retention**. The bound  $\tau_{\min, \text{abe}}$  can be expressed in terms of the molecular weight of the carrier gas (the fundamental property of the gas), its absolute temperature, and column length. Equation 13 also suggests that the standard deviation of a peak can never fall under about 90% of the time defined as the ratio of the column length,  $L$ , to the mean square speed,  $\mu_m$ , of carrier gas molecules.

If the components of a sample mixture and/or their capacity ratios (relative retentions) in a given column are known, then **more accurate higher solute-specific bounds**  $\tau_{\min}$ , eq 14, can be found for each component. For a given column length and carrier gas, a peak cannot be narrower than its solute-specific lower bound,  $\tau_{\min}$ , which **does not depend on the column diameter**.

Not only can the lower bounds for the peak widths be easily predicted, but their actual values as well. Specifically, if flow optimization, eq 5, for a given solute requires high column pressure drop, then the standard deviation,  $\tau_{\text{opt}}$ , of the peak can be found from eq 15. This value, again, is **independent of the column diameter**. It is interesting to notice from eq 15 that for a given solute, the optimum peak width,  $\tau_{\text{opt}}$ , exceeds its respective lower bound,  $\tau_{\min}$ , by about 41%. That means that **under high pressure drop conditions, there is no room for a significant peak width reduction beyond its Van Deemter optimum value**. One can conclude that (see theory and discussion below for more detailed conditions) **The only column dimension which affects peak widths in high pressure drop capillary GC is column length. Change in the column diameter alone does not affect the peak widths.**

This conclusion can be illustrated by the following examples. To improve peak resolution achieved with a Van Deemter optimized thin film capillary column operating under high pressure drop, one can choose another capillary column with smaller diameter but with the same length, stationary phase, and phase ratio. If the new column is also optimized, then the solute will elute with the **same peak width from both columns** (although, in the new column, all peaks will be further apart from each other, and, therefore, better resolved). The same is true if both columns were overoptimized.

To improve resolution, one can also increase column length while keeping its diameter, carrier gas mass flow, and other relevant conditions (see previous case) unchanged. In this case, **peak widths will increase proportionally to the increase in column length** (although, again, the time between the peaks will have even larger increase, so that the resolution will increase). Further discussion of the relations between column dimensions and resolution is outside of the scope of this report.

Independence of the peak width from the column diameter in eqs 11 and 13–15 can also be illustrated by the following analysis. For a given column length and solute capacity ratio, peak width is proportional to the quantity  $H/\bar{v}^2$ . In this ratio, plate height,  $H$ , is proportional to column diameter,  $d_c$ . Suppose that the column has optimum flow. Then  $\bar{v}_{\text{opt}}^2$  is<sup>6</sup> inversely proportional to  $d_c$  and in the relation  $\tau_{\text{opt}}^2 \propto H_{\text{opt}}/\bar{v}_{\text{opt}}^2$ , the column diameters in  $H_{\text{opt}}$  and  $\bar{v}_{\text{opt}}^2$  cancel each other. Consider, e.g., reduction in column diameter. It tends to reduce statistical zone broadening in *distance* proportional to the reduction in plate height. However, increased column pressure causes reduction in the carrier gas average velocity

(6) Schutjes, C. P. M.; Vermeer, E. A.; Rijks, J. A.; Cramers, C. A. *J. Chromatogr.* 1982, 253, 1–16.

(7) Guiochon, G.; Guillemin, C. L. *Quantitative gas chromatography for laboratory analysis and on-line control*; Elsevier: Amsterdam, 1988.

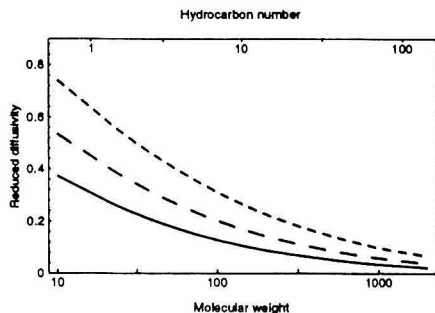


**Figure 1.** Reduced diffusivity,  $D_r$ , eq 10, of hydrocarbons in He (lower line),  $H_2$  (middle line) and in  $N_2$  (upper line). All data for collision diameters in eq 10 are taken from refs 3 and 4.  $d_m$ :  $2.88^{1/3} = 1.42$ ,  $7.07^{1/3} = 1.92$ ,  $17.9^{1/3} = 2.62$  for He,  $H_2$  and  $N_2$ , respectively, and  $d_0 = (3.96 + 20.46n)^{1/3}$  where  $n$  is hydrocarbon number.

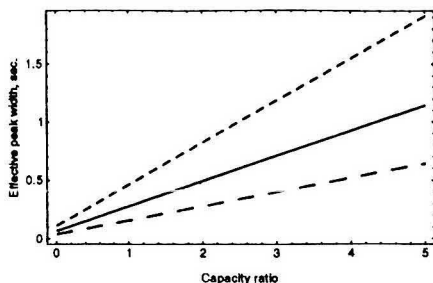


**Figure 2.** Effective peak width (area/height) of  $n$ -decane vs its capacity ratio at 100 °C for different carrier gases: middle line, He; lower line,  $H_2$ ; upper line,  $N_2$ . Effective peak width was calculated as  $(2\pi)^{1/2}\tau_{opt}$ , where  $\tau_{opt} = 2.5\tau_{opt}$ , where  $\tau_{opt}$  was calculated from eqs 15 and 13. Data for reduced diffusivity  $D_r$ , eq 10, were the same as in Figure 1.  $L = 10$  m.

(in spite of the mass flow increase). Reduced average velocity of the carrier gas proportionally reduces average velocity of migration of the solute. Reduced solute average velocity compensates for the reduction in the statistical zone broadening in distance resulting in unchanged peak width in time.

Graphical illustration of this discussion can be found in Figures 1–3. (Many commercially available integrators report peak width in units of  $w_{eff} = \text{area}/\text{height}$ , or effective peak width.<sup>8</sup> For Gaussian peaks,  $w_{eff} = (2\pi)^{1/2}\tau$ . To facilitate the comparison of the peak width values in Figures 2 and 3 with the experimentally available data, effective peak width is used in Figures 2 and 3.)

Notice that the simplicity of eqs 13 and 14 can be beneficial beyond the immediate needs of GC. For example, at  $k = 0$ , eq 14 becomes  $\tau_{min} = \tau_{min,ab}/D_r^{1/2}$ . Together with eq 10, it can be used as the basis for the alternative technique<sup>10</sup> of measurement of diffusion coefficients and collision diameters of gases.

**Boundaries for the Application of the Theoretical Results.** This theory requires high pressure drop, eq 1, and, therefore, strictly speaking, is valid only asymptotically when the ratio  $P_{in}/P_{out}$  approaches infinity (assuming, of course,

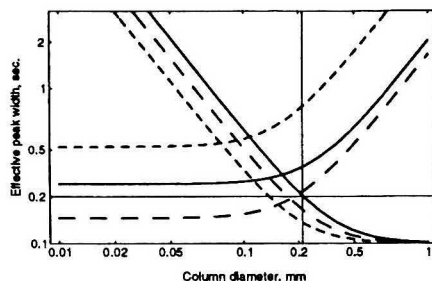


**Figure 3.** Effective peak widths,  $w_{eff}$  (rising curves), and inlet pressures,  $P_{in}$  (falling curves), vs column diameter,  $d_c$ , for  $n$ -decane at 100 °C with optimum flow, eq 5, of He (solid lines),  $H_2$  (long dashes), and  $N_2$  (short dashes).  $w_{eff}$  was calculated as  $w_{eff} = (2\pi)^{1/2}\tau_{opt}$  where  $\tau_{opt}$  was calculated from nonsimplified eqs 17 and 18 with  $D_{opt}$  calculated from known relations<sup>4</sup> and  $\eta$  taken from experimental data.<sup>11</sup>  $L = 10$  m. The horizontal line marks the level where  $P_{in} = 2P_{out} = 2$  atm. The vertical line at  $d_c = 0.21$  mm marks the intersection of the  $w_{eff,He}$  curve ( $w_{eff}$  for He) with the horizontal line. At this point,  $w_{eff,He} = 0.31$  s. To the left of this line (at  $d_c \leq 0.2$  mm)  $w_{eff,He}$  only slightly depends on  $d_c$ . Moving further to the left,  $P_{in}$  rapidly increases and the  $w_{eff,He}$  curve becomes practically flat (independent of  $d_c$ ) at  $w_{eff,He} = 0.24$  s.  $k = 1$ .

that the flow remains laminar). In practical calculations, though, one should take into account that most of the components in all equations have errors. Thus, the empirical equations for diffusivity alone can produce errors<sup>4</sup> of  $\geq 10\%$ . The errors in the analytical results from the theory fall within that range when  $P_{in}$  is 2 to 3 times higher than  $P_{out}$ , Figure 3.

Also included in the derivation of the general eq 11 were the assumptions that the carrier gas was ideal and thin stationary phase films were used. The former may exclude application of the theory to techniques, such as SFC (supercritical fluid chromatography), where behavior of the compressible mobile phase may significantly deviate from that of an ideal gas. The low film thickness can be essential for the validity of eq 11 for peaks with medium retention. However, it has no effect on the width of unretained or highly retained peaks.<sup>2</sup> Specifically, the film thickness does not affect the value of the absolute lower bound,  $\tau_{min,ab}$ , eq 13, for the peak width as that bound can be reached only by unretained solutes. Also, the film thickness does not affect the value,  $\tau_{min}(D_r, 0) = \tau_{min,ab}/(D_r)^{1/2}$ , eq 14, of the more accurate, solute-specific lower bound.

Other conditions in the theory, eqs 2 and 4, do not affect its general result, eq 11. Equation 4 was used in the derivation of the lower bounds, eqs 13 and 14, for the peak width. It can be viewed as the column overoptimization condition when these lower bounds can be achieved. Again, from the practical point of view,  $\tau$  in eq 11 gives a good approximation of the lower bounds in eqs 13 and 14 as long as column flow exceeds its Van Deemter optimum value by a factor of 2 or more.

Unlike all other conditions, the requirement in eq 2 that the molecular weights of a solute be larger than the molecular weight of the carrier gas may not be under the control of the operator and can be violated in practice (very light molecules migrate in, say, nitrogen). In the realistic GC, though, it almost never happens, especially with hydrogen or helium as a carrier gas. It must also be noticed that even the violation of this condition does not affect the expressions of the main results, eqs 11 and 13–16. Nor does it affect the conclusion of independence of peak widths and their lower bounds on the column diameter. It can only affect the accuracy of calculations if the simple formula, eq 10, was used instead of eq 9 for the calculation of the reduced diffusivity of the extremely light solutes.

(8) Blumberg, L. M. *Anal. Chem.* 1984, 56 (9), 1726–1729.

(9) Giddings, J. C.; Seager, S. L.; Stucki, L. R.; Stewart, G. H. *Anal. Chem.* 1960, 32, 867–870.

(10) Maynard, V. R.; Grushka, E. *Adv. Chromatogr.* 1975, 12, 99–140.

(11) Touloukian, Y. S.; Saxena, S. C.; Hestermans, P. *Viscosity*; IFI/Plenum: New York–Washington, 1975.

## CONCLUSION

The key conclusion in this report is: When optimization of a column flow in capillary GC requires high pressure drop, **widths of all peaks** depend on column length but **do not depend on column diameter**, as long as the column flow remains equal to or greater than its optimum value.

Expressions relating the peak widths and their lower bounds to the molecular properties of carrier gas and the solutes to be separated are derived and their implication is discussed.

## SYMBOLS

m	subscript indicating mobile phase
min	subscript indicating minimum
opt	subscript indicating optimum
out	subscript indicating column outlet
s	subscript indicating solute
D	diffusivity of a solute in a mobile phase, length <sup>2</sup> /time
D <sub>m</sub>	self-diffusivity of a mobile phase, length <sup>2</sup> /time
D <sub>r</sub>	reduced diffusivity of a solute, 1
d <sub>c</sub>	column internal diameter, length
d <sub>m</sub>	collision diameter of the mobile phase molecules, length
d <sub>s</sub>	collision diameter of the solute molecules, length
H	plate height, length
k	capacity ratio, 1
L	column length, length
M	molecular weight, mass/mole
N	column efficiency, 1
P	pressure, (mass/length)/time <sup>2</sup>
P <sub>in</sub>	column inlet pressure, (mass/length)/time <sup>2</sup>
R	gas constant (8.31431 J/K)/mol
T	temperature, temperature
t <sub>0</sub>	hold-up time, time
v	carrier gas velocity, length/time
$\bar{v}$	average carrier gas velocity, length/time
w <sub>eff</sub>	effective peak width, time
μ <sub>m</sub>	mean square speed of carrier gas molecules, length/time
η	carrier gas viscosity, (mass/length)/time
ρ	density, mass/length <sup>3</sup>
τ <sup>2</sup>	variance of a peak, time <sup>2</sup>

## APPENDIX

The following relations can be found in refs 7 and 9 and other text books on capillary GC

$$\tau^2 = \frac{9}{8} \frac{(P_{in}^4 - P_{out}^4)(P_{in}^2 - P_{out}^2)(1+k)^2 LH}{(P_{in}^3 - P_{out}^3)^2 \bar{v}^2},$$

$$P_{in}^2 = P_{out}^2 + \frac{64\eta\nu_{out}P_{out}L}{d_c^2},$$

$$\bar{v} = \frac{3}{2} \frac{P_{out}(P_{in}^2 - P_{out}^2)}{P_{in}^3 - P_{out}^3} \nu_{out} \quad (17)$$

$$H = \frac{2D_{out}}{\nu_{out}} + \frac{G(k)\nu_{out}d_c^2}{96(1+k)^2D_{out}}, \quad G(k) = 1 + 6k + 11k^2 \quad (18)$$

Equation 18 for  $H$  is valid for thin film columns only. Under condition eq 1, eqs 17 become

$$\tau^2 = \frac{9(1+k)^2 LH}{8\bar{v}^2}, \quad P_{in}^2 = \frac{64\eta\nu_{out}P_{out}L}{d_c^2},$$

$$\bar{v} = \frac{3}{2} \frac{P_{out}}{P_{in}} \nu_{out} \quad (19)$$

Combining the last two of these relations, one has

$$(\bar{v})^2 = \frac{9P_{out}^2\nu_{out}^2}{4} \frac{1}{P_{in}^2} = \frac{9P_{out}^2\nu_{out}^2}{4} \frac{d_c^2}{64\eta\nu_{out}P_{out}L} = \frac{9\nu_{out}^2P_{out}d_c^2}{256\eta L} \quad (20)$$

At the optimum carrier gas velocity, both additive terms on the right-hand side of the relation for  $H$ , eq 18, are equal to each other, i.e.

$$\frac{2D_{out}}{\nu_{out,opt}} = \frac{G(k)\nu_{out,opt}d_c^2}{96(1+k)^2D_{out}}$$

which allows for the following transformations of  $H$  in eq 18

$$H = \frac{2D_{out}}{\nu_{out,opt}} \frac{\nu_{out,opt}}{\nu_{out}} + \frac{G(k)\nu_{out}d_c^2}{96(1+k)^2D_{out}} = \frac{G(k)\nu_{out,opt}d_c^2}{96(1+k)^2D_{out}} \frac{\nu_{out,opt}}{\nu_{out}} + \frac{G(k)\nu_{out}d_c^2}{96(1+k)^2D_{out}} \left( \left( \frac{\nu_{out,opt}}{\nu_{out}} \right)^2 + 1 \right) \quad (21)$$

Substitution of eqs 20 and 21 in the expression for  $\tau^2$ , eq 19, yields

$$\tau^2 = \frac{9(1+k)^2}{8} LH \left( \frac{1}{\bar{v}} \right)^2 = \frac{9(1+k)^2 L}{8} \times \frac{G(k)\nu_{out}d_c^2}{96(1+k)^2D_{out}} \left( 1 + \left( \frac{\nu_{out,opt}}{\nu_{out}} \right)^2 \right) \frac{256\eta L}{9\nu_{out}P_{out}d_c^2} = \frac{\eta L^2 G(k)}{3D_{out}P_{out}} \left( 1 + \left( \frac{\nu_{out,opt}}{\nu_{out}} \right)^2 \right)$$

RECEIVED for review January 25, 1993. Accepted June 23, 1993.



# Ascorbic Acid Interferences in Hydrogen Peroxide Detecting Biosensors Based on Electrochemically Immobilized Enzymes

Francesco Palmisano and Pier G. Zambonin\*

Laboratorio di Chimica Analitica, Dipartimento di Chimica, Università degli Studi di Bari, Trav. 200 Re David, 4 70126 Bari, Italy

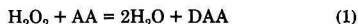
In spite of extensive research in mediated<sup>1-3</sup> and conducting salt<sup>4-7</sup> enzyme electrodes, peroxide detecting amperometric devices based on immobilized enzyme electrodes still remain the most common form of glucose biosensors. Hydrogen peroxide based glucose sensors pose, however, a challenge to eliminate faradaic interferences resulting from the presence of electrochemically active endogenous or exogenous compounds. Unfortunately, amperometric detection of hydrogen peroxide requires a rather positive applied potential: any substance capable of being oxidized at +650 mV vs SCE at a platinum surface (e.g. ascorbic acid, uric acid, cysteine, and acetaminophen<sup>8</sup>) may possibly act as an interferent.

In conventional glucose biosensors, faradaic interference effects are normally tackled by the use of discrete membranes (e.g. cellulose acetate) improving sensor discrimination against such interferences. An additional membrane, covering and protecting the enzyme layer, is also normally used.<sup>9</sup> However even in this "complete" configuration the sensor still suffers from residual faradaic interference effects which are particularly severe for acetaminophen.

The possibility of a one-step preparation of a glucose sensor has recently been demonstrated in the authors' laboratory.<sup>10,11</sup> It is based on the electrodeposition of a poly(*o*-phenylenediamine) (PPD) membrane able to entrap glucose oxidase (GOx) and to reject electroactive interferences and electrode fouling species (e.g. proteins). Reference 10 describes a new approach in immobilized enzyme sensors, namely the use of electrochemically grown nonconducting films as enzyme entrapment and permselective membranes.<sup>12</sup> The usefulness of this sensor for flow injection analysis of undiluted human serum (*i.e.* in the presence of proteins and several electroactive interferences) has been demonstrated.<sup>11,12</sup> Furthermore the sensor was characterized<sup>10</sup> by an unusually low response time of around 1 s.

Working in batch, an additional effect of ascorbic acid (AA), a depression of the response of immobilized enzyme biosensors based on hydrogen peroxide detection, was recently observed by Lowry and O'Neill.<sup>13</sup> On the basis of their studies they hypothesized that the H<sub>2</sub>O<sub>2</sub> produced at enzyme electrodes

can be depleted by a competing homogeneous reaction involving AA



*i.e.* consumption of electroactive species and production of the electroinactive dehydroascorbic acid (DAA).

These authors draw their general conclusions on a glucose sensor based on GOx immobilized in electropolymerized PPD with the procedure described in ref 10. We also observed<sup>10</sup> a depletion effect caused by a batch addition of AA, tentatively ascribed to a homogeneous phase reaction involving AA and O<sub>2</sub> which, however, proved too slow in the absence of proper catalysts<sup>14,15</sup> to significantly influence the sensor response. However even the kinetic data reported by Lowry and O'Neill (pseudo-first-order half-life time ca. 1 min) or by Tsukura et al.<sup>14</sup> (initial rate, at 1 mM in both reactants, around 10<sup>-8</sup> mol dm<sup>-3</sup> s<sup>-1</sup>) seem to indicate that even reaction 1 is too slow to markedly influence the Pt/GOx/PPD sensor whose response time<sup>10</sup> is on the order of a second.

We felt another effect was at the origin of the phenomena of current depression observed when working in batch.

In the following we show that the negative bias introduced by AA can be ascribed to "sensor modifications" caused by AA electrooxidation. Indirect (electrochemical) evidence and direct (ESCA) evidence show electrode fouling by products of AA electrooxidation.

## EXPERIMENTAL SECTION

**Reagents.** Glucose oxidase (GOx) from *Aspergillus niger*, type VII-S,  $\beta$ -D-glucose, ascorbic acid, and acetaminophen were obtained from Sigma Chemical Co. Glucose stock solutions were prepared and allowed to mutarotate at room temperature overnight before use. *o*-Phenylenediamine was obtained from Aldrich and purified before use by vacuum sublimation at 90 °C. All the other chemicals were of analytical grade. All the experiments were run in a phosphate buffer (*I* = 0.2 M, pH = 7.0). AA solutions were prepared immediately before use in containers protected from light by aluminum foil in order to avoid photoinduced oxidation.<sup>14,15</sup>

**Apparatus.** Unless otherwise specified the same electrochemical and ESCA systems described in refs 10 and 12 were used. XPS spectra were obtained on a Pt foil electrode, Ar<sup>+</sup> sputtered to reduce surface contamination, polarized at +0.65 V vs Ag/AgCl in a buffered ascorbate solution, then extracted under applied potential, rapidly washed with triple distilled water, and dried in nitrogen atmosphere just before introduction into the analysis chamber of the ESCA machine. Peak area values used for the determination of stoichiometric C/O ratios were corrected for the relevant sensitivity factors. In all experiments involving ascorbic acid the electrochemical cell was protected from light.

**Sensor Preparation.** GOx was immobilized in PPD films on a bare Pt disk electrode (1 mm diameter) as previously described.<sup>10</sup>

## RESULTS AND DISCUSSION

In agreement with the findings of Lowry and O'Neill,<sup>13</sup> calibration curves obtained by batch addition of glucose to

(1) Cass, A. E. G.; Davis, G.; Francis, G. D.; Hill, H. A. O.; Aston, W. J.; Higgins, I. J.; Plotkin, E. V.; Scott, L. D.; Turner, A. P. F. *Anal. Chem.* 1984, 56, 667.

(2) Cenas, N. K.; Pocius, A. K.; Kulyš, J. J. *J. Electroanal. Chem.* 1984, 173, 583.

(3) Hill, H. A. O.; Sanghera, G. S. In *Biosensors: A Practical Approach*; Cass, A. E. G., Ed.; Oxford University Press: New York, 1990; pp 19-46.

(4) Albery, W. J.; Bartlett, P. N.; Craston, D. H. *J. Electroanal. Chem.* 1985, 194, 223.

(5) Cenas, N. K.; Kulyš, J. J. *J. Electroanal. Chem.* 1981, 128, 103.

(6) Gunasingham, H.; Tan, C. *Anal. Chim. Acta* 1990, 229, 83.

(7) Boutelle, M. G.; Stanford, C.; Fillen, M.; Albery, W. J.; Bartlett, P. N. *Neurosci. Lett.* 1986, 72, 283.

(8) Moatti-Sirat, D.; Velho, G.; Reach, G. *Biosens. Bioelectron.* 1992, 7, 345.

(9) Bindra, S. D.; Zhang, V.; Wilson, G. S.; Stemberg, R.; Thevenot, D. R.; Moatti, D.; Reach, G. *Anal. Chem.* 1991, 63, 1692.

(10) Malitesta, C.; Palmisano, F.; Torsi, L.; Zambonin, P. G. *Anal. Chem.* 1990, 62, 2735.

(11) Centonze, D.; Guerrieri, A.; Malitesta, C.; Palmisano, F.; Zambonin, P. G. *Ann. Chim. (Rome)* 1992, 82, 219.

(12) Centonze, D.; Guerrieri, A.; Malitesta, C.; Palmisano, F.; Zambonin, P. G. *Fresenius J. Anal. Chem.* 1992, 342, 729.

(13) Lowry, G. P.; O'Neill, R. D. *Anal. Chem.* 1992, 64, 453.

(14) Tsukahara, K.; Wada, Y.; Kimura, M. *Bull. Chem. Soc. Jpn.* 1991, 64, 908.

(15) Deutschm J. C.; Kolhouse, F. J. *Anal. Chem.* 1993, 65, 321.

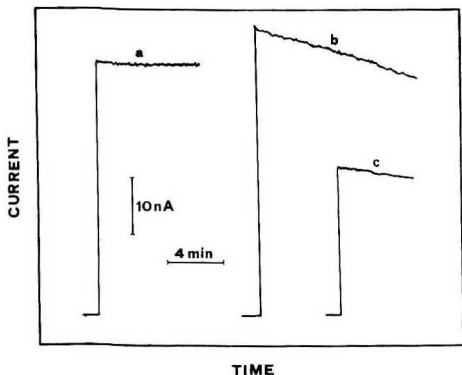


**Figure 1.** (a) Current-time response obtained on a Pt/GOx/PPD sensor (1 mm diameter) after addition of 10 mM glucose to a stirred phosphate buffer (pH = 7.0). (b) Current-time response obtained on the same sensor after the simultaneous addition of 10 mM glucose + 0.5 mM ascorbic acid to the stirred phosphate buffer. (c) Current-time response obtained after the addition of 10 mM glucose to the stirred phosphate buffer containing 0.5 mM AA. Before glucose addition the sensor was "conditioned" in the AA containing buffer for about 30 min at an applied potential of  $-0.7$  V vs Ag/AgCl.

a buffer containing 0.5 mM AA showed a lower sensitivity (i.e. reduced  $V_{\max}$ ) compared to those run in the absence of AA. However, the apparent loss in sensitivity of the electrode was found to be time dependent. In particular, the longer the time used to "stabilize" the electrode in the presence of AA before glucose addition, the more pronounced was the observed current depression.

Curve a in Figure 1 shows the current-time response of a Pt/GOx/PPD electrode for a rapid batch addition of 10 mM G to a stirred phosphate buffer; curve b shows the current-time response obtained on the same electrode after the simultaneous addition of 10 mM G + 0.5 mM AA; curve c shows the current-time response after addition of 10 mM G to a buffered 0.5 mM AA solution in which the electrode had been previously "conditioned" (electrooxidation of AA at the Pt electrode) for a certain time. Note that the maximum signal reached in this last case is lower than the steady-state value reached in curve a; also worth noting is that the signal is time dependent. Up to a certain limit (*vide infra*) the higher the "conditioning time" of the sensor in the presence of ascorbic acid, the lower were found both the maximum level reached in curve c after addition of glucose and the drift of the relevant current-time curve.

A time dependence was also found for the Pt/GOx/PPD response to AA only; instead of the expected square wave shape, a monotonically falling transient was obtained.

Recovery of the depressed glucose signal could, however, be observed as soon as the AA was removed; a signal similar to that of curve c in Figure 1 tends to slowly reach (typically in about 30 min) the response of a new sensor (e.g. that of curve a in Figure 1) when the conditioned sensor is brought in contact with a buffered glucose solution not containing AA.

Similar effects were observed on a bare Pt electrode. Figure 2A shows the time dependence of the AA response at a Pt RDE; Figure 2B shows that a response similar to Figure 2A was obtained when the same electrode was left for 8–10 min in a phosphate buffer not containing AA. Similar results were obtained at a stationary Pt foil electrode in a stirred solution. These current depression phenomena and their relevant "reversibility" observed at a bare electrode are interpreted as resulting from modification of the Pt surface.

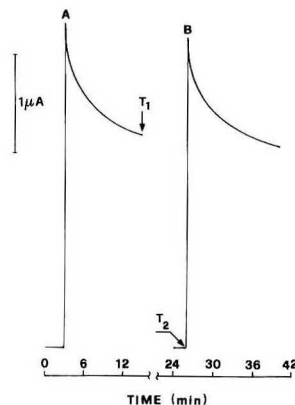


**Figure 2.** Current-time profiles obtained at a Pt RDE: applied potential, 0.65 V vs Ag/AgCl; rotation speed, 500 rpm. The maximum current level A was obtained just after addition of AA (final concentration 0.5 mM) to a phosphate buffer. At time  $T_1$  the AA containing buffer was removed and the electrode was rapidly washed, unwired, and then left in contact with a new aliquot of the buffer solution only added to the cell. At time  $T_2$  a new AA addition (final concentration 0.5 mM) was performed and the maximum current level B obtained.

Ascorbic acid is oxidized at Pt electrodes through a two-electron, two-proton reaction giving DAA which subsequently can form a dimer and/or convert into its mono- or dihydrated forms.<sup>16–19</sup> Desorption of DAA has been reported as the rate-determining step;<sup>16</sup> ref 19 gives evidence for the formation of adsorbed poisoning species. This information,<sup>16–19</sup> as well as the experimental findings reported in the present work, indicates that the observed signal depression phenomena can be ascribed to a sensor modification caused by the oxidation of AA with consequent fouling of the Pt surface by the products of the electrode reaction.

Direct evidence of electrode fouling was provided by ESCA measurements. Figure 3A shows the C1s region of an ESCA spectrum obtained on a Pt foil (our blank) cleaned in the analysis chamber of the ESCA machine by Ar ion sputtering. A residual, light surface contamination by hydrocarbons (peak 1) and C–OH containing substances (peak 2) is still present likely because of "knock-on" effects; no traces of C=O and O–C=O groups were detectable. Figure 3B shows the ESCA C1s spectrum recorded on the sputtered Pt foil, previously analyzed as blank and then used as an electrode, polarized for about 12 min at  $+0.65$  V vs Ag/AgCl in a buffer containing 0.5 mM of AA (situation corresponding to time  $T_1$  in Figure 2). Other than the unavoidable increase of the CH component (peak 1) due to hydrocarbons always present in the analysis chamber and of no significance in the present context, Figure 3B clearly indicates a net increase of the peaks 2, 3, and 4 and then the presence of an adsorbate containing C–O, C=O, and O–C=O functionalities as would be expected in the case of the electrooxidation product of AA. The same ESCA experiments performed to correspond to time  $T_2$  in Figure 2 (i.e. after maintaining for few minutes the Pt foil, used to electrooxidize AA, unwired and in contact with an AA free buffer solution) showed a C1s spectrum not different from

(16) Karabinas, P.; Jannakoudakis, D. *J. Electroanal. Chem.* 1984, 160, 159.

(17) Valls, M. J.; Feliu, J. M.; Aldaz, A.; Climent, M. A.; Clavilier, J. *J. Electroanal. Chem.* 1989, 260, 237.

(18) Takamura, K.; Sakamoto, M. *J. Electroanal. Chem.* 1980, 113, 273.

(19) Brezina, M.; Koryta, J.; Loucka, T.; Marsikova, D. *J. Electroanal. Chem.* 1972, 40, 13.

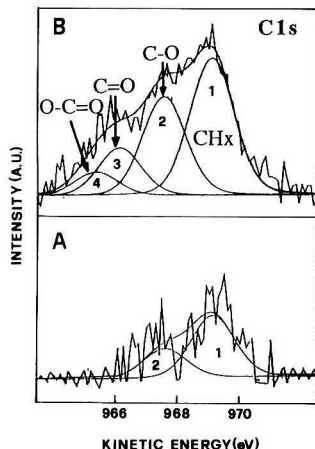


**Figure 3.** C1s region of the ESCA spectrum recorded on (A) Pt foil sputtered with Ar ions in the analysis chamber of the ESCA machine and (B) Pt foil electrode (the same used in part A) removed from the electrochemical cell at time  $T_1$  during an experiment similar to the one described in Figure 2.

the blank reported in Figure 3A. The absence of an adsorbate under the last conditions represents a direct proof of the "reversibility" of the adsorption (fouling) phenomenon.

It is worth noting that the experiment described in Figure 3B is performed under conditions (probably less than a monolayer of adsorbate) close to the instrumental limits of the ESCA technique. Results of Figure 3B are qualitative (*i.e.* evidence of an adsorbate containing C—O, C=O, and O—C=O functionalities) but are more difficult to treat in a quantitative way because of the modest signal-to-noise ratio. With this limit in mind, an identification of the adsorbed species (DAA, mono- or dihydrated DAA and dimeric DAA) has been however attempted. The peak area values for the C—O, C=O, and O—C=O components (measured in Figure 3B after blank correction) are close to the ratios 3:2:1, respectively. Furthermore the ratio between the total areas of these three carbon species and the total O1s peak area (corrected for the contribution of Pt oxide and of the C—OH component in the blank) was found to be C/O = 0.7. The expected ratios of the different C signals are 3:2:1 for DAA or its mono- and dihydrated form while the relevant stoichiometric C/O ratios are 1, 0.87, and 0.75, respectively. For the DDA dimer the corresponding ratios are expected to be 7:3:2 and 0.92. The above findings seem to indicate that a hydrated form of DAA is perhaps the most probable adsorbed species.

The evidence given above supports the model of reversible poisoning of the electrode by AA electrooxidation products. On the basis of this model, a reasonable self-consistent interpretation of the experimental findings can be offered. The "time dependence" of the current depression effects obtained in the presence of AA (*vide ante*) is accounted for by the "AA preconditioning time" of the sensor. In particular the results in Figure 1 can be rationalized as follows: the additivity of G and AA signals (pure faradaic effect) is observed in curve b just after the G + AA addition, after which a continuous decrease of the total signal occurs. These results, which might be interpreted as due to  $H_2O_2$  depletion through a homogeneous reaction, are ascribed to a continuous change in the sensor status caused by electrode fouling resulting from AA electrooxidation causing a more or less marked depression of all signals. Likewise the results of Figure 1c (addition of G to a buffer containing AA) can be explained on the basis of the given model; the preconditioning of the sensor (electrode partially fouled before the addition of G) accounts for (i) the initial current level less than the plateau of Figure 1a and (ii) the less pronounced signal drift with respect to Figure 1b.

The conclusions of the present paper are that the electrode fouling, caused by AA electrooxidation products, influences the response of Pt based  $H_2O_2$  detecting biosensors and can represent a potential problem particularly at very high ascorbate concentrations. Slow homogeneous processes, such as reaction 1, are unlikely to significantly influence a fast-response sensor;<sup>10-12</sup> however, on the basis of the kinetic data given in ref 13, an additional signal depression effect, due to  $H_2O_2$  chemical depletion, cannot be "*a priori*" excluded for sensors characterized by high response time.

Obviously the ultimate goal is the design of an electropolymerized membrane able to reject ascorbate without blocking the access of glucose to the immobilized enzyme. Work in progress in our laboratory indicates that biosensors based on overoxidized polypyrrole films, previously<sup>12</sup> found to be very efficient in rejecting ascorbate and other interferents in flow injection analysis, can also permit an accurate glucose determination in both batch and continuous flow systems including *in vivo* subcutaneous monitoring through microdialysis sampling.

#### ACKNOWLEDGMENT

D. Centonze and C. Malitesta are gratefully acknowledged for experimental help and useful discussions. Work was carried out with financial assistance from the CNR target project "Biotechnology and Bioinstrumentation".

RECEIVED for review April 27, 1993. Accepted June 29, 1993.

## TECHNICAL NOTES

### On-Line Peptide Mapping by Capillary Zone Electrophoresis

Lawrence N. Amankwa<sup>1</sup> and Werner G. Kuhr\*

Department of Chemistry, University of California, Riverside, California 92521

#### INTRODUCTION

Recently, we described an analytical procedure for immobilizing a proteolytic enzyme (trypsin) on the inner surface of a 50- $\mu\text{m}$ -i.d. fused-silica capillary for on-line digestion of picomole quantities of protein.<sup>1</sup> Trypsin was immobilized onto the surface of an aminoalkylsilane-treated fused-silica capillary via biotin-avidin-biotin technology. Subsequently the enzyme-modified capillary was used to digest  $\beta$ -casein simply by flowing a protein solution through it at a rate of 40 nL/min and collecting the effluent. This effluent contained the peptide fragments of the protein, which could be separated by capillary zone electrophoresis (CZE) to yield the tryptic map for characterization and identification of the protein. This method has numerous advantages over traditional homogeneous methods used for digesting proteins:<sup>2</sup> (1) the enzyme-modified fused-silica microreactor can be used for repeated digestions; (2) the eluted digest is totally free from contamination by the proteolytic enzyme; (3) the small size of the reactor makes it especially compatible for use in the analysis of small quantities (picomole) of protein as well as for analysis of small volumes of samples (typically, a few nanoliters). These advantages are particularly important when one is ascertaining subtle differences in protein structure (e.g., differences of a single residue between homologous proteins or differences resulting from posttranslational modifications).<sup>3,4</sup>

In our previous application of this enzyme-modified capillary reactor, the effluent (digest) from the reactor was collected in a microvial before reinjection onto a separation column for subsequent separation of the peptide fragments by CZE. It is obvious that this step, the collection of the effluent, will not only be impractical but will also be highly susceptible to sample loss and/or contamination, especially when one is confronted with the analysis of nanoliter-scale samples. Thus, it would be of great practical utility to be able to perform the digestion on-line with the separation of the digest. Several investigators have also explored the possibility of performing enzyme-mediated chemistry on-line with an electrophoretic separation. Nashabeh and El Rassi<sup>5</sup> have described a technique involving enzymophoresis of nucleic acids by tandem capillary enzyme reactor-capillary electrophoresis. Guzman et al. have used an on-line concentrator-reactor cell to perform digestions of nanogram quantities of protein on-line with a CZE separation.<sup>6</sup> The

coupling configuration described in these systems does not allow the use of different buffer components and/or pH's during the enzymatic reaction stage and during the separation stage. This requirement is particularly important in many enzyme reactions, since the pH required for optimum catalytic activity of the immobilized enzyme is generally different from that required for the separation of products from the reaction. This is especially true for digestions involving trypsin, since it has the greatest catalytic activity at pH's between 8 and 9 while the best separation for the peptide digest lies in the lower pH range (pH 2-4).<sup>4</sup>

The simplest way to use different buffers in the digestion and separation processes is to break the system into two distinct parts and couple the two capillaries together via a fluid joint. Numerous techniques for coupling micron-size fused-silica capillaries have been reported in the literature.<sup>7-11</sup> Unfortunately, none of these designs could be used for such an on-line sample introduction since it is important to have both quantitative mass transfer of sample across the joint when the sample is injected and complete isolation between the sample and the separation capillaries during the electrophoretic separation. Recently, we described a simple technique for transferring a solute across a wide capillary junction (ca. 50-200  $\mu\text{m}$ ).<sup>12</sup> The two capillaries were placed in close proximity by careful micropositioning, and the distance between them was controlled to submicron resolution. Very little diffusional sample loss in the gap was observed at low ionic strength, since the voltage gradient across the gap is large and the sample had little time for radial diffusion out of the junction. The utility of this approach is that it not only offers efficient mass transfer of the sample by electromigration but should also allow subsequent separation of the transferred sample in the second capillary without the need to move either capillary.

In this report, we have used the technique described above for coupling our enzyme-modified capillary reactor to a CZE fused-silica capillary for use for on-line protein digestion and separation of the digest by CZE. The enzyme-modified fused-silica microreactor was coupled through a 100- $\mu\text{m}$  solution gap to the separation capillary. First, the enzyme-modified capillary was filled with the protein solution and allowed to incubate at room temperature for  $\sim 2$  h, during which time proteolysis occurs. Subsequently, an aliquot of the digest was injected onto the separation capillary by applying a potential across the two free ends of both capillaries. The injected sample was then separated by applying the CZE

\* Current address: University of British Columbia, Biomedical Research Centre, 2222 Health Sciences Mall, Vancouver, British Columbia, V6T 1Z3 Canada.

(1) Amankwa, L. N.; Kuhr, W. G. *Anal. Chem.* 1992, 64, 1610-1613.  
(2) Cobb, K. A.; Novotny, M. *Anal. Chem.* 1989, 61, 2226-2231.  
(3) Huberman, A.; Aguilar, M. B. *J. Chromatogr.* 1988, 443, 337-342.  
(4) Wheat, T. E.; Young, P. M.; Astephen, N. E. *J. Liq. Chromatogr.* 1991, 14, 987-996.

(5) Nashabeh, W.; El Rassi, Z. *J. Chromatogr.* 1992, 596, 251-264.  
(6) Guzman, N. *Sixth Annual Symposium of the Protein Society* 1992, T-92. Guzman, N.; Hernandez, L.; Advis, J. P. *HPCE'93* 1993, W-58.

(7) Olefirowicz, T. M.; Ewing, A. G. *Anal. Chem.* 1990, 60, 1872-1876.

(8) Wallingford, R. A.; Ewing, A. G. *Anal. Chem.* 1987, 59, 1762-1766.

(9) Pentoney, S. L.; Huang, X.; Burgi, D. S.; Zare, R. S. *Anal. Chem.* 1988, 60, 2625-2630.

(10) Nickerson, B.; Jorgenson, J. W. *J. Chromatogr.* 1989, 480, 157-168.

(11) Albin, M.; Weinberger, R.; Saap, E.; Moring, S. *Anal. Chem.* 1991, 63, 417-422.

(12) Kuhr, W. G.; Licklider, L.; Amankwa, L. *Anal. Chem.* 1993, 65, 275-282.

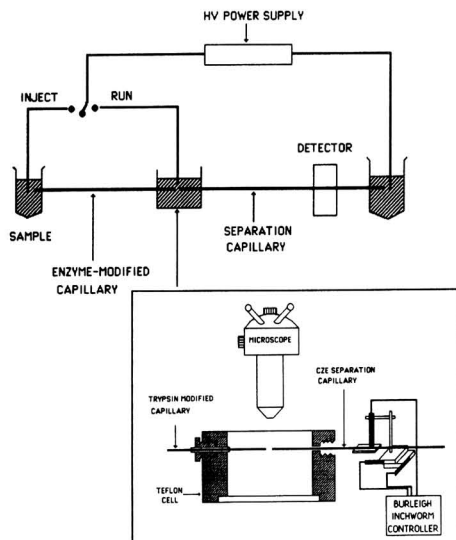


**Figure 1.** Schematic diagram of the coupled capillary CZE instrument. Two segments of 50- $\mu\text{m}$ -i.d. fused-silica capillary (one 50-cm segment used as a microreactor, the other 75-cm segment used as the separation column for CZE) were coupled via a fluid joint, which contained either distilled water or a 10-fold dilution of the separation buffer. Inset: A detailed schematic of the Teflon cell in which the digestion and the separation capillaries were coupled. One capillary was secured to the cell, while a three-axis Burleigh inchworm controller (roughly 50-nm step resolution) was used to align the end of the other capillary within either 1 (touching) or 100  $\mu\text{m}$  of the end of the first capillary. A stereomicroscope was used to visually inspect the positioning. Other details are given in the text.

separation potential across the gap solution and the other end of the separation capillary. Using this approach, we were able to perform on-line digestion and separation of picomole quantities protein by CZE in less than 3 h.

## EXPERIMENTAL SECTION

**Chemicals and Reagents.** Water was distilled and deionized (Millipore, Bedford, MA). Sodium bicarbonate, ammonium bicarbonate, sodium phosphate (monobasic and dibasic), acetone, ethylene glycol, and methanol were obtained from Fisher Scientific (Fairlawn, NJ). Hexadimethrine bromide (Polybrene),  $\beta$ -casein, trypsin (biotin-labeled), and ExtrAvidin were obtained from Sigma (St. Louis, MO); sulfosuccinimidyl 6-(biotinamido)-hexanoate (NHS-LC-biotin) was obtained from Pierce (Rockford, IL); sodium cyanide (Mallinkrodt, Paris, KY), 3-(aminopropyl)-triethoxysilane, (3-APTS; Aldrich Chemical Co., Milwaukee, WI), and 2,3-naphthalenedialdehyde (NDA; Molecular Probes, Inc., Eugene, OR) were used as received without further purification.

**Supplies and Equipment.** The CZE apparatus (Figure 1) used in this work was built locally and has been described in an earlier report.<sup>13</sup> Basically, it consists of a high-voltage power supply ( $\pm 50$  kV; Glassman High Voltage Inc., Model PSEH50R02.0, Whitehouse, NJ). The high-voltage end was isolated in a Plexiglas enclosure with an interlock on the door to ensure operator safety. Fused-silica capillary (50- $\mu\text{m}$  i.d., 360- $\mu\text{m}$  o.d.; Polymicro Technologies, Phoenix, AZ) was used for construction of the enzyme-modified microreactor or as the separation capillary.

**Trypsin-Modified Microreactor.** A detailed description of the procedure for immobilizing trypsin onto a fused-silica capillary was given previously.<sup>1</sup> Briefly, biotinylated trypsin was immobilized onto the inner surface of a fused-silica capillary that had

previously been treated successively with 3-APTS, biotin, and avidin. The 3-APTS treatment provided free amines on the surface of the capillary, allowing the covalent attachment of biotin through an amide bond. This was accomplished by perfusing the capillary with a 5.0 mg/mL solution of NHS-LC-biotin in 0.05 M  $\text{NaHCO}_3$  (pH 8.6) for 4 h at room temperature. After this treatment the capillary was rinsed with water and then treated with a 4 mg/mL solution of avidin in 0.05 M sodium phosphate buffer (pH 7.4) at a rate of  $\sim 40$  nL/min for 24 h at 4  $^\circ\text{C}$  using gravity flow. Finally, the avidin-coated capillary was rinsed with distilled water and then treated for 24 h at 4  $^\circ\text{C}$  with a 10 mg/mL solution of biotin-labeled trypsin in sodium phosphate buffer. Unbound trypsin was rinsed (by vacuum suction) from the capillary with  $\sim 10$  column volumes of buffer (0.05 M sodium phosphate, pH 7.4) and stored in the refrigerator until ready to use. This procedure produces a layer of trypsin bound to the surface of the capillary without exposing trypsin to the harsh chemicals necessary for the silica modification, thereby greatly increasing the viability of the surface-bound enzyme. Finally, a 10 mM aqueous solution of glycine was flowed through the digestion capillary for  $\sim 10$  min in order to block adsorption sites introduced during the enzyme immobilization process in the preparation of the reactor. This treatment has significantly reduced the effects of adsorption of small molecules, as reflected in shorter elution times of amino acids and peptides. However, no significant change in the migration of proteins was observed through the column. This might be expected, since proteins bind with some affinity to the active site of trypsin, which is on the capillary surface.

**Coupling Microreactor and Separation Capillaries.** The coupling of the microreactor and the separation capillaries was accomplished in a specially designed and electrically insulated Teflon cell (Figure 1, inset; total volume of  $\sim 10$  mL of buffer). One end of the enzyme-modified capillary reactor was rigidly connected to the Teflon cell. The separation capillary was mounted onto a three-axis micropositioner utilizing Burleigh inchworm motors (Burleigh, Fisher Park, NY). One end of the separation capillary was then inserted through a hole in this cell such that one end was directly aligned with that of the enzyme-modified capillary. The junction between the two capillaries was viewed through a stereomicroscope with a help of a microscope illuminator focused onto a diffusely reflective target located underneath the Teflon cell. The separation between the two capillaries was controlled with submicron resolution. The entire Teflon cell housing the capillary junction was mounted on four Kel-F supports attached to a Plexiglas platform to ensure complete electrical isolation of the capillary junction from ground.

**Preparation Of Tryptic Digest.** A 2 mg/mL solution of  $\beta$ -casein in 0.050 M ammonium bicarbonate buffer (pH 8.0) was boiled for 10 min in a water bath to denature the protein. A 150- $\mu\text{L}$  aliquot of the resulting solution was placed in a 200- $\mu\text{L}$  glass vial made from the tip of a Pasteur pipet. A 50-cm length of the enzyme-modified capillary was rinsed with ammonium bicarbonate buffer, and one end was connected to the vial containing the protein sample. The free end of the microreactor was connected to a house vacuum line in order to fill it by suction with the protein solution. Subsequently, the vial containing the protein solution was elevated relative to the other free end of the capillary reactor to ensure slow hydrodynamic flow ( $\sim 40$  nL/min) of the protein solution through the reactor into another vial. After  $\sim 5$  column volumes (5  $\mu\text{L}$ ) of the protein solution had flowed through the reactor, the free end of the capillary reactor was carefully connected to the Teflon cell while sample solution was still flowing through it, as shown in the inset of Figure 1. Following this, the two ends of the capillary reactor were leveled and maintained at the same height to minimize any nonelectroosmotic flow.

**Capillary Electrophoresis Separation.** All CZE separations were performed in fused-silica capillaries which were cleaned with 1 M NaOH and distilled water prior to use. All capillaries were dynamically modified with a cationic polymer by flowing either a MicroCoat solution (Applied Biosystems, Inc.) or a 2% solution of Polybrene in 2% ethylene glycol solution through the capillary for 30 min, followed by a 5-min distilled water rinse and a 10-min equilibration with the appropriate separation buffer (90 mM sodium phosphate, pH 7.4).

(13) Amankwa, L.; Scholl, J.; Kuhr, W. G. *Anal. Chem.* 1990, 62, 2189-2193.



Digest samples that were prepared off-line were injected into the separation capillary via electromigration. On-line injection of digests were accomplished as follows (Figure 1). Prior to on-line sample injection, the capillary was filled with the protein solution. Next, the ends of the capillary reactor and the separation capillary were brought to within 100  $\mu\text{m}$  of each other. Injection was performed by applying a high voltage ( $\sim 20$  kV) across both capillaries for a preset time ( $\sim 1$  min). During this time, an aliquot of the digest in the capillary reactor was transferred across the solution gap between the two capillaries into the separation capillary. During injection, the buffer in the Teflon cell was a 10-fold dilution of the buffer used for separation (yielding 9 mM sodium phosphate, pH 7.4). After injection, the buffer surrounding the capillary junction was carefully replaced with the separation buffer. The separation was then accomplished by applying a potential across only the separation capillary.

Detection was either by fluorescence or by UV absorbance. In cases where fluorescence was used, the peptides resulting from the tryptic digest were labeled with NDA prior to injection onto the separation capillary. Fluorescence detection was performed as described previously. Briefly, the 442-nm (50.6-mW) output of a HeCd laser (Omnichrome, Model 2056-8/25M, Chino, CA) was focused with a 1-cm focal-length quartz lens onto a spot 10 cm from the downstream end of the separation capillary (which has been previously cleared of the polyimide coating). The fluorescence signal was imaged through a 10 $\times$  microscope objective, a spatial, and two long-pass glass filters (Schott, No. G6495) onto a photomultiplier tube (Hamamatsu, R928). UV absorbance detection was accomplished on a locally assembled UV detector, essentially consisting of components of the detector for an Applied Biosystems Model 270A UV detector. Data were recorded on a strip chart recorder (Kipp & Zonen).

## RESULTS AND DISCUSSION

This work deals with the on-line digestion, injection, and separation of peptide digests. By performing all these steps on-line, one will be able to overcome most of the typical problems such as sample loss and contamination that normally plague the analysis of minute quantities of protein samples. On-line digestion is particularly advantageous in peptide mapping because of the high reproducibility requirement of the maps, and also because of the ever decreasing sizes of protein samples that are becoming available to the medical, bioanalytical, and the biotechnological communities. Several other investigators have already explored the possibility of performing enzyme-mediated chemistry on-line with an electrophoretic separation. Guzman et al. have reported the use of an on-line concentrator-reactor cell to perform digestions of nanogram quantities of protein on-line with a CZE separation.<sup>6</sup> Nashabeh and El Rassi<sup>5</sup> have described a technique involving enzymophoresis of nucleic acids by tandem capillary enzyme reactor-capillary electrophoresis. Ribonuclease T1, hexokinase, and adenosine deaminase were successfully immobilized on the inner walls of a short fused-silica capillary through glutaraldehyde attachment. In that report, the enzyme-modified capillary reactor was coupled in series with a CZE separation capillary via a PTFE tube, where substrates were introduced as thin plugs into the enzyme-modified capillary reactor. The catalyzed reaction occurred as the substrates migrated down the reactor either by hydrodynamic flow or by electromigration pass the connection point. The joint was then disconnected, and the separation of the enzymatic reaction products was subsequently performed by immersing the separation capillary in buffer. It is important to note that the coupling configuration used in these reports does not allow the use of different buffer components and/or pH's during the enzymatic reaction stage and during the separation stage. This requirement is particularly important in protein digestion, since the pH required for optimum catalytic activity of the immobilized

enzyme is generally different from that required for the separation of products from the reaction. This is especially true for digestions involving trypsin, since it has the greatest catalytic activity at pH's between 8 and 9 while the best separation for the peptide digest course in the lower pH range (pH 2–4).<sup>4</sup>

The simplest way to use different buffers in the digestion and separation processes is to break the system into two distinct parts, and couple the two capillaries together via a fluid joint. Numerous techniques for coupling micron-size fused-silica capillaries have been reported in the literature. Most of these designs involve mass transfer across a "tight electrically conductive joint" which was first developed for use with postcolumn electrochemical detectors for CZE.<sup>6–8</sup> Although, mass transfer across these joints (from one capillary segment to another) has been shown to be highly quantitative, mass transfer of buffer from the bathing solution into the capillary has proven to be very difficult because of the short distance between these joints (typically  $< 1 \mu\text{m}$ ). To overcome this problem, larger capillary joints (10–50  $\mu\text{m}$ ) have been developed for introducing various reagents surrounding these joints into the inside of the capillary.<sup>9–11</sup> These larger capillary joints can only be used to couple a precolumn capillary enzyme reactor to a separation if conditions are optimized such that (1) it will be possible to electromigrate only a small portion of the contents of the precolumn across the capillary junction into the separation capillary and (2) the separation can proceed without continuously siphoning of the contents of the precolumn reactor onto the separation capillary.

This can be accomplished by placing two capillaries in close proximity by careful micropositioning and controlling the distance between them with submicron resolution. When the ionic strength of the gap buffer is high, the alignment of the two capillaries is critical. A small misalignment can produce strong turbulence in the fluid flow, resulting in the formation of stagnant pools, eddies, and a whole host of complicated flow patterns. Once this occurs, the sample can be present in the gap for long periods of time, enough for significant losses due to diffusional dispersion to occur. This becomes far less problematic when the ionic strength of the gap buffer is decreased to 5–10 times less than the separation buffer.<sup>12</sup> A schematic diagram of the instrumental setup used in this work is shown in Figure 1, while a detailed schematic of the capillary junction is shown in the inset. The Teflon cell containing the capillary junction is designed such that the solution surrounding the capillary junction can be changed easily without disconnecting the capillaries or disturbing the alignment of the capillaries. The efficiency of the coupling process was evaluated by separating a tryptic digest of  $\beta$ -casein (prepared off-line) across a fluid gap on a set of coupled capillaries. Very little diffusional sample loss in the gap was observed under these conditions, as shown in Figure 2, where a digest of  $\beta$ -casein is separated on a segmented column that has either a minimal gap ( $< 1 \mu\text{m}$ ) or a large gap (100  $\mu\text{m}$ ) at low ionic strength. This occurs primarily because the voltage gradient across the gap is large, and the sample had little time for radial diffusion out of the junction. The utility of this approach is that it not only offers efficient mass transfer of the sample by electromigration but also allows subsequent separation of the transferred sample in the second capillary without the need to move either capillary to avoid siphoning additional material from the first capillary.

The assembly of a coupled digestion-separation system begins with a capillary with an immobilized proteolytic enzyme. We have immobilized a proteolytic enzyme (trypsin) on the inner surface of a 50- $\mu\text{m}$ -i.d. fused-silica capillary via biotin-avidin-biotin technology.<sup>1</sup> Biotin is attached to the silica surface after the surface is derivatized with an ami-

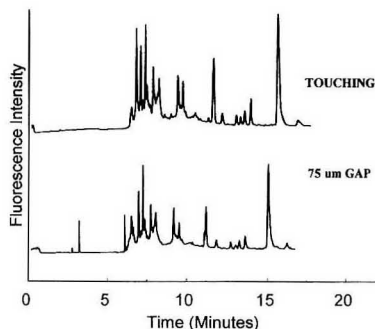


**Figure 2.** CZE electropherogram of an aliquot of the tryptic digest of a 20  $\mu$ M solution of  $\beta$ -casein (obtained off-line) on a coupled-capillary system. The peptides in the digest were derivatized with NDA, and a 1-s, 20-kV electrokinetic injection was performed onto a coupled separation column (two segments of unmodified capillary, each 50 cm, 50- $\mu$ m i.d., 360- $\mu$ m o.d.; total length 100 cm) using 0.050 M sodium phosphate, pH 7.4. The top electropherogram was obtained with the two column segments placed as close as possible ( $<1 \mu$ m), while the second electropherogram was obtained with a 75- $\mu$ m gap between the two capillaries. In both cases, the gap junction was immersed in deionized water. Samples were detected with laser-induced fluorescence ( $\lambda_{\text{ex}} = 442 \text{ nm}$ ), running voltage, 20 kV; current, 42.2  $\mu$ A.

nosilane (3-APTS). A consequence of this immobilization procedure is that the intrinsically net negative surface charge of silica is changed to a net positive charge. Consequently, the placement of the anode and cathode of the high-voltage power supply must be reversed to allow electromigration of sample onto the enzyme-modified capillary (i.e., the potential of the sampling reservoir is reversed to a negative voltage). The electroosmotic mobility for the microreactor was calculated to be  $1.55 \times 10^{-4} \text{ cm}^2/\text{V}\cdot\text{s}$  using a buffer containing 0.025 M ammonium bicarbonate and 0.025 mM sodium phosphate.

Since the electroosmotic flow in both digestion and separation capillaries must be in the same direction and relatively well-matched for efficient sample transfer across the capillary junction, it is necessary to reverse the electroosmotic flow in the separation capillary as well. The separation capillary can be modified dynamically with a cationic polymer to reverse the charge at the capillary surface.<sup>16,17</sup> This can be accomplished simply by flowing a dilute solution of the polymer [Microcoat or hexadimethrine bromide (Polybrene)] through the capillary prior to the separation. This reverses the direction of electroosmotic flow and reduces the amount of adsorption of basic peptides and proteins. This modification produced a capillary whose electroosmotic flow was reversed and had a magnitude roughly twice that of the microreactor.

The bottom electropherogram in Figure 3 shows the separation of a tryptic digest of  $\beta$ -casein obtained by on-line injection and mapping by the coupled capillary system. A 1-min injection time was found to be optimum for the on-line injection of the digest. The long sample time is very effective especially when the gap buffer was 10 times less concentrated than the separation buffer, since sample stacking can take place as the sample migrates across the more dilute buffer in the gap. After injection, the buffer surrounding the gap was

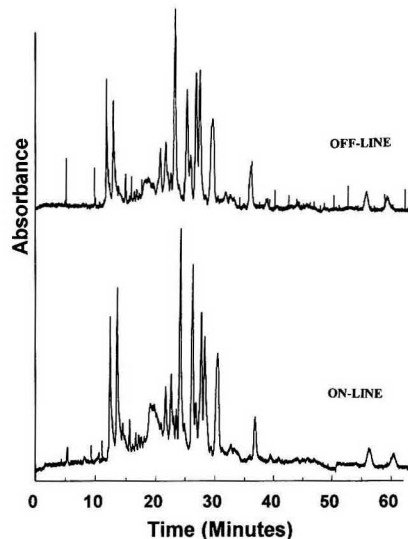


**Figure 3.** Electropherograms showing separations of a tryptic digest of  $\beta$ -casein. (top) This electropherogram was obtained by a normal 3-s, 20-kV injection of an aliquot of the tryptic digest (the digest was obtained off-line from 10  $\mu$ L of 2 mg/mL solution of  $\beta$ -casein eluted through a 50-cm, 50- $\mu$ m-i.d. microreactor). These separations were performed on a Polybrene-modified capillary (50- $\mu$ m i.d., 360- $\mu$ m i.d., length 75 cm.) using a separation buffer consisting of 0.090 M sodium phosphate, pH 7.4. Samples were detected (UV absorbance at 210 nm) at 60 cm from the injection end. Running voltage, -20 kV; current, 38.5  $\mu$ A. (bottom) This electropherogram represents an on-line injection (1 min at 10 kV) of the tryptic digest of a 2 mg/mL solution of  $\beta$ -casein eluted across a 100- $\mu$ m gap from a 50-cm, 50- $\mu$ m-i.d. microreactor coupled directly to the separation capillary. Otherwise, identical separation conditions were used as described above.

replaced with the separation buffer, then the separation potential (-20 kV) was applied across only the separation capillary. This compares well with the electropherogram shown in the top of Figure 3, which was obtained using a 20- $\mu$ L aliquot of a tryptic digest that was collected off-line, then injected and separated by CZE off-line using the same separation conditions. The mass transfer across the gap is quantitative and there is virtually no loss of separation efficiency or peak resolution due to the transfer of sample across the fluid gap under these conditions. It is also important to note that there is a complete absence of siphoning of the digest from the microreactor capillary during the separation. This is clearly indicated by the reproducibility of the baseline between electropherograms shown in Figure 3. The measured electroosmotic flow rate in the Polybrene-modified capillary was found to be about twice that measured for the digestion capillary. Although, the electroosmotic flow rates are different in the coupled capillaries, no significant effect on the efficiency of sample transfer was observed especially when longer injection times (1 min) were used. The stability of the Polybrene-modified separation capillary is also demonstrated by the relatively reproducible peak retention times between the two electropherograms. The stability of the separation capillary can be maintained easily by occasional regeneration of the polymer layer (either Microcoat or Polybrene) by a 3-min rinse with the polymer coating reagent after a 3-min rinse with 0.10 M NaOH.

One of the most important experimental parameters that must be carefully optimized is that all fluid reservoirs (i.e., sample solution, gap buffer and detector end) must be

(14) Wilchek, M.; Bayer, E. A. *Anal. Biochem.* **1988**, *171*, 1-32.

(15) Roach, M. C.; Harmony, M. D. *Anal. Chem.* **1987**, *59*, 411-415.

(16) Wiktorowicz, J. E.; Colburn, J. C. *Electrophoresis* **1990**, *11*, 769-773.

(17) Monnig, C. A., personal communication.

maintained at exactly the same height. This ensures that Poiseuille flow will not be generated during the experiment, since this will result in continuous siphoning of the digest into the separation capillary during the separation process. The effect of continuous sample siphoning during the separation stage is usually manifested in the form of a gradual rise in the baseline. Additionally, it was found that removal of the electrode from the sample reservoir during the separation ensured that no sample leaked out of the microreactor during the separation. Due to the very high electric fields present in both capillaries upon application of the separation potential, it was easiest to disconnect the sample electrode completely to avoid flow in the digestion capillary during the separation stage. Once this was done, very reproducible results were obtained.

### CONCLUSIONS

We have demonstrated that it is possible to interface two 50- $\mu\text{m}$ -i.d. fused-silica capillaries through a solution gap to allow on-line transfer of the contents of one capillary into the second. This approach was used for on-line digestion and mapping of a protein with capillary electrophoresis. Most of

the typical problems with protein digestions, including sample loss and contamination are overcome by performing both steps on-line. This technique is particularly advantageous in mapping proteins because of the high reproducibility requirement of the maps, and also because of the continuously decreasing size of protein samples that are presently of interest to the medical, bioanalytical and the biotechnological communities.

### ACKNOWLEDGMENT

This work was supported, in part, by a National Science Foundation Presidential Young Investigator Award (Grant CHE-897394), and a grant provided by Procter and Gamble Corp. The donations of the Inchworm Controller by Burleigh Instruments, the UV detector by Applied Biosystems, Inc., and the HeCd laser by Omnichrome Corp. are gratefully acknowledged.

RECEIVED for review February 10, 1993. Accepted July 5, 1993.

## In Situ Elimination of Metal Inhibitory Effects Using Ligand-Containing Carbon Paste Enzyme Electrodes

Joseph Wang\* and Qiang Chen

Department of Chemistry and Biochemistry, New Mexico State University, Las Cruces, New Mexico 88003

### INTRODUCTION

Enzyme-based biosensors are highly selective devices which rely on the specific binding of the target analyte (the substrate) to the active-site regions of the enzyme. Amperometric signals resulting from this biorecognition process have led to many useful enzyme electrodes.<sup>1-3</sup> The response of these devices is often affected by the presence of inhibitors, which combine with the free enzyme in a manner that prevents substrate binding. In particular, inorganic ions such as silver, mercury, lead, or copper possess strong affinity for many enzymes and thus greatly influence the velocity of many biocatalytic reactions.<sup>4</sup> Indeed, such inhibitory effects have been exploited for indirect assays of toxic metals.<sup>5-7</sup> However, for measurements of the substrate it is desirable to investigate means for circumventing the effect of such cations upon the performance of enzyme electrodes.

The objective of the present study is to describe an efficient and yet simple strategy to eliminate the interference of metals in amperometric biosensing. The method relies on the in situ removal of the interfering metal by a surface-bound complexing agent. The complexing agent is incorporated into the surface by mixing it within the enzyme-containing carbon paste matrix. Mixed enzyme/carbon paste electrodes are receiving considerable attention for the preparation of fast-responding reagentless biosensors.<sup>8-11</sup> More than 10 different enzymes have been incorporated in an active form within carbon paste matrices.<sup>8,11</sup> Several of them have recently reached the commercial stage.<sup>12</sup> Ligand-containing carbon paste electrodes have also been developed in connection with preconcentration/voltammetric measurements of target metal analytes.<sup>8,13-15</sup> For example, rapid collection and convenient measurements of nickel or gold ions can be accomplished at carbon pastes modified with dimethylglyoxime<sup>14</sup> or diethylenetriamine,<sup>15</sup> respectively. In the following sections we will illustrate that the coimmobilization of enzymes and complexing agents within the carbon paste environment represents a convenient approach for circumventing metal inhibition problems characterizing amperometric biosensors. Such development should facilitate the application of biosensors in complex samples containing high metal concentration.

### EXPERIMENTAL SECTION

**Apparatus.** Experiments were performed in a 10-mL cell [Model VC-2, Bioanalytical Systems (BAS)]. The enzyme electrode, reference electrode [Ag/AgCl, (3 M NaCl), Model RE-1, BAS], and platinum wire auxiliary electrode joined the cell through holes in its PTFE cover. A magnetic stirrer and stirring bar provided the convective transport. The electrodes were connected to a BAS CV-27 voltammograph and a BAS X-Y-t recorder.

**Electrode Preparation.** The modified carbon paste was prepared in two steps. The first involved a thorough mixing of 1.03 g of graphite powder (Acheson 38, Fisher), 0.67 g of mineral oil (Aldrich), and 0.30 g of potassium ferrocyanide (Baker). Subsequently, 150 mg of the initial paste was mixed with 10 mg of the enzyme (horseradish peroxidase, HRP) and 40 mg of disodium ethylenediaminetetraacetate (Fisher). A portion of the resulting paste was packed into the end of a 3-mm-i.d. Teflon tube. Electrical contact was established via a stainless steel wire. After the surface was smoothed (on a weight paper), it was coated with a Nafion film. For this purpose, 10  $\mu$ L of a 0.5% Nafion solution [prepared by diluting 50  $\mu$ L of the commercial Nafion (DuPont) solution in 400  $\mu$ L of ethanol and 50  $\mu$ L of deionized water] was placed on the active disk, and solvent was allowed to evaporate for 10 min.

**Reagents and Procedure.** Solutions were prepared from reagent-grade chemicals with deionized water. Hydrogen peroxide (Sigma), peracetic acid, and 2-butanone peroxide (Aldrich) were used without further purification. Nitrate salts were used to prepare the metal stock solutions. Horseradish peroxidase (EC 1.11.1.7, 96 units/mg) was obtained from Sigma. The supporting electrolyte was an ammonia buffer (0.1 M  $\text{NH}_3/\text{NH}_4\text{Cl}$ , pH 8.8) solution.

The desired working potential (usually -0.05 V) was applied, and transient currents were allowed to decay. Batch measurements of the peroxide substrates were subsequently carried out in the absence and presence of the metal inhibitors, with stirring at 300 rpm. All measurements were performed at room temperature.

### RESULTS AND DISCUSSION

The ability to circumvent the inhibition interference of metal cations at biocatalytic electrodes is illustrated in the following sections using horseradish peroxidase (HRP) as a model enzyme and in the presence of ethylenediaminetetraacetic acid (EDTA) as the complexing agent. The broad coordination action of EDTA makes it an ideal choice for the task of in situ removal of most cationic interferences. The carbon paste bioelectrode configuration is particularly useful for this task, as it allows controlled loading of HRP, EDTA, and the ferrocyanide mediator. The high amount of incorporated EDTA, and the immediate proximity of the enzyme and ligand sites, greatly facilitate the rapid and effective removal of metal cations approaching the surface. A schematic of the mixed enzyme/ligand carbon paste configuration is shown in Figure 1. This reagentless sensor operates in the amperometric mode for monitoring the peroxide substrate through cathodic detection of the enzymatically liberated ferrocyanide species (the oxidized form of the mediator) and electrochemical regeneration of the ferrocyanide. Various metal cations, e.g.,  $\text{Ni}^{2+}$ ,  $\text{Co}^{2+}$ , or  $\text{Mn}^{2+}$ , known to inhibit this

- (1) Kobos, R. K. *Trends Anal. Chem.* 1987, 6 (1), 6.
- (2) Turner, A. P.; Karube, I.; Wilson, G. S., Eds. *Biosensors: Fundamentals and Applications*; Oxford Press: Oxford, U.K., 1987.
- (3) Wang, J. *Electroanalytical Techniques in Clinical Chemistry and Laboratory Medicine*; VCH Publishers: New York, 1988.
- (4) Dixon, M.; Webb, E. *Enzymes*; Academic Press: New York, 1979; Chapter VIII.
- (5) Tran-Minh, C. *Ion-Select. Electrode Rev.* 1985, 7, 41.
- (6) Townshend, A.; Vaughan, A. *Talanta* 1970, 17, 289.
- (7) Dolmanova, I. F.; Shekhovtsova, T.; Kutcheryaeva, V. *Talanta* 1987, 34, 201.
- (8) Kalcher, K. *Electroanalysis* 1990, 2, 419.
- (9) Wang, J.; Wu, L.; Lu, Z.; Li, R.; Sanchez, J. *Anal. Chim. Acta* 1990, 228, 251.
- (10) Bremle, G.; Persson, B.; Gorton, L. *Electroanalysis* 1991, 3, 77.
- (11) Amine, A.; Kauffmann, J. M.; Patriarche, G. *J. Anal. Lett.* 1991, 24, 1293.
- (12) *Sugar Electrode*; Orion Research Inc.: Boston, MA, 1993.
- (13) Wang, J. Voltammetry Following Nonelectrolytic Preconcentration. In *Electroanalytical Chemistry*; Bard, A. J., Ed.; Marcel Dekker: New York, 1989; Vol. 16.
- (14) Baldwin, R. P.; Christensen, J.; Kryger, L. *Anal. Chem.* 1986, 58, 1790.
- (15) Kalcher, K. *Fresenius Z. Anal. Chem.* 1986, 325, 181.

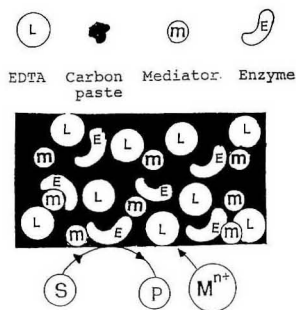


Figure 1. Schematic of the mixed enzyme/ligand/mediator carbon paste biosensor.

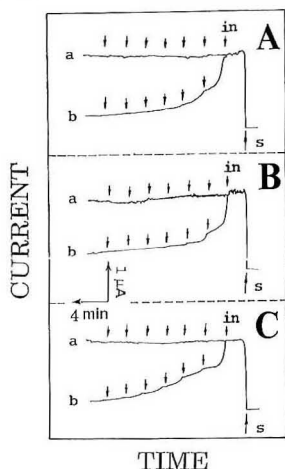


Figure 2. Current-time recordings at HRP/carbon paste electrodes containing 20 (a) and 0 wt % (b) EDTA upon increasing the cobalt (A), manganese (B), and nickel (C) ion concentration in  $1 \times 10^{-4}$  M steps. S represents the initial response to the substrate ( $1 \times 10^{-4}$  M hydrogen peroxide), while in represents the first inhibitor (metal ion) addition. Operating potential,  $-0.05$  V; stirring rate, 300 rpm; electrolyte, ammonia buffer (0.1 M, pH 8.8).

biocatalytic process<sup>16</sup> have been tested. Coefficient of inhibition ( $I_{0.5}$ ) values of 5300, 72, and 52  $\mu$ M have been reported for the interaction of HRP with  $\text{Ni}^{2+}$ ,  $\text{Co}^{2+}$ , and  $\text{Mn}^{2+}$ , respectively.<sup>17</sup> The high stability of EDTA complexes of these cations ( $K_f$  of  $10^{18.6}$ ,  $10^{18.3}$ , and  $10^{13.8}$ , respectively) greatly minimizes the competitive formation of the metal (inhibitor)-enzyme complex and hence circumvents the metal inhibition process.

Figure 2 illustrates the prevention of interferences by metal ions through the incorporation of EDTA within the carbon paste matrix. It displays the current response of HRP biosensors, with (a) and without (b) the incorporated ligand, to a  $1 \times 10^{-4}$  M addition of hydrogen peroxide (S), followed by seven repetitive additions of  $1 \times 10^{-4}$  M of the cobalt (A), manganese (B), and nickel (C) inhibitors (in). Both electrodes offer a similar response to the peroxide substrate, indicating that the presence of EDTA is not influencing the sensitivity and speed of the response. The steady-state signal is achieved

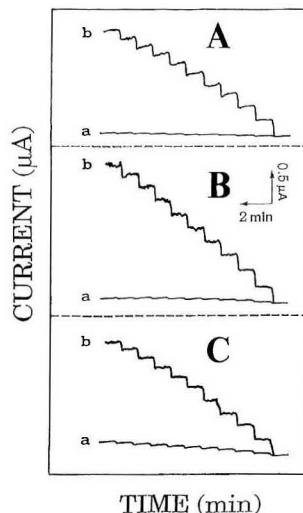


Figure 3. Current-time recordings at HRP/carbon paste containing 0 (a) and 20 wt % (b) EDTA upon increasing the hydrogen peroxide concentration in  $2 \times 10^{-5}$  M steps. Solutions containing  $4 \times 10^{-4}$  M cobalt (A), manganese (B), and nickel (C) ions. Other conditions, as in Figure 2.

within 20 s. However, at the plain (ligand-free) bioelectrode the response decreases rapidly upon adding the metal ions (with up to 90% diminution in the case of nickel). In contrast, the peroxide signal at the ligand-containing biosurface is not affected by the additions of the inhibitors. Apparently, the added cations are rapidly being "collected" by the surface-bound EDTA, instead of being attached to the enzyme (see Figure 1).

The practical biosensing utility of incorporating EDTA within the matrix of carbon paste enzyme electrodes is illustrated in Figure 3. This figure displays current-time tracings, obtained at the plain (a) and ligand-containing (b) carbon paste bioelectrodes, on successive  $2 \times 10^{-5}$  M additions of hydrogen peroxide [in the presence of  $4 \times 10^{-4}$  M cobalt (A), manganese (B), and nickel (C) ions]. The severity of the metal inhibition problem (in the absence of EDTA) precludes quantitation of the peroxide substrate. In contrast, the ligand-containing biosensor offers convenient measurement of these micromolar and submillimolar concentrations. Notice again the fast and sensitive response and the low noise level.

Calibration plots from the data of Figure 3, as well as from analogous experiments without the metals, are shown in Figure 4. Several points are noted from these data. First, the curves at the EDTA-containing electrode in the absence and presence of the metals are nearly identical (compare curves c and d). Second, in the absence of metals, the plain enzyme electrode yields a response larger (by ca. 15–20%) than the ligand-containing surface (compare curves b and c). Such behavior is attributed to the higher content (wt %) of the graphite sensing sites at the plain enzyme electrode. [Some exception from these points is noted in the case of manganese (B).] Third, poor sensitivity is observed in the presence of the metals at the plain carbon paste enzyme electrode (curves a), in comparison to the high sensitivity inherent to the EDTA-based biosensor (curves d). Overall, these plots clearly demonstrate the efficiency of the *in situ* metal collection by the surface-bound ligand. In addition, these data (and that of Figure 3) clearly indicate that interactions of the metals

(16) *Handbook of Enzyme Inhibitors*; Zollner, H., Ed.; VCH Publishers: New York, 1989; p 159.

(17) Guilbault, G.; Brignac, P.; Zimmer, M. *Anal. Chem.* 1968, 40, 190.



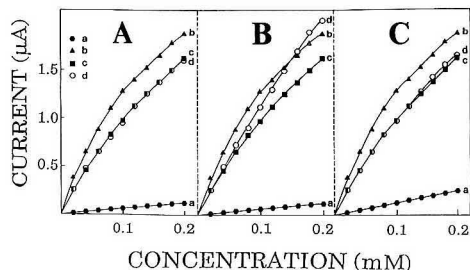


**Figure 4.** Calibration plots for hydrogen peroxide at HRP/carbon paste electrodes containing 0 (a, b) and 20 wt % (c, d) EDTA, in the presence (a, d) and absence (b, c) of  $4 \times 10^{-4}$  M cobalt (A), manganese (B), and nickel (C) ions. Other conditions, as in Figure 2.

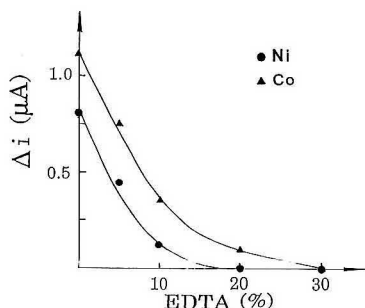


**Figure 5.** Effect of the EDTA loading (wt %) in the paste upon the suppression of the current ( $\Delta i$ ) for  $2 \times 10^{-4}$  M hydrogen peroxide in the presence of  $1 \times 10^{-3}$  M nickel (●) and cobalt (▲) ions. Other conditions, as in Figure 2.

with the ammonia buffer or with the surface-bound ferrocyanide have negligible effect upon the behavior reported in this paper.

The efficiency of the metal removal is also strongly affected by the paste composition. Figure 5 shows the effect of the EDTA content upon the suppression of the biosensing signal ( $\Delta i$ ) caused by nickel and cobalt. The enzyme inhibition by both metals rapidly decreases upon increasing the percentage of EDTA within the carbon paste. Negligible inhibition effects are observed for pastes containing more than 20 wt % of the complexing agent. Such profiles are expected from the increased binding capacity of the electrode. The high binding capacity assures sufficient surface "collection" sites, with no saturation upon prolonged exposures to metal-rich solutions. For example, no inhibition was indicated from the response to  $2 \times 10^{-3}$  M 2-butanone peroxide at the 30% EDTA-containing enzyme electrode after 20-min incubation in a stirred solution of  $1 \times 10^{-3}$  M nickel. A decrease in the binding capacity of the electrode is also not of major concern, considering the renewable character of carbon paste bioelectrodes. It should be noted also that the EDTA loading needed for effective prevention of the metal inhibition must be

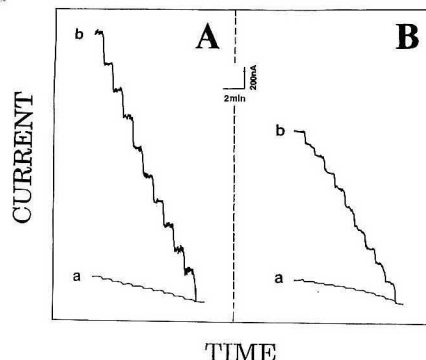


**Figure 6.** Current-time recordings at HRP/carbon paste electrodes containing 0 (a) and 20 wt % (b) EDTA upon increasing the peracetic acid (A) and 2-butanone peroxide (B) concentration in  $5 \times 10^{-5}$  M steps. Ammonia buffer solution containing  $4 \times 10^{-4}$  M cobalt (A) and manganese (B) ions. Other conditions, as in Figure 2.

adjusted to suit the requirement of each case (mass transport, nature of the metal and its level, etc.).

The biosensing of other substrates of HRP can also benefit from the elimination of metal inhibition effects. In particular, organic peroxides are of great environmental and industrial importance.<sup>18</sup> Figure 6 displays the amperometric response to increasing concentrations of peracetic acid (A) and 2-butanone peroxide (B), in the presence of  $4 \times 10^{-4}$  M manganese, at plain (a) and EDTA-containing (b) HRP electrodes. The advantages accrued from the use of the ligand-based biosensor are obvious.

In conclusion, the present study illustrates that ligand-containing bioelectrodes can be employed to circumvent enzyme inhibition processes and, hence, to impart high stability to biocatalytic sensors in the presence of interfering metals. Other ligands (e.g., dithizone) may offer similar advantages when inhibition by certain metals (e.g., mercury or silver) is concerned. While the concept presented here is within the framework of peroxidase, it could be extended to other important enzyme electrodes. Other buffer solutions, with a suitable pH for the enzyme activity, should be useful for this task. (The commonly used phosphate buffer was not employed because of heavy precipitation in the presence of high metal concentrations.) The mixed carbon paste biosensor configuration permits simultaneous incorporation of additional modifiers, as needed to eliminate other interferences (e.g., of ascorbic acid via the coimmobilization of ascorbic acid oxidase).

## ACKNOWLEDGMENT

This work was supported in part by the U.S. Environmental Protection Agency (Grant CR-817936-010). Mention of trade names or commercial products does not constitute endorsement or recommendation by the U.S. EPA.

RECEIVED for review May 12, 1993. Accepted July 6, 1993.

(18) Glaze, W. H. *Environ. Sci. Technol.* 1987, 21, 224.

## Radiochemical Determination of Low-Level Lead-210 in Environmental Water Samples

Dominic To

Radiochemistry Laboratory, Kansas Health and Environmental Laboratory,  
Kansas Department of Health and Environment, Topeka, Kansas 66620-0001

### INTRODUCTION

Lead-210 is a naturally occurring radionuclide of the uranium-238 series. The existence of lead-210 in environmental water results mainly from the decay of its precursor radon-222. In surface and shallow-well waters, lead-210 concentration is usually low due to the volatility of radon and/or rapid adsorption of the nuclide into sediments. However, in deeper wells, lead-210 concentration may reach as high as 200 pCi/L.<sup>1</sup> The high concentration of lead-210 in deeper wells may be attributed to the presence of high radon-222 activity.

Current National Primary Drinking Water Regulations require that the concentration of soluble  $\beta$  and photon-emitting radionuclides in drinking water not produce a dosage of more than 4 mrem effective dose equivalent (ede) per year.<sup>2</sup> At such level, the presence of even a minute amount of lead-210 in drinking water is of health and regulatory concern because the lead-210 concentration estimated to correspond to 4 mrem ede per year is 1 pCi/L. In order to determine whether water samples obtained from public water systems are in compliance with the regulations, an analytical method capable of determining lead-210 concentration below 1 pCi/L is necessary.

The lead-210 concentration in water can be measured directly by  $\gamma$ -ray spectrometry or liquid scintillation counting.<sup>3</sup> However, these direct counting methods do not achieve the 1 pCi/L sensitivity level due to uncertainties associated with measurement of the low-percent-abundant (4.1%) 46.5-keV photopeak resulting from decay of lead-210 and high backgrounds associated with the conventional liquid scintillation analyzer, respectively. Although lead-210 could also be determined directly by ICP-MS, to measure 1 pCi/L (13 fmol/L) would require another order of magnitude of preconcentration over the method being described to reach a detection limit of 10 ppt.

Alternatively, lead-210 concentration in environmental samples can be determined by measuring the activity of one of the daughters ( $^{210}\text{Bi}$  or  $^{210}\text{Po}$ ) of lead-210 after sufficient ingrowth period.<sup>4-6</sup> The lead-210 concentration is then extrapolated from the daughter activities. These indirect measurement methods, although sensitive enough to detect a low level of lead-210 in water samples, often involve lengthy and/or laborious steps.

The present paper describes a relatively simple and sensitive method for the determination of low-level lead-210 in environmental water samples. The method involves (i) concentration and separation of lead-210 from other naturally occurring radionuclides that may be present in the sample and (ii) isolation of bismuth-210 in the form of bismuth oxychloride from the sample, after a suitable ingrowth period, for  $\beta$  counting. The procedures for the concentration and separation of lead-210 are modified from those used by Goldin<sup>7</sup> to determine radium concentration in water.

### EXPERIMENTAL SECTION

**Apparatus.** A Tennelec Model LB5100 low-background  $\alpha/\beta$  counting system equipped with gas-flow detector and anticoincidence guard detector was used to count bismuth oxychloride. The  $\beta$  background of the  $\alpha/\beta$  counting system is less than 1 count/min. A Wallac Model 1409 liquid scintillation multichannel analyzer was used to count lead-210 and bismuth-210. Barium-133 radioactivity was determined by counting the samples with a Princeton Gamma-Tech Ge(Li) detector interfaced to a Nuclear Data 6600 computer-based data acquisition system. Chemical yields of lead carbonate and bismuth oxychloride were determined gravimetrically to 0.1-mg precision.

**Reagents and Solvents.** Lead-210, radium-226, natural uranium, and barium-133 standards were obtained from the National Institute of Standards and Technology. The concentrations of bismuth and lead carrier solutions were 10 and 20 mg/mL, respectively. Fresh radium-226 solution was prepared by adding a known quantity of radium-226 standard solution to 25 mL of distilled water in a centrifuge tube. Radium-226 was coprecipitated with barium and lead sulfate. Barium sulfate was separated from lead and converted to carbonate as described in the Sample Analysis section. The barium carbonate was dissolved in 1 M nitric acid. The radium-226 concentration was determined by  $\gamma$  counting of the resulting solution. The removal of lead-210 in the freshly prepared radium-226 solution was confirmed by the absence of the 46.5-keV lead-210 photopeak in the  $\gamma$ -ray spectrum. Further verification of lead-210 removal was made by analyzing an aliquot of the fresh radium-226 solution with the liquid scintillation analyzer. OptiPhase HiSafe3 scintillation cocktail (LKB-Wallac Scintillation Product) was used for all liquid scintillation counting. The result indicated the absence of lead-210 in the solution.

**Counter Efficiency.** The counting efficiency of the low-background counter was determined by counting  $^{210}\text{BiOCl}$  at different masses.  $^{210}\text{BiOCl}$  was prepared by adding a known quantity of  $^{210}\text{Pb}/^{210}\text{Bi}$  equilibrium standard solution to lead carbonate, which was prepared by boiling lead sulfate in a 2 M sodium carbonate solution. A few drops of 6 M HCl, followed by various amounts of bismuth carrier solution, were added to the lead carbonate. The resulting mixture was heated in a hot water bath until a clear solution was obtained. Distilled water was added to the solution to precipitate  $^{210}\text{BiOCl}$ .  $^{210}\text{BiOCl}$  was then filtered, weighed, and counted with the  $\alpha/\beta$  low-background counter. The counting efficiency over a range of  $^{210}\text{BiOCl}$  mass was determined after yield and decay correction.

**Sample Analysis.** Figure 1 shows the procedures for the analysis of lead-210 in 1-L water sample. A known quantity of lead-210 standard solution was added to the sample, followed by methyl orange indicator and 5 mL of 1 M citric acid. The sample was made basic with concentrated ammonium hydroxide solution. Sixty milligrams of lead and 20 mg of barium carriers were added, and the mixture was heated to boiling. Fifty milliliters of 18 N sulfuric acid was added to precipitate lead and barium sulfate, which was collected and washed with 10 mL of concentrated nitric acid and then distilled water. Fifteen milliliters of 0.05 M alkaline EDTA solution was added to dissolve the sulfate and then glacial acetic acid was added to reach a pH of 4.0. After further digestion, the barium sulfate was separated from lead by centrifuging and the supernatant fluid saved. To precipitate lead sulfate, the pH of the supernatant was adjusted to 1.0 with 18 N sulfuric acid and the mixture was digested for ~30 min with occasional stirring. The precipitation of lead sulfate marked the beginning of the bismuth-210 ingrowth period. After digestion, lead sulfate was separated and washed with two 15-mL portions of hot distilled water. Lead carbonate was obtained by heating the lead sulfate in 20 mL of 2 M sodium carbonate solution. After the chemical yield of lead was determined, the

(1) Personal communication. U.S. Environmental Protection Agency. Addendum to Occurrence of Man-Made Radionuclides in Public Drinking Water Supplies. EPA, 1991g, May 20, 1991.

(2) Fed. Regist. 1991, 56, (July 18), No. 138.

(3) Blais, J. S.; Marshall, W. D. *Anal. Chem.* 1988, 60, 1851-1855.

(4) Holtzman, R. B. *Health Phys.* 1963, 9, 385.

(5) Petrow, H. G.; Cover, A. *Anal. Chem.* 1965, 37, 1659-1660.

(6) Sill, C. W.; Willis, C. P. *Anal. Chem.* 1965, 37, 1661-1671.

(7) Goldin, A. S. *Anal. Chem.* 1961, 33, 406-409.

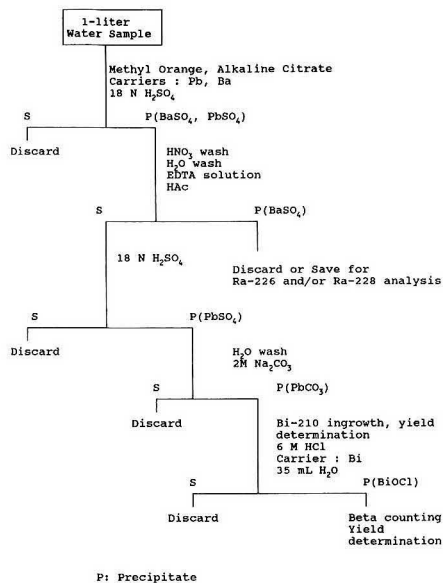


Figure 1. Analysis of lead-210 in environmental water sample.

lead carbonate was stored for sufficient time to allow bismuth-210 to ingrow.

At the end of the ingrowth period, a few drops of 6 M HCl and 5–10 mL of distilled water were added to the lead carbonate. Twenty milligrams of bismuth carrier was added, and the resulting mixture was digested in a hot water bath until a clear solution was obtained. About 35 mL of distilled water was then added to precipitate bismuth oxychloride. If bismuth oxychloride does not form after the solution is digested for 20 min, a few drops of concentrated ammonium hydroxide solution can be added to assist the formation of bismuth oxychloride. The formation of bismuth oxychloride marked the end of bismuth-210 ingrowth and the beginning of bismuth-210 decay. Bismuth oxychloride was separated by centrifuge and washed twice with 20 mL of hot distilled water. The oxychloride was then filtered, dried, weighed, and  $\beta$  counted. The lead-210 concentration was calculated by using the following equation:

$$^{210}\text{Pb (pCi/L)} = C/E(2.22) Y_1 Y_2 ID$$

where  $C$  is the net  $\beta$  count rate of  $^{210}\text{Bi}$ ;  $E$  is the counting efficiency of  $^{210}\text{BiOCl}$ ;  $Y_1$  and  $Y_2$  are the chemical yields of lead and bismuth, respectively;  $I$  is the ingrowth factor  $[1.0006(e^{-\lambda_1 t} - e^{-\lambda_2 t})]$ ,  $\lambda_1$  and  $\lambda_2$  are decay constants of  $^{210}\text{Pb}$  and  $^{210}\text{Bi}$ , respectively, and  $t$  is the ingrowth period; and  $D$  is the decay correction for  $^{210}\text{Bi}$ .

**Effect of pH on the Formation of Lead Sulfate in Alkaline EDTA Solution.** A known amount of lead carrier was mixed with 20 mL of distilled water in a centrifuge tube. To precipitate lead sulfate, 18 N sulfuric acid was added, and after separation, the lead sulfate was dissolved in 0.05 M alkaline EDTA solution. A known quantity of lead-210 standard solution, in equilibrium with its daughters, was added to the EDTA solution from which lead sulfate was reprecipitated by adding various amounts of 18 N sulfuric acid. The pH of the solution was measured and the lead sulfate was filtered, dried, and weighed. The percent recovery of lead was determined gravimetrically.

## RESULTS AND DISCUSSION

Environmental water samples often have high contents of sulfate which, if present, may cause premature precipitation of lead and barium carriers when added to these samples.

Table I. Effect of pH on the Recovery of Lead in EDTA Solution

pH of EDTA soln	% recovery <sup>a</sup> of lead as lead sulfate
1.5	84.7 ± 3.4
1.0	96.5 ± 4.4
0.5	96.3 ± 4.0

<sup>a</sup> These numbers represent the mean values and standard deviations at the 95% confidence level from three separate determinations.

Table II. Determination of  $^{210}\text{Pb}$  in Water Samples

lead-210 concn (pCi/L)		lead-210 concn (pCi/L)	
added	found <sup>a</sup>	added	found <sup>a</sup>
190.0	183.8 ± 7.0	9.6	9.8 ± 1.5
96.0	96.8 ± 4.1	5.8	6.3 ± 1.2
76.8	74.6 ± 3.0	1.0	1.3 ± 0.5
57.6	54.6 ± 3.0	28.0 <sup>b</sup>	25.2 ± 3.0
38.4	37.3 ± 1.9	11.5 <sup>b</sup>	11.2 ± 1.6
19.2	18.4 ± 4.1	5.8 <sup>b</sup>	5.4 ± 1.0
13.4	14.2 ± 2.3		

<sup>a</sup> Three separate determinations were performed. <sup>b</sup> These samples were spiked with natural uranium and radium-226.

Quantitative precipitation of lead and barium cannot be ensured if this occurs. To prevent early precipitation of the carriers, a masking agent such as alkaline citrate was mixed with water samples prior to the addition of carriers. Lead and barium would not precipitate until sulfuric acid was added to dissociate the metal-citrate complexes and precipitate lead and barium. After separation from the sample as sulfates, lead and barium were washed with concentrated nitric acid to remove polonium-210. Polonium-210, although primarily an  $\alpha$  emitter, may interfere with  $\beta$  counting of bismuth-210 when counted together with the latter, by absorption of the energy of  $\alpha$  particles by the counter window. This interference, although it can be corrected empirically, is undesirable for low-level  $\beta$  counting of bismuth-210.

Alkaline EDTA solution was used to complex lead and barium in solution. The influence of pH on the metal-EDTA complex stability provides the basis for the separation of lead-210 in solution from its daughters and other interfering radionuclides. Acetic acid was used to lower the pH of the EDTA solution. Precipitation of lead or barium was not observed until the solution pH reached 4. To ascertain that the precipitate contains only barium and, hence, radium, a known quantity of barium-133 standard solution was added to the water sample, which was analyzed using the procedures described. The barium sulfate residue and the EDTA solution from which the precipitate was separated were analyzed for barium-133 activity using the  $\gamma$ -ray spectrometer. Analysis of the  $\gamma$ -ray spectrum found no barium-133 activity in the EDTA solution, while over 90% of the added barium-133 activity was recovered in the precipitate. This result shows that complete separation of barium from the sample was achieved in EDTA solution by adjusting the pH to 4.

The effect of pH on the stability of the lead-EDTA complex in solution was also studied. Table I shows the percent recovery of lead as sulfate at various pH of the EDTA solution. As described in the Experimental Section, these samples were spiked with a known quantity of standard solution of lead-210 in equilibrium with its daughters bismuth-210 and polonium-210. Lead-210 and its daughters served as tracers to follow the chemical separation of lead in EDTA solution. Lead sulfate was counted with the  $\alpha/\beta$  low-background counter. No net  $\alpha$  counts were observed in the  $\alpha$  channel, indicating that polonium-210 was separated from lead-210. Lead sulfate was redissolved in alkaline EDTA solution after

**Table III. Advantages and Disadvantages of Existing Methods for Measuring Lead-210 in Water Samples**

method of analysis	advantage	disadvantage
(I) direct counting (1) $\gamma$ -ray spectrometry; liquid scintillation counting (2) ICP-MS	these methods usually require no or little sample preparation or chemical separation	low sensitivity  sample preconcentration required
(II) indirect measurement (1) polonium (2) Sill and Willis  (3) modified Petrow and Cover	low detection limit can be achieved with these methods	long waiting period laborious procedures (method used for mill effluent with high contents of heavy metals) lengthy steps of sample evaporation-digestion

being  $\alpha$  counted. An aliquot of EDTA solution was taken and analyzed with a liquid scintillation analyzer. The activities of lead-210 and bismuth-210 were determined. Only lead-210 activity was found present in the sample. The absence of polonium and bismuth activity in lead sulfate suggests that their EDTA complexes did not precipitate, even at such low pH. The separation of bismuth-210 from lead-210 ensures a pure lead-210 sample for bismuth-210 ingrowth.

Water samples obtained from wells often contain natural uranium and radium as well as lead-210. These naturally occurring isotopes are potential interferences to the separation of lead-210. To test the present method in the analysis of such samples, water samples containing known quantities of lead-210 were spiked with natural uranium standard solution free of lead-210 and freshly prepared radium-226 solution. Freshly prepared radium-226 solution was used in order to eliminate lead-210 that may be otherwise present in the radium-226 standard solution. The amount of lead-210 that ingrows into a prepared radium-226 solution within a 5-day period is  $\sim 0.01\%$  of the parent radium-226 activity.<sup>8</sup> The total radium-226 and uranium added to the sample were 53 and 77.8 pCi/L, respectively. Shown in Table II are experimental results of analyses of 1-L water samples that were spiked with lead-210 and those spiked with lead-210, uranium, and radium-226.

The experimental results agree within experimental error with the known lead-210 concentration. A two-tailed  $t$  test was used to test the data in Table II. The calculated  $t$  values range from 0.53 to 2.83, which are below the tabulated 10%  $t$  value ( $P = 0.1$ ) of 2.92, indicating no apparent bias in the method.

The presence of uranium and radium in the water samples does not appear to affect the results of the analyses. The effectiveness of separation of lead-210 from the uranium and radium isotopes was tested by counting the lead carbonate

with the  $\alpha/\beta$  low-background counter. No  $\alpha$  activity was found in the lead carbonate. The presence of other naturally occurring lead isotopes such as  $^{214}\text{Pb}$ ,  $^{212}\text{Pb}$ , and  $^{211}\text{Pb}$  will not interfere with the analysis either, since the half-lives of these isotopes are so short that they will decay away during the bismuth-210 ingrowth period.

The overall recoveries of lead and bismuth are 77.1% and 82.0%, respectively, from the sample analyses. The counting efficiency of bismuth-210 is 38% and the average  $\beta$  background of the  $\alpha/\beta$  counter is 1 count/min. Based on these figures, the minimum detection limit of the method is 0.6 pCi/L at the 95% confidence level.

## CONCLUSIONS

The study described in this paper demonstrates that lead-210, in an environmental water sample, can be separated from other naturally occurring radionuclides as lead sulfate by varying the pH of the EDTA solution that contains the lead-EDTA complex. After a suitable ingrowth period, bismuth-210 can be isolated as bismuth oxychloride, and the lead-210 concentration can be calculated from the daughter activity.

Summarized in Table III are the advantages and disadvantages of the existing methods for measuring lead-210 in water samples. The method reported here provides several advantages over the existing methods: (1) a higher sensitivity (detection limit less than 1 pCi/L), compared to the direct counting methods, can be achieved as a result of the relatively high chemical yields of lead and bismuth obtainable with the present method. Higher sensitivity also results because of the higher counting efficiency and the lower background of most of the commercially available low-background  $\alpha/\beta$  counters; (2) the need for a long waiting period (polonium method), and the time-consuming evaporation-digestion steps in the modified Petrow and Cover<sup>9</sup> method are avoided; and (3) the method can be coupled with the method recommended by the United States Environmental Protection Agency for the determination of radium-226 and radium-228 in water.<sup>10,11</sup>

RECEIVED for review March 10, 1993. Accepted June 17, 1993.

(8) Kirby, H. W. *Anal. Chem.* 1954, 26, 1063-1071.

(9) *Environmental Measurements Laboratory Procedures Manual*, 27th ed.; HASL-300; U.S. Department of Energy, Government Printing Office: Washington, DC, 1992; Vol. 1, pp 4.5.73-80.

(10) Percival, D. R.; Martin, D. B. *Anal. Chem.* 1974, 46, 1742-1749.

(11) Personal communication. Brooks, L. B.; Blanchard, R. L. A. *Procedures for the Determination of Radium-228*. U.S. Environmental Protection Agency, Environmental Monitoring and Support Laboratory, Cincinnati, OH, 1981.

# Lithium Ion Selective Optical Sensor Based on a Novel Neutral Ionophore and a Lipophilic Anionic Dye

Kazuhiko Watanabe, Eriko Nakagawa, Hiroyuki Yamada, Hideaki Hisamoto, and Koji Suzuki\*

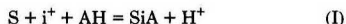
Department of Applied Chemistry, Keio University, 3-14-1 Hiyoshi, Kohoku-ku, Yokohama 223, Japan

## INTRODUCTION

Lithium salts such as  $\text{Li}_2\text{CO}_3$  have been used as a medicine for manic depressive and hyperthyroidism patients.<sup>1</sup> The  $\text{Li}^+$  concentration in the serum of manic depressive patients was reported to be 0.5–1.5 mM, with over 1.5 mM being a toxic range.<sup>1</sup> Thus, a  $\text{Li}^+$  sensor for monitoring  $\text{Li}^+$  in blood fluids is desired in the medical and clinical fields in order to monitor and control the  $\text{Li}^+$  concentration in the human body. For blood serum analysis, a high concentration of  $\text{Na}^+$  coexists. Therefore, an important characteristic for the development of a  $\text{Li}^+$  sensor is how to prevent or minimize any interference from  $\text{Na}^+$ , which has an ionic diameter similar to  $\text{Li}^+$  as well as having the same positive charge, being in the same periodical group of elements. The concentration of  $\text{Na}^+$  in normal blood (extracellular) is about 140 mM and the concentration of  $\text{Li}^+$ , which comes from the medicine, is at the millimolar level.<sup>1,2</sup> Thus, an ion selectivity ( $\text{Li}^+/\text{Na}^+$ ) of over 10 000 is needed for the selective  $\text{Li}^+$  determination at the millimolar level.<sup>2</sup>

Unfortunately, any electrodes developed to date have never been able to maintain this required selectivity. Some electrodes have been reported to have a  $\text{Li}^+/\text{Na}^+$  selectivity of over  $100^{2-9}$  (over 1000;<sup>7,9</sup> for a review, see ref 10). Therefore, the aim of this research was to develop an optical  $\text{Li}^+$  sensor ( $\text{Li}^+$ -selective optode) which is capable of determining low levels of  $\text{Li}^+$  in the serum of manic depressive patients, which has never been realized using ion-selective electrodes.

In our recent research, a high-performance  $\text{K}^+$  optical sensor was successfully developed using a highly selective neutral ionophore and a highly sensitive color-changeable anionic dye, in which the response mechanism is simply expressed by eq I based on the ion-pair formation reaction,<sup>11</sup> where S is a



neutral ionophore,  $\text{i}^+$  is the ion to be sensed, AH is a lipophilic anionic dye, and SiA is a produced association (ion-pair) species. Based on this equation, these types of optodes can be created not only for  $\text{K}^+$  but also for other specific sensors by replacing the ion-selective ionophore.

Here we report the first  $\text{Li}^+$ -selective optode in which a similar response mechanism is represented by eq I. This optical  $\text{Li}^+$  sensor can determine  $\text{Li}^+$  by basically measuring

the change in absorbance (516 nm) of the newly synthesized color-changeable anionic dye of the diphenylamine type (LAD-3; see Figure 1). As the  $\text{Li}^+$  ionophore, we designed and synthesized a 14-crown-4 derivative (PTM14C4; see Figure 1) having a bulky pinane and subunits at the ethano bridge of the crown ring, which prevents the formation of a 2:1 sandwich-type complex with large cations which do not fit the cavity size of the 14-crown-4. Consequently, a sensor having a high  $\text{Li}^+$  selectivity of over 10 000 could be achieved against all alkali metal and alkaline earth metal cations except  $\text{Li}^+$ . In addition, a flow-through-type optode was designed to realize practical continuous measurements of many aqueous samples with easy operation. The  $\text{Li}^+$  optode was prepared by packing pellicular-type ODS beads (30–40  $\mu\text{m}$ ) coated with a newly synthesized lipophilic organic liquid (TFPDE; see Figure 1) incorporating the ionophore (PTM14C4) and the dye (LAD-3) in a flow-through optical cell (volume 7  $\mu\text{L}$ ) having a quartz window attached directly to the tip of a bifurcated optical fiber (see Figure 2), so that the fast color change due to the  $\text{Li}^+$  concentration in the sample can be achieved. In this case, incident light of 516 nm was introduced through one of the bifurcated optical fibers and the resulting diffuse reflection light accompanying the absorbance change of the sensing beads was measured. This detection light mode was also effective for fast-response measurements.

Furthermore, the general response of these types of optodes was theoretically expressed with a formula, and the results were applied to the composition of the ion-sensing components to attain higher  $\text{Li}^+$  sensitivity. As a result, a flow-through-type, highly  $\text{Li}^+$  selective optode was developed and could be successfully applied to measure  $\text{Li}^+$ -spiked serum samples adjusted to the therapeutic concentration range found in manic depressive patients.

## THEORETICAL SECTION

**Sensor Response.** The response of the developed optical ion sensor based on the  $\text{Li}^+$ -selective neutral ionophore and the lipophilic anionic dye (LAD-3) can be represented by expanding the ion-pair extraction system previously reported as an optical  $\text{K}^+$  sensor using valinomycin and a lipophilic anionic dye, LAD,<sup>11</sup> which has a structure similar to that of LAD-3. The following equations can be adapted by any sensor systems based on a neutral ionophore and an anionic dye represented as eq I. For the case when an ion in aqueous solution forms a  $p:m$ - (ion:ionophore-) type complex with a neutral ionophore, the sensor response can be generally expressed as eq II and demonstrated as shown in Figure 3

$$p\text{i}^{z+} + m\text{S}_o + n\text{AH}_o = \text{S}_{m,p}\text{i}_p\text{A}_{n,o} + zp\text{H}^+ \quad (\text{II})$$

based on the ion-pair extraction reaction. Subscript o represents the organic phase, i is a cation to be sensed, S is a neutral ionophore, and AH is a lipophilic anionic dye of the protonated form. The measured chemical species on the optical ion sensor is the absorbance of  $\text{S}_{m,p}\text{i}_p\text{A}_{n,o}$  in eq II. Using activities of chemical species in relation to the formation of this species ( $a_{\text{S}_{m,p}\text{i}_p\text{A}_{n,o}}$ ), equilibrium constants can be represented as eqs 1–6, where  $a_i$ ,  $a_{\text{S}_o}$ ,  $a_{\text{AH}_o}$ , and  $a_{\text{H}^+}$  are activities of i, S, o,

(1) Amdisen, A. D. *Handbook of Lithium Therapy*; MTP Press: Lancaster, U.K., 1986.

(2) Metzger, E.; Ammann, D.; Asper, D.; Simon, W. *Anal. Chem.* 1986, 58, 132.

(3) Kimura, K.; Oishi, O.; Murata, T.; Shono, T. *Anal. Chem.* 1987, 59, 2331.

(4) Tohda, T.; Sasakura, H.; Suzuki, K.; Shirai, T. *Proc. 54th Chem. Soc. Jpn. Annu. Meet.* Tokyo, Japan, 1987; p473.

(5) Attiyat, A. S.; Christian, G. D.; Xie, R. Y.; Wen, X.; Bartsch, R. A. *Anal. Chem.* 1988, 60, 2561.

(6) Suzuki, K.; Hayashi, K.; Tohda, K.; Watanabe, K.; Ouchi, M.; Hakushi, T.; Inoue, Y. *Anal. Lett.* 1991, 24, 1085.

(7) Sugihara, H.; Okada, T.; Hiratani, K. *Chem. Lett.* 1987, 2391.

(8) Katakay, R.; Nicholson, P. E.; Parker, D.; Covington, A. *Analyst* 1991, 116, 135.

(9) Kobiro, K.; Tobe, Y.; Watanabe, K.; Yamada, H.; Suzuki, K. *Anal. Lett.*, in press.

(10) Umezawa, Y. *Handbook of Ion-Selective Electrodes: Selectivity Coefficients*; CRC Press: Boca Raton, FL, 1990.

(11) Suzuki, K.; Ohzora, H.; Tohda, K.; Miyazaki, K.; Watanabe, K.; Inoue, H.; Shirai, T. *Anal. Chim. Acta* 1990, 237, 155.



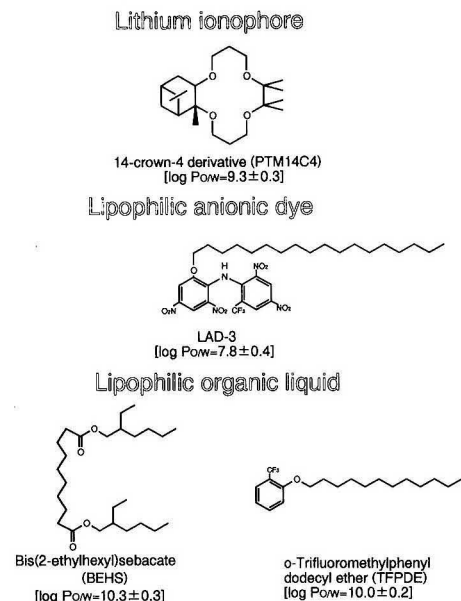


**Figure 1.** Chemical structures and lipophilicity values of the neutral lithium ionophore, lipophilic anionic dye, and lipophilic organic liquids used as the ion-sensing components for the  $\text{Li}^+$  optode.

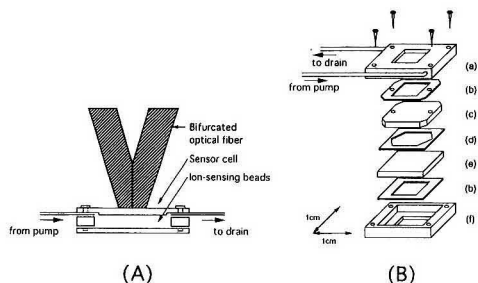


**Figure 2.** Schematic views of the flow-through-type optical sensor probe (A) and the optical sensor cell assembly (B): a, upper stainless steel cell body; b, silicon rubber packing; c, quartz glass window; d, Teflon spacer (0.05-mm thick); e, mirror with a hydrophobic surface; f, lower stainless steel cell body.

$$k_S = a_{S_o} / a_S \quad (1)$$

$$k_{AH} = a_{AH_o} / a_{AH} \quad (2)$$

$$k_{S_{mip}A_n} = a_{S_{mip}A_{n,o}} / a_{S_{mip}A_n} \quad (3)$$

$$\beta_{Si} = a_{S_{mip}^{zp+}} / a_S^m a_{i^{z+}}^p \quad (4)$$

$$K_a = (a_{A^-} - a_{H^+}) / a_{AH} \quad (5)$$

$$K_{ab} = a_{S_{mip}A_n} / a_{S_{mip}^{zp+}} a_{A^-}^n \quad (6)$$

$\text{AH}_o$ , and  $\text{H}^+$ , respectively,  $\beta_{Si}$  is the stability constant of  $\text{S}_{mip}^{zp+}$ ,  $K_{ab}$  is the association constant of  $\text{S}_{mip}^{zp+}$  and  $\text{A}^-$ ,  $K_a$  is the dissociation constant of the anionic dye,  $\text{AH}$ , and  $k_S$ ,  $k_{AH}$ , and  $k_{S_{mip}A_n}$  are the partition constants of  $\text{S}$ ,  $\text{AH}$ , and

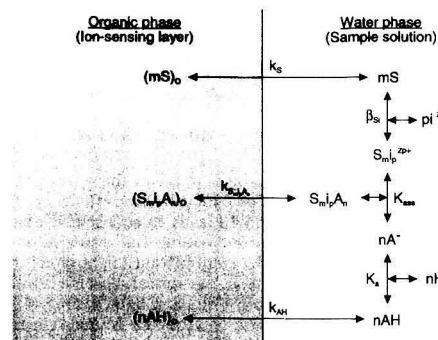


**Figure 3.** Ion extraction system for explaining the optical cation sensor response:  $\text{S}$ , neutral ionophore;  $\text{AH}$ , anionic dye of the protonated form;  $i^{z+}$ , ion to be sensed ( $z$ , charge number). The subscript  $o$  represents the organic phase. For factors and coefficients, see Results and Discussion.

$\text{S}_{mip}A_n$ , respectively, in the distribution equilibrium between the organic phase (lipophilic sensing phase) and the aqueous phase (sample solution). Hence, the activity of the species contributing to the absorbance change,  $a_{S_{mip}A_{n,o}}$ , can be expressed as eq 7 using eq 1–6. This equation is further

$$a_{S_{mip}A_{n,o}} = \frac{k_{S_{mip}A_n} K_{ab} \beta_{Si} K_a^n a_{i^{z+}}^p a_{S_o}^m a_{AH_o}^n}{k_S^m k_{AH}^n a_{H^+}^n} \quad (7)$$

modified as eq 12 with eq 7 representing the summarized constant,  $K$ , and eqs 9–11 relating the mass and charge balances of the chemical species.

$$K = \frac{k_{S_{mip}A_n} K_{ab} \beta_{Si} K_a^n}{k_S^m k_{AH}^n} \quad (8)$$

$$a_s^{\text{tot}} = a_{S_o} + m a_{S_{mip}A_{n,o}} = q_s C_s^{\text{tot}} \quad (9)$$

$$(a_{S_o} \gg a_s, a_{S_{mip}A_{n,o}} \gg a_{S_{mip}A_n}) \quad (9)$$

$$a_{AH}^{\text{tot}} = a_{AH_o} + m a_{S_{mip}A_{n,o}} = q_{AH} C_{AH}^{\text{tot}} \quad (10)$$

$$(a_{AH_o} \gg a_{AH}, a_{S_{mip}A_{n,o}} \gg a_{S_{mip}A_n}) \quad (10)$$

$$zp = n \quad (\text{for the electroneutrality}) \quad (11)$$

$$a_{S_{mip}A_{n,o}} = \frac{K a_{i^{z+}}^p (a_s^{\text{tot}} - m a_{S_{mip}A_{n,o}})^m (a_{AH}^{\text{tot}} - n a_{S_{mip}A_{n,o}})^n}{a_{H^+}^n} \quad (12)$$

$K$  represents the ion-pair extraction equilibrium constant,  $a_{AH}^{\text{tot}}$  and  $a_s^{\text{tot}}$  are the total anionic dye and the total neutral ionophore activities,  $C_s^{\text{tot}}$  and  $C_{AH}^{\text{tot}}$  are the total concentrations of the neutral ionophore and of the anionic dye, and  $q_s$  and  $q_{AH}$  are the activity factors of  $\text{S}$  and  $\text{AH}$  in the organic phase. The values of the activity factors are assumed to be nearly constant ( $q_s = q_{AH} \approx 1$ ) and not dependent on the concentrations of  $\text{S}$  and  $\text{AH}$  in the organic phase. The response of the sensor, in which the light was introduced through one branch of the bifurcated optical fiber and the transmittance light was detected through the ion-sensing phase from the other fiber, can be expressed as eq 14, based on the Lambert-Beer equation indicated as eq 13.<sup>11</sup>  $A$  represents the absorbance detected,  $\epsilon$  is the molar absorption coefficient of the dye ( $\text{S}_{mip}A_n$  form), and  $b$  is the effective

$$A = \Phi e b a_{S_{mip}A_n} \quad (13)$$

$$a_{i+j}^p = \frac{a_{H^+}^n A (\Phi e b)^{m+n-1}}{K (\Phi e b a_S^{\text{tot}} - m A)^m (\Phi e b a_{AH}^{\text{tot}} - n A)^n} \quad (14)$$

$$(\Phi e b a_S^{\text{tot}} \geq m A \geq 0, \quad \Phi e b a_{AH}^{\text{tot}} \geq n A \geq 0)$$

light path length of the organic phase as the sensing layer. The factor  $\Phi$  is the detection light collection efficiency. The combination of eqs 12 and 13 leads to eq 14, which is the fundamental equation for expressing the response of the optical sensor based on the transmittance light mode measurement. On the other hand, the optical sensor is based on the measurement of diffuse reflection light; therefore, the sensor response is expressed by Kubelka-Munk's equation (eq 15) instead of the Lambert-Beer equation (eq 13).<sup>13</sup> Thus,

$$f(r) = \frac{(1 - 10^{-A})^2}{2 \times 10^{-A}} = \frac{a_{S_{mip}A_n}}{\Psi} \quad (15)$$

$$a_{i+j}^p = \frac{a_{H^+}^n \Psi f(r)}{K (a_S^{\text{tot}} - m \Psi f(r))^m (a_{AH}^{\text{tot}} - n \Psi f(r))^n} \quad (16)$$

$$(a_S^{\text{tot}} > m \Psi f(r) \geq 0, \quad a_{AH}^{\text{tot}} > n \Psi f(r) \geq 0)$$

the response of the sensor investigated herein (see Figure 2) is represented as eq 16, where  $f(r)$  is the Kubelka-Munk factor measured as the sensor response in the absorbance mode and  $\Psi$  represents the instrument factor with consideration of straying and scattering of the incident light, the thickness of the ion-sensing layer, and the density of the particle packed in the cell. For both types of sensors based on the measurement of transmittance light or diffuse reflection light, the optical response is determined by six important factors: (1) the value of the constants ( $K$ ) relating ion-pair extraction equilibrium of the species of  $S_{mip}A_n$ , (2) the sample solution pH (proton activity  $a_{H^+}$ ), (3) the activity of the total anionic dye ( $a_{AH}^{\text{tot}}$ ), (4) the mixing ratio of the neutral ionophore and the anionic dye ( $a_S^{\text{tot}}/a_{AH}^{\text{tot}}$ ), (5) the stoichiometry (1: $m$ ) of the complex formed with the neutral ionophore,  $S$ , and the cation,  $i$  (in the case, the important species concerning the optical detection is  $S_{mip}A_n$  formed with the cationic complex species,  $S_{mip}^{zp+}$  and anionic dye,  $A$ , where  $S_{mip}A_n$  is electrically neutral in the bulk optode sensing phase and the value of  $n$  is the same as the number of the charge,  $zp^+$ ), and (6) the charge number ( $z$ ) of the ion,  $i$ , to be sensed.

**Sensor Selectivity.** Based on the theoretical response as expressed with eq 16, the ion selectivity coefficient ( $k_{i,j}$ , where  $i$  is the primary ion and  $j$  is the interfering ion) of the optical sensor is basically defined as eq 17, which can be

$$A = A_i + k_{i,j}^{\text{opt}} A_j \quad (17)$$

$$k_{i,j}^{\text{opt}} = a_i'/a_j \quad (= a_i'/a_j) \quad (18)$$

determined graphically in the same manner as the separate solution method SSM for an ion-selective electrode.<sup>14</sup> In this case, if the interfering ion ( $j$ ) has the same charge as that of the primary ion ( $i$ ), their response curves have to be drawn as shown in Figure 4a, and the ion-selectivity coefficient of the optical ion sensor ( $k_{i,j}^{\text{opt}}$ ) can simply be calculated with eq

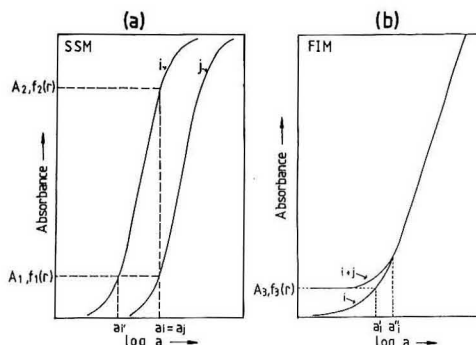


**Figure 4.** Typical relationship between the absorbance [ $A$ , or the Kubelka-Munk factor,  $f(r)$ ] as the sensor response and measured ion activity ( $a_i$  or  $a_j$ ) for understanding the selectivity coefficient,  $k_{i,j}^{\text{opt}}$  ( $i$ , primary ion;  $j$ , interfering ion), determined by (a) the separate solution method (SSM) or (b) the fixed interference method (FIM).

18, where  $A_i$  and  $A_j$  are the measured absorbances for cations  $i$  and  $j$ , respectively, at fixed ion concentrations ( $a_i = a_j$ ).  $A_1$  and  $A_2$  in Figure 4a are the absorbances corresponding to  $f_1(r)$  and  $f_2(r)$  for the optical sensor based on the diffuse reflection light mode measurement, and the corresponding activities,  $a_i (=a_j)$  and  $a_i'$ , are determined by the adjunct method with dashed lines described over the calibration graphs for the responding cations  $i$  and  $j$  in Figure 4a.

In general, when the primary ( $i$ ) and interfering ion ( $j$ ) form 1: $m_1$ - and 1: $m_2$ -type (ion:ionophore) complexes, respectively, where a neutral ionophore and the resulting charge numbers of these complexes are  $n_1$  and  $n_2$ , respectively, eq 18 is further expressed using eq 16 as eq 19a or 19b. This (eq

$$k_{i,j}^{\text{opt}} = \frac{f_1(r)(a_S^{\text{tot}} - m_1 \Psi f_2(r))^{m_1} (a_{AH}^{\text{tot}} - n_1 \Psi f_2(r))^{n_1}}{f_2(r)(a_S^{\text{tot}} - m_1 \Psi f_1(r))^{m_1} (a_{AH}^{\text{tot}} - n_1 \Psi f_1(r))^{n_1}} \quad (19a)$$

$$\left( = \frac{a_{H^+}^{n_1} K_j (a_S^{\text{tot}} - m_2 \Psi f_1(r))^{m_2} (a_{AH}^{\text{tot}} - n_2 \Psi f_1(r))^{n_2}}{a_{H^+}^{n_2} K_i (a_S^{\text{tot}} - m_1 \Psi f_1(r))^{m_1} (a_{AH}^{\text{tot}} - n_1 \Psi f_1(r))^{n_1}} \right) \quad (19b)$$

19a or 19b) is the basic equation calculated from the measured absorbances of the primary ion [ $A_1$  or  $f_1(r)$ ] and interfering ion [ $A_2$  or  $f_2(r)$ ]. When the measured ion concentration was fixed, the selectivity coefficient of the optical ion sensor could be determined using eq 19a or 19b, and the determined value itself is meaningful and comparable. However, there is a problem for the case where the selectivity factors vary with activities of the primary as well as the interfering ion, because they exhibit different response curve shapes. For a more reliable way to determine the selectivity coefficient, we recommend the graphical method shown in Figure 4b, which is similar to the fixed interference method (FIM) for an ion-selective electrode.<sup>14</sup> In this case, the two sensor response curves obtained with an aqueous solution containing only the primary ion ( $i$ ) and with an aqueous solution containing the primary ion as well as the interfering ion ( $i + j$ ), are used to determine the selectivity factor. The latter response curve exhibits a poorer response than the former one in the low-activity range because of the interference from the coexisting interfering ion. In this case, the selectivity coefficients can be determined using eq 20, where  $a_i'$  is an activity which

$$k_{i,j}^{\text{opt}} = a_i'/a_j \quad (20)$$

(12) Laubli, M. W.; Dinten, O.; Pretsch, E.; Simon, W. *Anal. Chem.* 1985, 57, 2756.

(13) Kubelka, P.; Munk, Z. Z. *Techn. Phys.* 1931, 12, 593.

(14) IUPAC Recommendation for Nomenclature of Ion-Selective Electrodes. *Pure Appl. Chem.* 1976, 48, 129.

exhibits the same absorbance [ $A_3$  or  $f_3(r)$  in Figure 4b] in the primary ion response ( $i$ ) curve when the coexisting interfering ion ( $j$ ) is fixed and affected by the response for  $i$ . In this case, the effective calibration activity range for the optical ion sensor is also determined, which is over the lowest activity,  $a_i''$  (determination limit; see Figure 4b), in the calibration curve for the primary ion, in which the absorbance obtained with the two response curves are quite identical.

## EXPERIMENTAL SECTION

**Reagents.** Reagents of the highest grade commercially available were used for syntheses of the new compounds and preparation of the aqueous test electrolytes. Distilled, deionized water had resistivity values of more than  $1.5 \times 10^7 \Omega \text{ cm}$  at 25 °C. Pericellular-type ODS bead was purchased from Merck (Perisorb RP-18; 30–40- $\mu\text{m}$  particle size, approximately 1–2- $\mu\text{m}$  porous surface region which was ODS-modified, approximately 14  $\text{m}^2/\text{g}$ , 0.05  $\text{mL/g}$  of pore volume). Bis(2-ethylhexyl) sebacate (BEHS; see Figure 1 for the structure; purchased from Tokyo Chemical Industry Co., Ltd., Tokyo, Japan) and a newly synthesized *o*-(trifluoromethyl)phenyl dodecyl ether (TFPDE) were used as the lipophilic organic liquids. The serum samples were supplied from Ortho Diagnostics Inc., Raritan, NJ.

**Synthesis of 14-Crown-4 Derivative.** The novel  $\text{Li}^+$  ionophore was synthesized according to the following procedures. Pinacol (Tokyo Chemical Industry), 6.15 mmol (0.73 g), and sodium hydride, 18.45 mmol (0.44g), were added in 10 mL of absolute tetrahydrofuran (THF) and stirred at ambient temperature for 30 min. Then 12.30 mmol (1.49 g) of allyl bromide dissolved in 3 mL of THF was further added in the reaction mixture and stirred at 80 °C for 36 h. After the addition of small amounts of methanol to the reaction mixture, the THF was evaporated. The resulting residue was extracted three times with ethyl acetate. After the organic phase was dried with  $\text{Na}_2\text{SO}_4$  and evaporation, the obtained residue was purified by silica gel column chromatography with hexane-ethyl acetate (4:1) as the eluent to yield 4,7-dioxo-5,5,6,6-tetramethyl-1,9-decane (0.57 g, 46.7%). This product, 2.88 mmol (0.57 g),  $\text{NaBH}_4$ , 2.59 mmol (0.10 g), and boron trifluoride ethyl ether complex, 3.44 mmol (0.49 g), were added to 3 mL of THF and stirred at ambient temperature for 2 h. After the addition of small amounts of deionized water, 2.1 mmol (0.08 g) of NaOH and 30%  $\text{H}_2\text{O}_2$  aqueous solution (0.90 mL) were added to the reaction mixture and the resultant mixture was stirred for 2 h. The product, 4,7-dioxo-5,5,6,6-tetramethyldecane-1,10-diol (compound **a**), was extracted from the reaction mixture with ethyl acetate and purified by silica gel column chromatography with hexane-ethyl acetate (1:1) as the eluent (yield: 0.28 g, 41.5%). 4,7-Dioxo-5,5,6,6-tetramethyldecane-1,10-diol bis(*p*-toluenesulfonate) (compound **b**) was prepared from compound **a** and *p*-toluenesulfonyl chloride in absolute pyridine (yield: 0.5 g, 54.2%). (1*R*,2*R*,3*S*,5*R*)-(-)-Pinnediol (Aldrich Chemical Co., Inc., Milwaukee, WI) (0.92 mmol) and 2.76 mmol of NaH were added to 10 mL of THF and the resultant mixture was refluxed for 30 min. Compound **b** (0.92 mmol) dissolved in 10 mL THF was added to the reaction mixture and the mixture was refluxed for 60 h. After small amounts of methanol were added, the reaction mixture was evaporated to dryness. The obtained residue was extracted with chloroform, and the organic phase was dried with  $\text{Na}_2\text{SO}_4$ . Finally, after evaporation of the organic phase, the primary product, 2,3-([1*R*)-(1*α*,2*α*,3*α*,5*α*)]-2,6,6-trimethylbicyclo-[3.1.1]heptano)-9,9,10,10-tetramethyl-1,4,8,11-tetraoxacyclotetradecane (PTM14C4; see Figure 1) was purified by silica gel column chromatography with hexane-ethyl acetate (20:1) as the eluent (yield: 87.0 mg, 25.6%). This final product was further purified using reversed-phase HPLC (column, ODS; eluent, methanol).

The analytical data for PTM14C4 obtained with  $^1\text{H}$  NMR (270 MHz,  $\text{CDCl}_3$ ), IR (KBr), and elemental analyses were as follows: mp 67.5–68.5 °C;  $^1\text{H}$  NMR,  $\delta$  0.92 (s, 3H,  $\text{CH}_3$ ), 1.12 (s, 3H,  $\text{CH}_3$ ), 1.18 (s, 3H,  $\text{CH}_3$ ), 1.20 (s, 3H,  $\text{CH}_3$ ), 1.22 (s, 3H,  $\text{CH}_3$ ), 1.25 (s, 3H,  $\text{CH}_3$ ), 1.32 (s, 3H,  $\text{CH}_3$ ), 1.52 (d, 1H, CH), 1.60–1.90 (m, 6H,  $\text{CH}_2$ ), 1.98–2.10 (m, 2H,  $\text{CH}_2$ ), 2.26–2.38 (m, 1H, CH), 3.30–4.10 (m, 9H,  $\text{OCH}_2$ ,  $\text{OCH}$ ); IR (KBr), 1107, 2850, 2917  $\text{cm}^{-1}$ .

Anal. Calcd for  $\text{C}_{22}\text{H}_{40}\text{O}_4$  (368.56): C, 71.70; H, 10.94. Found: C, 71.60; H, 10.78.

**Synthesis of a Lipophilic Anionic Dye (LAD-3).** LAD-3 was synthesized according to the following six-step reaction with *o*-nitrophenol as the starting material. *o*-Nitrophenol (3 g) and NaH (1.28 g) were added to 30 mL of absolute *N,N*-dimethylformamide (DMF) and stirred for 1 h at 0 °C. Stearyl bromide, 7.1 g, was added dropwise to this reaction mixture and the resultant mixture was refluxed for 24 h. After the addition of 2 mL of methanol to the reaction mixture and concentration, the product, *o*-nitrophenyloctadecylether (*o*-NPODE), was extracted from the reaction mixture with ethyl acetate and purified by silica gel chromatography with hexane-ethyl acetate (2:1) as the eluent (60% yield).

*o*-NPODE, 3 g, was dissolved in 20 mL of hexane and catalytically reduced to 2-octadecyloxyaniline (ODA) with 400 mg of 10% palladium carbon powder in an autoclave under 30 atm hydrogen atmosphere at ambient temperature for 24 h (100% yield). The following methods for obtaining LAD-3 with ODA were similar to the reported procedures for the synthesis of LAD.<sup>11</sup> The final product, *N*-2,4-dinitro-6-(octadecyloxy)phenyl-2',4'-dinitro-6'-(trifluoromethyl)phenylamine (LAD-3; see Figure 1), was extracted with chloroform and purified by silica gel chromatography with hexane-ethyl acetate (1:6) as the eluent (60% yield).

The analytical data for LAD-3 obtained with  $^1\text{H}$  NMR (270 MHz,  $\text{CDCl}_3$ ), IR (KBr), and elemental analyses were as follows: yellow needles; mp 90.5–92.0 °C;  $^1\text{H}$  NMR,  $\delta$  0.88 (t, 3H,  $\text{CH}_3$ ), 1.2–1.5 (br, 30H,  $\text{CH}_2$ ), 1.84 (m, 2H,  $\text{CH}_2$ ), 4.22 (t, 2H,  $\text{OCH}_2$ ), 7.11 (s, 1H, aromatic), 7.38 (s, 1H, aromatic), 7.58 (s, 1H, NH), 8.22 (s, 1H, aromatic), 9.04 (s, 1H, aromatic); IR (KBr), 1346, 1528, 1552, 1625, 2362, 2852, 2917, 3430  $\text{cm}^{-1}$ . Anal. Calcd for  $\text{C}_{41}\text{H}_{41}\text{N}_6\text{O}_8\text{F}_3$  (685.70): C, 54.46; H, 6.04; N, 10.09. Found: C, 54.30; H, 6.17; N, 10.21.

**Synthesis of *o*-(Trifluoromethyl)phenyl Dodecyl Ether (TFPDE).** Sodium hydride, 178 mg (7.4 mmol), and dodecyl bromide, 1.54 g (6.17 mmol), were added to a solution of 1.0 g (6.17 mmol) of *o*-(trifluoromethyl)phenol (Aldrich) in 15 mL of dimethylformamide and stirred at 70 °C for 3 h. The reaction mixture was evaporated, and the obtained residue was further extracted three times with chloroform. The organic phase was dried with anhydrous sodium sulfate and evaporated. Finally, the product, 1.7 g (5.14 mmol, viscous colorless oil, 83.5%) of TFPDE (see Figure 1), was purified by silica gel chromatography with hexane as the eluent.

The constitution of the synthesized lipophilic organic liquid was confirmed by  $^1\text{H}$  NMR (270 MHz,  $\text{CDCl}_3$ ), IR ( $\text{CHCl}_3$ ), and elemental analysis. For TFPDE:  $\nu_{\text{C-F}}$  1118, 1136,  $\nu_{\text{C-O}}$  1461, 1497, 1591, 1610,  $\nu_{\text{CH}_2}$  2855, 2928  $\text{cm}^{-1}$ ;  $^1\text{H}$  NMR,  $\delta$  0.88 (t, 3H,  $\text{CH}_3$ ), 1.25–1.40 (m, 16H,  $\text{CH}_2$ ), 1.40–1.55 (m, 2H,  $\text{CH}_2$ ), 1.75–1.90 (m, 2H,  $\text{CH}_2$ ), 4.05 (t, 2H,  $\text{OCH}_2$ ), 6.9–7.0 (m, 2H, aromatic), 7.40–7.50 (t, 1H, aromatic), 7.50–7.60 (d, 1H, aromatic). Anal. Calcd for  $\text{C}_{19}\text{H}_{29}\text{OF}_3$  (330.43): C, 69.15; H, 8.98. Found: C, 69.06; H, 8.85.

**Preparation of Lithium Ion Sensing Beads.** The  $\text{Li}^+$ -sensing organic liquid was prepared by dissolving PTM14C4 as the neutral lithium ionophore and LAD-3 in the lipophilic organic liquid of BEHS or TFPDE using a 10-mL glass vessel. The chemical structures of these organic liquid components are shown in Figure 1. The  $\text{Li}^+$ -sensing ODS beads were prepared by mixing pellicular ODS beads with the  $\text{Li}^+$ -sensing liquid having the following compositions in a glass vessel. Five kinds of  $\text{Li}^+$ -sensing beads were prepared: 100 mg of ODS beads, 40 mg of BEHS, 2.8  $\mu\text{mol}$  of PTM14C4, and 5.6  $\mu\text{mol}$  of LAD-3 as composition a; 200 mg of ODS beads, 80 mg of BEHS, 2.80  $\mu\text{mol}$  of PTM14C4, and 5.6  $\mu\text{mol}$  of LAD-3 as composition b; 200 mg of ODS beads, 80 mg of BEHS, 5.60  $\mu\text{mol}$  of PTM14C4, and 5.6  $\mu\text{mol}$  of LAD-3 as composition c; 200 mg of ODS beads, 80 mg of BEHS, 5.6  $\mu\text{mol}$  of PTM14C4, and 2.8  $\mu\text{mol}$  of LAD-3 as composition d; and 200 mg of ODS beads, 80 mg of TFPDE, 5.6  $\mu\text{mol}$  of PTM14C4, and 5.6  $\mu\text{mol}$  of LAD-3 as composition e.

**Structure of the Flow-Through-Type Fiber-Optic Lithium Ion Sensor.** The schematic structure of the fiber-optic  $\text{Li}^+$  sensor probe is shown in Figure 2A. The optical measurement system was almost the same as the optical  $\text{K}^+$  sensor reported previously which was constructed with a light source, the

bifurcated optical fibers, a light detector, and a flow-through cell sensor probe (different from the previous batchwise probe).<sup>11</sup> The diffuse reflection light on the surface of the  $\text{Li}^+$ -sensing beads, which corresponds to the response of the sensor, was measured with a photodiode detector through a monochromator attached to a double-beam spectrophotometer (U-2000; Hitachi Co., Ltd., Tokyo, Japan). The structures of the sensor cell assemblies are shown in Figure 2B. The  $\text{Li}^+$ -sensing beads were placed on the mirror as shown in Figure 2e and packed in a flow-through optical cell (volume  $7 \mu\text{L}$ ) having a quartz window (Figure 2c) attached directly to the tip of a bifurcated optical fiber. The flow-through cell was set in the shield box. A mirror as shown in Figure 2e had a hydrophobic surface modified with triethyloctadecylsilane in order to prevent the beads from flowing out of the cell. The reference flow-through cell had the same structures as that of the sample cell. The same beads but not containing LAD-3 were packed in the reference cell, which was filled with pH-adjusted 0.05 M Tris-HCl buffer solution and attached in the same way as that for the  $\text{Li}^+$  sensor fiber. The light from the same source as that of the  $\text{Li}^+$  sensor fiber was introduced into the reference detector of the double-beam spectrophotometer via a bifurcated fiber. As the light source, a 150-W xenon lamp equipped with a spectrofluorometer (FP-550; Jasco, Tokyo, Japan) was utilized.

For the flow-through system, pH-adjusted 0.05 M Tris-HCl buffer solution was pumped at a flow rate of 1.0 mL/min using a pulse-free liquid delivery pump (Tritorator; Jasco) attached to the flow system. All sample solutions were also prepared with pH-adjusted 0.05 M Tris-HCl buffer solution and introduced from an HPLC injector (Rheodyne, Type 7025) having a 2-mL injection loop. The flowing and sample solution pH were adjusted similarly in the range from 6.0 to 8.0 according to the respective investigation.

**Determination of Lipophilicities for Ion-Sensing Compounds.** The lipophilicities,  $\log P_{o/w}$  (distribution coefficient between organic liquid and water) of the synthesized compounds (a neutral lithium ionophore, a lipophilic anionic dye, and lipophilic organic liquids) were calculated from the  $R_f$  values of reversed-phase thin-layer chromatography (RP-TLC) according to the method reported by Simon et al.<sup>12</sup> The RP-TLC plates (KC18F, Whatman) were  $180 \times 200$  mm and were chromatographically developed with ethanol-water (90:10) as the mobile phase.

## RESULTS AND DISCUSSION

**Sensor Characteristics.** For  $\text{Li}^+$ -selective ionophores, some derivatives of the 14-crown-4 have been reported to have a very high  $\text{Li}^+$  selectivity of over 1000 against  $\text{Na}^+$ ,<sup>7,9</sup> which is a serious interference when the sensor is applied to measure  $\text{Li}^+$  in biological samples such as serum. We recently reported that introduction of a bulky subunit on the ethano bridge of a 14-crown-4 skeleton is very effective to attain high  $\text{Li}^+/\text{Na}^+$  selectivity.<sup>9,16</sup> Among all the 14-crown-4 derivatives, a decalino-14-crown-4 has the highest  $\text{Li}^+$  selectivity against  $\text{Na}^+$  ( $k_{\text{LiNa}}^{\text{pot}} = 2000$ ).<sup>9</sup> Similar excellent  $\text{Li}^+$  selectivity was observed for the pinane-14-crown-4 derivative, which has a pinane subunit on the ethano bridge of the cyclic skeleton.<sup>15</sup> The detection limit was  $1 \times 10^{-5}$  M  $\text{Li}^+$  on the optimal  $\text{Li}^+$  optodes for both these two 14-crown-4 derivatives. However, at least a 5 times lower detection limit ( $2 \times 10^{-6}$  M  $\text{Li}^+$ ) is desired for the accurate determination of  $\text{Li}^+$  (0.2–2 mM  $\text{Li}^+$ ) in the serum sample of manic depressive patients. As shown in Figures 6–8, the  $\text{Li}^+$  optode using a PTM 14-crown-4 as the ion-sensing  $\text{Li}^+$  ligand meets this required sensitivity. This indicates that a PTM14-crown-4 has a high  $K$  value in eq 16, where the ion-ionophore complex stability constant ( $\beta_{\text{Si}}$ ) or ion-ionophore-anionic dye complex ( $\text{SiA}$ ) stability is larger than those with a decalino-14-crown-4 or pinane 14-crown-4 derivative as the  $\text{Li}^+$  ionophore. S. Judging from their structures, the tetramethyl ethano subunit is effective for

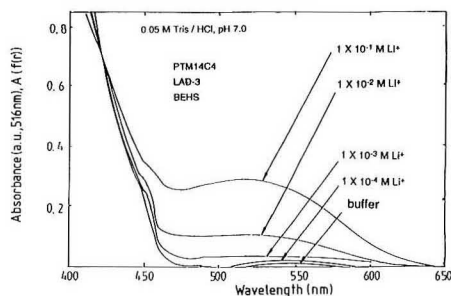


**Figure 5.** Absorption spectra obtained with the flow-through-type  $\text{Li}^+$  optode when different concentrations of  $\text{Li}^+$  ( $\text{LiCl}$ ) were introduced. All samples and flowing solutions contain 0.05 M Tris-HCl, pH 7.

increasing the stability of the  $\text{Li}^+$  complex. As for  $\text{Li}^+$  selectivity, the optical sensor based on the 14-crown-4 derivative (PTM14C4), LAD-3, and BEHS exhibits absolutely no response to all alkali metal and alkaline earth metal cations up to  $10^{-1}$  M except for  $\text{Li}^+$ . Thus, the selectivity coefficients of the sensor are at least less than 1:10 000 ( $\log k_{\text{Li},j}^{\text{pot}} \leq -4$ ;  $j$ , interfering ion).

On the other hand, the highly sensitive color-changeable dye synthesized and used was of the diphenylamine type, which deprotonates at neutral pH [ $pK_a = 6.91$ , in dioxane-0.05 M Tris-HCl (1:1); molar extinction coefficient  $2.13 \times 10^4 \text{ L mol}^{-1} \text{ cm}^{-1}$  at 516 nm]. This anionic dye, LAD-3, has a structure basically similar (see Figure 1) to the LAD dye which was previously reported and used for the optical  $\text{K}^+$  sensor.<sup>11</sup> The newly synthesized dye (LAD-3) has an octadecyl side chain that improves lipophilicity and realized a  $\log P_{o/w}$  value over 10<sup>7</sup>, so that sensor life was improved. The other favorable feature of the anionic dye is that it does not form a precipitating complex with any cations, so that the dye maintains homogeneity in the lipophilic organic liquid on the ODS bead as the ion-sensing component (we have synthesized many anionic dyes and chromoionophores, but most of them often form an insoluble complex with some cations, so that they can hardly be used as the optical sensor component).

Figure 5 shows the typical absorption spectra of the sensing beads based on PTM14C4 and LAD-3. These highly sensitive ion-sensing beads turn from pale yellow to red when they are put in a sample solution containing  $\text{Li}^+$ . As shown in the absorption curves of Figure 5, 480–550 nm is the most effective wavelength range for the sensing beads to detect  $\text{Li}^+$ . The absorbance maximum,  $\epsilon_{\text{max}}$ , of the sensing beads is 516 nm, which is the same as the  $\epsilon_{\text{max}}$  for LAD-3. As we expected, the time for the color change of the sensing beads themselves was very fast (within a few seconds), when the beads are separately dispersed. The base bead (Perisorb RP-18, Merck) is a special type. It is a pellicular-type ODS bead covered a polar material of about 1–2- $\mu\text{m}$  thickness on the surface of a 30–40- $\mu\text{m}$  hard core particle. The sensing organic liquid was thinly coated on the surface of the beads. Thus, a fast response was attained. PVC was often used as the sensing membrane material, which was also used in our former optical sensors.<sup>11,16,19</sup> In general, a PVC sensing membrane is highly lipophilic and the response

(16) Suzuki, K.; Tohda, K.; Tanda, Y.; Ohzora, H.; Nishihama, S.; Inoue, H.; Shirai, T. *Anal. Chem.* **1989**, *61*, 382–384.

(17) Ammann, D. *Ion-Selective Microelectrodes*; Springer-Verlag: New York, 1986; Chapter 7.

(18) Alder, J. F.; Schworath, D. C.; Narayanaswamy, R. E.; Moss, R. E.; Sutherland, I. O. *Analyst* **1987**, *112*, 1191.

(19) Miyazaki, K.; Tohda, K.; Ohzora, H.; Watanabe, K.; Inoue, H.; Suzuki, K. *Bunseki Kagaku* **1990**, *39*, 717.

(15) Yamada, H.; Kobori, K.; Tobe, Y.; Nagatuka, K.; Watanabe, K.; Suzuki, K. Presented at the 64th Annual Meeting for the Chemical Society of Japan, Niigata, Japan, Oct 1992; Abstr. 2C811.

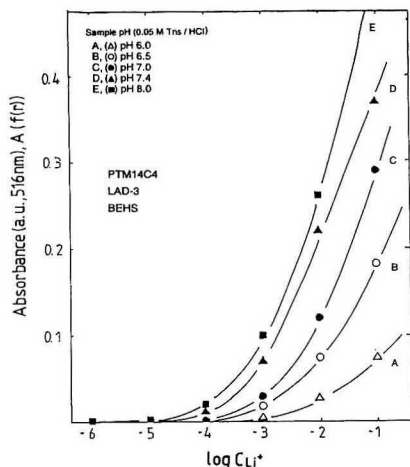


**Figure 6.** Typical response curves for  $\text{Li}^+$  obtained with the flow-through-type  $\text{Li}^+$  optode when the pH of the flowing solution was varied. All samples and flowing solutions contain 0.05 M Tris-HCl.

is not fast. In addition, a PVC membrane is gradually whitened and causes the sensitivity to decrease. The response time, of course, depends on the thickness of the sensing membrane, another negative factor that causes insensitivity, because it depends on the dye concentration and the membrane thickness. For these reasons, PVC was not used as the sensing membrane material.

Typical  $\text{Li}^+$  response curves are shown in Figure 6, where the sample pH was at five different values in the range from pH 6.0 to 8.0. As explained with eq 16, the sensor sensitivity increases with increasing pH of the sample. Though the higher pH is effective for  $\text{Li}^+$  detection sensitivity, a longer return time was needed for the color change for the  $\text{Li}^+$ -free blank buffer solution, which was used after the injection of a high-concentration  $\text{Li}^+$  sample of over  $10^{-2}$  M. Therefore, pH 7.0 or 7.4 is the optimal sample pH condition for the  $\text{Li}^+$  optode. A Tris buffer salt concentration of up to 0.2 M in the sample and flowing solution did not affect the color change of the sensing beads. As explained previously, the sensor sensitivity is expected to be affected by the contents of the  $\text{Li}^+$ -selective ionophore (PTM14C4) and the anionic dye (LAD-3). When the ionophore/dye ratio of 1:1 (0.035/0.035 in mol/L) was used for the sensing components, the sensor response was curve c (this curve is the same as curve C in Figure 6) in Figure 7, where the detection limit is  $1 \times 10^{-4}$  M  $\text{Li}^+$ . As expected from eq 16, varying the ratio of ionophore/dye increases sensitivity, and the resulting response curves b (ionophore/dye ratio of 1:2, 0.035/0.070 in mol/L) in Figure 7 had obviously increased sensor sensitivity. The highest sensitivity was observed in the sensor in the case where the sensing component of ionophore/dye was 0.067/0.134 (1:2; in mol/L) in which the anionic dye (LAD-3) as well as the ionophore contents were almost saturated.

One of other components which affects sensor sensitivity is the species of the lipophilic organic liquid used for dissolving the neutral ionophore and the anionic dye. All sensors used to obtain the response curves in Figures 5-7 utilized bis(2-ethylhexyl) sebacate as the organic liquid which was thinly coated on the ODS beads. The response curves in Figure 8 was obtained with the sensor, where the coating liquid of BEHS having a low polarity ( $\epsilon = 4$ ;  $\epsilon$ , dielectric constant) was replaced with *o*-(trifluoromethyl)phenyl dodecyl ether having

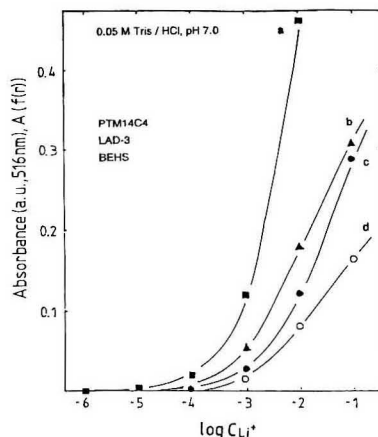


**Figure 7.** Typical response curves for  $\text{Li}^+$  obtained with the flow-through-type  $\text{Li}^+$  optode when the contents of the ion-sensing components (PTM14C4 and LAD-3) were varied. Mixing ratios of the ionophore (PTM14C4)/anionic dye (LAD-3) (in mol/L): a, 0.067/0.134; b, 0.035/0.070; c, 0.035/0.035; d, 0.070/0.035. All samples and flowing solutions contain 0.05 M Tris-HCl, pH 7.

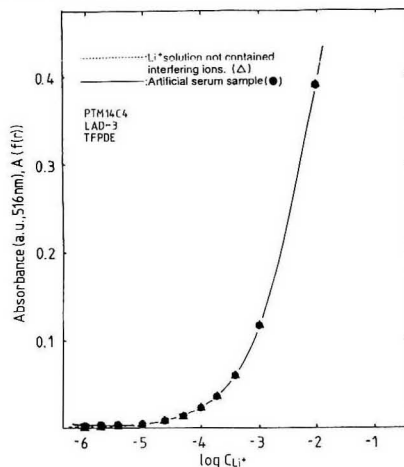


**Figure 8.** Typical response and calibration curves for  $\text{Li}^+$  obtained with the flow-through-type  $\text{Li}^+$  optode based on the  $\text{Li}^+$  ionophore (PTM14C4), anionic dye (LAD-3), and lipophilic organic liquid (TFPDE). Mixing ratio of the ion-sensing components, PTM14C4/LAD-3 (in mol/L), 0.035/0.035. Test samples contain 15 mM  $\text{Na}^+$ , 0.5 mM  $\text{K}^+$ , 0.12 mM  $\text{Ca}^{2+}$ , and 0.08 mM  $\text{Mg}^{2+}$  (1:10 dilution of typical artificial serum samples). All sample and flowing solutions contain 0.05 M Tris-HCl, pH 7.

a higher polarity compared with that of BEHS. The higher polarity liquid is favorable in sensitivity because it brings a large extraction constant ( $K$ ) for the ion-pair complex as the sensing chemical species (see eq 16). The new lipophilic organic liquid, TFPDE, was designed and synthesized on the basis of 2-nitrophenyl octyl ether (NPOE), which was often used as the membrane solvent for ion-selective electrodes of the poly(vinyl chloride) matrix membrane type. The nitro group produces the yellow color. Therefore, the polar group was replaced with a trifluoromethyl group to obtain novel colorless liquid, TFPDE (see Figure 1). In addition, the alkyl



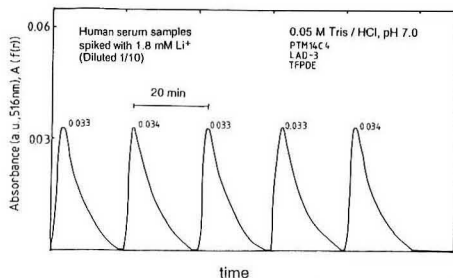


**Figure 9.** Typical response profiles for the human serum samples including  $\text{Li}^+$  obtained with the flow-through-type  $\text{Li}^+$  optode based on the  $\text{Li}^+$  ionophore (PTM14C4), anionic dye (LAD-3), and lipophilic organic liquid (TFPDE). Mixing ratio of the ion-sensing components, PTM14C4/LAD-3 (in mol/L)-0.035/0.035. All sample and flowing solutions contain 0.05 M Tris-HCl, pH 7.

chain of the dodecyl group was attached in the TFPDE molecule so that an optimal lipophilicity of over  $10^{10}$  in  $\log P_{o/w}$  value was attained. An alkyl chain longer than C12 (dodecyl) into this molecule is not favorable because it is no longer liquid at room temperature ( $20^\circ\text{C}$ ). The typical  $\text{Li}^+$  response curve of the sensor based on PTM14C4, LAD-3, and TFPDE as the sensing components is shown as the broken line in Figure 8. Compared with curve c in Figure 7, the sensor sensitivity was increased about 1 order of magnitude, and a lower detection limit ( $1 \times 10^{-6}$  M  $\text{Li}^+$ ) was attained. Because of the limiting solubility of LAD-3, this detection limit is the lowest among all prepared  $\text{Li}^+$  optodes. On the other hand, the  $\text{Li}^+$  selectivity of this sensor is slightly lower than that of the sensor using BEHS. The  $\text{Li}^+$  sensor using TFPDE responded to  $\text{Na}^+$  ( $\log k_{\text{Li}^+}^{\text{Na}^+} = -4.3$  by SSM at  $10^{-1}$  M cation concentration), but did not respond to all other alkali metal and alkaline earth metal cations except  $\text{Li}^+$  and  $\text{Na}^+$ .

**Sensor Application.** To prepare the calibration curve for  $\text{Li}^+$  in the serum of manic depressive patients, the typical serum ion concentration was adjusted and used to prepare the test samples of various  $\text{Li}^+$  concentrations. The typical response curve for the 10-times-diluted artificial serum samples is shown as the solid line in Figure 8. Through the test calibration solutions contained typical background ions of 10-times dilution of the upper level ion concentration for a normal human serum (15 mM  $\text{Na}^+$ , 0.5 mM  $\text{K}^+$ , 0.12 mM  $\text{Ca}^{2+}$ , and 0.08 mM  $\text{Mg}^{2+}$ ),<sup>17</sup> the  $\text{Li}^+$  response curve was in

perfect accordance with the response curve for  $\text{Li}^+$  without any interfering ions down to  $1 \times 10^{-6}$  M (0.01 mM)  $\text{Li}^+$ . Consequently, it was decided that this optical sensor can be used to measure serum samples containing 0.5–1.5 mM  $\text{Li}^+$ , which is the typical concentration range in the serum of manic depressive patients.<sup>1</sup> A typical response profile of the sensor for the 10-times-diluted  $\text{Li}^+$ -spiked human serum samples is shown in Figure 9. Concerning the reproducibility of the  $\text{Li}^+$  sensor, the relative standard deviations for the 10 measurements of the response to the 1:10 dilution serum samples containing  $2 \times 10^{-4}$  and  $1.8 \times 10^{-3}$  M  $\text{Li}^+$  were 1.3% and 1.4%, respectively. About 15 min was required for one determination of the serum sample containing  $1.8 \times 10^{-3}$  M  $\text{Li}^+$  serum samples diluted 1:10 with the Tris buffer solution.

The response time for the flow-through sensor was about 60–100 s, which was considered to be determined by the diffusion of the sample in the flowing solution as well as the packing state of the sensing beads, which depends on how the flowing solution travels through the packed-beads section in the flow-through optical cell. When the beads are separately dispersed, the time for the color change of the sensing beads was very fast (within a few seconds). Therefore, the response time could be improved by modifying the structure of the flow-through cell. The sensitivity of the  $\text{Li}^+$  optode was almost constant for at least 7 days (5–7 h of use per day), but lifetime studies of over 1 week have not been done.

## CONCLUSIONS

The flow-through-type  $\text{Li}^+$ -selective optode based on the ion-pair extraction reaction with the newly synthesized  $\text{Li}^+$ -selective neutral ionophore, PTM14C4, and an anionic dye, LAD-3 (see Figure 3), could detect  $\text{Li}^+$  in concentrations ranging from  $10^{-6}$  to  $10^{-1}$  M  $\text{Li}^+$  at pH 7.0 with 0.05 M Tris-HCl buffer as the flowing solution by measuring the absorbance change at 516 nm. The response characteristics were theoretically explained, and the expected response behavior was applied to prepare the sensitive  $\text{Li}^+$  sensor. This optode has an excellent  $\text{Li}^+$  selectivity of over  $10^4$  against all alkali metal and alkaline earth metal cations and could successfully be used to measure millimolar levels of  $\text{Li}^+$  in  $\text{Li}^+$ -spiked serum samples for manic depressive patients. Though similar cation-selective optodes using the absorbance mode of a color-changeable dye have been reported<sup>11,18–24</sup> (for recent reviews, see refs 21–24), high sensitivity and selectivity were only realized when a highly specific ion-selective ionophore and a highly sensitive dye adduct were successfully obtained.

## ACKNOWLEDGMENT

This work was partially supported by the Saneyoshi Scholarship Foundation and Asahi Glass Foundation, which are gratefully acknowledged.

RECEIVED for review February 2, 1993. Accepted July 1, 1993.

(20) Morf, W. E.; Seiler, K.; Rusterholz, B.; Simon, W. *Anal. Chem.* **1990**, *62*, 738.

(21) Wolfbeis, O. S. *Fiber Optic Chemical Sensors and Biosensors*; CRC Press: Boca Raton, FL, 1991; Vols. I and II.

(22) Janata, J. *Anal. Chem.* **1992**, *64*, 196R.

(23) Janata, J. *Anal. Chem.* **1992**, *64*, 921A.

(24) Arnold, M. A. *Anal. Chem.* **1992**, *64*, 1015A.

**CORRECTION**

**Analysis of Diffusional Broadening of Vesicular  
Packets of Catecholamines Released from Biological  
Cells during Exocytosis**

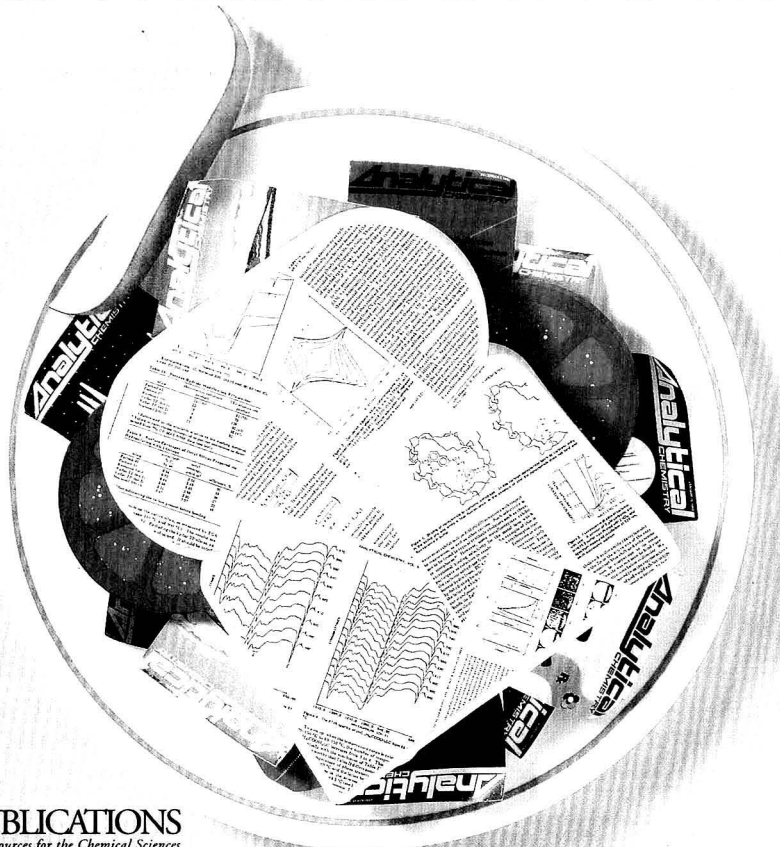
Timothy J. Schroeder, Jeffrey A. Jankowski, Kirk T.  
Kawagoe, R. Mark Wightman,\* Christine Lefrou, and  
Christian Amatore (*Anal. Chem.* **1992**, *64*, 3077–3083).

We have discovered an error in eq 3, which should read  
 $\log[(4\pi^{5/2}r^3/N_{\text{ves}})C_m] = 1.03 - 2.17 \log[l/r] - 1.06\{\log[l/r]\}^2$ .

## AUTHOR INDEX

- Amankwa, L. N., 2693  
 Amatore, C., 2711  
 Amster, I. J., 2608
- Bagnati, R., 2679  
 Belli, S. L., 2583  
 Berger, T. A., 2686  
 Berndt, H., 2590  
 Blumberg, L. M., 2686  
 Bright, F. V., 2671  
 Buttler, T. A., 2628
- Carnahan, J. W., 2596  
 Castoro, J. A., 2621  
 Chai, Y.-Q., 2572  
 Chen, E. T., 2563  
 Chen, Q., 2698  
 Chien, B. M., 2614  
 Collinson, M. M., 2576  
 Corley, J., 2601  
 Cornett, D. S., 2608
- Davoli, E., 2679  
 Duncan, M. A., 2608
- Ebersole, R. C., 2553  
 Effenhauser, C. S., 2637
- Fanelli, R., 2679  
 Foss, R. P., 2553  
 Frutos, M., 2643
- Gao, D., 2572  
 Gorton, L. G. O., 2628
- Harmon, B. J., 2655  
 Hisamoto, H., 2704
- Hurtubise, R. J., 2601
- Itoh, K., 2650
- Jankowski, J. A., 2711  
 Jiménez, M. I., 2643  
 Jinno, K., 2650  
 Johansson, K. A. J., 2628
- Kawagoe, K. T., 2711  
 Kuhr, W. G., 2693
- Lefrou, C., 2711  
 Li, J.-Z., 2572  
 Liu, D., 2572  
 Lubman, D. M., 2614  
 Luo, S.-K., 2590
- Manz, A., 2637  
 Marko-Varga, G. A., 2628  
 Martínez-Castro, I., 2643  
 Mason, P. B., 2596  
 McLean, M. A., 2676  
 Michael, S. M., 2614  
 Mo, Z., 2568  
 Moore, L. K., 2663
- Nagashima, H., 2650  
 Nakagawa, E., 2704  
 Narang, U., 2671  
 Nie, L., 2568
- Ohta, H., 2650
- Palmisano, F., 2690  
 Pardue, H. L., 2563  
 Patterson, D. H., 2655  
 Posta, J., 2590  
 Prasad, P. N., 2671
- Regnier, F. E., 2655
- Sanz, J., 2643  
 Schaldach, G., 2590  
 Schroeder, T. J., 2711  
 Sligar, S. G., 2676  
 Stayton, P. S., 2676  
 Suzuki, K., 2704  
 Synovec, R. E., 2663
- To, D., 2701
- Uemura, T., 2650
- Wang, J., 2553, 2698  
 Wang, R., 2671  
 Ward, M. D., 2553  
 Watanabe, K., 2704  
 Wei, W., 2568  
 Widmer, H. M., 2637  
 Wightman, R. M., 2576, 2711  
 Wilkins, C. L., 2621  
 Winans, R. E., 2596
- Yamada, H., 2704  
 Yao, S., 2568  
 Yu, R.-Q., 2572  
 Yuan, R., 2572
- Zambonin, P. G., 2690  
 Zhang, L., 2596  
 Zhu, W., 2568  
 Zirino, A., 2583

# POWER LUNCH



ACS  PUBLICATIONS  
Essential Resources for the Chemical Sciences

Fortify your analytical know-how with front-line research, new instrumentation methods, and emerging trends in the field.

*Analytical Chemistry* delivers the latest in measurement science — from its use in biotechnology and environmental science to materials science and clinical chemistry. More than food for thought, *Analytical Chemistry* brings innovative applications and how-to solutions you can adapt immediately and effectively to your own work. Take *Analytical Chemistry* to lunch! Call 1-800-333-9511 for subscription information. *Analytical Chemistry* is edited by Royce W. Murray, University of North Carolina, Chapel Hill.

*Analytical Chemistry* — The most powerful analytical tool you'll read.



# *Simultaneously Determine Carbon and Sulfur in Organic Materials With The New SC Series Analyzers From LECO®*

The LECO® SC Series of carbon and sulfur analyzers includes: the SC-444 Carbon and Sulfur Analyzer for simultaneous carbon and sulfur analysis of materials such as catalysts and soils; the SC-432DR Sulfur Analyzer which features a wide dynamic concentration range for low sulfur materials such as coke and oil, and high sulfur materials such as rubber; the SC-432 Sulfur Analyzer for mid-range sulfur materials such as coal; and the CR-412 Carbon Analyzer for the analysis of carbon in materials such as iron oxides, catalysts and soil.

Each of these systems provides the most advanced technology for meeting today's organic analysis requirements. Operation is made easy with the incorporation of icon-driven software, an efficient high-temperature combustion system with operating temperatures to 1500°C, and sensitive measurement through infrared absorption detection. By incorporating the optional autoloader, as many as 36 preweighed samples will be loaded and analyzed automatically, freeing the operator for extended time periods.

The LECO® SC Series is ideal for the analysis of carbon and/or sulfur in a wide variety of organic materials and brings the laboratory the speed and precision required to meet today's and tomorrow's needs. Call or write today to find out more about how the LECO® SC Series of carbon and sulfur analyzers can work for you.



ISO-9002  
No. FM 24045

BSI (British Standards Institute)



**LECO® Corporation 3000 Lakeview Avenue  
St. Joseph, MI 49085-2396 U.S.A.  
Phone: (616) 983-5531 Facsimile: (616) 983-3850**

CIRCLE 52 ON READER SERVICE CARD

27 C.D. 2536